Functional characterization of AMPA and kainate receptor gating properties

Patricia M.G.E. Brown

INTEGRATED PROGRAM IN NEUROSCIENCE

McGill University

Montreéal, Québec

October 2016

A thesis submitted to McGill University in partial fulfillment of the requirements of the degree of

DOCTOR OF PHILOSOPHY

To all my humans.

The difference between perseverance and obstinacy is that one comes from a strong will, and the other from a strong won't.

Henry Ward Beecher

ABSTRACT

Ionotropic glutamate receptors (iGluRs) mediate the majority of fast excitatory neurotransmission in the mammalian central nervous system (CNS). While AMPA-type (AMPARs) and NMDA-type iGluRs are critical for synaptic plasticity throughout the CNS, kainate-type (KARs) iGluRs modulate neuronal circuits. Despite sharing many structural features, AMPARs and KARs respond differently to the neurotransmitter, L-glutamate. In the CNS, AMPARs and KARs exist as heteromeric tetramers, associated with auxiliary proteins. Both these elements influence the activation and deactivation properties of the channels. As such, it is becoming clear that more information is needed to understand the roles of native synaptic iGluRs.

Using outside-out patch electrophysiology with an ultra-fast solution exchange system, we identified specific functional properties of heteromeric KARs formed of the most widely expressed subunits, GluK2 and GluK5. We found that the gating of GluK2/GluK5 heteromers is independent of external ions, which is in contrast with homomeric GluK2 receptors. Moreover, by coupling the analysis of macroscopic and microscopic current responses, we conclude that each subunit type within the tetramer has independent gating contributions.

Polyamine block is a common feature of many cation-selective ion channels, including AMPARs and KARs. Here, we show that KAR subunit heteromerization, and their association with auxiliary proteins, attenuate channel block by facilitating polyamine permeation. By combining electrophysiological data with Molecular Dynamics simulations, we demonstrate that relief of block in GluK2/GluK5 heteromers is due to a proline residue in GluK5, located in the

pore-lining region. *In silico*, this residue increases the pore flexibility and facilitates polyamine permeation.

We also found that the auxiliary proteins of AMPARs relieve polyamine block through enhanced polyamine permeation. At positive membrane potentials, this hinders Na^+ permeation, causing a decrease in the overall conductance. Our data identify an unappreciated role of polyamine permeation in shaping the signalling properties of cation-selective ion channels.

Three conclusions can be drawn from my results. First, the activation of heteromeric KARs does not rely on external ions and each subunit type can gate independently. Second, relief of polyamine block by KAR heteromerization and channel association with auxiliary proteins occurs through an increase in polyamine permeation. Finally, auxiliary proteins of AMPARs produce a similar increase in polyamine permeation, such that they interfere with Na^+ permeation at positive membrane potentials. The flux of polyamines through AMPARs may represent a yet unidentified mechanism of regulating intracellular polyamine levels in an activity-dependent manner. Taken together, these results improve our understanding of the functioning of native AMPARs and KARs, an essential step in the design of therapeutic approaches targeting these receptors.

ABRÉGÉ

Les récepteurs ionotropes glutamatergiques (iGluRs) sont responsables pour la majorité de la neurotransmission excitatrice dans le système nerveux central (SNC). Les iGluRs de type AMPA et NMDA sont essentiels à la plasticité synaptique, tandis que les récepteurs de type kainate (KARs) modulent les circuits neuronaux. Cependant, malgré plusieurs similarités structurelles, les AMPARs et les KARs répondent différemment au neurotransmetteur L-glutamate. Dans le SNC, les AMPARs et les KARs existent en tant qu'hétéromères tétramériques et sont associés à des protéines auxiliaires. Ces deux éléments influencent les propriétés d'activation et de désactivation des canaux. Par conséquent, il devient de plus en plus clair que de plus amples informations seront nécessaires à notre compréhension des rôles des iGluRs synaptiques.

À l'aide d'une approche électrophysiologique de type "outside-out patch" avec un système d'échange de solutions ultra-rapide, nous avons identifié des propriétés fonctionelles spécifiques aux KARs hétéromériques formés par les sous-unités les plus répandues, GluK2 et GluK5. Nous avons trouvé que l'activation de ces hétéromères est indépendante des ions externes, contrairement aux récepteurs homomériques GluK2. De plus, en combinant l'analyse des courants macroscopiques et microscopiques, nous concluons que chaque sous-unité du tétramère hétéromérique contribue indépendamment à l'activation du récepteur.

Le bloquage par les polyamines est une caractéristique commune aux canaux cationiques, tels les AMPARs et les KARs. Nous démontrons ici que l'hétéromérisation des sous-unités des KARs, ainsi que leur association aux protéines auxiliaires, atténuent ce bloquage en facilitant la pénétration des

polyamines. En combinant des données électrophysiologiques à des simulations de dynamique moléculaire, nous démontrons que le soulagement du bloquage chez les hétéromères GluK2/GluK5 peut être attribuée à une proline dans la sous-unité GluK5, située dans la région du pore. *In silico*, cet acide aminé augmente la flexibilité du pore, ce qui pourrait expliquer la pénétration accrue des polyamines.

Nous avons également découvert que les protéines auxiliaires des AMPARs soulagent le bloquage par les polyamines en facilitant leur pénétration. À des potentiels membranaires positifs, ceci gêne la pénétration du Na^+ et diminue la conductance. Nos données identifient un rôle sous-estimé de la pénétration des polyamines dans le fonctionnement des canaux cationiques.

Trois conclusions peuvent être tirées de mes résultats. Premièrement, l'activation des KARs hétéromères ne dépend pas des ions externes et chaque sous-unité agit indépendamment. Deuxièmement, le soulagement du bloquage polyamine-dépendant par l'hétéromérisation et l'association des canaux aux protéines auxiliaires provient d'une augmentation de la pénétration des polyamines. Finalement, les protéines auxiliaires des AMPARs augmentent la pénétration des polyamines, à un point tel qu'elles interfèrent avec le Na^+ à des potentiels membranaires positifs. Le flux des polyamines à travers les AMPARs pourraient représenter un mécanisme non-identifié jusqu'à maintenant, régulant le niveau de polyamines dans la cellule de façon activité-dépendante. Globalement, ces résultats enrichissent notre compréhension du fonctionnement des AMPARs et des KARs natifs, une étape essentielle à la conception d'approches thérapeutiques ciblant ces récepteurs.

TABLE OF CONTENTS

LIST OF TABLES

LIST OF FIGURES

LIST OF ABBREVIATIONS

η^2	estimated effect size
H_p	holding potential
K_d	dissociation constant
k_{off}	unbinding rate
k_{on}	binding rate
k_{perm}	permeation rate
V_{rev}	reversal potential
χ^2	chi-squared, goodness of fit
γDGG	γ-glutamylglycine
AMPA	α-amino-3-hydroxy-5-methyl-4-isoxazolepropionic acid
AMPAR	AMPA receptor
Arg	arginine
Asp	aspartate
ATD	amino-terminal domain
CNIH	cornichon homolog
CNQX	6-cyano-7-nitroquinoxaline-2,3-dione
CNS	central nervous system
Con-A	concanavalin-A
CTD	carboxy-terminal domain
CTZ	cyclothiazide
CUB	complement C1r/C1s, Uegf, Bmp1
Cys	cysteine

DαAA	D-α-aminoadipate
DH	dysiherbaine
DNQX	6,7-dinitroquinoxaline-2,3-dione
eGFP	enhanced green fluorescent protein
EM	electron microscopy
EPSC	excitatory post-synaptic current
ER	endoplamic reticulum
GDEE	glutamic acid diethyl ester
GK	guanylate kinase
Gln	glutamine
Glu	glutamate
Gly	glycine
GRIP	Glutamate receptor-interacting protein
HA	Human influenza hemagglutinin
iGluR	ionotropic glutamate receptor
KAR	kainate receptor
LBD	ligand-binding domain
LDLa	low-density lipoprotein receptor domain A
LTD	long-term depression
LTP	long-term potentiation
Lys	lysine
MD	molecular dynamics
MEM	minimal essential medium
Met	methionine
NBQX	2,3-dihydroxy-6-nitro-7-sulfamoyl-benzo[f]quinoxaline-2,3-dione
Neto1	neuropilin and tolloid-like 1

Neto2	neuropilin and tolloid-like 2
NMDA	*N*-methyl-D-aspartate
NMDAR	NMDA receptor
NSFA	non-stationary fluctuation analysis
PDB	protein data bank
PDZ	post synaptic density protein (PSD-95), Drosophila disc large tumor suppressor (Dlg1), and zonula occludens-1 protein (zo-1)
PhTX	philanthotoxin-343
PKA	protein kinase A
PKC	protein kinase C
POPC	1-palmitoyl-2-oleoyl-(*sn*)-glycero-3-phosphocholine
Put	putrescine
RMSD	root mean square deviation
SAP	synapse-associated protein
SH3	SRC Homology 3
SMD	steered molecular dynamics
Spd	spermidine
Spm	spermine
SUMO	small ubiquitin-like modifier
TARP	transmembrane AMPAR regulatory protein
TMD	transmembrane domain
WT	wild type

ACKNOWLEDGEMENTS

Surprisingly, this is one of the hardest parts to write, because you know everyone will read it and you want it to be perfect. However, as I learned while writing this thesis, perfection is subjective and probably unattainable. I will still try. After all, it is Thanksgiving...

This thesis, this PhD, this unique experience could not have happened without the many people that I have gotten to know along the way. During my time in the lab, the daily interactions with all of you were crucial in defining the person who I have become today. Therefore, I am grateful to everyone who has helped me grow (or reach things on the top shelf) in the past few years.

I thank Dr. Derek Bowie for believing in me and for convincing me to join his lab for graduate studies. The Bowie lab was a great environment for me to evolve as a person and as a scientist, something that was made possible by Derek and every individual who came through. In this lab, I learned that to be passionate and self-motivated can take you a long way.

I also thank the members of my committee, Dr. Ellis Cooper and Dr. David Stellwagen, who followed my progress and encouraged me over the years. During my committee meetings, I did not feel judged, but rather helped by their experience and wisdom.

I am very grateful to Anne-Marie Fay for teaching me electrophysiology when I first joined as an undergraduate student. A huge thank you to Dave MacLean, with whom many conversations, drinks, memories and laughs were shared (for example, "there was a fireball in the culture hood... but I have to go home now. Bye!"). I

will always look up to you as a mentor and as a friend. I'm very proud of you and I'm very proud to know you. I thank Ingrid Oswald, Adrian Wong and Alba Galan for completing this little first-generation Bowie lab family.

Thanks to Mark Aurousseau for all the help with molecular biology, many scientific (and non-scientific) discussions, and friendship. We hung in there and we made it until the end. Booya! It's too bad our Journal Club didn't get accepted in the Journal of Neuroscience, that would have been cool. I'm glad we tried anyways.

I am also grateful to all the other (past and present) members of the Bowie Lab who overlapped with me for being awesome (in no particular order): Brent, Erik, Ryan, Hugo, Loïs, Marika, Rafael, Bryan, Michael (Vito), Elizabeth, Selin, Joe, Mabel, and all the undergraduate students that came through the lab over the years. I also thank everyone in the student room who isn't a Bowie lab member, Sandra, Felix, Jing and Paola, for also being awesome. And, of course, I apologize if I have forgotten anyone!

Thank you to Dr. Maria Musgaard, Dr. Teresa Paramo and Dr. Philip Biggin (Oxford University) for their overseas help during our collaborations. I am especially grateful to Maria for her patience, fruitful discussions and the many simulations and movies.

I thank my whole family for being patient and encouraging, for believing in me, and for considering graduate studies as "being successful". You are my humans. I am especially grateful to my loving boyfriend and partner in crime, who put up with me very patiently and lovingly for all these years, through good and bad times, during weekly evening and weekend transfections and long work days. Thank you for supporting me in my great ambitions, and for helping me stay strong, calm and logical, especially in the final days of writing this masterpiece.

I would also like to give a huge (but still inadequate) thank you to my best

friend Filip. You helped me learn some new biochemistry and biophysics, and helped me open my "science eyes". Thank you for all the discussions about our projects and manuscripts, for your great company, your patience, your never-failing positive attitude, for all the shared memories and the many daily laughs. Thank you for teaching me German and encouraging me to always do better and to try harder. Thanks for being there for me, and for being my best friend and one of my humans. Dankeschön! Merci!

And last but not least, I thank the reader. For why write a thesis at all, if not for it to be devoured by other science-hungry fellow scientists, or examiners, or future doctoral candidates with related topics? I hope you will enjoy reading this thesis and that you will somehow find something useful within it.

Cheers! Santé! Prost!

AUTHOR CONTRIBUTIONS

This thesis is presented in manuscript-based format, as outlined in the McGill Thesis Guidelines. It is composed of one published article (Chapter 3) and two manuscripts (Chapters 2 and 4), which will be submitted in an altered form. I am the first author of all three manuscripts. A detailed description of the authors' contributions, as required by McGill guidelines, follows below.

In addition to these chapters, I have also included several publications in the appendix of this thesis. Though they were produced during my time in the lab, I contributed to various degrees to each of these articles, and they are not directly related to the main topic of this thesis. My contributions for each of these publications is outlined below. They are not in chronological order, but they are grouped by topic.

Main Thesis Contributions

Chapter 2: "Gating Contributions of GluK2 and GluK5 subunits in heteromeric KARs", is a manuscript that has not yet been submitted. In its present form, the author list is comprised of myself and Dr. Bowie. I performed all the experiments in this work. Both Dr. Bowie and I designed the experiments and interpreted results. I wrote the manuscript in its current form.

Chapter 3: "Kainate receptor pore-forming and auxiliary subunits regulate channel block by a novel mechanism" was published in the Journal of Physiology as:

Brown, P. M. G. E.; Aurousseau, M. R. P.; Musgaard, M.; Biggin, P. C. and Bowie, D. (2016) Kainate receptor pore-forming and auxiliary

subunits regulate channel block by a novel mechanism. *J Physiol.* 594, 1821-1840.

For this work, I performed all electrophysiological experiments and analysed the results. Dr. Aurousseau, Dr. Bowie and I designed the experiments and interpreted results. The MD simulations were designed by Dr. Philip Biggin and Dr. Maria Musgaard, and they were conducted by Dr. Musgaard. The mutations and constructs used in this study were made by Dr. Mark Aurousseau. I drafted the manuscript and Dr. Bowie and I revised it. The manuscript in its current form was approved by all the authors. I responded to reviewers and submitted all final corrections; all authors approved.

Chapter 4: "AMPAR auxiliary proteins relieve channel block by facilitating polyamine permeation" is a manuscript that has not yet been submitted. In its present form, the author list is comprised of myself, Dr. Hugo McGuire and Dr. Bowie. I performed all the electrophysiological experiments in this work. Dr. McGuire wrote programs (in Matlab) to fit the data, according to the two models (one that was previously published in Bahring et al. (1997) and one that was designed by Dr. McGuire and myself) outlined in the manuscript. All authors contributed to designing the experiments and interpreting the results. I wrote the manuscript in its current form.

Additional Contributions

Kainate receptors

Fay, A.-M. L. M.; Corbeil, C. R.; Brown, P.; Moitessier, N. and Bowie, D. (2009) Functional characterization and in silico docking of full and partial GluK2 kainate receptor agonists, *Mol Pharmacol*, 1096-1107.

As an undergraduate student, I performed and analysed the dose-response curves for GluK2 with D- and L-aspartate (Fig. 3 C and D). I helped review the final version of the manuscript.

Demmer, C. S.; Møoller, C.; Brown, P. M. G. E.; Han, L.; Pickering, D. S.; Nielsen, B.; Bowie, D.; Frydenvang, K.; Kastrup, J. S. and Bunch, L. (2015) Binding mode of an alpha-amino acid-linked quinoxaline-2,3-dione analogue at glutamate receptor subtype GluK1. ***ACS chemical neuroscience*****, 6, 845-854.**

For this work, I performed and analysed electrophysiological experiments for the functional characterization of two novel compounds at homomeric GluK1 and GluK2 KARs (Figure 4 and Table 2). I helped review the final version of the manuscript.

$GABA_A$ receptors

Lachance-Touchette, P.*; Brown, P.*; Meloche, C.; Kinirons, P.; Lapointe, L.; Lacasse, H.; Lortie, A.; Carmant, L.; Bedford, F.; Bowie, D. and Cossette, P. (2011) Novel alpha-1 and gamma-2 GABAA receptor subunit mutations in families with idiopathic generalized epilepsy. ***The European journal of neuroscience*****, 34, 237-249.**

I am a co-first author for this manuscript (*). As such, I designed, performed and analysed all the electrophysiological experiments in this article (Figs 5, 6, 7, 8 and 9, and Table 2). Dr. Lachance-Touchette performed the *in silico* analysis of $GABA_A$ receptor mutants, the genetic analysis, the PCR, and surface expression experiments. Dr. Lachance-Touchette, Dr. Cossette, Dr. Bowie and myself all contributed to the design and interpretation of the experiments and results. Dr. Lachance-Touchette and I drafted the manuscript and the four authors listed directly above revised the manuscript. Dr. Lachance-Touchette and I responded to the reviewers.

Accardi, M. V.; Daniels, B. A.; Brown, P. M. G. E.; Fritschy, J.-M.; Tyagarajan, S. K. and Bowie, D. (2014) Mitochondrial reactive oxygen species regulate the strength of inhibitory GABA-mediated synaptic transmission. ***Nature communications*****, 5, 3168.**

For this work, I performed all the electrophysiological experiments on recombinant $GABA_A$ receptors and analysed the data (Figure 6 C). I contributed to the design of these experiments, interpreted the results and helped review the final version of the manuscript.

Penna, A.; Wang, D.-S.; Yu, J.; Lecker, I.; Brown, P. M. G. E.; Bowie, D. and Orser, B. A. Hydrogen peroxide increases GABAA receptor-mediated tonic current in hippocampal neurons. (2014) ***The Journal of neuroscience : the official journal of the Society for Neuroscience*****, 34, 10624-10634.**

I performed preliminary experiments on recombinant $GABA_A$ receptors, which were not included in the final version of the manuscript. I contributed to the discussions and data interpretations, and helped review the final version of the manuscript.

Accardi, M. V.; Brown, P. M. G. E.; Miraucourt, L. S.; Orser, B. A. and Bowie, D. (2015) alpha6-Containing GABAA Receptors Are the Principal Mediators of Inhibitory Synapse Strengthening by Insulin in Cerebellar Granule Cells. ***The Journal of neuroscience : the official journal of the Society for Neuroscience*****, 35, 9676-9688.**

For this work, I performed all the electrophysiological experiments on recombinant $GABA_A$ receptors and analysed the data (Figure 2 A and Table 1). I

contributed to the design of these experiments, interpreted the results and helped review the final version of the manuscript.

PREFACE

The role of the nervous system is to allow an organism to interact with its environment. In mammals, it is an exquisitely complex network containing many types of neurons and glial cells, each playing a specific role in the transmission of information. This information can be transmitted electrically, for example through gap-junctions (Connors and Long, 2004), or more commonly, chemically, through the pre-synaptic release of neurotransmitter molecules that act through receptors to change the post-synaptic membrane potential. In the mammalian central nervous system, L-glutamate is the major excitatory neurotransmitter.

Glutamate-mediated rapid neurotransmission occurs through ionotropic glutamate receptors (iGluRs), which are divided into three families: NMDA, AMPA and kainate receptors (KARs). NMDA and AMPA receptors have been well-characterized as being the main mediators of excitatory transmission and synaptic plasticity, while KARs modulate synaptic transmission and neuronal circuits (Traynelis et al., 2010). Although an increasing number of studies have described the functional properties of recombinant AMPA and kainate receptors, it is becoming more obvious that synaptic receptors have different functional properties than those that are studied in a dish. For example, KAR-mediated synaptic currents tend to have much slower decay kinetics than their recombinant counterparts. How do we explain these differences? This was the main question that motivated me when I started my PhD in Dr. Bowie's lab. At the time, evidence was emerging, suggesting that synaptic KARs existed mainly as heteromeric complexes, and this could, at least in part, account for the differences

in kinetic properties (Barberis et al., 2008; Fernandes et al., 2009). Additionally, auxiliary proteins had been recently identified, interacting with AMPARs and KARs, and modifying their channel properties. A clearer picture of synaptic iGluRs was being painted, but many pieces of this puzzle were still missing.

The overarching aim of my thesis work was to understand how the different components of AMPA and kainate receptors affected their functional properties. Specifically, what are the mechanisms governing the changes in gating incurred by simply heteromerizing with distinct subunits? And how do auxiliary proteins also achieve this? To tackle these questions, I combined functional data with emerging structural information and Molecular Dynamics simulations through international collaborations.

This thesis is divided into **five chapters** and **Appendices**. **Chapter 1** contains background information about the structure and function of AMPARs and KARs, as well as the objectives and rationales. The following **three chapters** describe my experimental results on the functional properties of AMPARs and KARs. Each chapter is presented in manuscript format. The **Chapter 5** is a general discussion of the results and focuses on the gating properties of heteromeric KARs. I also discuss the physiological consequences of heteromerization on ion modulation, as well as the relevance of polyamine permeation. Finally, the **Appendices** contain re-prints and copyright waivers, and also additional articles that are related to my thesis work to various degrees.

CHAPTER 1
INTRODUCTION

1.1 Ionotropic Glutamate Receptors

Ionotropic glutamate receptors (iGluRs) are ligand-gated cation-selective channels that are found at many excitatory synapses in the central nervous system. They are gated by the neurotransmitter, L-glutamate, and play an important role in fast excitatory neurotransmission and in synaptic plasticity mechanisms, processes that are crucial for learning and memory (Traynelis et al., 2010). Based on their pharmacology, kinetic properties and sequence similarities, they are classified into three families, namely the NMDA, AMPA and kainate (KAR) receptors.

Each of these receptor types plays an important role in chemical synaptic neurotransmission. AMPA receptors open and close with sub-millisecond time scales, making them ideal for fast neuronal communication (Traynelis et al., 2010). In contrast, the behaviour of NMDA receptors is different in multiple ways. For example, these channels are blocked by Mg^{2+} ions at resting membrane potentials, and therefore require membrane depolarization in order to conduct current (Nowak et al., 1984; Mayer et al., 1984). For this reason, they are considered to be coincidence detectors of membrane depolarization and L-glutamate release. Additionally, they are highly Ca^{2+} permeable (Mayer and Westbrook, 1987) and have very slow activation and deactivation kinetics (Lester et al., 1990). Together at the same synapses, AMPA and NMDA receptors are the major players in synaptic plasticity (Traynelis et al., 2010). On the other hand, kainate receptors are known as modulators of neuronal excitability (Contractor et al., 2011). Their relative contribution to synaptic currents is small, but their slow deactivation kinetics allow for temporal summation (Contractor et al., 2011). Pre-synaptic KARs also regulate neurotransmitter release (Pinheiro and Mulle, 2008).

As iGluRs play important roles in the central nervous system (CNS), a disruption of their normal functioning can lead to various CNS disorders (Bowie, 2008). For example, several lines of evidence suggest that kainate receptors play a role in temporal lobe epilepsy (Mulle et al., 1998; Smolders et al., 2002; Epsztein et al., 2005). A thorough investigation of the functional properties of iGluRs, as well as the roles they play in neuronal communication, will help us understand how they contribute to these pathologies and promote rational therapeutic design.

1.1.1 Brief overview: the discovery of glutamate receptors

Nowadays, L-glutamate (L-Glu) is taken for granted as mediating the majority of fast excitatory neurotransmission in the mammalian CNS. However, this amino acid, found in high concentrations in the mammalian brain (Berl and Waelsch, 1958), was not always considered a neurotransmitter. L-Glu and many other related D- and L- amino acids were potent excitants of neurons (Curtis and Watkins, 1963). Since L-Glu was found in high concentrations throughout the brain and could depolarize almost all neurons, it could not be responsible for specific neurotransmission (Curtis et al., 1960; Curtis and Watkins, 1963; Watkins and Jane, 2006). Despite these early beliefs, L-Glu and L-Asp were shown to be released in a Ca^{2+} -dependent manner following electrical stimulation or depolarization (Watkins and Jane, 2006). Furthermore, high-affinity amino acid transporters were identified as a transmitter clearance mechanism, and the role of L-Glu as an excitatory neurotransmitter was reconsidered (Watkins, 1972).

The development of pharmacological tools was crucial in the identification and characterization of these excitatory amino acid transmitter receptors (Watkins and Jane, 2006). Two important compounds, *N*-methyl-D-aspartate (NMDA) and kainate, a toxin first isolated from the marine algae *Digenea simplex* by Murakami

and colleagues (1953), helped divide these receptors into "aspartate-preferring" and "glutamate-preferring" (or "NMDA" and "non-NMDA") receptors (Watkins and Jane, 2006; Lodge, 2009). Specifically, two neuronal cell types, spinal interneurons and Renshaw cells, showed differential sensitivities to these compounds (McCulloch et al., 1974). Quisqualic acid, isolated from the plant *Quisqualis indica*, produced similar effects as L-Glu on crayfish neuromuscular junctions (Shinozaki and Shibuya, 1974) and cat spinal neurons (McLennan and Lodge, 1979).

The NMDA receptors were further distinguished from the non-NMDA receptors with additional pharmacological properties, such as their weak preference of the antagonist, D-α-aminoadipate (DαAA) (Davies and Watkins, 1979), and block by Mg^{2+} (Evans et al., 1977). Furthermore, a subgroup of the receptors that were relatively insensitive to DαAA, those that were excited by L-Glu and quisqualate, were inhibited by glutamic acid diethyl ester (GDEE) (Hicks et al., 1978; McLennan and Lodge, 1979). Kainate-responsive receptors differed in their sensitivity to these antagonists, and it was postulated that L-Glu receptors and kainate receptors were different entities (McLennan and Lodge, 1979). The idea of three receptor types was further strengthened with the observation that the D and L forms of γ-glutamylglycine (γDGG) selectively inhibited responses to kainate and NMDA, but not L-Glu or quisqualate, in cat spinal neurons (Davies and Watkins, 1981). It was later discovered that quisqualate was also an agonist at metabotropic glutamate receptors (Sladeczek et al., 1985; Nicoletti et al., 1986), and the quisqualate receptors became the α-amino-3-hydroxy-5-methyl-4-isoxazolepropionic acid (AMPA) receptors, for their high responsiveness to this novel compound (Krogsgaard-Larsen et al., 1980; Lodge, 2009).

Though emerging pharmacological tools were useful in separating and characterizing synaptic iGluRs, the cloning of the channel subunits revealed their molecular identity.

1.1.2 Cloning of the glutamate receptor subunits

The first cloned subunit of the iGluR family was GluR-K1 (now GluA1) (Hollmann et al., 1989). This was done by injecting *Xenopus* oocytes with gradually decreasing sizes of cDNA libraries from the rat forebrain until a very small pool of cDNA resulted in oocytes that reversibly responded to L-Glu, kainate and domoate (Hollmann et al., 1989). Interestingly, this clone was initially believed to belong to the kainate-type family of iGluRs, because it did not respond to quisqualate (Hollmann et al., 1989). In the following years, multiple groups also identified this receptor subunit, each time giving it a new nomenclature (Lodge, 2009) (Figure 1–1). Additional AMPA receptor (AMPAR) subunits were then cloned and characterized, closely followed by the primary KAR and NMDAR subunits (Lodge, 2009). Interesgintly, KA-1 and KA-2 (GluK4 and GluK5, see Figure 1–1), were named this way because of their high affinity kainate binding sites (Werner et al., 1991; Herb et al., 1992). The various nomenclatures for all these iGluR subunits quickly became very confusing, and it was necessary to implement a standardized nomenclature, one which is arguably much more intuitive (Collingridge et al., 2009). Figure 1–1 illustrates the different classes of receptors and their subunits, as they are known today.

1.1.3 AMPARs and KARs in the CNS

The emergence of pharmacological tools, for example the quinoxalinediones, DNQX, CNQX and NBQX, and the 2,3-benzodiazepines, GYKI52466 and GYKI53655, were extremely valuable in separating synaptic contributions of

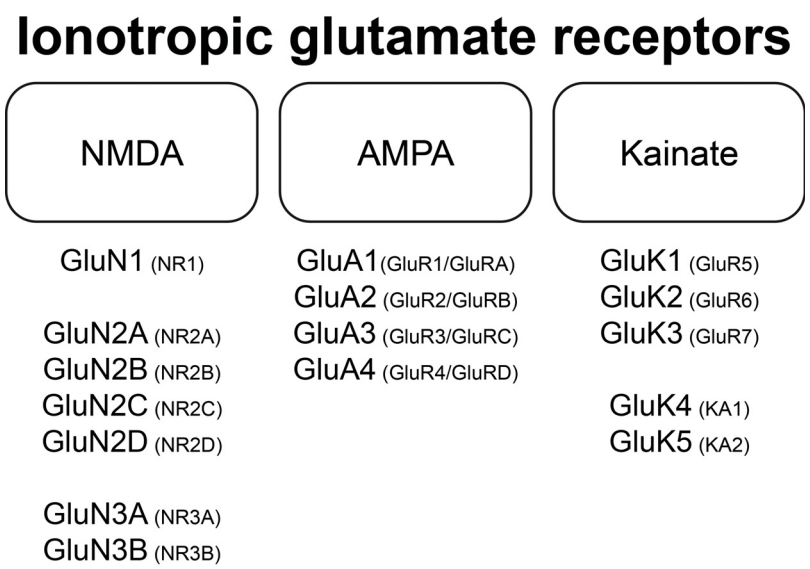

Figure 1–1: Ionotropic Glutamate Receptor Subunits
The current nomenclature of the subunits belonging to the NMDA, AMPA and Kainate-type iGluRs (Collingridge et al., 2009). Previous nomenclature is included in parentheses.

AMPA and kainate receptors (Lerma et al., 1997; Bleakman and Lodge, 1998; Lodge, 2009). For example, the GYKI compounds, AMPAR-selective antagonists, were used to isolate slow KAR-mediated responses in hippocampal CA3 neurons (Castillo et al., 1997; Vignes and Collingridge, 1997). Similarly, GluK1-selective antagonists (e.g. LY293558) and agonists (e.g. ATPA) could confirm the contribution of KARs to synaptic responses (Clarke et al., 1997).

Together with the specific agonists and antagonists, early cloning and *in situ* hybridization studies showed that the expression of AMPARs and KARs in the CNS is widespread and developmentally-regulated (Keinnen et al., 1990; Werner et al., 1991; Herb et al., 1992; Seeburg, 1993; Wisden and Seeburg, 1993; Bahn et al., 1994). A more recent study has used high-resolution quantitative mass spectrometry to characterize the spatio-temporal expression of native AMPAR complexes (Schwenk et al., 2014).

Overall, with the exception of the cerebellum, GluA2 is the most prevalent AMPAR subunit in various rodent brain regions including the cortex, the hippocampus and the striatum (Schwenk et al., 2014). GluA4 has the lowest expression in the brain, but seems to be in high relative abundance in the cerebellum (Schwenk et al., 2014). GluA1 and GluA3 have intermediate expressions throughout the brain (Schwenk et al., 2014), and their relative contribution to synaptic AMPAR currents may also be dynamically-regulated through plasticity mechanisms (Nicoll and Schmitz, 2005; Ehlers et al., 2007; Granger et al., 2013; Granger and Nicoll, 2014).

Native AMPARs are also associated with auxiliary proteins, which are also expressed differentially in various brain regions (Schwenk et al., 2014). For example, the transmembrane AMPAR regulatory protein (TARP) $\gamma 8$ is highly expressed in the cortex, the hippocampus and the striatum, but the expression of $\gamma 2$ and $\gamma 4$ dominate in the thalamus (Schwenk et al., 2014). The relative abundance of the various TARPs during development seems to be much more regulated than the AMPAR subunits themselves, with the expression of $\gamma 8$ increasing and $\gamma 4$ decreasing with age (Schwenk et al., 2014). Interestingly, Cornichon Homolog 3 (CNIH-3) is found in low abundance relative to CNIH-2 in all the brain regions that were tested (Schwenk et al., 2014). At synapses, the subunit composition and trafficking of AMPARs is regulated through both TARPs and CNIHs (Herring et al., 2013).

The expression of KAR subunits is more discrete than with AMPARs (Hollmann and Heinemann, 1994), with the exception of GluK5, which seems to be ubiquitous (Herb et al., 1992). The relative abundance of KAR mRNAs generally increases during development (Bahn et al., 1994). Interestingly, the mRNAs for both primary and secondary KAR subunits are observed in the same cell types (Seeburg, 1993;

Wisden and Seeburg, 1993; Bahn et al., 1994; Hollmann and Heinemann, 1994), suggesting that KARs most likely assemble as heteromers. In the rodent brain, the most widely expressed KAR subunits are GluK2 and GluK5 (Petralia et al., 1994).

Despite the lack of evidence for their protein expression, there is electrophysiological and pharmacological evidence of synaptic KARs. Notably, the development of selective AMPAR antagonists, such as the 2,3-benzodiazepines (Wilding and Huettner, 1995; Bleakman et al., 1996) enabled the characterization of isolated synaptic KAR-mediated responses (Paternain et al., 1995). Interestingly, KARs can be found at both pre- and post-synaptic sites (Nicoll and Schmitz, 2005) and act as modulators of neuronal excitability (Contractor et al., 2011). A great example demonstrating the role of KARs as neuronal circuit modulators is at the hippocampal mossy fibre synapses. Here, post-synaptic KARs produce L-Glu-evoked excitatory post-synaptic currents (EPSCs) with slow deactivation (Castillo et al., 1997; Vignes and Collingridge, 1997; Frerking and Ohliger-Frerking, 2002), while the activation of pre-synaptic KARs causes pre-synaptic facilitation (Contractor et al., 2003; Nicoll and Schmitz, 2005). These two processes contribute to the frequency facilitation at these synapses (Nicoll and Schmitz, 2005). The KARs involved are thought to be assembled from GluK2, GluK4 and GluK5 subunits (Darstein et al., 2003; Fernandes et al., 2009). Post-synaptic KARs are also found in the retina, amygdala, spinal cord and cortex (Frerking and Nicoll, 2000). Pre-synaptic GluK2/GluK5 KARs in cerebellar granule cells play an important role in the induction of long-term depression (LTD) (Crépel and Crepel, 2009).

In contrast to AMPAR-mediated EPSCs, the kinetic properties of KAR-mediated EPSCs are very different from those of recombinant homomeric GluK2 responses (Heckmann et al., 1996; Bowie, 2002; Swanson et al., 2002; Bowie

et al., 2003). Recent studies are showing that subunit composition, especially including the GluK4 and GluK5 subunits (Barberis et al., 2008; Fernandes et al., 2009), as well as the association of KARs with auxiliary proteins (Zhang et al., 2009), can account for these differences and gives insight into the functional mechanisms underlying the synaptic roles of KARs (for example, see Yan et al. (2013)).

1.1.4 Architecture and Topology

Not long after the cloning and functional classification of the iGluR subunits, a plethora of functional and structural evidence quickly expanded. However, the stoichiometry of the iGluRs was not always as clear as it is today. In fact, initial biochemical and functional evidence suggested that they assembled as pentamers (Blackstone et al., 1992; Wenthold et al., 1992; Brose et al., 1993; Wu and Chang, 1994; Sutcliffe et al., 1996; Ferrer-Montiel and Montal, 1996; Mano et al., 1996). At first, this made sense, since other ligand-gated ion channels, such as nicotinic acetylcholine receptors, were also thought to be pentamers (Changeux et al., 1987; Cooper et al., 1991). However, functional evidence for the tetrameric assembly of iGluRs soon emerged (Laube et al., 1998; Mano and Teichberg, 1998; Rosenmund et al., 1998). For example, electrophysiological analysis of recombinantly-expressed wild-type or mutant NMDAR subunits led to the conclusion that these receptors were composed of two GluN1 and two GluN2 subunits (Laube et al., 1998). Similarly, electrophysiological approaches were useful in determining the tetrameric organization of non-NMDARs (Mano and Teichberg, 1998; Rosenmund et al., 1998).

Ionotropic glutamate receptors have four main topological domains: the amino-terminal domain (ATD), the ligand-binding domain (LBD), the

transmembrane domain (TMD) and the C-terminal domain (CTD) (Figure 1–2). A detailed description of each one will follow.

With the observation that the S1 and S2 domains of the iGluR subunits were sufficient and necessary for agonist binding (see "LBD" section below) (Kuusinen et al., 1995; Paas, 1998), it became possible to obtain an X-ray crystal structure of an isolated GluA2 LBD in complex with the agonist, kainate (Armstrong et al., 1998). Shortly thereafter, 2-fold symmetrical dimeric structures of the GluA2 LBD were solved in the apo (unbound) state, in complex with the agonists, L-Glu, kainate and AMPA, as well as with an antagonist, DNQX (Armstrong and Gouaux, 2000). The analysis of functional mutant assembly suggested a dimers-of-dimers formation, occurring through critical NTD interactions (Ayalon and Stern-Bach, 2001). Interestingly, the various degrees of cleft closure observed with different ligands gave important insight into the structural mechanisms underlying the agonist selectivity and the activation properties of these channels (Armstrong and Gouaux, 2000; Hogner et al., 2002; Jin et al., 2002, 2003). Structures of isolated domains from related iGluRs emerged, for example GluR0 (Mayer et al., 2001) and GluK1 and GluK2 (Mayer, 2005), and suggested that the overall structure of these receptors is conserved.

In the following years, several biochemical and lower-resolution electron-microscopy (EM) experiments provided the first glimpse into the tetrameric nature of the full-length channel and its dimer-of-dimers arrangement (Safferling et al., 2001; Tichelaar et al., 2004; Nakagawa et al., 2005, 2006; Midgett and Madden, 2008). The first crystal structure of a full-length GluA2 receptor revealed the intricacies of the tetrameric complex with some unexpected features (Figure 1–2) (Sobolevsky et al., 2009). For example, "domain swapping" was observed between the ATDs and LBDs, and despite the identical primary sequence

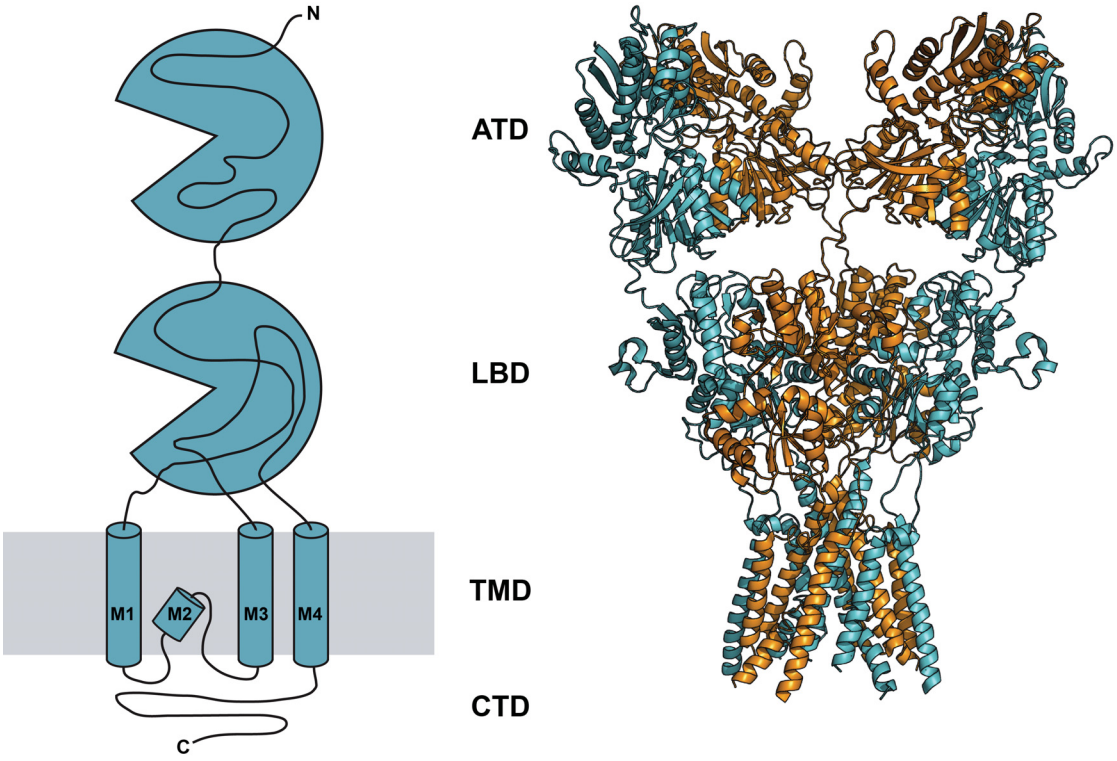

Figure 1–2: Structure of iGluRs
Left, Schematic illustration of the subunit topology of iGluRs. Right, Cryo-EM structure of the full-length GluA2 homotetramer (PDB # 5KBV). The A/C subunits are coloured in cyan; the B/D subunits are coloured in orange.

of the subunits within the homotetramer, there were differences in the structural arrangement of the different subunits, which led to their A/C and B/D designation (Sobolevsky et al., 2009) (Figure 1–2). Since then, multiple X-ray crystal and cryo-EM structures of AMPARs (Chen et al., 2014; Dürr et al., 2014; Twomey et al., 2016; Herguedas et al., 2016) and KARs (Meyerson et al., 2014, 2016) have been solved.

The details regarding the different domains of the iGluR are discussed in the following sections below. This thesis will focus on the AMPA and kainate receptors.

1.1.4.1 The Amino-Terminal Domain

The first 14–33 residues of all iGluRs constitute a signal peptide, which targets the receptor for membrane insertion before being removed (Traynelis et al., 2010). The numbering of the iGluR residues sometimes varies in reference to the "immature" (i.e. including the signal peptide residues) or "mature" peptide (i.e. beginning after the signal peptide). The ATD is assembled from the following 400–450 residues and has a structure similar to amino acid binding proteins (Traynelis et al., 2010).

The structure of this domain resembles that of the iGluR LBD clamshell structure with two distinct domains, the N-terminal R1 and the lower R2 domain, linking to the LBD (Sobolevsky et al., 2009; Karakas et al., 2009; Kumar et al., 2011). At the ATD level, the iGluRs have a 2-fold symmetrical arrangement (Sobolevsky et al., 2009; Karakas et al., 2009; Meyerson et al., 2016). More specifically, within one of the dimers, ATDs for each of the two subunits are not equivalent. There are multiple interactions between the ATDs within a dimer, and only the "proximal" ATDs (i.e. from subunits B and D) form contacts with the second ATD dimer (Figure 1–3) (Sobolevsky et al., 2009; Karakas et al., 2009; Karakas and Furukawa, 2014).

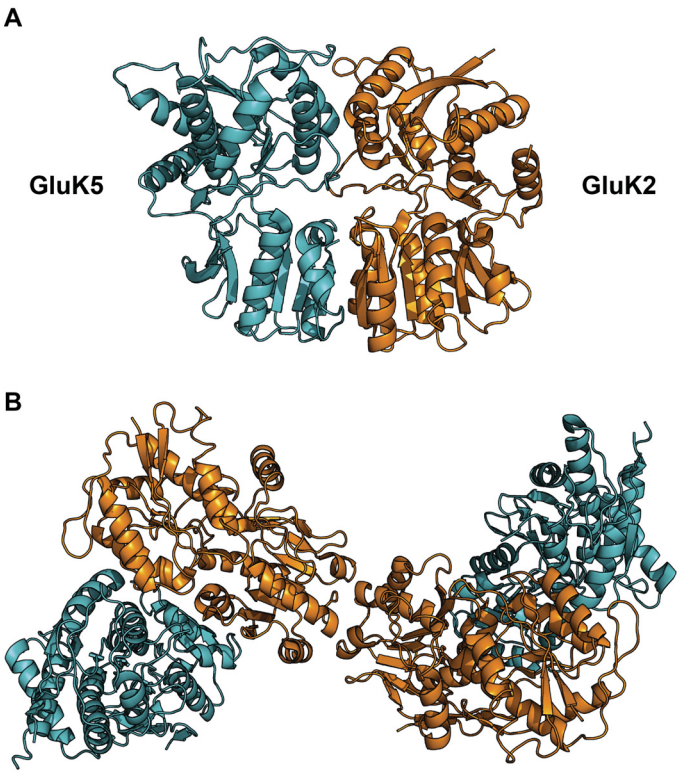

Figure 1–3: X-ray crystal structure of the GluK2/GluK5 ATD
A, X-ray crystal structure of an ATD dimer formed of GluK2 and GluK5 (PDB # 3QLU). B, Structure of the tetrameric GluK2/GluK5 ATD assembly (PDB # 3QLV). The GluK2 subunits are in orange and the GluK5 subunits are in cyan.

Although this extracellular domain is not essential for channel function (Pasternack et al., 2002; Matsuda et al., 2005; Rachline et al., 2005; Gielen et al., 2009; Yuan et al., 2009), it interacts with modulators and influences channel function (Traynelis et al., 2010). These studies have also provided insight into the specific roles of the ATD in the regulation of channel gating and assembly. Interestingly, a recent study also identified the signal peptide as playing a role in receptor assembly (He et al., 2016).

The ATD is the main place where the iGluRs are glycosylated as they are trafficked through the endoplasmic reticulum (ER) and Golgi (Everts et al., 1997). N-linked glycosylation impacts receptor trafficking, desensitization and channel open probability [(Hollmann and Heinemann, 1994; Everts et al., 1997; Leuschner and Hoch, 1999; Ayalon and Stern-Bach, 2001; Ayalon et al., 2005); see Traynelis et al. (2010) for a more thorough review]. Interestingly, some of the N-linked oligosaccharides are association sites for extracellular modulators. For example, the plant lectin, concanavalin-A (Con-A) (Partin et al., 1993; Everts et al., 1997, 1999), increases the steady-state current in KARs (Bowie et al., 1998), an effect that can be disrupted by the ablation of the glycosylation sites (Fay and Bowie, 2006). Other exogenous lectins, like wheat-germ agglutinin and succinyl concanavalin-A (Yue et al., 1995), as well as marine and vertebrate galectins, also modulate AMPAR and KAR function in a subunit-dependent manner (Ueda et al., 2013; Copits et al., 2014). Although the ATD of NMDARs contains multiple binding sites for allosteric modulators, such as Zn^{2+} and ifenprodil, no ions or small molecules are known to bind to the AMPA/kainate receptor ATD (Traynelis et al., 2010).

The ATDs of AMPA and NMDARs were also shown to interact with extracellular proteins such as N-cadherin (Saglietti et al., 2007) and the ephrin receptor (Dalva et al., 2000; Takasu et al., 2002), which may be important for their

roles in the development and maintenance of synapses. Specific subunit-subunit interactions at the level of the ATD are critical for the specificity of assembly between the subtypes of iGluRs (Ayalon et al., 2005) and could also promote heteromeric assemblies within these iGluR families (Kumar et al., 2011). ATDs could also play a role in the stabilization of the tetrameric structure (Sobolevsky et al., 2009).

1.1.4.2 The Ligand-Binding Domain

The LBD follows the ATD C-terminally (Figure 1–2). However, instead of being composed of a single stretch of residues, it is made up of 2 stretches of amino acids that are separated by the pore-forming sequences of the channel. These 2 regions, termed S1 and S2 (Stern-Bach et al., 1994), form the "upper" (D1) and "lower" (D2) lobes of a clamshell structure (Sobolevsky et al., 2009).

The S1 domain spans about 150 residues (Stern-Bach et al., 1994) after the ATD–LBD linker and leads into the S1-M1 linker (or pre-M1) (Sobolevsky et al., 2009). S2 emerges after the M3 segment and spans about 160 residues before leading into the M4 segment (Figure 1–2) (Stern-Bach et al., 1994). The S2-M3 linker is thought to be important for the conformational changes that lead to the opening of the channel pore (Sobolevsky et al., 2009); this will be discussed in more detail below. Together, the D1 and D2 domains form a clamshell structure, where agonists and competitive antagonists can dock (Armstrong and Gouaux, 2000; Furukawa and Gouaux, 2003; Du et al., 2005; Gonzalez et al., 2008; Sobolevsky et al., 2009). Encouragingly, the structures of the isolated LBDs are very close to that of the LBDs in the full-length GluA2 structures (Armstrong and Gouaux, 2000; Furukawa and Gouaux, 2003; Du et al., 2005; Gonzalez et al., 2008;

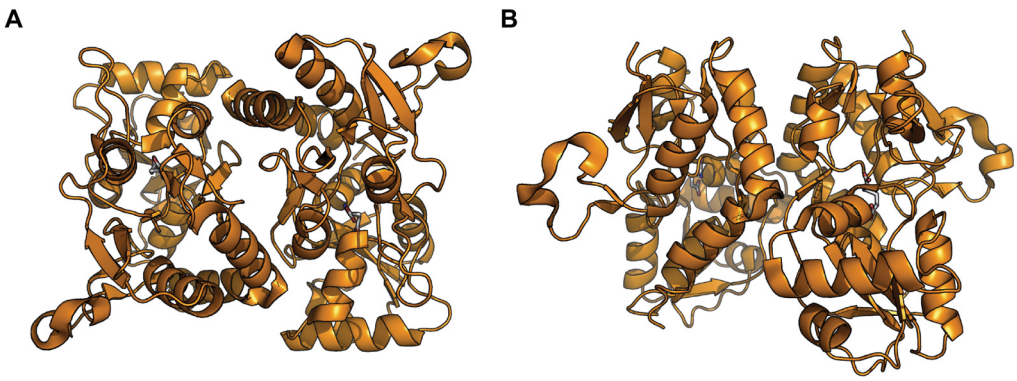

Figure 1–4: X-ray crystal structure of the GluA2 LBD
Homodimeric structure of GluA2 bound to L-Glu (PDB # 1FTJ). A, Top view. B, Side view.

Sobolevsky et al., 2009; Meyerson et al., 2014; Chen et al., 2014; Dürr et al., 2014; Herguedas et al., 2016; Twomey et al., 2016).

The binding of agonists occurs through several conserved residues within the cleft, a process that is similar in all iGluRs (Traynelis et al., 2010). This causes a conformational change, namely the closure of the clamshell *via* the movement of D2, leading to the opening of the channel pore (Armstrong and Gouaux, 2000). Subsequently, a re-opening of the cleft releases the agonist and leads to channel closure (Traynelis et al., 2010). Deactivation can occur in each subunit independently, resulting in gradually smaller conductance states as each agonist unbinds, as can be observed in single-channel openings (Rosenmund et al., 1998). Alternatively, the clamshell can remain closed, trapping the agonist and causing a "pulling" force to destabilize the D1–D1 dimer interface, which results in desensitization (Armstrong and Gouaux, 2000).

In AMPARs, agonist efficacy and antagonism is thought to depend on the degree of cleft closure. The first evidence for this came from the crystal structures of the isolated GluA2 LBD in the apo (unbound) state, or bound to agonists or antagonists (Armstrong and Gouaux, 2000). A comparison of the degree of cleft

closure suggested that the full agonist L-Glu caused a larger conformational change (i.e. a larger D2 movement toward D1) compared to partial agonists (20° for L-Glu versus 12° for kainate) (Armstrong and Gouaux, 2000). In contrast, the competitive antagonist DNQX resulted in a conformation that was much closer to the apo state (Armstrong and Gouaux, 2000), suggesting that the degree of cleft closure lies at the heart of the mechanism of activation in AMPARs. A similar phenomenon exists in KARs, where the partial agonists, kainate and domoate, produce intermediate clamshell closure compared to L-Glu (Mayer, 2005; Nanao et al., 2005; Fay et al., 2009). Antagonists also seem to prevent cleft closure in KARs (Mayer, 2005). Interestingly, many partial agonists of GluK2, small amino acids that are structurally related to L-Glu, seem to result in a cleft closure that is similar to L-Glu, suggesting that the interactions between the agonist and the residues in the clamshell are also important for determining agonist efficacy at KARs (Fay et al., 2009).

The D1–D1 dimer interface forms binding pockets for ions and allosteric modulators, which affect the stability of the LBD dimer and regulate the time-course of activation in AMPARs and KARs. For example, in AMPARs, the benzothiazide molecule, cyclothiazide (CTZ) binds at the dimer interface (Kovcs et al., 2004), presumably holding it together. This essentially abolishes desensitization, as suggested by non-decaying steady-state currents and single-channel openings that remain open until the agonist is removed (Yamada and Tang, 1993). In GluK2 KARs, the LBD dimer interface forms an ion-binding pocket, in which monovalent anions and cations bind (Plested et al., 2008). Here, the presence of one anion (Cl^-) and two cations (Na^+) (Plested and Mayer, 2007; Plested et al., 2008) is necessary for the activation of GluK2 (Wong et al., 2006,

2007). These ions are thought to increase the stability of the dimer interface and regulate the time course of KAR activation (Dawe et al., 2013).

Consistent with this, the substitution of the Na^+ ions for other cations (i.e. Li^+ , K^+ , Rb^+ , Cs^+) accelerates desensitization (Wong et al., 2006), presumably because the binding of these ions in the pocket is sub-optimal (Plested et al., 2008). Interestingly, AMPARs also have a putative ion-binding site, but only the smallest (Li^+) ions are able to bind and regulate channel gating (Dawe et al., 2016). Here, a network of electrostatic interactions at the LBD dimer interface, through conserved electronegative structural features, is critical for channel gating (Dawe et al., 2016). Although the LBD of the bacterial GluR0 has a similar structure and dimeric arrangement to that of the AMPA and kainate receptors (Mayer et al., 2001; Lee et al., 2008), its dimer interface is relatively electroneutral (Mayer et al., 2001), suggesting that it may not bind to external ions.

However, as I will discuss in Chapter 2 of this thesis, the ion-dependency of KARs is limited to homomeric GluK2 channels, since the heteromeric channels formed with GluK2 and GluK5 subunits display ion-independent gating. In addition, functional evidence shows that Li^+ ions, but not larger monovalent cations, are able to regulate the time-course of GluK2/GluK5 activation, suggesting that there may be structural similarities between the LBD dimer interface of GluK2/GluK5 and GluA2 receptors (see Chapters 2 and Discussion, and Dawe et al. (2016)). The ion sensitivity of heteromeric KARs formed of the GluK2 and GluK3 subunits, which are likely found pre-synaptically (Pinheiro et al., 2007), has not yet been tested.

1.1.4.3 The Transmembrane Domain

The TMD of iGluRs is formed by 3 transmembrane helices (M1, M3 and M4) and one re-entrant loop (M2) from each subunit, which assemble with a similar quaternary arrangement to the inverted K^+ -selective ion channel (Wo and Oswald, 1995; Kuner et al., 2003; Sobolevsky et al., 2009), as well as the *Bacillus cereus* NaK channel (Figure 1–5) (Siegler Retchless et al., 2012; Brown et al., 2016). The TMD of the homomeric GluA2 structure has a 4-fold symmetrical arrangement around the central pore cavity (Sobolevsky et al., 2009).

Structurally, the M2 helix lines the internal region of the pore and the M3 helix lines the external portion (Sobolevsky et al., 2009). At the level of the extracellular membrane boundary, the four M3 helices cross and occlude the channel pore; this presumably represents a closed channel state (Sobolevsky et al., 2009). The M1 and M4 helices are positioned on the exterior of M2 and M3, with the M4 segment of one subunit making contacts with the pore-forming helices of the adjacent subunit (Sobolevsky et al., 2009; Salussolia et al., 2011). Interestingly, the K^+ -selective bacterial glutamate receptor, GluR0 (Chen et al., 1999), as well as K^+ channels (Wo and Oswald, 1995; Kuner et al., 2003), share a similar architecture (though inverted) but lack the M4 segment. In AMPARs, the ablation of the M4 segment or mutation of M4 residues interacting with the M1 or M3 segments eliminates receptor surface trafficking and curtails their function (Salussolia et al., 2011). This segment is also critical for AMPAR dimers to assemble as tetramers (Salussolia et al., 2013) Together, this suggests that the M4 helices play an important structural role in AMPARs, and perhaps they help regulate channel stability.

There are 3 linkers that bridge the extracellular domains to the TMD. The S1–M1 linker, or pre-M1, forms a short helix that is positioned orthogonally to the

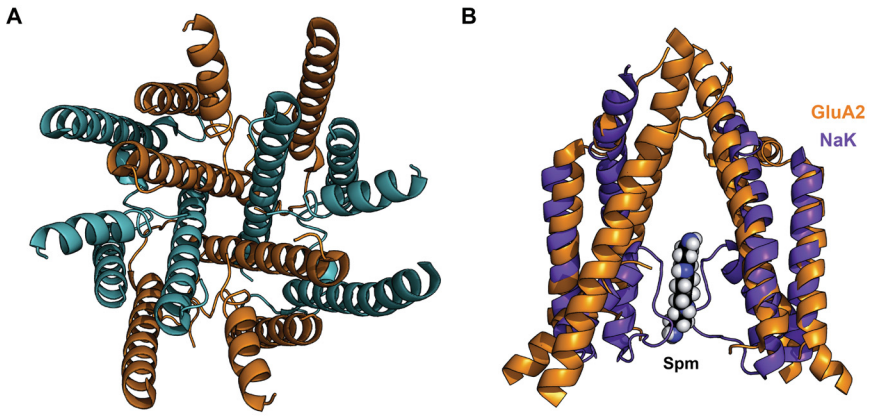

Figure 1–5: Structure of the iGluR pore
A, Structure of the GluA2 pore (view from cytoplasmic side, PDB # 5KBV). B, Subunits A and C from the GluA2 pore (orange, PDB # 3KG2) aligned with two equivalent subunits of the open *Bacillus cereus* NaK channel structure (purple, PDB # 3E86). A spermine molecule (Spm) is docked in the selectivity filter of the NaK channel, illustrating a potential binding site for polyamine blockers.

membrane plane and makes contacts with the C-terminal region of M3 and the N-terminal region of M4 (Sobolevsky et al., 2009). In the tetrameric GluA2 structure, these helices form a "cuff", which lines the exterior of the pore (Sobolevsky et al., 2009).

The M3–S2 and S2–M4 linkers are particularly interesting in that they are arranged with a 2-fold symmetry (Sobolevsky et al., 2009). In the distal (A/C) subunits, the M3–S2 linkers form short helices while in the proximal subunits (B/D), they are extended (Sobolevsky et al., 2009). In contrast, the S2–M4 linkers are extended in the A/C subunits but compact in the B/D subunits (Sobolevsky et al., 2009). This region is located just outside the extracellular boundary of the membrane and forms the transition from 2-fold to 4-fold symmetry (Sobolevsky et al., 2009). Given this, it is highly likely that these linkers are critical for channel opening, and that their 2-fold symmetry endows the distal and proximal subunits with distinct gating properties (Sobolevsky et al., 2009).

As mentioned above, the extracellular portion of the pore is made up of the M3 segment (Sobolevsky et al., 2009). The highly conserved SYTANLAAF motif is critical for the normal gating of iGluRs, with mutations resulting in changes in desensitization and activation (Huettner, 2015). The intracellular region of the pore is made up of residues from the M2 segment, but, apart from the short M2 helix, the structure of the pore-lining residues is disordered, (Sobolevsky et al., 2009), suggesting a higher motility in this region (Huettner, 2015).

Multiple residues along the channel pore are important in determining the modulation of channel gating by external factors. For example, substitutions in the pore-lining residues of M3 to positively-charged lysine (Lys) or arginine (Arg) residues can endow the AMPARs with anion permeability (Wilding et al., 2008) and alter Ca^{2+} permeability (Jatzke et al., 2003). In KARs, M3 residues are also involved in the strong inhibition by fatty acids (Wilding et al., 2010). Additionally, RNA editing at several positions in the M1, M2 and M3 segments are critical determinants of channel block by intracellular polyamines and divalent permeability (Köhler et al., 1993; Bowie and Mayer, 1995; Burnashev, 1996; Wilding et al., 2010). The pore properties of AMPARs and KARs will be discussed in more detail in the "Channel Gating" section of this chapter. Given the subunit specificity of RNA editing, alternative splicing and post-translational modifications, the stoichiometry of AMPA and kainate receptors, as well as their association with auxiliary proteins, are likely critical in determining the channel properties (Huettner, 2015). Indeed, the association of GluK2 and GluK5 as heteromers yields receptors with distinct gating properties (Barberis et al., 2008), which will be discussed in detail in the results Chapters of this thesis.

1.1.4.4 The Carboxy-Terminal Domain

The CTD, or C-tail, is the most variable of the iGluR domains (Traynelis et al., 2010). Indeed, the various C-tails of glutamate receptors come in many flavours, differing in both sequence and length. In addition, some subunits also undergo alternative splicing, which can alter the composition of the C-tail (Traynelis et al., 2010). Interestingly, with the exception of a small C-terminal peptide from GluN1 bound to Ca^{2+}/CaM (Ataman et al., 2007), very little structural information is known about the C-tail of iGluRs (Traynelis et al., 2010). Despite this, many studies have investigated the role of the splice variants and the many post-translational modifications that occur in this intracellular domain. A thorough review of all the C-terminal modifications and the roles of the CTD is beyond the scope of this thesis; for this reason, only a brief overview will be discussed.

Splice variants were identified for the GluA2 and GluA4 AMPAR subunits, and for all but the GluK4 subunit in KARs. The main consequence of the various C-tails is the presence or absence of sites for post-translational modifications, such as phosphorylation, palmitoylation and SUMOylation (Traynelis et al., 2010), but also potentially different interactions with scaffolding or auxiliary proteins. The CTD of AMPAR subunits contain multiple phosphorylation sites that are involved in the regulation of binding proteins (Traynelis et al., 2010). For example, glutamate receptor-interacting protein (GRIP) binding to GluA2 is weakened by the activity-dependent protein kinase C (PKC) phosphorylation of serine 880 (Matsuda et al., 1999; Chung et al., 2000), promoting the internalization of the complex (Chung et al., 2000). Generally, the phosphorylation state at any given site somehow regulates the trafficking, membrane insertion and recycling properties of AMPARs in a subunit-dependent, cell-dependent and developmentally-regulated manner (Malinow and Malenka, 2002; Traynelis et al., 2010). Several

phosphorylation sites are also found in the C-tails of the GluK1 (Rivera et al., 2007; Hirbec et al., 2003), GluK2 (Kornreich et al., 2007; Traynelis and Wahl, 1997) and GluK4 KAR subunits (Traynelis et al., 2010). Phosphorylation at these sites regulates the trafficking but also the gating properties of KARs. For example, protein kinase A (PKA)-dependent phosphorylation in the long splice variant of GluK2 (GluK2a) (Traynelis et al., 2010) increases whole-cell currents (Kornreich et al., 2007), potentially through an increase in channel open probability (Traynelis and Wahl, 1997).

In addition to being phosphorylated, AMPA and kainate receptors may also be palmitoylated, a modification resulting in the covalent attachment of fatty acids, such as palmitic acid, to cysteine (Cys) residues. This also impacts the localization of the channels through the binding of intracellular proteins (Hayashi et al., 2005). SUMOylation is the covalent attachment of small ubiquitin-like modifier (SUMO) proteins. GluK2 and GluK3 KAR subunits can be SUMOylated (Martin et al., 2007; Wilkinson et al., 2008); this is thought to regulate receptor endocytosis.

Generally, the CTD of iGluRs has been shown to interact with a large number of intracellular proteins, with roles including membrane trafficking and recycling, scaffolding and signalling (Traynelis et al., 2010). The trafficking and recycling of AMPAR subunits is critical for the expression of plasticity mechanisms like long-term potentiation (LTP) and LTD (Malinow and Malenka, 2002). This thesis will focus on the auxiliary proteins of AMPARs and KARs, TARPs and Netos, respectively; this will be discussed in more detail in a section below.

1.1.5 Assembly and Trafficking

The assembly of the iGluR tetramers is thought to first occur *via* ATD interactions (Ayalon and Stern-Bach, 2001; Ayalon et al., 2005), then through LBD

and TMD interactions (Greger and Esteban, 2007; Hansen et al., 2010). Receptor assembly occurs in the ER (Ma-Högemeier et al., 2010; Hansen et al., 2010). At this point, receptors also undergo quality control steps, such as ligand binding and channel activation and desensitization, before being trafficked to the plasma membrane. Indeed, mutations in KAR subunits that disrupt ligand binding or channel activation greatly reduce the trafficking of the receptor to the plasma membrane (Greger et al., 2002; Fleck et al., 2003; Grunwald and Kaplan, 2003; Mah et al., 2005; Valluru et al., 2005; Greger et al., 2006; Priel et al., 2006; Penn et al., 2008; Hansen et al., 2010; Traynelis et al., 2010). Also, mutations that affect dimerization (Fleck et al., 2003) or RNA editing (Lomeli et al., 1994; Greger et al., 2002) of AMPARs impacts their surface trafficking. Likewise, null mutations of ligand-binding residues in GluK2 are retained intracellularly (Fleck et al., 2003). In addition, mutants of both AMPA and kainate receptors with reduced or absent desensitization also traffic poorly (Traynelis et al., 2010). Two examples of this are the L483Y mutation in GluA2 (Greger et al., 2006) and the D776K mutation in GluK2 (Nayeem et al., 2009; Dawe et al., 2013). In contrast, mutant receptors with increased desensitization (i.e. the N754D mutation in GluA2 (Greger et al., 2006)) are able to traffic normally.

The trafficking of iGluRs is also regulated by trafficking and retention signals within the protein sequence. In KARs, the GluK2a subunit has a forward trafficking signal, which promotes its membrane insertion, as well as that of other retained subunits, such as GluK5, through heteromerization (Jaskolski et al., 2004). Multiple retention signals are responsible for the ER-retention of GluK5 (Ren et al., 2003; Nasu-Nishimura et al., 2006; Vivithanaporn et al., 2006). Interestingly, the ablation of these retention signals allows GluK5 tetramers to be inserted in the

plasma membrane (Reiner et al., 2012), but these surface receptors are not responsive to L-Glu (Ren et al., 2003).

Other factors that regulate proper localization and membrane insertion are post-translational modifications such as phosphorylation, palmitoylation, SUMOylation and glycosylation (Traynelis et al., 2010). AMPARs and KARs also associate with auxiliary proteins, which may also regulate their trafficking and localization; this will be briefly discussed in a section below.

1.1.6 Heteromerization

Although the existence of functional homomeric channels is possible, native AMPARs and KARs are likely found as heteromeric receptor complexes, assembled from their various respective subunits (Bahn et al., 1994; Seeburg, 1993; Wenthold et al., 1996; Fernandes et al., 2009; Lu et al., 2009).

1.1.6.1 AMPARs

AMPARs seem to assemble with a preferred subunit composition, the majority of which contain GluA2 subunits with either GluA1 or GluA3 (Wenthold et al., 1996; Greger et al., 2002; Lu et al., 2009). The GluA2 subunit is subject to post-transcriptional RNA editing at the Q/R site (Sommer et al., 1991). This process, which alters the sequence so that edited subunits harbour a positively-charged Arg (R) residue instead of a charge-neutral glutamine (Gln, Q) at the narrowest region in the pore (Sommer et al., 1991). In the rodent brain, virtually all GluA2 subunits are edited (i.e. contain an Arg, $> 99\%$), while the GluA1, GluA3 and GluA4 subunits remain unedited and contain a Gln residue at the pore apex (Sommer et al., 1991). The inclusion of GluA2 subunits in AMPARs reduces Ca^{+} permeability and polyamine-dependent inward rectification (Burnashev et al., 1992; Washburn et al., 1997). However, not all synapses express

GluA2-containing AMPARs, and GluA2-lacking Ca^{2+}-permeable AMPARs are expressed during development and synaptic plasticity (Isaac et al., 2007). The exact stoichiometry of AMPARs has been debated. For example, one study, using Ca^{2+} permeability, inward rectification and polyamine block as functional measures, concluded that the relative abundance of GluA2 in AMPARs was variable (Washburn et al., 1997). More recent studies have since suggested that AMPARs assemble with a fixed stoichiometry of 2:2 (Mansour et al., 2001; Greger et al., 2002, 2003, 2006), though the positioning of the subunits does not appear to be strict (Herguedas et al., 2016). Interestingly, Q/R editing is important in regulating the assembly of AMPAR but not KAR subunits (Greger et al., 2006; Ma-Högemeier et al., 2010; Ball et al., 2010).

1.1.6.2 KARs

In contrast to the AMPAR subunits, not all KAR subunits form functional homomers. The so-called "primary" subunits, which can form functional homomers when expressed in a recombinant system, are GluK1–3. On the other hand, the GluK4 and GluK5 subunits are considered as "secondary" subunits, because they do not function as homotetramers (Cui and Mayer, 1999; Paternain et al., 2000), even when they are found as tetramers at the cell surface (Ren et al., 2003; Reiner et al., 2012). Instead these subunits can co-assemble with primary subunits and form heteromeric channel complexes. In native systems, KARs most likely assemble as heteromers, since different subunits are often expressed in the same cells (Bahn et al., 1994; Seeburg, 1993). Additionally, the kinetic properties of KAR-mediated EPSCs are different from those of homomeric KARs (Castillo et al., 1997; Heckmann et al., 1996; Swanson et al., 2002). For example, whereas GluK2 homomers have very fast kinetic properties (deactivation time constant of $\approx$ 2.5 ms) (Heckmann

et al., 1996), the presence of the GluK5 subunit confers slow decay kinetics that resemble those observed in native KAR-EPSCs (deactivation slow time constants of $\approx$ 73–133 ms) (Bannister et al., 2005; Barberis et al., 2008). In fact, a knockout study suggest that post-synaptic KARs in the hippocampus function exclusively as heteromeric complexes composed of both primary and secondary subunits (Fernandes et al., 2009).

The most widely expressed KAR subunits are GluK2 and GluK5 (Seeburg, 1993; Petralia et al., 1994; Barberis et al., 2008). In line with this, an increasing number of studies has focused on a more detailed investigation of the properties of such heteromeric KARs (Swanson et al., 2002; Barberis et al., 2008; Fernandes et al., 2009; Mott et al., 2010; Fisher and Mott, 2011; Straub et al., 2011). Heteromers containing either GluK4 or GluK5 exhibit unique biophysical and pharmacological properties, most notably in their responsiveness to AMPA and slower deactivation kinetics (Herb et al., 1992; Barberis et al., 2008; Mott et al., 2010; Fernandes et al., 2009).

1.2 Auxiliary Proteins

Native iGluRs are not found alone, but instead exist as a part of a multi-protein synaptic complex (Jackson and Nicoll, 2011). The following sections will provide a brief overview of the structural and functional characteristics of the major auxiliary subunits of AMPARs and KARs that will be discussed in the Results chapters of this thesis.

1.2.1 AMPAR auxiliary proteins

The first auxiliary protein for AMPARs was identified through the *stargazer* mouse, in which a spontaneous mutation of the transmembrane protein stargazin (or γ2) renders it non-functional (Letts et al., 1998; Vandenberghe et al., 2005; Jackson

and Nicoll, 2011). Stargazin is the founding member of the TARP family of auxiliary subunits (Jackson and Nicoll, 2011). Additional homologous proteins were identified and further classified into functional groups. For example, γ2, γ3, γ4 and γ8 are part of the Type I TARPs; they impact the trafficking, targeting and functional properties of AMPARs and their exogenous expression in *stargazer* mice can rescue the otherwise absent AMPAR-mediated currents (Tomita et al., 2003; Kato et al., 2010; Jackson and Nicoll, 2011; Sumioka, 2013). Type II TARPs, γ5 and γ7, have a smaller impact on the function and localization of AMPARs (Kato et al., 2007, 2008; Soto et al., 2009; Jackson and Nicoll, 2011).

The best-known Type I TARP, γ2, is a transmembrane protein with 4 membrane-spanning regions (Letts et al., 1998). Recently, the structure of γ2 bound to an intact AMPAR was solved using cryo-EM (Twomey et al., 2016; Zhao et al., 2016). This will prove to be greatly useful in identifying the molecular mechanisms underlying their effects on AMPARs. Stargazin interacts with AMPAR subunits via several sites, the effects of which can be separated. The main interactions are thought to occur at the level of the TMD, with the TM3 and TM4 helices of γ2 interacting with M1 and M3 of GluA2, with additional interactions occur between the extracellular domain of γ2 and the D2 lobe of GluA2 (Twomey et al., 2016). Dawe et al. (2016) identified a positively-charged region in the D2 lobe of GluA2, namely the KGK motif, which is crucial for γ2 functional interactions. Consistent with this, Twomey et al. (2016) predicted that several negatively-charged residues in the extracellular loop of γ2 form an "electronegative patch", positioned just below the KGK motif of GluA2 (Twomey et al., 2016) (Figure 1–6). This motif is conserved in the Type I TARPs, which provides additional evidence that this interaction is important for having a functional impact on the AMPARs (Twomey et al., 2016). Indeed, a recent LRET study showed that

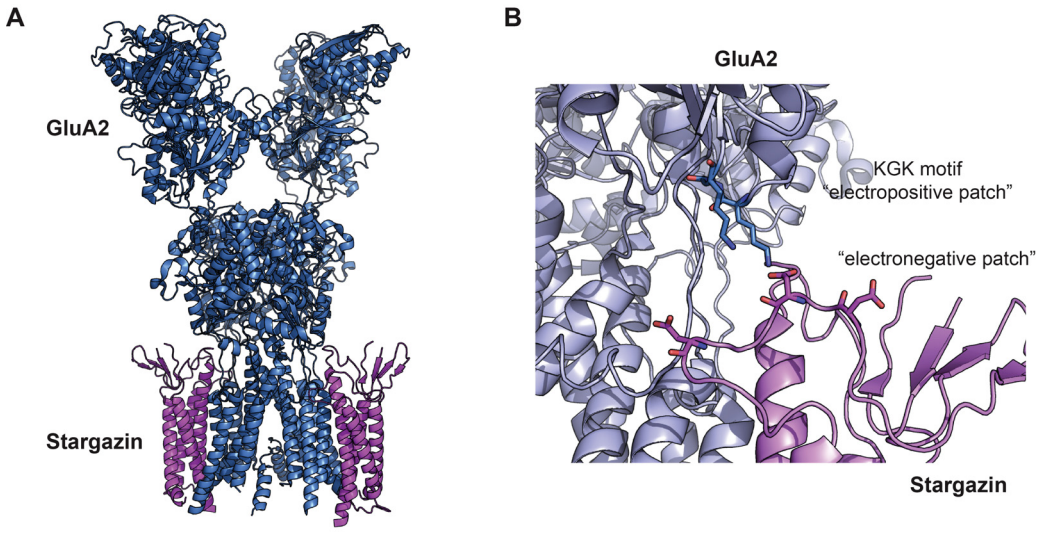

Figure 1–6: Structure of GluA2 with bound stargazin
A, Structure of the full-length GluA2 (blue) with two stargazin (magenta) bound, PDB # 5KBU). B, A closer view of the extracellular interacting domains of GluA2 and stargazin, highlighting the KGK motif in GluA2 (i.e. the "electropositive patch" (Dawe et al., 2016)), which is thought to interact with an "electronegative patch" in stargazin (Twomey et al., 2016).

γ2 promotes cleft closure and influences the gating properties of GluA2 receptors (MacLean et al., 2014). Interestingly, the disruption of this interaction by mutating the KGK motif abolishes the effect of γ2 on the gating properties of GluA2, but it does not affect its ability to relieve polyamine block (Dawe et al., 2016). In contrast, the C-tail of γ2 is critical for the attenuation of AMPAR polyamine block, ion permeation and single-channel conductance, potentially through interactions with the pore-lining residues of the AMPARs (Soto et al., 2014). These studies demonstrate that the functional effects of γ2 on AMPARs are separable.

More recently, another family of AMPAR auxiliary proteins was identified, namely the Cornichon homologs -2 and -3 (CNIH-2 and CNIH-3) (Schwenk et al., 2009). This family of proteins is related to the *Drosophila* Cornichon, which is involved in the ER export of the growth factor, Gurken (Bökel et al., 2006). The structure of CNIH-2 and CNIH-3 has not yet been solved, but they are predicted to

have 3 transmembrane helices (Schwenk et al., 2009), interacting with the TMD of AMPARs through membrane-boundary proximal residues on the extracellular and intracellular sides (Shanks et al., 2014). Heterologously-expressed CNIH-2 and CNIH-3 have a more profound impact on the decay kinetics of recombinant AMPARs compared to TARPs (Schwenk et al., 2009; Coombs et al., 2012). In addition, they increase the single-channel conductance and alleviate voltage-dependent polyamine block of Ca^{2+}-permeable AMPARs (Coombs et al., 2012). However, their synaptic roles are less well understood. For example, although CNIH-2 modulates AMPAR function, its cellular distribution remain uncertain (Jackson and Nicoll, 2011). Interestingly, CNIH-2, but not CNIH-3, is found in high relative abundance throughout the rodent brain (Schwenk et al., 2014). In addition to this, there may be an interplay between the CNIHs and TARPs, which affect the subunit composition of synaptic AMPARs (Herring et al., 2013).

Other potential AMPAR auxiliary subunits have also been identified, including SynDIG1 (Kalashnikova et al., 2010), GSG1L (Shanks et al., 2012), CKAMP44/Shisa9 (Pei and Grishin, 2012; von Engelhardt et al., 2010), SOL-1 (Zheng et al., 2006; Walker et al., 2006), SOL-2/Neto (Wang et al., 2012), Shisa6 (Klaassen et al., 2016) and Porcupine (Erlenhardt et al., 2016), but much less is known about their role in AMPAR function at synapses. For a review of the modulatory effects of some of these auxiliary proteins, see Haering et al. (2014).

1.2.2 KAR auxiliary proteins

The two related proteins, neuropillin and tolloid-like -1 and -2 (Neto1 and Neto2), were identified as KAR auxiliary subunits (Zhang et al., 2009; Tang et al., 2011). They are single-pass transmembrane proteins containing two extracellular

complement C1r/C1s, Uegf, Bmp1 (CUB) domains and a low-density lipoprotein receptor domain A (LDLa) domain (Stöhr et al., 2002). No further structural information is known. Interestingly, Neto1 also interacts with NMDARs, ensuring the proper abundance of GluN2A at post-synaptic densities, which is necessary for synaptic plasticity (Ng et al., 2009). Both Neto1 and Neto2 interact with the GluK1 and GluK2 KAR subunits (Zhang et al., 2009; Tang et al., 2011; Copits et al., 2011). Both auxiliary proteins regulate the trafficking and functional properties of KARs (Sheng et al., 2015) in a subunit-dependent manner (Fisher, 2015).

Generally speaking, they slow the decay kinetics of recombinant and synaptic KARs (Zhang et al., 2009; Straub et al., 2011). For Neto2, this results from an increase in the open probability and burst length of GluK2 single-channel currents (Zhang et al., 2009). Like TARPs, Netos also relieve voltage-dependent polyamine block of KARs (Fisher and Mott, 2012). Some positively-charged residues in the proximal C-tail of Netos are important for this relief of block (Fisher and Mott, 2012). Interestingly, the removal of these residues rescues polyamine block (Fisher and Mott, 2012), further demonstrating that effects on the pore and gating properties are separable. In Chapter 3 of this thesis, I show that this effect occurs by facilitating polyamine permeation through the channel pore, suggesting that interactions at the TMD level are critical in determining the pore architecture and functional properties of KARs. Consistent with this, interactions of Neto2 with the GluK2 M3-S2 linker, as well as with the D1–D1 dimer interface, are critical for its modulatory effects (Griffith and Swanson, 2015). The stoichiometry of Neto1 and Neto2 with homomeric and heteromeric KARs remains unknown.

SAP90 (also known as PSD-95) is a scaffolding protein of the synapse-associated protein (SAP) family that is found at excitatory post-synaptic

densities (Garcia et al., 1998). It contains three PDZ (post synaptic density protein (PSD-95), *Drosophila* disc large tumor suppressor (Dlg1), and zonula occludens-1 protein (zo-1)) domains followed by an SH3 (SRC Homology 3) domain and an inactive GK (guanylate kinase) domain (Garcia et al., 1998). The C-tail of some KAR subunits interacts with members of the SAP family through their different domains. For example, GluK2 co-immunoprecipitates with SAP90, SAP97 and SAP102 due to an interaction with its C-terminal ETMA sequence (Garcia et al., 1998). This interaction clusters the receptors and accelerates their recovery from desensitization (Garcia et al., 1998; Bowie et al., 2003). Conversely, the SH3 and GK domains of SAP90 and SAP97 interact with the C-tail of GluK5, which also results in clustering (Garcia et al., 1998; Mehta et al., 2001). Interestingly, the interaction between PSD-95 and GluK5 is weakened by the phosphorylation of the GluK5 CTD by CaMKII (Carta et al., 2013). This leads to an increased motility of the receptors and a decrease in synaptic GluK5-containing KARs, which is consistent with their implication in KAR-dependent LTD at mossy fibre–CA3 hippocampal synapses (Carta et al., 2013; Suzuki and Kamiya, 2016). Taken together, PSD-95, and other SAP family members, interact with the CTDs of certain KAR subunits through various domains and influence their localization (Carta et al., 2013; Aller et al., 2015) and to a lesser extent, their functional properties (Garcia et al., 1998; Bowie et al., 2003). Interestingly, PSD-95 can also interact with the TARP, $\gamma 2$, an interaction which influences the localization of the AMPAR complex at the post-synaptic density (Bats et al., 2007). A detailed review of these interactions, however, is beyond the scope of this thesis.

1.3 Channel Gating

1.3.1 Overview

The mechanisms governing the activation, deactivation and desensitization of iGluRs was pushed forward with the advent of X-ray crystal structures of the isolated GluA2 LBD bound to full and partial agonists and antagonists (Armstrong and Gouaux, 2000). As mentioned in the section above, channel gating occurs as a result of agonist binding (Armstrong and Gouaux, 2000). It has also been proposed that ligand-gated ion channels isomerize between closed and open states, with the binding of the ligand greatly increasing the probability of the receptor being in the open state by providing the energy necessary for the receptor to undergo conformational changes (Auerbach, 2013, 2015). AMPARs and KARs are thought to behave in a similar manner to one another, given their shared structural features.

For both AMPARs and KARs, the LBD dimers form the functional units of the receptor (Horning and Mayer, 2004; Mayer et al., 2006; Mayer, 2011), as the removal of the ATD still yields functional receptors (Pasternack et al., 2002; Matsuda et al., 2005; Du et al., 2005). Agonist docking results in the closure of the LBD clamshell (Armstrong and Gouaux, 2000; Du et al., 2005; Mayer et al., 2006; Du et al., 2008; Landes et al., 2011). This has been demonstrated in isolated AMPAR LBDs by crystal structures (Armstrong and Gouaux, 2000; Mayer et al., 2006) as well as fluorescence-based measurements (Du et al., 2008; Landes et al., 2011). In an intact receptor, where the LBDs are constrained by their adjacent domains (i.e. ATD and TMD), clamshell closure produces strain on the LBD dimer interface, which can be relieved by the upward motion of the D2 lobes, pulling on the LBD–TMD linkers to open the channel pore (i.e. activation) (Traynelis et al., 2010). Alternatively, the D1 lobes can move downward, thereby disrupting the integrity of the LBD dimer interface (Armstrong et al., 2006; Traynelis et al., 2010) (Figure 1–7).

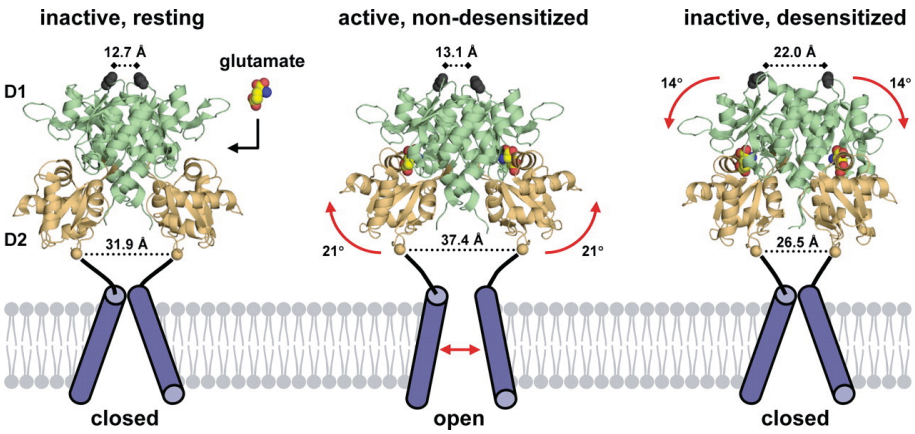

Figure 1–7: Conformational changes in AMPAR gating
Diagrams of the GluA2 LBD dimer corresponding the apo (resting) state (left, PDB # 1FT0) and the glutamate-bound active (PDB # 1FTJ) and desensitized (PDB # 2I3V) states. Figure taken from Traynelis et al. (2010).

Although this represents a simplification of channel gating, several lines of evidence are consistent with this general mechanism. For example, functional experiments using electrophysiology showed that mutations affecting the stability of the agonist-binding cleft reduced agonist efficacy/potency (Robert et al., 2005; Zhang et al., 2008; Weston et al., 2006a). Furthermore, the stabilization of the LBD dimer, either with an allosteric modulator or through mutations, is correlated with sustained channel activation in both macroscopic and single-channel experiments (Rosenmund et al., 1998; Smith et al., 2000a; Fucile et al., 2006; Prieto and Wollmuth, 2010; Nayeem et al., 2009; Stern-Bach et al., 1998; Sun et al., 2002; Gonzalez et al., 2010; Dawe et al., 2013). Indeed, the L507Y mutation in GluA2 is thought to increase the stability of the interface, thereby blocking receptor desensitization (Stern-Bach et al., 1998). CTZ is also thought to stabilize the dimer interface and reversibly blocks desensitization of AMPARs (Stern-Bach et al., 1998).

Additionally, several mutations in the GluK2 receptor also support this idea. For example, in the D776K substitution, the Lys residue acts as a surrogate cation

for the cation-binding pocket at the D1–D1 dimer interface (Nayeem et al., 2011), and this results in a non-desensitizing current (Nayeem et al., 2009; Dawe et al., 2013). The occupancy of the cation-binding pocket presumably stabilizes the LBD dimer interface, thereby preventing the channel from entering a desensitized state (Dawe et al., 2013). In contrast, the M770K mutation also acts as a surrogate cation but the occupancy of Lys770 in the cation-binding pocket is only partial (Nayeem et al., 2011). As a result, GluK2(M770K) channels are able to gate in the absence of external ions, but their activation is short-lived as desensitization occurs quickly when Lys770 ceases to occupy the cation-binding pocket (Wong et al., 2006, 2007; Nayeem et al., 2011; Dawe et al., 2013). The ion requirement for GluK2 gating will be further discussed below.

In the absence of allosteric modulators and in intact wild-type receptors, however, currents mediated by AMPARs and KARs are not sustained, but instead desensitize rapidly in the presence of agonist. Desensitization defines the transition of the receptors to an agonist-bound, not measurably conducting state. Structurally, this is thought to occur *via* the separation of the LBD dimer interface. In AMPARs, and especially in KARs, desensitization can be very profound, with receptor recovery rates ranging from sub-millisecond in GluA1 to tens of seconds in GluK2 (Bowie and Lange, 2002; Traynelis et al., 2010). This is different from deactivation, a process that can be thought of as the return of the receptor to the non-conducting apo state following the unbinding of the agonist. Deactivation and desensitization are very rapid for both recombinant AMPARs and KARs, occurring on the order of milliseconds or tens of milliseconds (Traynelis et al., 2010). Interestingly, native and heteromeric KARs exhibit slower deactivation kinetics (Bureau et al., 2000; Barberis et al., 2008); this will be further discussed in Chapter 2 of this thesis.

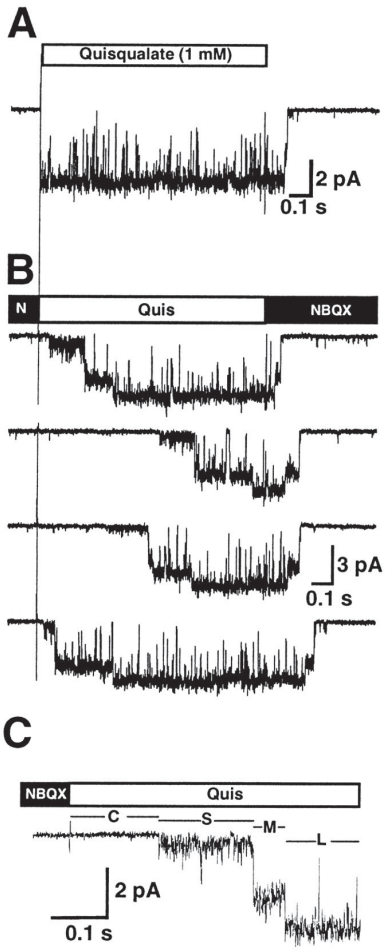

Figure 1–8: Conductance states in a non-desensitizing iGluR chimera
A, A single-channel recording from a GluK2/GluA3 chimera evoked by 1 mM quisqualate at a holding potential of -160 mV. B, Multiple responses jumping from the antagonist, NBQX, into the agonist, quisqualate. These jumps reveal intermediate a small, intermediate and large conductance states. C, Response from B on a different timescale. Modified from Rosenmund et al. (1998).

The binding of two agonist molecules is necessary for the channels to open (Clements et al., 1998). This was proposed by examining the activation kinetics of non-NMDARs in cultured hippocampal neurons and comparing them with gating models which had 1, 2 or 3 binding sites (Clements et al., 1998). Though this study could not determine the exact number of binding sites, Rosenmund and colleagues further developed this idea and suggested a tetrameric stoichiometry (Rosenmund et al., 1998). In this case, they built a non-desensitizing GluA3-GluK2 chimeric channel and studied single-channel responses (Rosenmund et al., 1998). To observe the rapid transitions between the 3 observed sub-conductance states, the agonist binding rate was slowed by imposing a much slower step, namely the unbinding of the high-affinity antagonist, NBQX (Rosenmund et al., 1998). The transition into the smallest conducting state occured with two time-constants, consistent with the idea that 2 molecules are necessary for activation, and the simplest explanation for the 3-conductance observation was therefore that these receptors are tetramers (Figure 1–8) (Rosenmund et al., 1998).

In AMPARs, the relative contribution of these conductance states is agonist-dependent, with higher conductances being more abundant in higher agonist concentrations (Rosenmund et al., 1998; Smith et al., 2000a). However, though the distribution of conductance levels in KARs does not appear to be agonist concentration-dependent, the results remain unclear due to the lack of pharmacological tools (such as CTZ for AMPARs) to remove desensitization (Smith et al., 2000a). These experiments could be performed with the non-desensitizing KAR mutant, D776K (Dawe et al., 2013).

1.3.2 The requirement for external ions

The gating properties of KARs, but not of AMPARs, are regulated by external cations and anions (Bowie, 2002; Paternain et al., 2003; Wong et al., 2006; Plested and Mayer, 2007; Wong et al., 2007; Plested et al., 2008; Dawe et al., 2013). Interestingly, AMPARs do seem to harbour the structural hallmarks of a cation-binding pocket, but in contrast with KARs, the occupancy of this pocket is not required for receptor activation (Wong et al., 2006; Dawe et al., 2016).

The first description of the phenomenon of ion sensitivity was published in 2002 (Bowie, 2002). In this study, it was discovered that ionic strength and species can modulate AMPAR and KAR peak responses (Bowie, 2002). However, in addition to this, the decay kinetics of KARs, but not of AMPARs, are also modulated by external ions (Bowie, 2002). Specifically, lowering the external ionic strength resulted in faster deactivation and desensitization rates of GluK2 receptors, while increasing it lead to slower decay kinetics (Bowie, 2002). Importantly, changing the chemical nature of the external ions (i.e. from Na^+ to Li^+ or Cs^+ and Cl^- to Br^- or F^-) also modulated the KAR gating properties (Bowie, 2002). Interestingly, both permeant and non-permeant cations and anions produce similar effects (Bowie, 2002). This phenomenon is voltage-independent and occurs only through external and not internal ions, suggesting that these ions are not influencing gating *via* the pore, but rather allosterically, through a site outside the membrane electric field (Bowie, 2002). A single methionine (Met) residue, at position 770 in GluK2, is critical for external ion modulation (Paternain et al., 2003). Mutating this residue to a Lys, as is found in AMPARs and NMDARs (i.e. GluK2 (M770K)), eliminates the modulation by external ions (Paternain et al., 2003; Wong et al., 2006). It was further demonstrated that external Na^+ ions are an absolute requirement for KAR gating and not simply allosteric modulators

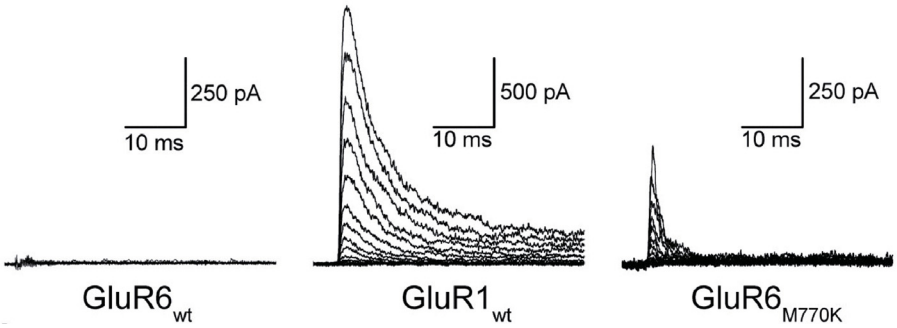

Figure 1–9: GluK2 KARs require external ions to gate
Membrane currents evoked by 1 mM L-Glu for GluK2 (GluR6, left), GluA1 (GluR1, middle) and GluK2 (M770K) (GluR6$_{M770K}$, right) at various holding potentials (range: -100 to +110 mV). Modified from Wong et al. (2006).

(Wong et al., 2006). Indeed, the removal of all external ions prevented the gating of GluK2, but not of GluA1 (Figure 1–9) (Wong et al., 2006).

Structural insight into the mechanism underlying the ion requirement came with the crystal structure of the GluK1 LBD dimer, to which an anion was bound (Plested and Mayer, 2007). A Cl^- or Br^- ion was found wedged at the interface between the two LBDs, interacting with residues in both protomers (Plested and Mayer, 2007). Non-stationary fluctuation analysis (NSFA) experiments suggested that external anion substitutions did not change the average unitary conductance of GluK2, but instead affected the number of receptors that were able to activate (Plested and Mayer, 2007). A separate study found that dimer interface mutants (GluK2(Y521C,L783C)), expected to hold the LBDs together during gating *via* a cross-dimer disulfide bridge, eliminated the ion requirement (Weston et al., 2006b). Taken together, these data strongly suggest that the Cl^- ions act at the dimer interface and hold it together.

Since the effects of cations and anions is similar in KARs (Bowie, 2002), and that single point mutations can abolish both effects, it was postulated that ion binding occurred through a dipole mechanism (Wong et al., 2007). Indeed, two cation-binding sites were identified at the LBD dimer interface, one for each protomer,

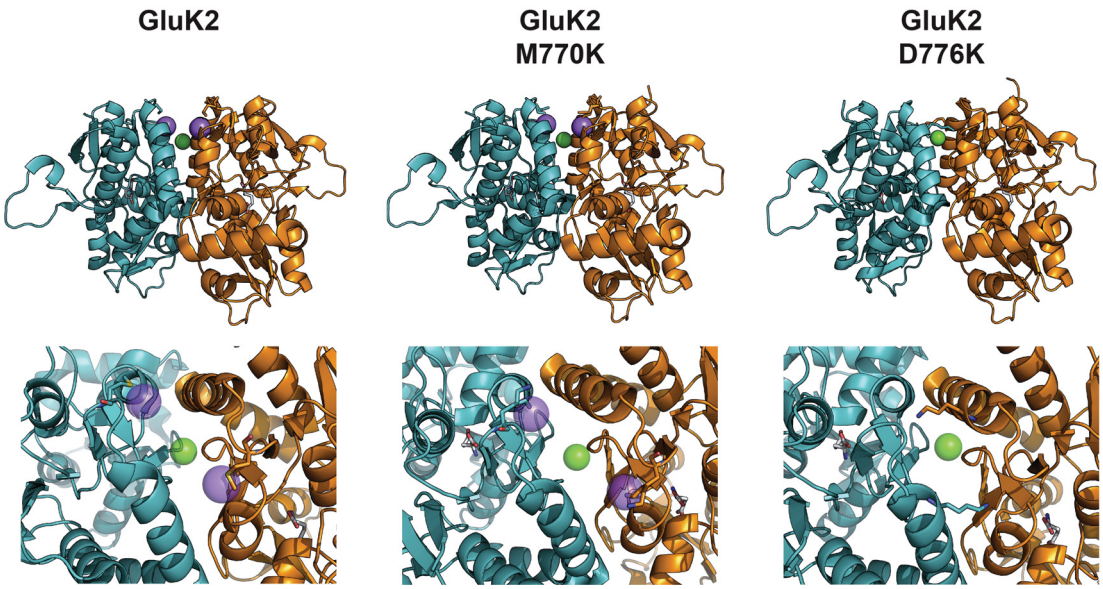

Figure 1–10: X-ray crystal structure of the wild-type and mutant GluK2 LBD
Top, Homodimeric structures from wild-type GluK2 (left, PDB # 2XXR), GluK2(M770K) (middle, PDB # 2XXU) and GluK2(D776K) (right, PDB # 2XXW). Bottom, Close-up of the ion-binding pocket (view from top), illustrating the position of the Met, Asp and Lys residues in relation with the Na^+ (purple ball) and Cl^- (green ball) monovalent ions.

with Na^+ being the optimal cation for these electronegative pockets (Plested et al., 2008). Interestingly, the Lys in GluK2(M770K) is acting as a tethered Rb^+ ion in terms of speeding the decay kinetics and eliminating anion sensitivity (Wong et al., 2007). Given that the larger Rb^+ ion has a much lower affinity for the cation-binding site compared to Na^+ (Plested et al., 2008), this provides a likely explanation for the behaviour of GluK2(M770K). Another GluK2 mutant, GluK2(D776K), was also found to relieve the ion requirement through a tethered charge in the cation-binding pocket (Nayeem et al., 2011; Dawe et al., 2013). The difference between these two "tethered charge" mutants is that the occupancy of the cation-binding pocket by the Lys in GluK2(M770K) is partial and short-lived, and maintained in GluK2(D776K) (Nayeem et al., 2011; Dawe et al., 2013).

An important observation was that the GluK2(D776K) substitution also rendered GluK2 non-desensitizing (Nayeem et al., 2009; Dawe et al., 2013).

Surprisingly, however, they also found that the macroscopically non-desensitizing double-cysteine mutant, GluK2(Y521C,L783C) (Weston et al., 2006b; Plested et al., 2008), could not sustain activation at the single-channel level as the GluK2(D776K) did (Dawe et al., 2013). Therefore, cross-linking the LBD dimer interface does not allow the receptor to fully activate, and the conformational restrictions probably do not allow them to desensitize.

Using these mutants as tools, the authors proposed a mechanism for activation and desensitization that was ion-dependent (Dawe et al., 2013). Briefly, external cations and anions are required for KAR activation. Desensitization occurs when the receptor is agonist-bound but cation-unbound (i.e. in the absence of external ions or if the cations unbind during a prolonged agonist application), while deactivation occurs when the receptor is cation-bound and the agonist unbinds (Dawe et al., 2013). The role of the ions is to maintain the LBD dimer together, and their unbinding promotes the separation of the LBDs (Dawe et al., 2013). Despite this being the case for the GluK2(Y521C,L783C) mutant, the positioning and lack of flexibility of the dimer interface is sufficient to relieve the ion requirement but not optimal for sustained activation (Dawe et al., 2013).

Although there is much less known about the ion sensitivity in heteromeric KARs, this will be discussed in Chapter 2 of this thesis. As mentioned in an earlier section, the ion sensitivity of KARs seems to be limited to homomeric channels. However, functional evidence shows that Li^+ ions, but not larger monovalent cations, are able to regulate the time-course of GluK2/GluK5 activation, suggesting that there may be structural similarities between the LBD dimer interface of GluK2/GluK5 and GluA2 receptors (see Chapter 2 and Discussion) (Dawe et al., 2016).

1.3.3 Polyamine block

1.3.3.1 Polyamines

Polyamines are organic non-protein cations containing two or more charged amine groups. In mammals, the naturally-occurring polyamines are putrescine (Put), spermidine (Spd) and spermine (Spm), with the most abundant being Spd and Spm (Pegg and McCann, 1982; Pegg, 2009). The synthesis pathway for these polyamines is well established and tightly regulated (Pegg, 2009), and imbalances in the synthesis or catabolism of polyamines lead to a variety of disorders, such as cancer (Nowotarski et al., 2013) and Snyder-Robinson Syndrome (SRS) (Snyder and Robinson, 1969; Cason et al., 2003). Polyamines are found in high concentrations in mammalian cells and are involved in a large number of cellular processes (Pegg, 2009). Given their cationic nature, they interact with negatively charged domains of biomolecules (Tabor and Tabor, 1984), including the pore regions of cation-selective ion channels, where they bind with micromolar affinity and hinder ion flow (Lopatin et al., 1994; Bowie and Mayer, 1995; Gomez and Hellstrand, 1995; Haghighi and Cooper, 1998; Lu and Ding, 1999; Kerschbaum et al., 2003; Fu et al., 2012). In this capacity, cytoplasmic polyamines are recognized as important determinants of neuronal signaling by regulating action potential firing rates (Fleidervish et al., 2008) as well as the strength of neurotransmission (Rozov and Burnashev, 1999; Aizenman et al., 2002). The following section will focus on the channel block by polyamines in non-NMDARs.

1.3.3.2 Channel block

Polyamine block of AMPARs and KARs is voltage-dependent and is displayed as the inward rectification of the current-voltage relationship (Bowie and Mayer (1995) and Figure 1–11). Polyamines are considered to be permeant channel blockers due to

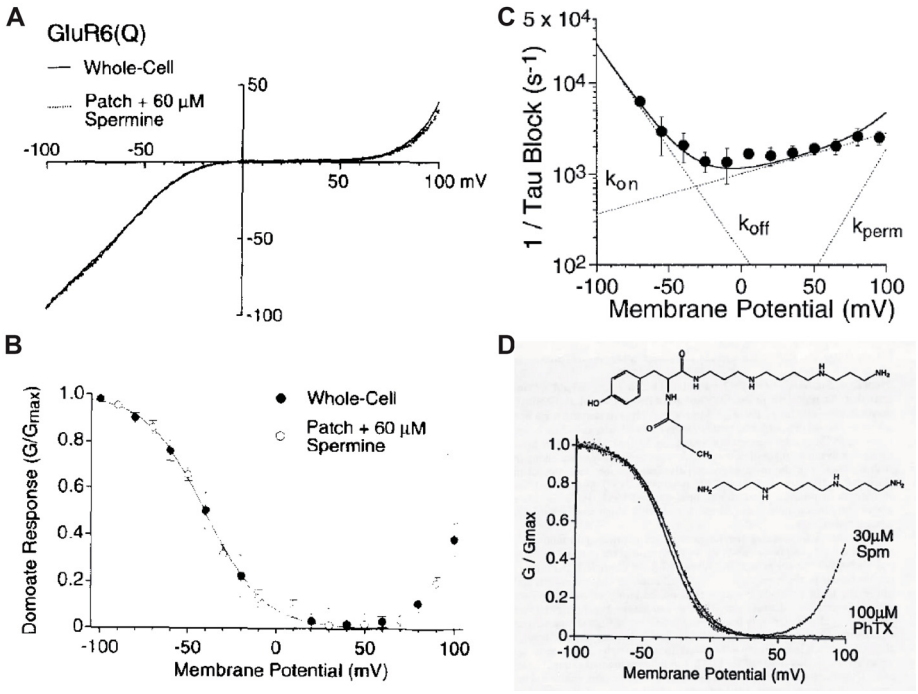

Figure 1–11: Block of GluK2(Q) by intracellular polyamines
A, Example electrophysiological recordings comparing I–V ramps (range: ± 100 mV) in HEK293 cells expressing GluK2(Q) (formerly GluR6(Q)) in the whole-cell configuration or in the outside-out patch configuration, for which 60 µM Spm was included in the patch pipette. 50 µM domoate was used as the agonist and voltage ramps were measured at the steady-state current. B, G–V plot for the data in A, fit with the Woodhull equation, estimating the free intracellular spermine concentration to be 62.1 µM. C, Polyamine block rates in GluK2(Q) in the presence of 20 µM $Spm_{(i)}$ as described by a single binding site model. According to the rate estimates of this model, polyamine permeation occurs at more positive membrane potentials. D, Relief of block at positive membrane potentials varies with the molecular size of the blocker (inset shows the chemical composition of Philanthotoxin-343 (PhTX, top) and spermine (Spm, bottom). G–V plots for GluK2(Q) with Spm or PhTX demonstrate relief of block due to the permeation of Spm but not of the much larger PhTX. Modified from Bowie and Mayer (1995) (A, B), Bowie et al. (1998) (C) and Bowie et al. (1999) (D).

their ability to both block and pass through the ion permeation pathway of cation-selective ion channels (Bowie et al., 1999). In the case of AMPARs and KARs, the degrees of polyamine block and permeation vary with the cross-sectional width and length (i.e. number of charges) of polyamines (Bowie and Mayer, 1995; Bahring et al., 1997). For almost all ion channels, cytoplasmic polyamine block is observed at negative and physiologically relevant membrane potentials, making it an ideal regulator of cellular excitability (Nichols and Lopatin, 1997; Bowie et al., 1999; Lu, 2004; Baronas and Kurata, 2014). In contrast, polyamine permeation occurs at extreme (>+50 mV) positive membrane potentials (Bahring et al. (1997) and Figure 1–11 C) and therefore has not been considered particularly significant. However, as will be discussed in Chapters 3 and 4 of this thesis, polyamine permeation also occurs at physiologically relevant membrane potentials when the ion channels are associated with auxiliary proteins. Given the relationship between block and permeation, the fraction of channels blocked by polyamines at any given membrane potential is the sum of these two opposing mechanisms.

The dynamics of this block were first described following a model for permeant ion blockers, a model developed to describe the voltage-dependent block of Na^+ channels by H^+ ions (Woodhull, 1973; Bahring et al., 1997). This model assumes that the ion blocker, H^+ ions in the case of the Na^+ channel, is able to permeate through the same pathway as the permeant ion, Na^+ , but that the energy barrier for H^+ to exit the pore is much larger than that for Na^+ (Woodhull, 1973). The same principle can be applied to polyamines (Bahring et al., 1997). The following simple model, based on the Woodhull model for permeant ion blockers (Woodhull, 1973), describes the relationship of the polyamine blocker (X) in relation to its binding site, with rates of onset of block (k_{on}), unbinding (k_{off}) and permeation (k_{perm}) (Bowie et al., 1998).

$$X_{in} \underset{k_{off}}{\overset{[B]k_{on}}{\rightleftharpoons}} X_{site} \overset{k_{perm}}{\rightleftharpoons} X_{out}$$

The probability for any given channel to not be blocked is estimated as the sum of exit rates (i.e. unbinding and permeation) divided by the sum of all rate constants. The contribution of each rate constant is illustrated in Figure 1–11 C. The fitting of G–V plots, as shown in Figure 1–11 B and D, with equations derived from this model provides critical information about the relationship between the pore and the blocker, such as the affinity of the blocker for its binding site and its relative position in the membrane electric field (Woodhull, 1973; Bahring et al., 1997). Using the Eyring rate theory to model polyamine block at equilibrium, it was initially estimated that there were two binding sites and three energy barriers (Bahring et al., 1997). However, estimating the rate constants directly, by using voltage steps in the presence of polyamines and observing blocker-induced decay with first-order kinetics, was consistent with one single binding site (Bowie et al., 1998). Although blocker permeation has been experimentally demonstrated with the observation of inward currents evoked in solutions where polyamines were the only external permeant cation (Bahring et al., 1997), the assumption remained that polyamines, like H^+ ions at Na^+ channels (Woodhull, 1973), did not contribute significantly to the overall current flowing through the channel. However, as will be discussed in Chapters 3 and 4 of this thesis, auxiliary proteins facilitate polyamine permeation through the channel pore and change the dynamics of channel block and permeation. In such cases, polyamines may contribute a significant conductance through the channel, causing an interaction with Na^+ permeation, which is especially visible at positive membrane potentials.

1.3.3.3 Q/R editing

Multiple residues along the pore have been shown to influence polyamine block (Wilding et al., 2010), and one of the best known is the Q/R site, which is found at the apex of the channel pore (Sobolevsky et al., 2009). This substitution abolishes polyamine sensitivity (Bowie and Mayer, 1995; Koh et al., 1995) and Ca^{2+} permeability (Köhler et al., 1993; Burnashev et al., 1995; Burnashev, 1996). The relationship between divalent permeability, polyamine block and editing state of the Q/R site has been ratified by extensive work on the AMPAR subunit GluA2, where the vast majority (>99%) of neuronal transcripts are in the edited form (Sommer et al., 1991).

Interestingly, RNA editing is limited to the AMPAR GluA2 subunit and the KAR GluK1 and GluK2 subunits (Sommer et al., 1991; Seeburg, 1993). While GluA2 is found almost exclusively in the edited (R) form (Sommer et al., 1991), editing of the KAR subunits is "incomplete" and developmentally-regulated (Bernard et al., 1999). For example, while the editing of the GluK1 and GluK2 subunits is 10% and 32% in the embryonic hippocampus, these levels increase to 50% and 90% in adulthood (Bernard et al., 1999). This amino acid substitution does not alter the functionally-measured pore size, which indicates that AMPARs and KARs may have a distinct selectivity mechanism involving residue interactions with distinct energy barriers, but not necessarily changes in the pore diameter (Huettner, 2015). Additional RNA editing in GluK2 (i.e. GluK2(V,C,Q)) can also determine divalent permeability and polyamine sensitivity, and these sites are also regulated to different extents (Köhler et al., 1993).

1.3.3.4 Relief of channel block

The degree of polyamine block is dynamically regulated, with two of the most prevalent mechanisms occurring through receptor subunit composition or by receptor association with auxiliary proteins (Perrais et al., 2010; Cull-Candy et al., 2006; Jackson and Nicoll, 2011). In KARs, polyamine block is relieved by the formation of heteromers that contain the GluK4 or GluK5 subunits (Barberis et al., 2008). In both AMPARs and KARs, the inclusion of edited subunits alleviates block (Bowie and Mayer, 1995; Kamboj et al., 1995; Donevan and Rogawski, 1995; Isa et al., 1995). In addition, relief of block can also occur through their co-assembly with auxiliary proteins, such as Neto1 and Neto2 for KARs (Fisher and Mott, 2012) and TARPs or CNIHs for AMPARs (Soto et al., 2007, 2009; Coombs et al., 2012). In both cases, the proximal regions of the C-terminal domains of the auxiliary proteins were found to be critical for their effect (Fisher and Mott, 2012; Soto et al., 2014).

Until recently (see Chapter 3), the mechanism underlying the attenuation of block at GluK2/GluK5 heteromers was still unknown (Barberis et al., 2008). The role of heteromerization, as well as the association of the ion channels with auxiliary proteins, in regulating polyamine block will be briefly discussed in the following sections and examined in further detail in Chapters 3 and 4 of this thesis.

1.3.4 Heteromerization

All the AMPARs subunits are able to form functional homomeric channels in recombinant systems, which have similar fast deactivation and desensitization kinetics (Traynelis et al., 2010). In contrast, only some of the KAR subunits (GluK1–3) can assemble in this way, and others (GluK4–5) must co-assemble with the former. At synapses, however, AMPARs and KARs are thought to exist as

heteromeric complexes (Seeburg, 1993; Wenthold et al., 1996; Fernandes et al., 2009; Lu et al., 2009).

1.3.4.1 AMPARs

Interestingly, Q/R editing of the GluA2 subunit also influences the assembly and favours heteromerization of AMPAR subunits (Traynelis et al., 2010). As previously mentioned, the presence of GluA2 subunits reduces Ca^{+} permeability and polyamine block (Burnashev et al., 1992; Geiger et al., 1995; Washburn et al., 1997). Additionally, noise analysis experiments showed that GluA2(Q)-containing AMPARs have a much lower single-channel conductance than GluA2-lacking (or GluA2(Q)-containing) AMPARs (Swanson et al., 1997b). At synapses, AMPARs display variable conductance levels (Vodyanoy et al., 1993; Smith et al., 2000b), something that may be attributed to the variable abundance of GluA2-containing receptors. The unitary conductance of synaptic AMPARs increases with LTP; this is thought to occur *via* a decrease in the number of GluA2-containing AMPARs and a concomitant increase in GluA2-lacking receptors (Benke et al., 1998). Subunit- and activity-dependent phosphorylation may also directly (and indirectly, by influencing assembly and trafficking) contribute to changes in the conductance of synaptic AMPARs (Malinow and Malenka, 2002; Traynelis et al., 2010).

1.3.4.2 KARs

While Q/R editing of the GluA2 subunit is critical in determining the function of synaptic AMPARs, editing of the KAR subunits is much less extensive and less well understood (Sommer et al., 1991; Puchalski et al., 1994; Schmitt et al., 1996). So far, only the GluK1 and GluK2 subunits were found to be edited to different extents and in a developmentally-regulated manner (Sommer et al., 1991; Seeburg, 1993; Bernard et al., 1999). It has yet to be tested whether the Q/R site of other

KAR subunits (i.e. GluK3–5) is edited or not. Similar to GluA2(R), GluK2(R) has a very low unitary conductance (Swanson et al., 1996).

At synapses, the assembly of primary and secondary KAR subunits appears to be a much more critical determinant of their functional properties. For example, heteromeric KARs containing GluK4 or GluK5 are responsive to AMPA and exhibit slower deactivation kinetics (Herb et al., 1992; Barberis et al., 2008; Fernandes et al., 2009; Mott et al., 2010). The secondary KAR subunits have a higher affinity for L-Glu than the primary subunits, and the dose-response curve for GluK2/GluK5 channels is left-shifted compared to that of homomeric GluK2 (Barberis et al., 2008; Mott et al., 2010; Fisher and Mott, 2011). The mechanisms underlying the unique gating properties of heteromeric channels are still emerging. For example, one possibility would be that the GluK4–5 subunits act merely as accessories, altering the responsiveness of the primary subunits, since it was thought that there were unable to gate (Figure 1–12 A) (Fisher and Mott, 2011). However, recent studies have supported an independent mechanism of activation, whereby both subunits contribute independently to the overall channel response (Swanson et al., 2002; Mott et al., 2010; Fisher and Mott, 2011). More specifically, GluK1–2 subunits are thought to be responsible for channel desensitization, while activation of the GluK4–5 subunits sustains channel activation (Mott et al., 2010; Fisher and Mott, 2011). Indeed, the specific activation of GluK4–5 subunits within KAR heteromers results in macroscopically non-decaying currents (Fisher and Mott, 2011). This was achieved pharmacologically (i.e. by blocking GluK2 with kynurenic acid or by using L-Glu concentrations that were too low to evoke currents in GluK2 homomers) and by introducing a point mutation in GluK2, E738D, which reduces the subunit's L-Glu affinity by 290-fold (Fisher and Mott, 2011). Interestingly, the initial evidence for this model suggested that GluK5 was

responsible for desensitizing the channel, because the application of L-Glu during a steady-state dysiherbaine current (DH, which binds with high affinity to GluK2) caused an initial fast current followed by a long-lived desensitization (Swanson et al., 2002).

The results from Chapter 2 of this thesis are consistent with an independent model of activation for the KAR subunits, and also provide further information regarding the specific gating contributions of each subunit. Based on these findings, I propose that each of the subunits is able to gate independently, but that the concerted activation of all four subunits leads to desensitization (Figure 1–12 C) (Fisher and Mott, 2011).

For GluK2 receptors, structural and functional evidence indicates that the time-course of activation and desensitization is controlled by external ions, which interact with the homomeric LBD interface (Wong et al., 2006, 2007; Plested et al., 2008; Nayeem et al., 2009, 2011; Dawe et al., 2013). However, the sensitivity of heteromeric KARs to external cations (Paternain et al., 2003) and anions (Plested and Mayer, 2007) is poorly understood. In Chapter 2 of this thesis, I report that the gating kinetics of GluK2/GluK5 heteromeric KARs is ion-independent and further suggest that there are important structural differences at the heteromeric LBD interface.

1.3.5 Auxiliary Proteins

The pore properties of synaptic AMPARs and KARs are modulated by auxiliary proteins, such as TARPs and CNIHs for AMPARs (Chen et al., 2000; Schwenk et al., 2009; Herring et al., 2013) and Netos for KARs (Zhang et al., 2009; Tang et al., 2011, 2012).

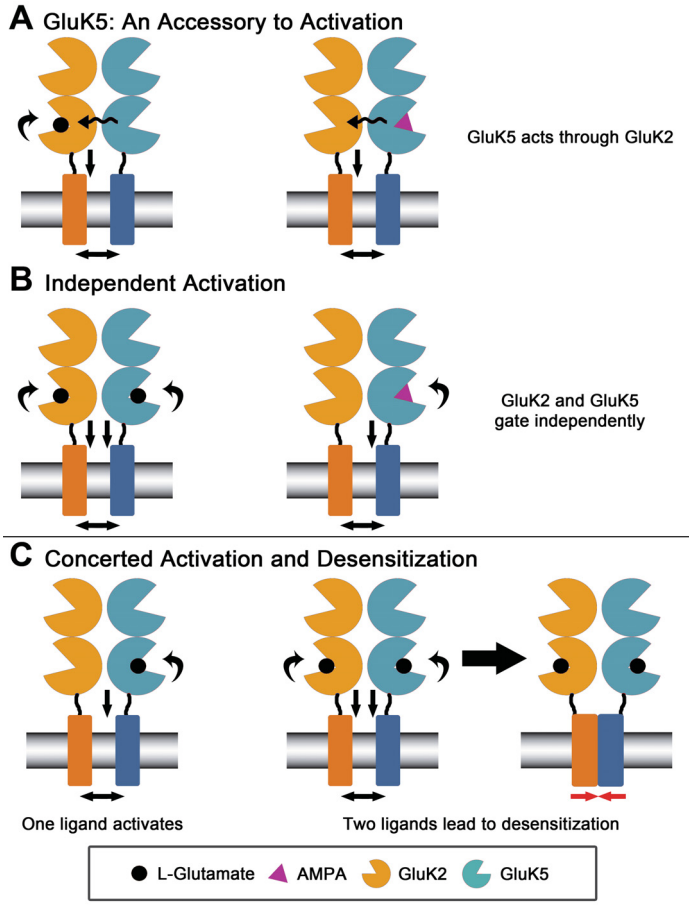

Figure 1–12: Gating models for heteromeric KARs
A, Accessory Model: GluK5 acts as an accessory to GluK2 gating, whereby GluK2 affects the gating response of GluK2 to glutamate. Also, the same model predicts that AMPA binding to GluK5 causes GluK2 to gate. B, Independent Model: GluK2 and GluK5 gate independently in response to agonist binding. C, Concerted Model: Despite both subunits being able to gate the channel independently, the simultaneous activation of both subunits results in desensitization. Black circles and magenta triangles represent L-glutamate and AMPA molecules, respectively. GluK2 and GluK5 subunits are represented by orange and cyan symbols. This model illustrates a single dimer from the KAR tetramer.

1.3.5.1 AMPARs

One of the hallmark effects of auxiliary proteins on the AMPARs is that they slow their desensitization kinetics and cause an increase in the steady-state current (Priel et al., 2005; Coombs et al., 2012). The TARP γ2 increases the unitary conductance and ion permeability of Ca^{2+}-permeable AMPARs (Soto et al., 2014). Results regarding the effect of γ2 on Ca^{2+} permeability are conflicting, with the first study showing no shift in reversal potential in high Ca^{2+} (Soto et al., 2007) while the other showed a significant increase in the relative Ca^{2+} permeability (Coombs et al., 2012). In addition, the presence of γ2 alleviates polyamine block (Soto et al., 2007). CNIH-3 also shifts polyamine block of GluA1 channels, albeit to a lesser extent than γ2 (Coombs et al., 2012). While CNIH-2 was shown to increase the Ca^{2+} permeability of GluA1, this has not been tested for CNIH-3 (Coombs et al., 2012). In both cases, the proximal residues of the auxiliary protein C-terminal regions are critical for these changes in the pore properties (Shanks et al., 2014; Soto et al., 2014), but the exact mechanism by which this occurs remains unclear. In Chapter 4 of this thesis, I demonstrate that the auxiliary proteins, γ2 and CNIH-3, increase polyamine permeation through the channel pore.

1.3.5.2 KARs

A similar phenomenon has been reported with KARs and their auxiliary proteins. For example, Neto2 also slows the decay kinetics and increases the steady state current of GluK2 (Zhang et al., 2009), as well as GluK1- and GluK5-containing channels (Straub et al., 2011). However, in GluK2, it does not achieve this by increasing the unitary conductance, but rather by significantly increasing the burst length and open probability (Zhang et al., 2009). Both Neto1 and Neto2 alter the L-Glu sensitivity of GluK1 and GluK5 in a subunit-dependent

manner (Fisher, 2015). In GluK2, both auxiliary proteins relieve polyamine block without affecting divalent permeability (Fisher and Mott, 2012). Interestingly, similar to the TARPs and CNIHs, the positively-charged proximal C-tail residues of the Netos are also critical for this effect and they are proposed to act in a charge-screening mechanism (Fisher and Mott, 2012). In Chatper 3 of this thesis, I also demonstrate that Neto2 facilitates polyamine permeation through the channel pore, though the structural mechanism remains unknown.

1.4 Rationale and Objectives

The goal of my thesis work is to understand how the different components of AMPA and kainate receptors affect their functional properties. In order to gain understanding of the gating of synaptic receptors, I focused on heteromeric receptors, and receptors that are in complexes with auxiliary proteins. The initial question was how each subunit within a heteromeric kainate receptor contributes to the gating and functional properties of the channel. Following this, we asked how subunit heteromerization itself, as well as receptor association with auxiliary proteins, relieve polyamine block of kainate and AMPARs.

Chapter 2

What are the specific contributions of the GluK2 and GluK5 subunits in a heteromeric KAR?

Early work on recombinant KARs described them as abundantly expressed and with fast kinetics, comparable to AMPARs (for example, Bowie (2002)). However, synaptic KAR-mediated responses are very small and generally much slower than AMPARs (Cossart et al., 2002). Synaptic KARs were already considered to be heteromeric complexes based on their localization (Seeburg, 1993; Bahn et al., 1994), and there were clues suggesting that the co-expression of certain subunits endowed the receptors with different functional properties. For example, GluK5-containing receptors are responsive to AMPA (Herb et al., 1992). It was discovered that a specific residue within the binding cleft of this subunit (N721 in GluK2) was responsible for the AMPA sensitivity (Swanson et al., 1997a), but since they could not form functional homomers, the mechanism through which AMPA binding could induce responses in heteromeric channels remained a mystery. An independent gating of the subunits was proposed, as the activation of specific

subunits produced different channel behaviours of activation and desensitization (Swanson et al., 2002; Mott et al., 2010; Fisher and Mott, 2011).

What causes synaptic KARs to have slow kinetics? When I started my thesis work, it had just been established that the co-expression of secondary subunits, GluK4 and GluK5, endowed the receptors with slow deactivation kinetics (Barberis et al., 2008; Fernandes et al., 2009). In order to characterize the molecular and structural mechanisms underlying the contribution of GluK5, I studied the functional properties of KAR heteromers formed of GluK2 and GluK5 subunits in a recombinant system. An ultra-fast solution exchange system, driven by a piezo-stack, was used to rapidly apply agonist solutions to outside-out patches, thereby mimicking synaptic neurotransmitter release. First, the functional properties of GluK2/GluK5 heteromers were tested under different agonist concentrations to reveal the GluK5 gating components. Next, since the decay kinetics of GluK2 are regulated by external ions, the ion-dependency of GluK2/GluK5 gating was tested. Finally, it has been proposed that the GluK5 subunits within heteromeric channels are non-desensitizing. To assess this, single-channel recordings of GluK2/GluK5 receptors were performed and a lower L-Glu concentration was used (300 µM) to reveal the gating of GluK5.

Chapter 3

How is polyamine block relieved in KARs that are heteromeric or associated with auxiliary proteins?

Recombinant KAR homomers are blocked by intracellular polyamines in a voltage-dependent manner (Bowie and Mayer, 1995; Bahring et al., 1997; Bowie et al., 1998). However, another characteristic of heteromeric KARs is that channel block is relieved, resulting in a much more linear I–V relationship (Barberis et al.,

2008). Interestingly, a similar relief of block is also observed when GluK2 homomers are co-expressed with the auxiliary proteins, Neto1 and Neto2 (Fisher and Mott, 2012). Positively-charged residues in the proximal region of the auxiliary protein C-terminal domains are believed to act as a charge screening mechanism to repel polyamines from the pore (Fisher and Mott, 2012). However, the mechanism underlying relief of block in GluK2/GluK5 heteromers remained unknown, and therefore, the aim of this chapter was to investigate this phenomenon. Electrophysiological recordings were combined with Molecular Dynamics to identify the molecular determinants underlying the relief of channel block.

Chapter 4

Do AMPAR auxiliary proteins facilitate polyamine permeation?

When investigating the polyamine block in KARs, we uncovered that the relief of block by auxiliary proteins occurred through a facilitation of polyamine permeation (Brown et al., 2016). Similar to KARs, the auxiliary proteins of AMPARs also relieve channel block (Soto et al., 2007; Coombs et al., 2012; Soto et al., 2014). The aim of this chapter was to assess whether polyamine permeation was also facilitated by the auxiliary proteins through AMPARs. Furthermore, we estimated the rates of polyamine block, unblock and permeation using a mathematical model.

CHAPTER 2
GATING CONTRIBUTIONS OF GLUK2 AND GLUK5 SUBUNITS IN HETEROMERIC KARS

Patricia M.G.E. Brown and Derek Bowie

To be submitted in modified form.

2.1 Foreword to Chapter 2

The study of recombinant AMPA and kainate receptors has been useful to characterize the functional properties of these channels and help establish a role for them in synaptic neurotransmission. However, the properties of recombinant KARs are different from synaptic KARs, something that can be attributed to subunit heteromerization (Barberis et al., 2008; Fernandes et al., 2009; Mott et al., 2010; Fisher and Mott, 2011; Fisher and Housley, 2013) and auxiliary proteins (Zhang et al., 2009; Tang et al., 2011; Fisher and Mott, 2012; Tang et al., 2012; Fisher, 2015).

When I first began my thesis work, our lab was interested in studying the biophysical properties of KARs, in order to gain a better understanding of their pre- and post-synaptic roles. For example, one of the main focus points was to identify the molecular basis of ion-dependent gating of GluK2 homomers. With this in mind, a potential role for KARs as sensors of changes in extracellular ion concentrations was proposed (Paternain et al., 2003; Plested et al., 2008; Bowie, 2010; MacLean, 2011). However, since it was becoming clear that native KARs were heteromers, I was motivated to study them, using a reductionist approach to gain insight into the molecular mechanisms underlying their gating.

GluK2 and GluK5 are the most widely expressed subunits (Petralia et al., 1994) and they form functional heteromers. One of the most prominent characteristics of GluK2/GluK5 KARs is their slow deactivation kinetics (Barberis et al., 2008). In this chapter, I report that the slow gating component in GluK2/GluK5 KARs are independently mediated by GluK5. As suggested by blocking the GluK2 component (Fisher and Mott, 2011), the specific activation of GluK5 subunits (i.e. using AMPA or 300 µM L-Glu) revealed slow deactivation kinetics. The time-course of GluK2 activation is regulated by external ions that

interact with the receptor at the dimer interface (Wong et al., 2006, 2007; Dawe et al., 2013). Although it has been observed that heteromeric KARs are less sensitive to ionic changes (Paternain et al., 2003), the results in this chapter show that the gating of GluK2/GluK5 is independent of external ions, suggesting that the heteromeric dimer interface is altered. Finally, previous studies have proposed a model in which GluK5 gating is non-desensitizing (Mott et al., 2010; Fisher and Mott, 2011). However, the single-channel records presented in this chapter suggest that specific GluK5 activation does not sustain channel opening, but rather allows the channels to re-open frequently after the agonist has been removed.

2.2 Abstract

Kainate receptors are modulators of synaptic transmission and are found at both pre- and post-synaptic sites. However, the kinetic properties of KAR-mediated EPSCs differ from those of recombinantly-expressed homomeric KARs. More recent evidence indicates that synaptic kainate receptors likely assemble as heteromeric complexes in combination with auxiliary proteins. In the hippocampus, the removal of the secondary (GluK4–GluK5) subunits abolishes KAR-mediated synaptic currents. Indeed, subunit composition is a critical determining factor for their functional and pharmacological properties. The most widely expressed KAR subunits, GluK2 and GluK5, assemble as heteromers with unique gating properties. Our data support that GluK5 subunits can gate independently and that the concerted activation of all subunits results in the desensitization of the channel. Furthermore, we find that the gating of GluK2/GluK5 KARs is ion-independent, suggesting that the LBD dimer interface is structurally altered compared to homomeric channels. Finally, GluK2/GluK5 receptors exhibit unique single-channel properties, with distinct behaviours that can be attributed to specific subunit types.

2.3 Introduction

Ionotropic glutamate receptors (iGluRs) mediate the vast majority of fast excitatory neurotransmission in the mammalian central nervous system (CNS). While AMPA- and NMDA-type iGluRs account for the majority of fast excitatory transmission, kainate-type (KARs) iGluRs are thought to act as neuronal circuit modulators (Frerking and Nicoll, 2000; Contractor et al., 2011). KAR-mediated EPSCs display slow kinetics at various synapses, and for this reason they are thought to play a role in synaptic integration (Castillo et al., 1997; Vignes and Collingridge, 1997; Frerking and Ohliger-Frerking, 2002).

Two separate gene families encode the five subunits that assemble to form the KAR tetramers. GluK1–GluK3 are considered to be the primary subunits because they can form functional homomeric and heteromeric channels. On the other hand, the secondary GluK4–GluK5 subunits form obligate heteromers with the primary subunits but are not functional as homomers (Cui and Mayer, 1999; Paternain et al., 2000). In native systems, KARs most likely assemble as heteromers since different subunits are often expressed in the same cells (Bahn et al., 1994; Seeburg, 1993). Additionally, the kinetic properties of KAR-mediated EPSCs are different from those of homomeric KARs (Castillo et al., 1997; Heckmann et al., 1996; Swanson et al., 2002). More recent knockout studies support that postsynaptic KARs function as heteromeric complexes composed of primary and secondary subunits (Fernandes et al., 2009; Fisher and Mott, 2011), with the most widely expressed subunits being GluK2 and GluK5 (Seeburg, 1993; Petralia et al., 1994; Barberis et al., 2008). In line with this, an increasing number of studies have focused on a more detailed investigation of the gating properties of such heteromeric KARs (Swanson et al., 2002; Barberis et al., 2008; Fernandes et al., 2009; Mott et al., 2010; Fisher and Mott, 2011; Straub et al., 2011).

The subunit composition of KARs has a profound effect on their functional properties. For example, heteromeric KARs containing GluK4 or GluK5 subunits exhibit unique biophysical and pharmacological properties, most notably in their responsiveness to AMPA and slower deactivation kinetics (Herb et al., 1992; Barberis et al., 2008; Fernandes et al., 2009; Mott et al., 2010). Though the mechanisms underlying the unique gating properties of heteromeric channels are still emerging, previous studies have supported an independent mechanism of activation, that is, that individual subunit types within a heteromeric complex can activate and contribute independently to the overall channel response (Swanson et al., 2002; Mott et al., 2010; Fisher and Mott, 2011). Specifically, GluK1–2 subunits are thought to be responsible for channel desensitization, while GluK4–5 subunits are responsible for sustained channel activation (Mott et al., 2010; Fisher and Mott, 2011). For GluK2 receptors, structural and functional evidence indicates that the time-course of activation and desensitization is controlled by external ions, which interact with the homomeric LBD interface (Wong et al., 2006, 2007; Plested et al., 2008; Nayeem et al., 2009, 2011; Dawe et al., 2013). Here, we report that the gating of GluK2/GluK5 heteromeric KARs is ion-independent, suggesting that there are important structural differences at the heteromeric LBD interface. Although our results are consistent with the independent subunit activation mechanism, we demonstrate that GluK5 does not sustain activation, but instead allows the receptor to open multiple times.

2.4 Methods

2.4.1 Plasmids and molecular biology

All experiments were performed using cDNA of rat GluK2 and GluK5 kainate-type ionotropic glutamate receptors. For electrophysiology, pRK5 plasmids containing the GluK2a(V,C,Q) and GluK5 cDNA each contained a downstream IRES sequence encoding mCherry and eGFP respectively, which were used to identify transfected cells.

2.4.2 Cell Culture and Transfection

HEK293T/17 cells (ATCC) were maintained in minimal essential medium (MEM) containing glutaMAX© supplemented with 10% fetal bovine serum (Invitrogen). Cells were plated at low density ($1.6 - 2.0 \times 10^4$ cells ml^{-1}) on poly-D-lysine-coated 35 mm plastic dishes and were transiently transfected 24 hours later using the calcium phosphate technique as previously described (Brown et al., 2016). A GluK2:GluK5 cDNA molar ratio of 1:10 was used for all co-transfections.

2.4.3 Electrophysiological recordings

Experiments were performed 36–48 h after transfection. Agonist solutions were rapidly applied to outside-out patches excised from transfected cells using a piezoelectric stack (Physik Instrumente, Auburn, MA, USA). Solution exchange (10–90% rise time of 250–350 μs) was determined in a separate experiment by measuring the liquid junction current. All recordings were performed using an Axopatch 200B (Molecular Devices, Sunnyvale, CA, USA) using thick-walled borosilicate glass pipettes (3–6 MΩ) coated with dental wax to reduce electrical noise. Current records were filtered at 5 kHz, digitized at 25 kHz and series resistance (3–12 MΩ) was compensated for by 95%. Recordings were performed at holding potentials of -20 or -60 mV. Data acquisition was performed using

pClamp9 or pClamp10 software (Molecular Devices) and tabulated using Microsoft Excel. All experiments were performed at room temperature.

All chemicals were purchased from Sigma-Aldrich (St Louis, MO, USA) unless otherwise indicated. External solutions contained (in mM) 150 NaCl, 5 HEPES, 0.1 $MgCl_2$ and 0.1 $CaCl_2$, pH 7.3–7.4. For ion substitution experiments, NaCl was replaced with LiCl, KCl, RbCl, CsCl, NaBr, NaF or NaI. The corresponding hydroxyde solutions (i.e. LiOH for LiCl) were used to adjust the pH. For experiments using 55 mM NaCl, sucrose was added to adjust the osmotic pressure to 295–300 mOsm and the internal solution remained the same. The internal solution contained (in mM) 115 NaCl, 10 NaF, 5 HEPES, 5 Na_4BAPTA (Life Technologies, Invitrogen, Burlington, ON, Canada), 1 $MgCl_2$, 0.5 $CaCl_2$ and 10 Na_2ATP, pH 7.3–7.4. The osmotic pressure of all solutions was adjusted to 295–300 mOsm with sucrose. Concentrated (10× or 100×) agonist stock solutions were prepared by dissolving agonist [L-glutamate (L-Glu) or α-amino-3-hydroxy-5-methyl-4-isoxazolepropionic acid (AMPA) (Tocris, Ellisville, MO, USA)] in the appropriate external solution, adjusting the pH to 7.3–7.4, and stored frozen at −20 °C. Stocks were thawed on the day of the experiment and used to prepare agonist-containing external solutions.

2.4.4 Data analysis, fitting and statistics

Current responses were fit with multiple exponential functions using Clampfit9 or Clampfit10 software. Correlations between the components of deactivation and the AMPA / L-Glu current ratio were analyzed using Origin 7 (OriginLab). Data were illustrated using Origin 7 and Adobe Illustrator. Statistical analysis was performed using the statistical software, SPSS Statistics.

2.5 Results

2.5.1 GluK5 contributes slow deactivation kinetics

The functional properties of GluK2/GluK5 kainate receptors (KARs) were studied using outside-out patches excised from HEK293T cells transfected with the cDNA encoding for the GluK2 and GluK5 subunits. To characterize the decay kinetics of GluK2/GluK5 in the continued presence of agonist (from here on referred to as "desensitization kinetics"), patches were subjected to prolonged (250 ms) L-Glu applications (1 mM; Figure 2–1, left panels). As previously described (Bowie et al., 2003), desensitization kinetics for GluK2 homomers were best fit with a double-exponential function with fast and slow time constants of 6.3 ± 0.3 ms and 46 ± 8 ms (92 % and 8 % of peak for τ_1 and τ_2, respectively, $n = 27$ patches; Table 2–1). GluK2/GluK5 responses evoked by 250 ms L-Glu applications were also fit with double-exponential functions having similar amplitudes to those of GluK2 (Table 2–1). However, the time constants were faster in GluK2/GluK5 responses, with a τ_1 of 2.8 ± 0.1 ms and a τ_2 of 31 ± 7 ms (Table 2–1), suggesting that the rates into desensitization are faster for GluK2/GluK5 receptors. In addition, while GluK2 responses typically displayed a steady-state current at 250 ms that was significantly larger than baseline (0.36 % ± 0.08 % of peak response; t-test, $t(26) = 4.242$, $P = 0.000248$, $n = 27$ patches; Figure 2–1 A, left panel) (Bowie et al., 2003), GluK2/GluK5 responses returned to baseline with no residual current (t-test, $t(82) = -1.988$, $P = 0.0502$, $n = 83$ patches; Figure 2–1 B and C, left panels). Taken together, these data indicate that the rate and degree of desensitization are faster and more profound when the GluK5 subunit is present in the receptor complex.

To mimic synaptic conditions, 1 mM L-Glu was applied for 1 ms. Example responses for GluK2 homomers and GluK2/GluK5 heteromers are shown in Figure 2–1 (middle panels). As previously described (Barberis et al., 2008), GluK2/GluK5

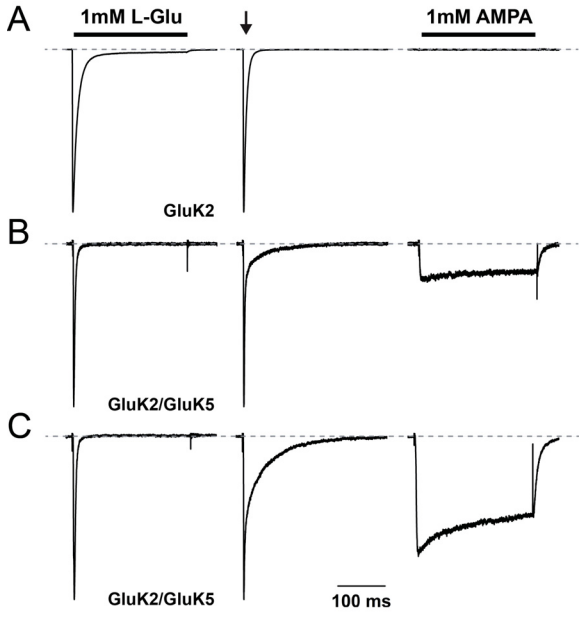

Figure 2–1: Recombinant GluK2/GluK5 KARs have variable kinetic and pharmacological properties
Example electrophysiological responses from GluK2 (A, patch # 100429p1) and GluK2/GluK5-containing (B and C, patches # 100330p4 and 111108p3, respectively) outside-out patches evoked by long (250 ms, left) and short (1 ms, middle) pulses of L-Glu (1 mM), as well as 250 ms pulses of AMPA (1 mM, right). Holding potential (Hp) = -20 or -60 mV.

heteromers displayed slow deactivation kinetics (i.e. the decay after the removal of the agonist) compared to GluK2 homomers. In addition, patches containing GluK2/GluK5 heteromeric receptors were responsive to α-amino-3-hydroxy-5-methyl-4-isoxazolepropionic acid (AMPA), while patches containing GluK2 homomers were not (Herb et al., 1992; Swanson et al., 1997a; Alt et al., 2004) (Figure 2–1, right panels). However, the deactivation kinetics and pharmacology of GluK2/GluK5 were variable between patches, as illustrated in Figure 2–1 B and C, where examples from two different GluK2/GluK5-containing patches are shown. Specifically, the overall deactivation rates of the L-Glu-evoked responses (left panels) and the AMPA responsiveness were different for each patch. The relationship between these functional properties were analyzed in greater detail in order to better understand the contribution of the individual subunit types.

Table 2–1: Desensitization kinetics of GluK2 and GluK2/GluK5

Receptor	$\tau_1 \pm$ SEM (ms)	%	$\tau_2 \pm$ SEM (ms)	%	n (patches)
GluK2	6.3 ± 0.3	92	46 ± 8	8	27
GluK2/GluK5	2.8 ± 0.1	92	31 ± 7	8	26

Desensitization kinetics represent current relaxations in the continued presence of 1 mM L-Glu (250 ms duration). Values are shown as mean ± SEM.

GluK2 deactivation responses were best fit with a double-exponential function with fast and slow time constants (τ_1 and τ_2) of 3.3 ± 0.2 ms and 21.1 ± 2.9 ms (3% of peak for τ_2, $n = 28$), respectively (Table 2–2 and Figure 2–2 A). In contrast, GluK2/GluK5 deactivation responses required an additional slower exponential component (τ_3, Figure 2–2 A) (Barberis et al., 2008). Interestingly, we found that while the time constant for this third component (τ_3) did not vary (linear regression, r = 0.0335, $P = 0.8984$, $n = 17$ patches), its relative amplitude (%A3) was positively correlated with AMPA responsiveness (defined as the AMPA / L-Glu ratio in a given patch; linear regression, $y = -2.54836 + 70.45256x$, r = 0.957, $P <$

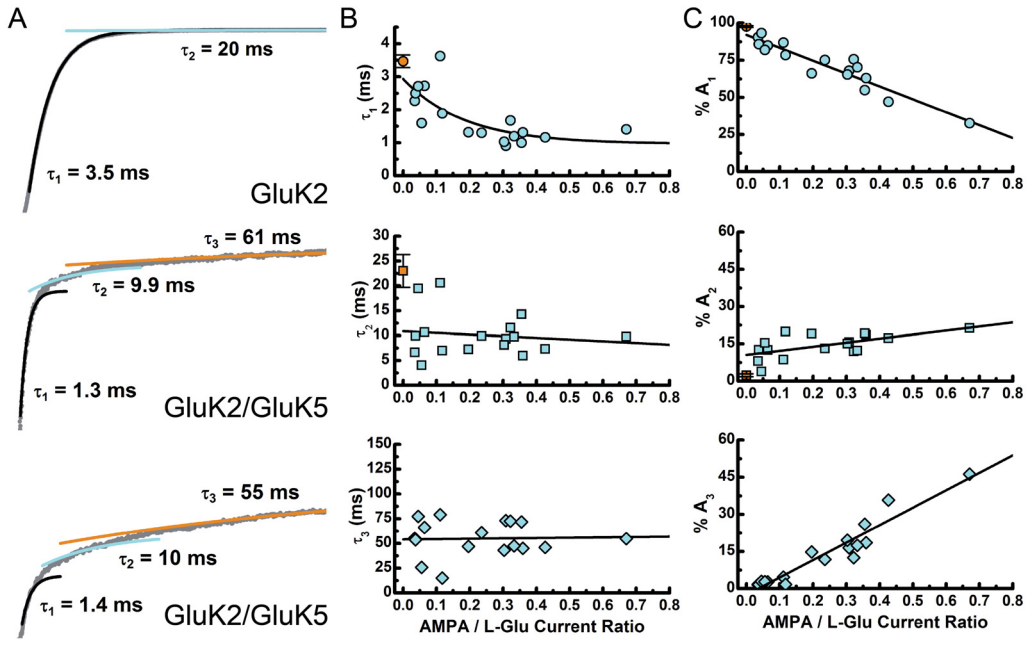

Figure 2–2: Exponential fits of GluK2 and GluK2/GluK5 deactivation
A, Exponential fits of the deactivation of GluK2 (top) and GluK2/GluK5 (middle and bottom) receptors after a 1 ms L-Glu (1 mM) pulse. Patches containing GluK2/GluK5 receptors required an additional slower exponential component (orange). B and C, Relationships between the exponential components (time constant, τ, B; relative amplitude, %A, C) and the AMPA/L-Glu current ratio obtained for individual GluK2/GluK5 patches (cyan data points). Exponential components for GluK2 receptors are shown in orange (mean ± SEM).

0.0001; Figure 2–2 B and C). Since the AMPA responsiveness can be directly related to the presence GluK2/GluK5 channels, this observation suggests that the additional slow exponential component corresponds to a specific gating contribution by the GluK5 subunit. Although the structural correlate of these exponential components remains unknown, they may represent the different gating modes or open states imparted by the individual subunits within the tetrameric complex. For example, while the fast component (τ_1) may represent an initial brief channel opening, the slowest component (τ_3) could be due to longer openings or channel re-openings. Figure 2–2 illustrates the correlation of each exponential component (τ; panel B) and its relative contribution (%A; panel C) with the AMPA responsiveness of a given patch.

As illustrated in Figure 2–2, the presence of GluK5 also had a significant impact on the intermediate (τ_2) and fast (τ_1) exponential components of deactivation. Similar to τ_3, there was no significant variation of the time constant for τ_2 with AMPA responsiveness in GluK2/GluK5 patches (linear correlation, r = -0.1341, $P = 0.6079$), but we did observe a significant positive correlation for %A2 (linear correlation, r = 0.6087, $P = 0.0095$; Figure 2–2). In contrast to τ_3, which is specific to the GluK5 subunit, τ_2 was present in both homomeric and heteromeric responses. However, the average τ_2 was significantly smaller for GluK2/GluK5 responses than for GluK2 responses (one-way ANOVA, $F_{2,63} = 12.29$, $P = 0.000031$, Bonferroni post-hoc pairwise comparisons, $P = 0.000062$; Table 2–2). These data suggest that the second exponential component, which is found in GluK2 responses, is modified by the presence of GluK5. It is unclear whether τ_2 represents a gating state incurred by GluK5, or whether GluK5 is directly influencing a state that exists in GluK2. Interestingly, we also found τ_2 to be faster in GluK2(M770K), an ion-insensitive mutant of GluK2, compared with the WT τ_2 ($P = 0.007$; Table 2–2).

Table 2–2: Deactivation kinetics of GluK2 and GluK2/GluK5

Receptor	$\tau_1 \pm$ SEM (ms)	%	$\tau_2 \pm$ SEM (ms)	%	$\tau_3 \pm$ SEM (ms)	%	n (patches)
GluK2	3.3 ± 0.2	97	21.1 ± 2.9	3	–	–	28
GluK2/GluK5	1.2 ± 0.1	44	9.7 ± 0.5	21	60 ± 2	35	35
GluK2(M770K)	1.1 ± 0.2	89	6.4 ± 0.7	11	–	–	5

Deactivation kinetics represent current relaxations back to baseline after a brief (1 ms) L-Glu pulse (1 mM). Values are shown as mean ± SEM.

Finally, the presence of GluK5 also significantly accelerated the fast time constant, τ_1, (exponential correlation, $r^2 = 0.5442$, $P = 0.0053$) while decreasing its relative amplitude (linear regression, r = -0.9398, $P < 0.0001$; Figure 2–2). Patches displaying a %A3 of over 30% were considered to be containing high levels of

GluK2/GluK5. In these patches, the mean τ_1 was significantly faster than that of GluK2 (one-way ANOVA, $F_{2,65} = 96.377$, $P = 3.59\text{E-}20$, Bonferroni post-hoc pairwise comparison, $P = 5.88\text{E-}20$; Figure 2–2 and Table 2–2). Interestingly, this fast time constant in GluK2/GluK5 was statistically indistinguishable from that of GluK2(M770K) ($P = 1.000$).

2.5.2 The slow component of deactivation is specific to GluK5

To identify the subunit responsible for the "ultra-fast" component of deactivation, outside-out patches were subjected to various concentrations of L-Glu. It has been proposed that GluK5 is the high-affinity, non-desensitizing subunit while GluK2 is the low-affinity, desensitizing subunit within the heterotetrameric channel (Fisher and Mott, 2011). Here, we used 0.3 mM L-Glu to preferentially activate GluK5 and 10 mM L-Glu to promote the activation of all four subunits (Barberis et al., 2008). The deactivation kinetics of currents elicited by 0.3 and 10 mM L-Glu were compared to those evoked by 1 mM L-Glu. The results from this experiment are shown in Figure 2–3 and Table 2–3.

As expected with GluK2 homomers, the current amplitudes of responses were strongly concentration-dependent (Figure 2–3 A). As before, responses were fit with double-exponential functions. Interestingly, although the time constants and their proportions were slightly affected by the L-Glu concentration (Figure 2–3 D, orange; Table 2–3, the overall deactivation kinetics did not change (Figure 2–3 A, Overlay and Table 2–3, weighted τ). The increase in τ_2 and its variability could be due to fitting an exponential with an extremely small relative amplitude ($\leq 1\%$ of the response) (Figure 2–3 and Table 2–3).

To probe GluK2/GluK5 receptors, responses were first assessed in 1 mM L-Glu and patches with high levels of heteromers (i.e. with a %A3 $\geq 30\%$) were subjected to the remaining L-Glu concentrations. In contrast to GluK2 homomers, GluK2/GluK5

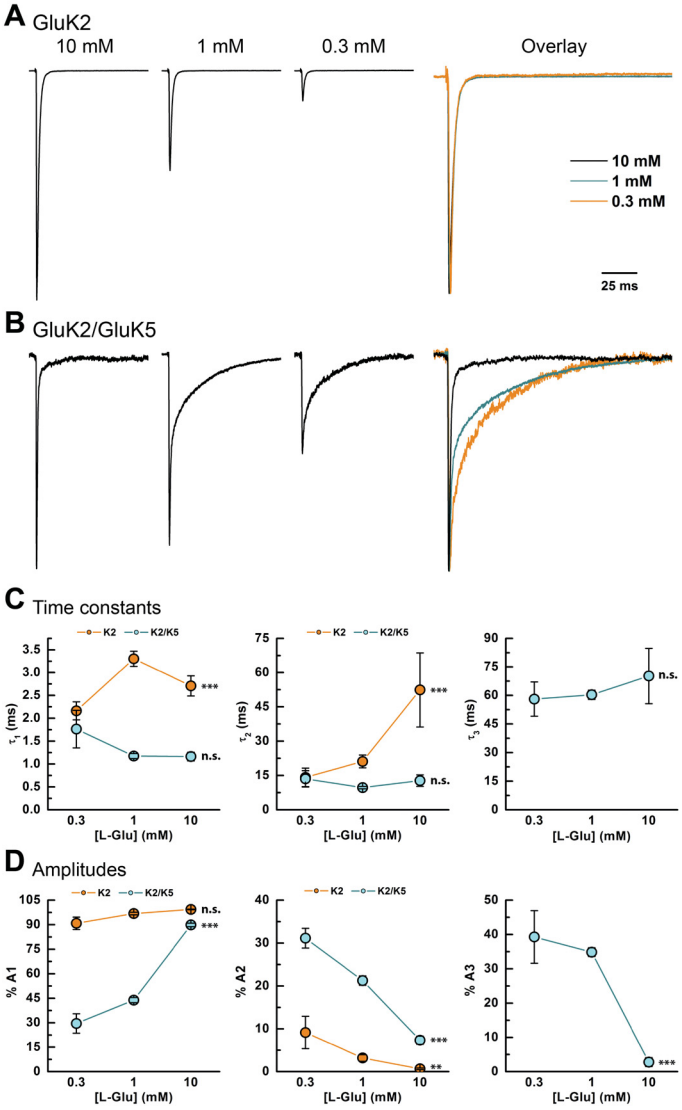

Figure 2–3: Deactivation kinetics of GluK2/GluK5 are glutamate-dependent
A and B, Example electrophysiological responses (A, GluK2, patch # 150316p3; B, GluK2/GluK5, patch # 121109p4) evoked by 10, 1 and 0.3 mM L-Glu (1 ms). Responses were standardized to the peak and the overlay is shown in the right panel. C and D, Each component of the multi-exponential fits of the deactivation (C, the time constants; D, the relative amplitudes) in relation to the L-Glu concentration, for GluK2 (orange) and GluK2/GluK5 (cyan). $**P < 0.01$, $***P < 0.001$, n.s. not significant.

peak responses were consistent with a shift in their apparent L-Glu affinity (Figure 2–3 B) (Barberis et al., 2008). Responses were fit with three exponential components, irrespective of L-Glu concentration (Figure 2–3 B). Interestingly, despite the obvious change in the deactivation kinetics (Figure 2–3 B, Overlay), the time constants for responses evoked by 10 and 0.3 mM L-Glu were not statistically different from those evoked by 1 mM L-Glu (2-way ANOVA, simple effects of Receptor at L-Glu; τ_1, $F_{2,85}$ = 2.117, P = 0.127); τ_2, $F_{2,79}$ = 0.256, P = 0.775; one-way ANOVA for τ_3, $F_{2,41}$ = 0.576, P = 0.566; Figure 2–3 C and Table 2–3). However, the relative amplitude of each component was greatly affected (2-way ANOVA, simple effects of Receptor at L-Glu; %A1, $F_{2,85}$ = 66.546, P = 4.06E-18; %A2, $F_{2,85}$ = 16.04, P = 0.000001; one-way ANOVA for %A3, $F_{2,42}$ = 22.718, P = 2.06E-7; Figure 2–3 D). Specifically, the relative contribution of the fastest exponential component, τ_1, became greater with higher L-Glu concentrations, going from 30% in 0.3 mM L-Glu to about 90% in saturating (10 mM) L-Glu (Figure 2–3 D and Table 2–3). Conversely, the relative contributions of the intermediate (τ_2) and slow (τ_3) components decreased with higher L-Glu concentration (Figure 2–3 D and Table 2–3). The effect of the L-Glu concentration on GluK2/GluK5 desensitization kinetics (i.e. with prolonged L-Glu applications) was similar, with the weighted τ being 5-fold larger in 0.3 mM compared to 10 mM L-Glu (Table 2–3). The desensitization kinetics of GluK2 were slightly slower with 1 mM L-Glu compared to 10 mM, but did not change any further with 0.3 mM L-Glu (Table 2–3).

As mentioned above, the fast component of deactivation of GluK2/GluK5 responses was akin to the fast deactivation of GluK2(M770K), which is thought to result from a change at the level of the LBD interface. Figure 2–4 A and B highlight the position of the ion-binding sites at the LBD dimer interface of GluK2 in an X-ray crystal structure (Nayeem et al., 2011). Since GluK2/GluK5

Table 2–3: Agonist dependence of KAR deactivation kinetics

	Deactivation kinetics								
Receptor	[L-Glu] (mM)	τ_1 ± SEM (ms)	%	τ_2 ± SEM (ms)	%	τ_3 ± SEM (ms)	%	Weighted τ (ms)	n (patches)
GluK2	10	2.7 ± 0.2	99	52 ± 16	1	–	–	3.0	7
	1	3.3 ± 0.2	97	21 ± 3	3	–	–	3.9	28
	0.3	2.2 ± 0.2	91	14 ± 4	9	–	–	3.3	11
GluK2/GluK5	10	1.2 ± 0.1	90	13 ± 2	7	70 ± 15	3	3.9	4
	1	1.2 ± 0.1	44	10 ± 1	21	60 ± 2	35	23.6	35
	0.3	1.8 ± 0.4	30	14 ± 4	31	58 ± 9	39	27.5	6
	Desensitization kinetics								
Receptor	[L-Glu] (mM)	τ_1 ± SEM (ms)	%	τ_2 ± SEM (ms)	%			Weighted τ (ms)	n (patches)
GluK2	10	3.9 ± 0.4	79	15 ± 5	21	–	–	4.8	7
	1	6.3 ± 0.3	92	46 ± 8	8	–	–	7.5	27
	0.3	5.6 ± 0.4	95	57 ± 16	5	–	–	7.1	12
GluK2/GluK5	10	1.5 ± 0.1	93	11 ± 3	7	–	–	2.0	3
	1	2.8 ± 0.1	92	31 ± 6	8	–	–	4.2	26
	0.3	7.5 ± 0.8	99	166 ± 54	1	–	–	9.9	3

heteromers assemble with a 2:2 fixed stoichiometry (Kumar et al., 2011; Reiner et al., 2012), we hypothesized that the dimer interface is formed as a heterodimer and predicted that the dependency of the heteromeric receptor to external ions should be altered.

2.5.3 Ion sensitivity is decreased in GluK2/GluK5

To test the ion sensitivity of GluK2/GluK5 receptors, outside-out patches were subjected to 1 mM L-Glu in the presence of various external ions, as previously done for GluK2 receptors (Figure 2–4) (Wong et al., 2006). Here, the relative peak amplitudes, the desensitization kinetics and the deactivation kinetics of GluK2- and GluK2/GluK5-containing patches were compared (Figure 2–4).

Example traces from GluK2 and GluK2/GluK5 responses from the same patch in three different external cations are illustrated in Figure 2–4 C. As previously shown (Paternain et al., 2003; Wong et al., 2006), the peak amplitudes of GluK2 (relative to responses obtained in 150 mM NaCl) were strongly dependent on the species of external ions (Figure 2–4 C and D). In addition, the desensitization kinetics (τ_1;

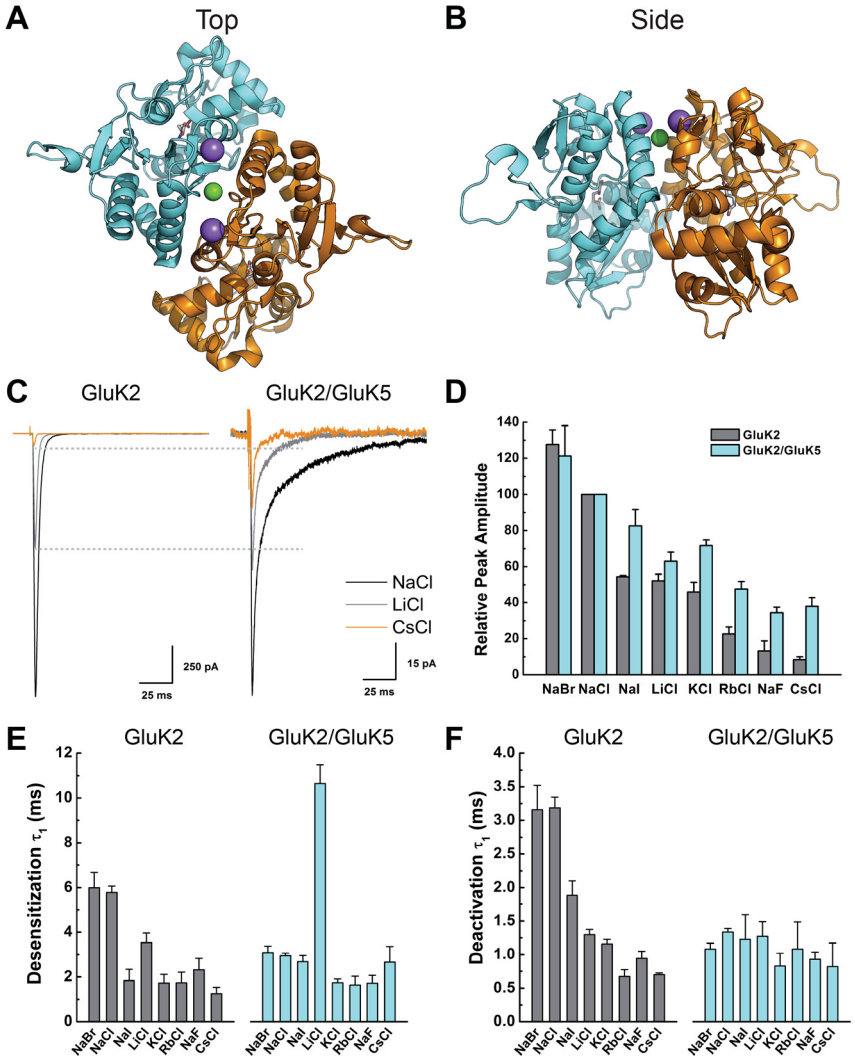

Figure 2–4: Ion sensitivity is decreased in GluK2/GluK5
A and B, Top and side views of the GluK2 LBD dimer (PDB # 2XXR) to illustrate the position of the ion-binding site. The Na^+ ions are in purple and the Cl^- ions are shown in green. L-Glu is illustrated as sticks. C, Example current traces from GluK2 (left, patch # 101126p2) and GluK2/GluK5 (right, patch # 110111p2) patches in the presence of external NaCl, LiCl and CsCl. D, Summary of the relative amplitudes for GluK2 (grey) and GluK2/GluK5 (cyan) in various external ions. All amplitudes are relative to NaCl. E and F, Summary of the fast component of desensitization kinetics (E) and of the deactivation kinetics (F) for GluK2 (grey) and GluK2/GluK5 (cyan) in various external ions.

Figure 2–4 E) and deactivation kinetics (τ_1; Figure 2–4 F) were generally faster in the presence of other monovalent cations and anions compared to the control Na^+ and Cl^- (present study and Wong et al. (2006)). Because the relative contribution of τ_2 was very low in GluK2 receptors, only τ_1 for the desensitization and deactivation kinetics of homomers and heteromers was used for this analysis.

Interestingly, GluK2/GluK5 peak responses were also affected by the species of external ions, but this effect was reduced (Figure 2–4 C and D), indicating that the presence of GluK5 attenuated the ion-dependency of the heteromeric receptor complex. Furthermore, the presence of variable amounts of homomeric GluK2 in heteromeric patches is likely to obscure the properties of pure GluK2/GluK5 receptor populations. Despite this, in stark contrast with homomeric GluK2 channels, the species of external cations and anions did not affect the fast component of the desensitization kinetics of GluK2/GluK5 responses (Figure 2–4 E), which were about 2-fold faster than GluK2 in 150 mM NaCl, as described above in Figure 2–2 and Table 2–1. One interesting exception was with LiCl, which resulted in a 3.5-fold slowing of the GluK2/GluK5 desensitization kinetics (Figure 2–4 E).

As described above, the deactivation τ_1 of GluK2/GluK5 in 150 mM NaCl was almost 3-fold faster than that of GluK2 (Figure 2–4 F). Additionally, this deactivation component was unaffected by a change in the species of external ions (Figure 2–4 F). The slower deactivation components, τ_2 and τ_3, could not be compared to any GluK2 equivalent and are therefore not reported here. Taken together, these results suggest that the fast component of gating in heteromeric KARs is not dependent on the species of external ions, a finding that is similar to the behaviour of the ion-insensitive GluK2(M770K) receptor (Wong et al., 2006).

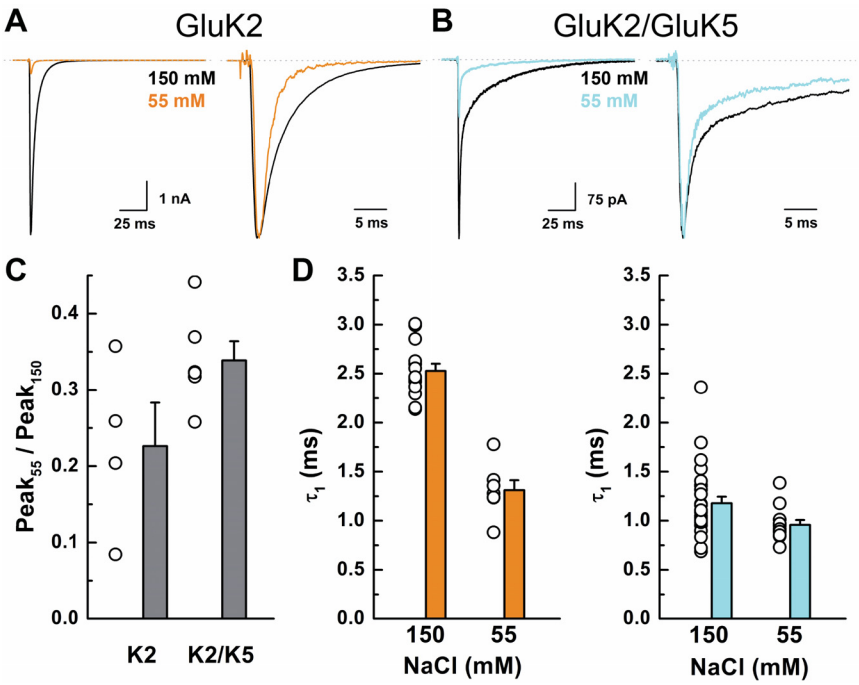

Figure 2–5: Sensitivity to ionic strength is reduced in GluK2/GluK5
A, B, Example L-Glu-evoked responses (1 mM, 1 ms) in 150 or 55 mM $NaCl_{(o)}$ for GluK2 (A, patch # 120911p2) and GluK2/GluK5 (B, patch # 111021p1). Responses in the left panels have been standardized to the peak. C, Summary of the peak ratio from 150 to 55 mM $NaCl_{(o)}$. D, Summary of the fast time constants of deactivation (τ_1) with GluK2 (left) and GluK2/GluK5 (right) in 150 or 55 mM $NaCl_{(o)}$. Columns are means and error bars are SEM.

In addition to being unaffected by the species of external ions, the desensitization kinetics of GluK2(M770K) are also independent of the external ionic strength (Wong et al., 2006). To test if this was also the case for GluK2/GluK5 receptors, outside-out patches were subjected to 1 mM L-Glu in the presence of 150 or 55 mM NaCl. The results from this experiment are summarized in Figure 2–5. For GluK2 receptors, peak current responses evoked in 55 mM NaCl were decreased, on average, to about 23% of the response in 150 mM NaCl (Figure 2–5 A and C). For GluK2/GluK5 receptors, this ratio was increased to about 34% (Figure 2–5 B and C), meaning that the decrease in the peak amplitude induced by lowering the ionic strength was not as pronounced. A two-tailed t-test was performed to evaluate whether the 55/150 mM current ratios were statistically different and yielded a P-value of 0.075 ($t(8)$ = -2.048). Although this difference was not different at the α-level of 0.05, the probability that they are the same is nevertheless very low. Given that GluK2/GluK5 patches most likely also contain some GluK2 homomers, we considered that the decrease in the current reduction that we observed in 55 mM NaCl was biologically relevant. With this, we concluded that lowering the NaCl concentration had a much lower effect on GluK2/GluK5 receptors than GluK2 homomers.

In addition to the decreased peak sensitivity to external ionic strength, we also noted a difference in the kinetic behaviour of GluK2/GluK5. Specifically, when subjected to 55 mM NaCl, the deactivation kinetics GluK2 responses were accelerated by almost 2-fold (Figure 2–5 D), going from a τ_1 of 2.50 $\pm$ 0.07 ms (n = 13) to 1.31 $\pm$ 0.10 ms (n = 7) in 150 and 55 mM NaCl, respectively. In contrast, the fast deactivation kinetics for GluK2/GluK5 were much less sensitive to the reduction in the ionic strength (Figure 2–5 D), with a τ_1 of 1.18 $\pm$ 0.07 ms (n = 27) and 0.96 $\pm$ 0.05 ms (n = 12) in 150 and 55 mM NaCl, respectively. A two-way ANOVA performed on the data revealed a significant interaction of the receptor

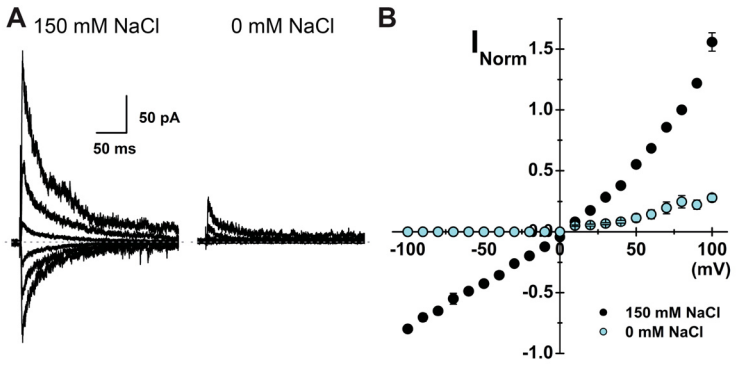

Figure 2–6: External ions are not required for GluK2/GluK5 gating
A, Example GluK2/GluK5 responses at various membrane potentials (range: -100 to +100 mV, 10 mV increments) in the presence (left) or absence (right) of external ions. B, Summary I-V plots for GluK2/GluK5 in the presence (black circles) or absence (cyan circles) or external ions ($n = 4$ patches). Data are shown as mean and SEM.

type and NaCl concentration ($F_{1,55} = 31.752$, $P = 6.2\text{E-}7$). A simple main effect analysis indicated that NaCl concentration had an effect at both receptor types ($F_{1,55} = 73.823$ (GluK2) and 4.569 (GluK2/GluK5); $P = 9.6\text{E-}12$ (GluK2) and 0.037 (GluK2/GluK5)). However, the estimated effect size (η^2) of NaCl concentration was much smaller for GluK2/GluK5, with η^2 values of 0.573 and 0.077 for GluK2 and GluK2/GluK5, respectively, indicating that the sensitivity of heteromeric KARs to ionic strength was reduced. Again, we considered that the presence of GluK2 contaminants could be skewing the results and that pure GluK2/GluK5 receptor populations would most likely be very mildly, if at all, affected by ionic strength.

Given the reduction in the ion sensitivity of patches containing high levels of GluK2/GluK5, we hypothesized that GluK2/GluK5 receptors themselves may be ion-insensitive and ion-independent. To test this, patches were subjected to 1 mM L-Glu in the absence of external anions and cations (Figure 2–6), as previously tested with GluK2 homomers (Wong et al., 2006; Dawe et al., 2013). In contrast with GluK2 receptors (Wong et al., 2006; Dawe et al., 2013), outward currents were elicited from

GluK2/GluK5 patches by 1 mM L-Glu in ion-free external solution (Figure 2–6, 0 mM NaCl). The reduction in the current amplitude compared to those evoked in the presence of 150 mM NaCl can be explained by the elimination of the contribution of GluK2 homomers within the patch, since they do not respond to L-Glu in the absence of external ions. These results demonstrate that GluK2/GluK5 receptors are functional in the absence of external ions, and thus that their gating is ion-independent.

2.5.4 GluK5-containing receptors have unique single-channel gating properties

External ions play an important role in the activation and desensitization of homomeric GluK2 channels (Wong et al., 2006, 2007; Dawe et al., 2013). Specifically, it is thought that the occupancy of the ion-binding pocket is critical for activation, and that subsequent unbinding of the cation while the agonist remains bound results in the desensitization of the channel (Dawe et al., 2013). Consistent with this, a mutation providing a surrogate cation in the ion-binding pocket (Nayeem et al., 2011), Asp776Lys (D776K), abolishes desensitization of GluK2 at the macroscopic and single-channel levels (Dawe et al., 2013). In contrast, the formation of a disulfide bridge to strengthen the LBD interface interactions, namely by introducing cysteine (Cys) residues at positions 521 and 783 of GluK2 (GluK2(Y521C/L783C)), hinders the activation of GluK2 and locks it out of the main open state (Dawe et al., 2013). Both receptors are able to gate in the absence of external ions (Dawe et al., 2013). Given the similarities between the macroscopic properties of these GluK2 mutants and GluK2/GluK5 receptors, we performed single-channel experiments to gain insight into the microscopic gating mechanisms governing heteromeric KARs.

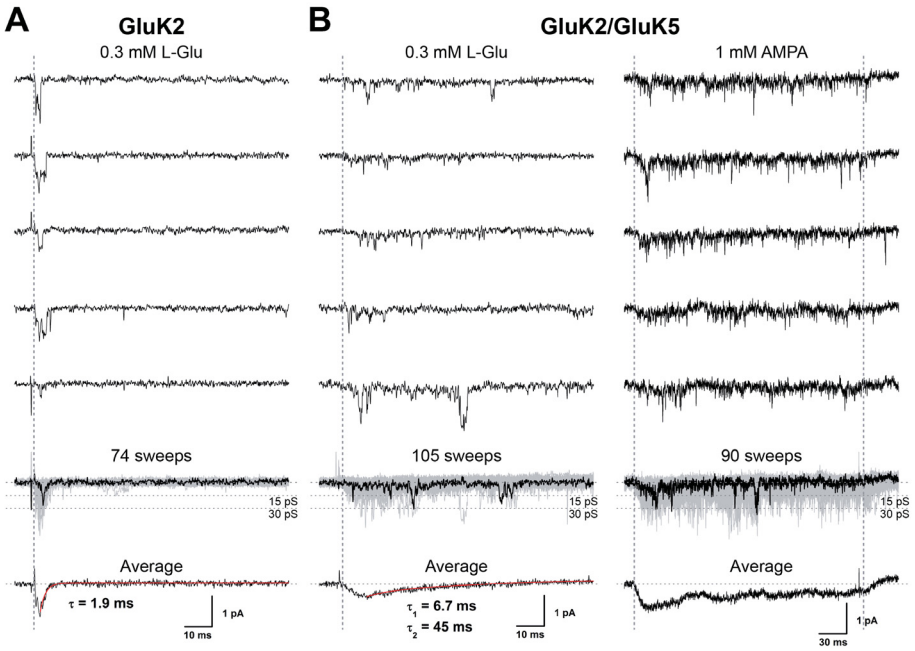

Figure 2–7: GluK2/GluK5 gates with unique single-channel properties
A, Example electrophysiological single-channel recordings; 5 non-consecutive trials are shown for GluK2 (0.3 mM L-Glu, 1 ms applications; patch # 140603p4) and 74 consecutive trials are superimposed below, with the average of all trials on the bottom. Four patches with 236 trials were analyzed for GluK2 (between 27 and 75 trials per patch). B, Examples for GluK2/GluK5 recordings (patch # 140704p2) in 0.3 mM L-Glu (1 ms, left) or 1 mM AMPA (250 ms, right). Five non-consecutive trials are shown above, with all consecutive trials superimposed below and the average of all trials on the bottom. Five patches were analyzed, with 502 trials for 0.3 mM L-Glu (between 90 and 105 trials per patch). The presence of GluK2/GluK5 channels was confirmed with 1 mM AMPA in each patch (272 trials in total, between 15 and 90 trials per patch).

Outside-out patches containing small numbers of GluK2 or GluK2/GluK5 were subjected to 0.3 mM L-Glu (1 ms jumps, holding potential (H_p) = -100 mV) to favour the activation of GluK5-containing receptors. Conventional single-channel analysis was not performed on the data because 0.3 mM L-Glu is sub-saturating for GluK2 and almost saturating for GluK2/GluK5 channels (Barberis et al., 2008; Fisher and Mott, 2011) and the conductance levels may not be comparable. Moreover, when a saturating L-Glu concentration was used, the contribution of GluK5 was reduced, as discussed above (Figure 2–3). For these reasons, the data were qualitatively assessed. Figure 2–7 summarizes these experiments.

In order to observe the rare GluK2 channel openings in 0.3 mM L-Glu, patches containing multiple channels were selected by first applying 1 mM L-Glu, followed by 0.3 mM L-Glu. Consistent with the macroscopic responses (Figure 2–3), microscopic GluK2 responses were brief and the channels did not re-open after the initial burst (Figure 2–7 A). These single-channel responses were similar to those previously observed for GluK2 with prolonged (250 ms) saturating (10 mM) L-Glu applications (Zhang et al., 2009; Daniels et al., 2013; Dawe et al., 2013). The average response from 236 trials ($n = 4$ patches) decayed with a τ of 1.9 $\pm$ 0.2 ms, similar to τ_1 in macroscopic patches at this L-Glu concentration (Figure 2–7 A and Table 2–3).

In contrast, currents elicited from GluK2/GluK5 receptors appeared very different (Figure 2–7 B). First, the openings were not restricted to the L-Glu application and were not synchronized (Figure 2–7 B). Channel openings were brief and continued to occur for several tens of milliseconds after L-Glu was removed (Figure 2–7 B). An average of 502 trials ($n = 5$ patches) yielded a weighted τ of 11 $\pm$ 2 ms, which was faster than the macroscopic deactivation of GluK2/GluK5, but much slower than the GluK2 responses (Figure 2–7 B and Table 2–3). For some patches (i.e. in Figure 2–7 B), the average response was fit with two exponentials, corresponding to τ_2 and τ_3 in macroscopic responses.

To confirm the presence of GluK2/GluK5 channels, patches were subjected to 1 mM AMPA (250 ms jumps, H_p = -100 mV; Figure 2–7 B). Interestingly, channel openings in the presence of AMPA were also very brief and occurred throughout the prolonged agonist application (Figure 2–7 B). Averaging of these responses yielded a current that was very similar to the macroscopic AMPA responses observed for GluK2/GluK5 receptors (272 trials, $n = 5$ patches; Figures 2–7 and 2–1). Together with the observed single-channel L-Glu responses for GluK2/GluK5, our findings

suggest that GluK5 is not non-desensitizing, as has been previously proposed (Mott et al., 2010; Fisher and Mott, 2011). Instead, our data show that GluK5 activation, either by a low L-Glu concentration or by AMPA, promotes the brief but frequent re-opening of the channel, even after the agonist has been removed (Figure 2–7 B).

2.6 Discussion

Our study provides an in-depth analysis of the specific contributions of the GluK2 and GluK5 subunits within a heteromeric KAR and provides insight into the functional mechanisms underlying KAR gating. First, we show that the activation of the GluK5 subunit is responsible for the slow deactivation kinetics in heteromeric KARs, while concerted activation of all subunits results in the desensitization of the channel and curtails the activation of GluK5. Second, the gating of GluK2/GluK5 heteromers is independent of external ions, indicating that there are underlying structural changes at the level of the ligand-binding domain (LBD) compared to homomeric GluK2 channels. Additionally, though homology models of GluK5 suggest that the ion-binding site may still be present in heteromeric channels, our experiments suggest that it may be asymmetrical. Finally, GluK2/GluK5 receptors exhibit distinct single-channel properties. In addition to having a higher affinity for L-Glu, activation of the GluK5 subunit allows the channel to re-open after the agonist has been removed. Taken together, our findings are consistent with an independent subunit activation within heteromeric KARs.

The assembly of kainate receptors as heteromeric complexes endows them with unique kinetic properties (present study and Barberis et al. (2008)). Interestingly, we found that GluK2/GluK5 responses decayed faster than GluK2 responses with prolonged L-Glu applications, suggesting that desensitization rates are faster in heteromeric channels. In contrast, their deactivation kinetics were slower, as previously demonstrated (Barberis et al., 2008), and correlated with their AMPA responsiveness, which is directly related to the presence of the GluK5 subunit (Herb et al., 1992; Swanson et al., 1997a). Given the fixed 2:2 stoichiometry of

GluK2/GluK5 receptors (Reiner et al., 2012), the presence of two receptor populations was assumed (i.e. GluK2 and GluK2/GluK5), and this allowed for the identification of patches containing a high GluK2/GluK5 content with minimal GluK2 contribution. Here, we found that short applications of 1 mM L-Glu yielded multi-exponential responses. Specifically, there was a slow exponential component of deactivation, for which the relative contribution was positively correlated with the presence of GluK5. However, the fast and intermediate exponential components were still present, as in GluK2, and were surprisingly accelerated by about 2-fold, suggesting that they were specific to heteromeric responses. As mentioned above, it is unclear whether the presence of GluK5 is modifying the open states that exist in GluK2 or whether these components are brought upon by the gating of the GluK5 subunit itself.

Our findings support that the concerted activation of all four subunits results in the desensitization of the channel, while the selective activation of two subunits, i.e. GluK5, allows the receptors to gate for longer times. Consistent with this, the desensitization and deactivation rates of GluK2/GluK5 receptors were strongly dependent on the L-Glu concentration. Since the GluK5 subunit has a higher affinity for L-Glu (Barberis et al., 2008; Fisher and Mott, 2011), applying L-Glu for shorter times (i.e. 1 ms) and at lower concentrations decreases the probability of GluK2 activation and allows the GluK5 subunits to gate undisturbed. This is consistent with previous studies that have proposed that the activation of GluK2 subunits within a heteromeric receptor complex results in channel desensitization (Mott et al., 2010; Fisher and Mott, 2012). However, our observation of the "ultra-fast" deactivation component was unexpected, since it is thought that GluK5 is responsible for the slow, and not the fast, deactivation in recombinant and native heteromeric KARs

(Barberis et al., 2008; Fernandes et al., 2009; Frerking and Nicoll, 2000). Our data suggest that this component results from the gating of GluK2 subunits within the heteromeric complex. Since the slow deactivation kinetics of GluK2/GluK5 are more prominent in sub-saturating L-Glu, it is possible that synaptic KARs are activated by sub-saturating agonist concentrations (i.e. that L-Glu concentrations may be lower than the estimated 1–5 mM (Clements et al., 1992; Clements, 1996) at KAR synapses).

Ion binding at the GluK2 LBD dimer interface is required for channel gating (Wong et al., 2006, 2007; Plested et al., 2008; Nayeem et al., 2009, 2011; Dawe et al., 2013). Furthermore, it has been proposed that the presence of a cation primes the receptor to gate (Dawe et al., 2013). Indeed, the introduction of single point mutations in GluK2 which act as tethered charges, namely M770K and D776K, circumvents the absolute requirement for external ions (Wong et al., 2006, 2007; Dawe et al., 2013). In GluK2(D776K), the Lys residue is predicted to be stably bound in the ion-binding pocket and this sustains channel activation (Dawe et al., 2013). On the other hand, while GluK2(M770K) gating is also ion-independent, this channel desensitizes very fast (Wong et al., 2006, 2007). X-ray crystallographic evidence suggests that while the Lys reaches into the ion-binding pocket and acts as a surrogate cation, its stability at this site is predicted to be short-lived, resulting in the partial occupancy of the ion-binding site (Nayeem et al., 2011). The removal of the positive charge (i.e. removal of the Na^+ or destabilization of the Lys interaction) ultimately causes the receptor enter a desensitized state (Dawe et al., 2013).

In this study, we found that the gating of GluK2/GluK5 was also ion-independent, suggesting that the ion-binding site is somehow altered in heteromeric receptors. An interesting exception to this was with Li^+ ions, which

slowed the desensitization kinetics of GluK2/GluK5, but not of GluK2, by almost 3.5-fold. Despite the ion-insensitivity of GluA1 receptors (Bowie, 2002), a similar phenomenon is seen with GluA2 receptors, where L-Glu-evoked currents in the presence of external LiCl causes a 7-fold slowing of the desensitization kinetics (Dawe et al., 2016). In this case, the putative ion-binding site is predicted to be smaller and to have a higher propensity to bind Li^+ than Na^+ ions (Dawe et al., 2016). In addition, the accelerated and ion-independent fast desensitization and deactivation components in GluK2/GluK5 are reminiscent of GluK2(M770K) ((Wong et al., 2006) and present study). Taken together, our observations suggest that the ion-binding site of GluK2/GluK5 shares some structural similarities with that of AMPARs. However, given the presence of two distinct subunit types in the heteromeric channel, it is likely that the LBD interface is asymmetrical compared to GluK2 or GluA2 homomers. Although there is no structural evidence to support this yet, the GluK5 subunit may alter at least one of the ion-binding sites and/or provide surrogate charges to satisfy the ion-binding pockets and bypass the requirement for external ions. As a consequence, external ions are not able to regulate the time-course of activation in GluK2/GluK5 heteromeric KARs.

Previously, it was demonstrated that GluK5 activation, in the absence of GluK2 activation, greatly decreases the desensitization of the channels (Mott et al., 2010; Fisher and Mott, 2011). In this study, we also found that the gating contribution of GluK5 could be revealed by lowering the agonist concentration or by specific activation with AMPA. However, our single-channel data do not support that GluK5 is a non-desensitizing subunit. Instead, our findings indicate that heteromer gating results in very fast and short-lived channel openings with frequent re-openings after the removal of the agonist. The specific pharmacological

activation of GluK5 also exhibits these brief openings and re-openings, which suggests that GluK5 is responsible for this type of gating. Although we cannot distinguish between closed and desensitized states, our data demonstrate that GluK5 activation does not lead to sustained activation of the channel. Additionally, the ion-independent gating of heteromers allows for the prolonged activity of GluK5. Taken together, we find that the unique gating properties of GluK2/GluK5 result from the interplay between the activation of GluK2 and GluK5 subunits within the channel. While our data underlines the importance of the LBD dimer interface, the precise interactions between the GluK2 and GluK5 subunits that are underlie this gating behaviour remains to be elucidated.

2.7 Author Contributions

P.M.G.E.B. designed and performed experiments, analysed data and wrote the paper; D.B. designed experiments and reviewed the manuscript.

2.8 Acknowledgements

This work was supported by an operating grant from the Canadian Institutes of Health Research (to D.B.). P.M.G.E.B. was supported by a graduate student fellowship from the Fonds de Recherche en Santé du Québec. D.B. is the recipient of a Canada Research Chair. We wish to thank members of the Bowie lab for insightful discussion of the manuscript.

CHAPTER 3
KAINATE RECEPTOR PORE-FORMING AND AUXILIARY SUBUNITS REGULATE CHANNEL BLOCK BY A NOVEL MECHANISM

Reproduced with permission.

Brown, PMGE, Aurousseau, MRP, Musgaard, M, Biggin, PC and Bowie, D. (2016)

J Physiol. Apr 1;594(7):1821-40. doi: 10.1113/JP271690. Epub 2016 Feb 2.

3.1 Foreword to Chapter 3

As mentioned earlier in the Preface, I was motivated to investigate the functional properties of recombinant KARs to better understand how they function in their native form, that is, as heteromeric complexes and with auxiliary proteins. In Chapter 2, I focused on the effects of gating that were brought upon by the heteromeric LBD dimer interface. In addition to this, there are molecular determinants of gating that are found in the pore region of the channel. For example, an RNA-editing mechanism that is active in GluA2 AMPAR subunits, as well as GluK1 and GluK2 KAR subunits (Sommer et al., 1991), substitutes the Gln residue for an Arg residue at the pore apex, which decreases Ca^{2+} permeability (Burnashev et al., 1992) and relieves polyamine block (Bowie and Mayer, 1995). However, the editing of KAR subunits is not absolute, given that the primary subunits are partially edited (Sommer et al., 1991; Puchalski et al., 1994; Schmitt et al., 1996), and the editing of the secondary subunits has not been tested.

For these reasons, we found it intriguing that despite containing unedited subunits, recombinant GluK2/GluK5 receptors were much less sensitive to polyamine block (Barberis et al., 2008). Similarly, unedited GluK2 homomers were also less sensitive to block when they were associated with the auxiliary proteins, Neto1 and Neto2 (Fisher and Mott, 2012). Here, a charge-screening mechanism was proposed to repel polyamines from the channel pore and thereby prevent polyamine block (Fisher and Mott, 2012).

In this chapter, we used a combination of electrophysiology and Molecular Dynamics to identify a proline (Pro) in the pore-lining region of GluK5, which is a critical determinant of polyamine sensitivity. Furthermore, using site-directed mutagenesis, we demonstrate that this residue is responsible for increasing the permeation of polyamines through the channel pore, a mechanism that has not

been considered in the past. Interestingly, auxiliary proteins also facilitate polyamine permeation at GluK2 homomers, which is at odds with the charge-screening mechanism proposed by Fisher and Mott (2012).

3.2 Key Points

- Kainate receptor heteromerization and auxiliary subunits, Neto1 and Neto2, attenuate polyamine ion-channel block by facilitating blocker permeation.
- Relief of polyamine block in GluK2/GluK5 heteromers results from a key proline residue that produces architectural changes in the channel pore α-helical region.
- Auxiliary subunits exert an additive effect to heteromerization, and thus relief of polyamine block is due to a different mechanism.
- Our findings have broad implications for work on polyamine block of other cation-selective ion channels.

3.3 Abstract

Channel block and permeation by cytoplasmic polyamines is a common feature of many cation-selective ion channels. Although the channel block mechanism has been studied extensively, polyamine permeation has been considered less significant as it occurs at extreme positive membrane potentials. Here, we show that kainate receptor (KAR) heteromerization and association with auxiliary proteins, Neto1 and Neto2, attenuate polyamine block by enhancing blocker permeation. Consequently, polyamine permeation and unblock occur at more negative and physiologically relevant membrane potentials. In GluK2/GluK5 heteromers, enhanced permeation is due to a single proline residue in GluK5 that alters the dynamics of the α-helical region of the selectivity filter. The effect of auxiliary proteins is additive, and therefore the structural basis of polyamine permeation and unblock is through a different mechanism. As native receptors are thought to assemble as heteromers in complex with auxiliary proteins, our data identify an unappreciated impact of polyamine permeation in shaping the signalling properties

of neuronal KARs and point to a structural mechanism that may be shared amongst other cation-selective ion channels.

3.4 Introduction

Polyamines are expressed ubiquitously in bacterial, plant and animal cells where they fulfill a variety of roles essential for life (TABOR and TABOR, 1964; Tabor and Tabor, 1985). Mammals possess two polyamines, the tetra- and tri-amines, spermine (Spm) and spermidine (Spd), respectively, that are derived from the diamine precursor, putrescine (Put), through tightly regulated biosynthetic pathways. Disruption in the synthesis or catabolism of polyamines leads to a variety of disease states from cancer to neurodevelopmental disorders (Nowotarski et al., 2013; Pegg, 2014), underlining their physiological importance. Given their cationic nature, polyamines interact with negatively charged domains of biomolecules (Tabor and Tabor, 1984) including the electrostatic pore regions of voltage- and ligand-gated ion channels where they bind and consequently block ion flow with micromolar affinity (Lopatin et al., 1994; Bowie and Mayer, 1995; Gomez and Hellstrand, 1995; Haghighi and Cooper, 1998; Lu and Ding, 1999; Kerschbaum et al., 2003; Fu et al., 2012). In this capacity, cytoplasmic polyamines are recognized as important determinants of neuronal signaling by regulating action potential firing rates (Fleidervish et al., 2008) as well as the strength of neurotransmission (Rozov and Burnashev, 1999; Aizenman et al., 2002).

Polyamines are often referred to as permeant channel blockers due to their ability to both block and traverse the ion-permeation pathway of cation-selective ion channels (Bowie et al., 1999). For almost all ion channels, cytoplasmic polyamine block is observed at negative and physiologically relevant membrane potentials, making it an ideal regulator of cellular excitability (Nichols and Lopatin, 1997; Bowie et al., 1999; Lu, 2004; Baronas and Kurata, 2014). In contrast, polyamine permeation occurs at extreme (>+50 mV) positive membrane potentials (Bahring et al., 1997) and therefore has not been considered particularly significant.

Given this arrangement, however, the fraction of channels blocked by polyamines at any given membrane potential is the sum of these two opposing mechanisms. Consequently, the overall level of polyamine block could, in principle, be shaped by any mechanism that enhances the relative contribution of polyamine permeation.

At glutamatergic synapses of the developing and mature CNS, polyamines have been well characterized to act as permeant channel blockers of both AMPA- and kainate-type (KARs) ionotropic glutamate receptors (iGluRs) (Bowie and Mayer, 1995; Kamboj et al., 1995; Koh et al., 1995). In each case, the degree of polyamine block is voltage-dependent and dynamically regulated, with two of the most prevalent mechanisms occurring through either changes in receptor subunit composition or by receptor association with auxiliary proteins (Cull-Candy et al., 2006; Perrais et al., 2010; Jackson and Nicoll, 2011). At KARs, polyamine block is attenuated by either the formation of heteromers that contain the GluK4 or GluK5 subunit (Barberis et al., 2008) or by co-assembly with auxiliary proteins, Neto1 and Neto2 (Fisher and Mott, 2012). Interestingly, removal of the positively charged Arg-Lys-Lys motif of Neto1 or Neto2 C-tail restores polyamine block, suggesting that relief of block may involve a charge screening mechanism that affects the pore (Fisher and Mott, 2012). Whether a similar electrostatic mechanism explains the attenuation of block at GluK2/GluK5 heteromers remains to be established.

Here, we have tested the hypothesis that KAR heteromers and auxiliary proteins attenuate channel block by a common mechanism. We show that in both cases relief of polyamine block results from an enhanced rate of polyamine permeation. Relief of block in heteromers is due to a proline residue from GluK5 that is predicted to alter the pore architecture, thereby facilitating polyamine permeation. The effect of auxiliary proteins is additive to that of the pore-forming subunits and we therefore conclude that they enhance polyamine permeation

through a different mechanism. As native receptors primarily assemble as heteromers in complex with auxiliary proteins, our data identify an unappreciated impact of polyamine permeation in shaping the signalling properties of KARs in neuronal circuits.

3.5 Methods

3.5.1 Plasmids and molecular biology

All experiments were performed using cDNA of rat GluK2 and GluK5 kainate-type iGluRs, mouse Neto1-HA and rat Neto2. For electrophysiology, GluK2a(V,C,Q) and GluK5 cDNA each contained a downstream internal ribosome entry site (IRES) sequence encoding mCherry and eGFP, respectively, which were used to identify transfected cells. cDNA of GluK2(G615P) and GluK5(P599G) were made using site-directed mutagenesis with all constructs verified by restriction digest analysis and sequencing.

3.5.2 Cell culture and transfection

HEK293T/17 cells (ATCC, Manassas, VA, USA) were maintained in minimal essential medium (MEM) containing glutaMAX© supplemented with 10% fetal bovine serum (Invitrogen, Carlsbad, CA, USA). Cells were plated at low density ($1.6 - 2.0 \times 10^4$ cells ml^{-1}) on poly-D-lysine-coated 35 mm plastic dishes and were transiently transfected 24 h later using the calcium phosphate technique. A GluK2:GluK5 or GluK2:Neto1/2 cDNA molar ratio of 1:10 was used for all co-transfections.

3.5.3 Electrophysiological recordings

Experiments were performed 36–48 h after transfection. Agonist solutions were rapidly applied to outside-out patches excised from transfected cells using a piezoelectric stack (Physik Instrumente, Auburn, MA, USA). Solution exchange (10–90% rise time of 250–350 μs) was determined in a separate experiment by measuring the liquid junction current. All recordings were performed using an Axopatch 200B (Molecular Devices, Sunnyvale, CA, USA) using thick-walled borosilicate glass pipettes (3–6 MΩ) coated with dental wax to reduce electrical

noise. Current records were filtered at 5 kHz, digitized at 25 kHz and series resistance (3–12 MΩ) was compensated for by 95%. Recordings were performed at a range of holding potentials from 100 to +100 mV to study polyamine channel block. Data acquisition was performed using pClamp9 or pClamp10 software (Molecular Devices) and tabulated using Excel. All experiments were performed at room temperature.

All chemicals were purchased from Sigma-Aldrich (St Louis, MO, USA) unless otherwise indicated. External solutions contained (in mM) 150 NaCl, 5 HEPES, 0.1 $MgCl_2$ and 0.1 $CaCl_2$, pH 7.3–7.4. The internal solution contained (in mM) 115 NaCl, 10 NaF, 5 HEPES, 5 Na_4BAPTA (Life Technologies, Invitrogen, Burlington, ON, Canada), 1 $MgCl_2$, 0.5 $CaCl_2$ and 10 Na_2ATP, pH 7.3–7.4. The osmotic pressure of all solutions was adjusted to 295–300 mOsm with sucrose. In experiments where polyamine block was examined, Na_2ATP in the internal solution was replaced with 60 µM Spm and the osmotic pressure adjusted to 295–300 mOsm with sucrose. For Ca^{2+} permeability experiments, the external solution contained (in mM) 105 NaCl, 30 $CaCl_2$, 5 HEPES and 0.1 $MgCl_2$, pH 7.3–7.4 (295 mOsm). For polyamine permeability experiments, the NaCl in the external solution was replaced by 90 mM Spm, pH was adjusted to 7.3–7.4 using the Spm free base and the osmotic pressure was adjusted with sucrose. Concentrated (10× or 100×) agonist stock solutions were prepared by dissolving agonist [L-glutamate or AMPA (Tocris, Ellisville, MO, USA)] in the appropriate external solution, adjusting the pH to 7.3–7.4, and stored frozen at −20 °C. Stocks were thawed on the day of the experiment and used to prepare agonist-containing external solutions. For heteromeric GluK2/GluK5 receptors, only patches where the contribution of the slowest exponential component (%A3) was above 25% were considered for analysis, unless otherwise stated.

3.5.4 Data analysis and fitting

Agonist-evoked membrane conductance (G) was calculated using eqn (1):

$$G = \frac{I}{(V - V_{\text{rev}})} \tag{3.1}$$

where I is the current at V holding potential and V_{rev} is the reversal potential.

Conductance-voltage (G–V) relationships were fit using Origin 7 (OriginLab, Northampton, MA, USA) with the following equation (from Bowie et al. (1998)):

$$G = \frac{Gmax}{1 + \frac{[Spm]}{K_d}} \tag{3.2}$$

where G_{max} is the maximal conductance, $[Spm]$ is the internal Spm concentration and K_d is the dissociation constant.

Binding (k_{on}) , unbinding (k_{off}) and permeation (k_{perm}) rates were defined as previously in Bowie et al. (1998):

$$k_{on} = a\ exp\left(\frac{V}{b}\right) \tag{3.3}$$

$$k_{off} = c\ exp\left(\frac{V}{d}\right) \tag{3.4}$$

$$k_{perm} = e\ exp\left(\frac{V}{f}\right) \tag{3.5}$$

To estimate k_{off} and k_{perm}, K_d was first calculated as:

$$K_d = \frac{\text{sum of exit rates}}{\text{Binding rate}}$$

which was redefined to eqn (6):

$$K_d = g\ exp\left(\frac{V}{h}\right) + L\ exp\left(\frac{V}{k}\right) \tag{3.6}$$

where

$$g = \frac{c}{a}$$

$$L = \frac{e}{a}$$

$$h = \frac{bd}{b-d}$$

$$k = \frac{bf}{b-f}$$

Binding rates were assumed to be constant for GluK2/GluK5, GluK2+Neto1 and GluK2+Neto2 (see Results for more details), and the values for a and b were taken from Bowie et al. (1998).

The voltage-dependent conductance of KARs under basal conditions is appreciably different between receptor types within the range ± 100 mV. This emphasizes the impact of auxiliary proteins in changing the basic gating properties of KARs and the importance of accounting for these significant differences in gating properties. The intrinsic G–V relationships were fit with eqn (7) using Origin 7:

$$y = 1 + (G_0 - 1)\ exp\left(\frac{x}{V}\right) \tag{3.7}$$

Where G_0 is the minimal conductance and V is the membrane potential. Values are summarized in Table 3–1.

Table 3–1: Fit parameters for intrinsic G–V relationships

	G_0	V
GluK2	1.0699	41.4
GluK2/GluK5	1.1168	55.7
GluK2+Neto1	1.0003	16.3
GluK2+Neto2	1.0094	25.5
GluK2/GluK5(P599G)	1.0240	38.4
GluK2(G615P)	1.0163	31.7
GluK2 - 300 µM	1.0736	37.6
GluK2/GluK5 - 300 µM	1.1282	60.0

The Ca^{2+} permeability relative to Na^{+} (P_{Ca}/P_{Na}) was determined using the constant field equation from Kamboj et al. (1995):

$$\frac{P_{Ca}}{P_{Na}} = \frac{[Na^{+}]_i}{[Ca^{2+}]_o} \times \frac{\left[exp\left(\frac{\Delta V_{rev}F}{RT}\right) \times \left(exp\left(\frac{\Delta V_{rev}F}{RT}\right) + 1\right)\right]}{4} \tag{3.8}$$

where P_{Ca} and P_{Na} are the permeability coefficients for Ca^{2+} and Na^{+} respectively; ΔV_{rev} is the reversal potential shift, F is Faradays constant, R is the gas constant and T is the temperature in Kelvin.

Relative Spm permeability (P_{Spm}/P_{Na}) was calculated from the reversal potential (V_{rev}) measurements in Spm-rich external solutions using the following equation from Bahring et al. (1997):

$$I_x = P_x z^2 \times \left(\frac{V_m F^2}{RT}\right) \times \left(\frac{[X]_i - [X]_o exp\left(\frac{-zFV_m}{RT}\right)}{1 - exp\left(\frac{-zFV_m}{RT}\right)}\right) \tag{3.9}$$

where I_x is the current carried by ion X at a membrane potential V_m, P_x is the corresponding permeability ($P_{Na} = 1$), $[X]_i$ and $[X]_o$ are the internal and external Spm concentrations, z is the valence, and F, R and T are as above. Experimentally determined reversal potentials were used for V_m. We obtained P_{Spm}/P_{Na} using the definition that $I_{Na} + I_{Spm} = 0$ at the reversal potential. The reversal potentials were corrected for liquid junction potentials that were determined experimentally.

All data were illustrated using Origin 7 and Adobe Illustrator.

3.5.5 Statistics

Statistical analysis was performed using the statistical software SPSS Statistics. Data were assumed to be distributed normally. The numbers provided for 'n' refer to the number of individual patches.

3.5.6 Molecular Dynamic Simulations

Molecular dynamics (MD) simulations were performed to study whether inserting proline residues into the α-helical region of the P-loop had an effect on the pore architecture. No atomic-resolution open-channel structure of an iGluR has been determined, so an open-channel structure of the non-selective NaK cation channel from *Bacillus cereus* determined to a resolution of 1.6 Å was used as a model system (PDB # 3E86) (Alam and Jiang, 2009a). Figure 3–7 below shows a structural alignment of the GluA2 (PDB # 3KG2) and the NaK (PDB # 3E86) channel pores. Given that they have very similar topologies, the NaK pore structure was used as this structure has the selectivity filter resolved at atomic resolution and is described as being in the open state as opposed to the GluA2 structure which is considered closed and where the selectivity filter region is unresolved.

To generate a membrane slab for further simulation, the tetrameric physiological unit of the NaK channel (residues 23–113, ignoring ions and other small molecules) was converted to Coarse Grain (CG) representation (Martini v2.1) (Monticelli et al., 2008) to allow for self-assembly and equilibration of a bilayer consisting of 200 1-palmitoyl-2-oleoyl-(*sn*)-glycero-3-phosphocholine (POPC) molecules around the protein structure. This system was simulated for 100 ns at 323 K in Gromacs v4.6.3 (Hess et al., 2008) to allow formation of a POPC bilayer (Stansfeld et al., 2015).

Following this, the system was converted back to atomistic representation using a CG2AT-align method (Stansfeld and Sansom, 2011) and this membrane slab was then used for further system setup with the different protein mutants aligned to the position of the protein. The (*4S*)-2-methyl-2,4-pentanediol molecule, observed in the crystal structure, was deleted. The crystal structure has four ions bound in the

filter region: one calcium ion in the external site, one sodium ion in the vestibule site, one caesium ion in site 3 and another sodium ion in site 4. To keep the ion composition simple, the calcium ion and the caesium ion were changed to potassium and sodium, respectively. Both monovalent and divalent cations can bind at the external site, but sodium does not appear to be a good binder at this site (Alam and Jiang, 2009b), and thus the calcium ion was exchanged for potassium. The vestibular site and sites 3 and 4 all appear to prefer sodium, so the caesium ion in site 3 was exchanged for sodium. Crystallographic water molecules were retained. The protein along with ions and protein-bound water molecules was inserted into the pre-generated POPC membrane slab, and water molecules for solvation were further added using the Solvate Plugin of VMD (Humphrey et al., 1996). Ions were added with the Autoionize Plugin in VMD to create a neutral system with an approximate ion concentration of 150 mM. The anion was chloride and because the NaK channel transports both sodium and potassium, approximately half of the cations were sodium and the other half potassium.

The system was then energy minimized for 5000 steps and equilibrated for 10 ns with protein heavy atoms along with ions bound to the filter harmonically restrained with a force constant of 7 kcal mol^{-1} $Å^{-2}$. Lipid molecules which, after 10 ns, were still stuck in odd positions between protein helices, resulting from the self-assembly process, were deleted and the system was energy minimized for 5000 steps and 500 ns of unbiased MD simulation was performed. This structure (with the oddly positioned lipid molecules removed) was further used for construction of the mutant systems using the Mutator Plugin of VMD. These systems were likewise energy minimized for 5000 steps followed by 500 ns of unbiased MD simulation. In addition to the NaK crystal structure (WT, mimicking the GluK2 homotetramer), we simulated the NaK structure with S57P in two opposing chains (A and C in 2Pro,

mimicking the GluK2/GluK2 heteromer if assuming a 2:2 assembly with GluK2–GluK5–GluK2–GluK5 packing at the membrane level) and the NaK structure with the S57P mutation imposed in all four chains [4Pro, mimicking the GluK2(G615P) homotetramer]. Each 500 ns simulation was repeated, so the final data set consisted of 2 × 500 ns for each of the protein constructs.

All atomistic simulations were performed with NAMD v2.9 (Phillips et al., 2005) using the CHARMM 36 force field (Klauda et al., 2010; Best et al., 2012) for protein and lipids and the TIP3P water model (Jorgensen et al., 1983). Simulations were performed in the NPT ensemble at a temperature of 310 K and a pressure of 1 atm. Langevin dynamics with a damping coefficient of 0.5 ps^{-1} was employed to control the temperature. The pressure was maintained using the Langevin piston NoséHoover method with a piston period of 100 fs and a damping timescale of 50 fs. LennardJones interactions were treated with a cutoff of 12 Å and the switching function applied from 10 Å, while full electrostatics were accounted for using Particle-Mesh Ewald (PME) (Darden et al., 1993) summation with a real-space cutoff of 12 Å and a 1 Å grid spacing. The pair list, with a cutoff of 14 Å, was updated every 20 fs. Periodic boundary conditions were applied in all simulations. The time step was 2 fs with full electrostatics calculated every second step. Water molecules were kept rigid by the SETTLE (Miyamoto and Kollman, 1992) algorithm and other bonds to hydrogen atoms by the SHAKE (Ryckaert et al., 1977) algorithm. Snapshots were collected every 5 ps.

3.5.6.1 Polyamine ligands

The structures for Spm, Spd and Put were downloaded the HIC-Up database (Kleywegt and Jones, 1998) (ideal coordinates, http://xray.bmc.uu.se/hicup/XXX/ where XXX = SPM, SPD, PUT), and hydrogen atoms were added in Maestro (Maestro, version 9.7, Schrödinger, LLC, New York, 2014). All amine nitrogen

atoms were treated as charged. Ligand topologies and parameters for the CHARMM General Force Field (CGenFF) (Vanommeslaeghe et al., 2010; Yu et al., 2012) v3.0.1 were generated using the CGenFF program v1.0.0 (Vanommeslaeghe and MacKerell Jr, 2012; Vanommeslaeghe et al., 2012) (https://cgenff.paramchem.org).

3.5.6.2 NaK-polyamine complexes

The most symmetrical and the most asymmetrical snapshot in terms of cross-pore distance (see Fig. 3–6 D below) was taken from each of the simulations of WT, 2Pro and 4Pro, leaving out the first 100 ns of simulation. Spm was inserted into the filter region by aligning the charged nitrogen atoms of Spm with the original position of the four cations in the filter. These four ions were then deleted to remove overlap and ensure charge neutrality, and furthermore water molecules in the filter overlapping with Spm were deleted. Spd and Put were inserted to the filter region of WT snapshots in a similar way, although due to the smaller number of nitrogen atoms in these ligands, central carbon atoms were used along with the nitrogen atoms in the alignment to original ion positions. For Spd, three of the original cations in the filter were deleted, and for Put, only two. No other ions were binding to the filter region in any of the complexes. The simulation systems were then energy minimized for 2000 steps followed by 30 ns of unbiased MD simulation.

All polyamines remained bound to the filter region throughout the 30 ns of relaxation. To probe the energetics involved in the unbinding of the polyamines from the filter, 15 ns of steered MD (SMD) simulations were performed on all NaK-polyamine complexes, starting after 30 ns of unbiased simulation. The SMD atoms, here the terminal nitrogen atom facing the pulling direction, were harmonically constrained with force constant of 7.2 kcal mol^{-1} Å^{-2}, corresponding to 500 pN Å^{-1}, to move with velocity 2.5 Å ns^{-1} in the negative direction along the

z-axis (towards the extracellular side for the NaK channel, corresponding to the intracellular side for the KAR channel). Forces were saved every 200 fs. To avoid the whole system being pulled along z, the C_α atoms of residues 23–28 were restrained harmonically with a force constant of 7.2 kcal mol^{-1} Å^{-2}.

The work was calculated from the force profiles by numerical integration according to:

$$W(t) = v \int_0^t f(t)dt \tag{3.10}$$

where v is the constant velocity (2.5 Å ns^{-1}), $f(t)$ is the force at the specific time step given in the SMD output and dt is the time step between the data points (200 fs).

3.6 Results

3.6.1 Heteromerization and auxiliary proteins attenuate inward rectification of KARs

To better understand how heteromerization and auxiliary proteins attenuate channel block, we studied KAR responses in outside-out membrane patches at a range of membrane potentials to observe when polyamines enter the pore to block it. To mimic the time course of neurotransmitter release in the synaptic cleft, 1 mM L-glutamate(L-Glu) was applied to excised patches for 1 ms and 60 µM Spm was included in the internal solution to match known cytoplasmic levels of the blocker (Bowie and Mayer, 1995). Figure 3–1 summarizes these experiments, where the degree of inward rectification induced by polyamine block of GluK2 homomers was compared to that of GluK2/GluK5 heteromers or GluK2 homomers co-assembled with the auxiliary proteins, Neto1 and Neto2.

In agreement with other studies, peak GluK2 receptor responses exhibited a bi-rectifying behaviour (range: -100 to +100 mV) due to the onset and relief of block at hyperpolarizing and depolarizing membrane potentials, respectively (Fig. 3–1 A and B) (Bowie and Mayer, 1995; Bowie et al., 1998). In contrast, I–V plots of GluK2/GluK5 heteromers (Fig. 3–1 C and D) or GluK2 with Neto1 or Neto2 (Fig. 3–1 E–G) (Barberis et al., 2008; Fisher and Mott, 2012) tended towards linearity. Rectification ratios were smallest for GluK2 homomers (0.20 ± 0.02, $n = 5$), highlighting that Spm channel block strongly opposes ion flow at positive membrane potentials (Fig. 3–1 A, B and H). This effect was much weaker with GluK2/GluK5 heteromers (rectification ratio = 0.89 ± 0.07, $n = 4$) and following co-assembly with auxiliary proteins (Neto1, 0.66 ± 0.02, $n = 12$; Neto2, 0.64 ± 0.03, $n = 7$) (Fig. 3–1 H), reaffirming that, in each case, polyamine block is significantly attenuated. Despite the similarity of the effects, it still remains to be

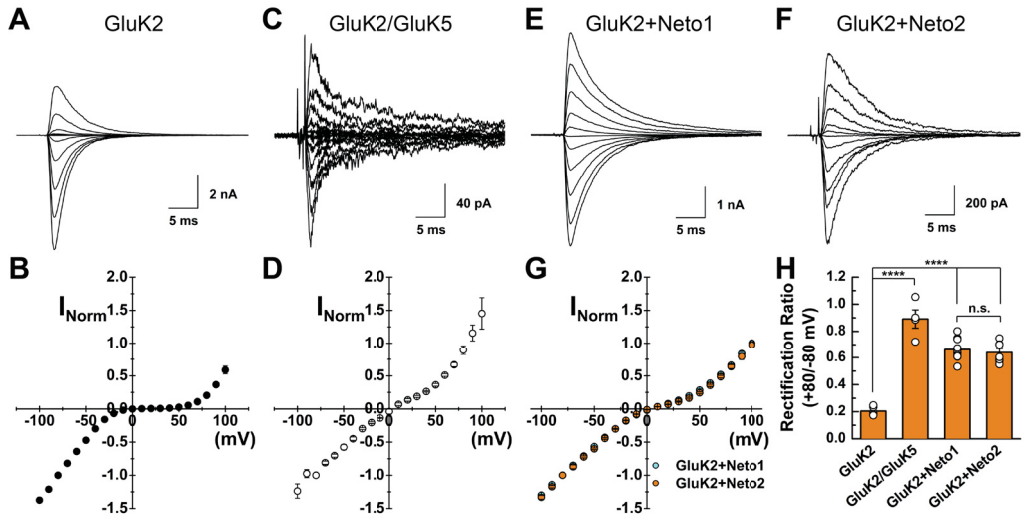

Figure 3–1: Heteromerization and auxiliary proteins reduce inward rectification of KARs

A, C, E, F, typical membrane currents evoked by 1 mM L-Glu (1 ms application) at various holding potentials (-100 to +100 mV, 20 mV increments) in the presence of 60 µM internal Spm. Patch numbers: GluK2, 120403p1; GluK2/GluK5, 120417p3; GluK2+Neto1, 130506p3; and GluK2+Neto2, 131104p3. B, D, G, average I–V plots for GluK2 (n = 5), GluK2/GluK5 (n = 4), GluK2+Neto1 (n = 12) and GluK2+Neto2 (n = 7). Data are presented as mean ± SEM. Current values are normalized to the current at -100 mV. H, to obtain the rectification ratio, the peak current at +80 mV was divided by that at -80 mV. Rectification ratios for individual patches are shown as empty circles; columns represent the mean and error bars indicate SEM. One-way ANOVA, $F_{3,24} = 60.819$, $P = 2.32\text{E-}11$, post hoc Tukey HSD pairwise comparisons: $****$ $P <$ 1.33E-8; n.s., not significant.

established if heteromerization and auxiliary proteins attenuate block by a similar or different mechanism.

To better understand the voltage-dependency of the onset and relief of block, we converted the I–V data from each dataset into G–V plots (Fig. 3–2). KARs exhibit significant outward rectification at positive membrane potentials in the absence of channel blockers (Bowie et al., 1998). To take this into account, we performed additional experiments to obtain control I–V data for all receptor combinations and then subtracted this non-linearity from data obtained in the presence of Spm (Figs 3–2 and 3–3). Corrected G–V plots were then fit with a single binding site model of channel block (Bowie et al., 1998) (see Methods) to estimate the equilibrium

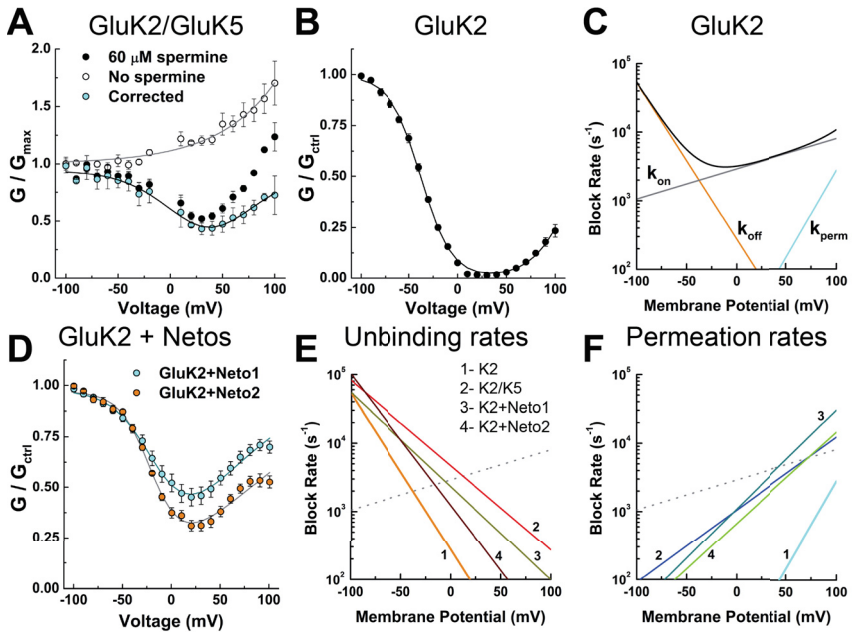

Figure 3–2: Association of GluK2 with GluK5 or auxiliary proteins reduces polyamine block by increasing permeation rates

A, conductancevoltage (G–V) plots for GluK2/GluK5 in the presence (black circles) and absence (white circles) of 60 μM internal Spm. Cyan circles represent the corrected G–V (n = 4), obtained by dividing the Spm G–V by the fit of the Spm-free G–V. B, corrected G–V plot for GluK2 (n = 5). C, rates of onset, unbinding and permeation for GluK2 (see Methods). k_{on} was estimated using values from Bowie et al. (1998). D, corrected G–V plots for GluK2+Neto1 (cyan, n = 12) and GluK2+Neto2 (orange, n = 7). All data are represented as the mean ± SEM. G–V plots were fit with eqn (2). E and F, comparison of the estimated unbinding (k_{off}, E) and permeation (k_{perm}, F) rates for GluK2 (1), GluK2/GluK5 (2), GluK2+Neto1 (3) and GluK2+Neto2 (4).

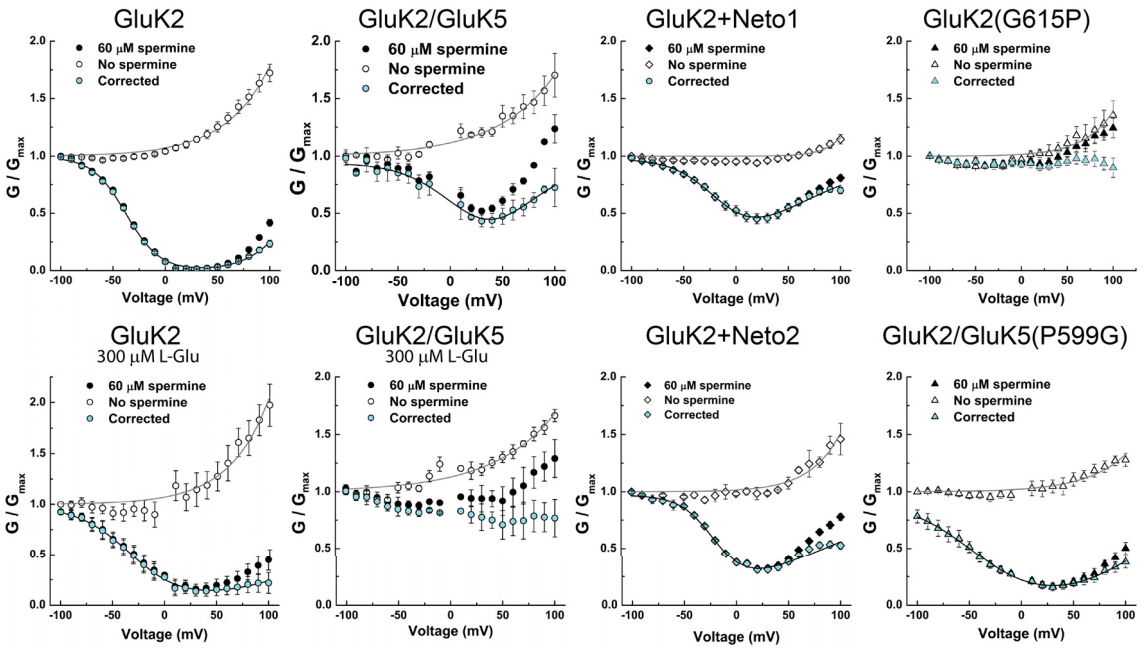

Figure 3–3: G–V corrections for intrinsic outward rectification in the absence of internal polyamines

G–V relationships in the absence (white symbols) or presence (black symbols) of internal polyamines were plotted. The corrected G–V relationships (cyan symbols) were obtained by dividing the value of the spermine G–V by the non-spermine G–V ($G_{corr} = G_{Spm}/G_{noSpm}$). Note the importance of performing this correction for each receptor type, as the intrinsic outward rectification properties differ.

dissociation constant of Spm at 0 mV ($K_{d(0mV)}$) as well as the voltage-dependency of the onset and relief of block (h and k, respectively; Table 3–2).

In agreement with previous work (Bowie et al., 1998), the $K_{d(0mV)}$ of Spm for GluK2 homomers was estimated to be 5.8 ± 0.3 µM, with voltage-dependencies of the onset and relief of block of -16 ± 0.5 and +20.4 ± 1.0 mV per e-fold change in membrane potential, respectively (Table 3–2). In comparison, KAR heteromerization and association with auxiliary proteins affected both Spm binding and the voltage-dependency of block. Fits of corrected G–V plots estimated the $K_{d(0mV)}$ of Spm to be 39 ± 2, 71 ± 13 and 119 ± 30 µM for GluK2+Neto2, GluK2+Neto1 and GluK2/GluK5 channels, respectively (Table 3–2), representing a 6- to 20-fold reduction in blocker affinity. Interestingly, heteromerization and

auxiliary protein association mainly affected the voltage-dependency of the relief of block (i.e. k), which was about 2- to 3-fold weaker compared to that of GluK2 homomers (Table 3–2). For example, fits of corrected G–V plots estimated the voltage-dependency of relief for GluK2/GluK5 heteromers to be +69.7 mV per e-fold change in membrane potential compared to +20.4 mV for GluK2 homomers. In keeping with this, selective activation of GluK2/GluK5 heteromers with either 1 mM AMPA (Herb et al., 1992) or 300 µM L-Glu (Barberis et al., 2008) estimated $K_{d(0mV)}$ to be 81 ± 40 and 170 ± 33 µM, respectively, with the voltage-dependency of relief corresponding to +56.8 and +107.7 mV per e-fold change in membrane potential, respectively (Table 3–2). In contrast, the differences between the voltage-dependency of onset of block (i.e. h) were more modest (Table 3–2), and the binding rates for Spm (k_{on}, Fig. 3–2 C) were assumed to be constant. The unbinding (k_{off}) and permeation rates (k_{perm}) were estimated using previous estimates of k_{on} (Fig. 3–2 C) (Bowie et al., 1998). Plots of unbinding (k_{off}) and permeation (k_{perm}) for Spm at GluK2 homomers predict that relief of block occurs only at extreme membrane potentials (i.e. >+50 mV), where the rates for k_{perm} become dominant (Fig. 3–2 C). In contrast, similar plots of k_{off} (Fig. 3–2 E) and k_{perm} (Fig. 3–2 F) with GluK2/GluK5 heteromers, GluK2+Neto1 or GluK2+Neto2 (Fig. 3–2 E and F) reveal that there are substantial shifts in estimates of unbinding and permeation rates that account for the overall attenuation in channel block. Specifically, there is a substantial hyperpolarizing shift in k_{perm} so that Spm permeation is expected to be appreciable even at membrane potentials of -50 mV (Fig. 3–2 F).

Given the specific nature of these effects, we reasoned that the attenuation of polyamine channel block by heteromerization or association with auxiliary proteins occurs because Spm permeation rates are enhanced under these conditions. To test

Table 3–2: Spermine affinities of kainate receptors

Receptor	Variable	mean	s.e.m.	n
GluK2	$K_{d(0mV)}$ (µM)	5.8	0.3	5
	h (mV)	-16.0	0.5	
	k (mv)	20.4	1.0	
GluK2/GluK5	$K_{d(0mV)}$ (µM)	119	30	5
	h (mV)	-25.9	3.8	
	k (mv)	69.7	36.0	
GluK2+Neto1	$K_{d(0mV)}$ (µM)	71	13	6
	h (mV)	-24.0	1.8	
	k (mv)	43.3	4.3	
GluK2+Neto2	$K_{d(0mV)}$ (µM)	39	2	7
	h (mV)	-18.5	1.1	
	k (mv)	48.6	5.3	
GluK2/GluK5(P599G)	$K_{d(0mV)}$ (µM)	19	2	4
	h (mV)	-32.3	3.8	
	k (mv)	41.4	4.7	
GluK2 (300 µM L-Glu)	$K_{d(0mV)}$ (µM)	21	6	3
	h (mV)	-24.2	1.9	
	k (mv)	56.2	14.1	
GluK2/GluK5 (300 µM L-Glu)	$K_{d(0mV)}$ (µM)	170	33	3
	h (mV)	-51.4	20.0	
	k (mv)	107.7	47.2	
GluK2/GluK5 (1 mM AMPA)	$K_{d(0mV)}$ (µM)	81	40	3
	h (mV)	-73.4	27.7	
	k (mv)	56.8	22.9	

Affinities were obtained using responses evoked by 1 ms applications of 1 mM L-Glu in 150 mM NaCl external solution. Values for h and k indicate the voltage dependency.

this experimentally, we performed bi-ionic reversal potential experiments to determine the extent to which KAR composition affected polyamine permeation rates.

3.6.2 Heteromerization and auxiliary proteins relieve channel block by facilitating polyamine permeation

To determine the permeability of Spm relative to that of Na^+ (P_{Spm}/P_{Na}), we measured the reversal potential of KAR responses in solutions where the main external permeant cation was either 150 mM Na^+ or 90 mM Spm. In all cases, the main permeant cation of the internal solution was 150 mM Na^+ (Fig. 3–4 and see Methods).

As expected, responses mediated by GluK2 (V_{rev} = -0.2 ± 1.5 mV, Fig. 3–4 A and C, inset), GluK2/GluK5 (V_{rev} = -0.5 ± 0.8 mV, Fig. 3–4 D and F, inset) and GluK2+Neto2 (V_{rev} = -0.7 ± 0.8 mV, Fig. 3–4 G and I, inset) in symmetrical 150 mM Na^+ solutions reversed close to 0 mV, demonstrating that Na^+ ions are equally permeable from both sides of the plasma membrane. In contrast, reversal potentials determined with external 90 mM Spm as the main permeant cation were dependent upon the KAR composition. With GluK2 homomers, we failed to observe a reliable inward current in 90 mM external Spm and therefore were unable to estimate P_{Spm}/P_{Na} (Fig. 3–4 B and C), an observation similar to a previous study of polyamine permeation (Bahring et al., 1997).

In keeping with this, preliminary experiments suggested that polyamines with fewer charged groups, namely Put (z = +2) and Spd (z = +3), were more permeant than Spm (z = +4). Reversal potentials with 90 mM external Put or Spd as the main permeant cation were -8.0 ± 2.7 mV (n = 2) and -34.4 ± 1.6 mV (n = 3), respectively, estimating P_{Put}/P_{Na} to be 0.23 ± 0.02 and P_{Spd}/P_{Na} to be 0.049 ± 0.002 for GluK2 homomers. This indicates that permeant channel blockers with smaller valencies have a greater tendency to permeate through the KAR channel, in agreement with prior work (Bahring et al., 1997; Cui et al., 1998). In contrast to GluK2 homomers, Spm-mediated inward currents were observed with both GluK2/GluK5 (Fig. 3–4 E and F) and GluK2+Neto2 (Fig. 3–4 H and I), with reversal potentials of -43.2 ± 1.2 mV (n = 3) and -33.6 ± 4.5 mV (n = 4), respectively. As a result, the calculated P_{Spm}/P_{Na} for GluK2/GluK5 and GluK2+Neto2 receptors were 0.024 ± 0.001 and 0.042 ± 0.009, respectively. Taken together, these data provide evidence that GluK2/GluK5 and GluK2+Neto2 receptors were more permeable to Spm compared to GluK2 homomers.

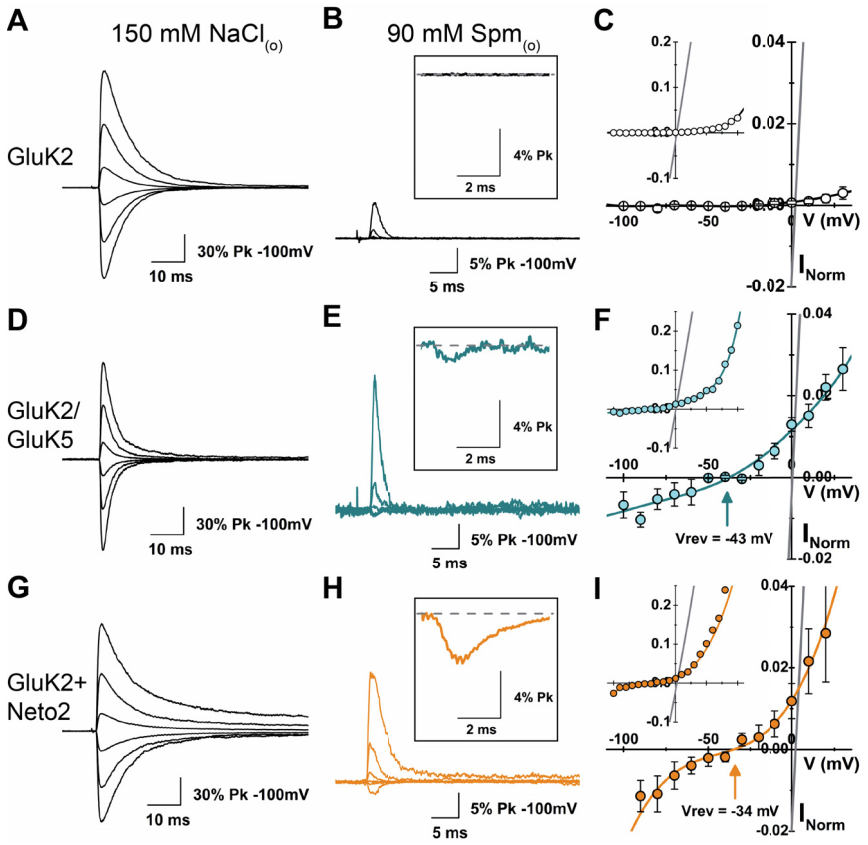

Figure 3–4: Spermine permeability is increased in GluK2/GluK5 and GluK2 + Neto2 Electrophysiological traces of GluK2 (A and B, patch # 130730p2), GluK2/GluK5 (D and E, patches # 121122p1 and 131206p2) and GluK2+Neto2 (G and H, patches # 131017p3 and 140410p9) evoked by 1 mM L-Glu (250 ms) at various holding potentials (-100 to +100 mV, 40 mV increments) in 150 mM NaCl external solution (left) or 90 mM Spm external solution (right). Insets show the current traces at -100 mV in 90 mM Spm. I–V plots in 90 mM external Spm for GluK2 (C, n = 4), GluK2/GluK5 (F, n = 3) and GluK2+Neto2 (I, n = 5). Arrows represent the reversal potentials for GluK2/GluK5 (V_{rev} = -43.2 mV) and GluK2+Neto2 (V_{rev} = -33.6 mV). Insets show the I–V plots ranging from -100 to +100 mV. Grey lines are the fits of the same receptor in the presence of 150 mM external NaCl. Data are represented as means ± SEM. Current values (both Na^+ and Spm currents) are normalized to the Na^+ current at 100 mV in the same patch.

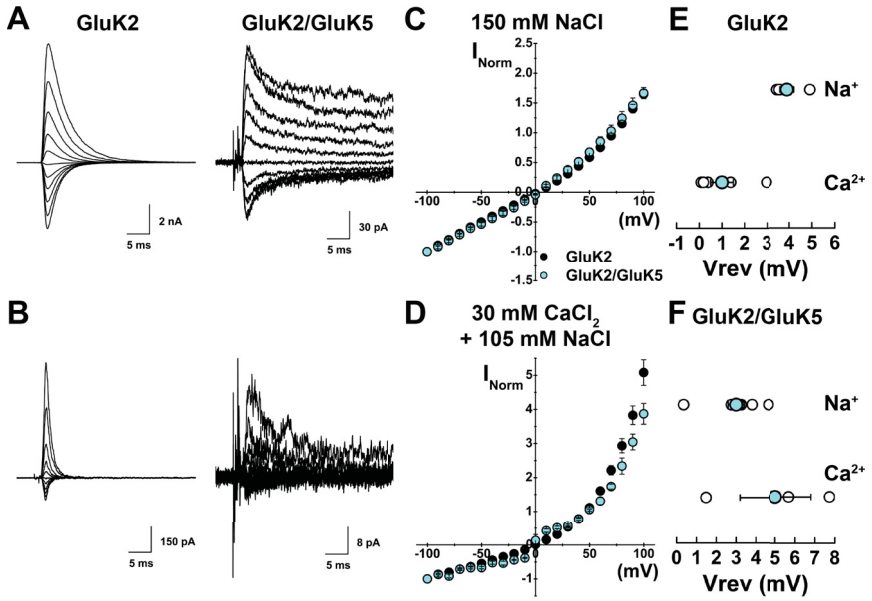

Figure 3–5: Ca^{2+} permeability is similar for GluK2 and GluK2/GluK5 kainate receptors

A, example membrane currents for GluK2 (left, patch # 120507p1) and GluK2/GluK5 (right, patch # 120522p2) evoked by 1 ms L-Glu applications (1 mM, in 150 mM NaCl) at various holding potentials (-100 to +100 mV, 20 mV increments) in the absence of internal polyamines. B, example membrane currents for GluK2 (left, same patch as in A) and GluK2/GluK5 (right, same patch as in A) evoked by 1 ms L-Glu applications (1 mM, in 30 mM $CaCl_2$) at various holding potentials (-100 to +100 mV, 20 mV increments) in the absence of internal polyamines. C, I–V relationships for GluK2 (black, $n = 4$) and GluK2/GluK5 (cyan, $n = 8$) in 150 mM NaCl external solution. D, I–V relationships for GluK2 (black, $n = 5$) and GluK2/GluK5 (cyan, $n = 3$) in 30 mM $CaCl_2$ external solution. Current values are normalized to the current at -100 mV. E and F, reversal potentials in 150 mM NaCl and 30 mM $CaCl_2$ external solutions for GluK2 (E) and GluK2/GluK5 (F). All data are represented as mean ± SEM.

A reduction in polyamine block is thought to go hand-in-hand with Ca^{2+} permeability in non-NMDA receptors (Burnashev, 1996). Despite these differences, KAR heteromerization or association with the auxiliary proteins do not attenuate Ca^{2+} permeability. For example, in Ca^{2+}-rich external solutions (i.e. 30 mM $CaCl_2$ + 105 mM NaCl), the reversal potential of GluK2 I–V plots was +1.0 ± 0.5 mV (n = 5) which was shifted to a slightly more positive potential of +5.0 ± 1.8 mV (n = 3) with GluK2/GluK5 heteromers (Fig. 3–5 E and F). As a result, the relative Ca^{2+} permeabilities (P_{Ca}/P_{Na}) of GluK2 homomers and GluK2/GluK5 heteromers were estimated to be 2.3 and 3.1, respectively. As a previous study has reported similar findings with the auxiliary proteins, Neto1 and Neto2 (Fisher and Mott, 2012), we concluded that differences in the pore properties of KARs induced by heteromerization or auxiliary proteins could not be revealed by studying divalent permeability; we therefore focused on polyamine block. Thus, KARs essentially behave as molecular sieves (Burnashev, 1996; Bahring et al., 1997) such that the movement of bulky permeating ions (i.e. Spm) is hindered in the permeation pathway while that of much smaller divalent cations, such as Ca^{2+} ions, is not. As explained below, we performed MD simulations to better understand this distinction by looking at how the pore region of KARs might be affected by modest changes in the ion-permeation pathway.

3.6.3 MD simulations predict a structural change in the channel pore

Sequence alignment of all KAR subunits was performed to identify differences between the GluK2 and GluK2/GluK5 receptors (Fig. 3–6 A). The most striking difference was found in the α-helical region of the re-entrant loop (P-loop; Fig. 3–6 A) where a glycine residue (i.e. GluK2 Gly615) is found in all primary subunits (GluK1-3) while a proline residue is found in the equivalent position (i.e. GluK5 Pro599) of secondary subunits (GluK4 and GluK5), which do not form functional

homomers. As each residue is located within a predicted α-helical region of the re-entrant P-loop of KARs (Panchenko et al., 1999) (Fig. 3–6 A), we reasoned that the Gly and Pro may exert differential effects on channel block and permeation. Specifically, we hypothesized that the Pro of the GluK5 subunit would result in structural changes in the heteromeric KAR pore regions, as has been proposed for Pro residues in other α-helical regions of ion-channels, such as the S6 helix of Shaker (Bright et al., 2002) and the M2 helix of KcsA K^+ channels (Fowler and Sansom, 2013).

To explore this, MD simulations were used to study how the introduction of the Pro residue may affect the pore structure and its dynamics (Fig. 3–6 B–D). As a high-resolution structure of the KAR pore region is not yet available, we performed MD simulations using the structure of the *Bacillus cereus* NaK channel pore [PDB # 3E86 (Alam and Jiang, 2009a), 1.6 Å resolution] as it has been used successfully to provide insight into the NMDA-type iGluR (Siegler Retchless et al., 2012). This structure has 4-fold symmetry, as expected for the GluK2 tetramer (Wilding et al., 2010) and furthermore illustrates an open conformation (Fig. 3–6 B and C). Although the iGluR pore structure has been compared to the KcsA structure (Sobolevsky et al., 2009), it also shares remarkable structural similarities with the NaK channel pore (Fig. 3–7). Moreover, because the NaK channel is a non-selective cation channel, its pore properties are expected to be closer to that of the iGluR. For these reasons, the NaK structure was used as a model of the pore in our MD simulations. To simulate a heteromer having a 2:2 stoichiometry, as is the case for GluK2/GluK5 KARs (Reiner et al., 2012), prolines were introduced into the equivalent α-helical positions of the NaK structure on opposing subunits (i.e. A and C), in agreement with prior work on KAR heteromers (Kumar et al., 2011).

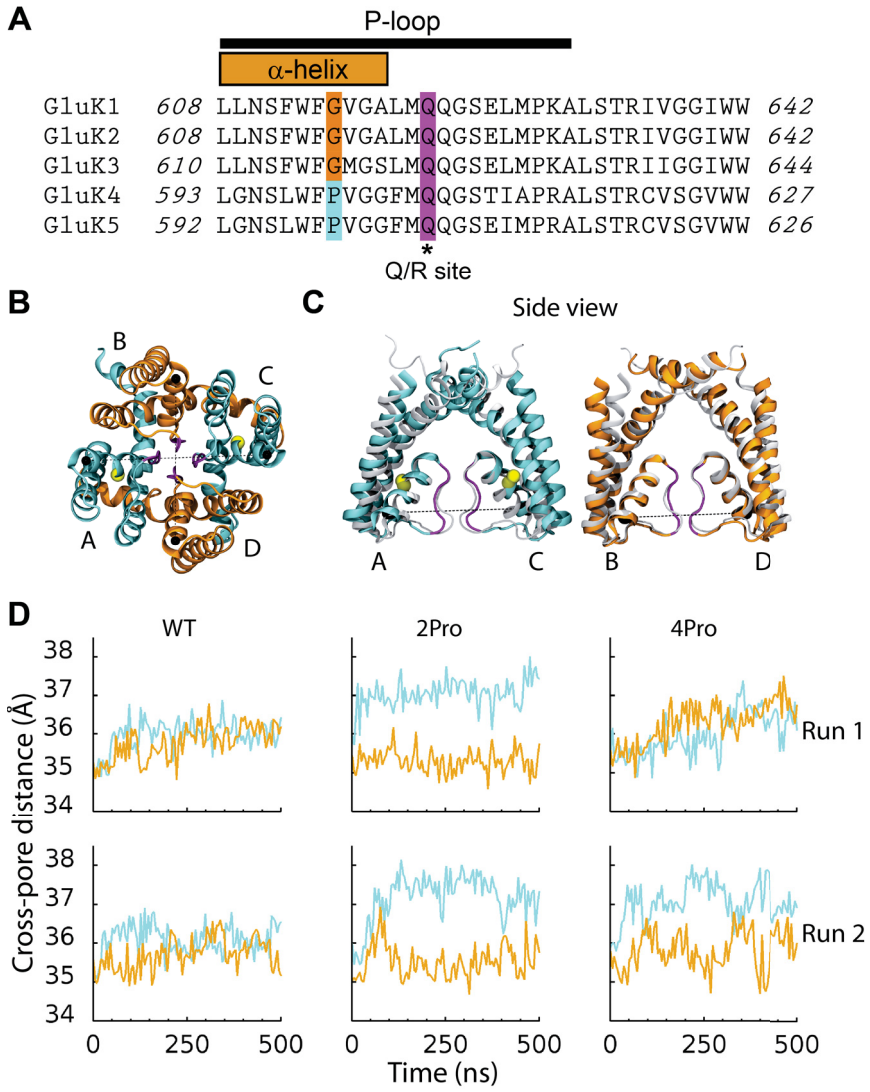

Figure 3–6: Prolines in GluK5 pore are predicted to alter pore dimensions
A, sequence alignment of the kainate receptor subunits. A proline is present in the secondary subunits where a conserved glycine is present in primary subunits. This residue is located within a region with a predicted α-helical structure of the P-loop. B, crystal structure of the NaK channel (PDB # 3E86). Proline residues were mutated in the equivalent α-helical structure of subunits A and C (yellow spheres). C, side view of the A/C (cyan) and B/D (orange) subunits of the inverted NaK pore before (grey) and after (coloured) 257 ns simulations. D, cross-pore distance measurements (see black spheres in C) were measured for 500 ns (two repeats for each condition).

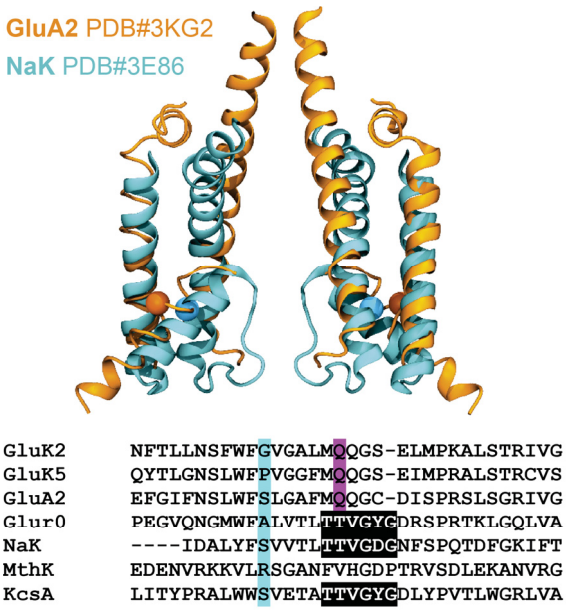

Figure 3–7: The NaK structure is similar to the GluA2 structure
The inverted structure of the open NaK channel (PDB # 3E86, cyan) is overlaid with that of the closed GluA2 (PDB # 3KG2, orange), illustrating that the two channels share a similar architecture. The proline position is indicated by a sphere. Only two chains are shown and for GluA2, only transmembrane helices M1–3 are included. The two structures are aligned using M2, C_α atoms of residues 573–586 in GluA2 and of residues 50–63 in the NaK channel. The position equivalent to the proline in GluK5 is highlighted by showing the C_α atom of this residue with a sphere (Ser580 in GluA2, Ser57 in NaK). A sequence alignment is shown, highlighting the Gly and Pro residues in GluK2 and GluK5, respectively, which correspond to an Ser in NaK.

Changes in cross-pore distances between the centre of mass of the α-carbons of residues 50–53 in opposing subunits are summarized in Fig. 3–6 D. As expected, the A/C and B/D cross-pore distances in the wild-type (WT) NaK pore quickly reached equilibrium and remained fairly constant for the rest of the 500 ns simulation (Fig. 3–6 D and supplementary Movies S1 and S2), consistent with a 4-fold symmetrical pore arrangement. In contrast, the pore adopted a 2-fold symmetry with prolines on opposing subunits (Fig. 3–6 D and Movies S1 and S2). For example, the mean distance between helices A/C increased by approximately 1 Å, while the distance between WT helices (B/D) decreased reciprocally (Fig. 3–6 D and Movies S1 and S2). Interestingly, the two simulation repeats with prolines introduced in all four helices illustrated two different outcomes (Fig. 3–6 D, 4Pro). In one case, helices adopted a 4-fold symmetry but with larger separation than the WT (Fig. 3–6 D, Run 1); in the second case, they adopted a 2-fold symmetry (Fig. 3–6 D, Run 2). Thus, despite the trajectories showing two different effects of proline insertions, they probably reflect the same result, namely that the Pro residue induces a more stochastic behaviour of the P-loop compared to the WT pore conformation.

To better understand how the Pro residues affect the dynamics of the NaK α-helical P-loop, we examined the root mean square deviation (RMSD) of each helix in comparison to the reference structure (Fig. 3–8; PDB # 3E86). Interestingly, the mean RMSD of Pro-containing helices in all simulations was about 0.5 Å, a 2-fold increase compared to the RMSD of WT helices (Fig. 3–8), indicating that they are able to move further away compared to their WT counterparts. Moreover, the RMSD fluctuation in the Pro-containing helices was much greater than in WT helices, spanning almost 0.2 Å, while the WT fluctuations spanned less than 0.1 Å (Fig. 3–8). Given this, we hypothesized that increased dynamics in the P-loop

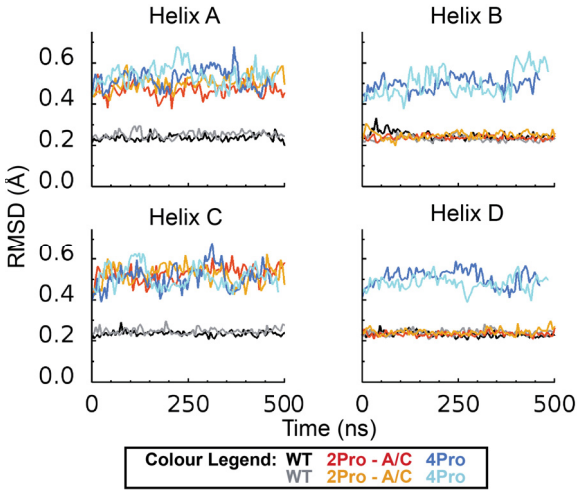

Figure 3–8: RMSD is larger in helices containing prolines
The RMSD values calculated for the C_α atoms of the P-loop helix (residues 50–62) of each chain of the NaK channel over the course of the 500 ns simulation. The alignment and RMSD calculation were performed for one chain at a time, aligning by residues 50–62 of the given helix for which the RMSD is calculated. WT helices are shown in black/grey, helices from the 2Pro simulation in red/orange and those of the 4Pro simulation in blue/cyan.

α-helices may be responsible for the enhanced polyamine permeation rates observed experimentally.

3.6.4 MD simulations predict increased polyamine permeation

To test whether Pro-induced changes in the position of the helices could facilitate blocker permeation, we compared the work required to pull pore-bound polyamines to the extracellular side of WT and mutant NaK pore regions, corresponding to the intracellular side in KARs (Fig. 3–9). Polyamines were also pulled to the intracellular side of the NaK pore, but the results from these experiments were inconclusive. From each of the WT trajectories in Fig. 3–6 D, the most symmetrical and the most asymmetrical snapshot (in terms of the cross-pore distance) was found and used as a starting structure, giving rise to a total of four different protein structures. Three polyamines of different structure and charge (Put, Spd and Spm) were modelled into the filter by overlaying with the original cations bound in the filter of the NaK structure (Fig. 3–9 A) (Alam and Jiang, 2009a). After 30 ns of relaxation, all

polyamines were still bound to the filter region. To probe the strength with which the polyamines bind to the filter, SMD simulations were subsequently performed. In the SMD simulations, polyamines were pulled out of the filter along the z-axis toward the intracellular side of the membrane (Movie S3). Each SMD simulation produced a force profile from which the work involved in the process was calculated (Fig. 3–9 B). The eight snapshots shown in Fig. 3–10 correspond to time steps at which the force peaks, each denoted in Fig. 3–9 B by an asterisk, along with snapshots before and near the end of the SMD simulation. From the SMD simulations with different polyamines, a clear trend in the work values was observed (Fig. 3–9 C and Movie S3), suggesting that, in the WT pore, it is easier for the smaller polyamines (Put and Spd) to pass through from the filter than Spm, in agreement with our data and that of others (Bahring et al., 1997). Similar SMD simulations were performed with Spm inserted into the most symmetrical or the most asymmetrical snapshots from the 2Pro and 4Pro trajectories from Fig. 3–6 D. As before, all Spm molecules were still bound to the filter region in the 12 different systems (4×WT, 4×2Pro, 4×4Pro) after 30 ns of relaxation. The calculated work values for pulling Spm to the solvent were lower for the 2Pro and 4Pro mutants than for the WT pore (Fig. 3–9 D). Thus, this model system suggests that the Pro residue in the α-helical region of the GluK5 P-loop may be enough to disturb Spm binding and ensure higher permeation and unblock in the GluK2/GluK5 heteromers.

3.6.5 Pro599 in the GluK5 pore is the main determinant of polyamine block

To assess whether GluK5 Pro599 is responsible for enhanced polyamine permeation, we measured the degree of channel block after substituting it with a Gly residue, as is found in GluK2 (Fig. 3–9 E–G). As anticipated, the degree of inward rectification of GluK2/GluK5(P599G) channels was significantly more

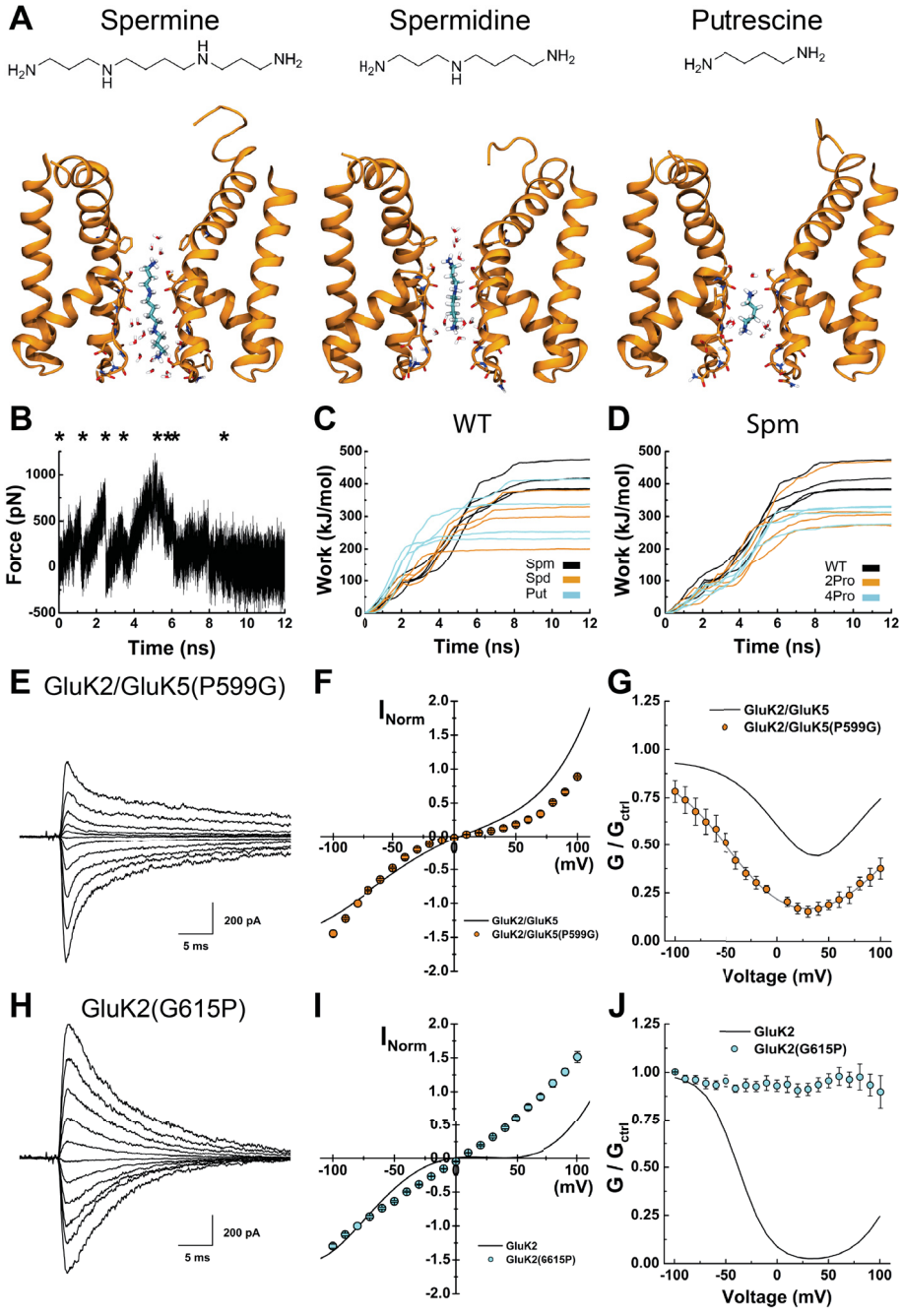
A
Spermine
Spermidine
Putrescine
B
Force (pN)
Time (ns)
C
WT
Work (kJ/mol)
Spm
Spd
Put
Time (ns)
D
Spm
Work (kJ/mol)
WT
2Pro
4Pro
Time (ns)
E
GluK2/GluK5(P599G)
200 pA
5 ms
F
I Norm
(mV)
GluK2/GluK5
GluK2/GluK5(P599G)
G
GluK2/GluK5
GluK2/GluK5(P599G)
G / G ctrl
Voltage (mV)
H
GluK2(G615P)
200 pA
5 ms
I
I Norm
(mV)
GluK2
GluK2(6615P)
J
GluK2
GluK2(G615P)
G / G ctrl
Voltage (mV)

pronounced than observed with WT heteromers (Fig. 3–9 F). This finding demonstrates that Pro599 is a critical determinant of polyamine block. Fits of the corrected G–V plot estimated the $K_{d(0mV)}$ of GluK2/GluK5(P599G) receptors to be 19 ± 2 µM, which was 4–5 fold more potent than WT heteromers with a $K_{d(0mV)}$ of 119 ± 30 µM (Fig. 3–9 G and Table 3–2). Interestingly, the $K_{d(0mV)}$ of Spm for GluK2/GluK5 (P599G) was statistically indistinguishable from GluK2 homomers [one-way ANOVA, $F_{7,28} = 8.506$, $P = 0.000014$; *post hoc* Tukey honest significant difference (HSD) pairwise comparison, $P = 1.000$; Table 3–2, indicating that the removal of Pro599 from GluK2/GluK5 heteromers enhances channel block. As a result, the differences between the G–V plots of GluK2 (Fig. 3–2 B) and mutant heteromers (Fig. 3–9 G) are found in the voltage-dependency of block (Table 3–2).

To test if the reverse substitution would render GluK2 receptors polyamine-insensitive, Gly615 was replaced with a Pro residue, as is found in GluK5 (Fig. 3–9 H–J). In contrast to WT GluK2, the I–V plot for GluK2(G615P) in the presence of 60 µM internal Spm was almost entirely linear, demonstrating that the introduction of Pro615 in the pore region of GluK2 eliminates polyamine

Figure 3–9 *(preceding page)*: Proline in the M2 helix controls spermine block and permeation
A, each of the three polyamines binding in the NaK filter region, from left to right: spermine (Spm), spermidine (Spd), putrescine (Put). For simplicity, only chains A and C of the protein are included and non-polar hydrogen atoms of the protein are omitted. Carbon atoms of the ligands are shown in cyan. B, an example of a force profile illustrating the force added when pulling Spm out of the WT filter towards the intracellular side. C, work profiles for pulling the three different polyamines to the intracellular side in the WT protein. Spm results are shown in black, Spd in orange and Put in cyan. The work involved in Spm release is generally larger than for release of the smaller polyamines. D, work profiles for pulling Spm to the intracellular side for the WT protein (black), the 2Pro mutant (orange) and the 4Pro mutant (cyan). E and H, example responses of GluK2/GluK5(P599G) (E, patch # 130610p7) and GluK2(G615P) (H, patch # 130606p2) at various holding potentials (-100 to +100 mV, 20 mV increments) in the presence of 60 µM internal spermine. Average I–V plots (F, I) and corrected G–V plots (G, J) for these receptors in the presence of internal spermine. Relationships for GluK2 and GluK2/GluK5 (grey lines in G and J) are shown for comparison. Data are represented as mean ± SEM. Current values are normalized to the current at -100 mV.

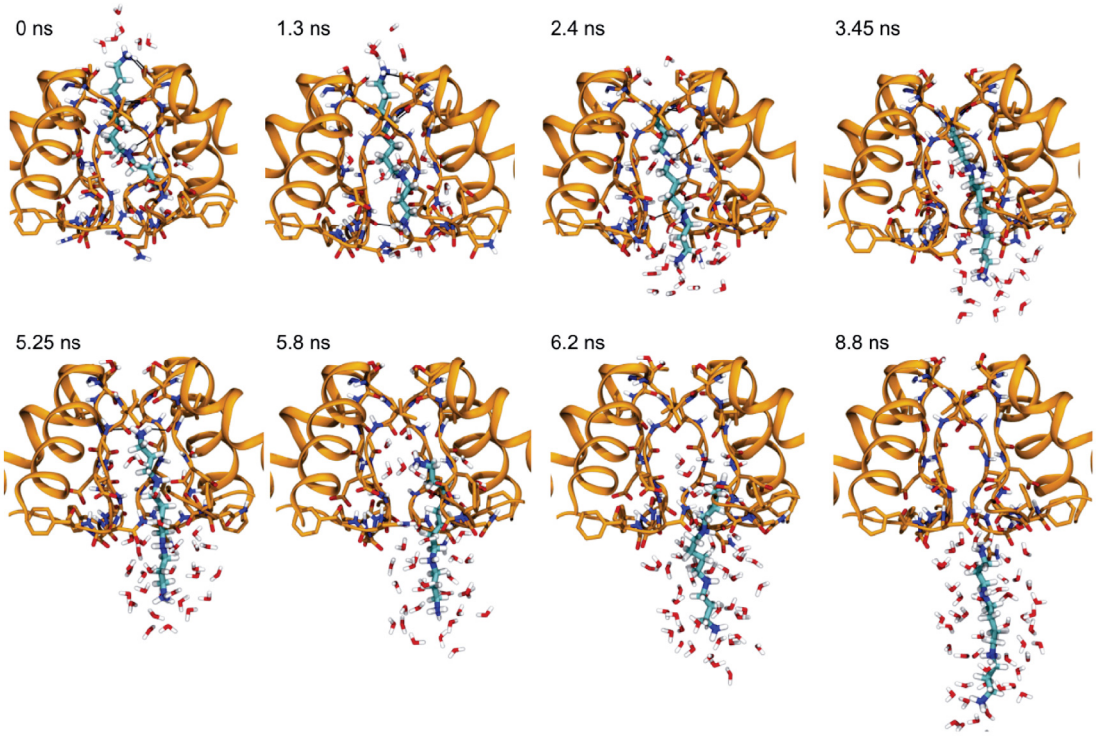

Figure 3–10: Snapshots illustrating the interactions as Spm is pulled toward the intracellular side of the membrane
Snapshots corresponding to the asterisks in Fig. 3–9 B. Spermine is shown with cyan carbon atoms. Hydrogen bonds between spermine and the protein [dist(H–O) < 2.5 Å] are indicated with black lines.

block (Fig. 3–9 I). In agreement with this, the corrected GluK2(G615P) G–V plot lacked voltage-dependency (Fig. 3–9 J), further underlining that this Pro residue is the principal determinant of Spm block in GluK2/GluK5 heteromers.

3.6.6 Auxiliary proteins and GluK5 relieve polyamine block by distinct mechanisms

To test whether auxiliary proteins relieve KAR channel block by a similar or different mechanism, we took advantage of the fact that GluK2(G615P) channels are unaffected by Spm block (Fig. 3–9 H–J). We reasoned that if auxiliary subunits attenuate Spm block by a different mechanism, their co-expression with GluK2(G615P) would increase the relative Spm permeability of the channel complex. Conversely, if they attenuate Spm block by a similar mechanism, the ability of Spm to permeate GluK2(G615P) channels would remain unchanged by co-expression with an auxiliary subunit.

In contrast to WT GluK2 (Fig. 3–11 A and D), Spm-mediated inward currents were readily observed at negative membrane potentials with GluK2(G615P) (Fig. 3–11 B and E). The reversal potential of GluK2(G615P) with 90 mM external Spm was -25.5 ± 2.4 mV (n = 5) (Fig. 3–11 B and E), estimating the P_{Spm}/P_{Na} to be 0.062 ± 0.008 (Fig. 3–11 G), similar to GluK2/GluK5 and GluK2+Neto2 (Fig. 3–11 G).

Interestingly, the magnitude of Spm-induced inward currents in patches containing GluK2 (G615P) channels co-expressed with Neto2 was increased by about 2-fold (Fig.3–11 C and F). For example, the Spm-mediated current at -100 mV was 8 ± 5% (n = 5) of the Na^+ -mediated current with GluK2(G615P) and 19 ± 12% (n = 7) with GluK2(G615P)+Neto2. In addition, the reversal potential observed with 90 mM external Spm was more positive for GluK2(G615P)+Neto2 than GluK2(G615P) alone (V_{rev} = -15.6 ± 2.3 mV; n = 4), estimating P_{Spm}/P_{Na} to

be 0.12 ± 0.02 (Fig. 3–11 G). One-way ANOVA performed on the relative Spm permeability revealed that P_{Spm}/P_{Na} for GluK2(G615P)+Neto2 was significantly larger than for GluK2(G615P), GluK2+Neto2 and GluK2/GluK5 (Fig. 3–11, see figure legend for P values). These results indicate that co-expression of KARs with Neto2 increases blocker permeation in an additive manner, suggesting that it is acting through a mechanism that is distinct from that of the Pro residues in GluK5 subunits.

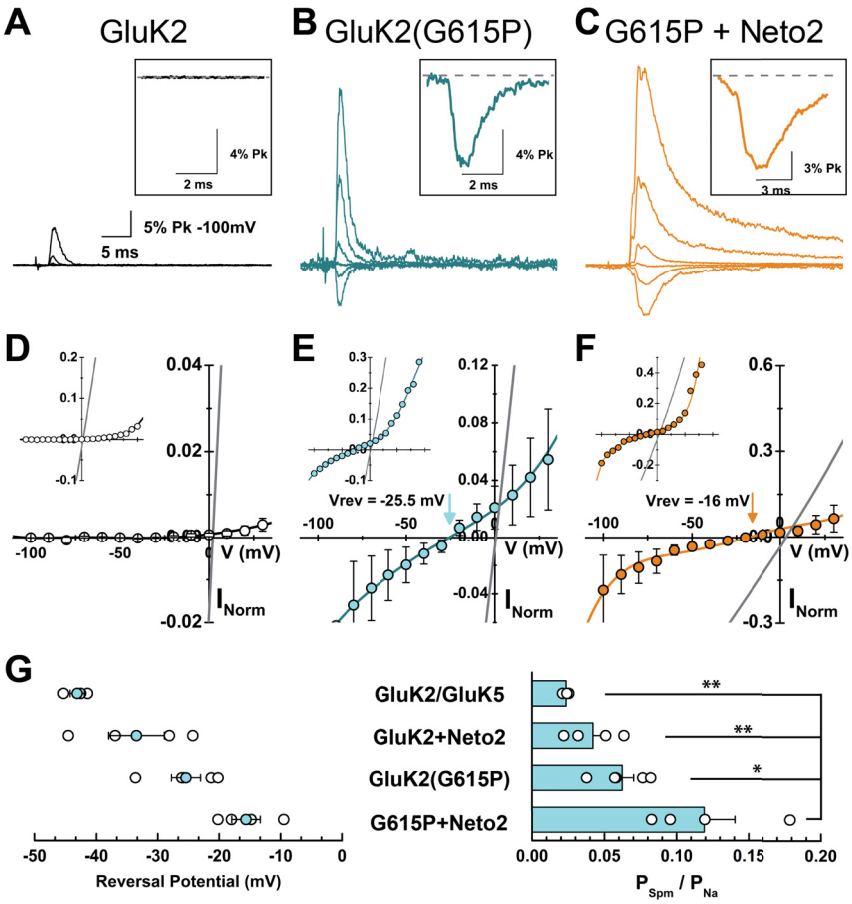

Figure 3–11: G615P mutation and Neto2 association increase spermine permeation of GluK2

Example responses of GluK2 (A, same data as in Fig. 3–4, GluK2(G615P) (B, patch # 130906p2) and GluK2(G615P)+Neto2 (C, patch # 140814p4) in 90 mM external Spm, at various holding potentials (-100 to +100 mV, 40 mV increments). Insets show the response in 90 mM external Spm at -100 mV. Average I–V plot for GluK2 (D, same data as in Fig. 3–4), GluK2(G615P) (E, $n = 5$) and GluK2(G615P)+Neto2 (F, $n = 4$) in 90 mM external Spm; arrows indicate reversal potentials for GluK2(G615P) (V_{rev} = -25.5 mV) and GluK2(G615P)+Neto2 (V_{rev} = -15.6 mV). Insets show the I–V plots ranging from -100 to +100 mV. Grey lines are the fits of the same receptor in the presence of 150 mM external NaCl. Data are represented as means and SEM. Current values (both Na^+ and Spm currents) are normalized to the Na^+ current at -100 mV in the same patch. G, left: summary plot showing the V_{rev} (in 90 mM Spm) for the various receptors tested. Right: summary plot showing the calculated relative Spm permeabilities (P_{Spm}/P_{Na}). One-way ANOVA, $F_{3,12} = 9.801$, $P = 0.002$; *post hoc* Tukey HSD pairwise comparisons: $*$ $P = 0.027$ and $**$ $P = 0.005$ and 0.002 for G615P+Neto2–GluK2+Neto2 and G5615P+Neto2–GluK2/GluK5 comparisons, respectively.

3.7 Discussion

The present study advances our understanding of polyamine block of KARs in several fundamental ways. First, we report that heteromerization and auxiliary proteins unexpectedly attenuate channel block by enhancing polyamine permeation rates. Second, MD simulations suggest that relief of block is due to a structural change in the α-helical region of the KAR pore, which is distinct from the charge-screening mechanism ascribed to GluA2-containing AMPARs. Our data identify that each of two GluK5 subunits in the GluK2/GluK5 heteromer possesses a critical proline residue that is predicted to push the helices outward, leading to a 2-fold symmetrical pore arrangement and increased pore helix fluctuation. Third and finally, heteromerization and auxiliary proteins relieve polyamine block by a distinct pathway. Consequently, Neto1 and Neto2 do not attenuate polyamine block by channelling their effect through the proline residue of GluK5 subunits.

3.7.1 The dynamic nature of polyamine block

Our study reveals that subunit composition affects the functional properties of KARs differently than AMPARs. In AMPARs, the Q/R site of the GluA2 subunit is >99% edited to an Arg but remains unedited in all other subunits (Sommer et al., 1991). This distinction is significant because it generates the two major AMPAR classes that are either GluA2-containing, polyamine-insensitive and divalent cation-impermeable or GluA2-lacking, polyamine-sensitive and divalent cation-permeable [(Cull-Candy et al., 2006) but see Bowie (2012)]. Importantly, polyamine-insensitivity of GluA2-containing AMPARs is thought to be due to the electrostatic effect of Arg at the Q/R site of GluA2, which repels polyamines in the narrowest region of the pore (Bowie et al., 1999). However, this reliance on the editing state of the Q/R site is not thought to be as important for KAR heteromers

because it is edited only 40% in GluK1 subunits with a range of estimates for GluK2 from <5 to 75% in the developing and adult rodent brain (Sommer et al., 1991; Puchalski et al., 1994; Schmitt et al., 1996). It has yet to be tested whether the Q/R site of other KAR subunits (i.e. GluK3–5) is edited or not. Our data demonstrate that GluK2/GluK5 heteromers attenuate polyamine block not by electrostatic repulsion but rather through a novel mechanism involving a structural change in the pore helices. Accordingly, the binding affinity for polyamines in the pore is reduced, enhancing their permeation rates. This is achieved through the distinctive cyclical structure of the proline side chain that is conformationally rigid and lacks the N–H hydrogen bond donor, and thus can uniquely distort α-helical structures. As proline residues are found exclusively in GluK4–5 subunits and are absent from GluK1–3 subunits, we predict that heteromers containing either GluK4 or GluK5 will exhibit a diminished level of polyamine block even if the Q/R site of all four subunits is unedited, as is the case in this study. This arrangement is distinct from AMPARs where the coupling of polyamine block and divalent cation permeability is governed by a common structural determinant, namely the Q/R site. As different structural domains govern polyamine block and Ca^{2+} permeability in KAR heteromers, native receptors will exhibit appreciable Ca^{2+} permeability that is unconstrained by significant voltage-dependent modifications in membrane conductance due to polyamine block.

3.7.2 Prolines in the KAR pore α-helices promote altered pore dynamics

MD simulations are consistent with a mechanism in which proline residues are arranged on opposing subunits of the NaK tetramer, resulting in a 2-fold symmetrical pore arrangement that alters the pore dynamics. In keeping with this, recent studies have shown that GluK2/GluK5 heteromers have a subunit copy

number of 2:2 (Reiner et al., 2012). Interestingly, prolines are found in many transmembrane α-helices of transport proteins and ion channels, as is the case in the present study, but are uncommon in water-soluble helices (Brandl and Deber, 1986; Barlow and Thornton, 1988; Tieleman et al., 2001). They are most frequently located on the hydrophilic side of the helix (Woolfson and Williams, 1990), where they destabilize the helix and tend to produce hinges, kinks or swivels (Cordes et al., 2002). Given these observations, we hypothesized that the proline found in the re-entrant P-loop of the GluK5 subunit might result in a similar structural rearrangement in the KAR channel pore, as has been proposed for the S6 α-helix in Shaker (Bright et al., 2002) and the M2 helix in KcsA potassium channels (Fowler and Sansom, 2013). In the latter case, the introduction of prolines in the M2 helices predicted the formation of kinks and helical rearrangement after only 10 ns of MD simulation, with the pore helices adopting 2-fold symmetry instead of 4-fold symmetry (Fowler and Sansom, 2013). Similarly, the introduction of prolines in the P-loop of the NaK channel pore, which was used in the present study as a model of the KAR channel pore, resulted in small changes in the position of the outer region of the helices. Accordingly, our data suggest that reduced channel block and enhanced polyamine permeation rates occur through an increased structural flexibility of the pore α-helices due to proline residues that bring about an asymmetrical re-arrangement and enlargement of the KAR channel pore.

3.7.3 Auxiliary proteins and polyamine block

Auxiliary proteins of AMPARs and KARs are not pore-forming components of the channel (Chen et al., 2000; Tomita et al., 2003; Zhang et al., 2009) and therefore it has been unclear how they cause attenuation of polyamine channel block. The proximal end of the C-terminal region of the TARP, γ-2 or stargazin, has been shown

to attenuate polyamine block of AMPARs through a mechanism that involves a direct interaction with the intracellular domain of GluA1 or GluA4 subunits (Soto et al., 2014). A similar finding has been reported with Neto2, where positive residues in the proximal intracellular C-terminal domain are implicated in reducing polyamine block (Fisher and Mott, 2012). Although it is still unclear how these residues affect inward rectification of GluK2 channels, we found that the auxiliary protein achieves this by increasing the blocker permeation, which seems at odds with the charge screening hypothesis. Our data demonstrate that Neto1 and Neto2 exert a structural effect on the channel pore that is distinct from that seen in GluK2/GluK5 heteromers. Exactly how auxiliary proteins achieve this remains to be investigated. However, given the similarity between the effect of auxiliary proteins on KARs and AMPARs, we predict that TARPs and cornichons are likely to attenuate polyamine block of AMPARs by the same mechanism, i.e. by increasing polyamine permeation.

3.8 Author Contributions

P.M.G.E.B. designed and performed experiments, analysed data and wrote the paper; M.R.P.A. designed experiments and wrote the paper; M.M. designed and performed experiments, analysed data and wrote the paper; P.C.B. and D.B. designed experiments and wrote the paper. All authors have approved the final version of the manuscript, agree to be accountable for all aspects of the work and qualify for authorship.

3.9 Acknowledgements

This work was supported by operating grants from the Canadian Institutes of Health Research (to D.B.), the Leverhulme Trust RPG-059 (P.C.B and M.M.) and the Medical Research Council (MR/M0004331, P.C.B). P.M.G.E.B. was supported by a graduate student fellowship from the Fonds de Recherche en Santé du Québec and M.R.P.A. was supported by a Banting and Best graduate fellowship from the CIHR. D.B. is the recipient of a Canada Research Chair. M.M. was supported by a post-doctoral fellowship from the Alfred Benzon Foundation. This work made use of the facilities of ARCHER (www.archer.ac.uk) granted via the UK High-End Computing Consortium for Biomolecular Simulation, HECBioSim (hecbiosim.ac.uk, grant no. EP/L000253/1) and HECToR, the UKs national high-performance computing service, funded by the Office of Science and Technology through EPSRCsHigh End Computing Programme. We also acknowledge the use of the IRIDIS High Performance Computing Facility, Advanced Research Computing, Oxford, the National Service for Computational Chemistry Software and the Blue Joule facility at the Hartree Centre. We thank R. McInnes for the Neto1-HA plasmid and J. R. Howe for the Neto2 plasmid. We wish to thank members of the Bowie lab for insightful discussion of the manuscript.

3.10 Supporting information

The following supporting information is available in the online version of this article.

Movie S1. MD simulation of the NaK channel with 2 Pro substitutions. This movie illustrates the MD simulation of the 2Pro mutant of the NaK channel over 500 ns. Ser57 was substituted with a Pro residue in opposing subunits A and C, and the C_α of the inserted Pro is shown as a yellow sphere. The NaK structure is inverted so that the orientation of the helices matches that of the kainate receptor. The four subunits of the tetramer are shown as pairs of opposing subunits. The A and C subunits are on the left (cyan) and the B and D subunits are on the right (orange). The original protein structure is shown in white; the selectivity filter is highlighted in magenta. The Pro-containing α-helices (cyan, including the selectivity filter) tend to move outward, while the WT helices (orange) tend to move inward.

Movie S2. MD simulation of the NaK with 2 Pro substitutions, intracellular view. This movie illustrates the same MD simulation as in Movie S1, viewed from the intracellular side. The Pro-containing helices (cyan) seem to bend back, pulling the selectivity filter (magenta) away from the original crystal structure (white). In contrast, the selectivity filter for the WT helices tends to move slightly closer, causing a more asymmetrical arrangement of the filter, which in turn may affect polyamine permeation.

Movie S3. SMD simulation pulling pore-bound polyamines to the intracellular side. This movie illustrates the binding (from left to right) of Spm, Spd and Put to the WT NaK pore region simulated for 30 ns of relaxation before being pulled to the intracellular side. Ligands are illustrated with cyan carbon atoms and for clarity only chains A and C are shown. Protein residues in the filter are shown with

licorice representation along with other protein residues and water molecules within 4 Å of the ligands.

CHAPTER 4
AMPAR AUXILIARY PROTEINS RELIEVE CHANNEL BLOCK BY FACILITATING POLYAMINE PERMEATION

Patricia M.G.E. Brown, Hugo McGuire and Derek Bowie

To be submitted in a modified form.

4.1 Foreword to Chapter 4

Interestingly, despite having very different structures (Straub and Tomita, 2012), the auxiliary proteins of KARs and AMPARs exert similar effects on their receptors. For example, on a macroscopic level, both AMPARs and KARs display slower decay kinetics and accentuated steady-state currents (Tomita et al., 2005; Schwenk et al., 2009; Zhang et al., 2009; Straub et al., 2011; Coombs et al., 2012). On a microscopic level, however, they are acting through different mechanisms. Specifically, both TARPs and CNIHs increase the unitary conductance of AMPARs (Coombs et al., 2012; Soto et al., 2014), while Neto2 increases the channel burst length and open probability without affecting the conductance (Zhang et al., 2009).

Similar to those of KARs, the auxiliary proteins of AMPARs also relieve polyamine block (Soto et al., 2007; Coombs et al., 2012; Soto et al., 2014). In the previous chapter, we uncovered that polyamine permeation through the KAR pore is facilitated by the auxiliary protein, Neto2. Given this, we asked whether the relief of channel block could also be due to facilitated polyamine permeation through AMPARs by the auxiliary proteins, stargazin (or γ2) and CNIH-3.

By performing similar permeation experiments as in Chapter 3, we demonstrate in this chapter that the auxiliary proteins of AMPARs also facilitate blocker permeation. Moreover, AMPARs are generally more permeable to polyamines than KARs, even in the absence of auxiliary proteins. Furthermore, given the availability of pharmacological tools to block desensitization in AMPARs, we were able to measure the voltage- (and polyamine) -dependent current decay in GluA2 currents, which allowed us to estimate the rates of binding, unbinding and permeation of the blocker, as previously described for kainate receptors using the partial agonist domoate (Bowie et al., 1998). In analysing the polyamine block for AMPARs with auxiliary proteins, we observed a decrease in conductance in the

G–V relationship at very positive membrane potentials, which could not be explained by the current model. To explain our data, we built upon the existing model by taking into account that auxiliary proteins increase the conductance of polyamines. These results are surprising and could be of particular interest, since polyamines play important cellular roles and a general polyamine transporter has not yet been identified for mammalian cells (Poulin et al., 2012).

4.2 Key Points

- Auxiliary proteins of AMPARs, $\gamma 2$ and CNIH-3, relieve channel block by enhancing blocker permeation at GluA2(Q) receptors.
- Polyamine block of GluA2(Q) receptors in the presence of auxiliary proteins is not well described by a single binding site model for a permeant blocker, as previously characterized with GluK2 KARs.
- A new model, which includes a polyamine conductance, is more appropriate to describe the relief of polyamine block at positive potentials.
- This mechanism is common between auxiliary proteins of non-NMDA iGluRs.
- AMPARs with auxiliary proteins may participate in the regulation of intracellular polyamine levels.

4.3 Abstract

Many cation-selective ion channels exhibit inward rectification, a phenomenon that is attributed to the voltage-dependent block by intracellular polyamines. For non-NMDAR ionotropic glutamate receptors (iGluRs), polyamines have been well-characterized to act as permeant channel blockers. However, an increasing number of studies demonstrate that synaptic iGluRs associate with auxiliary proteins, and that these interactions effectively reduce polyamine block. Although the mechanisms underlying this relief of channel block remain unclear, it was recently shown that the KAR auxiliary proteins, Neto1 and Neto2, attenuate polyamine block by enhancing blocker permeation through the channel pore. Here, we show that the auxiliary proteins of AMPARs, $\gamma 2$ and CNIH-3, also facilitate polyamine permeation through the channel. Using a new model of channel block that includes a polyamine conductance, we propose that high polyamine permeation at positive membrane potentials hinders Na^+ permeation, causing a

reduction in the overall channel conductance. Although the exact structural mechanism remains to be investigated, our study provides insight into a functional mechanism underlying the relief of polyamine block that is shared among the auxiliary proteins of iGluRs, and that could also apply to other cation-selective ion channels. Furthermore, given the unexpectedly high levels of polyamine permeation, AMPARs with auxiliary proteins could be used by cells to regulate intracellular polyamine levels.

4.4 Introduction

AMPA receptors mediate the vast majority of fast excitatory neurotransmission in the CNS. They are tetrameric ion channels, assembled as a combination of pore-forming subunits (GluA1-4), which associate with auxiliary proteins (Fukata et al., 2005; Vandenberghe et al., 2005; Schwenk et al., 2009; Traynelis et al., 2010). The functional properties of synaptic AMPARs depend strongly on their subunit composition and editing status (Traynelis et al., 2010). For example, a post-transcriptional RNA editing mechanism changes the codon encoding for a glutamine (Q) residue to that for an arginine (R) at this site, resulting in the loss of polyamine affinity, and thus channel rectification (Bowie and Mayer, 1995), as well as Ca^{2+} permeability (Burnashev et al., 1995). The relationship between divalent permeability, polyamine block and editing state of the Q/R site has been ratified by extensive work on the α-amino-3-hydroxy-5-methyl-4-isoxazolepropionic acid (AMPA) receptor subunit GluA2, where the vast majority ($> 99\%$) of neuronal transcripts are in the edited form (Sommer et al., 1991).

The proper trafficking and pore properties of AMPARs are also dependent on their association with auxiliary proteins, such as the transmembrane AMPAR regulatory proteins (TARPs) and cornichon homologs (CNIH) (Chen et al., 2000; Schwenk et al., 2009; Herring et al., 2013). For example, the TARP, $\gamma 2$ or stargazin, increases the single-channel conductance (Soto et al., 2014) while reducing the polyamine block in calcium-permeable AMPARs, without altering their divalent permeability (Soto et al., 2007). The cornichon homolog, CNIH-3, also shifts polyamine block of GluA1 channels, albeit to a lesser extent than $\gamma 2$ (Coombs et al., 2012). In both cases, the proximal residues of the auxiliary protein C-terminal regions are critical for these changes in the pore properties (Shanks

et al., 2014; Soto et al., 2014). The exact mechanism by which this occurs remains unclear. A similar phenomenon has been reported with KARs and their auxiliary proteins (Fisher and Mott, 2012). For example, Neto2 significantly increases the burst length of GluK2 channels (Zhang et al., 2009) and reduces polyamine block without affecting divalent permeability (Fisher and Mott, 2012). Interestingly, the positively-charged proximal C-tail residues of Neto2 (and Neto1) are also critical for this effect and they are proposed to act in a charge-screening mechanism, thereby repelling the positively-charged polyamines from the channel pore and preventing polyamine block (Fisher and Mott, 2012). Furthermore, the relief of polyamine block in GluK2 channels is accompanied by an important increase in blocker permeation when Neto2 is present (Brown et al., 2016). Given the similarities between the effects of auxiliary proteins on AMPAR and KAR pores, we hypothesized that the auxiliary proteins of AMPARs also increase blocker permeation, resulting in an apparent reduction in polyamine affinity at AMPARs.

In this study, we found that the co-expression of AMPARs with the auxiliary proteins, $\gamma 2$ and CNIH-3, resulted in a significant increase in polyamine permeation, with an even greater magnitude than has been observed with KARs (Brown et al., 2016). In addition, we found that the permeation of polyamines produced a significant conductance through the channel pore and that the single conductance model, previously used to describe the conductance of sodium and polyamine block of ionotropic glutamate receptors (iGluRs) (Bowie et al., 1998), did not represent our data. Given this, we propose a new two-conductance model to describe polyamine block of iGluRs, which takes into account the polyamine conductance. With this model, we observed that the rates of unbinding and permeation were increased when both auxiliary proteins were present, which is consistent with the increase in polyamine permeation and decreased affinity. Our

study provides insight into the mechanism governing the relief of polyamine block in AMPARs by auxiliary proteins.

4.5 Materials and Methods

4.5.1 Plasmids and molecular biology

All experiments were performed using cDNA of rat GluA2, GluA2-γ2 (in tandem) (Dawe et al., 2016) and CNIH-3. The GluA2 plasmid contained a downstream P2A sequence and the sequence encoding for GCaMP6s to identify transfected cells. GluA2-γ2 was co-transfected with a plasmid encoding eGFP.

4.5.2 Cell culture and transfection

HEK293T/17 cells (ATCC, Manassas, VA, USA) were maintained in minimal essential medium (MEM) containing glutaMAX© supplemented with 10% fetal bovine serum (Invitrogen, Carlsbad, CA, USA). Cells were plated at low density ($1.6 - 2.0 \times 10^4$ cells ml^{-1}) on poly-D-lysine-coated 35 mm plastic dishes and were transiently transfected 48 h later using the calcium phosphate technique. A GluA2:CNIH-3 cDNA molar ratio of 1:2 was used and 30 µM 6,7-dinitroquinoxaline-2,3-dione (DNQX) was included in the medium after transfection to prevent cell death.

4.5.3 Electrophysiological recordings

Experiments were performed 24–48 h after transfection. Agonist solutions were rapidly applied to outside-out patches excised from transfected cells using a piezoelectric stack (Physik Instrumente, Auburn, MA, USA). Solution exchange (10–90% rise time of 250–350 µs) was determined by measuring the liquid junction current at the end of an experiment. All recordings were performed using an Axopatch 200B (Molecular Devices, Sunnyvale, CA, USA) using thick-walled borosilicate glass pipettes (3–6 MΩ) coated with dental wax to reduce electrical noise. Current records were filtered at 10 kHz and digitized at 100 kHz for block rate experiments and filtered at 5 kHz and digitized at 25 kHz for Spm permeation

experiments. Series resistance (3–12 MΩ) was compensated by 95%. Recordings were performed at a range of holding potentials from -100 to +130 mV to study polyamine channel block. Data acquisition was performed using pClamp10 software (Molecular Devices) and tabulated using Excel (Microsoft Corp). All experiments were performed at room temperature.

All chemicals were purchased from Sigma-Aldrich (St Louis, MO, USA) unless otherwise indicated. The external solution contained (in mM) 150 NaCl, 5 HEPES, 0.1 $MgCl_2$ and 0.1 $CaCl_2$, pH 7.3–7.4. The internal solution contained (in mM) 115 NaCl, 10 NaF, 5 HEPES, 5 Na_4BAPTA (Life Technologies, Invitrogen, Burlington, ON, Canada), 1 $MgCl_2$, 0.5 $CaCl_2$ and 10 Na_2ATP, pH 7.3–7.4. The osmotic pressure of all solutions was adjusted to 295–300 mOsm with sucrose. In polyamine block experiments, Na_2ATP in the internal solution was replaced with 10–100 µM Spm (from a concentrated stock solution) and the osmotic pressure was adjusted to 295–300 mOsm with sucrose. For polyamine permeation experiments, the NaCl in the external solution was replaced by 90 mM Spm, pH was adjusted to 7.3–7.4 using the Spm free base and the osmotic pressure was adjusted with sucrose. Concentrated (10×) agonist stock solutions were prepared by dissolving L-glutamate (L-Glu) in the appropriate external solution, adjusting the pH to 7.3–7.4 and stored frozen at −20 °C. Stocks were thawed on the day of the experiment and used to prepare agonist-containing external solutions.

4.5.4 Data analysis and fitting

Relative Spm permeability (P_{Spm}/P_{Na}) was calculated from the reversal potential (V_{rev}) measurements in Spm-rich external solutions using the following equation from Bahring et al. (1997) (equation 4.1):

$$I_x = P_x z^2 \times \left(\frac{V_m F^2}{RT}\right) \times \left(\frac{[X]_i - [X]_o exp\left(\frac{-zFV_m}{RT}\right)}{1 - exp\left(\frac{-zFV_m}{RT}\right)}\right) \tag{4.1}$$

where I_x is the current carried by ion X at a membrane potential V_m; P_x the corresponding permeability ($P_{Na} = 1$); $[X]_i$ and $[X]_o$ the internal and external Spm concentrations; z, the valence, F, Faraday's constant; R, the gas constant and T, the temperature in Kelvin. Experimentally determined reversal potentials were used for V_m. We obtained P_{Spm}/P_{Na} using the definition that $I_{Na} + I_{Spm} = 0$ at the reversal potential. The reversal potentials were corrected for liquid junction potentials that were determined experimentally.

Agonist-evoked membrane conductance (G) was calculated using equation 4.2:

$$G = \frac{I}{(V - V_{\text{rev}})} \tag{4.2}$$

where I is the current at V holding potential and V_{rev} is the reversal potential.

4.5.4.1 Single conductance model of polyamine block

Conductance-voltage (G–V) relationships were fit using Origin 7 (OriginLab, Northampton, MA, USA) with the following equation (from Bowie et al. (1998)) (equation 4.3):

$$G = \frac{Gmax}{1 + \frac{[Spm]}{K_d}} \tag{4.3}$$

where G_{max} is the maximal conductance, $[Spm]$ is the internal Spm concentration and K_d is the dissociation constant.

K_d was defined as:

$$K_d = \frac{k_{off} + k_{perm}}{k_{on}} = \frac{\text{sum of exit rates}}{\text{binding rate}}$$

and was then redefined to (equation 4.4):

$$K_d = g\ exp\left(\frac{V}{h}\right) + L\ exp\left(\frac{V}{k}\right) \tag{4.4}$$

Voltage (V)-dependent binding (k_{on}), unbinding (k_{off}) and permeation (k_{perm}) rates were defined as previously in (Bowie et al., 1998; Brown et al., 2016) (equations 4.5, 4.6 and 4.7):

$$k_{on} = a\ exp\left(\frac{V}{b}\right) \tag{4.5}$$

$$k_{off} = c\ exp\left(\frac{V}{d}\right) \tag{4.6}$$

$$k_{perm} = e\ exp\left(\frac{V}{f}\right) \tag{4.7}$$

A summary of fitted constants a, b, c, d, e and f is shown in Table 4–3.

Auxiliary proteins affect the voltage-dependent conductance of KARs under basal conditions within the range of ± 100 mV (Brown et al., 2016). To account for these differences, the intrinsic G–V relationships were fit with the following equation (equation 4.8) using Origin 7 (OriginLab):

$$G = 1 + (G_0 - 1)\ exp\left(\frac{V}{V_c}\right) \tag{4.8}$$

Where G_0 is the minimal conductance and V_c is a voltage constant. Values are summarized in Table 4–1.

Current relaxations over time t by polyamine block were fit to the function $I(t, V)$ (equation 4.9):

$$I(t, V) = (I_0 - I_\infty)\ e^{-\left([Spm]k_{on} + k_{off} + k_{perm}\right)t} + I_\infty \tag{4.9}$$

Where I_0 is the current value before blocker entry and I_∞ is the stable current value after decay by blocker entry. I_0 was estimated using an exponential fit. I_∞ can

be represented as follows (equation 4.10):

$$I_\infty = \frac{I_0}{1 + \frac{[Spm]}{K_d}} \tag{4.10}$$

All the fits were done using the Levenberg-Marquardt method. To compare the fit block rate constants with those obtained using the G–V relationships, we redefined the constants in equation 4.4 to the following (equations 4.11, 4.12, 4.13 and 4.14):

$$g = \frac{c}{a} \tag{4.11}$$

$$L = \frac{e}{a} \tag{4.12}$$

$$h = \frac{bd}{b-d} \tag{4.13}$$

$$k = \frac{bf}{b-f} \tag{4.14}$$

4.5.4.2 Two-conductance model of polyamine block

Conductance-voltage (G–V) relationships were fit using Matlab with the following equation (equation 4.15).

$$\frac{G}{G_{max}} = \frac{k_{off}\left([Spm]k_{on} + k_1\right) + k_1 k_{perm} + \frac{G_{Spm}}{G_{Na}}\left(k_{perm}\left([Spm]k_{on} + k_{1'}\right) + k_{1'}k_{off}\right)}{\left([Spm]k_{on} + k_{1'} + k_1\right)\left([Spm]k_{on} + k_{off} + k_{perm}\right)} \tag{4.15}$$

Where G_{max} is the maximal conductance, $[Spm]$ is the internal Spm concentration and k_{on}, k_{off}, k_{perm}, k_1 and $k_{1'}$ are as defined in equations 4.5, 4.6 and 4.7 and Figure 4–3 A. G_{Spm}/G_{Na} is the ratio of conductance of Spm over Na^+ and was obtained using the equations as follows:

$$\frac{G_{Spm}}{G_{Na}}\left(V \neq 0\right) = \left| 16\left(\frac{P_{Spm}}{P_{Na}}\right)\left(\frac{[Spm]_i\left(1 - e^{-FV/RT}\right)}{\left(1 - e^{-4FV/RT}\right)\left([Na]_i - [Na]_o e^{-4FV/RT}\right)}\right)\right| \tag{4.16}$$

$$\frac{G_{Spm}}{G_{Na}}(V=0) = \left| 16 \left(\frac{P_{Spm}}{P_{Na}} \right) \left(\frac{[Spm]_i}{4\left([Na]_i - [Na]_o\right)} \right) \right| \tag{4.17}$$

Where P_{Spm}/P_{Na} was taken from the permeability experiments as described above.

Current relaxations over time t by polyamine block were fit to the function $I_2(t,V)$:

$$I_2(t,V) = I_0 \Bigg[\left(m_1 \left(1 - n_{Na\infty}\right) - \frac{G_{Spm}}{G_{Na}} m_2 n_{Spm\infty} \right) e^{-\mu_1 t} + \left(\left(1-m_1\right)\left(1-n_{Na\infty}\right) - \frac{G_{Spm}}{G_{Na}}\left(1-m_2\right) n_{Spm\infty} \right) e^{-\mu_2 t} + n_{Na\infty} + \frac{G_{Spm}}{G_{Na}} n_{Spm\infty} \Bigg] \tag{4.18}$$

Where

$$\mu_1 = k_{1'} + k_1 + [Spm]k_{on} \tag{4.19}$$

$$\mu_2 = [Spm]k_{on} + k_{off} + k_{perm} \tag{4.20}$$

$$m_1 = \frac{\left(\frac{\left([Spm]k_{on}+k_{off}+k_{perm}\right)(k_{1'}+k_1+[Spm]k_{on})(k_{1'}+[Spm]k_{on})}{k_{1'}\left([Spm]k_{on}+k_{off}+k_{perm}\right)+[Spm]k_{on}([Spm]k_{on}+k_1+k_{perm})} - \mu_2 \right)}{\mu_1 - \mu_2} \tag{4.21}$$

$$m_2 = \frac{\left(\frac{k_{1'}\left([Spm]k_{on}+k_{off}+k_{perm}\right)(k_{1'}+k_1+[Spm]k_{on})}{k_{perm}([Spm]k_{on}+k_{1'})+k_{1'}k_{off}} - \mu_2 \right)}{\mu_1 - \mu_2} \tag{4.22}$$

$$n_{Na\infty} = \frac{k_{off}\left([Spm]k_{on}+k_1\right) + k_1 k_{perm}}{\left([Spm]k_{on}+k_{1'}+k_1\right)\left([Spm]k_{on}+k_{off}+k_{perm}\right)} \tag{4.23}$$

$$n_{Spm\infty} = \frac{k_{perm}\left([Spm]k_{on} + k_{1'}\right) + k_{1'}k_{off}}{\left([Spm]k_{on} + k_{1'} + k_1\right)\left([Spm]k_{on} + k_{off} + k_{perm}\right)} \tag{4.24}$$

All the fits were done using the Levenberg-Marquardt method. A program that performs these tasks was written in the Matlab language. We will make this program as well as its source code available on demand.

All data were illustrated using Origin 7 (OriginLab) and Adobe Illustrator.

4.5.5 Statistics

Statistical analysis was performed using the statistical software SPSS Statistics. Data were assumed to be distributed normally. The numbers provided for n refer to the number of individual patches.

4.6 Results

4.6.1 Auxiliary proteins increase Spm permeation through GluA2 receptors

To investigate the mechanism by which auxiliary proteins relieve polyamine block of AMPARs, the two auxiliary subunits, γ2 and CNIH-3, were selected as representatives of the transmembrane AMPA receptor-associated protein (TARP) and cornichon homolog (CNIH) classes of auxiliary proteins, respectively. To estimate polyamine permeation at GluA2 AMPARs, outside-out patches excised from HEK293T cells transfected with GluA2(Q), GluA2-γ2 or GluA2+CNIH-3 were subjected to 10 mM L-Glu applications (200 ms). The functional presence of γ2 (Tomita et al., 2005) or CNIH-3 (Schwenk et al., 2009; Coombs et al., 2012) was confirmed by the slowed decay kinetics and sustained steady-state currents of L-Glu -evoked responses at the start of each experiment (Figure 4–1 A–C). To measure the Spm permeability relative to that of Na^+ (P_{Spm}/P_{Na}), we measured the reversal potentials (V_{rev}) of each receptor complex in solutions where the main external permeant cation was Na^+ (150 mM) or Spm (90 mM). The results from this experiment are summarized in Figure 4–1.

Responses for all receptor complexes reversed near 0 mV in symmetrical Na^+ solutions (Figure 4–1 J). Interestingly, the V_{rev} for GluA2+CNIH-3 in Na^+ external solution was positively shifted compared to that of GluA2 alone or with γ2 [Figure 4–1 J; $V_{rev} = +2.0 \pm 0.1$ mV ($n = 6$), $+2.1 \pm 0.4$ mV ($n = 7$) and $+4.2 \pm 0.6$ mV ($n = 9$) for GluA2, GluA2-γ2 and GluA2+CNIH-3, respectively; one-way ANOVA, $F_{2,19} = 4.022$, $P = 0.03495$; post-hoc Tukeys HSD pairwise comparisons, $P = 0.061$]. This is consistent with the increased mean single-channel conductance observed when CNIH-3 is co-expressed with the unedited (Q) forms of GluA1 and GluA2 receptors (Coombs et al., 2012).

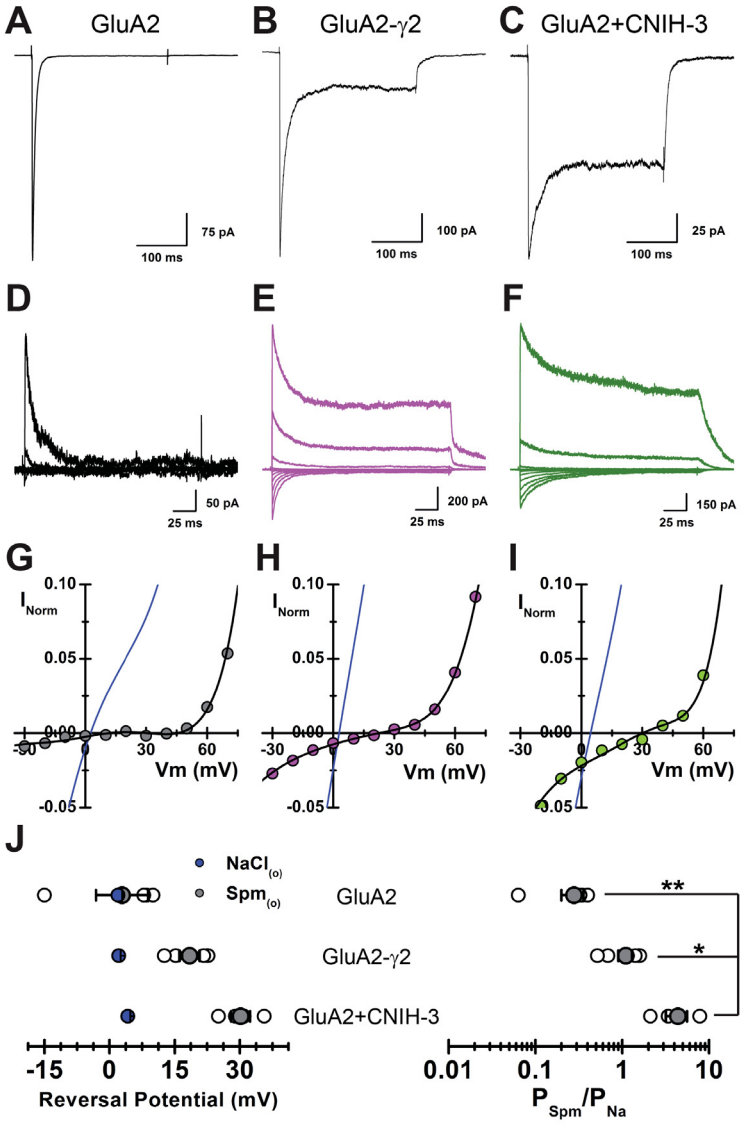

Figure 4–1: Spermine permeation through GluA2(Q) is increased by auxiliary proteins A, B, C, Example electrophysiological responses from GluA2 (A, patch # 150911p1), GluA2-γ2 (B, patch # 151126p5) and GluA2+CNIH-3 (C, patch # 151109p4) evoked by 10 mM L-Glu (250 ms, holding potential (Hp) = -60 mV) in the presence of 150 mM $NaCl_{(o)}$. D, E, F, Example traces from GluA2 (D, patch # 151016p2), GluA2-γ2 (E, patch # 151008p5) and GluA2+CNIH-3 (F, patch # 151009p9) at various potentials (range: -100 to +100 mV, 10 mV increments) in the presence of 90 mM $Spm_{(o)}$. G, H, I, Corresponding I–V plots (near the reversal potential (V_{rev}) for the patches shown in D, E and F are shown in grey (G, GluA2), magenta (H, GluA2-γ2) and green (I, GluA2+CNIH-3). Average fits of the I–V plots in the presence of $NaCl_{(o)}$ are displayed in blue. J, Summary of the V_{rev} (left) and relative Spm permeability (P_{Spm}/P_{Na}; right) values. V_{rev} values in the presence of $NaCl_{(o)}$ are displayed in blue. $*P = 0.014$, $**P = 0.005$.

Spm-mediated inward currents were readily observed at GluA2 channels with Spm as the main external permeant cation (Figure 4–1 D and G), reversing at +2.7 ± 5.9 mV ($n = 4$). Using equation 4.1 (see Methods), the P_{Spm}/P_{Na} for GluA2 was estimated to be 0.28 ± 0.08 (Figure 4–1 J). This is in stark contrast to homomeric GluK2 receptors, for which the relative Spm permeability was found to be very low, if at all detectable (Bahring et al., 1997; Brown et al., 2016). The V_{rev} for the current responses was shifted to more positive potentials when the auxiliary proteins were present [V_{rev} = +18.4 ± 2.4 mV ($n = 5$) and +30.2 ± 2.2 mV ($n = 4$) for GluA2-γ2 (Figure 4–1 E and H) and GluA2+CNIH-3 (Figure 4–1 F and I), respectively], estimating the P_{Spm}/P_{Na} to be 1.1 ± 0.2 and 4.4 ± 1.2, respectively (Figure 4–1 J). These represent 4-fold and 16-fold increases in Spm permeation, which was significantly larger with GluA2+CNIH-3 compared to GluA2-γ2 and GluA2 alone (one-way ANOVA, $F_{2,10} = 10.133$, $P = 0.004$; post-hoc Tukeys HSD pairwise comparisons, $P = 0.005$ and 0.014 for the GluA2+CNIH-3 - GluA2 and GluA2+CNIH-3 GluA2-γ2 comparisons; $P = 0.636$ for the GluA2 GluA2-γ2 comparison). Taken together, our data demonstrate that the auxiliary proteins, γ2 and CNIH-3, increase blocker permeation through the GluA2 channel pore, an effect that is similar to that of Neto2 at GluK2 KARs (Brown et al., 2016).

4.6.2 Spermine block of GluA2 is reduced with auxiliary proteins γ2 and CNIH-3

To study the kinetics of polyamine block at AMPARs, as well as equilibrium open-channel block, outside-out patches excised from HEK293T cells transfected with GluA2(Q), GluA2-γ2 or GluA2+CNIH-3 were subjected to 10 mM L-Glu applications in the presence of 100 µM cyclothiazide (CTZ, to attenuate desensitization) and the holding potential was stepped from +130 mV to -100 mV in 10 mV increments. Figure 4–2 summarizes the results from this experiment.

As previously described for GluK2 (Bowie et al., 1998), GluA2 currents did not decay in the absence of internal polyamines (Figure 4–2 B). Here, the current-voltage (I–V) relationship was outwardly rectifying (Figure 4–2 C). In contrast, current relaxations decayed when 10–30 µM spermine (Spm; $n = 7$) was included in the internal pipette. I–V plots for peak responses were outwardly rectifying, similar to that observed in the absence of internal polyamines (Figure 4–2 C), indicating that most of the polyamine block has not yet occurred within 100–200 µs at these Spm concentrations. In contrast, I–V plots constructed with responses at equilibrium (40–45 ms after the voltage step) in the presence of 30 µM $Spm_{(i)}$ (Figure 4–2 B) displayed strong inward rectification (Figure 4–2 C), consistent with polyamine block of AMPARs (Bowie and Mayer, 1995).

As was the case for GluA2 alone, currents following voltage steps did not decay in the absence of $Spm_{(i)}$ when auxiliary proteins were present (Figure 4–2 E and H). However, although the current did decay in the presence of 30 µM $Spm_{(i)}$, this decay was largely attenuated, especially in the case of γ2 (Figure 4–2 E and H). Interestingly, in contrast with what has been observed with GluA4 and γ2 (Soto et al., 2007), the degree of intrinsic outward rectification of GluA2 was reduced by the presence of γ2 and CNIH-3 (Figure 4–2 F and I). These differences in the intrinsic voltage-dependent gating are also observed with various KAR complexes (Bahring et al., 1997; Bowie et al., 1998; Brown et al., 2016). In agreement with other studies (Soto et al., 2007; Coombs et al., 2012; Soto et al., 2014), the degree of inward rectification of GluA2 I–V plots caused by 30 µM $Spm_{(i)}$ was also attenuated by the presence of auxiliary proteins, especially for GluA2-γ2 (Figure 4–2 F and I).

To first characterize the equilibrium block at these receptors, conductance-voltage (G–V) plots of the steady-state currents were constructed in order to obtain estimates of the blocker affinity at GluA2 receptor complexes

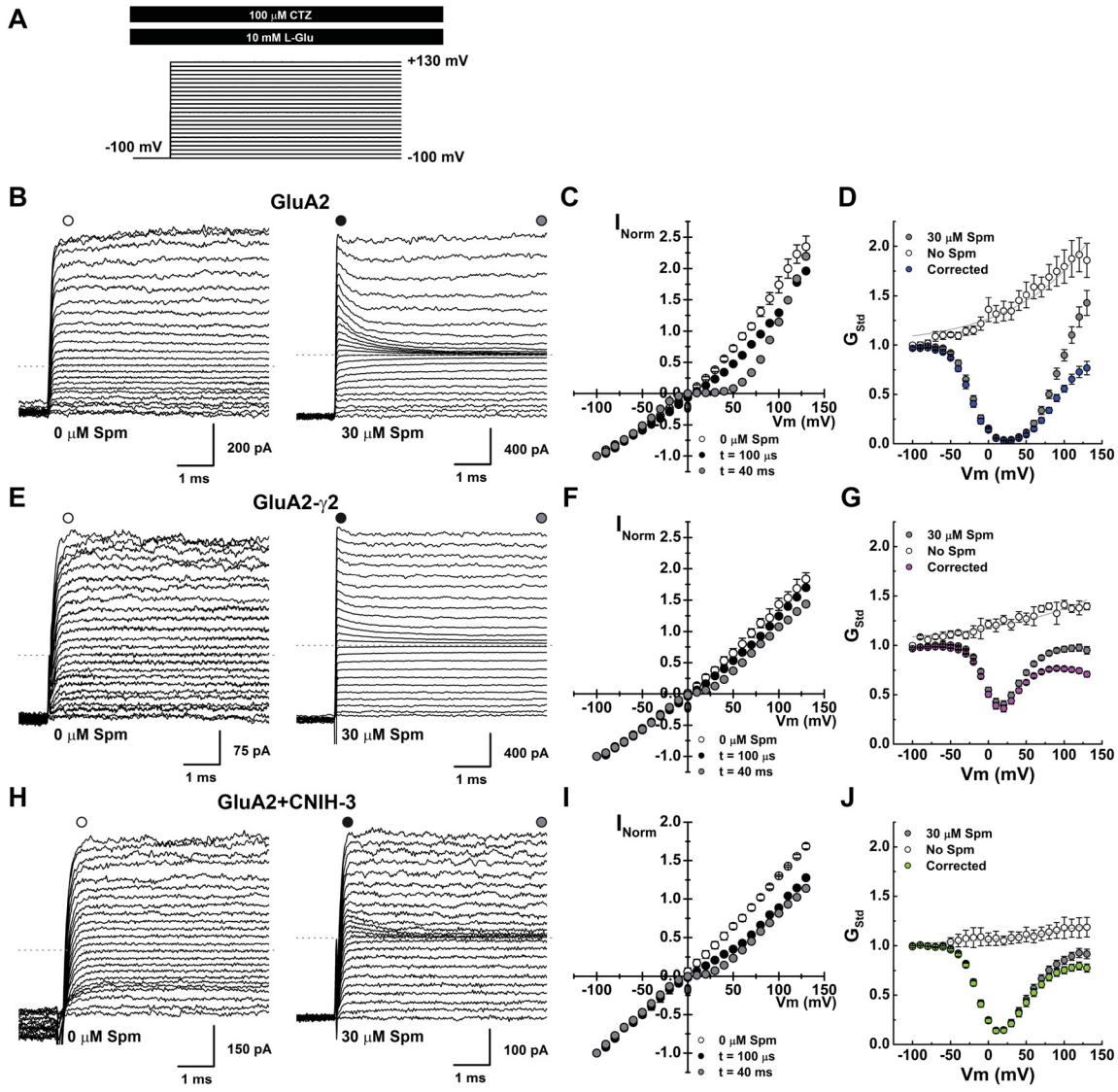

Figure 4–2: Polyamine block of GluA2 receptors is attenuated by auxiliary proteins
A, Responses from outside-out patches were evoked by 10 mM L-Glu in the presence of 10 μM cyclothiazide (CTZ) at a *Hp* of -100 mV. At equilibrium, patches were subjected to voltage steps (range: -100 mV to +130 mV, 10 mV increments). B, E, H, Example voltage-step responses in the absence (left) or presence (right) of 30 μM $Spm_{(i)}$ for GluA2 (B, patches # 150724p1 (Ctrl) and 150911p1 (Spm)), GluA2-γ2 (E, patches # 150723p3 (Ctrl) and 151126p5 (Spm)) and GluA2+CNIH-3 (H, patches # 151203p1 (Ctrl) and 151109p4 (Spm)). C, F, I, I–V plots for each receptor complex (C, GluA2; F, GluA2-γ2; I, GluA2+CNIH-3). Average I–V plots in the absence of $Spm_{(i)}$ are shown in white circles (GluA2, $n = 5$; GluA2-γ2, $n = 4$; GluA2+CNIH-3, $n = 3$). I–V plots of the peak responses (100–200 μs after the voltage steps) are in black and equilibrium I–V plots are in grey, for the patches shown in B, E and H. D, G, J, Average G–V plots for each receptor complex (D, GluA2, blue; G, GluA2-γ2, magenta; J, GluA2+CNIH-3, green). G–V plots in the absence of $Spm_{(i)}$ are in white, raw G–V plots with 30 μM $Spm_{(i)}$ are in grey and corrected G–V plots (see Methods) are coloured. Data in I–V and G–V plots are shown as mean and SEM.

(Figure 4–2 D, G and J). G–V plots in the presence of internal Spm were corrected for the intrinsic outward rectification displayed by GluA2 receptors (Figure 4–2 D), as previously described (Bowie et al., 1998; Brown et al., 2016). The intrinsic G–V properties of GluA2 (Figure 4–2 D), GluA2-γ2 (Figure 4–2 G) and GluA2+CNIH-3 (Figure 4–2 J) were described with equation 4.8 (see Methods); a summary of the constants is listed in Table 4–1. The differences in the intrinsic voltage-dependent gating properties with various receptor complexes underline the importance of correcting individual G–V plots, thereby allowing for a more accurate characterization of polyamine block for every channel complex.

Table 4–1: Fit parameters for intrinsic G–V relationships

Receptor	G_0	V
GluA2	1.2674	96.2
GluA2-γ2	1.1815	140.0
GluA2+CNIH-3	1.0604	104.3

4.6.3 Analysis of spermine block at AMPARs with a single conductance model

Corrected G–V plots were fit with a single binding site model (Figure 4–3 A) to estimate the dissociation constant for Spm at 0 mV ($K_{d(0mV)}$), as previously described (Bowie et al., 1998; Brown et al., 2016). For GluA2, the fits were able to follow the experimental data and yielded estimates of $K_{d(0mV)}$ for Spm that were not significantly different between various $\text{Spm}_{(i)}$ concentrations, with $K_{d(0mV)}$ values of 2.8 ± 0.4 µM (n = 3), 3.9 ± 1.1 µM (n = 3) and 4.3 ± 0.6 µM (n = 5) for 10, 20 and 30 µM $\text{Spm}_{(i)}$ respectively (one-way ANOVA, $F_{2,8}$ = 1.101, P = 0.378). Figure 4–3 B shows the average G–V plot for GluA2 with 30 µM $\text{Spm}_{(i)}$. The fit parameters for GluA2 Spm block were therefore pooled and the average estimate of $K_{d(0mV)}$ was 3.6 ± 0.4 µM (n = 12; Table 4–2), similar to that observed with GluK2 receptors (Brown et al., 2016). As an internal test of the single conductance model,

the parameters obtained from individual G–V fits at various Spm concentrations were used to simulate G–V curves at 30 µM Spm (Figure 4–3 B, right). Here, we found that the simulated G–V was reasonably representative of the data (Figure 4–3 B) and concluded that the single conductance model of polyamine block was adequate to study the characteristics of polyamine block at GluA2 receptors.

This model was also used to characterize the channel block at GluA2-γ2 and GluA2+CNIH-3 channel complexes. As for GluA2, $K_{d(0mV)}$ values were independent of the Spm concentration (10–100 µM $\text{Spm}_{(i)}$, not shown) and the estimates were pooled. The average $K_{d(0mV)}$ for Spm were estimated to be 34.3 ± 2.9 µM ($n = 18$) and 9.6 ± 1.5 µM ($n = 13$) for GluA2-γ2 and GluA2+CNIH-3, respectively (Table 4–2). As previously shown (Coombs et al., 2012), CNIH-3 was less effective than γ2 at reducing polyamine block of GluA2 despite its larger impact on the decay kinetics and steady-state current (Figure 4–1 and Table 4–2). However, while the model was able to fit the GluA2 G–V plots well, it was inadequate with the GluA2-γ2 and GluA2+CNIH-3 G–V plots. Specifically, the fits were poor at positive membrane potentials and could not account for the decrease in conductance at these membrane potentials (Figure 4–3 C and D, left). In addition, simulated G–V curves for 30 µM Spm, using parameters from the fits, did not represent the data (Figure 4–3 C and D, right). In fact, all simulated curves returned toward the maximal conductance, which was not the case for the experimentally-observed data. This suggests that the single conductance model of polyamine block is not adequate to describe polyamine block at these receptor complexes. More specifically, the model cannot account for the reduction in the conductance at positive potentials (Figure 4–3 B–D, left).

4.6.4 A two-conductance model of polyamine block

Given the large increase in the relative Spm permeation with auxiliary proteins (Figure 4–1), we postulated that Spm permeation through the channel pore, in

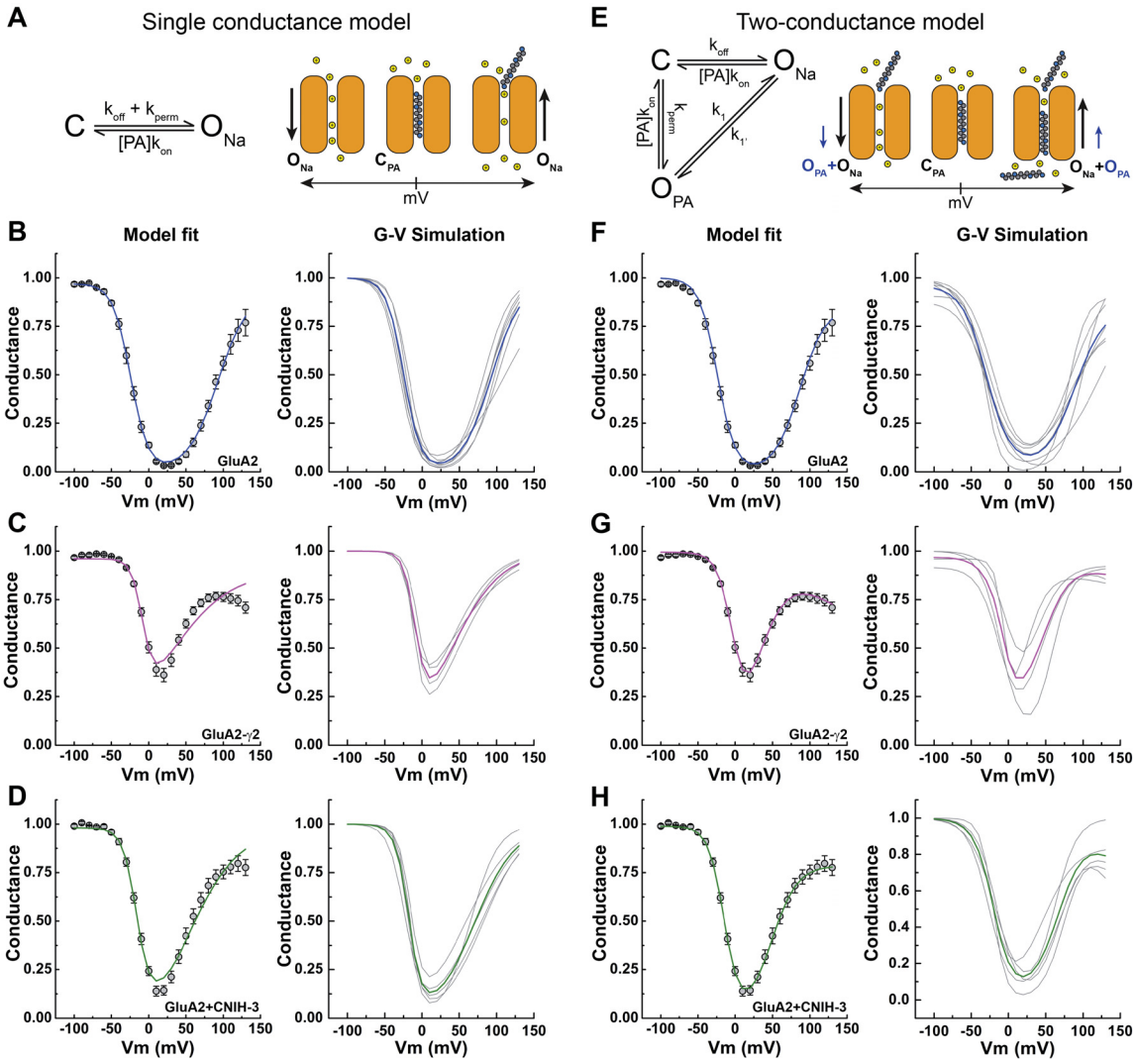

Figure 4–3: Two models of polyamine block
A, The single conductance model. C denotes a closed (non-conducting) state and O_{Na} denotes a Na^+ -conducting state. The binding, unbinding and permeation rates are denoted as k_{on}, k_{off} and k_{perm}, respectively. PA, polyamine. A graphical representation of the model is shown on the right. B, C, D, Fits of the corrected G–V plots (same data as in Figure 4–2) with the single conductance model for GluA2, GluA2-gγ2 and GluA2+CNIH-3, respectively, are shown on the left. As an internal control, G–V plots were simulated with the values obtained with the fit for each patch (right, grey) with the mean shown in colour. E, The two-conductance model. C denotes a closed (non-conducting) state, O_{Na} denotes a Na^+ -conducting state and O_{PA} denotes a PA-conducting state. The binding, unbinding and permeation rates are as in A; k_1 and $k_{1'}$ are transition rates between O_{Na} and O_{PA}. A graphical representation of the model is shown on the right. F, G, H, Fits of the corrected G–V plots (same data as in Figure 4–2) with the two-conductance model for GluA2, GluA2-γ2 and GluA2+CNIH-3, respectively, are shown on the left. As an internal control, G–V plots were simulated with the values obtained with the fit for each patch (right, grey) with the mean shown in colour.

addition to that of Na^+ , could carry a significant current. To address this, we incorporated a second conductance to the initial model of polyamine block (Figure 4–3 E) and used this two-conductance model to fit the corrected G–V plots for GluA2, GluA2-γ2 and GluA2+CNIH-3 (Figure 4–3 F, G and H).

Table 4–2: Spermine affinities for GluA2 with auxiliary proteins

	Single conductance model		
	$K_{d(0mV)}$		
	mean	SEM	n
GluA2	3.7	0.4	12
GluA2-γ2	34.4	2.9	18
GluA2+CNIH-3	9.6	1.5	13

	Two-conductance model		
	$K_{d(0mV)}$		
	mean	SEM	n
GluA2	1.8	0.2	12
GluA2-γ2	17.9	1.5	19
GluA2+CNIH-3	7.1	2.1	14

In all cases, fits represented the data well (Figure 4–3 F, G and H). For GluA2, the fits were similar with both models. However, the two-conductance model yielded better fits in the cases of GluA2-γ2 and GluA2+CNIH-3. As with the single conductance model, the parameters obtained from the two-conductance model G–V fits at various $Spm_{(i)}$ concentrations were used to simulate G–V curves at 30 µM Spm as an additional internal test. Here, we found that the two-conductance model was able to predict the decrease in conductance occurring at positive potentials in all three cases (Figure 4–3 F, G and H, right). Parameters obtained from fitting with the two-conductance model were used to estimate $K_{d(0mV)}$ for Spm at GluA2, GluA2-γ2 and GluA2+CNIH-3 (Table 4–2). The $K_{d(0mV)}$ values obtained with the single- and two-conductance models are compared in Table 4–2. The $K_{d(0mV)}$ for all receptor complexes were estimated to be smaller with the two-conductance model (Table 4–2). Specifically, the $K_{d(0mV)}$ for GluA2

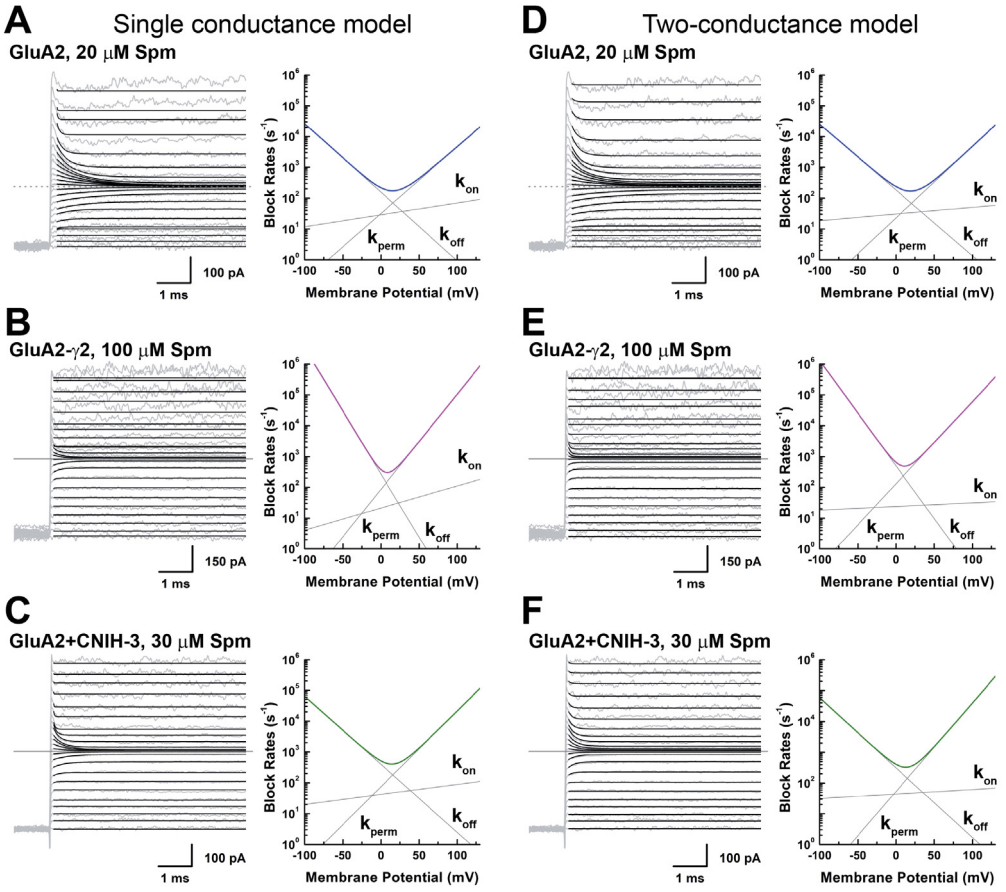

Figure 4–4: Fits of current relaxations for the single- and two-conductance models
A, B, C, Single-conductance model fits of the current relaxations following voltage steps for GluA2 (patch # 151023p3), GluA2-γ2 (patch # 150924p1) and GluA2+CNIH-3 (patch # 151201p2), respectively (right panels). The left panels illustrate the block rates (k_{on}, k_{off} and k_{perm}) as well as the sum of rates, as estimated from the fits. D, E, F, Two-conductance model fits of the current relaxations in the same patches (right panels). The left panels illustrate the block rates estimated from the fits using the two-conductance model.

and GluA2-γ2 were decreased by 2-fold and the $K_{d(0mV)}$ for GluA2+CNIH-3 was decreased by about 25% (Table 4–2). Given that the two-conductance model yielded better fits of the equilibrium channel block (G–V plots, Figure 4–3), we concluded that these values represent a more accurate estimate of the dissociation constants. Despite these differences in the $K_{d(0mV)}$ when using either the single- or two-conductance model, we observed the same outcome with the auxiliary proteins, that is, that they decreased the affinity for Spm at GluA2 receptors (Table 4–2).

4.6.5 Rate constants of spermine block

In addition to studying the equilibrium channel block, we estimated the rate constants for the binding (k_{on}), unbinding (k_{off}) and permeation (k_{perm}) of Spm by fitting the current relaxations following voltage steps with exponential functions (Figure 4–4), as was done previously for GluK2 KARs (Bowie et al., 1998). As mentioned above, most of the polyamine block has not yet occurred at the peak, about 100–200 μs following the voltage step (Figure 4–2) and channel block reached equilibrium within 2–5 ms (Figure 4–4). Examples of the current relaxation fits are shown in Figure 4–4. Estimates of the parameters obtained with either the single conductance model (A, B and C) or the two-conductance model (D, E and F) are illustrated in Figure 4–4 and the values for the rate constants are summarized in Table 4–3.

Table 4–3: Spermine block rates in GluA2 with auxiliary proteins

	Single conductance model								
	k_{on}		k_{off}		k_{perm}				n
	a $(\mu M \cdot s)^{-1}$	b (mV)	c (s^{-1})	d (mV)	e (s^{-1})	f (mV)			
GluA2	28.7	112.7	155.7	-19.5	31.8	20.1			7
SEM	4.6	13.5	30.0	1.2	15.9	2.8			
GluA2-γ2	21.4	60.7	267.2	-10.6	86.9	14.1			4
SEM	8.9	14.5	113.0	1.9	30.2	1.6			
GluA2+CNIH-3	42.1	134.9	396.2	-19.7	74.6	17.7			5
SEM	7.8	62.6	130.2	3.0	33.9	2.8			
	Two-conductance model								
	k_{on}		k_{off}		k_{perm}				n
	a $(\mu M \cdot s)^{-1}$	b (mV)	c (s^{-1})	d (mV)	e (s^{-1})	f (mV)	k_1	$k_{1'}$	
GluA2	30.5	199.1	183.6	-20.3	22.8	18.7	4550091510	29528482	7
SEM	6.4	94.1	43.7	1.2	8.8	2.1	1934743567	20398475	
GluA2-γ2	24.0	369.2	498.7	-12.7	131.0	16.3	167001174	41560257	4
SEM	8.4	223.4	147.4	1.3	24.6	2.0	163671579	41233074	
GluA2+CNIH-3	44.0	291.4	313.3	-19.1	53.2	15.1	2098100966	1293706	5
SEM	16.5	139.0	80.7	2.5	28.9	1.8	1977756638	1061300	

Current relaxations were fit with a single-exponential function for the single conductance model (Figure 4–4 A, B and C) and with a double-exponential function for the two-conductance model (Figure 4–4 D, E and F). The rate constants for k_{on}, k_{off} and k_{perm}, as well as the sum of all the constants, are illustrated on the right

of each panel. While both models yielded similar fits and rate constants (Figure 4–4 and Table 4–3), the two-conductance model was able to fit the data slightly more precisely, resulting in a better goodness of fit value (reduced χ^2). For GluA2, the global reduced χ^2 for all fitted traces was 91 considering the single conductance model and 72 for the two-conductance model. This was also true for GluA2-γ2 and GluA2+CNIH-3 (χ^2 = 72 and 68, and 63 and 49, respectively). We therefore concluded that the two-conductance model provided a more precise description of the data and a more accurate estimate of the rate constants. In all cases, k_{on} was similar and largely voltage-independent (Figure 4–4 and Table 4–3). In addition, both models estimated as expected that the rate constants for k_{off} and k_{perm} were larger for GluA2-γ2 and GluA2+CNIH-3 compared to GluA2 alone (Figure 4–4 and Table 4–3).

4.6.6 Auxiliary proteins increase spermine conductance

The two-conductance model of polyamine block includes 3 states: one closed (C, non-conducting) state and two open states (O_{Na} and O_{PA}). We used fits of the G–V relationships using this model to estimate the proportion of the total conductance that is attributed to Na^+ (G_{Na}) or Spm (G_{Spm}), as well as the proportion of open channels in each of the two open states, O_{Na} and O_{PA}. Summary plots are shown in Figure 4–5.

Since Spm was only in the internal solution, the Spm conductance was only present at positive potentials. The vast majority of the conductance through GluA2 channels was carried by Na^+ , with a very small proportion that was attributed to Spm at very positive potentials (Figure 4–5 A). However, in the presence of the auxiliary proteins, this small proportion of G_{Spm} was increased in a voltage-dependent manner, suggesting that polyamine permeation can occur at a more physiological range of membrane potentials when GluA2 is complexed with

γ2 or CNIH-3 (Figure 4–5 B and C). While this increase in G_{Spm} seemed to plateau around +130 mV for GluA2 and GluA2-CNIH-3, it continued to increase for GluA2-γ2 (Figure 4–5 A–C).

The proportion of open channels that were in the O_{PA} state was unexpectedly high and increased in a voltage-dependent manner (Figure 4–5 D–F). In fact, the proportion of O_{PA} started to plateau around 13.6% at +130 mV for GluA2 (Figure 4–5 D). This proportion of Spm-conducting channels was slightly increased to 26.8% and 21.3% with GluA2-γ2 and GluA2+CNIH-3, respectively (Figure 4–5 E and F). Interestingly, while the proportion of channels in the O_{PA} state also plateaued with CNIH-3 (Figure 4–5 E), it continued to increase with γ2 (Figure 4–5 F). Taken together, our analysis of the G–V fits suggests that the Spm conductance is greatly increased by both auxiliary proteins, and highlights differences in their voltage-dependent behaviours. Therefore, we conclude that Spm conductance through GluA2 channels is non-negligible, especially with γ2 and CNIH-3.

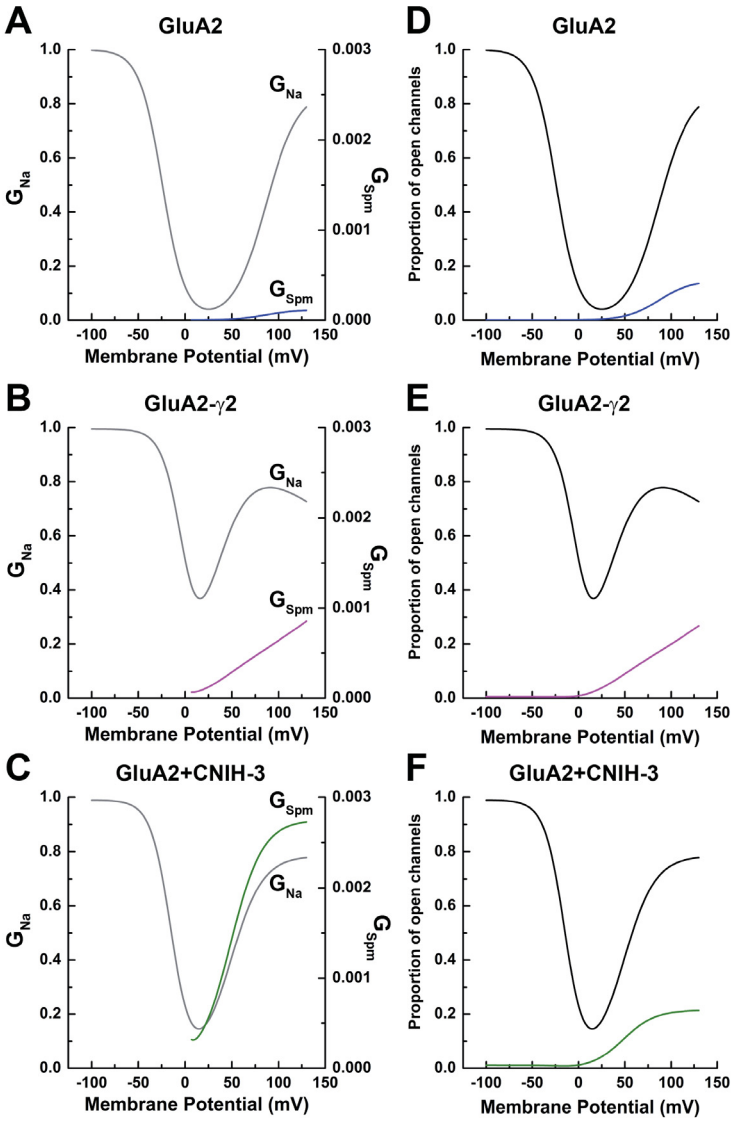

Figure 4–5: Spermine conductance is increased by auxiliary proteins
A, B, C, Relative conductances of Na^+ (left axis, grey traces) and Spm (right axis, coloured traces) for GluA2, GluA2-γ2 and GluA2+CNIH-3, respectively, calculated from simulations with the two-conductance model of polyamine block. D, E, F, Proportion of open channels that are conducting either Na^+ (black traces) or Spm (coloured traces), calculated from simulations with the two-conductance model of polyamine block.

4.7 Discussion

Our study provides insight into the mechanism underlying the relief of polyamine block in calcium-permeable AMPARs. First, we demonstrated that Spm permeation through GluA2 channels is facilitated by the auxiliary proteins, γ2 and CNIH-3. When we characterized channel block by internal polyamines, we found that the single conductance model, which was previously used to describe polyamine block in KARs (Bowie et al., 1998; Brown et al., 2016), could not accurately describe the block at AMPARs associated with auxiliary proteins. Therefore, we proposed a new model, in which a conductance for polyamine permeation is taken under consideration. Using this two-conductance model, we found that the association of AMPARs with auxiliary proteins leads to an increase in the polyamine unbinding and permeation rates. Finally, our results suggest that there is a voltage-dependent increase in the Spm conductance with auxiliary proteins, which is responsible for the decrease in the overall conductance at positive membrane potentials. Taken together, our findings demonstrate that the auxiliary proteins of AMPARs relieve channel block by increasing polyamine permeation. Although the structural mechanism underlying this phenomenon remains unclear, this phenomenon has also been observed for other iGluRs (Brown et al., 2016) and we propose that such a mechanism may also apply to other cation-selective ion channels associated with auxiliary proteins.

We measured Spm-mediated currents at GluA2(Q) channels with a reversal potential near 0 mV, indicating that the Spm permeation of GluA2 was much larger than that of GluK2 (Bahring et al., 1997; Brown et al., 2016). This was unexpected, since the pore diameters of AMPARs and KARs are thought to be very similar (Burnashev, 1996). In addition, γ2 and CNIH-3 further increased the

Spm permeation through the channel, with CNIH-3 having the greatest effect with an increase of 16-fold compared to GluA2 alone. Interestingly, we also observed a slight positive shift in the Na^+ reversal potential when GluA2 was co-expressed with CNIH-3, consistent with an increased mean channel conductance (Coombs et al., 2012). The Na^+ reversal potential was not shifted with $\gamma 2$, despite a similar increase in the mean channel conductance of AMPARs (Soto et al., 2014). In the case of $\gamma 2$, the calculated pore diameter was not changed (Soto et al., 2014), suggesting a reduction of the energy barrier for Spm permeation by other means than a widening of the pore. It is for instance possible that the atomic structure of the pore allows Spm to be partially dehydrated more efficiently when $\gamma 2$ is present. The effect of CNIH-3 on the pore diameter of AMPARs remains unknown, but given the slight shift in the Na^+ reversal potential, a small change at the level of the pore might be expected.

Previously, the kinetics of open-channel polyamine block at iGluRs have been characterized using a single binding site model for a permeant blocker (Bowie et al., 1998). However, we found that this model was inadequate to describe the polyamine block of AMPARs in the presence of auxiliary proteins. In fact, we found that it was necessary for the conductance of Spm permeation to be taken into account in order for the model to properly explain the data. Specifically, we observed a decrease in the overall conductance of GluA2 channels at positive membrane potentials with $\gamma 2$ or CNIH-3, resulting in a biphasic G–V plot. This can be explained by the voltage-dependent increase in Spm permeation that occurs simultaneously. The energy barrier for the permeation of large polycations like Spm is expected to be much greater than that of Na^+ ions, and the presence of the polyamine in the channel pore would hinder the permeation pathway by competing

with Na^+ ions, resulting in a net decrease in channel conductance as Spm goes through the channel pore. A similar, much more pronounced biphasic G–V relationship was observed with the blockade of cGMP-gated channels by internal polyamines (Lu and Ding, 1999). To explain this phenomenon, it was suggested that intracellular Spm adopts permeant or non-permeant conformations, the latter being responsible for the increase in the proportion of blocked channels at positive membrane potentials (Lu and Ding, 1999).

Here, we report that Spm block at homomeric GluA2(Q) receptors is very similar to that observed for GluA1(Q) receptors (Bowie and Mayer, 1995). The auxiliary proteins, γ2 and CNIH-3, lowered the Spm affinity of GluA2(Q), as was observed with GluA1 (Coombs et al., 2012). However, γ2 resulted in a much greater relief of channel block despite its more modest effect on the decay kinetics and steady-state current of macroscopic GluA2 responses (present study and Coombs et al. (2012)). These observations suggest that the effect of auxiliary proteins on the pore properties can be separated from their effects on the channel gating properties, a phenomenon that has recently been reported for γ2 (Dawe et al., 2016), as well as for the auxiliary proteins of KARs, Neto1 and Neto2 (Fisher and Mott, 2012). This likely occurs through a different set of interactions between the ion channel and the auxiliary proteins (Fisher and Mott, 2012; Shanks et al., 2014; Griffith and Swanson, 2015). For example, at inward rectifying K^+ channels, polyamines can bind at several locations along the selectivity filter depending their length (Kurata et al., 2006, 2013). Similarly, several conserved residues along the M3 helix of iGluRs are also crucial in determining polyamine block (Wilding et al., 2010). By interacting with channel pores, auxiliary proteins may alter their architecture and have an impact on the polyamine binding environment. Neto2 interacts with the M3–S2 linker of

KARs (Griffith and Swanson, 2015), which may, in turn, affect the positioning of the pore-lining helices. It is currently thought that positively-charged residues in their C-terminal regions, which are expected to interact with the cytoplasmic part of the channel pore, could relieve channel block by a charge-screening mechanism (Fisher and Mott, 2012; Soto et al., 2014). In light of our results, it is also possible that the auxiliary proteins are altering the binding site(s) for polyamines, thereby facilitating their permeation. The precise interactions responsible for the relief of channel block have yet to be identified.

Although outward Spm permeation was not directly measured in our experiments, fits of the G–V plots estimated that Spm was indeed permeating the GluA2 channel, and that both $\gamma 2$ and CNIH-3 increased this conductance in a similar manner as with external polyamines. Despite the relatively very small Spm conductance, the proportion of channels in the O_{PA} state was unexpectedly high, especially since Na^+ ions were in 5000-fold excess (i.e. 150 mM NaCl vs. 30 µM Spm) in the internal solution. To explain this, the local concentration of Spm around the pores should be significantly increased compared to the solution concentration. This could be the result of high affinity interactions between the channel and Spm molecules.

The permeation of Spm through GluA2 channels associated with auxiliary proteins was unexpectedly high, especially with CNIH-3. This could be of particular interest, since a general polyamine transporter has not yet been identified for mammalian cells (Poulin et al., 2012). Based on some general properties, such as voltage- and pH-dependence, as well as interactions with monovalent and divalent cations (Poulin et al., 2012), native AMPARs and KARs that are in complexes with auxiliary proteins (Brown et al., 2016) could be

interesting candidates for playing an important role in polyamine transport. Further experiments investigating the specificity and transport potential of the naturally-occurring polyamines (i.e. with Put, Spd and Spm (TABOR and TABOR, 1964; Pegg, 2009)) are required.

4.8 Author Contributions

P.M.G.E.B. designed and performed experiments, analysed data and wrote the paper; H.M. wrote the fitting programs in MatLab, analysed data and wrote the paper; D.B. designed experiments and reviewed the manuscript.

4.9 Acknowledgements

This work was supported by an operating grant from the Canadian Institutes of Health Research (to D.B.). H.M. is the recipient of a post-doctoral fellowship from the Natural Sciences and Engineering Research Council of Canada (NSERC).

CHAPTER 5
GENERAL DISCUSSION

In the three chapters that were presented in this thesis, I examined the functional properties of KARs and AMPARs. As I mentioned earlier, these excitatory receptors are widely distributed throughout the mammalian central nervous system and play a central role in the effective and intricate communication between neurons. As such, two important aspects to consider are their subunit composition and their auxiliary subunits. My findings address both of these factors and provide insight into the structural mechanisms underlying the function of these receptors. Although the targeted structure/function study of specific neurotransmitter receptors may seem a bit short-sighted, there are greater implications and considerations that are worth discussing.

In the following sections, I will discuss four topics. First, I will briefly describe a gating model for heteromeric KARs, highlighting the specific structural and functional roles of each subunit within a tetrameric channel. Next, I will address the structural and physiological implications of KAR ion-sensitivity (or lack thereof), and I will speculate on the relevance of polyamine permeation through AMPARs and KARs. Finally, I will discuss the possibility of using structure/function findings, like the ones presented in thesis, to allow the progression of rational compound design.

5.1 A conceptual model of heteromeric KAR gating

In Chapter 2 of this thesis, we characterized the functional contribution of the different subunits forming GluK2/GluK5 KARs. Specifically, their individual contributions were teased apart pharmacologically, by using AMPA or by lowering the L-Glu concentration to reveal GluK5-specific responses. Analysing the functional properties of the heteromers under various conditions allowed us to interpret the specific roles of each subunit within the channel. The model that I

will describe here is, by no means, as complex as the one proposed by Mott et al. (2010), nor is it a mathematical model. Instead, it represents a unified theory of independent subunit gating, which combines observations from multiple studies. Here, it applies directly to GluK2/GluK5 receptors, but it could also be broadened to include other heteromeric iGluR complexes.

Early clues regarding independent subunit contributions came with the observation that KARs containing the secondary subunits, GluK4 or GluK5, had different kinetic and pharmacological properties. For example, heteromeric KARs containing the GluK5 subunit are responsive to AMPA, while homomeric GluK2 recepters are not (Herb et al., 1992), suggesting that the activation of GluK5 alone is sufficient for channel gating. The heteromerization of GluK2 and GluK5 also results in slow deactivation kinetics, which more closely represent the kinetics of KAR EPSCs (Barberis et al., 2008). Generally speaking, within a GluK2/GluK5 tetramer, the GluK2 subunits are thought to be responsible for desensitizing the channel, while the GluK5 subunits are non-desensitizing (Mott et al., 2010; Fisher and Mott, 2011).

Initially, however, GluK5 was thought to desensitize the channel (Swanson et al., 2002). It was observed that the high-affinity KAR agonist, disyherbaine (DH), could produce a long-lasting desensitization of homomeric GluK1 and GluK2, but not GluK2/GluK5 receptors (Swanson et al., 2002). Interestingly, DH produced a long-lasting (10–20 minutes) tonic current at GluK1/GluK5 receptors, during which L-Glu application would result in a transient activation followed by rapid desensitization (Swanson et al., 2002). The affinity of DH for GluK1 subunits is much higher than for GluK5, so it was interpreted that DH forms a stable complex with GluK1, resulting in tonic activation, and that L-Glu application during this activation was acting through the GluK5 subunit, which desensitized the channel (Swanson et al., 2002).

Some years later, Barberis et al. (2008) observed that, despite having similar desensitization kinetics as homomeric GluK2 receptors, GluK2/GluK5 receptors displayed much slower deactivation kinetics. To explain this behaviour, Mott et al. (2010) developed a gating model, in which desensitizing subunits had a lower affinity for L-Glu (GluK2) and non-desensitizing subunits had a higher affinity for L-Glu (GluK5). In line with this, GluK2/GluK5 receptors have a higher sensitivity to L-Glu (Barberis et al., 2008; Mott et al., 2010; Fisher and Mott, 2011). Moreover, selective activation of the GluK5 subunit reduces desensitization (Fisher and Mott, 2011). In fact, GluK2/GluK5 responses are almost non-decaying with L-Glu concentrations that are too low to evoke currents from GluK2 (i.e. 1 µM) (Fisher and Mott, 2011), or when AMPA is used (Herb et al. (1992) and Chapter 2 of this thesis). Additionally, the fact that desensitization is also reduced when GluK2 is blocked pharmacologically (i.e. with kynurenic acid), or through a mutation that reduces its L-Glu affinity by 260-fold (E738D) (Mah et al., 2005), strongly suggests that channel activation is sustained through GluK5 (Fisher and Mott, 2011). Taken together, the simplest explanation for these observations is that GluK2 and GluK5 gate independently, and that GluK2 desensitizes the channel.

The results from Chapter 2 are consistent with this model of independent subunit activation, with the exception that the single-channel recordings reveal that GluK5 activation is not sustained. The observations presented here are consistent with a previous analysis of the single-channel properties of heteromeric KARs (Swanson et al., 1996). Using a combination of noise analysis and discrete single-channel records, the authors determined that GluK5 does not significantly change the conductance and single-channel behaviour of KARs compared to homomeric GluK2 channels (Swanson et al., 1996). When associated with GluK1, GluK5 was found to shorten the burst length of domoate-induced responses

(Swanson et al., 1996). It is not surprising that homomeric and heteromeric KARs display similar microscopic behaviours, since their macroscopic currents also behave in a similar manner in the continued presence of agonist (see Figure 2–1 in Chapter 2 for example). The results presented in Chapter 2 provide additional information regarding the continued activation of heteromeric GluK2/GluK5 channels after brief L-Glu pulses. Specifically, GluK5-mediated openings are very brief, with frequent re-openings for several tens of milliseconds after the removal of L-Glu. Channel openings are very similar in the continued presence of AMPA, suggesting that GluK5 is responsible for such brief and frequent openings. Although we cannot distinguish between closed and desensitized states, we can conclude that GluK5 activation does not lead to sustained activation of the channel. Interestingly, GluK2/GluK5 channel openings are reminiscent of those evoked from GluK2 (Y521C,L783C), in which a cross-link at the dimer interface prevents proper channel gating (Dawe et al., 2013). Given this, there could be structural similarities underlying the gating of GluK5, for example through an unstable cleft closure of GluK5 LBDs or through structural differences at the heteromeric dimer interface (see section below).

If GluK5 can cause frequent channel openings (i.e. with AMPA or after short L-Glu pulses), why are responses to longer L-Glu pulses not slower? Our findings support that the selective activation of two subunits (i.e. GluK5) allows the receptors to gate for longer times, while the concerted activation of all four subunits results in the desensitization of the channel. Since the GluK5 subunit has a higher affinity for L-Glu (Barberis et al., 2008; Fisher and Mott, 2011), applying L-Glu for shorter times (i.e. 1–1.5 ms) and at lower concentrations decreases the probability of GluK2 activation and allows the GluK5 subunits to gate undisturbed. Consistent with this is the observation that recovery from desensitization of GluK2/GluK5 receptors

is much faster than that of GluK2 with short L-Glu applications (Barberis et al., 2008). Though this idea is based on the original heteromeric gating models of Mott et al. (2010) and Fisher and Mott (2011), it is still consistent with the observations of Swanson et al. (2002). For example, during the tonic DH activation of GluK1, two subunits (GluK1) are active. With L-Glu application, the other two subunits (GluK5) are also activated and the concerted activation of all four subunits, despite being with two different agonists, results in channel desensitization.

Taken together, as illustrated in the schematic in Figure 1–12 C, the observations presented in Chapter 2 of this thesis suggest that while the specific activation of two subunits within the tetramer (i.e. GluK2 or GluK5) activates the channel, the concerted activation of all four subunits leads to channel desensitization.

Hints of the structural correlates of the different gating of KAR subunits already began to emerge with the first full-length crystal structure of the GluA2 tetramer (Sobolevsky et al., 2009). As described in the introduction, subunits with identical amino acid sequences have different structural features based on their positioning in the tetramer. For example, the proximal subunits (B/D) have M3–S2 linkers that are extended compared to those of the distal subunits (A/C), which are helical in nature (Sobolevsky et al., 2009). As such, the proximal subunits are thought to have a greater impact on channel gating and desensitization than the distal subunits (Sobolevsky et al., 2009; Chen et al., 2014; Herguedas et al., 2016). In GluK2 homomers, the proximal subunits are believed to undergo drastic conformational changes, which are central in the desensitization of the channel (Meyerson et al., 2016). Interestingly, crystal structures of isolated GluK2/GluK5 ATDs indicate that the positioning of GluK5 is preferentially distal (Kumar et al., 2011).

There are multiple reasons that can explain the gating behaviour of GluK5. First, GluK5 has a higher L-Glu affinity than GluK2 (Barberis et al., 2008; Mott et al., 2010; Fisher and Mott, 2011). Second, the proximal positioning of the GluK2 subunits is predicted to have a greater impact on channel gating and desensitization (Herguedas et al., 2016). Whether the particular single-channel behaviour of GluK5 arises from specific subunit properties, or simply through their preferred A/C positioning, is still unknown. Finally, external ions are known to govern activation and desensitization in KARs (Bowie, 2002; Paternain et al., 2003; Wong et al., 2006; Plested and Mayer, 2007; Wong et al., 2007; Plested et al., 2008; Dawe et al., 2013). However, the findings from Chapter 2 demonstrate that heteromeric KAR gating is independent of external ions. In the next section, I will discuss the possible structural implications of these observations.

5.2 KARs and the external ions

A question that has been prominent with KARs ever since it was discovered that their gating was ion-dependent (Bowie, 2002) is: "What is the physiological role of ion-dependent KAR gating?" Given the dependence of KARs to external ions, they have been proposed to act as "ion sensors" (Paternain et al., 2003; Plested et al., 2008; Bowie, 2010; MacLean, 2011). For example, during spreading depression or high frequency stimulation, the concentration of ions can change dramatically (Somjen, 2001). Indeed, decreases in Na^+ by about 100 mM in 2–3 seconds have been measured extracellularly (Herreras and Somjen, 1993a,b), in which case KAR responses may be depressed (Paternain et al., 2003). With KARs playing roles in regulating excitability, sensing the high levels of activity and subsequently modulating pre-synaptic release or cell excitability represents an attractive hypothesis.

However, synaptic KARs are thought to exist as heteromeric entities (Bahn et al., 1994; Seeburg, 1993; Wenthold et al., 1996; Barberis et al., 2008; Fernandes et al., 2009; Lu et al., 2009). The evidence is also showing that the gating of heteromeric KARs is much less sensitive to the removal of external Na^+ (Paternain et al., 2003), and that it is, in fact, not dependent on the presence of external ions (Chapter 2 of this thesis). Therefore, where the kinetics and amplitude of GluK2 responses would become faster and smaller, respectively, with a decrease in extracellular Na^+ (see Chapter 2), GluK2/GluK5 responses would remain robust and slow, and this is inconsistent with the idea that synaptic KARs are ion sensors.

The sensitivity and dependence to external ions in GluK2 has provided great insight into the structural and functional properties of KARs, especially regarding the LBD dimer interface, as discussed in the Introduction. In combination with structural studies (Kumar et al., 2011; Meyerson et al., 2016), the results presented in Chapter 2 suggest that the formation of a heterodimeric interface leads to the receptor being independent of external ions. Structurally, the presence of GluK5 could supersede the requirement for external ions by providing a surrogate charge or by reshaping the ion-binding pocket.

The functional evidence for this comes from the observation that Li^+ ions slow the decay kinetics (compared to Na^+ ions) in the continued presence of L-Glu. A similar phenomenon was observed with the ion-independent AMPARs (Dawe et al., 2016). Here, the exchange of Na^+ for Li^+ in the external solution resulted in slower desensitization kinetics of GluA2 (Dawe et al., 2016). A Li^+ ion was modelled into the putative cation-binding pocket at the dimer interface of GluA2 (Assaf et al., 2013) in a position that is equivalent to the cation-binding pocket of GluK2 (Dawe et al., 2016). Despite this, MD simulations suggest that neither Na^+ nor the smaller Li^+ remain stably bound at this site, and the substitution of a critical Lys residue

to a Met (K759M), as is found in the equivalent position of GluK2, promotes the binding of Li^+ (Dawe et al., 2016). This could then stabilize the dimer interface, thereby slowing the entry into desensitization (Dawe et al., 2016). These observations suggest that there is a putative (or vestigial) cation-binding pocket in AMPARs that is smaller than in KARs, and in which a Lys satisfies the pocket in a similar manner as in GluK2 (M770K).

The fact that the desensitization kinetics of GluK2/GluK5 heteromers are also slowed in the presence of Li^+ , but not other cations, suggests that there are structural similarities between the LBD dimer interfaces of heteromeric KARs and AMPARs. For example, despite the dimer interface residues being conserved, the GluK2 and GluK5 LBDs may assemble asymmetrically, or in a way that results in a more restricted cation-binding pocket, where only the smaller Li^+ ions can bind. Additionally, though this has not been tested, and very little structural information exists regarding heteromeric LBDs (though see Kristensen et al. (2016) for a homodimeric structure of the GluK4 LBD), GluK5 may satisfy the putative cation-binding pocket in a similar way as GluA2.

What about heteromeric KARs that are assembled from primary subunits? For exapmle, there is functional and genetic evidence that pre-synaptic KARs at hippocampal mossy fibre synapses are assembled from the GluK2 and GluK3 subunits (Pinheiro et al., 2007; Contractor et al., 2011). The ion sensitivity of such heteromers has not yet been assessed, however, given that they are more closely related to each other than to the secondary subunits (Alberstein et al., 2015), they may indeed be ion-dependent. If this was the case, KARs could be classified into two functional categories, with heteromers composed of primary subunits being modulated by external ions and heteromers containing secondary subunits being ion-independent. In addition to these potential differences, primary- and

secondary-containing heteromers also diverge in their functional properties, including polyamine block, decay kinetics and agonist affinity [for example, see Barberis et al. (2008) and Perrais et al. (2010)]. Thus, the subunit composition of KARs could determine the functional properties of the channels and define their specific roles as regulators of neuronal excitability.

5.3 The importance of polyamine permeation

As mentioned in the Introduction, AMPARs and KARs are blocked by cytoplasmic polyamines in a voltage-dependent manner (Bowie and Mayer, 1995). Here, polyamines are considered to be permeant channel blockers due to their ability to block and pass through the pore of cation-selective ion channels (Bowie et al., 1999). The dynamics of channel block are governed by the rates of polyamine binding, unbinding and permeation (Brown et al. (2016); Chapters 3 and 4). For homomeric AMPARs and KARs, polyamine permeation occurs only at extremely positive membrane potentials (Bahring et al., 1997), while channel block is observed in the physiological membrane potential range (Bowie et al., 1999). In Chapters 3 and 4 of this thesis, we uncovered that the polyamine permeation rates were increased with KAR heteromers and when homomeric AMPARs and KARs were associated with auxiliary proteins, resulting in an overall decrease in channel block.

A similar decrease in conductance was observed at cGMP-gated channels (Lu and Ding, 1999). Here, the authors proposed that intracellular Spm can adopt permeant and non-permeant conformations, with the proportion of the non-permeant form increasing at positive membrane potentials (Lu and Ding, 1999). Previously, it was also assumed that the conductance of permeant ion blockers, like H^+ ions or polyamines, was negligible (Woodhull, 1973; Bahring

et al., 1997). However, in order to explain the decrease in AMPAR and KAR conductance at positive membrane potentials, we propose a new model describing polyamine block, which takes into account the conductance of polyamines through the channel pore. Here, the energy barrier for the permeation of large polycations like Spm is expected to be much greater than that of Na^+ ions, and their presence in the pore would hinder the permeation pathway by competing with Na^+ ions, resulting in a net decrease in channel conductance.

What is the significance of polyamine permeation? In mammals, intracellular polyamines, such as Spm, Spd and Put, play important roles at cation-selective ion channels, but also in cell signalling, transcription, proliferation and differentiation, and cell survival (Pegg, 2009, 2016). Their levels are determined by the tightly-regulated synthesis and catalysis pathways, but also by transport across the cell membrane (Pegg, 2009). The latter of these processes is not well understood (Pegg, 2009), and a general polyamine transporter has not yet been identified for mammalian cells (Poulin et al., 2012).

The permeation of Spm through GluA2 channels associated with auxiliary proteins is unexpectedly high, especially with CNIH-3. This property, combined with other characteristics including voltage- and pH-dependence, as well as interactions with monovalent and divalent cations (Poulin et al., 2012), native AMPARs and KARs in complex with auxiliary proteins could be interesting candidates for playing an important role in polyamine transport. For example, elevated polyamine levels have been associated with multiple types of cancer (Nowotarski et al., 2013). However, targeting the polymaine synthesis and catalysis pathways has not been successful in developing cancer treatments, since polyamine transport is increased when synthesis is blocked (Nowotarski et al., 2013). Interestingly, the expression of several iGluR subunits has also been detected in

several peripheral cancer cell lines, where they may be implicated in cellular proliferation and migration (Ribeiro et al., 2016). Could the influx of polyamines through AMPARs be important in the increased proliferation of cancer cells? Further experiments are required to explore the role of these iGluR complexes in polyamine homeostasis in both normal and disease states.

5.4 Why is structure/function important?

Why should we study the functional and structural properties of ion channels in such detail? Generally speaking, these studies advance our basic knowledge of the structure and function of these receptors, but also helps us understand how they contribute to normal or disease conditions. For example, as presented in Appendix C, the functional characterization of single point mutations in $GABA_A$ receptor subunits of patients with idiopathic generalized epilepsy gave us insight into the roles these channels play in this disease (Lachance-Touchette et al., 2011). Similarly, iGluRs have been implicated in several disease states, including temporal-lobe epilepsy (Bowie, 2010; Contractor et al., 2011). The use of new genome editing technologies such as CRISPR-Cas (Sander and Joung, 2014) and engineering glutamate-sensitive fluorescent reporters (Hires et al., 2008) and light-activated glutamate receptors (Gascón-Moya et al., 2015), for example, will help put the structural and functional properties of these receptors into a more physiological context.

The development of subunit-specific agonists and antagonists has proved indispensable for the isolation and characterization of the iGluR families (Lodge, 2009; Traynelis et al., 2010). Nowadays, the rational design of novel subunit-specific compounds combined with X-ray crystallographic approaches provide additional useful tools but also gives us insight into the functional mechanisms underlying

their effect (for example, see Demmer et al. (2015)). In this case, novel compounds derived from quinoxalines were designed in the hope of obtaining antagonists with novel subunit selectivity, and a new mode of ligand binding was identified (Demmer et al., 2015). *In silico* docking studies (for example, Fay et al. (2009)) and Molecular Dynamics simulations (for example, Brown et al. (2016)) are great tools to make predictions about the molecular mechanisms underlying channel function.

Rational compound design could also take a different, and perhaps more realistic turn. Specifically, recent studies like the ones presented in this thesis underline the importance of subunit heteromerization and auxiliary proteins. This could be used in at least two ways. For example, compounds targeted to act at the dimer interface of heteromeric, but not homomeric channels, could greatly increase the specificity of their actions in native conditions. Alternatively, the identification of specific regions of interaction between receptors and their auxiliary proteins, like the KGK motif in GluA2 that interacts with $\gamma 2$ and is correlated with specific functional outcomes (Dawe et al., 2016), provides novel opportunities to disrupt or enhance the normal function of these channels in their native forms. A great example of this is the recent design of inhibitors that target the interaction between the scaffolding protein, gephyrin, and the inhibitory glycine and $GABA_A$ neurotransmitter receptors (Maric et al., 2015). These interaction-specific compounds have great potential as therapeutic compounds (Maric et al., 2015). These avenues should be further explored for the future development of novel pharmacological tools but also as new therapeutic targets.

5.5 CONCLUSION

In this thesis, I have presented results that further our understanding of the function of native KARs and AMPARs. Here, I have proposed a general model

describing how each subunit type contributes to heteromeric KAR gating. The similarities in the gating modes of GluK2/GluK5, GluK2 mutants and even GluA2 gives us insight into their the structural mechanism underlying the gating mode of GluK5. The structural and functional roles of GluK2 and GluK5 subunits could be based on their positioning within the tetramer, as well as their subunit-specific characteristics. In the absence of a structure of the full-length GluK2/GluK5, MD simulations could be relied upon to predict the molecular mechanisms underlying their gating upon agonist binding. Additionally, fluorescence measurements of the conformational changes induced by agonist binding at GluK2 or GluK5 could shed light onto the structural differences between homomeric and heteromeric KARs.

Polyamines are important determinants of neuronal signalling by regulating action potential firing rates and modulating neurotransmission through their well-characterized role as permeant blockers of cation-selective ion channels. However, channel block of AMPARs and KARs, as heteromeric complexes and associated with auxiliary proteins, is greatly reduced. Here, I demonstrate that this relief of block, especially in AMPARs with TARPs or CNIHs, results from an unexpected increase in polyamine permeation. Higher intracellular polyamine levels have been associated with some peripheral cancer types. Interestingly, AMPAR antagonists can block cell proliferation and migration in such cases. Could KAR and AMPAR complexes be involved in polyamine homeostasis in mammalian cells? The cellular significance of the polyamine permeation through AMPARs still remains to be explored. For example, can the activation of AMPARs, with TARPs or CNIHs, result in a considerable increase in intracellular polyamines? Could this increase in polyamines favour cell proliferation?

To conclude, the work presented in my thesis explores simple questions regarding the function of ion channels, but the conclusions we can make and the hypotheses we can build from them are of great physiological importance.

SUMMARY OF ORIGINAL CONTRIBUTIONS

I. I found that the deactivation kinetics of GluK2/GluK5 KARs can be fit with three exponential components, with the gating of the GluK5 subunit is responsible for the slowest component (Chapter 2).

II. I show that the contribution of GluK2 and GluK5 to the exponential componets of heteromeric responses are concentration-dependent (Chapter 2).

III. I found that the specific activation of the GluK5 subunit results in rapid and frequent single-channel openings (Chapter 2). Since GluK5 has a higher L-Glu affinity than GluK2, this explains why GluK2/GluK5 channels display slow deactivation kinetics.

IV. I propose that the different subunits within a heteromeric GluK2/GluK5 KAR can gate independently and contribute differently to channel gating (Chapter 2 and Chapter 5). Specifically, the activation of two subunits activates the channel, while the concerted activation of all four subunits results in desensitization.

V. I found that the gating of GluK2/GluK5 heteromers is independent of external ions (Chapter 2).

VI. I found that only Li^+ ions can slow the desensitization kinetics of GluK2/GluK5 receptors, suggesting that the putative ion-binding pocket of these heteromers may have structural similarities with that of the AMPAR (Chapter 2).

VII. I identified that a proline residue in the pore region of GluK5 subunits is responsible for relieving polyamine block in heteromeric KARs (Chapter 3).

VIII. I found that relief of polyamine block in heteromeric GluK2/GluK5, and in GluK2 homomers that are associated with the auxiliary protein, Neto2, occurs through an increase in polyamine permeation through the channel pore (Chapter 3).

IX. I found that this proline residue in the pore region of GluK5 is also resonsible for increasing the permeation of polyamines through the channel pore (Chapter 3).

X. I found that the increases in polyamine permeation in heteromeric KARs and with Neto2 are additive, suggesting that heteromerization and auxiliary proteins are acting through structurally distinct mechanisms (Chapter 3).

XI. I found that the auxiliary proteins of AMPARs, $\gamma 2$ and CNIH-3, relieve polyamine block of GluA2 homomers by facilitating polyamine permeation through the channel pore (Chapter 4).

XII. I characterized the rates of onset of block, unbinding and permeation of polyamines at GluA2 receptors, with and without auxiliary proteins, using a single binding site model for a permeant blocker (Chapter 4).

XIII. I propose a new model to describe polyamine block, which takes into consideration that polyamine conductance through the channel pore is significant (Chapter 4).

REFERENCES

Accardi, M. V., Brown, P. M. G. E., Miraucourt, L. S., Orser, B. A., and Bowie, D. (2015). alpha6-containing gabaa receptors are the principal mediators of inhibitory synapse strengthening by insulin in cerebellar granule cells. *The Journal of neuroscience : the official journal of the Society for Neuroscience*, 35:9676–9688.

Accardi, M. V., Daniels, B. A., Brown, P. M. G. E., Fritschy, J.-M., Tyagarajan, S. K., and Bowie, D. (2014). Mitochondrial reactive oxygen species regulate the strength of inhibitory gaba-mediated synaptic transmission. *Nature communications*, 5:3168.

Aizenman, C. D., Muñoz-Elías, G., and Cline, H. T. (2002). Visually driven modulation of glutamatergic synaptic transmission is mediated by the regulation of intracellular polyamines. *Neuron*, 34(4):623–634.

Alam, A. and Jiang, Y. (2009a). High-resolution structure of the open NaK channel. *Nat Struct Mol Biol*, 16(1):30–34.

Alam, A. and Jiang, Y. (2009b). Structural analysis of ion selectivity in the nak channel. *Nat Struct Mol Biol*, 16(1):35–41.

Alberstein, R., Grey, R., Zimmet, A., Simmons, D. K., and Mayer, M. L. (2015). Glycine activated ion channel subunits encoded by ctenophore glutamate receptor genes. *Proceedings of the National Academy of Sciences of the United States of America*, 112:E6048–E6057.

Aller, M. I., Pecoraro, V., Paternain, A. V., Canals, S., and Lerma, J. (2015). Increased dosage of high-affinity kainate receptor gene grik4 alters synaptic transmission and reproduces autism spectrum disorders features. *J Neurosci*,

35(40):13619–13628.

Alt, a., Weiss, B., Ogden, a. M., Knauss, J. L., Oler, J., Ho, K., Large, T. H., and Bleakman, D. (2004). Pharmacological characterization of glutamatergic agonists and antagonists at recombinant human homomeric and heteromeric kainate receptors in vitro. *Neuropharmacology*, 2004/03/23(6):793–806.

Armstrong, N. and Gouaux, E. (2000). Mechanisms for activation and antagonism of an ampa-sensitive glutamate receptor: crystal structures of the glur2 ligand binding core. *Neuron*, 28(1):165–181.

Armstrong, N., Jasti, J., Beich-Frandsen, M., and Gouaux, E. (2006). Measurement of conformational changes accompanying desensitization in an ionotropic glutamate receptor. *Cell*, 127:85–97.

Armstrong, N., Sun, Y., Chen, G. Q., and Gouaux, E. (1998). Structure of a glutamate-receptor ligand-binding core in complex with kainate. *Nature*, 395(6705):913–917.

Assaf, Z., Larsen, A. P., Venskutonyt, R., Han, L., Abrahamsen, B., Nielsen, B., Gajhede, M., Kastrup, J. S., Jensen, A. A., Pickering, D. S., Frydenvang, K., Gefflaut, T., and Bunch, L. (2013). Chemoenzymatic synthesis of new 2,4-syn-functionalized (s)-glutamate analogues and structure-activity relationship studies at ionotropic glutamate receptors and excitatory amino acid transporters. *Journal of medicinal chemistry*, 56:1614–1628.

Ataman, Z. A., Gakhar, L., Sorensen, B. R., Hell, J. W., and Shea, M. A. (2007). The nmda receptor nr1 c1 region bound to calmodulin: structural insights into functional differences between homologous domains. *Structure*, 15(12):1603–1617.

Auerbach, A. (2013). The energy and work of a ligand-gated ion channel. *Journal of molecular biology*, 425:1461–1475.

Auerbach, A. (2015). Activation of endplate nicotinic acetylcholine receptors by agonists. *Biochemical pharmacology*, 97:601–608.

Ayalon, G., Segev, E., Elgavish, S., and Stern-Bach, Y. (2005). Two regions in the n-terminal domain of ionotropic glutamate receptor 3 form the subunit oligomerization interfaces that control subtype-specific receptor assembly. *The Journal of biological chemistry*, 280:15053–15060.

Ayalon, G. and Stern-Bach, Y. (2001). Functional assembly of ampa and kainate receptors is mediated by several discrete protein-protein interactions. *Neuron*, 31(1):103–113.

Bahn, S., Volk, B., and Wisden, W. (1994). Kainate receptor gene expression in the developing rat brain. *J Neurosci*, 1994/09/01(9):5525–5547.

Bahring, R., Bowie, D., Benveniste, M., and Mayer, M. L. (1997). Permeation and block of rat GluR6 glutamate receptor channels by internal and external polyamines. *J Physiol*, 502 (Pt 3:575–589.

Ball, S. M., Atlason, P. T., Shittu-Balogun, O. O., and Molnár, E. (2010). Assembly and intracellular distribution of kainate receptors is determined by rna editing and subunit composition. *J Neurochem*, 114(6):1805–1818.

Bannister, N. J., Benke, T. A., Mellor, J., Scott, H., Gürdal, E., Crabtree, J. W., Isaac, J. T. R., Gurdal, E., Crabtree, J. W., Isaac, J. T. R., Gürdal, E., Crabtree, J. W., Isaac, J. T. R., Gurdal, E., Crabtree, J. W., and Isaac, J. T. R. (2005). Developmental changes in AMPA and kainate receptor-mediated quantal transmission at thalamocortical synapses in the barrel cortex. *J Neurosci*, 2005/05/27(21):5259–5271.

Barberis, A., Sachidhanandam, S., and Mulle, C. (2008). GluR6/KA2 kainate receptors mediate slow-deactivating currents. *J Neurosci*, 2008/06/20(25):6402–6406.

Barlow, D. J. and Thornton, J. M. (1988). Helix geometry in proteins. *Journal of Molecular Biology*, 201(3):601–619.

Baronas, V. A. and Kurata, H. T. (2014). Inward rectifiers and their regulation by endogenous polyamines. *Front Physiol*, 5:325.

Bats, C., Groc, L., and Choquet, D. (2007). The interaction between stargazin and psd-95 regulates ampa receptor surface trafficking. *Neuron*, 53:719–734.

Benke, T. A., Lthi, A., Isaac, J. T., and Collingridge, G. L. (1998). Modulation of ampa receptor unitary conductance by synaptic activity. *Nature*, 393:793–797.

Berl, S. and Waelsch, H. (1958). Determination of glutamic acid, glutamine, glutathione and gamma-aminobutyric acid and their distribution in brain tissue. *Journal of neurochemistry*, 3:161–169.

Bernard, A., Ferhat, L., Dessi, F., Charton, G., Represa, A., Ben-Ari, Y., and Khrestchatisky, M. (1999). Q/r editing of the rat glur5 and glur6 kainate receptors in vivo and in vitro: evidence for independent developmental, pathological and cellular regulation. *Eur J Neurosci*, 11(2):604–616.

Best, R. B., Zhu, X., Shim, J., Lopes, P. E. M., Mittal, J., Feig, M., and Mackerell, Jr, A. D. (2012). Optimization of the additive charmm all-atom protein force field targeting improved sampling of the backbone ϕ, ψ and side-chain $\chi(1)$ and $\chi(2)$ dihedral angles. *J Chem Theory Comput*, 8(9):3257–3273.

Blackstone, C. D., Moss, S. J., Martin, L. J., Levey, A. I., Price, D. L., and Huganir, R. L. (1992). Biochemical characterization and localization of a non-n-methyl-d-aspartate glutamate receptor in rat brain. *J Neurochem*, 58(3):1118–1126.

Bleakman, D., Ballyk, B. a., Schoepp, D. D., Palmer, A. J., Bath, C. P., Sharpe, E. F., Woolley, M. L., Bufton, H. R., Kamboj, R. K., Tarnawa, I., and Lodge, D. (1996). Activity of 2,3-benzodiazepines at native rat and recombinant human glutamate receptors in vitro: Stereospecificity and selectivity profiles.

Neuropharmacology, 35(12):1689–1702.

Bleakman, D. and Lodge, D. (1998). Neuropharmacology of ampa and kainate receptors. *Neuropharmacology*, 37:1187–1204.

Bökel, C., Dass, S., Wilsch-Bräuninger, M., and Roth, S. (2006). Drosophila cornichon acts as cargo receptor for er export of the tgfalpha-like growth factor gurken. *Development*, 133(3):459–470.

Bowie, D. (2002). External anions and cations distinguish between AMPA and kainate receptor gating mechanisms. *J Physiol*, 2002/03/19(Pt 3):725–733.

Bowie, D. (2008). Ionotropic glutamate receptors & CNS disorders. *CNS Neurol Disord Drug Targets*, 2008/06/10(2):129–143.

Bowie, D. (2010). Ion-dependent gating of kainate receptors. *The Journal of physiology*, 588:67–81.

Bowie, D. (2012). Redefining the classification of AMPA-selective ionotropic glutamate receptors. *J.Physiol*, 590(Pt 1):49–61.

Bowie, D., Bähring, R., and Mayer, M. (1999). Block of kainate and ampa receptors by polyamines and insect toxins.

Bowie, D., Garcia, E. P., Marshall, J., Traynelis, S. F., and Lange, G. D. (2003). Allosteric regulation and spatial distribution of kainate receptors bound to ancillary proteins. *J Physiol*, 2003/02/04(Pt 2):373–385.

Bowie, D. and Lange, G. D. (2002). Functional stoichiometry of glutamate receptor desensitization. *J Neurosci*, 2002/04/30(9):3392–3403.

Bowie, D., Lange, G. D., and Mayer, M. L. (1998). Activity-dependent modulation of glutamate receptors by polyamines. *J Neurosci*, 1998/10/08(20):8175–8185.

Bowie, D. and Mayer, M. L. (1995). Inward rectification of both AMPA and kainate subtype glutamate receptors generated by polyamine-mediated ion channel block. *Neuron*, 15(2):453–462.

Brandl, C. J. and Deber, C. M. (1986). Hypothesis about the function of membrane-buried proline residues in transport proteins. *Proc Natl Acad Sci U S A*, 83(4):917–921.

Bright, J. N., Shrivastava, I. H., Cordes, F. S., and Sansom, M. S. (2002). Conformational dynamics of helix S6 from Shaker potassium channel: simulation studies. *Biopolymers*, 64(6):303–313.

Brose, N., Gasic, G. P., Vetter, D. E., Sullivan, J. M., and Heinemann, S. F. (1993). Protein chemical characterization and immunocytochemical localization of the nmda receptor subunit nmda r1. *J Biol Chem*, 268(30):22663–22671.

Brown, P. M. G. E., Aurousseau, M. R. P., Musgaard, M., Biggin, P. C., and Bowie, D. (2016). Kainate receptor pore-forming and auxiliary subunits regulate channel block by a novel mechanism. *J Physiol*, 594(7):1821–1840.

Bureau, I., Dieudonne, S., Coussen, F., and Mulle, C. (2000). Kainate receptor-mediated synaptic currents in cerebellar Golgi cells are not shaped by diffusion of glutamate. *Proc Natl Acad Sci U S A*, 2000/06/07(12):6838–6843.

Burnashev, N. (1996). Calcium permeability of glutamate-gated channels in the central nervous system. *Curr Opin Neurobiol*, 6(3):311–317.

Burnashev, N., Monyer, H., Seeburg, P. H., and Sakmann, B. (1992). Divalent ion permeability of ampa receptor channels is dominated by the edited form of a single subunit. *Neuron*, 8:189–198.

Burnashev, N., Zhou, Z., Neher, E., and Sakmann, B. (1995). Fractional calcium currents through recombinant GluR channels of the NMDA, AMPA and kainate receptor subtypes. *J Physiol*, 485 (Pt 2:403–418.

Carta, M., Opazo, P., Veran, J., AthanÃ©, A., Choquet, D., Coussen, F., and Mulle, C. (2013). Camkii-dependent phosphorylation of gluk5 mediates plasticity of kainate receptors. *EMBO J*, 32(4):496–510.

Cason, A. L., Ikeguchi, Y., Skinner, C., Wood, T. C., Holden, K. R., Lubs, H. A., Martinez, F., Simensen, R. J., Stevenson, R. E., Pegg, A. E., and Schwartz, C. E. (2003). X-linked spermine synthase gene (sms) defect: the first polyamine deficiency syndrome. *European journal of human genetics : EJHG*, 11:937–944.

Castillo, P. E., Malenka, R. C., and Nicoll, R. a. (1997). Kainate receptors mediate a slow postsynaptic current in hippocampal CA3 neurons. *Nature*, 1997/07/10(6638):182–186.

Changeux, J.-P., Giraudat, J., and Dennis, M. (1987). The nicotinic acetylcholine receptor: molecular architecture of a ligand-regulated ion channel. *Trends in Pharmacological Sciences*, 8(12):459–465.

Chen, G. Q., Cui, C., Mayer, M. L., and Gouaux, E. (1999). Functional characterization of a potassium-selective prokaryotic glutamate receptor. *Nature*, 402(6763):817–821.

Chen, L., Chetkovich, D. M., Petralia, R. S., Sweeney, N. T., Kawasaki, Y., Wenthold, R. J., Bredt, D. S., and Nicoll, R. a. (2000). Stargazin regulates synaptic targeting of AMPA receptors by two distinct mechanisms. *Nature*, 408(6815):936–943.

Chen, L., Dürr, K. L., and Gouaux, E. (2014). X-ray structures of ampa receptor-cone snail toxin complexes illuminate activation mechanism. *Science*, 345(6200):1021–1026.

Chung, H. J., Xia, J., Scannevin, R. H., Zhang, X., and Huganir, R. L. (2000). Phosphorylation of the ampa receptor subunit glur2 differentially regulates its interaction with pdz domain-containing proteins. *J Neurosci*, 20(19):7258–7267.

Clarke, V. R., Ballyk, B. A., Hoo, K. H., Mandelzys, A., Pellizzari, A., Bath, C. P., Thomas, J., Sharpe, E. F., Davies, C. H., Ornstein, P. L., Schoepp, D. D., Kamboj, R. K., Collingridge, G. L., Lodge, D., and Bleakman, D. (1997). A

hippocampal glur5 kainate receptor regulating inhibitory synaptic transmission. *Nature*, 389:599–603.

Clements, J. (1996). Transmitter timecourse in the synaptic cleft: its role in central synaptic function. *Trends Neurosci*, 19(5):163–171.

Clements, J., Feltz, A., Sahara, Y., and Westbrook, G. (1998). Activation kinetics of ampa receptor channels reveal the number of functional agonist binding sites. *J Neurosci*, 18(1):119–127.

Clements, J., Lester, R., Tong, G., Jahr, C., and Westbrook, G. (1992). The time course of glutamate in the synaptic cleft. *Science*, 258(5087):1498–1501.

Collingridge, G. L., Olsen, R. W., Peters, J., and Spedding, M. (2009). A nomenclature for ligand-gated ion channels. *Neuropharmacology*, 56(1):2–5.

Connors, B. W. and Long, M. A. (2004). Electrical synapses in the mammalian brain. *Annual review of neuroscience*, 27:393–418.

Contractor, A., Mulle, C., and Swanson, G. T. (2011). Kainate receptors coming of age: milestones of two decades of research. *Trends Neurosci.*, 34(3):154–163.

Contractor, A., Sailer, A. W., Darstein, M., Maron, C., Xu, J., Swanson, G. T., and Heinemann, S. F. (2003). Loss of kainate receptor-mediated heterosynaptic facilitation of mossy-fiber synapses in ka2-/- mice. *The Journal of neuroscience : the official journal of the Society for Neuroscience*, 23:422–429.

Coombs, I. D., Soto, D., Zonouzi, M., Renzi, M., Shelley, C., Farrant, M., and Cull-Candy, S. G. (2012). Cornichons modify channel properties of recombinant and glial ampa receptors. *J Neurosci*, 32(29):9796–9804.

Cooper, E., Couturier, S., and Ballivet, M. (1991). Pentameric structure and subunit stoichiometry of a neuronal nicotinic acetylcholine receptor. *Nature*, 350(6315):235–238.

Copits, B. A., Robbins, J. S., Frausto, S., and Swanson, G. T. (2011). Synaptic targeting and functional modulation of gluk1 kainate receptors by the auxiliary neuropilin and tolloid-like (neto) proteins. *J Neurosci*, 31(20):7334–7340.

Copits, B. A., Vernon, C. G., Sakai, R., and Swanson, G. T. (2014). Modulation of ionotropic glutamate receptor function by vertebrate galectins. *J Physiol*, 592(10):2079–2096.

Cordes, F. S., Bright, J. N., and Sansom, M. S. P. (2002). Proline-induced distortions of transmembrane helices. *Journal of Molecular Biology*, 323(5):951–960.

Cossart, R., Epsztein, J., Tyzio, R., Becq, H., Hirsch, J., Ben-Ari, Y., and Crépel, V. (2002). Quantal release of glutamate generates pure kainate and mixed AMPA/kainate EPSCs in hippocampal neurons. *Neuron*, 35(1):147–159.

Crépel, F. and Crepel, F. (2009). Role of presynaptic kainate receptors at parallel fiber-purkinje cell synapses in induction of cerebellar LTD: interplay with climbing fiber input. *J Neurophysiol*, 2009/06/19(2):965–973.

Cui, C., Bahring, R., and Mayer, M. L. (1998). The role of hydrophobic interactions in binding of polyamines to non NMDA receptor ion channels. *Neuropharmacology*, 37(10-11):1381–1391.

Cui, C. and Mayer, M. L. (1999). Heteromeric kainate receptors formed by the coassembly of GluR5, GluR6, and GluR7. *The Journal of neuroscience : the official journal of the Society for Neuroscience*, 19(19):8281–8291.

Cull-Candy, S., Kelly, L., and Farrant, M. (2006). Regulation of ca2+-permeable ampa receptors: synaptic plasticity and beyond. *Curr Opin Neurobiol*, 16(3):288–297.

Curtis, D. R., Phillis, J. W., and Watkins, J. C. (1960). The chemical excitation of spinal neurones by certain acidic amino acids. *The Journal of physiology*, 150:656–682.

Curtis, D. R. and Watkins, J. C. (1963). Acidic amino acids with strong excitatory actions on mammalian neurones. *The Journal of physiology*, 166:1–14.

Dalva, M. B., Takasu, M. A., Lin, M. Z., Shamah, S. M., Hu, L., Gale, N. W., and Greenberg, M. E. (2000). Ephb receptors interact with nmda receptors and regulate excitatory synapse formation. *Cell*, 103(6):945–956.

Daniels, B. A., Andrews, E. D., Aurousseau, M. R., Accardi, M. V., and Bowie, D. (2013). Crosslinking the ligand-binding domain dimer interface locks kainate receptors out of the main open state. *J Physiol*, 591(Pt 16):3873–3885.

Darden, T., York, D., and Pedersen, L. (1993). Particle mesh ewald: An n log (n) method for ewald sums in large systems. *The Journal of chemical physics*, 98(12):10089–10092.

Darstein, M., Petralia, R. S., Swanson, G. T., Wenthold, R. J., and Heinemann, S. F. (2003). Distribution of kainate receptor subunits at hippocampal mossy fiber synapses. *The Journal of neuroscience : the official journal of the Society for Neuroscience*, 23:8013–8019.

Davies, J. and Watkins, J. C. (1979). Selective antagonism of amino acid-induced and synaptic excitation in the cat spinal cord. *The Journal of physiology*, 297:621–635.

Davies, J. and Watkins, J. C. (1981). Differentiation of kainate and quisqualate receptors in the cat spinal cord by selective antagonism with gamma-d(and l)-glutamylglycine. *Brain research*, 206:172–177.

Dawe, G. B., Musgaard, M., Andrews, E. D., Daniels, B. A., Aurousseau, M. R. P., Biggin, P. C., and Bowie, D. (2013). Defining the structural relationship between kainate-receptor deactivation and desensitization. *Nat Struct Mol Biol*, 20(9):1054–1061.

Dawe, G. B., Musgaard, M., Aurousseau, M. R. P., Nayeem, N., Green, T., Biggin, P. C., and Bowie, D. (2016). Distinct structural pathways coordinate the activation

of ampa receptor-auxiliary subunit complexes. *Neuron*, 89(6):1264–1276.

Demmer, C. S., Moller, C., Brown, P. M. G. E., Han, L., Pickering, D. S., Nielsen, B., Bowie, D., Frydenvang, K., Kastrup, J. S., and Bunch, L. (2015). Binding mode of an alpha-amino acid-linked quinoxaline-2,3-dione analogue at glutamate receptor subtype gluk1. *ACS chemical neuroscience*, 6:845–854.

Donevan, S. D. and Rogawski, M. A. (1995). Intracellular polyamines mediate inward rectification of ca(2+)-permeable alpha-amino-3-hydroxy-5-methyl-4-isoxazolepropionic acid receptors. *Proceedings of the National Academy of Sciences of the United States of America*, 92:9298–9302.

Du, M., Rambhadran, A., and Jayaraman, V. (2008). Luminescence resonance energy transfer investigation of conformational changes in the ligand binding domain of a kainate receptor. *The Journal of biological chemistry*, 283:27074–27078.

Du, M., Reid, S. A., and Jayaraman, V. (2005). Conformational changes in the ligand-binding domain of a functional ionotropic glutamate receptor. *J Biol Chem*, 280(10):8633–8636.

Dürr, K. L., Chen, L., Stein, R. A., De Zorzi, R., Folea, I. M., Walz, T., Mchaourab, H. S., and Gouaux, E. (2014). Structure and dynamics of ampa receptor glua2 in resting, pre-open, and desensitized states. *Cell*, 158(4):778–792.

Ehlers, M. D., Heine, M., Groc, L., Lee, M.-C., and Choquet, D. (2007). Diffusional trapping of glur1 ampa receptors by input-specific synaptic activity. *Neuron*, 54:447–460.

Epsztein, J., Represa, A., Jorquera, I., Ben-Ari, Y., Crepel, V., and Crépel, V. (2005). Recurrent mossy fibers establish aberrant kainate receptor-operated synapses on granule cells from epileptic rats. *J Neurosci*, 2005/09/09(36):8229–8239.

Erlenhardt, N., Yu, H., Abiraman, K., Yamasaki, T., Wadiche, J. I., Tomita, S., and Bredt, D. S. (2016). Porcupine controls hippocampal ampar levels, composition, and synaptic transmission. *Cell Rep*, 14(4):782–794.

Evans, R. H., Francis, A. A., and Watkins, J. C. (1977). Selective antagonism by mg2+ of amino acid-induced depolarization of spinal neurones. *Experientia*, 33:489–491.

Everts, I., Petroski, R., Kizelsztein, P., Teichberg, V. I., Heinemann, S. F., and Hollmann, M. (1999). Lectin-induced inhibition of desensitization of the kainate receptor glur6 depends on the activation state and can be mediated by a single native or ectopic n-linked carbohydrate side chain. *J Neurosci*, 19(3):916–927.

Everts, I., Villmann, C., and Hollmann, M. (1997). N-glycosylation is not a prerequisite for glutamate receptor function but is essential for lectin modulation. *Mol Pharmacol*, 52(5):861–873.

Fay, A.-M. L. and Bowie, D. (2006). Concanavalin-a reports agonist-induced conformational changes in the intact glur6 kainate receptor. *J Physiol*, 572(Pt 1):201–213.

Fay, A.-M. L. M., Corbeil, C. R., Brown, P., Moitessier, N., and Bowie, D. (2009). Functional characterization and in silico docking of full and partial GluK2 kainate receptor agonists. *Mol Pharmacol*, 2009/02/20(5):1096–1107.

Fernandes, H. B., Catches, J. S., Petralia, R. S., Copits, B. a., Xu, J., Russell, T. a., Swanson, G. T., and Contractor, A. (2009). High-affinity kainate receptor subunits are necessary for ionotropic but not metabotropic signaling. *Neuron*, 2009/09/26(6):818–829.

Ferrer-Montiel, A. V. and Montal, M. (1996). Pentameric subunit stoichiometry of a neuronal glutamate receptor. *Proc Natl Acad Sci U S A*, 93(7):2741–2744.

Fisher, J. L. (2015). The auxiliary subunits neto1 and neto2 have distinct, subunit-dependent effects at recombinant gluk1- and gluk2-containing kainate receptors. *Neuropharmacology*, 99:471–480.

Fisher, J. L. and Housley, P. R. (2013). Agonist binding to the gluk5 subunit is sufficient for functional surface expression of heteromeric gluk2/gluk5 kainate receptors. *Cellular and molecular neurobiology*, 33:1099–1108.

Fisher, J. L. and Mott, D. D. (2011). Distinct Functional Roles of Subunits within the Heteromeric Kainate Receptor. *J.Neurosci.*, 31(47):17113–17122.

Fisher, J. L. and Mott, D. D. (2012). The auxiliary subunits Neto1 and Neto2 reduce voltage-dependent inhibition of recombinant kainate receptors. *J.Neurosci.*, 32(37):12928–12933.

Fleck, M. W., Cornell, E., and Mah, S. J. (2003). Amino-acid residues involved in glutamate receptor 6 kainate receptor gating and desensitization. *J Neurosci*, 23(4):1219–1227.

Fleidervish, I. A., Libman, L., Katz, E., and Gutnick, M. J. (2008). Endogenous polyamines regulate cortical neuronal excitability by blocking voltage-gated na+ channels. *Proc Natl Acad Sci U S A*, 105(48):18994–18999.

Fowler, P. W. and Sansom, M. S. P. (2013). The pore of voltage-gated potassium ion channels is strained when closed. *Nat Commun*, 4(May):1872.

Frerking, M. and Nicoll, R. a. (2000). Synaptic kainate receptors. *Current Opinion in Neurobiology*, 10(3):342–351.

Frerking, M. and Ohliger-Frerking, P. (2002). AMPA receptors and kainate receptors encode different features of afferent activity. *J Neurosci*, 2002/08/28(17):7434–7443.

Fu, L. Y., Cummins, T. R., and Moczydlowski, E. G. (2012). Sensitivity of cloned muscle, heart and neuronal voltage-gated sodium channels to block by polyamines:

a possible basis for modulation of excitability in vivo. *Channels (Austin, Tex.)*, 6(1):41–49.

Fucile, S., Miledi, R., and Eusebi, F. (2006). Effects of cyclothiazide on glur1/ampa receptors. *Proceedings of the National Academy of Sciences of the United States of America*, 103:2943–2947.

Fukata, Y., Tzingounis, A. V., Trinidad, J. C., Fukata, M., Burlingame, A. L., Nicoll, R. A., and Bredt, D. S. (2005). Molecular constituents of neuronal ampa receptors. *J Cell Biol*, 169(3):399–404.

Furukawa, H. and Gouaux, E. (2003). Mechanisms of activation, inhibition and specificity: crystal structures of the nmda receptor nr1 ligand-binding core. *EMBO J*, 22(12):2873–2885.

Garcia, E. P., Mehta, S., Blair, L. a. C., Wells, D. G., Shang, J., Fukushima, T., Fallon, J. R., Garner, C. C., and Marshall, J. (1998). SAP90 binds and clusters kainate receptors causing incomplete desensitization. *Neuron*, 1998/11/10(4):727–739.

Gascón-Moya, M., Pejoan, A., Izquierdo-Serra, M., Pittolo, S., Cabré, G., Hernando, J., Alibés, R., Gorostiza, P., and Busqué, F. (2015). An optimized glutamate receptor photoswitch with sensitized azobenzene isomerization. *The Journal of organic chemistry*, 80:9915–9925.

Geiger, J. R., Melcher, T., Koh, D. S., Sakmann, B., Seeburg, P. H., Jonas, P., and Monyer, H. (1995). Relative abundance of subunit mrnas determines gating and ca2+ permeability of ampa receptors in principal neurons and interneurons in rat cns. *Neuron*, 15:193–204.

Gielen, M., Siegler Retchless, B., Mony, L., Johnson, J. W., and Paoletti, P. (2009). Mechanism of differential control of nmda receptor activity by nr2 subunits. *Nature*, 459(7247):703–707.

Gomez, M. and Hellstrand, P. (1995). Effects of polyamines on voltage-activated calcium channels in guinea-pig intestinal smooth muscle. *Pflugers Arch*, 430(4):501–507.

Gonzalez, J., Du, M., Parameshwaran, K., Suppiramaniam, V., and Jayaraman, V. (2010). Role of dimer interface in activation and desensitization in ampa receptors. *Proceedings of the National Academy of Sciences of the United States of America*, 107:9891–9896.

Gonzalez, J., Rambhadran, A., Du, M., and Jayaraman, V. (2008). Lret investigations of conformational changes in the ligand binding domain of a functional ampa receptor. *Biochemistry*, 47(38):10027–10032.

Granger, A. J. and Nicoll, R. A. (2014). Expression mechanisms underlying long-term potentiation: a postsynaptic view, 10 years on. *Philosophical transactions of the Royal Society of London. Series B, Biological sciences*, 369:20130136.

Granger, A. J., Shi, Y., Lu, W., Cerpas, M., and Nicoll, R. A. (2013). Ltp requires a reserve pool of glutamate receptors independent of subunit type. *Nature*, 493:495–500.

Greger, I. H., Akamine, P., Khatri, L., and Ziff, E. B. (2006). Developmentally regulated, combinatorial rna processing modulates ampa receptor biogenesis. *Neuron*, 51(1):85–97.

Greger, I. H. and Esteban, J. A. (2007). Ampa receptor biogenesis and trafficking. *Current opinion in neurobiology*, 17:289–297.

Greger, I. H., Khatri, L., Kong, X., and Ziff, E. B. (2003). Ampa receptor tetramerization is mediated by q/r editing. *Neuron*, 40:763–774.

Greger, I. H., Khatri, L., and Ziff, E. B. (2002). Rna editing at arg607 controls ampa receptor exit from the endoplasmic reticulum. *Neuron*, 34(5):759–772.

Griffith, T. N. and Swanson, G. T. (2015). Identification of critical functional determinants of kainate receptor modulation by auxiliary protein neto2. *J Physiol*, 593(22):4815–4833.

Grunwald, M. E. and Kaplan, J. M. (2003). Mutations in the ligand-binding and pore domains control exit of glutamate receptors from the endoplasmic reticulum in c. elegans. *Neuropharmacology*, 45(6):768–776.

Haering, S. C., Tapken, D., Pahl, S., and Hollmann, M. (2014). Auxiliary subunits: shepherding ampa receptors to the plasma membrane. *Membranes (Basel)*, 4(3):469–490.

Haghighi, A. P. and Cooper, E. (1998). Neuronal nicotinic acetylcholine receptors are blocked by intracellular spermine in a voltage-dependent manner. *J Neurosci*, 18(11):4050–4062.

Hansen, K. B., Furukawa, H., and Traynelis, S. F. (2010). Control of assembly and function of glutamate receptors by the amino-terminal domain. *Molecular pharmacology*, 78:535–549.

Hayashi, T., Rumbaugh, G., and Huganir, R. L. (2005). Differential regulation of ampa receptor subunit trafficking by palmitoylation of two distinct sites. *Neuron*, 47(5):709–723.

He, X.-Y., Li, Y.-J., Kalyanaraman, C., Qiu, L.-L., Chen, C., Xiao, Q., Liu, W.-X., Zhang, W., Yang, J.-J., Chen, G., Jacobson, M. P., and Shi, Y. S. (2016). Glua1 signal peptide determines the spatial assembly of heteromeric ampa receptors. *Proceedings of the National Academy of Sciences of the United States of America*, 113:E5645–E5654.

Heckmann, M., Bufler, J., Franke, C., and Dudel, J. (1996). Kinetics of homomeric GluR6 glutamate receptor channels.

Herb, A., Burnashev, N., Werner, P., Sakmann, B., Wisden, W., and Seeburg, P. H. (1992). The KA-2 subunit of excitatory amino acid receptors shows widespread expression in brain and forms ion channels with distantly related subunits. *Neuron*, 1992/04/01(4):775–785.

Herguedas, B., García-Nafría, J., Cais, O., Fernández-Leiro, R., Krieger, J., Ho, H., and Greger, I. H. (2016). Structure and organization of heteromeric ampa-type glutamate receptors. *Science*, 352(6285):aad3873.

Herreras, O. and Somjen, G. G. (1993a). Analysis of potential shifts associated with recurrent spreading depression and prolonged unstable spreading depression induced by microdialysis of elevated k+ in hippocampus of anesthetized rats. *Brain research*, 610:283–294.

Herreras, O. and Somjen, G. G. (1993b). Propagation of spreading depression among dendrites and somata of the same cell population. *Brain research*, 610:276–282.

Herring, B. E., Shi, Y., Suh, Y. H., Zheng, C.-Y., Blankenship, S. M., Roche, K. W., and Nicoll, R. A. (2013). Cornichon proteins determine the subunit composition of synaptic ampa receptors. *Neuron*, 77(6):1083–1096.

Hess, B., Kutzner, C., van der Spoel, D., and Lindahl, E. (2008). Gromacs 4: algorithms for highly efficient, load-balanced, and scalable molecular simulation. *J Chem Theory Comput*, 4(3):435–447.

Hicks, T. P., Hall, J. G., and McLennan, H. (1978). Ranking of excitatory amino acids by the antagonists glutamic acid diethylester and d-alpha-aminoadipic acid. *Canadian journal of physiology and pharmacology*, 56:901–907.

Hirbec, H., Francis, J. C., Lauri, S. E., Braithwaite, S. P., Coussen, F., Mulle, C., Dev, K. K., Coutinho, V., Meyer, G., Isaac, J. T. R., Collingridge, G. L., Henley, J. M., and Couthino, V. (2003). Rapid and differential regulation of ampa and kainate receptors at hippocampal mossy fibre synapses by pick1 and grip. *Neuron*,

37(4):625–638.

Hires, S. A., Zhu, Y., and Tsien, R. Y. (2008). Optical measurement of synaptic glutamate spillover and reuptake by linker optimized glutamate-sensitive fluorescent reporters. *Proceedings of the National Academy of Sciences of the United States of America*, 105:4411–4416.

Hogner, A., Kastrup, J. S., Jin, R., Liljefors, T., Mayer, M. L., Egebjerg, J., Larsen, I. K., and Gouaux, E. (2002). Structural basis for ampa receptor activation and ligand selectivity: crystal structures of five agonist complexes with the glur2 ligand-binding core. *J Mol Biol*, 322(1):93–109.

Hollmann, M. and Heinemann, S. (1994). Cloned glutamate receptors.

Hollmann, M., O'Shea-Greenfield, A., Rogers, S. W., and Heinemann, S. (1989). Cloning by functional expression of a member of the glutamate receptor family. *Nature*, 342(6250):643–648.

Horning, M. S. and Mayer, M. L. (2004). Regulation of ampa receptor gating by ligand binding core dimers. *Neuron*, 41(3):379–388.

Huettner, J. E. (2015). Glutamate receptor pores. *J Physiol*, 593(1):49–59.

Humphrey, W., Dalke, A., and Schulten, K. (1996). Vmd: visual molecular dynamics. *J Mol Graph*, 14(1):33–8, 27–8.

Isa, T., Iino, M., Itazawa, S., and Ozawa, S. (1995). Spermine mediates inward rectification of ca(2+)-permeable ampa receptor channels. *Neuroreport*, 6:2045–2048.

Isaac, J. T. R., Ashby, M. C., and McBain, C. J. (2007). The role of the glur2 subunit in ampa receptor function and synaptic plasticity. *Neuron*, 54:859–871.

Jackson, A. C. and Nicoll, R. A. (2011). The expanding social network of ionotropic glutamate receptors: Tarps and other transmembrane auxiliary subunits. *Neuron*, 70(2):178–199.

Jaskolski, F., Coussen, F., Nagarajan, N., Normand, E., Rosenmund, C., and Mulle, C. (2004). Subunit composition and alternative splicing regulate membrane delivery of kainate receptors. *The Journal of neuroscience : the official journal of the Society for Neuroscience*, 24:2506–2515.

Jatzke, C., Hernandez, M., and Wollmuth, L. P. (2003). Extracellular vestibule determinants of ca2+ influx in ca2+-permeable ampa receptor channels. *J Physiol*, 549(Pt 2):439–452.

Jin, R., Banke, T. G., Mayer, M. L., Traynelis, S. F., and Gouaux, E. (2003). Structural basis for partial agonist action at ionotropic glutamate receptors. *Nat Neurosci*, 6(8):803–810.

Jin, R., Horning, M., Mayer, M. L., and Gouaux, E. (2002). Mechanism of activation and selectivity in a ligand-gated ion channel: structural and functional studies of glur2 and quisqualate. *Biochemistry*, 41(52):15635–15643.

Jorgensen, W. L., Chandrasekhar, J., Madura, J. D., Impey, R. W., and Klein, M. L. (1983). Comparison of simple potential functions for simulating liquid water. *The Journal of chemical physics*, 79(2):926–935.

Kalashnikova, E., Lorca, R. A., Kaur, I., Barisone, G. A., Li, B., Ishimaru, T., Trimmer, J. S., Mohapatra, D. P., and DÃaz, E. (2010). Syndig1: an activity-regulated, ampa- receptor-interacting transmembrane protein that regulates excitatory synapse development. *Neuron*, 65(1):80–93.

Kamboj, S. K., Swanson, G. T., and Cull-Candy, S. G. (1995). Intracellular spermine confers rectification on rat calcium-permeable AMPA and kainate receptors. *The Journal of physiology*, 486 (Pt 2:297–303.

Karakas, E. and Furukawa, H. (2014). Crystal structure of a heterotetrameric NMDA receptor ion channel. *Science*, 344(6187):992–997.

Karakas, E., Simorowski, N., and Furukawa, H. (2009). Structure of the zinc-bound amino-terminal domain of the nmda receptor nr2b subunit. *EMBO J*, 28(24):3910–3920.

Kato, A. S., Gill, M. B., Yu, H., Nisenbaum, E. S., and Bredt, D. S. (2010). Tarps differentially decorate ampa receptors to specify neuropharmacology. *Trends Neurosci*, 33(5):241–248.

Kato, A. S., Siuda, E. R., Nisenbaum, E. S., and Bredt, D. S. (2008). Ampa receptor subunit-specific regulation by a distinct family of type ii tarps. *Neuron*, 59(6):986–996.

Kato, A. S., Zhou, W., Milstein, A. D., Knierman, M. D., Siuda, E. R., Dotzlaf, J. E., Yu, H., Hale, J. E., Nisenbaum, E. S., Nicoll, R. A., and Bredt, D. S. (2007). New transmembrane ampa receptor regulatory protein isoform, gamma-7, differentially regulates ampa receptors. *J Neurosci*, 27(18):4969–4977.

Keinnen, K., Wisden, W., Sommer, B., Werner, P., Herb, A., Verdoorn, T. A., Sakmann, B., and Seeburg, P. H. (1990). A family of ampa-selective glutamate receptors. *Science (New York, N.Y.)*, 249:556–560.

Kerschbaum, H. H., Kozak, J. A., and Cahalan, M. D. (2003). Polyvalent cations as permeant probes of mic and trpm7 pores. *Biophys J*, 84(4):2293–2305.

Klaassen, R. V., Stroeder, J., Coussen, F., Hafner, A.-S., Petersen, J. D., Renancio, C., Schmitz, L. J. M., Normand, E., Lodder, J. C., Rotaru, D. C., Rao-Ruiz, P., Spijker, S., Mansvelder, H. D., Choquet, D., and Smit, A. B. (2016). Shisa6 traps ampa receptors at postsynaptic sites and prevents their desensitization during synaptic activity. *Nat Commun*, 7:10682.

Klauda, J. B., Venable, R. M., Freites, J. A., O'Connor, J. W., Tobias, D. J., Mondragon-Ramirez, C., Vorobyov, I., MacKerell, Jr, A. D., and Pastor, R. W. (2010). Update of the charmm all-atom additive force field for lipids: validation

on six lipid types. *J Phys Chem B*, 114(23):7830–7843.

Kleywegt, G. J. and Jones, T. A. (1998). Databases in protein crystallography. *Acta Crystallographica Section D: Biological Crystallography*, 54(6):1119–1131.

Koh, D. S., Burnashev, N., and Jonas, P. (1995). Block of native Ca(2+)-permeable AMPA receptors in rat brain by intracellular polyamines generates double rectification. *J Physiol*, 486 (Pt 2:305–312.

Köhler, M., Burnashev, N., Sakmann, B., and Seeburg, P. H. (1993). Determinants of Ca2+ permeability in both TM1 and TM2 of high affinity kainate receptor channels: diversity by RNA editing. *Neuron*, 10(3):491–500.

Kornreich, B. G., Niu, L., Roberson, M. S., and Oswald, R. E. (2007). Identification of c-terminal domain residues involved in protein kinase a-mediated potentiation of kainate receptor subtype 6. *Neuroscience*, 146(3):1158–1168.

Kovcs, I., Simon, A., Szrics, E., Barabs, P., Hja, L., Nyikos, L., and Kardos, J. (2004). Cyclothiazide binding to functionally active ampa receptor reveals genuine allosteric interaction with agonist binding sites. *Neurochemistry international*, 44:271–280.

Kristensen, O., Kristensen, L. B., Møollerud, S., Frydenvang, K., Pickering, D. S., and Kastrup, J. S. (2016). The structure of a high-affinity kainate receptor: Gluk4 ligand-binding domain crystallized with kainate. *Structure (London, England : 1993)*, 24:1582–1589.

Krogsgaard-Larsen, P., Honor, T., Hansen, J. J., Curtis, D. R., and Lodge, D. (1980). New class of glutamate agonist structurally related to ibotenic acid. *Nature*, 284:64–66.

Kumar, J., Schuck, P., and Mayer, M. L. (2011). Structure and assembly mechanism for heteromeric kainate receptors. *Neuron*, 71(2):319–331.

Kuner, T., Seeburg, P. H., and Guy, H. R. (2003). A common architecture for k+ channels and ionotropic glutamate receptors? *Trends Neurosci*, 26(1):27–32.

Kurata, H. T., Akrouh, A., Li, J. B. W., Marton, L. J., and Nichols, C. G. (2013). Scanning the topography of polyamine blocker binding in an inwardly rectifying potassium channel. *J Biol Chem*, 288(9):6591–6601.

Kurata, H. T., Marton, L. J., and Nichols, C. G. (2006). The polyamine binding site in inward rectifier k+ channels. *J Gen Physiol*, 127(5):467–480.

Kuusinen, A., Arvola, M., and Keinänen, K. (1995). Molecular dissection of the agonist binding site of an ampa receptor. *EMBO J*, 14(24):6327–6332.

Lachance-Touchette, P., Brown, P., Meloche, C., Kinirons, P., Lapointe, L., Lacasse, H., Lortie, A., Carmant, L., Bedford, F., Bowie, D., and Cossette, P. (2011). Novel alpha-1 and gamma-2 gabaa receptor subunit mutations in families with idiopathic generalized epilepsy. *The European journal of neuroscience*, 34:237–249.

Landes, C. F., Rambhadran, A., Taylor, J. N., Salatan, F., and Jayaraman, V. (2011). Structural landscape of isolated agonist-binding domains from single ampa receptors. *Nature chemical biology*, 7:168–173.

Laube, B., Kuhse, J., and Betz, H. (1998). Evidence for a tetrameric structure of recombinant nmda receptors. *J Neurosci*, 18(8):2954–2961.

Lee, J. H., Kang, G. B., Lim, H.-H., Jin, K. S., Kim, S.-H., Ree, M., Park, C.-S., Kim, S.-J., and Eom, S. H. (2008). Crystal structure of the glur0 ligand-binding core from nostoc punctiforme in complex with l-glutamate: structural dissection of the ligand interaction and subunit interface. *J Mol Biol*, 376(2):308–316.

Lerma, J., Morales, M., Vicente, M. A., and Herreras, O. (1997). Glutamate receptors of the kainate type and synaptic transmission. *Trends in neurosciences*, 20:9–12.

Lester, R. A., Clements, J. D., Westbrook, G. L., and Jahr, C. E. (1990). Channel kinetics determine the time course of nmda receptor-mediated synaptic currents.

Nature, 346:565–567.

Letts, V., Felix, R., Biddlecome, G., Arikkath, J., Mahaffey, C., Valenzuela, A., Bartlett, 2nd, F., Mori, Y., Campbell, K., and Frankel, W. (1998). The mouse stargazer gene encodes a neuronal ca2+-channel gamma subunit. *Nat Genet*, 19(4):340–347.

Leuschner, W. D. and Hoch, W. (1999). Subtype-specific assembly of alpha-amino-3-hydroxy-5-methyl-4-isoxazole propionic acid receptor subunits is mediated by their n-terminal domains. *The Journal of biological chemistry*, 274:16907–16916.

Lodge, D. (2009). The history of the pharmacology and cloning of ionotropic glutamate receptors and the development of idiosyncratic nomenclature. *Neuropharmacology*, 56(1):6–21.

Lomeli, H., Mosbacher, J., Melcher, T., Höger, T., Geiger, J. R., Kuner, T., Monyer, H., Higuchi, M., Bach, A., and Seeburg, P. H. (1994). Control of kinetic properties of ampa receptor channels by nuclear rna editing. *Science (New York, N.Y.)*, 266:1709–1713.

Lopatin, A. N., Makhina, E. N., and Nichols, C. G. (1994). Potassium channel block by cytoplasmic polyamines as the mechanism of intrinsic rectification. *Nature*, 372(6504):366–369.

Lu, W., Shi, Y., Jackson, A. C., Bjorgan, K., During, M. J., Sprengel, R., Seeburg, P. H., and Nicoll, R. A. (2009). Subunit composition of synaptic AMPA receptors revealed by a single-cell genetic approach. *Neuron*, 62(2):254–268.

Lu, Z. (2004). Mechanism of rectification in inward-rectifier k+ channels. *Annu Rev Physiol*, 66:103–129.

Lu, Z. and Ding, L. (1999). Blockade of a retinal cgmp-gated channel by polyamines. *J Gen Physiol*, 113(1):35–43.

Ma-Högemeier, Z.-L., Körber, C., Werner, M., Racine, D., Muth-Köhne, E., Tapken, D., and Hollmann, M. (2010). Oligomerization in the endoplasmic reticulum and intracellular trafficking of kainate receptors are subunit-dependent but not editing-dependent. *J Neurochem*, 113(6):1403–1415.

MacLean, D. M. (2011). *Allosteric modulation of kainate receptors by external ions*. Phd dissertation, McGill University, Montreal, Canada.

MacLean, D. M., Ramaswamy, S. S., Du, M., Howe, J. R., and Jayaraman, V. (2014). Stargazin promotes closure of the ampa receptor ligand-binding domain. *J Gen Physiol*, 144(6):503–512.

Mah, S. J., Cornell, E., Mitchell, N. A., and Fleck, M. W. (2005). Glutamate receptor trafficking: endoplasmic reticulum quality control involves ligand binding and receptor function. *J Neurosci*, 25(9):2215–2225.

Malinow, R. and Malenka, R. C. (2002). Ampa receptor trafficking and synaptic plasticity. *Annu Rev Neurosci*, 25:103–126.

Mano, I., Lamed, Y., and Teichberg, V. I. (1996). A venus flytrap mechanism for activation and desensitization of alpha-amino-3-hydroxy-5-methyl-4-isoxazole propionic acid receptors. *J Biol Chem*, 271(26):15299–15302.

Mano, I. and Teichberg, V. I. (1998). A tetrameric subunit stoichiometry for a glutamate receptor-channel complex. *Neuroreport*, 9(2):327–331.

Mansour, M., Nagarajan, N., Nehring, R. B., Clements, J. D., and Rosenmund, C. (2001). Heteromeric ampa receptors assemble with a preferred subunit stoichiometry and spatial arrangement. *Neuron*, 32:841–853.

Maric, H. M., Kasaragod, V. B., Haugaard-Kedström, L., Hausrat, T. J., Kneussel, M., Schindelin, H., and Strømgaard, K. (2015). Design and synthesis of high-affinity dimeric inhibitors targeting the interactions between gephyrin and inhibitory neurotransmitter receptors. *Angewandte Chemie (International ed. in*

English), 54:490–494.

Martin, S., Nishimune, A., Mellor, J. R., and Henley, J. M. (2007). SUMOylation regulates kainate-receptor-mediated synaptic transmission. *Nature*, 447(7142):321–325.

Matsuda, S., Kamiya, Y., and Yuzaki, M. (2005). Roles of the n-terminal domain on the function and quaternary structure of the ionotropic glutamate receptor. *J Biol Chem*, 280(20):20021–20029.

Matsuda, S., Mikawa, S., and Hirai, H. (1999). Phosphorylation of serine-880 in glur2 by protein kinase c prevents its c terminus from binding with glutamate receptor-interacting protein. *J Neurochem*, 73(4):1765–1768.

Mayer, M. L. (2005). Crystal structures of the GluR5 and GluR6 ligand binding cores: molecular mechanisms underlying kainate receptor selectivity. *Neuron*, 2005/02/22(4):539–552.

Mayer, M. L. (2011). Structure and mechanism of glutamate receptor ion channel assembly, activation and modulation. *Current opinion in neurobiology*, 21:283–290.

Mayer, M. L., Ghosal, A., Dolman, N. P., and Jane, D. E. (2006). Crystal structures of the kainate receptor GluR5 ligand binding core dimer with novel GluR5-selective antagonists. *J Neurosci*, 2006/03/17(11):2852–2861.

Mayer, M. L., Olson, R., and Gouaux, E. (2001). Mechanisms for ligand binding to glur0 ion channels: crystal structures of the glutamate and serine complexes and a closed apo state. *J Mol Biol*, 311(4):815–836.

Mayer, M. L. and Westbrook, G. L. (1987). Permeation and block of N-methyl-D-aspartic acid receptor channels by divalent cations in mouse cultured central neurones.

Mayer, M. L., Westbrook, G. L., and Guthrie, P. B. (1984). Voltage-dependent block by Mg2+ of NMDA responses in spinal cord neurones. *Nature*,

1984/05/17(5965):261–263.

McCulloch, R. M., Johnston, G. A., Game, C. J., and Curtis, D. R. (1974). The differential sensitivity of spinal interneurones and renshaw cells to kainate and n-methyl-d-aspartate. *Experimental brain research*, 21:515–518.

McLennan, H. and Lodge, D. (1979). The antagonism of amino acid-induced excitation of spinal neurones in the cat. *Brain research*, 169:83–90.

Mehta, S., Wu, H., Garner, C. C., and Marshall, J. (2001). Molecular mechanisms regulating the differential association of kainate receptor subunits with SAP90/PSD-95 and SAP97. *J Biol Chem*, 2001/03/30(19):16092–16099.

Meyerson, J. R., Chittori, S., Merk, A., Rao, P., Han, T. H., Serpe, M., Mayer, M. L., and Subramaniam, S. (2016). Structural basis of kainate subtype glutamate receptor desensitization. *Nature*, 537:567–571.

Meyerson, J. R., Kumar, J., Chittori, S., Rao, P., Pierson, J., Bartesaghi, A., Mayer, M. L., and Subramaniam, S. (2014). Structural mechanism of glutamate receptor activation and desensitization. *Nature*, 514(7522):328–334.

Midgett, C. R. and Madden, D. R. (2008). The quaternary structure of a calcium-permeable ampa receptor: conservation of shape and symmetry across functionally distinct subunit assemblies. *J Mol Biol*, 382(3):578–584.

Miyamoto, S. and Kollman, P. A. (1992). Settle: an analytical version of the shake and rattle algorithm for rigid water models. *Journal of computational chemistry*, 13(8):952–962.

Monticelli, L., Kandasamy, S. K., Periole, X., Larson, R. G., Tieleman, D. P., and Marrink, S.-J. (2008). The martini coarse-grained force field: Extension to proteins. *J Chem Theory Comput*, 4(5):819–834.

Mott, D. D., Rojas, A., Fisher, J. L., Dingledine, R. J., and Benveniste, M. (2010). Subunit-specific desensitization of heteromeric kainate receptors. *The Journal of*

physiology, 588(Pt 4):683–700.

Mulle, C., Sailer, A., Perez-Otano, I., Dickinson-Anson, H., Castillo, P. E., Bureau, I., Maron, C., Gage, F. H., Mann, J. R., Bettler, B., and Heinemann, S. F. (1998). Altered synaptic physiology and reduced susceptibility to kainate-induced seizures in GluR6-deficient mice. *Nature*, 392(6676):601–605.

Nakagawa, T., Cheng, Y., Ramm, E., Sheng, M., and Walz, T. (2005). Structure and different conformational states of native ampa receptor complexes. *Nature*, 433(7025):545–549.

Nakagawa, T., Cheng, Y., Sheng, M., and Walz, T. (2006). Three-dimensional structure of an ampa receptor without associated stargazin/tarp proteins. *Biol Chem*, 387(2):179–187.

Nanao, M. H., Green, T., Stern-Bach, Y., Heinemann, S. F., and Choe, S. (2005). Structure of the kainate receptor subunit glur6 agonist-binding domain complexed with domoic acid. *Proc Natl Acad Sci U S A*, 102(5):1708–1713.

Nasu-Nishimura, Y., Hurtado, D., Braud, S., Tang, T. T.-T., Isaac, J. T. R., and Roche, K. W. (2006). Identification of an endoplasmic reticulum-retention motif in an intracellular loop of the kainate receptor subunit KA2. *J Neurosci*, 2006/06/30(26):7014–7021.

Nayeem, N., Mayans, O., and Green, T. (2011). Conformational flexibility of the ligand-binding domain dimer in kainate receptor gating and desensitization. *J.Neurosci.*, 31(8):2916–2924.

Nayeem, N., Zhang, Y., Schweppe, D. K., Madden, D. R., and Green, T. (2009). A nondesensitizing kainate receptor point mutant. *Mol.Pharmacol.*, 76(3):534–542.

Ng, D., Pitcher, G. M., Szilard, R. K., SertiÃ©, A., Kanisek, M., Clapcote, S. J., Lipina, T., Kalia, L. V., Joo, D., McKerlie, C., Cortez, M., Roder, J. C., Salter,

M. W., and McInnes, R. R. (2009). Neto1 is a novel cub-domain nmda receptor-interacting protein required for synaptic plasticity and learning. *PLoS Biol*, 7(2):e41.

Nichols, C. G. and Lopatin, A. N. (1997). Inward rectifier potassium channels. *Annu.Rev.Physiol*, 59:171–191.

Nicoletti, F., Meek, J., Iadarola, M., Chuang, D., Roth, B., and E, C. (1986). Coupling of inositol phospholipid metabolism with excitatory amino acid recognition sites in rat hippocampus. *J Neurochem*, 46(1):40–6.

Nicoll, R. a. and Schmitz, D. (2005). Synaptic plasticity at hippocampal mossy fibre synapses. *Nature reviews. Neuroscience*, 6(11):863–876.

Nowak, L., Bregestovski, P., Ascher, P., Herbet, A., and Prochiantz, A. (1984). Magnesium gates glutamate-activated channels in mouse central neurones. *Nature*, 307:462–465.

Nowotarski, S. L., Woster, P. M., and Casero, Jr, R. A. (2013). Polyamines and cancer: implications for chemotherapy and chemoprevention. *Expert Rev Mol Med*, 15:e3.

Paas, Y. (1998). The macro- and microarchitectures of the ligand-binding domain of glutamate receptors. *Trends Neurosci*, 21(3):117–125.

Panchenko, V. A., Glasser, C. R., Partin, K. M., and Mayer, M. L. (1999). Amino acid substitutions in the pore of rat glutamate receptors at sites influencing block by polyamines. *J.Physiol*, 520 Pt 2:337–357.

Partin, K. M., Patneau, D. K., Winters, C. a., Mayer, M. L., and Buonanno, a. (1993). Selective modulation of desensitization at AMPA versus kainate receptors by cyclothiazide and concanavalin A. *Neuron*, 11(6):1069–1082.

Pasternack, A., Coleman, S. K., Jouppila, A., Mottershead, D. G., Lindfors, M., Pasternack, M., and Keinänen, K. (2002). Alpha-amino-3-hydroxy-5-methyl-4-isoxazolepropionic acid (ampa) receptor channels lacking the n-terminal domain. *J Biol Chem*, 277(51):49662–49667.

Paternain, A. V., Cohen, A., Stern-Bach, Y., and Lerma, J. (2003). A role for extracellular na+ in the channel gating of native and recombinant kainate receptors. *J Neurosci*, 23(25):8641–8648.

Paternain, A. V., Herrera, M. T., Nieto, M. a., and Lerma, J. (2000). GluR5 and GluR6 kainate receptor subunits coexist in hippocampal neurons and coassemble to form functional receptors. *J Neurosci*, 2000/01/11(1):196–205.

Paternain, A. V., Morales, M., and Lerma, J. (1995). Selective antagonism of AMPA receptors unmasks kainate receptor-mediated responses in hippocampal neurons. *Neuron*, 1995/01/01(1):185–189.

Pegg, A. E. (2009). Mammalian polyamine metabolism and function. *IUBMB.Life*, 61(9):880–894.

Pegg, A. E. (2014). The function of spermine. *IUBMB Life*, 66(1):8–18.

Pegg, A. E. (2016). Functions of polyamines in mammals. *The Journal of biological chemistry*, 291:14904–14912.

Pegg, A. E. and McCann, P. P. (1982). Polyamine metabolism and function. *The American journal of physiology*, 243:C212–C221.

Pei, J. and Grishin, N. V. (2012). Unexpected diversity in shisa-like proteins suggests the importance of their roles as transmembrane adaptors. *Cell Signal*, 24(3):758–769.

Penn, A. C., Williams, S. R., and Greger, I. H. (2008). Gating motions underlie ampa receptor secretion from the endoplasmic reticulum. *EMBO J*, 27(22):3056–3068.

Penna, A., Wang, D.-S., Yu, J., Lecker, I., Brown, P. M. G. E., Bowie, D., and Orser, B. A. (2014). Hydrogen peroxide increases gabaa receptor-mediated tonic current in hippocampal neurons. *The Journal of neuroscience : the official journal of the Society for Neuroscience*, 34:10624–10634.

Perrais, D., Veran, J., and Mulle, C. (2010). Gating and permeation of kainate receptors: differences unveiled. *Trends Pharmacol.Sci.*, 31(11):516–522.

Petralia, R. S., Wang, Y. X., and Wenthold, R. J. (1994). Histological and ultrastructural localization of the kainate receptor subunits, KA2 and GluR6/7, in the rat nervous system using selective antipeptide antibodies. *J.Comp Neurol.*, 349(1):85–110.

Phillips, J. C., Braun, R., Wang, W., Gumbart, J., Tajkhorshid, E., Villa, E., Chipot, C., Skeel, R. D., Kalé, L., and Schulten, K. (2005). Scalable molecular dynamics with namd. *J Comput Chem*, 26(16):1781–1802.

Pinheiro, P. S. and Mulle, C. (2008). Presynaptic glutamate receptors: physiological functions and mechanisms of action. *Nature reviews. Neuroscience*, 9:423–436.

Pinheiro, P. S., Perrais, D., Coussen, F., Barhanin, J., Bettler, B., Mann, J. R., Malva, J. O., Heinemann, S. F., and Mulle, C. (2007). GluR7 is an essential subunit of presynaptic kainate autoreceptors at hippocampal mossy fiber synapses. *Proc.Natl.Acad.Sci.U.S.A*, 104(29):12181–12186.

Plested, A. J., Vijayan, R., Biggin, P. C., and Mayer, M. L. (2008). Molecular basis of kainate receptor modulation by sodium.

Plested, A. J. R. and Mayer, M. L. (2007). Structure and mechanism of kainate receptor modulation by anions. *Neuron*, 2007/03/16(6):829–841.

Poulin, R., Casero, R., and Soulet, D. (2012). Recent advances in the molecular biology of metazoan polyamine transport. *Amino Acids*, 42(2-3):711–723.

Priel, A., Kolleker, A., Ayalon, G., Gillor, M., Osten, P., and Stern-Bach, Y. (2005). Stargazin reduces desensitization and slows deactivation of the ampa-type glutamate receptors. *The Journal of neuroscience : the official journal of the Society for Neuroscience*, 25:2682–2686.

Priel, A., Selak, S., Lerma, J., and Stern-Bach, Y. (2006). Block of kainate receptor desensitization uncovers a key trafficking checkpoint. *Neuron*, 52(6):1037–1046.

Prieto, M. L. and Wollmuth, L. P. (2010). Gating modes in ampa receptors. *The Journal of neuroscience : the official journal of the Society for Neuroscience*, 30:4449–4459.

Puchalski, R. B., Louis, J. C., Brose, N., Traynelis, S. F., Egebjerg, J., Kukekov, V., Wenthold, R. J., Rogers, S. W., Lin, F., and Moran, T. (1994). Selective rna editing and subunit assembly of native glutamate receptors. *Neuron*, 13(1):131–147.

Rachline, J., Perin-Dureau, F., Le Goff, A., Neyton, J., and Paoletti, P. (2005). The micromolar zinc-binding domain on the nmda receptor subunit nr2b. *J Neurosci*, 25(2):308–317.

Reiner, A., Arant, R. J., and Isacoff, E. Y. (2012). Assembly Stoichiometry of the GluK2/GluK5 Kainate Receptor Complex. *Cell Rep.*, 1(3):234–240.

Ren, Z., Riley, N. J., Garcia, E. P., Sanders, J. M., Swanson, G. T., and Marshall, J. (2003). Multiple trafficking signals regulate kainate receptor KA2 subunit surface expression. *J Neurosci*, 23(16):6608–6616.

Ribeiro, M. P. C., Custdio, J. B. A., and Santos, A. E. (2016). Ionotropic glutamate receptor antagonists and cancer therapy: time to think out of the box? *Cancer chemotherapy and pharmacology*.

Rivera, R.-o., Rozas, J. L., and Lerma, J. (2007). Pkc-dependent autoregulation of membrane kainate receptors. *EMBO J*, 26(20):4359–4367.

Robert, A., Armstrong, N., Gouaux, J. E., and Howe, J. R. (2005). Ampa receptor binding cleft mutations that alter affinity, efficacy, and recovery from desensitization. *The Journal of neuroscience : the official journal of the Society for Neuroscience*, 25:3752–3762.

Rosenmund, C., Stern-Bach, Y., and Stevens, C. F. (1998). The tetrameric structure of a glutamate receptor channel. *Science (New York, N.Y.)*, 280(5369):1596–1599.

Rozov, A. and Burnashev, N. (1999). Polyamine-dependent facilitation of postsynaptic ampa receptors counteracts paired-pulse depression. *Nature*, 401(6753):594–598.

Ryckaert, J.-P., Ciccotti, G., and Berendsen, H. J. (1977). Numerical integration of the cartesian equations of motion of a system with constraints: molecular dynamics of n-alkanes. *Journal of Computational Physics*, 23(3):327–341.

Safferling, M., Tichelaar, W., Kümmerle, G., Jouppila, A., Kuusinen, A., Keinänen, K., and Madden, D. R. (2001). First images of a glutamate receptor ion channel: oligomeric state and molecular dimensions of glurb homomers. *Biochemistry*, 40(46):13948–13953.

Saglietti, L., Dequidt, C., Kamieniarz, K., Rousset, M.-C., Valnegri, P., Thoumine, O., Beretta, F., Fagni, L., Choquet, D., Sala, C., Sheng, M., and Passafaro, M. (2007). Extracellular interactions between glur2 and n-cadherin in spine regulation. *Neuron*, 54(3):461–477.

Salussolia, C. L., Corrales, A., Talukder, I., Kazi, R., Akgul, G., Bowen, M., and Wollmuth, L. P. (2011). Interaction of the m4 segment with other transmembrane segments is required for surface expression of mammalian α-amino-3-hydroxy-5-methyl-4-isoxazolepropionic acid (ampa) receptors. *J Biol Chem*, 286(46):40205–40218.

Salussolia, C. L., Gan, Q., Kazi, R., Singh, P., Allopenna, J., Furukawa, H., and Wollmuth, L. P. (2013). A eukaryotic specific transmembrane segment is required for tetramerization in ampa receptors. *The Journal of neuroscience : the official journal of the Society for Neuroscience*, 33:9840–9845.

Sander, J. D. and Joung, J. K. (2014). Crispr-cas systems for editing, regulating and targeting genomes. *Nature biotechnology*, 32:347–355.

Schmitt, J., Dux, E., Gissel, C., and Paschen, W. (1996). Regional analysis of developmental changes in the extent of glur6 mrna editing in rat brain. *Brain Res Dev Brain Res*, 91(1):153–157.

Schwenk, J., Baehrens, D., Haupt, A., Bildl, W., Boudkkazi, S., Roeper, J., Fakler, B., and Schulte, U. (2014). Regional diversity and developmental dynamics of the ampa-receptor proteome in the mammalian brain. *Neuron*, 84:41–54.

Schwenk, J., Harmel, N., Zolles, G., Bildl, W., Kulik, A., Heimrich, B., Chisaka, O., Jonas, P., Schulte, U., Fakler, B., and Klöcker, N. (2009). Functional proteomics identify cornichon proteins as auxiliary subunits of ampa receptors. *Science*, 323(5919):1313–1319.

Seeburg, P. H. (1993). The TINS/TiPS Lecture. The molecular biology of mammalian glutamate receptor channels. *Trends Neurosci*, 1993/09/01(9):359–365.

Shanks, N. F., Cais, O., Maruo, T., Savas, J. N., Zaika, E. I., Azumaya, C. M., Yates, 3rd, J. R., Greger, I., and Nakagawa, T. (2014). Molecular dissection of the interaction between the ampa receptor and cornichon homolog-3. *J Neurosci*, 34(36):12104–12120.

Shanks, N. F., Savas, J. N., Maruo, T., Cais, O., Hirao, A., Oe, S., Ghosh, A., Noda, Y., Greger, I. H., Yates, 3rd, J. R., and Nakagawa, T. (2012). Differences in ampa and kainate receptor interactomes facilitate identification of ampa receptor

auxiliary subunit gsg1l. *Cell Rep*, 1(6):590–598.

Sheng, N., Shi, Y. S., Lomash, R. M., Roche, K. W., and Nicoll, R. A. (2015). Neto auxiliary proteins control both the trafficking and biophysical properties of the kainate receptor gluk1. *Elife*, 4.

Shinozaki, H. and Shibuya, I. (1974). A new potent excitant, quisqualic acid: effects on crayfish neuromuscular junction. *Neuropharmacology*, 13:665–672.

Siegler Retchless, B., Gao, W., and Johnson, J. W. (2012). A single GluN2 subunit residue controls NMDA receptor channel properties via intersubunit interaction. *Nat Neurosci*, 15(3):406–13, S1–2.

Sladeczek, F., Pin, J., Rcasens, M., Bockaert, J., and S, W. (1985). Glutamate stimulates inositol phosphate formation in striatal neurones. *Nature*, 317(6039):717–9.

Smith, T. C., Wang, L. Y., and Howe, J. R. (2000a). Heterogeneous conductance levels of native AMPA receptors. *J.Neurosci.*, 20(6):2073–2085.

Smith, T. C., Wang, L. Y., and Howe, J. R. (2000b). Heterogeneous conductance levels of native ampa receptors. *The Journal of neuroscience : the official journal of the Society for Neuroscience*, 20:2073–2085.

Smolders, I., Bortolotto, Z. A., Clarke, V. R. J., Warre, R., Khan, G. M., O'Neill, M. J., Ornstein, P. L., Bleakman, D., Ogden, A., Weiss, B., Stables, J. P., Ho, K. H., Ebinger, G., Collingridge, G. L., Lodge, D., and Michotte, Y. (2002). Antagonists of glu(k5)-containing kainate receptors prevent pilocarpine-induced limbic seizures. *Nature neuroscience*, 5:796–804.

Snyder, R. D. and Robinson, A. (1969). Recessive sex-linked mental retardation in the absence of other recognizable abnormalities. report of a family. *Clinical pediatrics*, 8:669–674.

Sobolevsky, A. I., Rosconi, M. P., and Gouaux, E. (2009). X-ray structure, symmetry and mechanism of an AMPA-subtype glutamate receptor. *Nature*, 462(7274):745–756.

Somjen, G. G. (2001). Mechanisms of spreading depression and hypoxic spreading depression-like depolarization. *Physiological reviews*, 81:1065–1096.

Sommer, B., Kohler, M., Sprengel, R., and Seeburg, P. H. (1991). RNA editing in brain controls a determinant of ion flow in glutamate-gated channels. *Cell*, 67(1):11–19.

Soto, D., Coombs, I. D., Gratacos-Batlle, E., Farrant, M., and Cull-Candy, S. G. (2014). Molecular Mechanisms Contributing to TARP Regulation of Channel Conductance and Polyamine Block of Calcium-Permeable AMPA Receptors. *J Neurosci*, 34(35):11673–11683.

Soto, D., Coombs, I. D., Kelly, L., Farrant, M., and Cull-Candy, S. G. (2007). Stargazin attenuates intracellular polyamine block of calcium-permeable AMPA receptors. *Nat.Neurosci.*, 10(10):1260–1267.

Soto, D., Coombs, I. D., Renzi, M., Zonouzi, M., Farrant, M., and Cull-Candy, S. G. (2009). Selective regulation of long-form calcium-permeable ampa receptors by an atypical tarp, gamma-5. *Nat Neurosci*, 12(3):277–285.

Stansfeld, P. J., Goose, J. E., Caffrey, M., Carpenter, E. P., Parker, J. L., Newstead, S., and Sansom, M. S. P. (2015). Memprotmd: Automated insertion of membrane protein structures into explicit lipid membranes. *Structure*, 23(7):1350–1361.

Stansfeld, P. J. and Sansom, M. S. P. (2011). From coarse grained to atomistic: A serial multiscale approach to membrane protein simulations. *J Chem Theory Comput*, 7(4):1157–1166.

Stern-Bach, Y., Bettler, B., Hartley, M., Sheppard, P. O., O'Hara, P. J., and Heinemann, S. F. (1994). Agonist selectivity of glutamate receptors is specified by

two domains structurally related to bacterial amino acid-binding proteins. *Neuron*, 13(6):1345–1357.

Stern-Bach, Y., Russo, S., Neuman, M., and Rosenmund, C. (1998). A point mutation in the glutamate binding site blocks desensitization of AMPA receptors. *Neuron*, 21(4):907–918.

Stöhr, H., Berger, C., Froehlich, S., and Weber, B. H. F. (2002). A novel gene encoding a putative transmembrane protein with two extracellular cub domains and a low-density lipoprotein class a module: isolation of alternatively spliced isoforms in retina and brain. 286(2):223–231.

Straub, C. and Tomita, S. (2012). The regulation of glutamate receptor trafficking and function by TARPs and other transmembrane auxiliary subunits. *Curr.Opin.Neurobiol.*, 22(3):488–495.

Straub, C., Zhang, W., and Howe, J. R. (2011). Neto2 modulation of kainate receptors with different subunit compositions. *J Neurosci*, 31(22):8078–8082.

Sumioka, A. (2013). Auxiliary subunits provide new insights into regulation of ampa receptor trafficking. *J Biochem*, 153(4):331–337.

Sun, Y., Olson, R., Horning, M., Armstrong, N., Mayer, M., and Gouaux, E. (2002). Mechanism of glutamate receptor desensitization. *Nature*, 417:245–253.

Sutcliffe, M. J., Wo, Z. G., and Oswald, R. E. (1996). Three-dimensional models of non-nmda glutamate receptors. *Biophys J*, 70(4):1575–1589.

Suzuki, E. and Kamiya, H. (2016). Psd-95 regulates synaptic kainate receptors at mouse hippocampal mossy fiber-ca3 synapses. *Neuroscience research*, 107:14–19.

Swanson, G. T., Feldmeyer, D., Kaneda, M., and Cull-Candy, S. G. (1996). Effect of rna editing and subunit co-assembly single-channel properties of recombinant kainate receptors. *The Journal of physiology*, 492 (Pt 1):129–142.

Swanson, G. T., Gereau, R. W., Green, T., Heinemann, S. F., Gereau IV, R. W., Green, T., and Heinemann, S. F. (1997a). Identification of amino acid residues that control functional behavior in GluR5 and GluR6 kainate receptors. *Neuron*, 1997/11/14(4):913–926.

Swanson, G. T., Green, T., Sakai, R., Contractor, A., Che, W., Kamiya, H., and Heinemann, S. F. (2002). Differential activation of individual subunits in heteromeric kainate receptors. *Neuron*, 2002/06/14(4):589–598.

Swanson, G. T., Kamboj, S. K., and Cull-Candy, S. G. (1997b). Single-channel properties of recombinant ampa receptors depend on rna editing, splice variation, and subunit composition. *The Journal of neuroscience : the official journal of the Society for Neuroscience*, 17:58–69.

Tabor, C. W. and Tabor, H. (1984). Polyamines. *Annu Rev Biochem*, 53:749–790.

Tabor, C. W. and Tabor, H. (1985). Polyamines in microorganisms. *Microbiol Rev*, 49(1):81–99.

TABOR, H. and TABOR, C. W. (1964). Spermidine, spermine, and related amines. *Pharmacol Rev*, 16:245–300.

Takasu, M. A., Dalva, M. B., Zigmond, R. E., and Greenberg, M. E. (2002). Modulation of nmda receptor-dependent calcium influx and gene expression through ephb receptors. *Science*, 295(5554):491–495.

Tang, M., Ivakine, E., Mahadevan, V., Salter, M. W., and McInnes, R. R. (2012). Neto2 interacts with the scaffolding protein GRIP and regulates synaptic abundance of kainate receptors. *PLoS One*, 7(12):e51433.

Tang, M., Pelkey, K. a., Ng, D., Ivakine, E., McBain, C. J., Salter, M. W., and McInnes, R. R. (2011). Neto1 is an auxiliary subunit of native synaptic kainate receptors. *The Journal of neuroscience : the official journal of the Society for Neuroscience*, 31(27):10009–10018.

Tichelaar, W., Safferling, M., Keinänen, K., Stark, H., and Madden, D. R. (2004). The three-dimensional structure of an ionotropic glutamate receptor reveals a dimer-of-dimers assembly. *J Mol Biol*, 344(2):435–442.

Tieleman, D. P., Shrivastava, I. H., Ulmschneider, M. R., and Sansom, M. S. (2001). Proline-induced hinges in transmembrane helices: possible roles in ion channel gating. *Proteins*, 44(2):63–72.

Tomita, S., Adesnik, H., Sekiguchi, M., Zhang, W., Wada, K., Howe, J. R., Nicoll, R. A., and Bredt, D. S. (2005). Stargazin modulates ampa receptor gating and trafficking by distinct domains. *Nature*, 435(7045):1052–1058.

Tomita, S., Chen, L., Kawasaki, Y., Petralia, R. S., Wenthold, R. J., Nicoll, R. a., and Bredt, D. S. (2003). Functional studies and distribution define a family of transmembrane AMPA receptor regulatory proteins. *Journal of Cell Biology*, 161(4):805–816.

Traynelis, S. F. and Wahl, P. (1997). Control of rat glur6 glutamate receptor open probability by protein kinase a and calcineurin. *J Physiol*, 503 (Pt 3):513–531.

Traynelis, S. F., Wollmuth, L. P., McBain, C. J., Menniti, F. S., Vance, K. M., Ogden, K. K., Hansen, K. B., Yuan, H., Myers, S. J., Dingledine, R., and Sibley, D. (2010). Glutamate receptor ion channels: structure, regulation, and function. *Pharmacol Rev*, 2010/08/19:405–496.

Twomey, E. C., Yelshanskaya, M. V., Grassucci, R. A., Frank, J., and Sobolevsky, A. I. (2016). Elucidation of ampa receptor-stargazin complexes by cryo-electron microscopy. *Science*, 353(6294):83–86.

Ueda, T., Nakamura, Y., Smith, C. M., Copits, B. A., Inoue, A., Ojima, T., Matsunaga, S., Swanson, G. T., and Sakai, R. (2013). Isolation of novel prototype galectins from the marine ball sponge cinachyrella sp. guided by their modulatory activity on mammalian glutamate-gated ion channels. *Glycobiology*, 23(4):412–425.

Valluru, L., Xu, J., Zhu, Y., Yan, S., Contractor, A., and Swanson, G. T. (2005). Ligand binding is a critical requirement for plasma membrane expression of heteromeric kainate receptors. *J Biol Chem*, 280(7):6085–6093.

Vandenberghe, W., Nicoll, R. A., and Bredt, D. S. (2005). Stargazin is an ampa receptor auxiliary subunit. *Proc Natl Acad Sci U S A*, 102(2):485–490.

Vanommeslaeghe, K., Hatcher, E., Acharya, C., Kundu, S., Zhong, S., Shim, J., Darian, E., Guvench, O., Lopes, P., Vorobyov, I., et al. (2010). Charmm general force field: A force field for drug-like molecules compatible with the charmm all-atom additive biological force fields. *Journal of computational chemistry*, 31(4):671–690.

Vanommeslaeghe, K. and MacKerell Jr, A. D. (2012). Automation of the charmm general force field (cgenff) i: bond perception and atom typing. *Journal of chemical information and modeling*, 52(12):3144–3154.

Vanommeslaeghe, K., Raman, E. P., and MacKerell Jr, A. D. (2012). Automation of the charmm general force field (cgenff) ii: assignment of bonded parameters and partial atomic charges. *Journal of chemical information and modeling*, 52(12):3155–3168.

Vignes, M. and Collingridge, G. L. (1997). The synaptic activation of kainate receptors. *Nature*, 1997/07/10(6638):179–182.

Vivithanaporn, P., Yan, S., and Swanson, G. T. (2006). Intracellular trafficking of ka2 kainate receptors mediated by interactions with coatomer protein complex i (copi) and 14-3-3 chaperone systems. *The Journal of biological chemistry*, 281:15475–15484.

Vodyanoy, V., Bahr, B. A., Suppiramaniam, V., Hall, R. A., Baudry, M., and Lynch, G. (1993). Single channel recordings of reconstituted ampa receptors reveal low and high conductance states. *Neuroscience letters*, 150:80–84.

von Engelhardt, J., Mack, V., Sprengel, R., Kavenstock, N., Li, K. W., Stern-Bach, Y., Smit, A. B., Seeburg, P. H., and Monyer, H. (2010). Ckamp44: a brain-specific protein attenuating short-term synaptic plasticity in the dentate gyrus. *Science*, 327(5972):1518–1522.

Walker, C. S., Francis, M. M., Brockie, P. J., Madsen, D. M., Zheng, Y., and Maricq, A. V. (2006). Conserved sol-1 proteins regulate ionotropic glutamate receptor desensitization. *Proc Natl Acad Sci U S A*, 103(28):10787–10792.

Wang, R., Mellem, J. E., Jensen, M., Brockie, P. J., Walker, C. S., Hoerndli, F. J., Hauth, L., Madsen, D. M., and Maricq, A. V. (2012). The sol-2/neto auxiliary protein modulates the function of ampa-subtype ionotropic glutamate receptors. *Neuron*, 75(5):838–850.

Washburn, M. S., Numberger, M., Zhang, S., and Dingledine, R. (1997). Differential dependence on glur2 expression of three characteristic features of ampa receptors. *The Journal of neuroscience : the official journal of the Society for Neuroscience*, 17:9393–9406.

Watkins, J. C. (1972). Metabolic regulation in the release and action of excitatory and inhibitory amino acids. *The Biochemical journal*, 128:71P–73P.

Watkins, J. C. and Jane, D. E. (2006). The glutamate story. *British journal of pharmacology*, 147 Suppl 1:S100–S108.

Wenthold, R. J., Petralia, R. S., Blahos II, J., and Niedzielski, A. S. (1996). Evidence for multiple AMPA receptor complexes in hippocampal CA1/CA2 neurons. *J.Neurosci.*, 16(6):1982–1989.

Wenthold, R. J., Yokotani, N., Doi, K., and Wada, K. (1992). Immunochemical characterization of the non-nmda glutamate receptor using subunit-specific antibodies. evidence for a hetero-oligomeric structure in rat brain. *J Biol Chem*, 267(1):501–507.

Werner, P., Voigt, M., Keinanen, K., Wisden, W., and Seeburg, P. H. (1991). Cloning of a putative high-affinity kainate receptor expressed predominantly in hippocampal CA3 cells. *Nature*, 351(6329):742–744.

Weston, M. C., Gertler, C., Mayer, M. L., and Rosenmund, C. (2006a). Interdomain interactions in ampa and kainate receptors regulate affinity for glutamate. *The Journal of neuroscience : the official journal of the Society for Neuroscience*, 26:7650–7658.

Weston, M. C., Schuck, P., Ghosal, A., Rosenmund, C., and Mayer, M. L. (2006b). Conformational restriction blocks glutamate receptor desensitization. *Nature structural & molecular biology*, 13(12):1120–1127.

Wilding, T. J., Chen, K., and Huettner, J. E. (2010). Fatty acid modulation and polyamine block of GluK2 kainate receptors analyzed by scanning mutagenesis. *J.Gen.Physiol*, 136(3):339–352.

Wilding, T. J., Fulling, E., Zhou, Y., and Huettner, J. E. (2008). Amino acid substitutions in the pore helix of glur6 control inhibition by membrane fatty acids. *J Gen Physiol*, 132(1):85–99.

Wilding, T. J. and Huettner, J. E. (1995). Differential antagonism of alpha-amino-3-hydroxy-5-methyl-4- isoxazolepropionic acid-preferring and kainate-preferring receptors by 2,3-benzodiazepines. *Molecular pharmacology*, 47:582–587.

Wilkinson, K. A., Nishimune, A., and Henley, J. M. (2008). Analysis of sumo-1 modification of neuronal proteins containing consensus sumoylation motifs. *Neurosci Lett*, 436(2):239–244.

Wisden, W. and Seeburg, P. H. (1993). A complex mosaic of high-affinity kainate receptors in rat brain. *J Neurosci*, 1993/08/01(8):3582–3598.

Wo, Z. G. and Oswald, R. E. (1995). Unraveling the modular design of glutamate-gated ion channels. *Trends Neurosci*, 18(4):161–168.

Wong, A. Y. C., Fay, A.-M. L. M., and Bowie, D. (2006). External ions are coactivators of kainate receptors. *The Journal of neuroscience : the official journal of the Society for Neuroscience*, 26(21):5750–5755.

Wong, A. Y. C., MacLean, D. M., and Bowie, D. (2007). Na+/Cl- dipole couples agonist binding to kainate receptor activation. *J Neurosci*, 2007/06/22(25):6800–6809.

Woodhull, A. M. (1973). Ionic blockage of sodium channels in nerve. *The Journal of general physiology*, 61:687–708.

Woolfson, D. N. and Williams, D. H. (1990). The influence of proline residues on alpha-helical structure. *FEBS Lett*, 277(1-2):185–188.

Wu, T. Y. and Chang, Y. C. (1994). Hydrodynamic and pharmacological characterization of putative alpha-amino-3-hydroxy-5-methyl-4-isoxazolepropionic acid/kainate-sensitive l-glutamate receptors solubilized from pig brain. *Biochem J*, 300 (Pt 2):365–371.

Yamada, K. A. and Tang, C. M. (1993). Benzothiadiazides inhibit rapid glutamate receptor desensitization and enhance glutamatergic synaptic currents. *The Journal of neuroscience : the official journal of the Society for Neuroscience*, 13:3904–3915.

Yan, D., Yamasaki, M., Straub, C., Watanabe, M., and Tomita, S. (2013). Homeostatic control of synaptic transmission by distinct glutamate receptors. *Neuron*, 78:687–699.

Yu, W., He, X., Vanommeslaeghe, K., and MacKerell, A. D. (2012). Extension of the charmm general force field to sulfonyl-containing compounds and its utility in biomolecular simulations. *Journal of computational chemistry*, 33(31):2451–2468.

Yuan, H., Hansen, K. B., Vance, K. M., Ogden, K. K., and Traynelis, S. F. (2009). Control of nmda receptor function by the nr2 subunit amino-terminal domain. *J Neurosci*, 29(39):12045–12058.

Yue, K. T., MacDonald, J. F., Pekhletski, R., and Hampson, D. R. (1995). Differential effects of lectins on recombinant glutamate receptors. *Eur J Pharmacol*, 291(3):229–235.

Zhang, W., Cho, Y., Lolis, E., and Howe, J. R. (2008). Structural and single-channel results indicate that the rates of ligand binding domain closing and opening directly impact ampa receptor gating. *The Journal of neuroscience : the official journal of the Society for Neuroscience*, 28:932–943.

Zhang, W., St-Gelais, F., Grabner, C. P., Trinidad, J. C., Sumioka, A., Morimoto-Tomita, M., Kim, K. S., Straub, C., Burlingame, A. L., Howe, J. R., and Tomita, S. (2009). A transmembrane accessory subunit that modulates kainate-type glutamate receptors. *Neuron*, 2009/02/17(3):385–396.

Zhao, Y., Chen, S., Yoshioka, C., Baconguis, I., and Gouaux, E. (2016). Architecture of fully occupied glua2 ampa receptor-tarp complex elucidated by cryo-em. *Nature*.

Zheng, Y., Brockie, P. J., Mellem, J. E., Madsen, D. M., Walker, C. S., Francis, M. M., and Maricq, A. V. (2006). Sol-1 is an auxiliary subunit that modulates the gating of glr-1 glutamate receptors in caenorhabditis elegans. *Proc Natl Acad Sci U S A*, 103(4):1100–1105.

APPENDIX A
Reprint of thesis article

JPn Neuroscience
The Journal of Physiology

J Physiol 594.7 (2016) pp 1821–1840

Kainate receptor pore-forming and auxiliary subunits regulate channel block by a novel mechanism

Patricia M. G. E. Brown[1,3], Mark R. P. Aurousseau[2,3], Maria Musgaard[4], Philip C. Biggin[4] and Derek Bowie[3]

[1]*Integrated Program in Neurosciences, McGill University, Montréal, Québec, Canada H3G 0B1*
[2]*Graduate Program in Pharmacology, McGill University, Montréal, Québec, Canada H3G 0B1*
[3]*Department of Pharmacology and Therapeutics, McGill University, Montréal, Québec, Canada H3G 0B1*
[4]*Department of Biochemistry, University of Oxford, Oxford OX1 3QU, UK*

Key points

- Kainate receptor heteromerization and auxiliary subunits, Neto1 and Neto2, attenuate polyamine ion-channel block by facilitating blocker permeation.
- Relief of polyamine block in GluK2/GluK5 heteromers results from a key proline residue that produces architectural changes in the channel pore α-helical region.
- Auxiliary subunits exert an additive effect to heteromerization, and thus relief of polyamine block is due to a different mechanism.
- Our findings have broad implications for work on polyamine block of other cation-selective ion channels.

Abstract Channel block and permeation by cytoplasmic polyamines is a common feature of many cation-selective ion channels. Although the channel block mechanism has been studied extensively, polyamine permeation has been considered less significant as it occurs at extreme positive membrane potentials. Here, we show that kainate receptor (KAR) heteromerization and association with auxiliary proteins, Neto1 and Neto2, attenuate polyamine block by enhancing blocker permeation. Consequently, polyamine permeation and unblock occur at more negative and physiologically relevant membrane potentials. In GluK2/GluK5 heteromers, enhanced permeation is due to a single proline residue in GluK5 that alters the dynamics of the α-helical region of the selectivity filter. The effect of auxiliary proteins is additive, and therefore the structural basis of polyamine permeation and unblock is through a different mechanism. As native receptors are thought to assemble as heteromers in complex with auxiliary proteins, our data identify an unappreciated impact of polyamine permeation in shaping the signalling properties of neuronal KARs and point to a structural mechanism that may be shared amongst other cation-selective ion channels.

(Received 4 October 2015; accepted after revision 7 December 2015; first published online 18 December 2015)
Corresponding authors D. Bowie: Department of Pharmacology & Therapeutics, Bellini Building, Room 164, McGill University, 3649 Promenade Sir William Osler, Montréal, Québec, Canada H3G 0B1.
Email: derek.bowie@mcgill.ca; P. C. Biggin: Department of Biochemistry, University of Oxford, Oxford OX1 3QU, UK.
Email: philip.biggin@bioch.ox.ac.uk

Abbreviations iGluR, ionotropic glutamate receptor; KAR, kainate receptor; L-Glu, L-glutamate; MD, molecular dynamics; POPC, 1-palmitoyl-2-oleoyl-*sn*-glycero-3-phosphocholine; Put, putrescine; RMSD, root mean square deviation; SMD, steered molecular dynamics; Spm, spermine; Spd, spermidine.

M.M. and M.R.P.A. contributed equally and are arranged alphabetically.

DOI: 10.1113/JP271690

Introduction

Polyamines are expressed ubiquitously in bacterial, plant and animal cells where they fulfil a variety of roles essential for life (Tabor & Tabor, 1964, 1985). Mammals possess two polyamines, the tetra- and tri-amines, spermine (Spm) and spermidine (Spd), respectively, that are derived from the diamine precursor, putrescine (Put), through tightly regulated biosynthetic pathways. Disruption in the synthesis or catabolism of polyamines leads to a variety of disease states from cancer to neurodevelopmental disorders (Nowotarski *et al.* 2013; Pegg, 2014), underlining their physiological importance. Given their cationic nature, polyamines interact with negatively charged domains of biomolecules (Tabor & Tabor, 1984) including the electrostatic pore regions of voltage- and ligand-gated ion channels where they bind and consequently block ion flow with micromolar affinity (Lopatin *et al.* 1994; Bowie & Mayer, 1995; Gomez & Hellstrand, 1995; Haghighi & Cooper, 1998; Lu & Ding, 1999; Kerschbaum *et al.* 2003; Fu *et al.* 2012). In this capacity, cytoplasmic polyamines are recognized as important determinants of neuronal signalling by regulating action potential firing rates (Fleidervish *et al.* 2008) as well as the strength of neurotransmission (Rozov & Burnashev, 1999; Aizenman *et al.* 2002).

Polyamines are often referred to as permeant channel blockers due to their ability to both block and traverse the ion-permeation pathway of cation-selective ion channels (Bowie *et al.* 1999). For almost all ion channels, cytoplasmic polyamine block is observed at negative and physiologically relevant membrane potentials, making it an ideal regulator of cellular excitability (Nichols & Lopatin, 1997; Bowie *et al.* 1999; Lu, 2004; Baronas & Kurata, 2014). In contrast, polyamine permeation occurs at extreme ($>+50$ mV) positive membrane potentials (Bahring *et al.* 1997) and therefore has not been considered particularly significant. Given this arrangement, however, the fraction of channels blocked by polyamines at any given membrane potential is the sum of these two opposing mechanisms. Consequently, the overall level of polyamine block could, in principle, be shaped by any mechanism that enhances the relative contribution of polyamine permeation.

At glutamatergic synapses of the developing and mature CNS, polyamines have been well characterized to act as permeant channel blockers of both AMPA- and kainate-type (KARs) ionotropic glutamate receptors (iGluRs) (Bowie & Mayer, 1995; Kamboj *et al.* 1995; Koh *et al.* 1995). In each case, the degree of polyamine block is voltage-dependent and dynamically regulated, with two of the most prevalent mechanisms occurring through either changes in receptor subunit composition or by receptor association with auxiliary proteins (Cull-Candy *et al.* 2006; Perrais *et al.* 2010; Jackson & Nicoll, 2011). At KARs, polyamine block is attenuated by either the formation of heteromers that contain the GluK4 or GluK5 subunit (Barberis *et al.* 2008) or by co-assembly with auxiliary proteins, Neto1 and Neto2 (Fisher & Mott, 2012). Interestingly, removal of the positively charged Arg–Lys–Lys motif of the Neto1 or Neto2 C-tail restores polyamine block, suggesting that relief of block may involve a charge screening mechanism that affects the pore (Fisher & Mott, 2012). Whether a similar electrostatic mechanism explains the attenuation of block at GluK2/GluK5 heteromers remains to be established.

Here, we have tested the hypothesis that KAR heteromers and auxiliary proteins attenuate channel block by a common mechanism. We show that in both cases relief of polyamine block results from an enhanced rate of polyamine permeation. Relief of block in heteromers is due to a proline residue from GluK5 that is predicted to alter the pore architecture, thereby facilitating polyamine permeation. The effect of auxiliary proteins is additive to that of the pore-forming subunits and we therefore conclude that they enhance polyamine permeation through a different mechanism. As native receptors primarily assemble as heteromers in complex with auxiliary proteins, our data identify an unappreciated impact of polyamine permeation in shaping the signalling properties of KARs in neuronal circuits.

Methods

Plasmids and molecular biology

All experiments were performed using cDNA of rat GluK2 and GluK5 kainate-type iGluRs, mouse Neto1-HA and rat Neto2. For electrophysiology, GluK2a(V,C,Q) and GluK5 cDNA each contained a downstream internal ribosome entry site (IRES) sequence encoding mCherry and eGFP, respectively, which were used to identify transfected cells. cDNA of GluK2(G615P) and GluK5(P599G) were made using site-directed mutagenesis with all constructs verified by restriction digest analysis and sequencing.

Cell culture and transfection

HEK293T/17 cells (ATCC, Manassas, VA, USA) were maintained in minimal essential medium (MEM) containing glutaMAX© supplemented with 10% fetal bovine serum (Invitrogen, Carlsbad, CA, USA). Cells were plated at low density ($1.6–2.0\times10^4$ cells ml^{-1}) on poly-D-lysine-coated 35 mm plastic dishes and were transiently transfected 24 h later using the calcium phosphate technique. A GluK2:GluK5 or GluK2:Neto1/2 cDNA molar ratio of 1:10 was used for all co-transfections.

Electrophysiological recordings

Experiments were performed 36–48 h after transfection. Agonist solutions were rapidly applied to

outside-out patches excised from transfected cells using a piezoelectric stack (Physik Instrumente, Auburn, MA, USA). Solution exchange (10–90% rise time of 250–350 μs) was determined in a separate experiment by measuring the liquid junction current. All recordings were performed using an Axopatch 200B (Molecular Devices, Sunnyvale, CA, USA) using thick-walled borosilicate glass pipettes (3–6 MΩ) coated with dental wax to reduce electrical noise. Current records were filtered at 5 kHz, digitized at 25 kHz and series resistance (3–12 MΩ) was compensated for by 95%. Recordings were performed at a range of holding potentials from −100 to +100 mV to study polyamine channel block. Data acquisition was performed using pClamp9 or pClamp10 software (Molecular Devices) and tabulated using Excel. All experiments were performed at room temperature.

All chemicals were purchased from Sigma-Aldrich (St Louis, MO, USA) unless otherwise indicated. External solutions contained (in mM) 150 NaCl, 5 HEPES, 0.1 $MgCl_2$ and 0.1 $CaCl_2$, pH 7.3–7.4. The internal solution contained (in mM) 115 NaCl, 10 NaF, 5 HEPES, 5 Na_4BAPTA (Life Technologies, Invitrogen, Burlington, ON, Canada), 1 $MgCl_2$, 0.5 $CaCl_2$ and 10 Na_2ATP, pH 7.3–7.4. The osmotic pressure of all solutions was adjusted to 295–300 mOsm with sucrose. In experiments where polyamine block was examined, Na_2ATP in the internal solution was replaced with 60 μM Spm and the osmotic pressure adjusted to 295–300 mOsm with sucrose. For Ca^{2+} permeability experiments, the external solution contained (in mM) 105 NaCl, 30 $CaCl_2$, 5 HEPES and 0.1 $MgCl_2$, pH 7.3–7.4 (295 mOsm). For polyamine permeability experiments, the NaCl in the external solution was replaced by 90 mM Spm, pH was adjusted to 7.3–7.4 using the Spm free base and the osmotic pressure was adjusted with sucrose. Concentrated (10× or 100×) agonist stock solutions were prepared by dissolving agonist [L-glutamate or AMPA (Tocris, Ellisville, MO, USA)] in the appropriate external solution, adjusting the pH to 7.3–7.4, and stored frozen at −20°C. Stocks were thawed on the day of the experiment and used to prepare agonist-containing external solutions. For heteromeric GluK2/GluK5 receptors, only patches where the contribution of the slowest exponential component (%A3) was above 25% were considered for analysis, unless otherwise stated.

Data analysis and fitting

Agonist-evoked membrane conductance (G) was calculated using eqn (1):

$$G = \frac{I}{(V - V_{rev})} \quad (1)$$

where I is the current at V holding potential and V_{rev} is the reversal potential.

Conductance–voltage (G–V) relationships were fit using Origin 7 (OriginLab, Northampton, MA, USA) with the following equation (from Bowie *et al.* 1998):

$$G = \frac{G_{max}}{1 + \frac{[Spm]}{K_d}} \quad (2)$$

where G_{max} is the maximal conductance, $[Spm]$ is the internal Spm concentration and K_d is the dissociation constant.

Binding (k_{on}), unbinding (k_{off}) and permeation (k_{perm}) rates were defined as previously (Bowie *et al.* 1998):

$$k_{on} = a \exp\left(V/b\right) \quad (3)$$

$$k_{off} = c \exp\left(V/d\right) \quad (4)$$

$$k_{perm} = e \exp\left(V/f\right) \quad (5)$$

To estimate k_{off} and k_{perm}, K_d was first calculated as:

$$K_d = \frac{sum\ of\ exit\ rates}{Binding\ rate}$$

which was redefined to eqn (6):

$$K_d = g \exp\left(V/h\right) + L \exp\left(V/k\right) \quad (6)$$

where

$$g = \frac{c}{a}$$

$$L = \frac{e}{a}$$

$$h = \frac{bd}{b - d}$$

$$k = \frac{bf}{b - f}$$

Binding rates were assumed to be constant for GluK2/GluK5, GluK2+Neto1 and GluK2+Neto2 (see Results for more details), and the values for a and b were taken from Bowie *et al.* (1998).

The voltage-dependent conductance of KARs under basal conditions is appreciably different between receptor types within the range ±100 mV. This emphasizes the impact of auxiliary proteins in changing the basic gating properties of KARs and the importance of accounting for these significant differences in gating properties. The intrinsic G/V relationships were fit with eqn (7) using Origin 7:

$$y = \left(1 + (G_0 - 1) \exp\left(\frac{x}{V}\right)\right) \quad (7)$$

where G_0 is the minimal conductance and V is the membrane potential. Values are summarized in Table 1.

The Ca^{2+} permeability relative to Na^+ (P_{Ca}/P_{Na}) was determined using the constant field equation from Kamboj *et al.* (1995):

$$\frac{P_{Ca}}{P_{Na}} = \frac{\left[Na^+\right]_i}{\left[Ca^{2+}\right]_o} \times \frac{\left[\exp\left(\frac{\Delta V_{rev} F}{RT}\right) \times \left(\exp\left(\frac{\Delta V_{rev} F}{RT}\right) + 1\right)\right]}{4} \quad (8)$$

where P_{Ca} and P_{Na} are the permeability coefficients for Ca^{2+} and Na^+, respectively, ΔV_{rev} is the reversal potential shift, F is Faraday's constant, R is the gas constant and T is the temperature in Kelvin.

Relative Spm permeability (P_{Spm}/P_{Na}) was calculated from the reversal potential (V_{rev}) measurements in Spm-rich external solutions using the following equation from Bahring *et al.* (1997):

$$I_x = P_x z^2 \left(\frac{V_m F^2}{RT}\right) \left(\frac{[X]_i - [X]_o \exp\left(\frac{-zF V_m}{RT}\right)}{1 - \exp\left(\frac{-zF V_m}{RT}\right)}\right) \quad (9)$$

where I_x is the current carried by ion X at a membrane potential V_m, P_x is the corresponding permeability ($P_{Na} = 1$), $[X]_i$ and $[X]_o$ are the internal and external Spm concentrations, z is the valence, and F, R and T are as above. Experimentally determined reversal potentials were used for V_m. We obtained P_{Spm}/P_{Na} using the definition that $I_{Na} + I_{Spm} = 0$ at the reversal potential. The reversal potentials were corrected for liquid junction potentials that were determined experimentally.

All data were illustrated using Origin 7 and Adobe Illustrator.

Table 1. Fit parameters for intrinsic *G–V* relationships

	G_0	V
GluK2	1.0699	41.4
GluK2/GluK5	1.1168	55.7
GluK2+Neto1	1.0003	16.3
GluK2+Neto2	1.0094	25.5
GluK2/GluK5(P599G)	1.0240	38.4
GluK2(G615P)	1.0163	31.7
GluK2 – 300 μM	1.0736	37.6
GluK2/GluK5 – 300 μM	1.1282	60.0

Table 2. Spermine affinities of kainate receptors

Receptor		Mean	SEM	*n*
GluK2	K_d (0 mV) (μM)	5.8	0.3	5
	h (mV)	−16.0	0.5	
	k (mV)	20.4	1.0	
GluK2/GluK5	K_d (0 mV) (μM)	119	30	5
	h (mV)	−25.9	3.8	
	k (mV)	69.7	36.0	
GluK2+Neto1	K_d (0 mV) (μM)	71	13	6
	h (mV)	−24.0	1.8	
	k (mV)	43.3	4.3	
GluK2+Neto2	K_d (0 mV) (μM)	39	2	7
	h (mV)	−18.5	1.1	
	k (mV)	48.6	5.3	
GluK2/GluK5(P599G)	K_d (0 mV) (μM)	19	2	4
	h (mV)	−32.3	3.8	
	k (mV)	41.4	4.7	
GluK2 (300 μM L-Glu)	K_d (0 mV) (μM)	21	6	3
	h (mV)	−24.2	1.9	
	k (mV)	56.2	14.1	
GluK2/GluK5 (300 μM L-Glu)	K_d (0 mV) (μM)	170	33	3
	h (mV)	−51.4	20.0	
	k (mV)	107.7	47.2	
GluK2/GluK5 (1 mM AMPA)	K_d (0 mV) (μM)	81	40	3
	h (mV)	−73.4	27.7	
	k (mV)	56.8	22.9	

Affinities were obtained using responses evoked by 1 ms applications of 1 mM L-Glu in 150 mM NaCl external solution. Values for '*h*' and '*k*' indicate the voltage dependency.

Statistics

Statistical analysis was performed using the statistical software SPSS Statistics. Data were assumed to be distributed normally. The numbers provided for '*n*' refer to the number of individual patches.

Molecular dynamics simulations

Molecular dynamics (MD) simulations were performed to study whether inserting proline residues into the α-helical region of the P-loop had an effect on the pore architecture. No atomic-resolution open-channel structure of an iGluR has been determined, so an open-channel structure of the non-selective NaK cation channel from *Bacillus cereus* determined to a resolution of 1.6 Å was used as a model system (PDB #3E86) (Alam & Jiang, 2009*a*). Figure 7 below shows a structural alignment of the GluA2 (PDB #3KG2) and the NaK (PDB #3E86) channel pores. Given that they have very similar topologies, the NaK pore structure was used as this structure has the selectivity filter resolved at atomic resolution and is described as being in the open state as opposed to the GluA2 structure which is considered closed and where the selectivity filter region is unresolved.

To generate a membrane slab for further simulation, the tetrameric physiological unit of the NaK channel (residues 23–113, ignoring ions and other small molecules) was converted to Coarse Grain (CG) representation (Martini v2.1) (Monticelli *et al.* 2008) to allow for self-assembly and equilibration of a bilayer consisting of 200 1-palmitoyl-2-oleoyl-*sn*-glycero-3-phosphocholine (POPC) molecules around the protein structure. This

system was simulated for 100 ns at 323 K in Gromacs v4.6.3 (Hess *et al.* 2008) to allow formation of a POPC bilayer (Stansfeld *et al.* 2015).

Following this, the system was converted back to atomistic representation using a CG2AT-align method (Stansfeld & Sansom, 2011) and this membrane slab was then used for further system setup with the different protein mutants aligned to the position of the protein. The (4*S*)-2-methyl-2,4-pentanediol molecule, observed in the crystal structure, was deleted. The crystal structure has four ions bound in the filter region: one calcium ion in the external site, one sodium ion in the vestibule site, one caesium ion in site 3 and another sodium ion in site 4. To keep the ion composition simple, the calcium ion and the caesium ion were changed to potassium and sodium, respectively. Both monovalent and divalent cations can bind at the external site, but sodium does not appear to be a good binder at this site (Alam & Jiang, 2009*b*), and thus the calcium ion was exchanged for potassium. The vestibular site and sites 3 and 4 all appear to prefer sodium, so the caesium ion in site 3 was exchanged for sodium. Crystallographic water molecules were retained. The protein along with ions and protein-bound water molecules was inserted into the pre-generated POPC membrane slab, and water molecules for solvation were further added using the Solvate Plugin of VMD (Humphrey *et al.* 1996). Ions were added with the Autoionize Plugin in VMD to create a neutral system with an approximate ion concentration of 150 mM. The anion was chloride and because the NaK channel transports both sodium and potassium, approximately half of the cations were sodium and the other half potassium.

The system was then energy minimized for 5000 steps and equilibrated for 10 ns with protein heavy atoms along with ions bound to the filter harmonically restrained with a force constant of 7 kcal mol^{-1} $Å^{-2}$. Lipid molecules which, after 10 ns, were still stuck in odd positions between protein helices, resulting from the self-assembly process, were deleted and the system was energy minimized for 5000 steps and 500 ns of unbiased MD simulation was performed. This structure (with the oddly positioned lipid molecules removed) was further used for construction of the mutant systems using the Mutator Plugin of VMD. These systems were likewise energy minimized for 5000 steps followed by 500 ns of unbiased MD simulation. In addition to the NaK crystal structure (WT, mimicking the GluK2 homotetramer), we simulated the NaK structure with S57P in two opposing chains (A and C in 2Pro, mimicking the GluK2/GluK2 heteromer if assuming a 2:2 assembly with GluK2–GluK5–GluK2–GluK5 packing at the membrane level) and the NaK structure with the S57P mutation imposed in all four chains [4Pro, mimicking the GluK2(G615P) homotetramer]. Each 500 ns simulation was repeated, so the final data set consisted of 2×500 ns for each of the protein constructs.

All atomistic simulations were performed with NAMD v2.9 (Phillips *et al.* 2005) using the CHARMM 36 force field (Klauda *et al.* 2010; Best *et al.* 2012) for protein and lipids and the TIP3P water model (Jorgensen *et al.* 1983). Simulations were performed in the NPT ensemble at a temperature of 310 K and a pressure of 1 atm. Langevin dynamics with a damping coefficient of 0.5 ps^{-1} was employed to control the temperature. The pressure was maintained using the Langevin piston Nosé–Hoover method with a piston period of 100 fs and a damping timescale of 50 fs. Lennard–Jones interactions were treated with a cutoff of 12 Å and the switching function applied from 10 Å, while full electrostatics were accounted for using Particle-Mesh Ewald (PME) (Darden *et al.* 1993) summation with a real-space cutoff of 12 Å and a 1 Å grid spacing. The pairlist, with a cutoff of 14 Å, was updated every 20 fs. Periodic boundary conditions were applied in all simulations. The time step was 2 fs with full electrostatics calculated every second step. Water molecules were kept rigid by the SETTLE (Miyamoto & Kollman, 1992) algorithm and other bonds to hydrogen atoms by the SHAKE (Ryckaert *et al.* 1977) algorithm. Snapshots were collected every 5 ps.

Polyamine ligands

The structures for Spm, Spd and Put were downloaded from the HIC-Up database (Kleywegt & Jones, 1998) ('ideal coordinates', http://xray.bmc.uu.se/hicup/XXX/ where XXX = SPM, SPD, PUT), and hydrogen atoms were added in Maestro (Maestro, version 9.7, Schrödinger, LLC, New York, 2014). All amine nitrogen atoms were treated as charged. Ligand topologies and parameters for the CHARMM General Force Field (CGenFF) (Vanommeslaeghe *et al.* 2010; Yu *et al.* 2012) v3.0.1 were generated using the CGenFF program v1.0.0 (Vanommeslaeghe & MacKerell, 2012; Vanommeslaeghe *et al.* 2012) (https://cgenff.paramchem.org).

NaK–polyamine complexes

The most symmetrical and the most asymmetrical snapshot in terms of cross-pore distance (see Fig. 6*D* below) was taken from each of the simulations of WT, 2Pro and 4Pro, leaving out the first 100 ns of simulation. Spm was inserted into the filter region by aligning the charged nitrogen atoms of Spm with the original position of the four cations in the filter. These four ions were then deleted to remove overlap and ensure charge neutrality, and furthermore water molecules in the filter overlapping with Spm were deleted. Spd and Put were inserted to the filter region of WT snapshots in a similar way, although due to the smaller number of nitrogen atoms in these ligands, central carbon atoms were used along with the nitrogen atoms in the alignment to original ion positions. For Spd,

three of the original cations in the filter were deleted, and for Put, only two. No other ions were binding to the filter region in any of the complexes. The simulation systems were then energy minimized for 2000 steps followed by 30 ns of unbiased MD simulation.

All polyamines remained bound to the filter region throughout the 30 ns of relaxation. To probe the energetics involved in the unbinding of the polyamines from the filter, 15 ns of steered MD (SMD) simulations were performed on all NaK–polyamine complexes, starting after 30 ns of unbiased simulation. The SMD atoms, here the terminal nitrogen atom facing the pulling direction, were harmonically constrained with force constant of 7.2 kcal mol^{-1} Å^{-2}, corresponding to 500 pN Å^{-1}, to move with velocity 2.5 Å ns^{-1} in the negative direction along the *z*-axis (towards the extracellular side for the NaK channel, corresponding to the intracellular side for the KAR channel). Forces were saved every 200 fs. To avoid the whole system being pulled along *z*, the C_α atoms of residues 23–28 were restrained harmonically with a force constant of 7.2 kcal mol^{-1} Å^{-2}.

The work was calculated from the force profiles by numerical integration according to:

$$W(t) = v\int_0^t f\ (t)\,\mathrm{d}t \qquad (10)$$

where v is the constant velocity (2.5 Å ns^{-1}), $f(t)$ is the force at the specific time step given in the SMD output and dt is the time step between the data points (200 fs).

Results

Heteromerization and auxiliary proteins attenuate inward rectification of KARs

To better understand how heteromerization and auxiliary proteins attenuate channel block, we studied KAR responses in outside-out membrane patches at a range of membrane potentials to observe when polyamines enter the pore to block it. To mimic the time course of neurotransmitter release in the synaptic cleft, 1 mM L-glutamate (L-Glu) was applied to excised patches for 1 ms and 60 μM Spm was included in the internal solution to match known cytoplasmic levels of the blocker (Bowie & Mayer, 1995). Figure 1 summarizes these experiments, where the degree of inward rectification induced by polyamine block of GluK2 homomers was compared to that of GluK2/GluK5 heteromers or GluK2 homomers co-assembled with the auxiliary proteins, Neto1 and Neto2.

In agreement with other studies, peak GluK2 receptor responses exhibited a bi-rectifying behaviour (range: −100 to + 100 mV) due to the onset and relief of block at hyperpolarizing and depolarizing membrane potentials, respectively (Fig. 1*A* and *B*) (Bowie & Mayer, 1995; Bowie *et al.* 1998). In contrast, *I–V* plots of GluK2/GluK5 heteromers (Fig. 1*C* and *D*) or GluK2 with Neto1 or Neto2 (Fig. 1*E–G*) (Barberis *et al.* 2008; Fisher & Mott, 2012) tended towards linearity. Rectification ratios were smallest for GluK2 homomers (0.20 ± 0.02, n = 5), highlighting that Spm channel block strongly opposes ion flow at positive membrane potentials (Fig. 1*A*, *B* and *H*). This effect was much weaker with GluK2/GluK5 heteromers (rectification ratio = 0.89 ± 0.07, n = 4) and following co-assembly with auxiliary proteins (Neto1, 0.66 ± 0.02, n = 12; Neto2, 0.64 ± 0.03, n = 7) (Fig. 1*H*), reaffirming that, in each case, polyamine block is significantly attenuated. Despite the similarity of the effects, it still remains to be established if heteromerization and auxiliary proteins attenuate block by a similar or different mechanism.

To better understand the voltage-dependency of the onset and relief of block, we converted the *I–V* data from each dataset into *G–V* plots (Fig. 2). KARs exhibit significant outward rectification at positive membrane potentials in the absence of channel blockers (Bowie *et al.* 1998). To take this into account, we performed additional experiments to obtain control *I–V* data for all receptor combinations and then subtracted this non-linearity from data obtained in the presence of Spm (Figs 2 and 3). Corrected *G–V* plots were then fit with a single binding site model of channel block (Bowie *et al.* 1998) (see Methods) to estimate the equilibrium dissociation constant of Spm at 0 mV ($K_{d(0mV)}$) as well as the voltage-dependency of the onset and relief of block (*h* and *k*, respectively; Table 2).

In agreement with previous work (Bowie *et al.* 1998), the $K_{d(0mV)}$ of Spm for GluK2 homomers was estimated to be 5.8 ± 0.3 μM, with voltage-dependencies of the onset and relief of block of −16 ± 0.5 and +20.4 ± 1.0 mV per *e*-fold change in membrane potential, respectively (Table 2). In comparison, KAR heteromerization and association with auxiliary proteins affected both Spm binding and the voltage-dependency of block. Fits of corrected *G–V* plots estimated the $K_{d(0mV)}$ of Spm to be 39 ± 2, 71 ± 13 and 119 ± 30 μM for GluK2+Neto2, GluK2+Neto1 and GluK2/GluK5 channels, respectively (Table 2), representing a 6- to 20-fold reduction in blocker affinity. Interestingly, heteromerization and auxiliary protein association mainly affected the voltage-dependency of the relief of block (i.e. *k*), which was about 2- to 3-fold weaker compared to that of GluK2 homomers (Table 2). For example, fits of corrected *G–V* plots estimated the voltage-dependency of relief for GluK2/GluK5 heteromers to be +69.7 mV per *e*-fold change in membrane potential compared to +20.4 mV for GluK2 homomers. In keeping with this, selective activation of GluK2/GluK5 heteromers with either 1 mM AMPA (Herb *et al.* 1992) or 300 μM L-Glu (Barberis *et al.* 2008) estimated $K_{d(0\ mV)}$ to be 81 ± 40 and 170 ± 33 μM, respectively, with the voltage-dependency of relief corresponding to +56.8 and +107.7 mV per *e*-fold

change in membrane potential, respectively (Table 2). In contrast, the differences between the voltage-dependency of onset of block (i.e. h) were more modest (Table 2), and the binding rates for Spm (k_{on}, Fig. 2*C*) were assumed to be constant. The unbinding (k_{off}) and permeation rates (k_{perm}) were estimated using previous estimates of k_{on} (Fig. 2*C*) (Bowie *et al.* 1998). Plots of unbinding (k_{off}) and permeation (k_{perm}) for Spm at GluK2 homomers predict that relief of block occurs only at extreme membrane potentials (i.e. $>$ +50 mV), where the rates for k_{perm} become dominant (Fig. 2*C*). In contrast, similar plots of k_{off} (Fig. 2*E*) and k_{perm} (Fig. 2*F*) with GluK2/GluK5 heteromers, GluK2+Neto1 or GluK2+Neto2 (Fig. 2*E* and *F*) reveal that there are substantial shifts in estimates of unbinding and permeation rates that account for the overall attenuation in channel block. Specifically, there is a substantial hyperpolarizing shift in k_{perm} so that Spm permeation is expected to be appreciable even at membrane potentials of −50 mV (Fig. 2*F*).

Given the specific nature of these effects, we reasoned that the attenuation of polyamine channel block by heteromerization or association with auxiliary proteins occurs because Spm permeation rates are enhanced under these conditions. To test this experimentally, we performed bi-ionic reversal potential experiments to determine the extent to which KAR composition affected polyamine permeation rates.

Heteromerization and auxiliary proteins relieve channel block by facilitating polyamine permeation

To determine the permeability of Spm relative to that of Na^+ (P_{Spm}/P_{Na}), we measured the reversal potential of KAR responses in solutions where the main external permeant cation was either 150 mM Na^+ or 90 mM Spm. In all cases, the main permeant cation of the internal solution was 150 mM Na^+ (Fig. 4 and see Methods).

As expected, responses mediated by GluK2 (V_{rev} = −0.2 ± 1.5 mV, Fig. 4*A* and *C*, inset), GluK2/GluK5 (V_{rev} = −0.5 ± 0.8 mV, Fig. 4*D* and *F*, inset) and GluK2+Neto2 (V_{rev} = −0.7 ± 0.8 mV, Fig. 4*G* and *I*, inset) in symmetrical 150 mM Na^+ solutions reversed close to 0 mV, demonstrating that Na^+ ions are equally permeable from both sides of the plasma membrane. In contrast, reversal potentials determined with external 90 mM Spm as the main permeant cation were dependent upon the KAR composition. With GluK2 homomers, we failed to observe a reliable inward current in 90 mM external Spm and therefore were unable to estimate P_{Spm}/P_{Na} (Fig. 4*B* and *C*), an observation similar to a previous study of

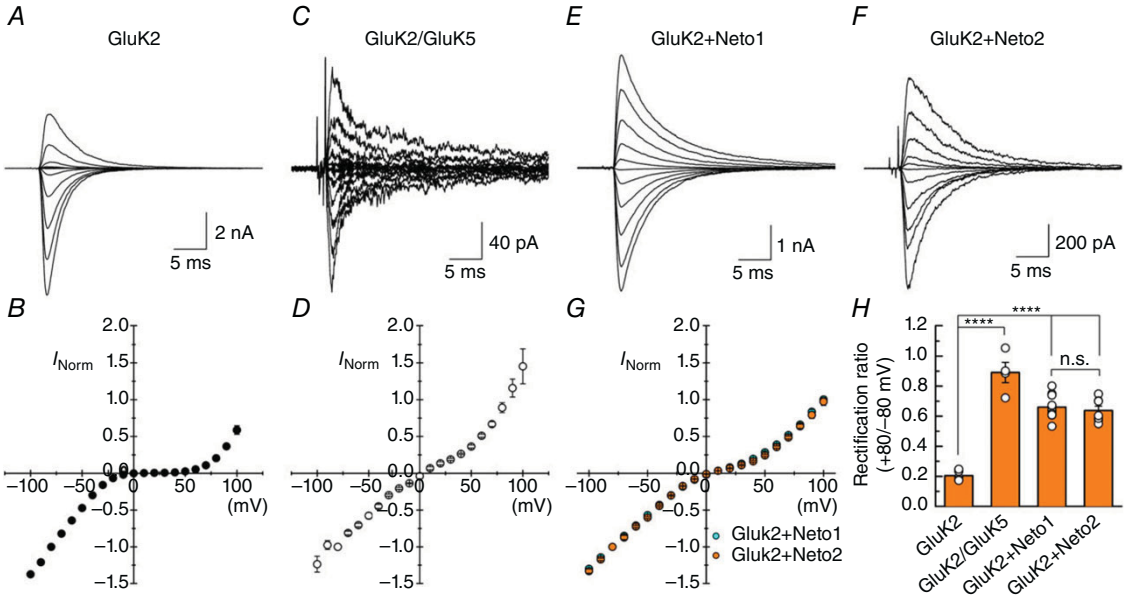

Figure 1. Heteromerization and auxiliary proteins reduce inward rectification of KARs
A, *C*, *E*, *F*, typical membrane currents evoked by 1 mM L-Glu (1 ms application) at various holding potentials (−100 to +100 mV, 20 mV increments) in the presence of 60 μM internal Spm. Patch numbers: GluK2, 120403p1; GluK2/GluK5, 120417p3; GluK2+Neto1, 130506p3; and GluK2+Neto2, 131104p3. *B*, *D*, *G*, average *I*–*V* plots for GluK2 (n = 5), GluK2/GluK5 (n = 4), GluK2+Neto1 (n = 12) and GluK2+Neto2 (n = 7). Data are presented as mean ± SEM. Current values are normalized to the current at −100 mV. *H*, to obtain the rectification ratio, the peak current at +80 mV was divided by that at −80 mV. Rectification ratios for individual patches are shown as empty circles; columns represent the mean and error bars indicate SEM. One-way ANOVA, $F_{3,24}$ = 60.819, P = 2.32E-11, *post hoc* Tukey HSD pairwise comparisons: ****P < 1.33E-8; n.s., not significant.

polyamine permeation (Bahring *et al.* 1997). In keeping with this, preliminary experiments suggested that polyamines with fewer charged groups, namely Put ($z = +2$) and Spd ($z = +3$), were more permeant than Spm ($z = +4$). Reversal potentials with 90 mM external Put or Spd as the main permeant cation were -8.0 ± 2.7 mV ($n = 2$) and -34.4 ± 1.6 mV ($n = 3$), respectively, estimating P_{Put}/P_{Na} to be 0.23 ± 0.02 and P_{Spd}/P_{Na} to be 0.049 ± 0.002 for GluK2 homomers. This indicates that permeant channel blockers with smaller valencies have a greater tendency to permeate through the KAR channel, in agreement with prior work (Bahring *et al.* 1997; Cui *et al.* 1998). In contrast to GluK2 homomers, Spm-mediated inward currents were observed with both GluK2/GluK5 (Fig. 4*E* and *F*) and GluK2+Neto2 (Fig. 4*H* and *I*), with reversal potentials of -43.2 ± 1.2 mV ($n = 3$) and -33.6 ± 4.5 mV ($n = 4$), respectively. As a result, the calculated P_{Spm}/P_{Na} for GluK2/GluK5 and GluK2+Neto2 receptors were 0.024 ± 0.001 and 0.042 ± 0.009, respectively. Taken together, these data provide evidence that GluK2/GluK5 and GluK2+Neto2 receptors were more permeable to Spm compared to GluK2 homomers.

A reduction in polyamine block is thought to go hand-in-hand with Ca^{2+} permeability in non-NMDA receptors (Burnashev, 1996). Despite these differences, KAR heteromerization or association with the auxiliary proteins do not attenuate Ca^{2+} permeability. For example, in Ca^{2+}-rich external solutions (i.e. 30 mM $CaCl_2$ + 105 mM NaCl), the reversal potential of GluK2 *I–V* plots was $+1.0 \pm 0.5$ mV ($n = 5$) which was shifted to a slightly more positive potential of $+5.0 \pm 1.8$ mV ($n = 3$) with GluK2/GluK5 heteromers (Fig. 5*E* and *F*). As a result, the relative Ca^{2+} permeabilities (P_{Ca}/P_{Na}) of GluK2 homomers and GluK2/GluK5 heteromers were estimated to be 2.3 and 3.1, respectively. As a previous study has reported similar findings with the auxiliary proteins, Neto1 and Neto2 (Fisher & Mott, 2012), we concluded that differences in the pore properties of KARs induced by heteromerization or auxiliary proteins could not be revealed by studying divalent permeability; we therefore focused on polyamine block. Thus, KARs essentially

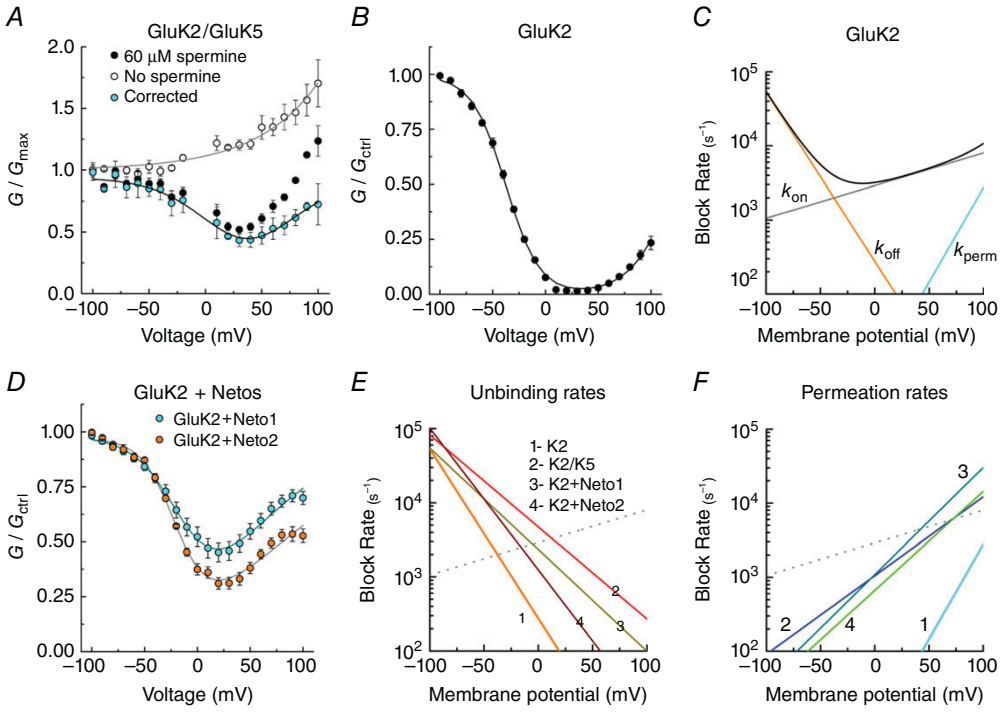

Figure 2. Association of GluK2 with GluK5 or auxiliary proteins reduces polyamine block by increasing permeation rates
A, conductance–voltage (*G–V*) plots for GluK2/GluK5 in the presence (black circles) and absence (white circles) of 60 μM internal Spm. Cyan circles represent the corrected *G–V* ($n = 4$), obtained by dividing the Spm *G–V* by the fit of the Spm-free *G–V*. *B*, corrected *G–V* plot for GluK2 ($n = 5$). *C*, rates of onset, unbinding and permeation for GluK2 (see Methods). k_{on} was estimated using values from Bowie *et al.* (1998). *D*, corrected *G–V* plots for GluK2+Neto1 (cyan, $n = 12$) and GluK2+Neto2 (orange, $n = 7$). All data are represented as the mean ± SEM. *G–V* plots were fit with eqn (2). *E* and *F*, comparison of the estimated unbinding (k_{off}, *E*) and permeation (k_{perm}, *F*) rates for GluK2 (1), GluK2/GluK5 (2), GluK2+Neto1 (3) and GluK2+Neto2 (4).

behave as molecular sieves (Burnashev, 1996; Bahring *et al.* 1997) such that the movement of bulky permeating ions (i.e. Spm) is hindered in the permeation pathway while that of much smaller divalent cations, such as Ca^{2+} ions, is not. As explained below, we performed MD simulations to better understand this distinction by looking at how the pore region of KARs might be affected by modest changes in the ion-permeation pathway.

MD simulations predict a structural change in the channel pore

Sequence alignment of all KAR subunits was performed to identify differences between the GluK2 and GluK2/GluK5 receptors (Fig. 6*A*). The most striking difference was found in the α-helical region of the re-entrant loop (P-loop; Fig. 6*A*) where a glycine residue (i.e. GluK2 Gly615) is found in all primary subunits (GluK1-3) while a proline residue is found in the equivalent position (i.e. GluK5 Pro599) of secondary subunits (GluK4 and GluK5), which do not form functional homomers. As each residue is located within a predicted α-helical region of the re-entrant P-loop of KARs (Panchenko *et al.* 1999) (Fig. 6*A*), we reasoned that the Gly and Pro may exert differential effects on channel block and permeation. Specifically, we hypothesized that the Pro of the GluK5 subunit would result in structural changes in the heteromeric KAR pore regions, as has been proposed for Pro residues in other α-helical regions of ion-channels, such as the S6 helix of Shaker (Bright *et al.* 2002) and the M2 helix of KcsA K^+ channels (Fowler & Sansom, 2013).

To explore this, MD simulations were used to study how the introduction of the Pro residue may affect the pore structure and its dynamics (Fig. 6*B–D*). As a high-resolution structure of the KAR pore region is not yet available, we performed MD simulations using the structure of the *Bacillus cereus* NaK channel pore [PDB 3E86 (Alam & Jiang, 2009*a*), 1.6 Å resolution] as it has been used successfully to provide insight into the NMDA-type iGluR (Siegler Retchless *et al.* 2012). This structure has 4-fold symmetry, as expected for the GluK2 tetramer (Wilding *et al.* 2014) and furthermore illustrates an open conformation (Fig. 6*B* and *C*). Although the iGluR pore structure has been compared to the KcsA structure (Sobolevsky *et al.* 2009), it also shares remarkable structural similarities with the NaK channel pore (Fig. 7). Moreover, because the NaK channel is a non-selective cation channel, its pore properties are expected to be closer to that of the iGluR. For these reasons, the NaK structure was used as a model of the pore in our MD simulations. To simulate a heteromer having a 2:2 stoichiometry, as is the case for GluK2/GluK5 KARs (Reiner *et al.* 2012), prolines

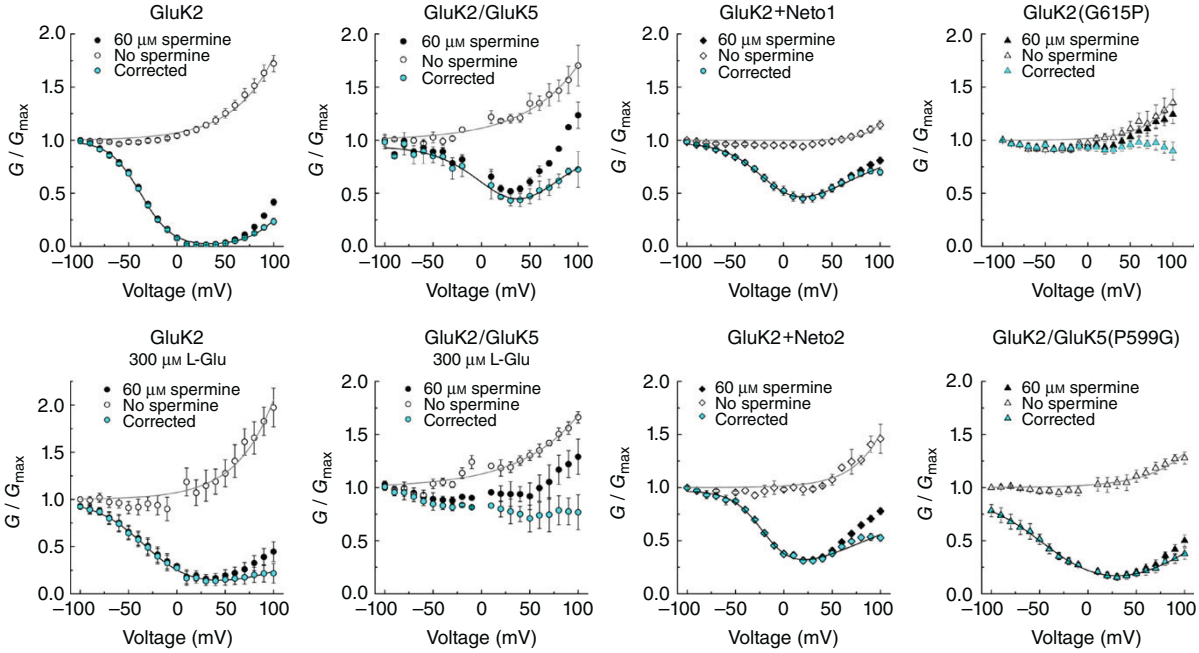

Figure 3. *G–V* corrections for intrinsic outward rectification in the absence of internal polyamines
G–V relationships in the absence (white symbols) or presence (black symbols) of internal polyamines were plotted. The corrected *G–V* relationships (cyan symbols) were obtained by dividing the value of the spermine *G–V* by the non-spermine *G–V* ($G_{corr} = G_{Spm}/G_{noSpm}$). Note the importance of performing this correction for each receptor type, as the intrinsic outward rectification properties differ.

were introduced into the equivalent α-helical positions of the NaK structure on opposing subunits (i.e. A and C), in agreement with prior work on KAR heteromers (Kumar *et al.* 2011).

Changes in cross-pore distances between the centre of mass of the α-carbons of residues 50–53 in opposing subunits are summarized in Fig. 6*D*. As expected, the A/C and B/D cross-pore distances in the wild-type (WT) NaK pore quickly reached equilibrium and remained fairly constant for the rest of the 500 ns simulation (Fig. 6*D* and supplementary Movies S1 and S2), consistent with a 4-fold symmetrical pore arrangement. In contrast, the pore adopted a 2-fold symmetry with prolines on opposing subunits (Fig. 6*D* and Movies S1 and S2). For example, the mean distance between helices A/C increased by approximately 1 Å, while the distance between WT helices (B/D) decreased reciprocally (Fig. 6*D* and Movies S1 and S2). Interestingly, the two simulation repeats with prolines introduced in all four helices illustrated two different outcomes (Fig. 6*D*, 4Pro). In one case, helices adopted

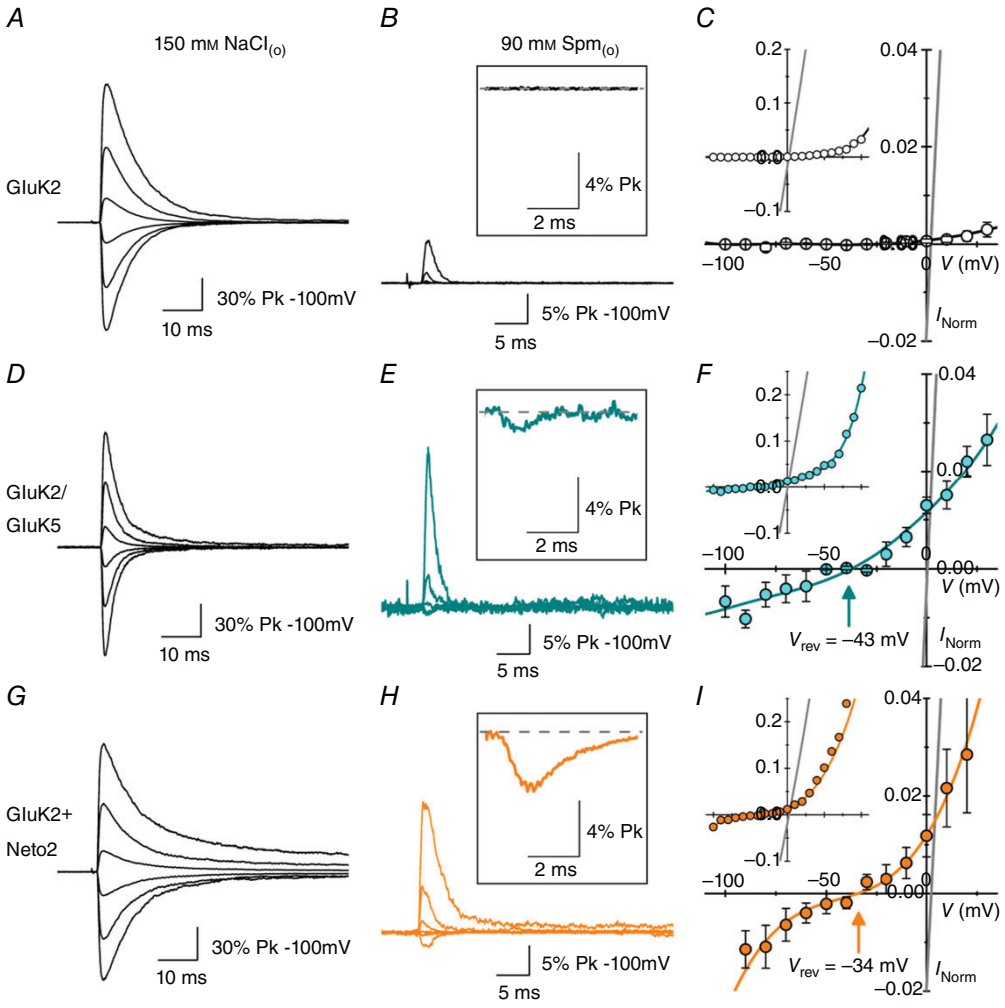

Figure 4. Spermine permeability is increased in GluK2/GluK5 and GluK2+Neto2
Electrophysiological traces of GluK2 (*A* and *B*, patch 130730p2), GluK2/GluK5 (*D* and *E*, patches 121122p1 and 131206p2) and GluK2+Neto2 (*G* and *H*, patches 131017p3 and 140410p9) evoked by 1 mM L-Glu (250 ms) at various holding potentials (−100 to +100 mV, 40 mV increments) in 150 mM NaCl external solution (left) or 90 mM Spm external solution (right). Insets show the current traces at −100 mV in 90 mM Spm. *I–V* plots in 90 mM external Spm for GluK2 (*C*, $n = 4$), GluK2/GluK5 (*F*, $n = 3$) and GluK2+Neto2 (*I*, $n = 5$). Arrows represent the reversal potentials for GluK2/GluK5 ($V_{rev} = -43.2$ mV) and GluK2+Neto2 ($V_{rev} = -33.6$ mV). Insets show the *I–V* plots ranging from −100 to +100 mV. Grey lines are the fits of the same receptor in the presence of 150 mM external NaCl. Data are represented as means ± SEM. Current values (both Na^+ and Spm currents) are normalized to the Na^+ current at −100 mV in the same patch.

a 4-fold symmetry but with larger separation than the WT (Fig. 6*D*, Run 1); in the second case, they adopted a 2-fold symmetry (Fig. 6*D*, Run 2). Thus, despite the trajectories showing two different effects of proline insertions, they probably reflect the same result, namely that the Pro residue induces a more stochastic behaviour of the P-loop compared to the WT pore conformation.

To better understand how the Pro residues affect the dynamics of the NaK α-helical P-loop, we examined the root mean square deviation (RMSD) of each helix in comparison to the reference structure (Fig. 8; PDB #3E86). Interestingly, the mean RMSD of Pro-containing helices in all simulations was about 0.5 Å, a 2-fold increase compared to the RMSD of WT helices (Fig. 8), indicating that they are able to move further away compared to their WT counterparts. Moreover, the RMSD fluctuation in the Pro-containing helices was much greater than in WT helices, spanning almost 0.2 Å, while the WT fluctuations spanned less than 0.1 Å (Fig. 8). Given this, we hypothesized that increased dynamics in the P-loop α-helices may be responsible for the enhanced polyamine permeation rates observed experimentally.

MD simulations predict increased polyamine permeation

To test whether Pro-induced changes in the position of the helices could facilitate blocker permeation, we compared the work required to pull pore-bound polyamines to the extracellular side of WT and mutant NaK pore regions, corresponding to the intracellular side in KARs (Fig. 9). Polyamines were also pulled to the intracellular side of the NaK pore, but the results from these experiments were inconclusive. From each of the WT trajectories in Fig. 6*D*, the most symmetrical and the most asymmetrical snapshot (in terms of the cross-pore distance) was found and used as a starting structure, giving rise to a total of four different protein structures. Three polyamines of different structure and charge (Put, Spd and Spm) were modelled into the filter by overlaying with the original cations bound in the filter of the NaK structure (Fig. 9*A*) (Alam & Jiang, 2009*a*). After 30 ns of relaxation, all polyamines were still bound to the filter region. To probe the strength with which the polyamines bind to the filter, SMD simulations were subsequently performed. In the

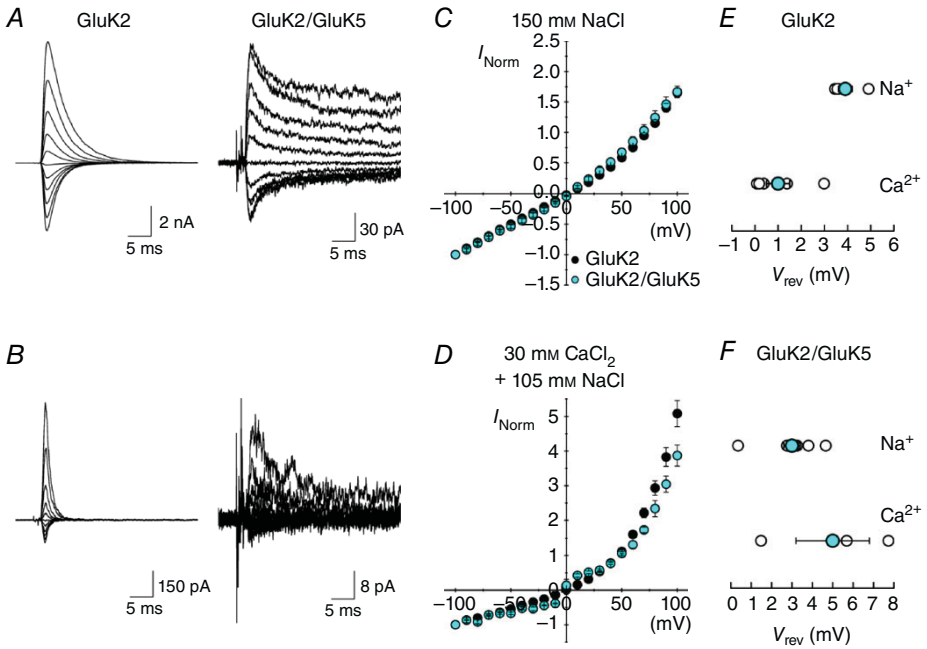

Figure 5. Ca^{2+} permeability is similar for GluK2 and GluK2/GluK5 kainate receptors
A, example membrane currents for GluK2 (left, patch 120507p1) and GluK2/GluK5 (right, patch 120522p2) evoked by 1 ms L-Glu applications (1 mM, in 150 mM NaCl) at various holding potentials (−100 to +100 mV, 20 mV increments) in the absence of internal polyamines. *B*, example membrane currents for GluK2 (left, same patch as in *A*) and GluK2/GluK5 (right, same patch as in *A*) evoked by 1 ms L-Glu applications (1 mM, in 30 mM $CaCl_2$) at various holding potentials (−100 to +100 mV, 20 mV increments) in the absence of internal polyamines. *C*, *I–V* relationships for GluK2 (black, $n = 4$) and GluK2/GluK5 (cyan, $n = 8$) in 150 mM NaCl external solution. *D*, *I–V* relationships for GluK2 (black, $n = 5$) and GluK2/GluK5 (cyan, $n = 3$) in 30 mM $CaCl_2$ external solution. Current values are normalized to the current at −100 mV. *E* and *F*, reversal potentials in 150 mM NaCl and 30 mM $CaCl_2$ external solutions for GluK2 (*E*) and GluK2/GluK5 (*F*). All data are represented as mean ± SEM.

SMD simulations, polyamines were pulled out of the filter along the *z*-axis toward the intracellular side of the membrane (Movie S3). Each SMD simulation produced a force profile from which the work involved in the process was calculated (Fig. 9*B*). The eight snapshots shown in Fig. 10 correspond to time steps at which the force peaks, each denoted in Fig. 9*B* by an asterisk, along with snapshots before and near the end of the SMD simulation. From the SMD simulations with different polyamines, a clear trend in the work values was observed (Fig. 9*C* and Movie S3), suggesting that, in the WT pore, it is easier for the smaller polyamines (Put and Spd) to pass through from the filter than Spm, in agreement with our data and that of others (Bahring *et al.* 1997). Similar SMD simulations were performed with Spm inserted into the most symmetrical or the most asymmetrical snapshots from the 2Pro and 4Pro trajectories from Fig. 6*D*. As before, all Spm molecules were still bound to the filter region in the 12 different systems (4×WT, 4×2Pro, 4×4Pro) after 30 ns of relaxation. The calculated work values for pulling Spm to the solvent were lower for the 2Pro and 4Pro mutants than for the WT pore (Fig. 9*D*). Thus, this model system suggests that the Pro residue in the α-helical region of the GluK5 P-loop may be enough to disturb Spm binding and ensure higher permeation and unblock in the GluK2/GluK5 heteromers.

Pro599 in the GluK5 pore is the main determinant of polyamine block

To assess whether GluK5 Pro599 is responsible for enhanced polyamine permeation, we measured the degree of channel block after substituting it with a Gly residue, as is found in GluK2 (Fig. 9*E*–*G*). As anticipated, the degree of inward rectification of GluK2/GluK5(P599G) channels was significantly more pronounced than observed with WT heteromers (Fig. 9*F*). This finding demonstrates that Pro599 is a critical determinant of polyamine block. Fits of the corrected *G*–*V* plot estimated the $K_{d(0mV)}$ of GluK2/GluK5(P599G) receptors to be 19 ± 2 μM, which was 4–5 fold more potent than WT heteromers with a $K_{d(0mV)}$ of 119 ± 30 μM (Fig. 9*G* and Table 2).

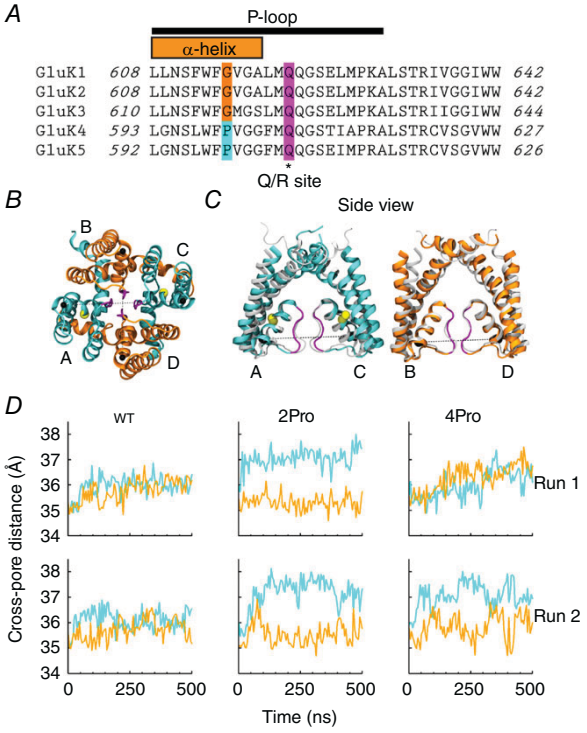

Figure 6. Prolines in GluK5 pore are predicted to alter pore dimensions
A, sequence alignment of the kainate receptor subunits. A proline is present in the secondary subunits where a conserved glycine is present in primary subunits. This residue is located within a region with a predicted α-helical structure of the P-loop. *B*, crystal structure of the NaK channel (PDB#3E86). Proline residues were mutated in the equivalent α-helical structure of subunits A and C (yellow spheres). *C*, side view of the A/C (cyan) and B/D (orange) subunits of the inverted NaK pore before (grey) and after (coloured) 257 ns simulations. *D*, cross-pore distance measurements (see black spheres in *C*) were measured for 500 ns (two repeats for each condition).

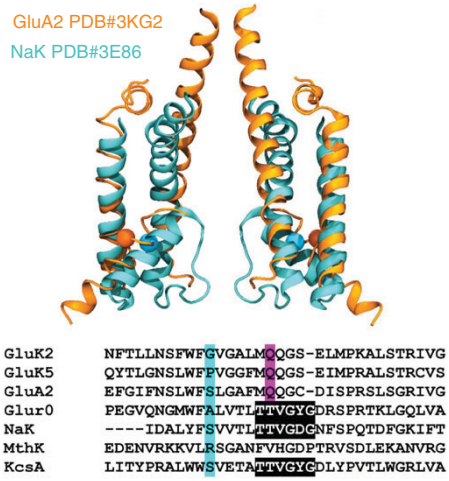

Figure 7. The NaK structure is similar to the GluA2 structure
The inverted structure of the open NaK channel (PDB #3E86, cyan) is overlaid with that of the closed GluA2 (PDB #3KG2, orange), illustrating that the two channels share a similar architecture. The proline position is indicated by a sphere. Only two chains are shown and for GluA2, only transmembrane helices M1–3 are included. The two structures are aligned using M2, C_α atoms of residues 573–586 in GluA2 and of residues 50–63 in the NaK channel. The position equivalent to the proline in GluK5 is highlighted by showing the C_α atom of this residue with a sphere (Ser580 in GluA2, Ser57 in NaK). A sequence alignment is shown, highlighting the Gly and Pro residues in GluK2 and GluK5, respectively, which correspond to an Ser in NaK.

Interestingly, the $K_{d(0mV)}$ of Spm for GluK2/GluK5 (P599G) was statistically indistinguishable from GluK2 homomers [one-way ANOVA, $F_{7,28} = 8.506$, $P = 0.000014$; *post hoc* Tukey honest significant difference (HSD) pairwise comparison, $P = 1.000$; Table 2], indicating that the removal of Pro599 from GluK2/GluK5 heteromers enhances channel block. As a result, the differences between the *G–V* plots of GluK2 (Fig. 2*B*) and mutant heteromers (Fig. 9*G*) are found in the voltage-dependency of block (Table 2).

To test if the reverse substitution would render GluK2 receptors polyamine-insensitive, Gly615 was replaced with a Pro residue, as is found in GluK5 (Fig. 9*H–J*). In contrast to WT GluK2, the *I–V* plot for GluK2(G615P) in the presence of 60 μM internal Spm was almost entirely linear, demonstrating that the introduction of Pro615 in the pore region of GluK2 eliminates polyamine block (Fig. 9*I*). In agreement with this, the corrected GluK2(G615P) *G–V* plot lacked voltage-dependency (Fig. 9*J*), further underlining that this Pro residue is the principal determinant of Spm block in GluK2/GluK5 heteromers.

Auxiliary proteins and GluK5 relieve polyamine block by distinct mechanisms

To test whether auxiliary proteins relieve KAR channel block by a similar or different mechanism, we took advantage of the fact that GluK2(G615P) channels are unaffected by Spm block (Fig. 9*H–J*). We reasoned that if auxiliary subunits attenuate Spm block by a different mechanism, their co-expression with GluK2(G615P) would increase the relative Spm permeability of the channel complex. Conversely, if they attenuate Spm block by a similar mechanism, the ability of Spm to permeate GluK2(G615P) channels would remain unchanged by co-expression with an auxiliary subunit.

In contrast to WT GluK2 (Fig. 11*A* and *D*), Spm-mediated inward currents were readily observed at negative membrane potentials with GluK2(G615P) (Fig. 11*B* and *E*). The reversal potential of GluK2(G615P) with 90 mM external Spm was -25.5 ± 2.4 mV ($n = 5$) (Fig. 11*B* and *E*), estimating the P_{Spm}/P_{Na} to be 0.062 ± 0.008 (Fig. 11*G*), similar to GluK2/GluK5 and GluK2+Neto2 (Fig. 11*G*).

Interestingly, the magnitude of Spm-induced inward currents in patches containing GluK2(G615P) channels co-expressed with Neto2 was increased by about 2-fold (Fig. 11*C* and *F*). For example, the Spm-mediated current at -100 mV was $8 \pm 5\%$ ($n = 5$) of the Na^+-mediated current with GluK2(G615P) and $19 \pm 12\%$ ($n = 7$) with GluK2(G615P)+Neto2. In addition, the reversal potential observed with 90 mM external Spm was more positive for GluK2(G615P)+Neto2 than GluK2(G615P) alone ($V_{rev} = -15.6 \pm 2.3$ mV; $n = 4$), estimating P_{Spm}/P_{Na} to be 0.12 ± 0.02 (Fig. 11*G*). One-way ANOVA performed on the relative Spm permeability revealed that P_{Spm}/P_{Na} for GluK2(G615P)+Neto2 was significantly larger than for GluK2(G615P), GluK2+Neto2 and GluK2/GluK5 (Fig. 11, see figure legend for *P* values). These results indicate that co-expression of KARs with Neto2 increases blocker permeation in an additive manner, suggesting that it is acting through a mechanism that is distinct from that of the Pro residues in GluK5 subunits.

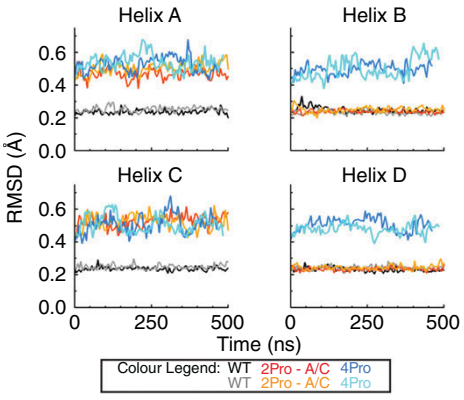

Figure 8. RMSD is larger in helices containing prolines
The RMSD values calculated for the C_α atoms of the P-loop helix (residues 50–62) of each chain of the NaK channel over the course of the 500 ns simulation. The alignment and RMSD calculation were performed for one chain at a time, aligning by residues 50–62 of the given helix for which the RMSD is calculated. WT helices are shown in black/grey, helices from the 2Pro simulation in red/orange and those of the 4Pro simulation in blue/cyan.

Discussion

The present study advances our understanding of polyamine block of KARs in several fundamental ways. First, we report that heteromerization and auxiliary proteins unexpectedly attenuate channel block by enhancing polyamine permeation rates. Second, MD simulations suggest that relief of block is due to a structural change in the α-helical region of the KAR pore, which is distinct from the charge-screening mechanism ascribed to GluA2-containing AMPARs. Our data identify that each of two GluK5 subunits in the GluK2/GluK5 heteromer possesses a critical proline residue that is predicted to push the helices outward, leading to a 2-fold symmetrical pore arrangement and increased pore helix fluctuation. Third and finally, heteromerization and auxiliary proteins relieve polyamine block by a distinct pathway. Consequently, Neto1 and Neto2 do not attenuate polyamine block by channelling their effect through the proline residue of GluK5 subunits.

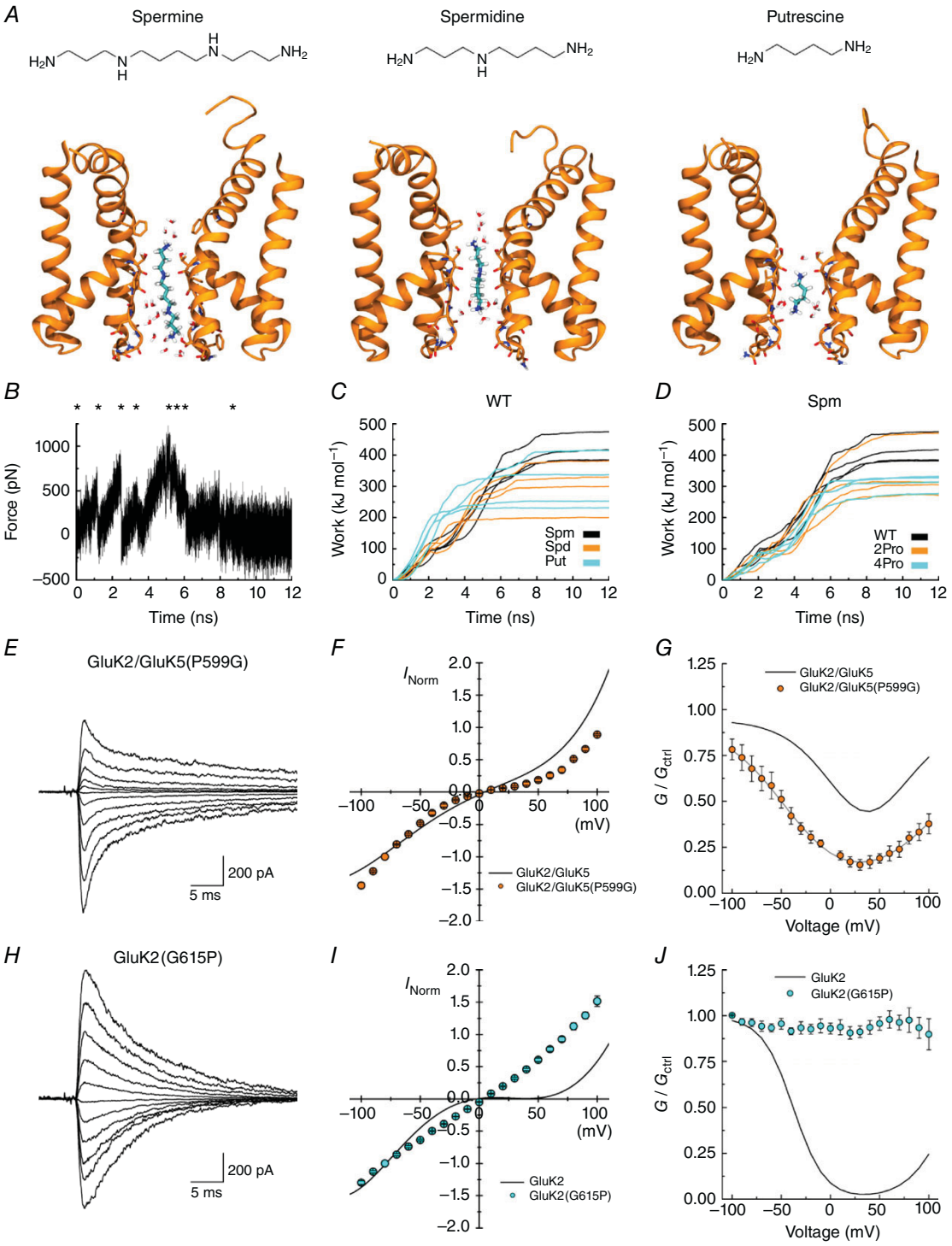

Figure 9. Proline in the M2 helix controls spermine block and permeation
A, each of the three polyamines binding in the NaK filter region, from left to right: spermine (Spm), spermidine (Spd), putrescine (Put). For simplicity, only chains A and C of the protein are included and non-polar hydrogen atoms of the protein are omitted. Carbon atoms of the ligands are shown in cyan. *B*, an example of a force profile

The dynamic nature of polyamine block

Our study reveals that subunit composition affects the functional properties of KARs differently than AMPARs. In AMPARs, the Q/R site of the GluA2 subunit is >99% edited to an Arg but remains unedited in all other subunits (Sommer *et al.* 1991). This distinction is significant because it generates the two major AMPAR classes that are either GluA2-containing, polyamine-insensitive and divalent cation-impermeable or GluA2-lacking, polyamine-sensitive and divalent cation-permeable (Cull-Candy *et al.* 2006) (but see Bowie, 2012). Importantly, polyamine-insensitivity of GluA2-containing AMPARs is thought to be due to the electrostatic effect of Arg at the Q/R site of GluA2, which repels polyamines in the narrowest region of the pore (Bowie *et al.* 1999). However, this reliance on the editing state of the Q/R site is not thought to be as important for KAR heteromers because it is edited only 40% in GluK1 subunits with a range of estimates for GluK2 from <5 to 75% in the developing and adult rodent brain (Sommer *et al.* 1991; Puchalski *et al.* 1994; Schmitt *et al.* 1996). It has yet to be tested whether the Q/R site of other KAR subunits (i.e. GluK3-5) is edited or not. Our data demonstrate that GluK2/GluK5 heteromers attenuate polyamine block not by electrostatic repulsion but rather through a novel mechanism involving a structural change in the pore helices. Accordingly, the binding affinity for polyamines in the pore is reduced, enhancing their permeation rates. This is achieved through the distinctive cyclical structure of the proline side chain that is conformationally rigid and lacks the N–H hydrogen bond donor, and thus can uniquely distort α-helical structures. As proline residues are found exclusively in GluK4–5 subunits and are absent from

illustrating the force added when pulling Spm out of the WT filter towards the intracellular side. *C*, work profiles for pulling the three different polyamines to the intracellular side in the WT protein. Spm results are shown in black, Spd in orange and Put in cyan. The work involved in Spm release is generally larger than for release of the smaller polyamines. *D*, work profiles for pulling Spm to the intracellular side for the WT protein (black), the 2Pro mutant (orange) and the 4Pro mutant (cyan). *E* and *H*, example responses of GluK2/GluK5(P599G) (E, patch 130610p7) and GluK2(G615P) (*H*, patch 130606p2) at various holding potentials (−100 to +100 mV, 20 mV increments) in the presence of 60 μM internal spermine. Average *I–V* plots (*F*, *I*) and corrected *G–V* plots (*G*, *J*) for these receptors in the presence of internal spermine. Relationships for GluK2 and GluK2/GluK5 (grey lines in *G* and *J*) are shown for comparison. Data are represented as mean ± SEM. Current values are normalized to the current at −100 mV.

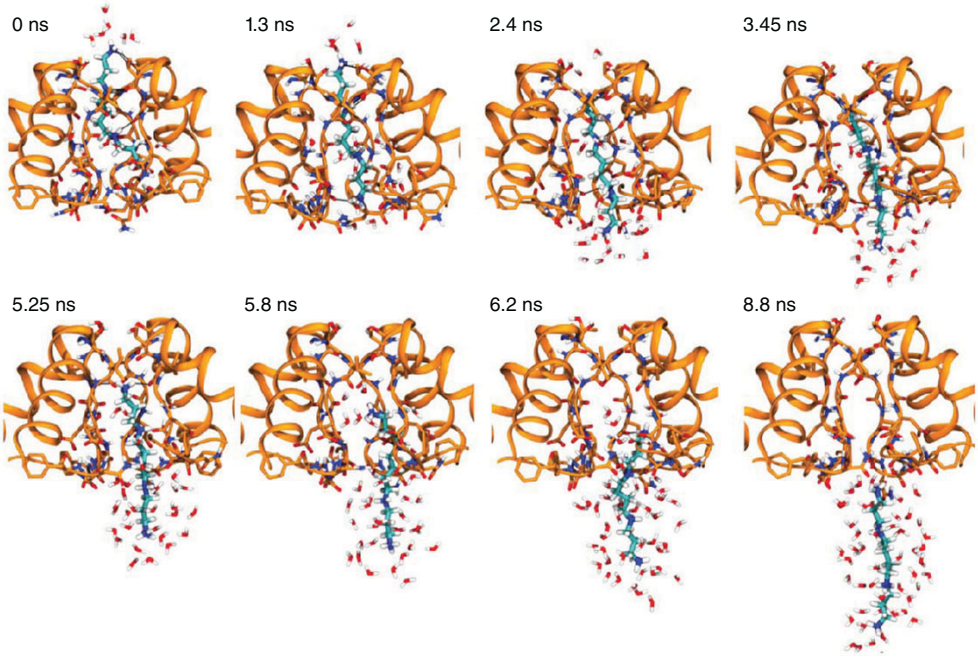

Figure 10. Snapshots illustrating the interactions as Spm is pulled toward the intracellular side of the membrane
Snapshots corresponding to the asterisks in Fig. 9*B*. Spermine is shown with cyan carbon atoms. Hydrogen bonds between spermine and the protein [dist(H–O) < 2.5 Å] are indicated with black lines.

GluK1–3 subunits, we predict that heteromers containing either GluK4 or GluK5 will exhibit a diminished level of polyamine block even if the Q/R site of all four subunits is unedited, as is the case in this study. This arrangement is distinct from AMPARs where the coupling of polyamine block and divalent cation permeability is governed by a common structural determinant, namely the Q/R site. As different structural domains govern polyamine block and Ca^{2+} permeability in KAR heteromers, native receptors will exhibit appreciable Ca^{2+} permeability that is unconstrained by significant voltage-dependent modifications in membrane conductance due to polyamine block.

Prolines in the KAR pore α-helices promote altered pore dynamics

MD simulations are consistent with a mechanism in which proline residues are arranged on opposing subunits of

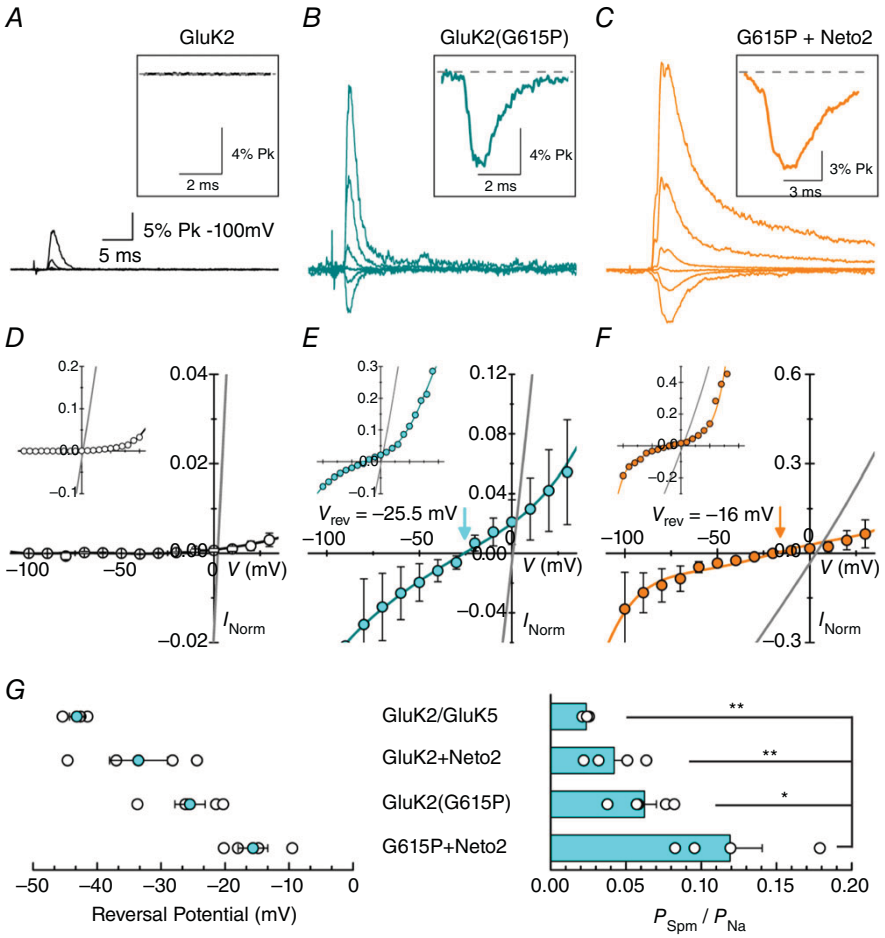

Figure 11. G615P mutation and Neto2 association increase spermine permeation of GluK2
Example responses of GluK2 (*A*, same data as in Fig. 3, GluK2(G615P) (*B*, patch 130906p2) and GluK2(G615P)+Neto2 (*C*, patch 140814p4) in 90 mM external Spm, at various holding potentials (−100 to +100 mV, 40 mV increments). Insets show the response in 90 mM external Spm at −100 mV. Average *I–V* plot for GluK2 (*D*, same data as in Fig. 3), GluK2(G615P) (*E*, $n = 5$) and GluK2(G615P)+Neto2 (*F*, $n = 4$) in 90 mM external Spm; arrows indicate reversal potentials for GluK2(G615P) ($V_{rev} = -25.5$ mV) and GluK2(G615P)+Neto2 ($V_{rev} = -15.6$ mV). Insets show the *I–V* plots ranging from −100 to +100 mV. Grey lines are the fits of the same receptor in the presence of 150 mM external NaCl. Data are represented as means and SEM. Current values (both Na^+ and Spm currents) are normalized to the Na^+ current at −100 mV in the same patch. *G*, left: summary plot showing the V_{rev} (in 90 mM Spm) for the various receptors tested. Right: summary plot showing the calculated relative Spm permeabilities (P_{Spm}/P_{Na}). One-way ANOVA, $F_{3,12} = 9.801$, $P = 0.002$; *post hoc* Tukey HSD pairwise comparisons: $^*P = 0.027$ and $^{**}P = 0.005$ and 0.002 for G615P+Neto2–GluK2+Neto2 and G5615P+Neto2–GluK2/GluK5 comparisons, respectively.

the NaK tetramer, resulting in a 2-fold symmetrical pore arrangement that alters the pore dynamics. In keeping with this, recent studies have shown that GluK2/GluK5 heteromers have a subunit copy number of 2:2 (Reiner *et al.* 2012). Interestingly, prolines are found in many transmembrane α-helices of transport proteins and ion channels, as is the case in the present study, but are uncommon in water-soluble helices (Brandl & Deber, 1986; Barlow & Thornton, 1988; Tieleman *et al.* 2001). They are most frequently located on the hydrophilic side of the helix (Woolfson & Williams, 1990), where they destabilize the helix and tend to produce hinges, kinks or swivels (Cordes *et al.* 2002). Given these observations, we hypothesized that the proline found in the re-entrant P-loop of the GluK5 subunit might result in a similar structural rearrangement in the KAR channel pore, as has been proposed for the S6 α-helix in Shaker (Bright *et al.* 2002) and the M2 helix in KcsA potassium channels (Fowler & Sansom, 2013). In the latter case, the introduction of prolines in the M2 helices predicted the formation of kinks and helical rearrangement after only 10 ns of MD simulation, with the pore helices adopting 2-fold symmetry instead of 4-fold symmetry (Fowler & Sansom, 2013). Similarly, the introduction of prolines in the P-loop of the NaK channel pore, which was used in the present study as a model of the KAR channel pore, resulted in small changes in the position of the outer region of the helices. Accordingly, our data suggest that reduced channel block and enhanced polyamine permeation rates occur through an increased structural flexibility of the pore α-helices due to proline residues that bring about an asymmetrical re-arrangement and enlargement of the KAR channel pore.

Auxiliary proteins and polyamine block

Auxiliary proteins of AMPARs and KARs are not pore-forming components of the channel (Chen *et al.* 2000; Tomita *et al.* 2003; Zhang *et al.* 2009) and therefore it has been unclear how they cause attenuation of polyamine channel block. The proximal end of the C-terminal region of the TARP, γ-2 or stargazin, has been shown to attenuate polyamine block of AMPARs through a mechanism that involves a direct interaction with the intracellular domain of GluA1 or GluA4 subunits (Soto *et al.* 2014). A similar finding has been reported with Neto2, where positive residues in the proximal intracellular C-terminal domain are implicated in reducing polyamine block (Fisher & Mott, 2012). Although it is still unclear how these residues affect inward rectification of GluK2 channels, we found that the auxiliary protein achieves this by increasing the blocker permeation, which seems at odds with the charge screening hypothesis. Our data demonstrate that Neto1 and Neto2 exert a structural effect on the channel pore that is distinct from that seen in GluK2/GluK5 heteromers. Exactly how auxiliary proteins achieve this remains to be investigated. However, given the similarity between the effect of auxiliary proteins on KARs and AMPARs, we predict that TARPs and cornichons are likely to attenuate polyamine block of AMPARs by the same mechanism, i.e. by increasing polyamine permeation.

References

Aizenman CD, Munoz-Elias G & Cline HT (2002). Visually driven modulation of glutamatergic synaptic transmission is mediated by the regulation of intracellular polyamines. *Neuron* **34**, 623–634.

Alam A & Jiang Y (2009*a*). High-resolution structure of the open NaK channel. *Nat Struct Mol Biol* **16**, 30–34.

Alam A & Jiang Y (2009*b*). Structural analysis of ion selectivity in the NaK channel. *Nat Struct Mol Biol* **16**, 35–41.

Bahring R, Bowie D, Benveniste M & Mayer ML (1997). Permeation and block of rat GluR6 glutamate receptor channels by internal and external polyamines. *J Physiol* **502**, 575–589.

Barberis A, Sachidhanandam S & Mulle C (2008). GluR6/KA2 kainate receptors mediate slow-deactivating currents. *J Neurosci* **28**, 6402–6406.

Barlow DJ & Thornton JM (1988). Helix geometry in proteins. *J Mol Biol* **201**, 601–619.

Baronas VA & Kurata HT (2014). Inward rectifiers and their regulation by endogenous polyamines. *Front Physiol* **5**, 325.

Best RB, Zhu X, Shim J, Lopes PE, Mittal J, Feig M & Mackerell AD, Jr (2012). Optimization of the additive CHARMM all-atom protein force field targeting improved sampling of the backbone φ, ψ and side-chain $\chi(1)$ and $\chi(2)$ dihedral angles. *J Chem Theory Comput* **8**, 3257–3273.

Bowie D (2012). Redefining the classification of AMPA-selective ionotropic glutamate receptors. *J Physiol* **590**, 49–61.

Bowie D, Bahring R & Mayer ML (1999). Block of AMPA and kainate receptors by polyamines and arthropod toxins. In *Handbook of Experimental Pharmacology, Ionotropic Glutamate Receptors in the CNS*, ed. Jonas P & Monyer H, pp. 251–373. Springer, Berlin.

Bowie D, Lange GD & Mayer ML (1998). Activity-dependent modulation of glutamate receptors by polyamines. *J Neurosci* **18**, 8175–8185.

Bowie D & Mayer ML (1995). Inward rectification of both AMPA and kainate subtype glutamate receptors generated by polyamine-mediated ion channel block. *Neuron* **15**, 453–462.

Brandl CJ & Deber CM (1986). Hypothesis about the function of membrane-buried proline residues in transport proteins. *Proc Natl Acad Sci USA* **83**, 917–921.

Bright JN, Shrivastava IH, Cordes FS & Sansom MS (2002). Conformational dynamics of helix S6 from Shaker potassium channel: simulation studies. *Biopolymers* **64**, 303–313.

Burnashev N (1996). Calcium permeability of glutamate-gated channels in the central nervous system. *Curr Opin Neurobiol* **6**, 311–317.

Chen L, Chetkovich DM, Petralia RS, Sweeney NT, Kawasaki Y, Wenthold RJ, Bredt DS & Nicoll RA (2000). Stargazin regulates synaptic targeting of AMPA receptors by two distinct mechanisms. *Nature* **408**, 936–943.

Cordes FS, Bright JN & Sansom MSP (2002). Proline-induced distortions of transmembrane helices. *J Mol Biol* **323**, 951–960.

Cui C, Bahring R & Mayer ML (1998). The role of hydrophobic interactions in binding of polyamines to non NMDA receptor ion channels. *Neuropharmacology* **37**, 1381–1391.

Cull-Candy S, Kelly L & Farrant M (2006). Regulation of Ca^{2+}-permeable AMPA receptors: synaptic plasticity and beyond. *Curr Opin Neurobiol* **16**, 288–297.

Darden T, York D & Pedersen L (1993). Particle mesh Ewald: an N·log(N) method for Ewald sums in large systems. *J Chem Phys* **98**, 10089–10092.

Fisher JL & Mott DD (2012). The auxiliary subunits Neto1 and Neto2 reduce voltage-dependent inhibition of recombinant kainate receptors. *J Neurosci* **32**, 12928–12933.

Fleidervish IA, Libman L, Katz E & Gutnick MJ (2008). Endogenous polyamines regulate cortical neuronal excitability by blocking voltage-gated Na^+ channels. *Proc Natl Acad Sci USA* **105**, 18994–18999.

Fowler PW & Sansom MS (2013). The pore of voltage-gated potassium ion channels is strained when closed. *Nat Commun* **4**, 1872.

Fu LY, Cummins TR & Moczydlowski EG (2012). Sensitivity of cloned muscle, heart and neuronal voltage-gated sodium channels to block by polyamines: a possible basis for modulation of excitability *in vivo*. *Channels (Austin)* **6**, 41–49.

Gomez M & Hellstrand P (1995). Effects of polyamines on voltage-activated calcium channels in guinea-pig intestinal smooth muscle. *Pflugers Arch* **430**, 501–507.

Haghighi AP & Cooper E (1998). Neuronal nicotinic acetylcholine receptors are blocked by intracellular spermine in a voltage-dependent manner. *J Neurosci* **18**, 4050–4062.

Herb A, Burnashev N, Werner P, Sakmann B, Wisden W & Seeburg PH (1992). The KA-2 subunit of excitatory amino acid receptors shows widespread expression in brain and forms ion channels with distantly related subunits. *Neuron* **8**, 775–785.

Hess B, Kutzner C, van der Spoel D & Lindahl E (2008). GROMACS 4: algorithms for highly efficient, load-balanced, and scalable molecular simulation. *J Chem Theory Comput* **4**, 435–447.

Humphrey W, Dalke A & Schulten K (1996). VMD: visual molecular dynamics. *J Mol Graph* **14**, 33–38.

Jackson AC & Nicoll RA (2011). The expanding social network of ionotropic glutamate receptors: TARPs and other transmembrane auxiliary subunits. *Neuron* **70**, 178–199.

Jorgensen WL, Chandrasekhar J, Madura JD, Impey RW & Klein ML (1983). Comparison of simple potential functions for simulating liquid water. *J Chem Phys* **79**, 926–935.

Kamboj SK, Swanson GT & Cull-Candy SG (1995). Intracellular spermine confers rectification on rat calcium-permeable AMPA and kainate receptors. *J Physiol* **486**, 297–303.

Kerschbaum HH, Kozak JA & Cahalan MD (2003). Polyvalent cations as permeant probes of MIC and TRPM7 pores. *Biophys J* **84**, 2293–2305.

Klauda JB, Venable RM, Freites JA, O'Connor JW, Tobias DJ, Mondragon-Ramirez C, Vorobyov I, MacKerell AD, Jr & Pastor RW (2010). Update of the CHARMM all-atom additive force field for lipids: validation on six lipid types. *J Phys Chem B* **114**, 7830–7843.

Kleywegt GJ & Jones TA (1998). Databases in protein crystallography. *Acta Crystallogr D Biol Crystallogr* **54**, 1119–1131.

Koh DS, Burnashev N & Jonas P (1995). Block of native Ca^{2+}-permeable AMPA receptors in rat brain by intracellular polyamines generates double rectification. *J Physiol* **486**, 305–312.

Kumar J, Schuck P & Mayer ML (2011). Structure and assembly mechanism for heteromeric kainate receptors. *Neuron* **71**, 319–331.

Lopatin AN, Makhina EN & Nichols CG (1994). Potassium channel block by cytoplasmic polyamines as the mechanism of intrinsic rectification. *Nature* **372**, 366–369.

Lu Z (2004). Mechanism of rectification in inward-rectifier K^+ channels. *Annu Rev Physiol* **66**, 103–129.

Lu Z & Ding L (1999). Blockade of a retinal cGMP-gated channel by polyamines. *J Gen Physiol* **113**, 35–43.

Miyamoto S & Kollman PA (1992). Settle: an analytical version of the SHAKE and RATTLE algorithm for rigid water models. *J Comput Chem* **13**, 952–962.

Monticelli L, Kandasamy SK, Periole X, Larson RG, Tieleman DP & Marrink S-J (2008). The MARTINI coarse-grained force field: extension to proteins. *J Chem Theor Comput* **4**, 819–834.

Nichols CG & Lopatin AN (1997). Inward rectifier potassium channels. *Annu Rev Physiol* **59**, 171–191.

Nowotarski SL, Woster PM & Casero RA Jr (2013). Polyamines and cancer: implications for chemotherapy and chemoprevention. *Expert Rev Mol Med* **15**, e3.

Panchenko VA, Glasser CR, Partin KM & Mayer ML (1999). Amino acid substitutions in the pore of rat glutamate receptors at sites influencing block by polyamines. *J Physiol* **520**, 337–357.

Pegg AE (2014). The function of spermine. *IUBMB Life* **66**, 8–18.

Perrais D, Veran J & Mulle C (2010). Gating and permeation of kainate receptors: differences unveiled. *Trends Pharmacol Sci* **31**, 516–522.

Phillips JC, Braun R, Wang W, Gumbart J, Tajkhorshid E, Villa E, Chipot C, Skeel RD, Kale L & Schulten K (2005). Scalable molecular dynamics with NAMD. *J Comput Chem* **26**, 1781–1802.

Puchalski RB, Louis JC, Brose N, Traynelis SF, Egebjerg J, Kukekov V, Wenthold RJ, Rogers SW, Lin F, Moran T, Morrison JH & Heinemann SF (1994). Selective RNA editing and subunit assembly of native glutamate receptors. *Neuron* **13**, 131–147.

Reiner A, Arant RJ & Isacoff EY (2012). Assembly stoichiometry of the GluK2/GluK5 kainate receptor complex. *Cell Rep* **1**, 234–240.

Rozov A & Burnashev N (1999). Polyamine-dependent facilitation of postsynaptic AMPA receptors counteracts paired-pulse depression. *Nature* **401**, 594–598.
Ryckaert J-P, Ciccotti G & Berendsen HJC (1977). Numerical integration of the cartesian equations of motion of a system with constraints: molecular dynamics of n-alkanes. *J Comput Phys* **23**, 327–341.
Schmitt J, Dux E, Gissel C & Paschen W (1996). Regional analysis of developmental changes in the extent of GluR6 mRNA editing in rat brain. *Brain Res Dev Brain Res* **91**, 153–157.
Siegler Retchless B, Gao W & Johnson JW (2012). A single GluN2 subunit residue controls NMDA receptor channel properties via intersubunit interaction. *Nat Neurosci* **15**, 406–413, S401–402.
Sobolevsky AI, Rosconi MP & Gouaux E (2009). X-ray structure, symmetry and mechanism of an AMPA-subtype glutamate receptor. *Nature* **462**, 745–756.
Sommer B, Kohler M, Sprengel R & Seeburg PH (1991). RNA editing in brain controls a determinant of ion flow in glutamate-gated channels. *Cell* **67**, 11–19.
Soto D, Coombs ID, Gratacos-Batlle E, Farrant M & Cull-Candy SG (2014). Molecular mechanisms contributing to TARP regulation of channel conductance and polyamine block of calcium-permeable AMPA receptors. *J Neurosci* **34**, 11673–11683.
Stansfeld PJ, Goose JE, Caffrey M, Carpenter EP, Parker JL, Newstead S & Sansom MS (2015). MemProtMD: automated insertion of membrane protein structures into explicit lipid membranes. *Structure* **23**, 1350–1361.
Stansfeld PJ & Sansom MSP (2011). From coarse grained to atomistic: a serial multiscale approach to membrane protein simulations. *J Chem Theor Comput* **7**, 1157–1166.
Tabor CW & Tabor H (1984). Polyamines. *Annu Rev Biochem* **53**, 749–790.
Tabor CW & Tabor H (1985). Polyamines in microorganisms. *Microbiol Rev* **49**, 81–99.
Tabor H & Tabor CW (1964). Spermidine, spermine, and related amines. *Pharmacol Rev* **16**, 245–300.
Tieleman DP, Shrivastava IH, Ulmschneider MR & Sansom MS (2001). Proline-induced hinges in transmembrane helices: possible roles in ion channel gating. *Proteins* **44**, 63–72.
Tomita S, Chen L, Kawasaki Y, Petralia RS, Wenthold RJ, Nicoll RA & Bredt DS (2003). Functional studies and distribution define a family of transmembrane AMPA receptor regulatory proteins. *J Cell Biol* **161**, 805–816.
Vanommeslaeghe K, Hatcher E, Acharya C, Kundu S, Zhong S, Shim J, Darian E, Guvench O, Lopes P, Vorobyov I & Mackerell AD, Jr (2010). CHARMM general force field: a force field for drug-like molecules compatible with the CHARMM all-atom additive biological force fields. *J Comput Chem* **31**, 671–690.
Vanommeslaeghe K & MacKerell AD (2012). Automation of the CHARMM general force field (CGenFF) I: Bond perception and atom typing. *J Chem Inform Model* **52**, 3144–3154.
Vanommeslaeghe K, Raman EP & MacKerell AD (2012). Automation of the CHARMM general force field (CGenFF) II: Assignment of bonded parameters and partial atomic charges. *J Chem Inform Model* **52**, 3155–3168.
Wilding TJ, Lopez MN & Huettner JE (2014). Radial symmetry in a chimeric glutamate receptor pore. *Nat Commun* **5**, 3349.
Woolfson DN & Williams DH (1990). The influence of proline residues on alpha-helical structure. *FEBS Lett* **277**, 185–188.
Yu W, He X, Vanommeslaeghe K & MacKerell AD (2012). Extension of the CHARMM general force field to sulfonyl-containing compounds and its utility in biomolecular simulations. *J Comput Chem* **33**, 2451–2468.
Zhang W, St-Gelais F, Grabner CP, Trinidad JC, Sumioka A, Morimoto-Tomita M, Kim KS, Straub C, Burlingame AL, Howe JR & Tomita S (2009). A transmembrane accessory subunit that modulates kainate-type glutamate receptors. *Neuron* **61**, 385–396.

Additional information

Competing interests

The authors declare no competing financial interests.

Author Contributions

P.M.G.E.B. designed and performed experiments, analysed data and wrote the paper; M.R.P.A. designed experiments and wrote the paper; M.M. designed and performed experiments, analysed data and wrote the paper; P.C.B. and D.B. designed experiments and wrote the paper. All authors have approved the final version of the manuscript, agree to be accountable for all aspects of the work and qualify for authorship.

Acknowledgements

This work was supported by operating grants from the Canadian Institutes of Health Research (to D.B.), the Leverhulme Trust RPG-059 (P.C.B and M.M.) and the Medical Research Council (MR/M0004331, P.C.B). P.M.G.E.B. was supported by a graduate student fellowship from the Fonds de Recherche en Santé du Québec and M.R.P.A. was supported by a Banting and Best graduate fellowship from the CIHR. D.B. is the recipient of a Canada Research Chair. M.M. was supported by a post-doctoral fellowship from the Alfred Benzon Foundation. This work made use of the facilities of ARCHER (www.archer.ac.uk) granted via the UK High-End Computing Consortium for Biomolecular Simulation, HECBioSim (hecbiosim.ac.uk, grant no. EP/L000253/1) and HECToR, the UK's national high-performance computing service, funded by the Office of Science and Technology through EPSRC's High End Computing Programme. We also acknowledge the use of the IRIDIS High Performance Computing Facility, Advanced Research Computing, Oxford, the National Service for Computational Chemistry Software and the Blue Joule facility at the Hartree Centre. We thank R. McInnes for the Neto1-HA plasmid and J. R. Howe for the Neto2 plasmid. We wish to thank members of the Bowie lab for insightful discussion of the manuscript.

Supporting information

The following supporting information is available in the online version of this article.

Movie S1. MD simulation of the NaK channel with 2 Pro substitutions. This movie illustrates the MD simulation of the 2Pro mutant of the NaK channel over 500 ns. Ser57 was substituted with a Pro residue in opposing subunits A and C, and the Cα of the inserted Pro is shown as a yellow sphere. The NaK structure is inverted so that the orientation of the helices matches that of the kainate receptor. The four subunits of the tetramer are shown as pairs of opposing subunits. The A and C subunits are on the left (cyan) and the B and D subunits are on the right (orange). The original protein structure is shown in white; the selectivity filter is highlighted in magenta. The Pro-containing α-helices (cyan, including the selectivity filter) tend to move outward, while the WT helices (orange) tend to move inward.

Movie S2. MD simulation of the NaK with 2 Pro substitutions, intracellular view. This movie illustrates the same MD simulation as in Movie S1, viewed from the intracellular side. The Pro-containing helices (cyan) seem to bend back, pulling the selectivity filter (magenta) away from the original crystal structure (white). In contrast, the selectivity filter for the WT helices tends to move slightly closer, causing a more asymmetrical arrangement of the filter, which in turn may affect polyamine permeation.

Movie S3. SMD simulation pulling pore-bound polyamines to the intracellular side. This movie illustrates the binding (from left to right) of Spm, Spd and Put to the WT NaK pore region simulated for 30 ns of relaxation before being pulled to the intracellular side. Ligands are illustrated with cyan carbon atoms and for clarity only chains A and C are shown. Protein residues in the filter are shown with licorice representation along with other protein residues and water molecules within 4 Å of the ligands.

APPENDIX B
Ligand Binding at the Agonist-Binding Cleft

Foreword to Appendix B

I first joined the lab as an undergraduate student, interested in doing an Honours Project for my B.Sc. in Biology. During this 8-month period, I learned electrophysiology and studied kainate receptors. As it turns out, I was a fast learner and was able to perform experiments efficiently, so at the end of my Honours Project, I was asked to help finish some experiments for a manuscript that was going to be submitted shortly. Since then, I have helped others on multiple occasions.

In this appendix, you will find reprints of published articles to which I have contributed and that pertain to ligand binding in KARs. The first article in this appendix is the first article to which I contributed. At the time, there was evidence that the degree of cleft closure in AMPARs was the mechanism behind partial agonism (Armstrong and Gouaux, 2000; Jin et al., 2003; Fay et al., 2009). However, despite their similarities with AMPARs, KARs may function differently. Indeed, this study shows that the efficacy of many partial agonists, especially with small amino acid ligands, is not correlated with cleft closure, with the exception of kainate and domoate, which are associated with more open conformations due to steric hindrance (Fay et al., 2009).

The following article presents novel amino acid-functionalized quinoxalines that act as antagonists at GluK1 and GluK2 receptors. One of these antagonists binds in the ligand-binding pocket with an unexpected orientation and causes variable domain openings (Demmer et al., 2015), suggesting that the mechanism for their antagonism may be to destabilize the clamshell closure.

Anne-Marie L. Fay, Christopher R. Corbeil, Patricia Brown, Nicolas Moitessier, and Derek Bowie, Functional Characterization and In Silico Docking of Full and Partial GluK2 Kainate Receptor Agonists, *Mol Pharmacol* 2009, 75:1096-1107; DOI: 10.1124/mol.108.054254

0026-895X/09/7505-1096–1107$20.00
MOLECULAR PHARMACOLOGY
Copyright © 2009 The American Society for Pharmacology and Experimental Therapeutics
Mol Pharmacol 75:1096–1107, 2009

Vol. 75, No. 5
54254/3464655
Printed in U.S.A.

Functional Characterization and In Silico Docking of Full and Partial GluK2 Kainate Receptor Agonists

Anne-Marie L. Fay, Christopher R. Corbeil, Patricia Brown, Nicolas Moitessier, and Derek Bowie

Departments of Pharmacology and Therapeutics (A.-M.L.F., P.B., D.B.) and Chemistry (C.R.C., N.M.), McGill University, Montréal, Québec, Canada

Received December 18, 2008; accepted February 18, 2009

ABSTRACT

Two structural models have been developed to explain how agonist binding leads to ionotropic glutamate receptor (iGluR) activation. At α-amino-3-hydroxy-5-methyl-4-isoxazolepropionic acid (AMPA) iGluRs, full and partial agonists close the agonist-binding domain (ABD) to different degrees whereas agonist-induced domain closure is apparently fixed at *N*-methyl-D-aspartate receptors. Although kainate (KA) iGluRs are thought to behave like AMPA receptors, the issue has not been formally tested because of the paucity of available receptor agonists. Here we identify a series of structurally related full and partial agonists at GluK2 (formerly GluR6) KARs and predict their docking mode using the in silico ligand-docking program FITTED. As expected, the neurotransmitter L-Glu behaved as a full agonist but modest reduction (e.g., L-serine or L-aspartate) or elongation (e.g., L-α-aminoadipate) in chain length generated weak partial agonists. It is noteworthy that in silico ligand-docking predicted that most partial agonists select for the closed and not, as expected, the open or intermediate conformations of the GluK2 ABD. Experiments using concanavalin-A to directly report conformations in the intact GluK2 receptor support this prediction with the full agonist, L-Glu, indistinguishable in this regard from weak partial agonists, D- and L-Asp. Exceptions to this were KA and domoate, which failed to elicit full closure as a result of steric hindrance by a key tyrosine residue. Our data suggest that alternative structural models need to be considered to describe agonist behavior at KARs. Finally, our study identifies the responsiveness to several neurotransmitter candidates establishing the possibility that endogenous amino acids other than L-Glu may regulate native KARs at central synapses.

iGluRs mediate the vast majority of excitatory neurotransmission in the mammalian brain and have been implicated in numerous CNS disorders (Bowie, 2008). Given this, much research has focused on their structure-function properties because, among other benefits, it provides a rational approach to drug discovery. Insight into their structure was first advanced by homology modeling using the bilobed domain of bacterial amino acid binding proteins as a template (Stern-Bach et al., 1994). Subsequently, the agonist-binding domain (ABD) of the GluA2 (Collingridge et al., 2009) (formerly GluR2 or GluRB) AMPAR was crystallized, revealing the predicted clamshell-like structure of globular domains 1 and 2 that close upon agonist binding (Armstrong and Gouaux, 2000). Since then, a similar approach has permitted the atomic resolution of ABDs of all iGluR family members, including the KAR (Mayer, 2005; Nanao et al., 2005), NMDAR (Inanobe et al., 2005), and, more recently, the δ-2 orphan iGluR (Naur et al., 2007). From these studies, two structural models of agonist behavior have emerged. At the NR1 NMDAR subunit, full and partial agonists differ little in the conformational change they elicit in the ABD (Inanobe et al., 2005). In contrast, at AMPARs, agonist efficacy is thought to reside in the conformations adopted by the ABD, full agonists more effective at promoting domain closure than partial agonists (Armstrong and Gouaux, 2000; Jin et al., 2003).

Although KARs are thought to behave like AMPARs, the structural basis of agonist efficacy of this receptor family has

This work was supported by the Canadian Institutes of Health Research (CIHR); the Fonds de la Recherche en Santé du Québec; the CIHR-funded Chemical Biology program; and a Canada Research Chair award.

Article, publication date, and citation information can be found at http://molpharm.aspetjournals.org.

doi:10.1124/mol.108.054254.

ABBREVIATIONS: iGluR, ionotropic glutamate receptor; CNS, central nervous system; ABD, agonist-binding domain; AMPA, α-amino-3-hydroxy-5-methyl-4-isoxazolepropionic acid; AMPAR, AMPA receptor; KA, kainate; KAR, kainate receptor; Dom, domoate; NMDA, *N*-methyl-D-aspartate; NMDAR, *N*-methyl-D-aspartate receptor; QA, quisqualic acid; SYM 2081, (2*S*,4*R*)-4-methylglutamic acid; BAPTA, 1,2-bis(2-aminophenoxy)-ethane-*N*,*N*,*N*′,*N*′-tetraacetic acid; RMSD, root-mean-square deviation; SOS, L-serine-*O*-sulfate; L-Cys, L-cysteic acid; SSC, *S*-sulfo-L-cysteic acid; HCSA, L-homocysteine sulfinic acid; HC, L-homocysteic acid; Con-A, concanavalin-A; CNQX, 6-cyano-7-nitroquinoxaline-2,3-dione; PhTX, philanthotoxin; FITTED, Flexibility Induced Through Targeted Evolutionary Description.

not been firmly established for several reasons. First and foremost, there are fewer agonist-bound crystal structures available to make the comparison. To date, the ABD of GluK1 and/or GluK2 bound by the full agonist L-Glu and partial agonists KA and domoic acid (Dom) have been resolved at atomic resolution (Mayer, 2005; Nanao et al., 2005). Other structures for quisqualic acid (QA) and SYM 2081 have also been described (Mayer, 2005) but it is not yet clear whether they act as full or partial agonists. Second, the extent of domain closure elicited by the full agonist, L-Glu, differs from partial agonist, KA, by only 3° (Mayer, 2005), which is modest in comparison with the effect of the same agonists at AMPARs (e.g., L-Glu versus KA, 8° difference) (Armstrong and Gouaux, 2000). An added complication is that the apo state of the KAR ABD has yet to be resolved; therefore, the extent of domain closure is given with respect to the GluA2 AMPAR apo state. Third and finally, KARs require external anions and cations as well as the neurotransmitter L-glutamate for activation (Wong et al., 2006), a property not shared by AMPARs (Bowie, 2002). Given this, it is possible that the degree of activation of KARs is shaped not only by the agonist molecule but also by external ions.

Here, we have tested the functionality of a range of L-Glu analogs as a first step in understanding the structural basis of agonist behavior at KARs. To complement this data, we also used the in silico ligand-docking program FITTED to predict the conformation of the ABD preferred by each agonist. It is noteworthy that this combined approach suggests unexpectedly that most partial agonists select for the closed and not the open or intermediate conformation of GluK2 ABD. This finding suggests that agonist efficacy at KARs may not be solely determined by the extent of closure in the GluK2 ABD; therefore, alternative structural models may need to be considered.

Materials and Methods

Cell Culture and Transfection. Techniques used to culture and transfect mammalian cells to express GluR6 KARs have been described in detail elsewhere (Bowie, 2002). In brief, tsA201 cells, a transformed human embryonic kidney 293 cell line stably expressing a simian virus 40 temperature-sensitive T antigen (provided by R. Horn, Jefferson Medical College, Philadelphia, PA) were maintained at a confluence of 70 to 80% in minimal essential medium with Earle's salts, 2 mM glutamine, and 10% fetal bovine serum supplemented with penicillin (100 units/ml) and streptomycin (100 μg/ml). After plating at low density (2×10^4 cells/ml) on plastic dishes, cells were transfected with cDNA encoding unedited rat glutamate receptor subunit 6 using the calcium phosphate technique as described previously (Bowie, 2002). The cDNA for enhanced green fluorescent protein (S65T mutant) was routinely cotransfected to identify transfected cells. In this and all subsequent publications from our laboratory, we adopt the recommended change to iGluR nomenclature (Collingridge et al., 2009). Consequently, GluR6 will be referred to as GluK2 and the GluR-B or GluR2 AMPAR subunit as GluA2.

Electrophysiological Solutions and Techniques. All ligands tested in this study were dissolved in external solutions containing 150 mM NaCl and 5 mM HEPES with low concentrations of $CaCl_2$ and $MgCl_2$ (0.1 mM each) to avoid divalent block. For dose-response relationships to D- and L-Asp (Fig. 3D), however, agonists were applied at concentrations (i.e., >100 mM) that would cause a shift in reversal potential as a result of changes in the driving force for the main permeant ion, Na^+. To avoid this, the ionic strength of all solutions was increased to 200 mM, with the desired agonist concentration balanced by the appropriate amount of NaCl. All concentrated ligand solutions were adjusted to pH 7.3 with NaOH before being stored at −20°C. Saturating agonist concentrations chosen for L-Glu (10 mM), kainate (1 mM), domoate (50 μM) were at least 5-fold higher than published EC_{50} values at GluK2 receptors. We confirmed empirically that these concentrations were saturating by doubling the agonist concentration in each case and observing that peak response amplitudes were unchanged. For sulfur-containing amino acids, QA, SYM 2081, and L-α-aminoadipate, saturating levels were determined empirically by increasing concentrations until a maximal response was observed. In cases in which millimolar concentrations of agonist were required for activation (e.g., 40 mM L-cysteic acid), the reported response amplitudes were corrected for the shift in the reversal potential observed. Internal pipette solution contained 115 mM NaCl, 10 mM NaF, 5 mM HEPES, 5 mM Na_4BAPTA, 0.5 mM $CaCl_2$, 1 mM $MgCl_2$, and 10 mM Na_2ATP to chelate endogenous polyamines. The pH and osmotic pressure of internal and external solutions were adjusted to 7.3 and 295 mOsmol/kg, respectively. Concanavalin-A (Con-A) (Sigma, St. Louis) was prepared in glucose free saline solution and filtered (0.2 μm filter, Corning) immediately before use as described previously (Bowie et al., 2003). All recordings were performed with an Axopatch 200B amplifier (Axon Instruments Inc., CA) using thin-walled borosilicate glass pipettes (2–5 MΩ) coated with dental wax to reduce electrical noise. Control and agonist solutions were rapidly applied to outside-out patches excised from transfected tsA201 cells as described previously (Bowie, 2002). Solution exchange (10–90% rise-time = 25–50 μs) was determined routinely at the end of the experiment by measuring the liquid junction current (or exchange current) between the control and agonist-containing solution in which total Na^+-content was reduced by 5%. Current records were filtered at 5 kHz, digitized at 25 to 50 kHz and series resistances (3–10 MΩ) compensated by 95%. Most recordings were performed at −20 mV membrane potential to ensure adequate voltage clamp control of peak currents. Data acquisition was performed using pClamp9 software (Molecular Devices, Sunnyvale, CA). All experiments were carried out at room temperature (22 to 23°C).

Overview of the Docking Program FITTED. Conformational changes in the ligand-binding domain of iGluRs have been investigated through X-ray crystallography. Previous X-ray data have revealed two fundamental features pertaining to the ligand-binding domain of iGluRs, which has made it difficult to accurately model these proteins. First, the model must allow for protein flexibility, because it is well established that the ligand-binding domain can adopt a range of degree of clamshell closure. Moreover, given that water molecules have been shown to play a key role in stabilizing the ligand in the binding cleft of both AMPA and KARs (Mayer, 2005), the docking program would have to allow for displacement and movement of waters. Until recently, docking software that simultaneously accounted for these features in their search algorithm was not available. However, the development of a genetic algorithm based docking program called FITTED 2.0 (Flexibility Induced Through Targeted Evolutionary Description), which performs all these functions has recently been described previously (Corbeil et al., 2007). This docking tool can uniquely accommodate for displaceable bridging water molecules, whereas treating the ligand/protein as a realistically dynamic system, and therefore provides the most appropriate docking approach to investigate iGluRs. For data shown in this study, we used FITTED version 2.0 using the semiflexible docking option with displaceable waters and, in each case, the pharmacophore-oriented docking function was used (Corbeil et al., 2007).

Protein and Ligand Structure Preparation before Docking. The X-ray structures of GluK2 complexes were retrieved from the Protein Data Bank (codes 1s50, 1s7y, 1sd3, 1s9t, 1tt1, 1yae) and hydrogen atoms were added with their position optimized through energy minimization. The result was visually inspected, as described previously to ensure the optimum hydrogen bond network (Corbeil et al., 2007). Six bridging water molecules found to be conserved

throughout most of the ligand-protein complexes were retained for the docking study. All protein structures were prepared using ProCESS (a module of FITTED), and the ligands were fully ionized and prepared with SMART (a module of FITTED) (Corbeil et al., 2007).

Docking Amino Acid Ligands using FITTED. The data obtained from docking experiments are summarized in Table 1. Six protein structures initially resolved with five different agonists were used as input files [i.e., 1s7y (L-Glu), 1s9t (QA), 1sd3 (SYM 2081), 1tt1 (kainate), 1yae_a (domoate, conformation 1), and 1yae_b (domoate, conformation 2)]. All the original Protein Data Bank files pertain to KAR dimer structures solved with different ligands (Mayer, 2005) with the exception of 1yae, which was solved as a hexamer (Nanao et al., 2005). To compare GluK2 monomers within a given polymer, protein superimposition was achieved by aligning the α-carbons of the residues found with at least one atom within 10 Å from the ligand. With the exception of 1yae, all the monomers within a given polymer were identical. Therefore, only one of the monomers/dimer was retained for the docking studies. As for 1yae, two monomers (1yae_a and 1yae_b) were retained as input files to allow for greater protein fluctuations within the binding pocket. The five agonists (L-Glu, QA, SYM 2081, KA, and domoate) were docked using six protein structures as input files (1s7y, 1s9t, 1sd3, 1tt1, 1yae_a, and 1yae_b). As previously reported, comparison of the crystal structures reveals three distinct protein conformations that we will refer to as closed, intermediate, and open. Consistent with the identical degree of domain closure observed with the binding of L-Glu (1s7y), SYM 2081 (1sd3), or QA (1s9t) at GluK2 crystals, the computed root-mean-square deviation (RMSD) between the active site of all three protein structures were small (1s7y and 1sd3, 0.24 Å; 1s7y and 1s9t, 0.46 Å; 1sd3 and 1s9t, 0.51 Å). For the remainder of the text, the term "closed" conformation will be used to refer to any of these three protein conformations. In agreement with crystallographic studies (Nanao et al., 2005), the "open" state will denote the conformation observed with domoate-bound crystals (RMSD between 1s7y and 1yae, 1.6 Å). Finally, the conformation adopted by the kainate-bound GluR6 crystal conformation will be termed "intermediate" (RMSD between 1s7y and 1tt1, 0.91 Å).

We assessed the validity of FITTED 2.0 for GluK2 KARs in several ways. First, we performed statistical analysis comparing the ligand bound in the actual crystal structures with the docked ligand predicted by FITTED. A ligand pose was considered successfully docked when the RMSD relative to the ligand bound in the actual crystal structure was below 2.0 Å (Table 1) (Corbeil et al., 2007). Second, the protein structure was considered to be accurately selected when the population favored that specific protein conformation over others (Corbeil et al., 2007). Third, we compared the number and position of water molecules in the crystal structure with that predicted by FITTED. In all cases, FITTED correctly predicted the number and position of water molecules. For each pose, FITTED used the RankScore function to yield a docking score, an estimation of the free energy of binding including entropic contributions (Table 1). It is noteworthy that although the scoring function has been trained to reproduce free energies of binding, the accuracy level is not high enough to make highly accurate predictions within two orders of magnitude in K_i. In addition, the apparent agonist affinity (see Fig. 3) is not governed only by the free energy of agonist binding but also by multiple aspects of ion-channel behavior that include channel gating properties and desensitization. A minimum set of 10 runs was carried out for each ligand (Corbeil et al., 2007). An initial population of 500 was enough for docking of all GluK2 KAR ligands to reach the convergence criterion. Moreover, a maximum of 500 generations was used to reach convergence for each ligand.

Assumptions of Molecular Docking Strategy. To perform molecular ligand docking experiments, four assumptions were made. First, our modeling strategy pertained to transposing the information obtained from resolved crystal with the behavior of the mature receptor under physiological conditions. Our electrophysiological recordings from GluK2 KARs were performed under physiological pH 7.3 to 7.4, whereas most of the GluK2 S1S2 isolated cores were crystallized under conditions that were significantly more acidic (ranging from 4.0 to 6.5). To assess the effect (if any) of these pH fluctuations, we compared the two GluK2 KAR crystals in complex with L-Glu that were cocrystallized at distinct pH (1s50, pH 8.0; 1s7y, pH 4.8) (Mayer, 2005). Visual inspection of the superimposed protein-ligand complexes revealed no significant differences between the two structures. We therefore used the 1s7y structure and did not further consider 1s50 in our analysis. Second, our modeling experiments assumed that all the amino acids tested bind in the same cavity between the S1S2 domains (i.e., the orthosteric site) as previously reported for other ligands cocrystallized with GluK2 KARs. Third, because the apo state of GluK2 KARs has yet to be resolved, the degree of domain closure of the agonist-binding domain was obtained in comparison with the apo state of GluA2 AMPA receptor. Fourth, we have assumed that L-Glu analogs bind to one of the three known GluK2 conformations identified through X-ray crystallography (open, intermediate, and closed). The computed RMSD between the active sites of structures for L-Glu (1s7y), SYM 2081 (1sd3) and QA (1s9t) were small (1s7y and 1sd3, 0.24 Å; 1s7y and 1s9t, 0.46 Å;

TABLE 1
Functional and structural properties of GluK2 KAR agonists
Functional properties of responses elicited by the sixteen GluK2 receptor agonists examined in this study. Structural information obtained with FITTED are also provided. All data are expressed as the mean ± S.E.M.

Agonist, Concentration Range	Peak		Ligand Category	Conformation		RMSD	Docking Score (FITTED)
				Selected (FITTED)	Experimental (Crystallography)		
	%	*n*					
L-Glu,10 mM	100	43	Full	Closed	Closed	0.34	−5.73
SYM 2081, 1–3 mM	102.0 ± 7.7	3	Full	Closed	Closed	0.24	−6.52
QA, 1–3 mM	90.0 ± 1.1	3	Full	Closed	Closed	2.0	−8.70
L-Cys, 10–60 mM	73.6 ± 1.9	4	Partial	Closed			−5.60
SSC, 1–2 mM	64.1 ± 7.6	5	Partial	Closed			−8.06
HCSA, 10–40 mM	58.0 ± 5.4	5	Partial	Closed			−6.84
KA, 1–3 mM	39.1 ± 2.0	10	Partial	Intermediate	Intermediate	0.46	−8.33
HC, 10–40 mM	34.4. ± 3.4	8	Partial	Closed			−6.62
CSA, 10–40 mM	31.72 ± 3.75	3	Partial	Closed			−6.97
Dom, 50–150 μM	15.3 ± 1.9	8	Partial	Open	Open	1.2	−8.88
L-Aminoadipate, 10–40 mM	14.05 ± 0.19	4	Partial	Closed			−6.70
D-Asp, 10 mM	3.6 ± 1.15	6	Partial	Closed			−6.29
L-Asp, 10 mM	0.95 ± 0.39	5	Partial	Closed			−5.13
SOS, 1–20 mM	0.52 ± 0.7	3	Partial	Closed			−7.24
L-Ser, 10 mM	0.26 ± 0.3	3	Partial	Closed			−5.01
D-Ser, 10 mM	0.05 ± 0.5	3	Partial	Closed			−4.96

1sd3 and 1s9t, 0.51 Å), and therefore their domain closure was considered indistinguishable in agreement with previous structural analysis (Mayer, 2005).

Results

L-Glu Analogs Exhibit a Wide Range of Agonist Activity at GluK2 Receptors. In an effort to identify receptor ligands that exhibit the full range of agonist behavior, we studied the kinetic properties of a number of commercially available L-Glu analogs (see *Materials and Methods*). In all cases, agonists were applied at saturating concentrations and at frequencies that permit full recovery from desensitization. Figure 1 shows the extended structure of the selected amino acids all of which possess a common L-Glu backbone. We purposely chose this group of amino acids because they would provide information on how agonist efficacy is shaped by changes in chain length, atom substitution, as well as the addition of side groups and/or sulfur groups. Agonist activity of several of these amino acids have been previously reported at AMPARs, NMDARs, and metabotropic glutamate receptors (Patneau and Mayer, 1990; Kingston et al., 1998) but not yet at KARs.

Almost all amino acids tested elicited membrane currents that consisted of a rapidly rising peak response, which declined in the presence of the agonist to a new equilibrium level (Fig. 2 upper, Table 1). In some cases, as with L-serine-*O*-sulfate (SOS) and stereoisomers of serine (Ser) and aspartate (Asp), responses were difficult to resolve because of their small amplitude (even in high-expressing patches), which made detailed kinetic analysis problematic (Figs. 2 and 3). Nevertheless, a wide range of agonist efficacy was observed among all the amino acids tested (Fig. 2, bottom). For example, five sulfur-containing amino acids exhibited the following rank order of efficacy: L-cysteic acid (L-Cys, 40 mM) > *S*-sulfo-L-cysteic acid (SSC; 20 mM) > L-homocysteine sulfinic acid (HCSA; 40 mM) > L-homocysteic acid (HC; 20 mM) > SOS (1 mM) based on peak response amplitude with saturating agonist concentrations (Fig. 2, top). As mentioned above, SOS evoked barely detectable responses demonstrating that even modest changes to the agonist structure has pronounced effects on agonist efficacy (Fig. 2, top). In this case, replacement of the sulfur atom at the ω-position with an oxygen converted the partial agonist, SSC, into the poorly stimulating SOS. Except for SYM2081 and QA, all other

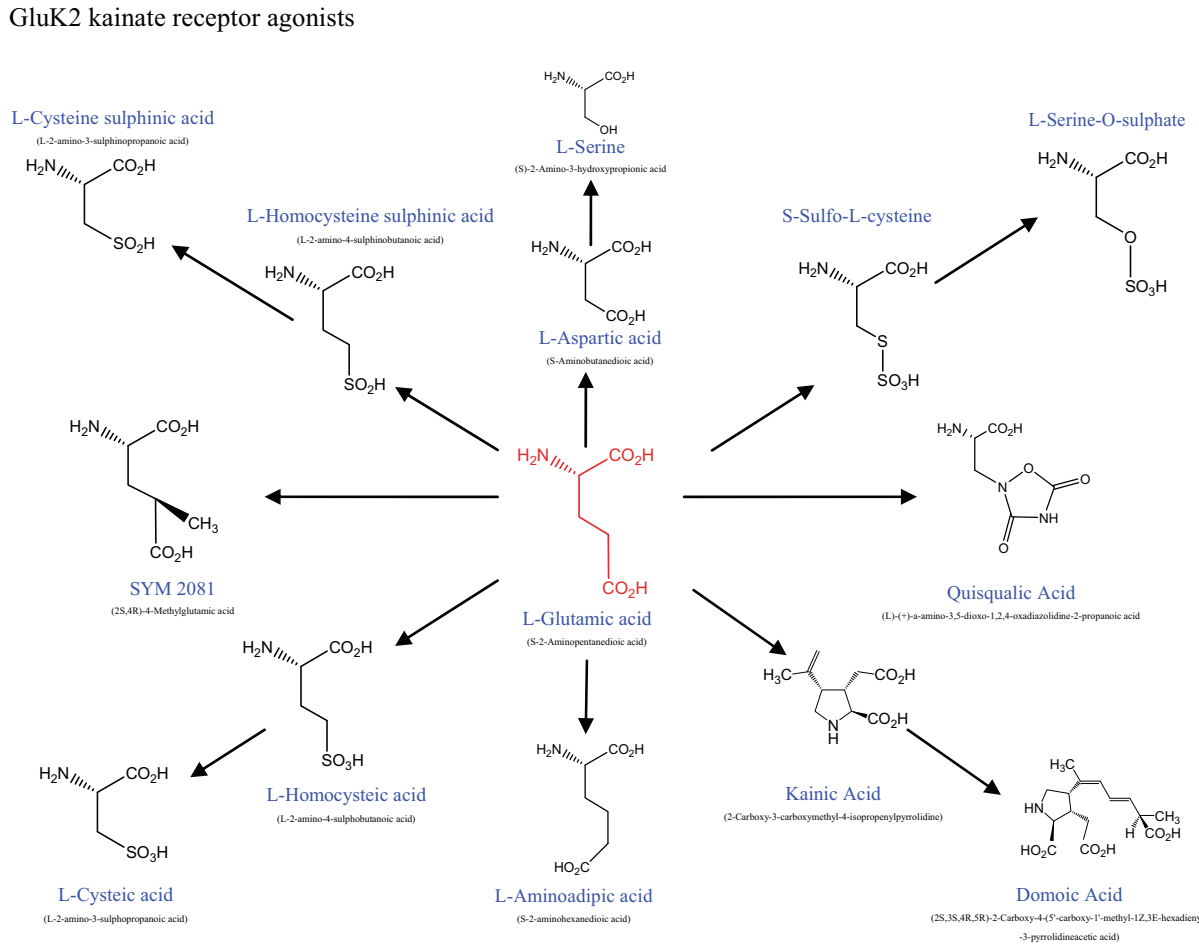

Fig. 1. Extended structure of GluK2 receptor agonists. Schematic diagram showing the extended structure of all the amino acids selected for investigation. All amino acids are structural analogs of L-Glu and thus were chosen purposely to provide information on how changes in chain length, atom substitution, and the addition of side groups and/or sulfur groups affect agonist efficacy. Each structure is identified by both its common and IUPAC nomenclature.

agonists tested were partial agonists because they elicited peak responses smaller than that observed with L-Glu (one sample t test, $p < 0.01$; Fig. 2, bottom). Finally, modest reduction (e.g., L-serine and L-aspartate) or elongation (e.g., L-α-aminoadipate) in chain length of the L-Glu structure generates weak partial agonists suggesting that the KAR ABD is optimized for the binding of this amino acid.

Desensitization Does Not Profoundly Affect Estimates of Peak Response Amplitude. Although solution exchanges performed in this study were rapid, relative rates of activation and desensitization may vary among different agonists. Consequently, agonists designated as poorly conducting (i.e., weak partial agonists) may, in fact, behave as full agonists if studied in the absence of desensitization. To address this issue, we looked more closely at SOS and the stereoisomers (i.e., D and L) of both Asp and Ser, which were ideal for this purpose because these ligands represent the five weakest responding agonists, which, as explained above, may reflect genuine partial agonist activity or result from rapid rates into desensitization. To delineate between these two possibilities, we examined agonist responses after treatment with the plant lectin, concanavalin-A (Con-A).

Although Con-A does not block desensitization or shift apparent agonist affinity, it irreversibly increases current flow through GluK2 KARs (Bowie et al., 2003). We reasoned that this property would permit better resolution of re-

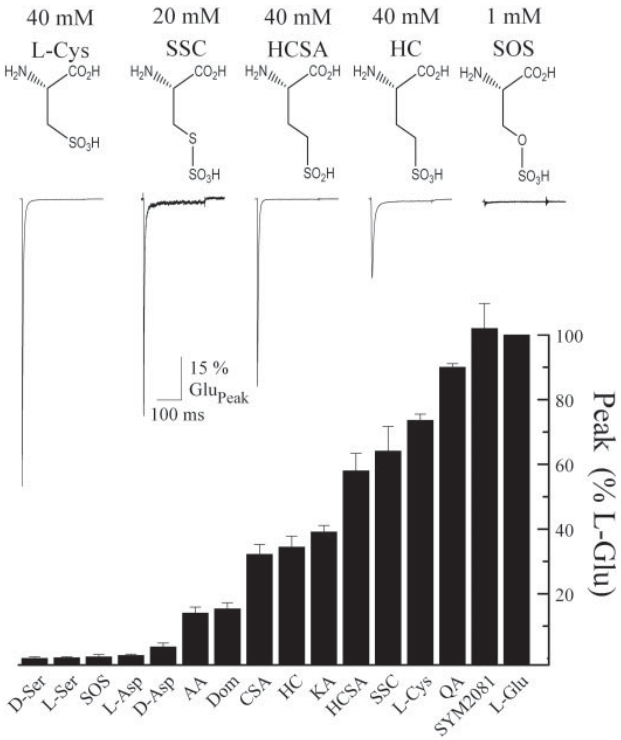

Fig. 2. Response profile of an extended series of GluK2 kainate receptor agonists. Top, structure-function relationship of five sulfur-containing amino acids aligned in order of peak agonist responsiveness. To allow comparison between experiments, membrane currents were normalized to the peak L-Glu response in each recording. Patch numbers were 04622p4 (L-Cys), 04629p2 (HCSA), 060720p1 (HC), 060720p4 (SSC)b, and 04621p1 (SOS). Bottom, summary bar graph comparing the peak response amplitude observed with saturating concentrations of each amino acid (n = 8–43 patch recordings). The data are arranged in increasing order of responsiveness, from very weak partial agonists (stereoisomers of serine and aspartate as well as SOS) to QA, SYM 2081, and L-Glu, which are full agonists. All data are expressed as the mean ± S.E.M.

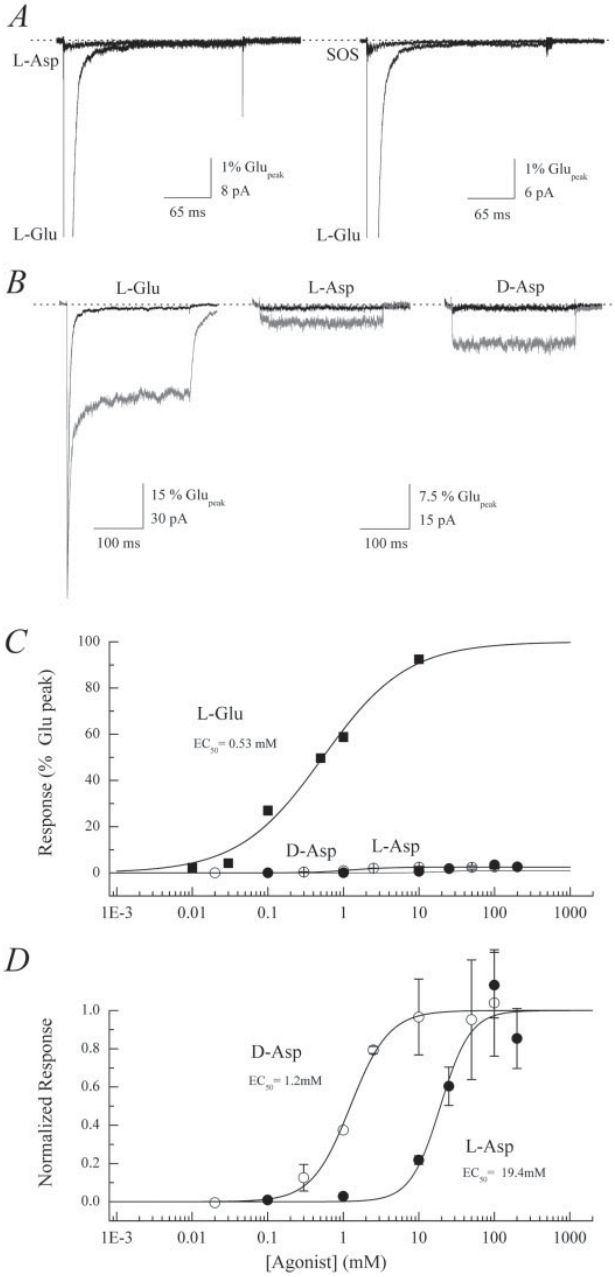

Fig. 3. Stereoisomers of aspartate are partial agonists at GluK2 kainate receptors. A, representative membrane currents elicited by 10 mM L-Glu, 10 mM L-Asp, and 1 mM SOS (patch numbers 080425p2). The dotted line denotes the zero current level. B, typical electrophysiological recordings elicited by 10 mM L-Glu, L-Asp, and D-Asp (10 mM each) before (black line) and after (gray line) Concanavalin-A (3 min) treatment in the same patch (patch number 080425p2). Con-A treatment reveals that both D- and L-Asp elicit rapidly rising, nondesensitizing membrane currents that quickly deactivate upon cessation of the agonist application. C and D, activation curves to L-Glu as well as D- and L-Asp reveal that stereoisomers of Asp are weak partial agonists with significantly lower affinity than with the full agonist L-Glu.

sponses elicited by weakly responding agonists. Before Con-A treatment, typical responses elicited by each of these agonists were small in amplitude, which made accurate analysis of their kinetic properties problematic as shown in Fig. 3A for 10 mM L-Asp and SOS. To allow comparison, membrane currents elicited by the full agonist, L-Glu (10 mM), in the same patch recording are shown superimposed (Fig. 3A). As anticipated, Con-A treatment (10 μM, 3–5 mins) increased current flow through GluK2 receptors activated by SOS and stereoisomers of both Asp and Ser, making it possible to routinely study their peak responses (Fig. 3B). From detailed analysis of the stereoisomers of Asp, two important characteristics of their response were revealed that unequivocally demonstrate that they behave as partial agonists. First, stereoisomers of Asp elicited rapidly rising, nondesensitizing membrane currents showing that these agonists are not weakly responding because of the rapid onset of desensitization (Fig. 3B). Second, construction of activation curves for each agonist revealed that maximal responses in each case were significantly smaller than with L-Glu (Fig. 3C). Compared with the maximal response elicited by L-Glu, responses to saturating concentrations of D- and L-Asp were 2.5 ± 0.1% and 3.0 ± 0.3% (n = 4–6), respectively. In addition, estimated EC_{50} values (Hill coefficient, n_H) for D-Asp and L-Asp were 1.2 ± 0.1 mM (n_H = 1.7 ± 0.3) and 19.4 ± 4.7 mM (n_H = 2.2 ± 1.1), respectively, compared 0.5 ± 0.1 mM (n_H = 0.8 ± 0.1) for L-Glu (Fig. 3, C and D). Taken together, these observations directly demonstrate that D -and L-isomers of Asp elicit responses of small amplitude because they are partial agonists and not due to the rapid onset of desensitization.

In Silico Ligand-Docking Correctly Identifies Conformations Adopted by the Gluk2 Agonist-Binding Domain. To combine this functional data with in silico ligand-docking using FITTED, we first focused on receptor agonists previously cocrystallized with the isolated ligand binding core of GluK2 (Mayer, 2005; Nanao et al., 2005). From electrophysiology recordings, we already identified kainate (1 mM KA) and domoate (50 μM Dom) as partial agonists at GluK2 receptors with L-glutamate (10 mM L-Glu), SYM 2081 (3 mM), and quisqualate (3 mM QA) all behaving as full agonists when applied at saturating concentrations (Fig. 4, A and B). Peak KA and Dom responses were 39.1 ± 2.0% (n = 10) and 15.3 ± 1.9% (n = 8) respectively of the maximal full agonist response (Fig. 4B, Table 1). Previous structural work

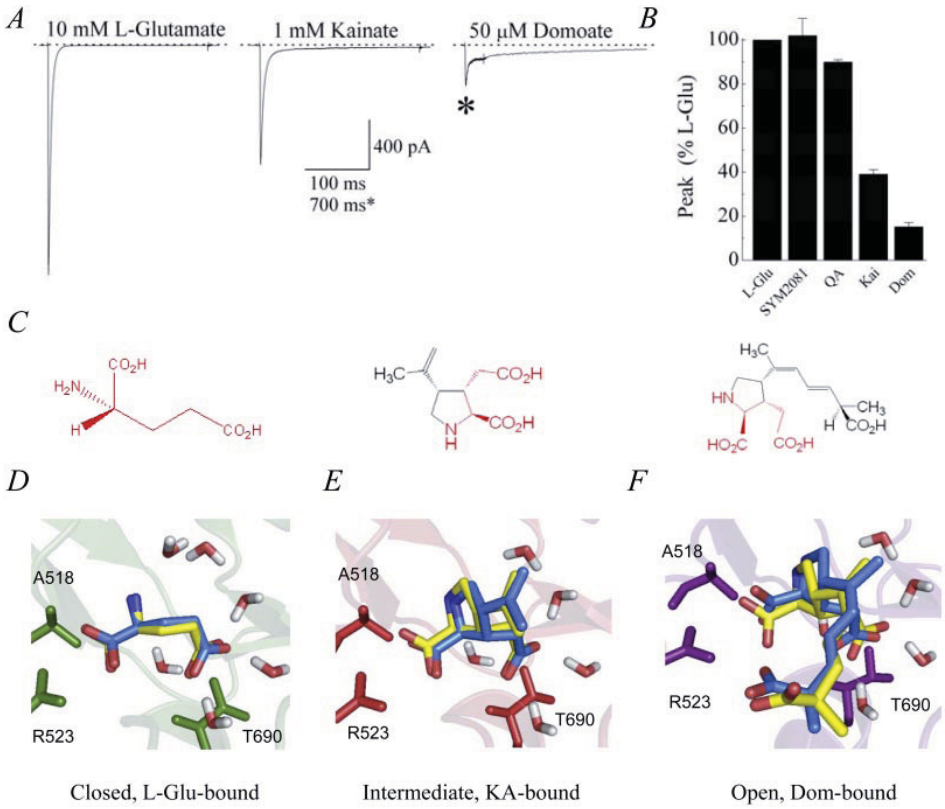

Fig. 4. FITTED accurately predicts conformations adopted by the GluK2 agonist-binding domain. A, membrane currents evoked by L-Glu (10 mM, 250-ms duration, H_p = −20 mV), KA (1 mM), and Dom (50 μM) in the same outside-out patch containing homomeric GluK2 channels (patch number 030724p2). *, Dom response is drawn on a different time base. B, summary plot showing peak responses evoked by five agonists, all of which have been cocrystallized with the GluK2 KAR: L-Glu (n = 13), SYM 2081 (n = 3), QA (n = 3), KA (n = 13), and Dom (n = 8). All data are expressed as the mean ± S.E.M. C, extended molecular structures showing that kainate and domoate have a common L-Glu backbone (red labeling). D to F, superimposition of the GluK2 agonist-binding pocket containing L-Glu, KA, and Dom where the solved crystal structures are compared with that docked by FITTED. In this and subsequent figures, the numbering of amino acid residues begins at the start site of the open reading frame and therefore includes the signal peptide. The solved crystal structures are shown in yellow, whereas the modeled structures are in blue. Key residues as well as agonist and water molecules are shown as sticks. L-Glu, KA, and Dom selected the closed (green), intermediate (red), and the open conformations (purple), respectively. Note that binding of KA and Dom displaces one of the key surrogate water molecules, which are present in the L-Glu-bound crystal. Nonpolar hydrogens are omitted for clarity.

has shown that Dom induces domain closure of 12.3°, KA elicits an intermediate closure of 23.3°, whereas the degree of domain closure with SYM 2081, QA, and L-Glu are between 26.2° to 26.6° (Mayer, 2005; Nanao et al., 2005). Consequently, our electrophysiological data support the current view that agonist efficacy is determined by the degree of closure in the GluK2 ABD (Mayer, 2005; Nanao et al., 2005).

To look at domain closure and binding mode, we performed in silico ligand-docking with the same series of receptor agonists using FITTED (Fig. 4, D–F). FITTED is a suite of programs that is unique in that the fitting process permits flexibility in macromolecules (side chains and main chains) and the presence of bridging water molecules while treating protein/ligand complexes as realistic dynamic systems (Corbeil et al., 2007). These characteristics are particularly relevant to the iGluR ABD because ligand and protein flexibility as well as water molecule mobility are critical determinants of agonist behavior (Arinaminpathy et al., 2006). In practical terms, agonists were docked to previously published structures of GluK2 that together represent the closed, intermediate or open conformation of the ABD (see *Materials and Methods* for details). It is important to emphasize that the final structure only ever represents a composite of these input structures and that FITTED cannot predict a completely novel structure. Upon convergence of the fitting process, we were able to assign a preferred conformation of the GluK2 ABD to each agonist.

In agreement with published X-ray crystal structures (Mayer, 2005; Nanao et al., 2005), the full agonist, L-Glu, selected the closed conformation (Fig. 4D), whereas the partial agonists, KA and Dom, selected intermediate and open conformations, respectively. Superimposition of the agonist-receptor complexes observed with FITTED and published X-ray crystal structures reveal that the structures obtained by each approach were indistinguishable (Fig. 4, D–F). In support of this, comparison of the computed RMSDs between the crystal and docked structures for L-Glu, KA and Dom were 0.34, 0.46, and 1.2 Å, respectively (Table 1) indicating that the ligand pose was accurately selected for each agonist. A closer view of the GluK2 ligand-binding pocket (Fig. 4, D–F) reveals key water molecules and selected amino acid residues involved in ligand recognition. For example, Arg523 and Ala518 are involved in H-bonding with the α-carboxyl group of all ligands. In contrast, Thr690 is involved in both direct hydrogen bonding with the γ-carboxyl group and indirect interactions through surrogate water molecules. Two other full agonists previously crystallized, SYM 2081 and QA, also selected the closed clamshell conformation with small computed RMSDs (SYM 2081, 0.24 Å; QA, 2.0 Å; Table 1). Taken together, our findings validate the use of FITTED in providing information on the conformational state adopted by the GluK2 ABD bound by different receptor agonists.

Agonist Efficacy and Predictions of Domain Closure Do Not Correlate. We next broadened our analysis to include all L-Glu analogs. With the exception of KA and Dom, FITTED predicted that all amino acids bind preferentially to the closed conformation, suggesting that agonist efficacy and the degree of closure in the GluK2 ABD are apparently not correlated (Fig. 5). At first glance, this result was perplexing, because it suggests that weak partial agonists, such as stereoisomers of Asp or Ser, elicit similar degrees of conformational change as L-Glu (Fig. 5B). Our immediate concern was

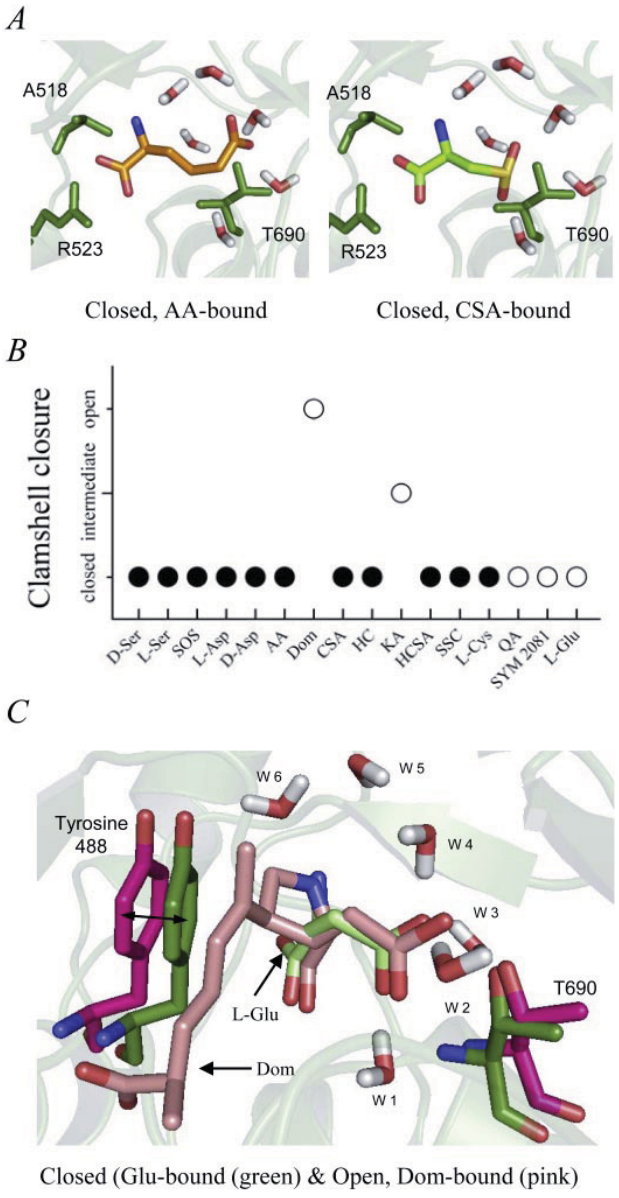

Fig. 5. Tyrosine 488 prevents full cleft closure with domoate and kainate. A, docking of L-aminoadipate (AA; left) and CSA (right) to GluK2 KARs using FITTED selects the closed conformation (green) in each case. The modeled structures are shown in orange and green, respectively. B, summary plot showing the conformation selected by each L-Glu analog using FITTED. Agonists previously cocrystallized with GluK2 are labeled as open circles, whereas the conformation selected by newly identified ligands is denoted by a filled circle. C, superimposition of the GluK2 ABD in complex with L-Glu (green) and Dom (pink). Note that different shading intensities have been used to distinguish between amino acid residues in the GluK2 ABD from the agonist molecule. In addition, only the protein backbone of the closed conformation is illustrated. Note that the pyrrolidine ring of Dom elicits a displacement of the Tyr488 residue as well as a water molecule (W6) normally found in the L-Glu-bound crystal structure. It is noteworthy that KA has the same effect though to a lesser extent because of to its smaller side-chain that extends from the pyrrolidine ring. Agonists, water molecules, and selected key residues are shown as sticks. Nonpolar hydrogens have been omitted for clarity.

that the outcome of the modeling represented a local minimum in the fitting process that is nonsensical from a biological perspective. However, we excluded this on two counts. First, FITTED already predicted the correct docking orientation of ligands previously crystallized with the GluK2 ABD (see Figure 4). Second, the binding mode of all other docked agonists was comparable with the binding orientation observed with L-Glu as would be expected. Typical binding orientation is illustrated by a visual inspection of the GluK2 ligand-binding pocket docked with L-α-aminoadipate and L-homocysteine sulfinic (Fig. 5A). In each case, the α-carboxyl groups of both partial agonists are predicted to form H-bonds with Ala518, Arg523, and AlaA689 (Fig. 5A), whereas the α-amino group is predicted to interact with Pro516 and Glu738 (data not shown). As expected, FITTED predicts that the terminal-carbon interacts with Thr690 via direct H-bonding and surrogate water molecules.

An additional concern was that the limited number of structures of the KAR ABD may bias the outcome of our analysis with FITTED. Although important to consider, we feel that this issue is not critical in our case, because the structures we have used cover an appreciable range of cleft closure in the GluK2 ABD from 12.3° for Dom to 26.2° to 26.6° for L-Glu (Mayer, 2005; Nanao et al., 2005). Furthermore, these structures represent the preferred conformations of full agonists (i.e., L-Glu, SYM 2081, and QA) to moderate and weak partial agonists (e.g., KA, Dom). FITTED does not provide information on whether the ABD adopts discrete or a limitless range of conformations after agonist binding. Nor does it identify any putative twist motion proposed from molecular dynamics to occur with partial agonists acting on GluA2 AMPARs (Bjerrum and Biggin, 2008). However, given these limitations, FITTED still permits us to examine the more general issue of whether there is any proposed relationship between cleft closure and agonist efficacy.

It is not wholly surprising that FITTED predicts that weak partial agonists, such as Asp or Ser, elicit the same degree of domain closure as full agonists, such as L-Glu, especially because almost all ligands used in this study have compact structures. Consequently, it is reasonable that most of the agonists we have docked using FITTED prefer the closed rather than the open or intermediate conformation of the KAR ABD. This conclusion is supported by recent work on AMPARs that has established the precedence that agonist efficacy need not be correlated with the degree of cleft closure (Zhang et al., 2008). Specifically, Zhang et al. (2008) found that mutation of the Thr686 residue of the GluA2 AMPAR renders L-Glu a partial agonist but yet structural changes elicited are indistinguishable from wild-type receptors. The exceptions to this at GluK2 receptors are KA and Dom, which prefer the intermediate and open conformations. However, as explained below, this observation can be simply accounted for by steric hindrance within the KAR ABD that limits the closure achieved by more bulky ligands, such as KA and Dom.

Domain Closure Is Determined by Ligand Interaction with Tyrosine 488. If the degree of closure in the ABD is not correlated with agonist efficacy, what is the basis for differences in closure observed with some agonists? Visual inspection of the ligand-bound complexes predicted by FITTED reveals an important property of the GluK2 ABD unique to Dom- and KA-bound structures (Fig. 5C). Specifically, the large side chain that extends from position 4 on the pyrrolidine ring of Dom causes a translational motion of Tyr488 that prevents complete closure of the GluK2 ABD. Likewise, the shorter side chain extending from the pyrrolidine ring of KA also causes steric hindrance but to a lesser extent accounting for the intermediate closure of the ABD. In contrast, all other amino acids tested, including the full agonist L-Glu, do not interact directly with Tyr488 and, because of their compact structure, allow complete closure of the agonist-binding pocket (Fig. 5B). The exception to this is QA, which possesses a bulky oxadiazolidine ring (Fig. 1). In this case, however, the ring structure of QA occupies a different region of the GluK2 ABD from the pyrrolidine ring of Dom and KA. Consequently, QA binds to GluK2 permitting complete closure of the ABD.

Conformational Changes Elicited by D- and L-Asp Are Indistinguishable from L-Glu. Although docking experiments with FITTED predicts that weak partial agonists, such as D- and L-Asp, bind to the closed conformation of the GluK2 ABD, it was nevertheless important to demonstrate this experimentally. To do this, we examined GluK2 responses after pretreatment with Con-A (Fig. 6). Con-A binds to a number of *N*-glycosylated residues in and around the GluK2 ABD (Fay and Bowie, 2006). In the resting or apo state of the GluK2 ABD, access to these sites is unrestricted; as a result, Con-A can bind to the receptor. Con-A binding in turn leads to the up-regulation of GluK2 responses as we have described previously (Bowie et al., 2003; Fay and Bowie, 2006). A typical experiment showing this effect is illustrated in Fig. 6A. Note that the equilibrium/peak response ratio to 10 mM L-Glu increased to 21.8 ± 2.9% after pretreatment with Con-A (10 μM, 3 mins) (Fig. 6, A and C). Conversely, if appreciable conformational changes are induced in the GluK2 ABD, such as occurs after L-Glu binding (Fay and Bowie, 2006), Con-A access to its binding sites are significantly restricted. As a consequence, pretreatment with Con-A has only a modest effect on the GluK2 response. In the example shown in Fig. 6A, the equilibrium/peak response ratio to L-Glu observed after pretreatment with Con-A was increased only to 6.7 ± 1.8% (Fig. 6, A and C).

State-dependent modulation by Con-A was therefore used to report the conformational changes elicited by D- and L-Asp. As positive controls, we compared the amount of modulation observed when GluK2 receptors were preincubated with Con-A and one of three agonists (i.e., 10 mM L-Glu, 1 mM KA, or 50 μM Dom) (Fig. 6, A and C). We have shown previously that Con-A modulation of GluK2 receptors preincubated with Glu, KA, or Dom corresponds to the closed, intermediate, or open states of the ABD, respectively (Fay and Bowie, 2006) (Fig. 6C). As negative controls, we examined pharmacological compounds that would not be expected to induce significant closure of the GluK2 ABD that were the competitive antagonist, 6-cyano-7-nitroquinoxaline-2,3-dione (CNQX), as well as the ion-channel blocker philanthotoxin (PhTX). Although CNQX induces modest closure in the AMPAR ABD by acting as a partial agonist (Menuz et al., 2007), this effect has not been observed at KARs; consequently, we have assumed it behaves as a competitive antagonist.

As expected, preincubation with CNQX or PhTX did not interfere with the degree of modulation of GluK2 receptors by Con-A (Fig. 6, B and C). In support of this, the degree of Con-A modulation observed with CNQX or PhTX was similar

to that observed for the open conformation of the GluK2 ABD but statistically distinct from the closed or intermediate (Table 2). These findings suggest that occupancy of the pore with a channel blocker or the ABD with a competitive antagonist does not evoke appreciable closure of the GluK2 ABD. In contrast, preincubation with either D- or L-Asp significantly reduced the degree of Con-A modulation (Fig. 6, B and C). In support of this, the degree of Con-A modulation observed with D-Asp or L-Asp was similar to that observed for the closed conformation of the GluK2 ABD but statistically distinct from the open or intermediate (Table 2). This finding further supports the central tenet of our study that weak partial agonists, such as D- and L-Asp, elicit conformational changes in the GluK2 ABD that are indistinguishable from conformations elicited by the full agonist, L-Glu.

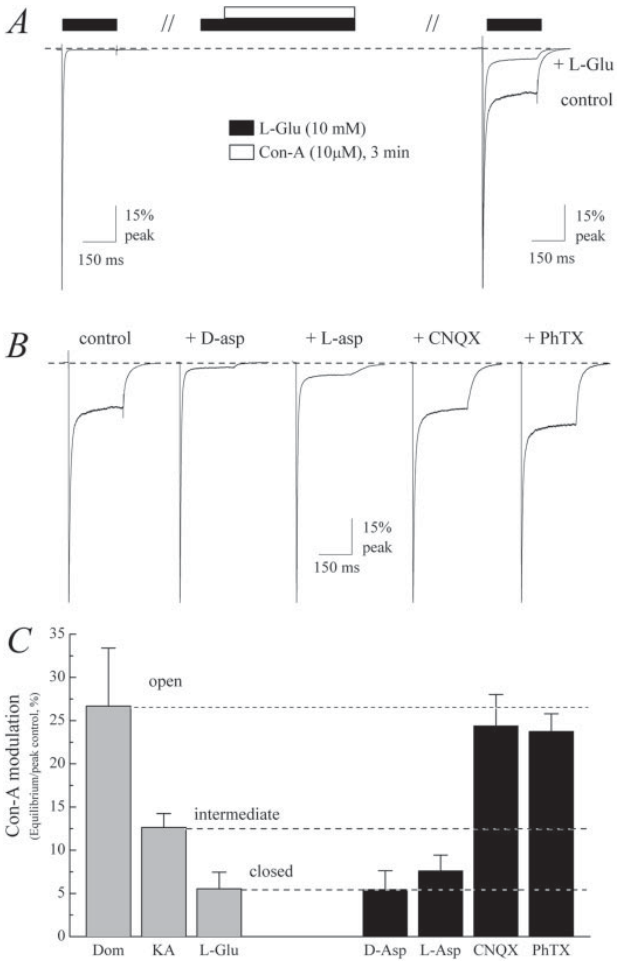

Fig. 6. Conformational changes elicited by L-Glu and stereoisomers of Asp to the GluK2 agonist-binding pocket are indistinguishable. A, typical experiment showing how modulation by Con-A reports conformational changes in the GluK2 ABD (for details, see Fay and Bowie, 2006). Con-A binds to a number of *N*-glycosylated residues in and around the GluK2 ABD. If agonist is bound, access to these sites is restricted; as a result, Con-A has a much weaker effect on the L-Glu equilibrium response. In the example shown, the equilibrium response is much smaller after coapplication of Con-A and L-Glu (10 mM; patch number 030724p2) than when Con-A is applied alone (control; patch number 01817p6). Filled and open bars indicate the application period of 10 mM L-Glu and 10 μM Con-A, respectively. The dotted line denotes the zero current level. The first and third applications of 10 mM Glu had a duration of 250 ms. B, experimental traces showing the extent of Con-A modulation as described in A, with D-Asp (patch number 071018p3), L-Asp (patch number 07906p1), CNQX (patch number 07913p2), and philanthotoxin (PhTX, patch number 07104p1) compared with control. C, Summary bar graphs showing the extent of Con-A modulation after cotreatment with various pharmacological agents (L-Glu, $n = 13$; D-Asp, $n = 4$; L-Asp, $n = 4$; CNQX, $n = 3$; PhTX, $n = 3$). The dotted lines on the graph denote the extent of Con-A modulation observed for the open, intermediate, and closed conformations of the GluK2 ABD, which we have described previously (A.-M.L. Fay and D. Bowie, 2006). CNQX and PhTX adopt the open conformation of the GluK2 ABD because their degree of Con-A modulation exactly matches that observed with Dom. In contrast, both D- and L-Asp adopt the closed conformation because modulation with Con-A is statistically indistinguishable from that observed with L-Glu. All data are expressed as the mean ±S.E.M.

Although these observations are consistent with Con-A reporting conformational changes in the GluK2 ABD, it was nevertheless important to evaluate alternate explanations. For example, it is possible that Con-A modulation reveals that stereoisomers of Asp adopt a desensitized conformation similar to that L-Glu instead of reporting the extent of cleft closure. This possibility, however, is unlikely for three main reasons. First, there is no available evidence to suggest that conformational changes in the dimer interface that accompany the onset of AMPA or KAR desensitization are agonist-dependent (Armstrong et al., 2006; Weston et al., 2006), which would be required to explain Con-A's effects. Second, Con-A binding and consequently modulation of GluK2 is almost entirely eliminated by mutation of three key N-terminal amino acid residues that do not participate in forming the dimer interface (Fay and Bowie, 2006). Although residues distant from the dimer interface may still regulate KAR desensitization, GluK2 receptors that lack the N-terminal desensitize normally (Plested and Mayer, 2007), suggesting that this region of the intact receptor is not functionally coupled to the dimer interface. Third and finally, Con-A does not affect rates into or out of desensitization (Bowie et al., 2003; Fay and Bowie, 2006), which would not be expected if lectin binding reports separation in the dimer interface. Given this, the most parsimonious explanation of our data is that Con-A reports conformational changes in the ABD of GluK2 receptor as discussed in detail elsewhere (Fay and Bowie, 2006).

Discussion

To our knowledge, this study is the first to identify a series of structurally related amino acids that exhibit the entire range of agonist behavior at KARs. Analysis of their struc-

TABLE 2
Statistical comparisons between the degree of Con-A modulation observed with different GluK2 receptor ligands

The ability of stereoisomers of Asp, CNQX, and PhTX to affect Con-A modulation of GluK2 receptors was compared with the modulation observed with L-Glu, KA, and Dom using Student's *t* test. The modulation observed by preincubating with stereoisomers of Asp was statistically significant from that observed with KA and Dom but indistinguishable from L-Glu. In contrast, the modulation observed by pre-incubating with CNQX or PhTX was statistically significant from that observed with L-Glu and KA but indistinguishable from Dom.

Ligand	L-Glu (Closed)	KA (Intermediate)	Dom (Open)
D-Asp	N.S.	*	*
L-Asp	N.S.	*	*
PhTX	**	**	N.S.
CNQX	**	**	N.S.

N.S., not significant.
* Significant at $P < 0.05$.
** Significant at $P < 0.01$.

ture-function relationship reveals that the agonist binding pocket of KARs is ideally suited to respond to the neurotransmitter, L-Glu, because modest changes in its chain length generates weak partial agonists. Using both in silico docking as well as measurements of conformations in the intact receptor, we show that the majority of full and partial agonists select for the closed conformation of the GluK2 ABD. Although this finding is not wholly surprising given the compact structures of most ligands tested, it is inconsistent with agonist efficacy being solely determined by the extent of closure in the KAR ABD. Exceptions to this were the partial agonists, KA and Dom, which select for the open and intermediate conformations, respectively. However this finding can be simply explained by steric hindrance due to the Tyr 488 residue in domain 1 of the GluK2 ABD. Our findings suggest the value in looking more closely at the relationship between agonist efficacy and the extent of agonist-induced domain closure in KARs.

Can Other Mechanisms Account for Agonist Efficacy at Kainate Receptors? Although the view that agonist efficacy is governed by closure in the ABD has gained much popularity, recent work on AMPARs has identified a different mechanism (though not mutually exclusive) (Robert et al., 2005; Zhang et al., 2008) that may also account for full and partial agonist behavior at KARs. In essence, it is argued that the time the ABD remains in the closed conformation determines several gating properties of AMPARs including agonist efficacy, deactivation rates as well as apparent agonist affinity. For L-Glu, closed-cleft stability is optimized by direct and indirect interactions with domains 1 and 2 of the AMPAR ABD, which permit L-Glu to attain full agonist activity while exhibiting rapid unbinding (Robert et al., 2005; Zhang et al., 2008), essential features for any fast-acting neurotransmitter. In the specific case of AMPARs, mutation of a key threonine (i.e., Thr686) residue in domain 2 of the GluR2 ABD, disrupts the optimization established between the ligand and receptor. As a result, L-Glu is rendered a weak partial agonist with much lower affinity (Robert et al., 2005).

There are several reasons to suggest that basic elements of the mechanism proposed by Zhang et al. (2008) may also account for differences in efficacy between L-Glu and stereoisomers of Asp reported in this study. First, activation curves of partial agonists D- and L-Asp are shifted rightward compared with the full agonist L-Glu (Fig. 3, C and D), suggesting that, in this case, agonist efficacy and affinity may be tightly correlated. Second, deactivation rates for stereoisomers of Asp (e.g., D-Asp, $\tau = 1.2 \pm 0.3$ ms) were faster than with L-Glu ($\tau = 2.6 \pm 0.2$ ms) (Bowie, 2002). Third and finally, the more extended structure of L-Glu permits more contact points (direct and indirect) to be established with the GluK2 ABD than with D- or L-Asp (Fig. 7). This difference in agonist binding would be expected to weaken the stability of the closed GluK2 ABD. It is noteworthy that L-Asp formed considerably less contacts than D-Asp or L-Glu, which may explain its weaker responsiveness based on analysis of activation curves (Fig. 3D). Although more work is required to rigorously test this model, it provides a valuable framework for future work on agonist behavior at KARs.

Are Amino Acids Other Than L-Glu Suitable Neurotransmitter Candidates at Kainate Receptors? Several of the amino acids examined in this study are endogenous to the CNS and have been previously evaluated as neurotrans-

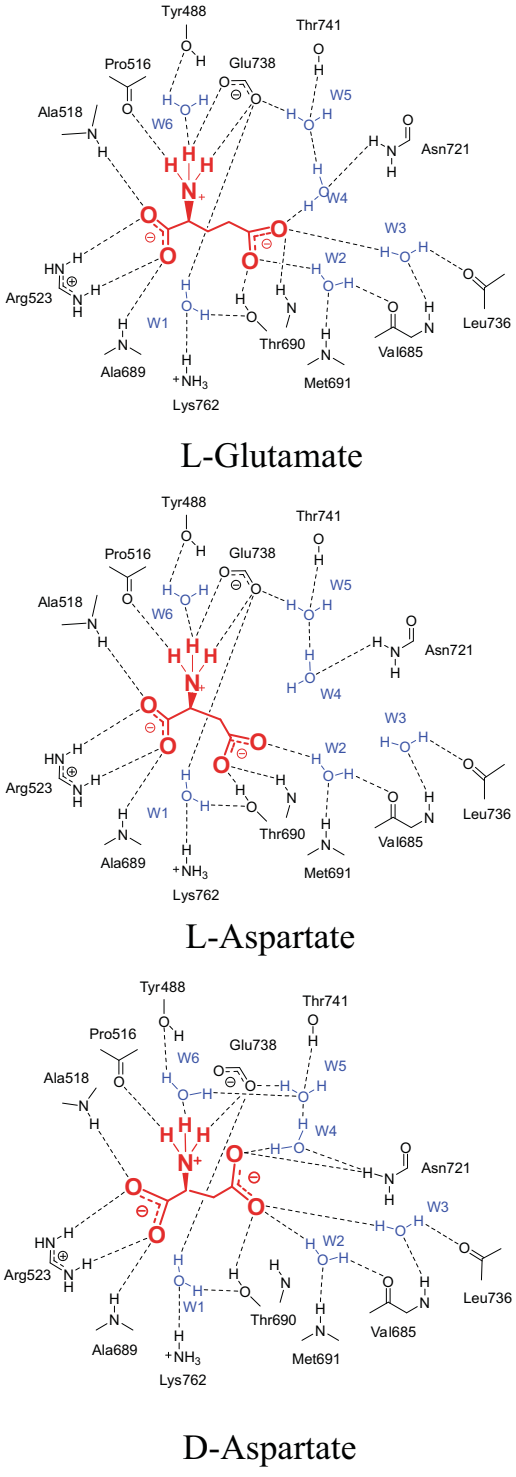

Fig. 7. Stereoisomers of Asp establish fewer contact points with the GluK2 agonist binding pocket than L-Glu. Two-dimensional topographical maps of the GluK2 ABD shows that the number of contact points and the binding orientation of the full agonist, L-Glu, and partial agonists, D- and L-Asp. Topographical maps were deduced from structure complexes obtained with FITTED. Note the number of contact points made by D- and L-Asp was fewer than with L-Glu. In addition, the binding orientation is different between L- and D-Asp, which would be expected for stereoisomers of the same amino acid.

mitter candidates at glutamatergic synapses. The candidature of sulfur-containing amino acids, which include L-Cys, HC, SSC, and HCSA, was considered after mechanisms that lead to their release, uptake, and responsiveness (see below) were identified (Do et al., 1986; Bouvier et al., 1991). Recent attention has focused on their potent activation of metabotropic glutamate receptors (e.g., Kingston et al., 1998). However, earlier work demonstrated that they also activate iGluRs (Thompson and Kilpatrick, 1996). At the time, most investigators argued for their greater ability to activate NMDARs than AMPARs (Patneau and Mayer, 1990); however, their effect on KARs was never tested, because evidence for the existence of this iGluR subclass had yet to emerge (Bowie, 2008). In view of this, our data on homomeric GluK2 receptors suggests the value in testing the responsiveness of native KARs to sulfur-containing amino acids. It is noteworthy that the most potent sulfur-containing amino acid in our experiments, L-Cys, is a very weak partial agonist on homomeric GluR1 AMPARs (A.-M.L. Fay and D. Bowie, unpublished observations). Therefore, it would be interesting in future work to determine whether different non-NMDA receptor subtypes discriminate among sulfur-containing amino acids.

In comparison, there is more compelling evidence linking the stereoisomers of both serine and aspartate to roles in glutamatergic transmission (Boehning and Snyder, 2003). D-Ser was considered in this capacity only after it was shown to act as a coagonist at the glycine binding site of NMDARs (McBain et al., 1989). Because D-serine is expressed in discrete populations of glial cells opposed to NMDARs (Schell et al., 1997a), it has been categorized as a gliotransmitter (Mothet et al., 2000; Panatier et al., 2006). The role of D-Asp is more elusive, although it is found in the developing and adult brain (Schell et al., 1997b). Accumulation of D-Asp in CNS tissue has marked behavioral consequences, such as impaired motor coordination (Weil et al., 2006), which is consistent with its putative role as a transmitter at the climbing fibers of the cerebellum (Wiklund et al., 1982). Likewise, L-Asp's role in neurotransmission has centered on NMDARs (Fleck et al., 1993), although it elicits a high calcium conductance in cerebellar Purkinje cells that apparently involves a novel iGluR (Yuzaki et al., 1996). Our study shows that D- and L-forms of each amino acid are weak partial agonists and, although these properties are not normally expected of a neurotransmitter candidate, it may be interesting to evaluate their roles at native KAR-containing synapses.

Conclusion

It is puzzling that not all iGluR subunits respond to the neurotransmitter L-Glu. In fact, neither the NR1 NMDAR subunit nor the orphan-class δ-2 (δ2) subunit even binds L-Glu. Because the ancestral iGluR, GluR0, possesses an L-Glu binding pocket (Chen et al., 1999), it is conceivable that evolving NR1 and δ2 subunits sacrificed this ability to serve more specialized roles in the mammalian CNS. In this regard, it is interesting that NMDARs (McBain et al., 1989) and orphan-class δ2 iGluR (Naur et al., 2007) retained their ability to bind D-Ser. Likewise, AMPARs (P. Brown and D. Bowie, unpublished observations) and KARs (present study) are also gated by D-Ser (and D-Asp) suggesting that these naturally occurring D-amino acids discriminate little among iGluR families. Whether this observation is a peculiarity of iGluRs that holds little biological significance or hints at a broader role for D-amino acids at glutamatergic synapses awaits future investigation.

Acknowledgments

We are grateful to David MacLean, Mark Aurousseau, and Elizabeth Andrews for discussions during the course of this work and Drs. G. Miller and R. Blunck for comments on the manuscript. We thank the Réseau québécois de calcul de haute performance for allocation of computer resources for this study.

References

Arinaminpathy Y, Sansom MS, and Biggin PC (2006) Binding site flexibility: molecular simulation of partial and full agonists within a glutamate receptor. *Mol Pharmacol* **69:**11–18.
Armstrong N and Gouaux E (2000) Mechanisms for activation and antagonism of an AMPA-sensitive glutamate receptor: crystal structures of the GluR2 ligand binding core. *Neuron* **28:**165–181.
Armstrong N, Jasti J, Beich-Frandsen M, and Gouaux E (2006) Measurement of conformational changes accompanying desensitization in an ionotropic glutamate receptor. *Cell* **127:**85–97.
Bjerrum EJ and Biggin PC (2008) Rigid body essential X-ray crystallography: distinguishing the bend and twist of glutamate receptor ligand binding domains. *Proteins* **72:**434–446.
Boehning D and Snyder SH (2003) Novel neural modulators. *Annu Rev Neurosci* **26:**105–131.
Bouvier M, Miller BA, Szatkowski M, and Attwell D (1991) Electrogenic uptake of sulphur-containing analogues of glutamate and aspartate by muller cells from the salamander retina. *J Physiol* **444:**441–457.
Bowie D (2002) External anions and cations distinguish between AMPA and kainate receptor gating mechanisms. *J Physiol* (*Lond*) **539:**725–733.
Bowie D (2008) Ionotropic glutamate receptors & CNS disorders. *CNS Neurol Disord Drug Targets* **7:**129–143.
Bowie D, Garcia EP, Marshall J, Traynelis SF, and Lange GD (2003) Allosteric regulation and spatial distribution of kainate receptors bound to ancillary proteins. *J Physiol* (*Lond*) **547:**373–385.
Chen GQ, Cui C, Mayer ML, and Gouaux E (1999) Functional characterization of a potassium-selective prokaryotic glutamate receptor. *Nature* **402:**817–821.
Collingridge GL, Olsen RW, Peters J, and Spedding M (2009) A nomenclature for ligand-gated ion channels. *Neuropharmacology* **56:**2–5.
Corbeil CR, Englebienne P, and Moitessier N (2007) Docking ligands into flexible and solvated macromolecules. 1. Development and validation of FITTED 1.0. *J Chem Inf Model* **47:**435–449.
Do KQ, Mattenberger M, Streit P, and Cuénod M (1986) In vitro release of endogenous excitatory sulfur-containing amino acids from various rat brain regions. *J Neurochem* **46:**779–786.
Fay AM and Bowie D (2006) Concanavalin-A reports agonist-induced conformational changes in the intact glur6 kainate receptor. *J Physiol* **572:**201–213.
Fleck MW, Henze DA, Barrionuevo G, and Palmer AM (1993) Aspartate and glutamate mediate excitatory synaptic transmission in area CA1 of the hippocampus. *J Neurosci* **13:**3944–3955.
Inanobe A, Furukawa H, and Gouaux E (2005) Mechanism of partial agonist action at the NR1 subunit of NMDA receptors. *Neuron* **47:**71–84.
Jin R, Banke TG, Mayer ML, Traynelis SF, and Gouaux E (2003) Structural basis for partial agonist action at ionotropic glutamate receptors. *Nat Neurosci* **6:**803–810.
Kingston AE, Lowndes J, Evans N, Clark B, Tomlinson R, Burnett JP, Mayne NG, Cockerham SL, and Lodge D (1998) Sulphur-containing amino acids are agonists for group 1 metabotropic receptors expressed in clonal RGT cell lines. *Neuropharmacology* **37:**277–287.
Mayer ML (2005) Crystal structures of the glur5 and glur6 ligand binding cores: molecular mechanisms underlying kainate receptor selectivity. *Neuron* **45:**539–552.
McBain CJ, Kleckner NW, Wyrick S, and Dingledine R (1989) Structural requirements for activation of the glycine coagonist site of *N*-methyl-D-aspartate receptors expressed in *Xenopus* oocytes. *Mol Pharmacol* **36:**556–565.
Menuz K, Stroud RM, Nicoll RA, and Hays FA (2007) TARP auxiliary subunits switch AMPA receptor antagonists into partial agonists. *Science* **318:**815–817.
Mothet JP, Parent AT, Wolosker H, Brady RO Jr, Linden DJ, Ferris CD, Rogawski MA, and Snyder SH (2000) D-Serine is an endogenous ligand for the glycine site of the *N*-methyl-D-aspartate receptor. *Proc Natl Acad Sci U S A* **97:**4926–4931.
Nanao MH, Green T, Stern-Bach Y, Heinemann SF, and Choe S (2005) Structure of the kainate receptor subunit GluR6 agonist-binding domain complexed with domoic acid. *Proc Natl Acad Sci U S A* **102:**1708–1713.
Naur P, Hansen KB, Kristensen AS, Dravid SM, Pickering DS, Olsen L, Vestergaard B, Egebjerg J, Gajhede M, Traynelis SF, et al. (2007) Ionotropic glutamate-like receptor delta2 binds D-serine and glycine. *Proc Natl Acad Sci U S A* **104:**14116–14121.
Panatier A, Theodosis DT, Mothet JP, Touquet B, Pollegioni L, Poulain DA, and Oliet SH (2006) Glia-derived D-serine controls NMDA receptor activity and synaptic memory. *Cell* **125:**775–784.
Patneau DK and Mayer ML (1990) Structure-activity relationships for amino acid

transmitter candidates acting at *N*-methyl-D-aspartate and quisqualate receptors. *J Neurosci* **10:**2385–2399.
Plested AJ and Mayer ML (2007) Structure and mechanism of kainate receptor modulation by anions. *Neuron* **53:**829–841.
Robert A, Armstrong N, Gouaux JE, and Howe JR (2005) AMPA receptor binding cleft mutations that alter affinity, efficacy, and recovery from desensitization. *J Neurosci* **25:**3752–3762.
Schell MJ, Brady RO, Jr., Molliver ME, and Snyder SH (1997a) D-Serine as a neuromodulator: regional and developmental localizations in rat brain glia resemble NMDA receptors. *J Neurosci* **17:**1604–1615.
Schell MJ, Cooper OB, and Snyder SH (1997b) D-Aspartate localizations imply neuronal and neuroendocrine roles. *Proc Natl Acad Sci U S A* **94:**2013–2018.
Stern-Bach Y, Bettler B, Hartley M, Sheppard PO, O'Hara PJ, and Heinemann SF (1994) Agonist-selectivity of glutamate receptors is specified by two domains structurally related to bacterial amino acid binding proteins. *Neuron* **13:**1345–1357.
Thompson GA and Kilpatrick IC (1996) The neurotransmitter candidature of sulphur-containing excitatory amino acids in the mammalian central nervous system. *Pharmacol Ther* **72:**25–36.
Weil ZM, Huang AS, Beigneux A, Kim PM, Molliver ME, Blackshaw S, Young SG, Nelson RJ, and Snyder SH (2006) Behavioural alterations in male mice lacking the gene for D-aspartate oxidase. *Behav Brain Res* **171:**295–302.
Weston MC, Schuck P, Ghosal A, Rosenmund C, and Mayer ML (2006) Conformational restriction blocks glutamate receptor desensitization. *Nat Struct Mol Biol* **13:**1120–1127.
Wiklund L, Toggenburger G, and Cuénod M (1982) Aspartate: possible neurotransmitter in cerebellar climbing fibers. *Science* **216:**78–80.
Wong AY, Fay AM, and Bowie D (2006) External ions are coactivators of kainate receptors. *J Neurosci* **26:**5750–5755.
Yuzaki M, Forrest D, Curran T, and Connor JA (1996) Selective activation of calcium permeability by aspartate in purkinje cells. *Science* **273:**1112–1114.
Zhang W, Cho Y, Lolis E, and Howe JR (2008) Structural and single-channel results indicate that the rates of ligand binding domain closing and opening directly impact AMPA receptor gating. *J Neurosci* **28:**932–943.

Address correspondence to: Dr. Derek Bowie, Department of Pharmacology and Therapeutics, McIntyre Medical Sciences Building, Room 1317, McGill University, 3655 Promenade Sir William Osler, Montreal, Québec, Canada H3A 1Y6. E-mail: derek.bowie@mcgill.ca

The following article is reprinted with permission from:

Demmer, C. S.; Møller, C.; Brown, P. M. G. E.; Han, L.; Pickering, D. S.; Nielsen, B.; Bowie, D.; Frydenvang, K.; Kastrup, J. S. & Bunch, L. Binding mode of an alpha-amino acid-linked quinoxaline-2,3-dione analogue at glutamate receptor subtype GluK1. *ACS chemical neuroscience,* **2015***, 6*, 845-854

ACS Chemical Neuroscience

Research Article

pubs.acs.org/chemneuro

Binding Mode of an α-Amino Acid-Linked Quinoxaline-2,3-dione Analogue at Glutamate Receptor Subtype GluK1

Charles S. Demmer,[†] Charlotte Møller,[‡] Patricia M. G. E. Brown,[#] Liwei Han,[∥] Darryl S. Pickering,[∥] Birgitte Nielsen,[§] Derek Bowie,[#] Karla Frydenvang,[‡] Jette S. Kastrup,*[,‡] and Lennart Bunch*[,†]

[†]Chemical Neuroscience Group, [‡]Biostructural Research Group, [§]Medicinal Chemistry Group, [∥]Molecular and Cellular Pharmacology Group, and [⊥]Molecular Pharmacology Group, Department of Drug Design and Pharmacology, Faculty of Health and Medical Sciences, University of Copenhagen, Copenhagen, Denmark

[#]Bowie Lab, Department of Pharmacology & Therapeutics, Faculty of Medicine, McGill University, Montreal, Canada H3G 0B1

Supporting Information

ABSTRACT: Two α-amino acid-functionalized quinoxalines, **1a** (CNG-10301) and **1b** (CNG-10300), of a quinoxaline moiety coupled to an amino acid moiety were designed, synthesized, and characterized pharmacologically. While **1a** displayed low affinity at native AMPA, KA, and NMDA receptors, and at homomeric GluK1,3 receptors, the affinity for GluK2 was in the midmicromolar range (K_i = 136 μM), **1b** displayed low to midmicromolar range binding affinity at all the iGluRs (K_i = 9−126 μM). In functional experiments (outside-out patches excised from transfected HEK293T cells), 100 μM **1a** partially blocked GluK1 (33% peak response), while GluK2 was unaffected (96% peak response). Furthermore, **1a** was shown not to be an agonist at GluK1 and GluK2 at 100 μM. On the other hand, 100 μM **1b** fully antagonized GluK1 (8% peak response) but only partially blocked GluK2 (33% peak response). An X-ray structure at 2.3 Å resolution of **1b** in the GluK1-LBD (ligand-binding domain) disclosed an unexpected binding mode compared to the predictions made during the design phase; the quinoxaline moiety remains to act as an amino acid bioisostere, but the amino acid moiety is oriented into a new area within the GluK1 receptor. The structure of the GluK1-LBD with **1b** showed a large variation in domain openings of the three molecules from 25° to 49°, demonstrating that the GluK1-LBD is capable of undergoing major domain movements.

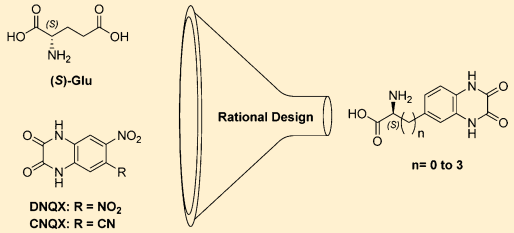

KEYWORDS: *Design, synthesis, radioligand binding, X-ray crystallography, domain opening*

INTRODUCTION

The common α-amino acid (*S*)-glutamate (Glu) is the major excitatory neurotransmitter of the mammalian central nervous system (CNS). The glutamatergic neurotransmitter system is involved in a vast number of neurological processes such as memory and learning, plasticity, and motor function,[1,2] and thus also in the pathogenesis of many neurological and psychiatric disorders. The class of fast-acting ionotropic Glu receptors (iGluRs) is divided into three groups that again comprise a number of subunits [AMPA receptors GluA1−4, kainic acid (KA) receptors[3−5] GluK1−5, and NMDA receptors[6] GluN1, GluN2A-D, and GluN3A,B]. The iGluRs form ligand-gated ion channels consisting of four subunits, with each subunit having an extracellular region composed of the N-terminal domain and the ligand-binding domain (LBD), a transmembrane region, and a C-terminal region. The LBD forms a clamshell-like domain with the glutamate-binding site located within two lobes designated D1 and D2.

A number of competitive antagonists that discriminate among the AMPA, KA, and NMDA receptors have been reported.[7] However, it remains a challenge to discover antagonists, which display selectivity among the subunits within one of these groups. In fact, only GluK1-selective competitive antagonists have been reported to date [e.g., LY466195[8] (Figure 1 and Table 1].[7] There is therefore an unmet need for the creative design of new chemical scaffolds that eventually can be developed into antagonists with a novel subunit selectivity profile. Such chemical probes are key tools in the elucidation of the role and function of Glu receptors in health and disease.

RESULTS AND DISCUSSION

Design. Some 20 years ago, a series of substituted quinoxaline-2,3(1*H*,4*H*)-diones [DNQX and CNQX (Figure 1 and Table 1)] were identified as potent competitive AMPA/KA receptor antagonists.[9] Interestingly, the quinoxaline-2,3-(1*H*,4*H*)-dione moiety acts as an α-amino acid bioisostere[10] as disclosed by X-ray crystallographic studies.[11,12]

A potentially new class of iGluR antagonists was designed with the general molecular formula I (Figure 2). Via the linkage of an α-amino acid to the quinoxaline-2,3(1*H*,4*H*)-dione

Received: September 23, 2014
Accepted: March 26, 2015

DOI: 10.1021/acschemneuro.5b00038
ACS Chem. Neurosci. XXXX, XXX, XXX−XXX

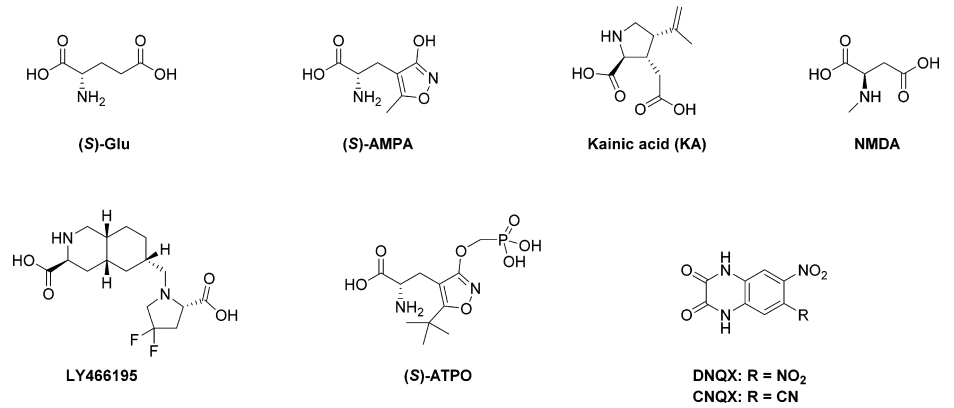

Figure 1. Chemical structures of Glu, AMPA, KA, NMDA, and competitive antagonists LY466195, (*S*)-ATPO, DNQX, and CNQX.

Table 1. Pharmacological Profiles of LY466195, ATPO, DNQX, CNQX, 1a (CNG-10301), and 1b (CNG-10300) at the iGluRs, Together with Binding Affinities of 1b at the GluK1-LBD[a]

	AMPA IC_{50}[b]	KA IC_{50}[b]	NMDA K_i[b]	GluA2 K_i[c]	GluK1 K_i[c]	GluK2 K_i[c]	GluK3 K_i[c]	GluK1-LBD K_i[c]
LY466195[d]	–	–	–	270	0.05	–	8.9	–
ATPO	16	>100	>100	60.3 ± 4.7	2.55 ± 0.43	>100	>1,000	–
DNQX	0.25[e]	0.53[e]	4.1[e]	0.254 ± 0.014	0.652 ± 0.028	2.10 ± 0.32	0.362 ± 0.033	–
CNQX	0.40[e]	0.27[e]	13[e]	0.333 ± 0.028	1.28 ± 0.30	1.49 ± 0.01	0.637 ± 0.050	–
1a (CNG-10301)	203 [3.69 ± 0.03]	>300	>200	>100 (80 ± 8%)	>100 (74 ± 3%)	136 ± 22	>100 (71 ± 5%)	–
1b (CNG-10300)	26 [4.59 ± 0.06]	126 [3.90 ± 0.02]	78 [4.12 ± 0.08]	21.3 ± 2.4	16.1 ± 1.0	9.52 ± 1.15	59.0 ± 3.2	37.1 ± 7.8

[a]All values are in micromolar. [b]Mean values ± the standard error of the mean (SEM) of three individual experiments. The following radioligands were used: AMPA receptors, [^{3}H]AMPA; KA receptors, [^{3}H]KA; NMDA receptors, [^{3}H]CGP 39653. [c]Mean values ± SEM of at least three experiments, conducted in triplicate at 12−16 ligand concentrations. In parentheses are values of percent residual specific binding at 100 μM ligand. The following radioligands were used: GluA2, [^{3}H]AMPA; GluK1−3, [^{3}H]-(2*S*,4*R*)-4-methyl-Glu (SYM2081) or [^{3}H]KA. Hill coefficients were not different from unity. [d]From ref 8. [e]Functional data from ref 9.

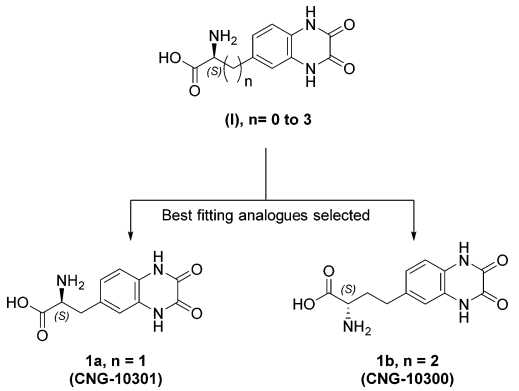

Figure 2. Design of α-amino acid-functionalized quinoxalines **1a** (CNG-10301) and **1b** (CNG-10300) as potential AMPA/KA antagonists.

moiety, the latter was initially assumed to act as a carboxylic acid bioisostere engaging in hydrogen bonding directly to the amino acid residues of the D2 domain of the receptor, or via water molecules. The pK_a value of an unsubstituted quinoxaline-2,3(1*H*,4*H*)-dione skeleton has been determined to be 9.2,[13] which calculates to approximately 1% of the ionized form at physiological pH 7.4.[10] The suitable linker length was investigated by performing a stochastic conformational search of chemical structures of the general formula I, for n = 0−3 (Figure 2). While a large variety of AMPA/KA receptor antagonists have been crystallized with GluA2-LBD and/or GluK1-LBD, the two distinct antagonists, ATPO [K_i = 2.6 μM affinity for GluK1, Protein Data Bank (PDB) entry 1VSO][14] and LY466195 (K_i = 0.05 μM affinity for GluK1,[8] PDB entry 2QS4),[15] were used as templates in the design. The study led to the conclusion that the linker length of n = 1, compound **1a** (Figure 3A) and the linker length of n = 2, compound **1b** (Figure 3B) were both attractive. In detail, one low-energy conformation of **1a** fit the pharmacophore dictated by LY466195, whereas four low-energy conformations of **1b** could be superimposed on LY466195, two being the most favorable. In comparison with LY466195, **1a** and **1b** present their hydrogen bonding functionalities to the receptor with altered distances and angles (Figure 3A,B). Such properties are in particular interesting as we were aiming to discover new scaffolds with unprecedented receptor subtype selectivity profiles.

Synthesis. A retrosynthetic analysis of target compounds **1a** and **1b** suggested the use of a protected natural α-amino acid (commercially available) as a direct source of chirality, and a Negishi cross coupling between the 6-quinoxaline moiety and the side chain of the amino acid was planned as the key step.[16,17] The synthesis of **1a** and **1b** commenced with the reduction of the carboxylic acid functionality of BOC-Asp-OBn

DOI: 10.1021/acschemneuro.5b00038
ACS Chem. Neurosci. XXXX, XXX, XXX−XXX

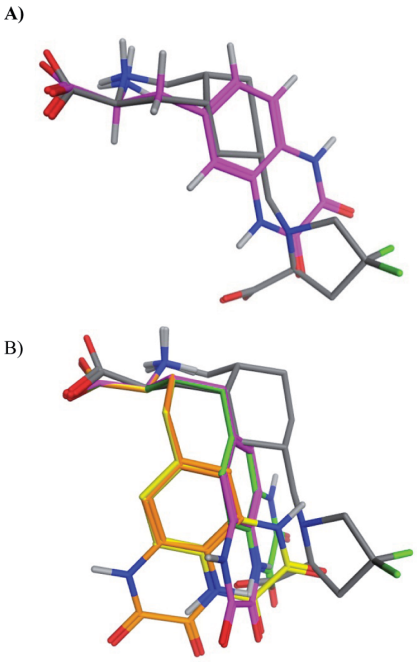

Figure 3. (A) Superimposition of a low-energy conformation of **1a** (purple) on LY466195 (gray; PDB entry 2QS4). Both compounds are colored according to atom type. (B) Superimposition of four low-energy conformations of **1b** ($\Delta\Delta G$ = 0−1 kcal/mol; yellow, orange, purple, and green) on LY466195.

2 to give the corresponding alcohol **3b**, using isobutyl chloroformate as an activator.[18] The crude product was used without further purification as this led to formation of the corresponding cyclization product due to the acidic nature of silica gel. The iodo-amino acids, **4a** and **4b**, were then generated from their corresponding alcohols **3a** (commercially available) and **3b**, respectively, by reaction with iodine under neutral conditions (triphenylphosphine and imidazole).[19] The quinoxaline moiety was successfully introduced by a palladium coupling with the organic zinc nucleophile (Negishi) from **4a** or **4b** and 6-bromo-2,3-dimethoxyquinoxaline **9**.[17] The palladium-catalyzed cross coupling was first tried out on **7** but proved to be unsuccessful, presumably because of the competing coordination of the 2,3-dicarbonyl oxygens. Possibly expectedly, 2,3-dichloroquinoxaline **8** was also unsuccessful as a coupling partner, giving a complex product mixture. Finally, **5a** and **5b** were fully deprotected in a one-pot reaction under acidic conditions, providing the HCl salt of the two target structures **1a** and **1b** (Scheme 1).

Pharmacology. With the two target compounds **1a** and **1b** in hand, they were characterized pharmacologically at rat synaptosomes (native AMPA, KA, and NMDA receptors). The compounds were also assessed at cloned homomeric GluA2 and GluK1−3 receptors, and all results are summarized in Table 1. Analogue **1a** displayed a low affinity for native iGluRs (IC_{50} or K_i of >200 μM) and cloned homomeric GluA2 and GluK1,3 receptors (K_i > 100 μM), and medium-range micromolar affinity for GluK2 (K_i = 136 μM). Analogue **1b** displayed medium-range micromolar affinity for native AMPA, KA, and NMDA receptors. The binding affinity of **1b** for AMPA receptors was confirmed at the cloned homomeric GluA2 receptor (K_i = 21 μM). At cloned homomeric GluK1−3 receptors, **1b** displayed medium-range binding affinity for GluK1−3 with K_i values of 16, 9.5, and 59 μM, respectively (Table 1). Finally, in a functional EAAT assay,[20] both **1a** and **1b** displayed no appreciable activity as inhibitors at subtypes EAAT1−3 [IC_{50} > 1000 μM (results not shown)].

Upon comparison with the four antagonists employed in the design phase [LY466195, ATPO, CNQX, and DNQX (Figure 1 and Table 1)], the broad profile of **1b** is comparable to that of DNQX and CNQX. On the other hand, a slightly GluK2 preferring profile of **1a** is surprising because LY466195 is highly

Scheme 1. Synthesis of 1a and 1b[a]

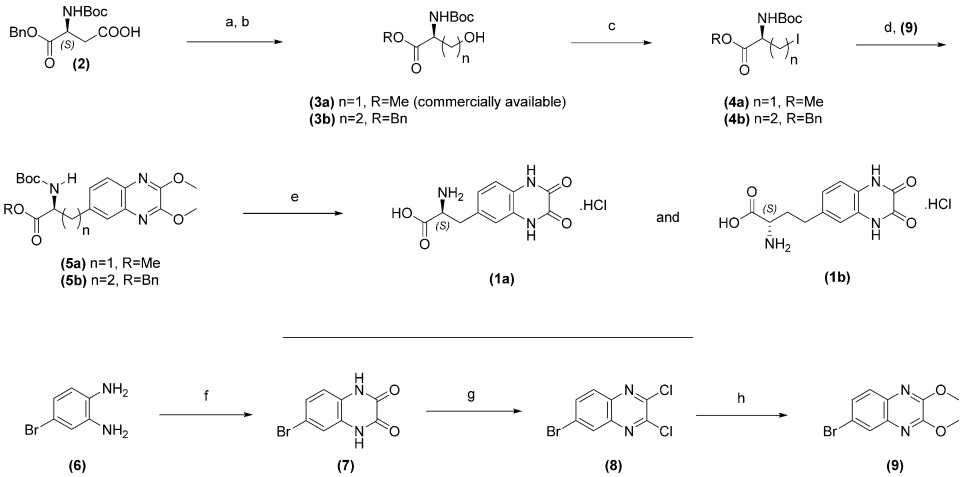

[a]Reagents and conditions: (a) *N*-methylmorpholine, isobutyl chloroformate, THF; (b) $NaBH_4$, MeOH; (c) PPh_3, imidazole, I_2, DCM (80% for R = Me, 49% over two steps for R = Bn); (d) Zn dust, I_2, Pd_2dba_3, SPhos, **9**, DMF (41% for R = Me, 35% for R = Bn); (e) 4 N HCl, H_2O, dioxane for **1a** (89%), recrystallization with propylene oxide for **1b** (68%); (f) diethyl oxalate (96%); (g) thionyl chloride, DMF (catalytic) (90%); (h) MeOK, MeOH (93%).

DOI: 10.1021/acschemneuro.5b00038
ACS Chem. Neurosci. XXXX, XXX, XXX−XXX

selective for GluK1 and ATPO binds to the GluK1 and AMPA receptors.

Functional Characterization at GluK1 and GluK2. We characterized the functionality of **1a** and **1b** at recombinantly expressed KA receptors. Outside-out patches excised from HEK293T cells transfected with GluK1 or GluK2 were subjected to fast Glu applications (250 ms, 1 mM Glu) in the absence or presence of 100 μM **1a** or **1b**, and peak currents were measured (Figure 4) and are summarized in Table 2.

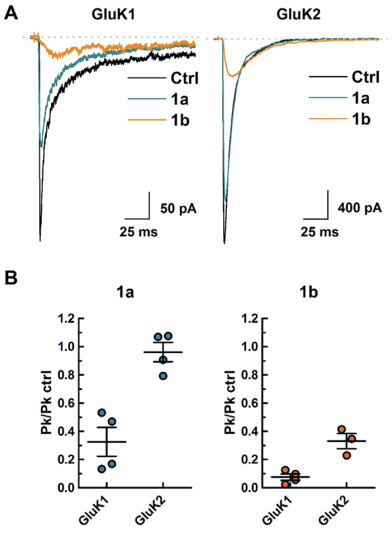

Figure 4. Antagonism of GluK1 and GluK2 by **1a** and **1b**. (A) Example GluK1 and GluK2 responses evoked by 1 mM Glu (patches 141215p2 and 141201p1, respectively) under control conditions (black) and in the presence of 100 μM **1a** (cyan) or **1b** (orange). (B) Summary of relative peak responses of GluK1 and GluK2 in the presence of 100 μM **1a** (left) or **1b** (right). Data points represent individual observations; lines and error bars represent the mean and SEM.

Table 2. Mean Relative Peak Responses Evoked by 1 mM Glu in the Presence of 100 μM 1a or 1b

	GluK1			GluK2		
	mean	SEM	*n*	mean	SEM	*n*
1a (CNG-10301)	0.33	±0.10	4	0.96	±0.07	4
1b (CNG-10300)	0.08	±0.02	4	0.33	±0.05	3

Surprisingly, 100 μM **1a** partially blocked GluK1, while GluK2 was unaffected (Figure 4B). On the other hand, **1b** fully antagonized GluK1 but only partially blocked GluK2 (Figure 4B). Of note, **1b** also slowed the rise time of both GluK1 and GluK2 responses by almost 13- and 6-fold, respectively (GluK1, 0.60 ± 0.08 and 7.8 ± 4.5 ms in control and **1b**, respectively; GluK2, 0.96 ± 0.05 and 5.6 ± 0.3 ms in control and **1b**, respectively). This is consistent with **1b** being a competitive antagonist at both GluK1 and GluK2 receptors.

We also investigated **1a** as a potential agonist at GluK1 and GluK2. At a concentration of 100 μM, **1a** alone did not produce any response at either GluK1 (n = 3) or GluK2 (n = 5) at a holding potential of −100 mV. Moreover, preliminary experiments using Concanavalin-A to enhance small agonist responses, as previously described,[21] did not change this outcome. On the basis of these results, we conclude that within the resolution of our system, **1a** is an antagonist and not a partial agonist at GluK1.

X-ray Structure of the GluK1-LBD with 1b. Today, approximately 300 structures of LBDs of iGluRs have been determined. Such high-resolution structures (1−2.5 Å) are valuable for gaining detailed information about ligand binding and hydrogen bonding, including binding site water networks. For comparison, structures of full-length GluA2 have been crystallized with three agonists and one antagonist only at medium to low resolution (3.2−3.9 Å).[22−24] However, a similar binding mode of the ligands as well as similar domain and subunit arrangements at the soluble LBD and full-length receptors was seen, which supports the use of LBDs for detailed studies.

Of compounds **1a** and **1b**, only **1b** was successfully crystallized with the GluK1-LBD at 2.28 Å resolution. The crystal contains three molecules (A−C) in the asymmetric unit of the crystal (Table S1 of the Supporting Information). Molecules A and C form a biologically relevant dimer with each other, whereas molecule B forms a dimer with a symmetry-related molecule B. Compound **1b** was found to bind with a similar binding affinity at the GluK1-LBD (37 μM) and at cloned homomeric GluK1 receptors (16 μM) (Table 1).

Compound **1b** could unambiguously be located at the three binding sites (Figure 5A−C). The ligand is positioned in such a way that the quinoxaline-2,3-dione part of **1b** forms contacts to the essential Arg523, in the same manner as seen in the structure of the GluA2-LBD with DNQX.[12] In this way, the α-amino acid moiety of **1b** can be regarded as a substituent on the quinoxaline-2,3-dione skeleton. The contacts to the quinoxaline-2,3-dione part of **1b** involve polar interactions between both oxygen atoms of **1b** and the Arg523 side chain as well as an interaction from the 2-one of **1b** to the backbone nitrogen atom of Thr518. Furthermore, the 3-one atom forms a contact with a water molecule in molecule B (Figure 5B), which is not seen in molecule A or C (Figure 5A,C). The 1-nitrogen atom of **1b** forms a contact with the backbone carbonyl oxygen atom of Pro516, whereas the 4-nitrogen atom interacts with a water molecule in molecules A and B. The side chain of Glu738 is twisted away from the ligand (Figure 5D) as previously also observed upon binding of UBP318 in the GluK1-LBD,[15] but in contrast to what was seen in other structures of GluK1 with antagonists, e.g., GluK1-LBD in complex ATPO,[14] where this residue forms direct contacts with the ligand (Figure 5D).

As GluK1 is an α-amino acid-binding receptor, a binding mode positioning the α-amino acid of **1b** toward Arg523 was predicted as one of the possible binding modes (see section on *In silico* study in the Supporting Information), and Glu738 was thought to bind to the ligand α-amino group of **1b**. Instead, the structure reveals that the α-amino acid moiety of **1b** binds in a small cavity inside the binding pocket (Figures 5D and 6). The *in silico* study showed that only when docking back into the **1b**−GluK1-LBD X-ray structure could the X-ray-determined binding mode of **1b** be reproduced. Following the concept of induced fit of ligand−protein binding, this is however not unexpected as three key parameters in this process are difficult to model: (1) receptor domain closure, (2) organization of water matrix and hydrogen bonding network in the binding pocket, and (3) overall entropy of the system whether this is positively or negatively contributing to the total free energy of binding.

DOI: 10.1021/acschemneuro.5b00038
ACS Chem. Neurosci. XXXX, XXX, XXX−XXX

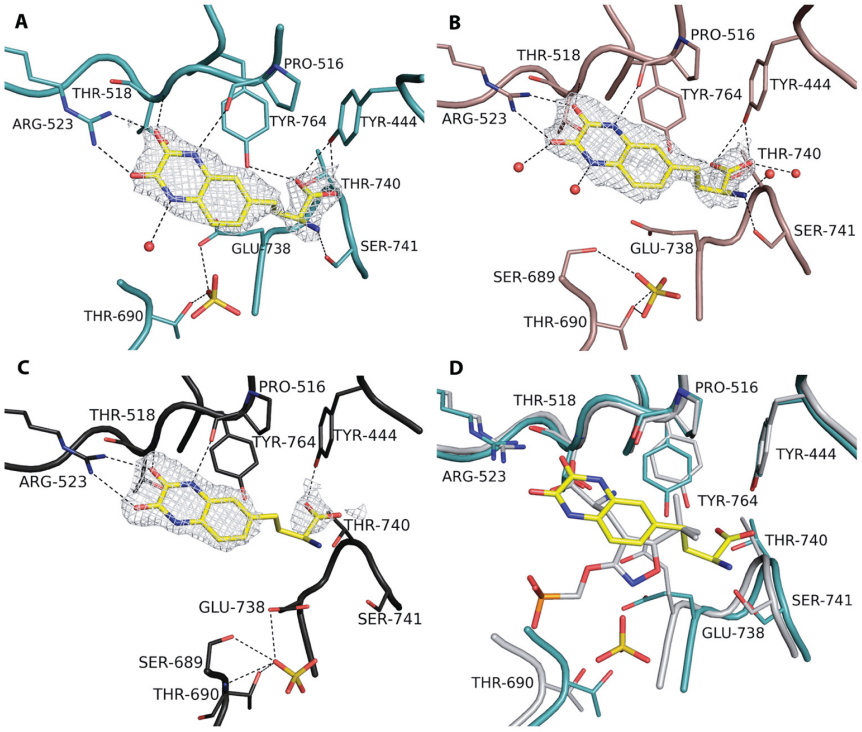

Figure 5. X-ray crystal structure of **1b** in the LBD of GluK1. (A–C) **1b** is shown as sticks with carbon atoms colored yellow. Selected binding site residues are illustrated with carbon atoms colored cyan (molecule A), salmon (molecule B), and dark gray (molecule C). The backbone trace is shown as a ribbon. Oxygen atoms are colored red, nitrogen atoms blue, and sulfur atoms yellow. Water molecules are displayed as red spheres, and a sulfate ion located in the binding site is shown as sticks. Potential hydrogen bonds within 3.2 Å are shown as dashed lines. Furthermore, a standard Phenix $2F_o - F_c$ omit map (gray) carved around the ligand at a 1.6 Å radius is shown: molecules (A) A, (B) B, and (C) C. (D) Superimposition of the structures of the GluK1-LBD with **1b** (molecule A, color coding as in panel A) and the GluK1-LBD with ATPO (PDB entry 1VSO,[14] molecule A, carbon atoms colored light gray). See Figure S1 of the Supporting Information for the final $2F_o - F_c$ electron density map of the three molecules of **1b**.

The α-amino group of **1b** in molecules A and B makes contacts with the side chain hydroxyl group of Ser741 and also a water molecule in molecule B (Figure 5A,B), whereas no close contacts with the α-amino group are seen in molecule C (Figure 5C). The α-carboxylate group of **1b** forms contacts with side chain hydroxyl groups of Tyr444, Thr740, and Tyr764 as well as a water molecule in molecule B. In molecule C, a close contact with Tyr444 (2.6 Å) is seen, whereas the contacts with Thr740 (3.6 Å) and Tyr764 (3.6 Å) are weaker. A sulfate ion is found in the binding pocket, which is located 6–8 Å from **1b** in the vicinity of Thr690 (Figure 5A–C) and forms similar contacts in all three molecules. Upon comparison of the present structure with the structure of the GluK1-LBD in complex with other antagonists, it is seen that a distal substituent of most antagonists is positioned where the sulfate ion is located in the structure of the GluK1-LBD with **1b** (Figure 6). The sulfate ion is found in a similar region as the phosphonate group of ATPO in the GluK1-LBD but in a different location (Figure 5D). In the structures of the GluA2-LBD with DNQX and NS1209, a sulfate ion is positioned at the same site as the phosphonate group of ATPO in the GluA2-LBD.[25] However, the phosphonate group of ATPO adopts different locations in the GluA2-LBD and GluK1-LBD[14] and also different from the sulfate ion in the GluK1-LBD structure with **1b**. Therefore, it seems that incorporation of an anionic moiety into a compound would favor binding at both GluA2 and GluK1 but may result in different receptor contacts.

Whereas agonists induce a closure of domain D2 toward domain D1, antagonists stabilize an open form of the LBD. D1–D2 domain openings were calculated for molecules A–C of the GluK1-LBD structure with antagonist **1b** bound using the GluK1-LBD structure with glutamate (PDB entry 2F36, molecule A)[26] as a reference structure. The domain opening of the three molecules was seen to be significantly different (25.4°, 29.0°, and 49.3° for molecules A–C, respectively) (Figure 7). Domain openings of GluK1-LBD have previously been found to vary from 25° to 31°.[15] Therefore, the domain opening of 49° in molecule C in the structure presented here is surprisingly large but at the same time demonstrates that the GluK1-LBD is capable of undergoing major domain movements. In the crystal, the entrances to the binding sites of molecules B and C are facing each other, and thus, this crystal packing might affect closure of molecule C. Also, the average B value (55 Å^2) of D2 in molecule C is significantly larger than those of the three D1 domains and the other two D2 domains in the structure (35–39 Å^2). This observation indicates high flexibility of domain D2 in molecule C, consistent with a large domain opening and weaker contacts of **1b** in molecule C compared to in molecules A and B.

DOI: 10.1021/acschemneuro.5b00038
ACS Chem. Neurosci. XXXX, XXX, XXX–XXX

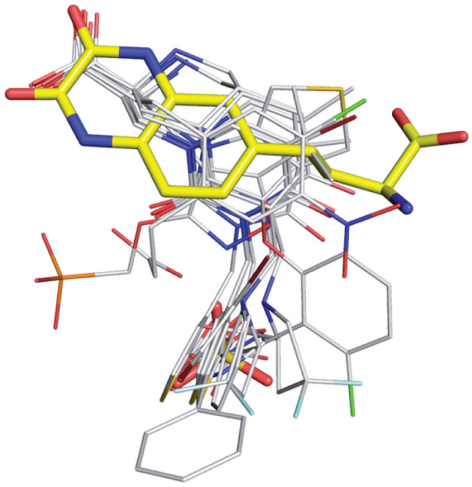

Figure 6. Superimposition on domain D1 of all 10 available antagonist structures at rat GluK1-LBD (molecule A) to illustrate that the amino acid part of **1b** points into an area of the binding pocket that has not previously been explored by antagonists. All reported antagonists have substituents pointing in the direction of the sulfate ion. Only ligand atoms are shown for the sake of clarity (yellow sticks, **1b** and sulfate ion; thin gray lines, PDB entries 1VSO, 2F34, 2F3S, 2QS1, 2QS2, 2QS3, 2QS4, 3S2V, 4DLD, and 4MF3).

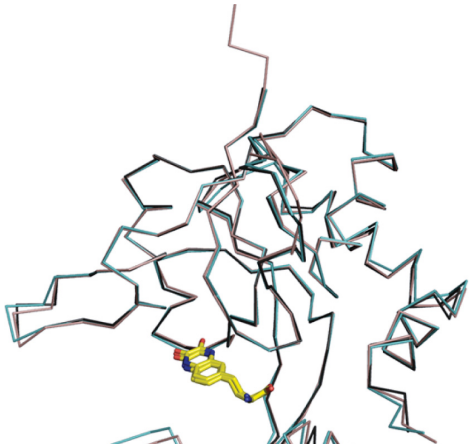

Figure 7. Molecules A–C of the GluK1-LBD structure with **1b** superimposed on domain D1 residues. Molecule A is colored cyan, molecule B salmon, and molecule C dark gray. **1b** is shown as yellow sticks.

Crystallization of **1b** with the GluA2-LBD was also attempted. The diffraction data showed the GluA2 LBD to be in an open cleft conformation; however, a lack of interpretable electron density in the binding site prevented modeling of **1b** into the structure (data not shown). On the basis of a comparison of amino acid residues in the GluK1-LBD and GluA2-LBD, only one difference is seen within 4 Å of **1b**: Ser741 in GluK1, which corresponds to a methionine in GluA2 (Met708). The α-amino group in **1b** forms a hydrogen bond with the side chain hydroxyl group of Ser741 in GluK1 (Figure 5). Thus, this hydrogen bond is not possible in the GluA2-LBD and might suggest a different binding mode of **1b** in GluA2 compared to that in GluK1. However, it has been observed that Met708 in GluA2 can undergo major side chain conformational changes,[27] and therefore, the α-amino acid substituent might point into a similar region in GluA2 as observed for GluK1. This would be in agreement with a similar binding affinity of **1b** in GluA2 and GluK1 (Table 1).

CONCLUSION

Discovery of iGluR antagonists that display an unprecedented receptor subtype selectivity profile continues to be a challenging task. By means of creativity together with structural insight into the iGluRs and the binding modes of their ligands, amino acid-functionalized quinoxalines **1a** (CNG-10301) and **1b** (CNG-10300) were designed and successfully synthesized. Analogue **1a** displayed midrange micromolar affinity for the GluK2 subtype and low affinity for GluK1 and GluK3. However, in a functional setup, **1a** antagonized GluK1 but not GluK2 (33 and 96% peak responses at 100 μM, respectively). Analogue **1b** showed binding affinities for native AMPA, KA, and NMDA and the three GluK1–3 subtypes in the low to medium micromolar range. At 100 μM, **1b** fully antagonized GluK1 and partially antagonized GluK2. An X-ray crystal structure of the GluK1-LBD with **1b** revealed an unexpected binding mode and a large variation in domain openings of the three molecules from 25° to 49°, demonstrating that the GluK1-LBD is capable of undergoing major domain movements.

In all, the new insight presented herein is valuable for the future design and synthesis of subtype-selective iGluR antagonists.

EXPERIMENTAL SECTION

Chemistry. All reactions involving dry solvents or sensitive agents were performed under a nitrogen atmosphere, and glassware was dried prior to use. Commercially available chemicals were used without further purification. THF and DMF were dried using 3 Å molecular sieves. Reactions were monitored by analytical thin-layer chromatography (TLC, Merck silica gel 60 F_{254} aluminum sheets). Flash chromatography was conducted using Merck silica gel 60A (20–45 μm). ^{1}H NMR spectra were recorded on a 300 MHz Avance Bruker spectrometer and ^{13}C NMR spectra on a 75 MHz Avance Bruker spectrometer. The purity of all tested compounds was determined by elementary analysis to be >95%.

(*S*)-Benzyl 2-[(*tert*-Butoxycarbonyl)amino]-4-hydroxybutanoate (3b). To a solution of (*S*)-4-(benzyloxy)-3-[(*tert*-butoxycarbonyl)amino]-4-oxobutanoic acid **2** (2.00 g, 6.18 mmol) in dry THF (30 mL) at −15 °C was added *N*-methylmorpholine (0.680 mL, 6.18 mmol) followed by isobutyl chloroformate (0.810 mL, 6.18 mmol) (milky solution). The solution was stirred for 20 min, and $NaBH_4$ (0.700 g, 18.5 mmol) was added portionwise followed by a slow dropwise addition of MeOH (62 mL) over 45 min. The reaction mixture was stirred for 40 min at −15 °C before the reaction was quenched by the addition of an aqueous solution of HCl (11 mL, 1 M). The mixture was concentrated under reduced pressure, and the residue was extracted with EtOAc (3 × 30 mL). The combined

DOI: 10.1021/acschemneuro.5b00038
ACS Chem. Neurosci. XXXX, XXX, XXX–XXX

organic layers were successively washed with an aqueous solution of HCl (1 × 40 mL, 1 M), H_2O (2 × 50 mL), an aqueous solution of 5% $NaHCO_3$ (1 × 50 mL), and finally H_2O (3 × 50 mL). It was dried over $MgSO_4$, filtered, and evaporated under reduced pressure, leading to a yellow oil. The crude was used without purification.

General Procedure for the Displacement of the Primary Hydroxy Group with Iodine. To a solution of PPh_3 (2.02 g, 7.70 mmol) and imidazole (0.520 g, 7.70 mmol) in DCM (29 mL) at 0 °C was added I_2 (1.95 g, 7.70 mmol) (orange milky solution). The reaction mixture was warmed to room temperature and stirred for 10 min. The mixture was recooled to 0 °C, and a solution of the corresponding alcohol (6.16 mmol) in DCM (6 mL) was added dropwise over 15 min. The solution was stirred at 0 °C for 90 min and then at room temperature for 2 h. The reaction mixture was filtered off through a pad of Celite (2 cm) using a solution of ether and petroleum ether (1:1) as the eluent. The organic phase was evaporated under reduced pressure without being heated.

*(S)-Methyl 2-[(tert-Butoxycarbonyl)amino]-3-iodopropanoate (**4a**).* Purified by flash column chromatography (ether/petroleum ether, 1:4) (R_f = 0.19). White solid (2.85 g, 80%). Mp: 51 °C (Lit. 51 °C). ^{1}H NMR (300 MHz, $CDCl_3$): δ 5.34 (d, J = 7.06 Hz, 1H), 4.55−4.47 (m, 1H), 3.79 (s, 3H), 3.62−3.50 (m, 2H), 1.45 (s, 9H).

*(S)-Benzyl 2-[(tert-Butoxycarbonyl)amino]-4-iodobutanoate (**4b**).* Purified by flash column chromatography (EtOAc/petroleum ether, 1:5) (R_f = 0.5). White solid (1.3 g, 49% over two steps). Mp: 54 °C (Lit. 54 °C). ^{1}H NMR (300 MHz, $CDCl_3$): δ 7.39−7.32 (m, 5H), 5.22 (dd, J = 2.91 Hz, 1H), 5.13−5.03 (m, 1H), 4.41−4.35 (m, 1H), 3.21−3.08 (m, 2H), 2.41−2.35 (m, 1H), 2.25−2.17 (m, 1H), 1.45 (s, 9H).

General Procedure for the Negishi Cross Coupling Reaction. Zinc dust (0.61 g, 9.30 mmol) was added to a nitrogen-purged vial. Dry DMF (3.25 mL) was added followed by a catalytic amount of I_2 (40 mg, 0.15 mmol) (the solution turned yellow and then black again). The corresponding iodine compound, **4a** or **4b** (3.10 mmol), was immediately added followed by another catalytic amount of I_2 (40 mg, 0.15 mmol) (the solution turned yellow-green and then black again; exothermicity was felt because of zinc insertion). Pd_2dba_3 (73 mg, 0.08 mmol), SPhos (62 mg, 0.150 mmol), and 6-bromo-2,3-dimethoxyquinoxaline **9** (0.290 g, 1.08 mmol) were added to the vial, and the solution was heated at 50 °C for 4 h. The reaction mixture was filtered off through a pad of Celite (2 cm), washed with DMF, and evaporated under reduced pressure. Water (10 mL) was added, and the solution was extracted with Et_2O (3 × 20 mL). Combined organic phases were washed with brine, dried over $MgSO_4$, filtered, and evaporated under reduced pressure.

*(S)-Methyl 2-[(tert-Butoxycarbonyl)amino]-3-(2,3-dimethoxyquinoxalin-6-yl)propanoate (**5a**).* Purified twice by flash column chromatography [AcOEt/heptane, 3:7 (R_f = 0.30), and then toluene/AcOEt, 85:15 (R_f = 0.35)]. White solid (0.5 g, 41%). Mp: 56.4 °C. $[\alpha]_D^{25}$ = +67.5 (c = 0.306 g/100 mL, CH_2Cl_2). ^{1}H NMR (300 MHz, $CDCl_3$): δ 7.69 (d, J = 8.34 Hz, 1H), 7.55 (br s, 1H), 7.26 (dd, J = 8.33, 1.98 Hz, 1H), 5.02 (d, J = 7.99 Hz, 1H), 4.66 (dd, J = 13.73, 6.05 Hz, 1H), 4.14 (s, 6H), 3.74 (s, 3H), 3.24 (dq, J = 13.97, 6.07 Hz, 2H), 1.42 (9H, s). ^{13}C NMR (75 MHz, $CDCl_3$): δ 172.1, 154.9, 149.9, 149.7, 136.9, 136.1, 134.6, 127.8, 126.7, 126.3, 79.9, 54.4, 54.1, 52.2, 38.1, 28.2.

*(S)-Benzyl 2-[(tert-Butoxycarbonyl)amino]-4-(2,3-dimethoxyquinoxalin-6-yl)butanoate (**5b**).* Purified four times by flash column chromatography [twice with EtOAc/heptane, 3:7 (R_f = 0.33), then DCM/MeOH (5%) (R_f = 0.38), and then toluene/EtOAc, 9:1 (R_f = 0.30)]. Orange glass solid (1.0 g, 35%). Mp: 67.6 °C. $[\alpha]_D^{25}$ = +22.0 (c = 0.4 g/100 mL, CH_2Cl_2). ^{1}H NMR (300 MHz, $CDCl_3$): δ 7.65 (d, J = 8.35 Hz, 1H), 7.52 (br s, 1H), 7.38−7.34 (m, 4H), 7.26 (s, 1H), 7.26−7.15 (m, 1H), 5.16 (dd, J = 19.42, 12.28 Hz, 2H), 5.14 (br s, 1H), 4.44 (dd, J = 12.99, 7.03 Hz, 1H), 4.14 (s, 6H), 2.88−2.67 (m, 2H), 2.34−2.15 (m, 1H), 2.10−1.95 (m, 1H), 1.46 (s, 9H). ^{13}C NMR (75 MHz, $CDCl_3$): δ 172.3, 155.2, 149.8, 149.5, 139.4, 137.0, 135.5, 135.2, 128.5, 128.3, 128.2, 127.4, 126.2, 125.4, 79.9, 67.0, 54.0, 53.2, 34.2, 31.3, 28.2.

*(S)-2-Amino-3-(2,3-dioxo-1,2,3,4-tetrahydroquinoxalin-6-yl)-propanoic Acid Hydrochloride (**1a**).* To a solution of (*S*)-methyl 2-[(*tert*-butoxycarbonyl)amino]-3-(2,3-dimethoxyquinoxalin-6-yl)-propanoate **5a** (0.400 g, 1.02 mmol) in dioxane (19 mL) was added an aqueous solution of HCl (19 mL, 4 N), and the reaction mixture was heated under gentle reflux conditions overnight. The reaction mixture was evaporated, and the residue was triturated with Et_2O (3 × 5 mL), leading to a pure white HCl salt (250 mg, 89%). Mp: 278 °C dec. $[\alpha]_D^{25}$ = +48.0 (c = 0.167 g/100 mL, DMSO). ^{1}H NMR (300 MHz, d_6-DMSO): δ 12.00 (s, 1H), 11.95 (s, 1H), 8.33 (br s, 3H), 7.07 (d, J = 8.60 Hz, 1H), 7.01−6.96 (m, 2H), 4.08 (br s, 1H), 3.07 (d, J = 6.42 Hz, 2H). ^{13}C NMR (75 MHz, d_6-DMSO): δ 170.1, 155.1, 154.9, 129.7, 125.5, 124.7, 124.2, 116.1, 115.3, 53.2, 35.2. Anal. Calcd for $C_{12}H_{13}N_3O_4{\cdot}0.34H_2O{\cdot}1.62HCl$): C, 43.88; H, 4.7; N, 12.79. Found: C, 43.58; H, 4.38; N, 13.12.

*(S)-2-Amino-4-(2,3-dioxo-1,2,3,4-tetrahydroquinoxalin-6-yl)-butanoic Acid Hydrochloride (**1b**).* To a solution of (*S*)-benzyl 2-[(*tert*-butoxycarbonyl)amino]-4-(2,3-dimethoxyquinoxalin-6-yl)-butanoate **5b** (0.250 g, 0.52 mmol) in dioxane (12 mL) was added an aqueous solution of HCl (12 mL, 4 N), and the solution was heated under gentle reflux conditions overnight. The reaction mixture was then evaporated, and the residue was triturated with Et_2O (3 × 5 mL). The crude was obtained as a light orange powder (96%).

The crude (150 mg, 0.5 mmol) was dissolved in H_2O (8 mL) and the mixture stirred at room temperature. Propylene oxide (35 μL, 5.0 mmol) was slowly added to the reaction mixture, and the solution was stirred for 30 min. The reaction mixture was left overnight without stirring for crystallization and then filtered with a filter paper, and crystals were washed with H_2O (3 × 2 mL). The crystals were dissolved in an aqueous solution of HCl (1.5 mL, 1 M) and evaporated to dryness. The solid was dissolved in H_2O (2 mL) and freeze-dried to afford a light brown solid (106 mg, 68%). Mp: 263 °C dec. $[\alpha]_D^{25}$ = +35.8 (c = 0.142 g/100 mL, H_2O). ^{1}H NMR (300 MHz, d_6-DMSO): δ 11.95 (s, 1H), 11.91 (s, 1H), 8.48 (br s, 3H), 7.07 (d, J = 7.97 Hz, 3H), 6.95 (br s, 1H), 6.94 (br dd, J = 9.13, 1.48 Hz, 1H), 3.87 (signal hidden by the solvent peak, 1H), 2.82−2.67 (m, 1H), 2.67−2.53 (m, 1H), 2.10−1.96 (m, 2H). ^{1}H NMR (300 MHz, D_2O): δ 7.00 (ddd, J = 8.27, 1.68, 1.68 Hz, 1H), 6.94 (dd, J = 8.31, 1.51 Hz, 1H), 6.87 (br d, J = 1.39 Hz, 1H), 3.99 (dd, J = 6.25, 6.25 Hz, 1H), 2.81−2.55 (m, 2H), 2.13−1.99 (m, 2H). ^{13}C NMR (75 MHz, d_6-DMSO): δ 170.7, 155.3, 155.0, 135.4, 125.6, 124.0, 123.1, 115.3, 114.6, 51.6, 32.0, 30.0. Anal. Calcd for $C_{12}H_{14}ClN_3O_4{\cdot}1.5H_2O{\cdot}0.81HCl$): C, 40.84; H, 4.67; N, 11.41. Found: C, 40.46; H, 5.04; N, 11.79.

*6-Bromoquinoxaline-2,3(1H,4H)-dione (**7**).* A solution of 2-amino-4-bromoaniline **6** (3.0 g, 16.0 mmol) in diethyl oxalate (15 mL) was refluxed for 4 h. The reaction mixture was allowed to cool to room temperature, after which EtOAc (25 mL) was added. The precipitate was filtered and washed with EtOAc (3 × 20 mL) and dried under vacuum to give a brown powder (3.75 g, 96%). ^{1}H NMR (300 MHz, d_6-DMSO): δ 11.97 (s, 1H), 11.94 (s, 1H), 7.26−7.18 (m, 2H), 7.03 (d, J = 9.03 Hz, 1H). Mp: >400 °C dec (Lit. >350 °C).

*6-Bromo-2,3-dichloroquinoxaline (**8**).* To a mixture of 6-bromoquinoxaline-2,3(1*H*,4*H*)-dione **7** (5.33 g, 22.11 mmol) in thionyl chloride (74 mL) was added a catalytic amount of DMF (three drops). The reaction mixture was heated under reflux for 8 h, cooled to room temperature, and poured very slowly into an ice/water bath. The solid was filtered, dissolved in EtOAc (500 mL), and dried with $MgSO_4$. The organic phase was filtered and evaporated to afford the desired product, 6-bromo-2,3-dichloroquinoxaline **8**, as a light orange-brown solid (1.03 g, 90%). Mp: 131 °C (Lit. 132 °C). ^{1}H NMR (300 MHz, d_6-DMSO): δ 8.34 (d, J = 2.01 Hz, 1H), 8.05 (dd, J = 8.91, 2.06 Hz, 1H), 8.00 (d, J = 8.89 Hz, 1H).

*6-Bromo-2,3-dimethoxyquinoxaline (**9**).* To a solution of the intermediate 6-bromo-2,3-dichloroquinoxaline **8** (2.25 g, 8.09 mmol) in anhydrous methanol (34 mL) was added a solution of 25% MeOK in MeOH (6.90 mL, 22.6 mmol). The reaction mixture was refluxed for 3 h and cooled to room temperature. H_2O (50 mL) was added, and the suspension was filtered before being washed with water (3 × 20 mL). The solid was dried overnight using a vacuum oven to give the desired product, 6-bromo-2,3-dimethoxyquinoxaline **9**, as a brown powder (2.02 g, 93%). Mp: 105 °C (Lit. 114−115 °C, solvent of

DOI: 10.1021/acschemneuro.5b00038
ACS Chem. Neurosci. XXXX, XXX, XXX−XXX

methanol). ^{1}H NMR (300 MHz, d_6-DMSO): δ 7.90 (br s, 1H), 7.67 (d, J = 9.09 Hz, 1H), 7.63 (d, J = 8.77 Hz, 1H), 4.03 (s, 6H).

Pharmacology. Radioligand displacement studies were performed as previously described at native rat brain AMPA, KA, and NMDA receptors and at recombinant rat homomeric GluA2$(R)_o$, GluK1$(Q)_{1b}$, GluK2$(VCR)_a$, and GluK3$_a$ receptors as well as the GluK1-LBD.[28] For recombinant kainate receptor assays, [^{3}H]SYM2081 was used as the radioligand while [^{3}H]AMPA was employed for the GluA2$(R)_o$ binding assay.

Cell Culture and Transfection. HEK293T/17 cells (ATCC) were maintained in minimal essential medium (MEM) containing glutaMAX supplemented with 10% fetal bovine serum (Invitrogen). Cells were plated at a low density (1.6−2.0 × 10^4 cells/mL) on poly-D-lysine-coated 35 mm plastic dishes and were transiently transfected 24 h later using the calcium phosphate technique as previously described.[29] Rat cDNA encoding for GluK1−2a and GluK2a subunits was cotransfected with cDNA encoding enhanced green fluorescent protein (eGFP) to identify transfected cells.

Electrophysiological Recordings. Experiments were performed 36−48 h after transfection. Agonist solutions were rapidly applied to outside-out patches excised from transfected cells using a piezoelectric stack (Physik Instrumente). Solution exchange (10−90% rise time of 250−350 μs) was determined in a separate experiment by measuring the liquid junction current. All recordings were performed using an Axopatch 200B (Molecular Devices) using thick-walled borosilicate glass pipettes (3−6 MΩ) coated with dental wax to reduce electrical noise. Current records were filtered at 5 kHz, digitized at 25 kHz, and series resistance (3−12 MΩ) compensated by 95%. Recordings were performed at a holding potential of −100 mV. All experiments were performed at room temperature. All chemicals used for electrophysiology were purchased from Sigma-Aldrich unless otherwise indicated. The external solution contained 150 mM NaCl, 5 mM HEPES, 0.1 mM $MgCl_2$, and 0.1 mM $CaCl_2$ (pH 7.3−7.4). The internal solution contained 115 mM NaCl, 10 mM NaF, 5 mM HEPES, 5 mM Na_4BAPTA (Life Technologies), 1 mM $MgCl_2$, 0.5 mM $CaCl_2$, and 10 mM Na_2ATP (pH 7.3−7.4). The osmotic pressure of all solutions was adjusted to 295−300 mOsm with sucrose. Concentrated (100×) L-Glu stocks were prepared and stored at −20 °C; stocks were thawed and diluted on the day of the experiment. Concentrated (3 mM in DMSO) stocks of **1a** and **1b** were prepared and stored at −20 °C; stocks were thawed on the day of the experiment and added to the control and agonist external solutions for a final concentration of 100 μM. As a control, an equivalent amount of DMSO was added to the external solutions not containing **1a** or **1b**. To test whether **1a** was a partial agonist at GluK1 and GluK2 receptors, 100 μM **1a** was applied to outside-out patches alone. The presence of receptors in the patch was confirmed by obtaining a response with 1 mM L-Glu. The plant lectin, Concanavalin-A, was dissolved at ∼1 mg/mL in an external solution and applied to the patch for 1−2 min. Data were acquired using pClamp10 software (Molecular Devices) and tabulated using Excel (Microsoft Corp.).

X-ray Structure Determination. The rat GluK1-LBD (GRIK1_RAT, UNP P22756, segment S1 residues 430−544 and segment S2 residues 667−805) was expressed and purified in the presence of Glu as previously described.[30] Crystallization of GluK1-LBD in complex with **1b** was performed using the hanging drop vapor diffusion method at 6 °C. A protein solution consisting of 5 mg/mL GluK1-LBD, 5.2 mM **1b**, 10 mM HEPES, 20 mM NaCl, and 1 mM EDTA (pH 7.0) was prepared and used for crystallization experiments. Crystals used for diffraction studies were obtained under the following conditions: 24.4% PEG4000, 0.3 M ammonium sulfate, and 0.1 M phosphate citrate buffer (pH 4.5). The crystals were flash-cooled with liquid nitrogen after immersion in cryo buffer (1 μL of reservoir solution containing 1 μL of UCP). Flash-cooled crystals were stored in liquid nitrogen until data were collected.

An X-ray diffraction data set to 2.28 Å resolution was collected on beamline I911-3 at MAX-lab (Lund, Sweden). The data were processed with XDS[31] and scaled using SCALA[32] in CCP4i.[33] The structure was determined by molecular replacement using PHASER[34] within CCP4i and the structure of the GluK1-LBD in complex with (*S*)-ATPO as a search model (PDB entry 1VSO, molecule A; protein atoms only).[14] The search model was defined as two domains, D1 and D2. Three molecules were found in the asymmetric unit of the crystal. Visual inspection of the structure in COOT[35] revealed well-defined electron density for the structure in most areas and clear density corresponding to **1b**. The ligand coordinates were created in Maestro (Maestro version 9.2, Schrödinger, LLC, New York, NY) and fit into the electron density. Topology and parameter files for **1b** were obtained using eLBOW.[36] The model used for molecular replacement lacked two loops (residues 493−497 and 712−714), and these residues were built in manually. The structure was refined in PHENIX[37] with isotropic *B* factors and validated using tools in COOT and PHENIX. The final structure was also validated on the PDB ADIT validation server. Statistics of data collection and refinement can be found in Table S1 of the Supporting Information. D1−D2 domain openings were calculated using the DynDom server.[38]

***In Silico* Conformational Search Study.** Conformational searches and superimposition studies were performed using the software package MOE 2013.08 (Molecular Operating Environment, Chemical Computing Group). The built-in function "stochastic search" was used with the standard setup: mmff94x force field, solvation set to GB/SA, and energy cutoff of >7 kcal/mol.

■ ASSOCIATED CONTENT

Ⓢ Supporting Information

Crystal data, data collection, and refinement statistics of GluK1-LBD in complex with **1b** (Table S1), final 2Fo-Fc electron density of the three molecules of **1b** (Figure S1), and *in silico* study of the binding mode of **1b** (Table S2 and Figure S2). This material is available free of charge via the Internet at http://pubs.acs.org.

Accession Codes

The structure of the GluK1-LBD in complex with **1b** (CNG-10300) has been deposited in as Protein Data Bank entry 4QF9.

■ AUTHOR INFORMATION

Corresponding Authors

*Phone: +45 35336244. Fax: +45 35336041. E-mail: lebu@sund.ku.dk.

*E-mail: jsk@sund.ku.dk (for X-ray crystallography).

Author Contributions

C.S.D. (medicinal chemistry) and C.M. (X-ray crystallography) contributed equally to this work.

Funding

We thank the Lundbeck Foundation, the Carlsberg Foundation, The University of Copenhagen Programme of Excellence (GluTarget), the Hørslev Foundation, and Danscatt for financial support.

Notes

The authors declare no competing financial interest.

■ ACKNOWLEDGMENTS

Diffraction data were collected at the MAX-lab synchrotron facility in Lund, Sweden. Heidi Peterson is thanked for technical assistance.

■ ABBREVIATIONS

AMPA, α-amino-3-hydroxy-5-methyl-4-isoxazolepropionic acid; CNS, central nervous system; EAATs, excitatory amino acid transporters; Glu, (*S*)-glutamate; iGluRs, ionotropic Glu receptors; KA, kainic acid; LBD, ligand-binding domain; mGluRs, metabotropic Glu receptors; NMDA, *N*-methyl-D-aspartate

DOI: 10.1021/acschemneuro.5b00038
ACS Chem. Neurosci. XXXX, XXX, XXX−XXX

REFERENCES

(1) Anggono, V., and Huganir, R. L. (2012) Regulation of AMPA receptor trafficking and synaptic plasticity. *Curr. Opin. Neurobiol. 22*, 461−469.

(2) Lovinger, D. M. (2010) Neurotransmitter roles in synaptic modulation, plasticity and learning in the dorsal striatum. *Neuropharmacology 58*, 951−961.

(3) Jane, D. E., Lodge, D., and Collingridge, G. L. (2009) Kainate receptors: Pharmacology, function and therapeutic potential. *Neuropharmacology 56*, 90−113.

(4) Contractor, A., Mulle, C., and Swanson, G. T. (2011) Kainate receptors coming of age: Milestones of two decades of research. *Trends Neurosci. 34*, 154−163.

(5) Matute, C. (2011) Therapeutic Potential of Kainate Receptors: Therapeutic Potential of Kainate Receptors. *CNS Neurosci. Ther. 17*, 661−669.

(6) Ogden, K. K., and Traynelis, S. F. (2011) New advances in NMDA receptor pharmacology. *Trends Pharmacol. Sci. 32*, 726−733.

(7) Larsen, A. M., and Bunch, L. (2011) Medicinal Chemistry of Competitive Kainate Receptor Antagonists. *ACS Chem. Neurosci. 2*, 60−74.

(8) Weiss, B., Alt, A., Ogden, A. M., Gates, M., Dieckman, D. K., Clemens-Smith, A., Ho, K. H., Jarvie, K., Rizkalla, G., and Wright, R. A. (2006) Pharmacological characterization of the competitive GLUK5 receptor antagonist decahydroisoquinoline LY466195 in vitro and in vivo. *J. Pharmacol. Exp. Ther. 318*, 772−781.

(9) Randle, J. C., Guet, T., Cordi, A., and Lepagnol, J. M. (1992) Competitive inhibition by NBQX of kainate/AMPA receptor currents and excitatory synaptic potentials: Importance of 6-nitro substitution. *Eur. J. Pharmacol. 215*, 237−244.

(10) Poulie, C. B. M., and Bunch, L. (2013) Heterocycles as nonclassical bioisosteres of α-amino acids. *ChemMedChem 8*, 205−215.

(11) Hogner, A., Greenwood, J. R., Liljefors, T., Lunn, M.-L., Egebjerg, J., Larsen, I. K., Gouaux, E., and Kastrup, J. S. (2003) Competitive antagonism of AMPA receptors by ligands of different classes: Crystal structure of ATPO bound to the GluR2 ligand-binding core, in comparison with DNQX. *J. Med. Chem. 46*, 214−221.

(12) Armstrong, N., and Gouaux, E. (2000) Mechanisms for activation and antagonism of an AMPA-sensitive glutamate receptor: Crystal structures of the GluR2 ligand binding core. *Neuron 28*, 165−181.

(13) Cordi, A. A., Desos, P., Randle, J. C., and Lepagnol, J. (1995) Structure-activity relationships in a series of 3-sulfonylamino-2-(1H)-quinolones, as new AMPA/kainate and glycine antagonists. *Bioorg. Med. Chem. 3*, 129−141.

(14) Hald, H., Naur, P., Pickering, D. S., Sprogøe, D., Madsen, U., Timmermann, D. B., Ahring, P. K., Liljefors, T., Schousboe, A., and Egebjerg, J. (2007) Partial agonism and antagonism of the ionotropic glutamate receptor iGluR5 structures of the ligand-binding core in complex with domoic acid and 2-amino-3-[5-*tert*-butyl-3-(phosphonomethoxy)-4-isoxazolyl]propionic acid. *J. Biol. Chem. 282*, 25726−25736.

(15) Alushin, G. M., Jane, D., and Mayer, M. L. (2011) Binding site and ligand flexibility revealed by high resolution crystal structures of GluK1 competitive antagonists. *Neuropharmacology 60*, 126−134.

(16) Jackson, R. F., Moore, R. J., Dexter, C. S., Elliott, J., and Mowbray, C. E. (1998) Concise synthesis of enantiomerically pure phenylalanine, homophenylalanine, and bishomophenylalanine derivatives using organozinc chemistry: NMR studies of amino acid-derived organozinc reagents. *J. Org. Chem. 63*, 7875−7884.

(17) Ross, A. J., Lang, H. L., and Jackson, R. F. (2010) Much improved conditions for the Negishi cross-coupling of iodoalanine derived zinc reagents with aryl halides. *J. Org. Chem. 75*, 245−248.

(18) Broadrup, R. L., Wang, B., and Malachowski, W. P. (2005) A general strategy for the synthesis of azapeptidomimetic lactams. *Tetrahedron 61*, 10277−10284.

(19) Adamczyk, M., Johnson, D. D., and Reddy, R. E. (2000) A concise synthesis of (S)-(−)-3-(2-carboxy-4-pyrrolyl)-alanine. *Tetrahedron: Asymmetry 11*, 3063−3068.

(20) Jensen, A. A., and Braüner-Osborne, H. (2004) Pharmacological characterization of human excitatory amino acid transporters EAAT1, EAAT2 and EAAT3 in a fluorescence-based membrane potential assay. *Biochem. Pharmacol. 67*, 2115−2127.

(21) Fay, A.-M. L., Corbeil, C. R., Brown, P., Moitessier, N., and Bowie, D. (2009) Functional characterization and in silico docking of full and partial GluK2 kainate receptor agonists. *Mol. Pharmacol. 75*, 1096−1107.

(22) Sobolevsky, A. I., Rosconi, M. P., and Gouaux, E. (2009) X-ray structure, symmetry and mechanism of an AMPA-subtype glutamate receptor. *Nature 462*, 745−756.

(23) Yelshanskaya, M. V., Li, M., and Sobolevsky, A. I. (2014) Structure of an agonist-bound ionotropic glutamate receptor. *Science 345*, 1070−1074.

(24) Dürr, K. L., Chen, L., Stein, R. A., De Zorzi, R., Folea, I. M., Walz, T., Mchaourab, H. S., and Gouaux, E. (2014) Structure and dynamics of AMPA receptor GluA2 in resting, pre-open, and desensitized states. *Cell 158*, 778−792.

(25) Kasper, C., Pickering, D. S., Mirza, O., Olsen, L., Kristensen, A. S., Greenwood, J. R., Liljefors, T., Schousboe, A., Wätjen, F., Gajhede, M., Sigurskjold, B. W., and Kastrup, J. S. (2006) The structure of a mixed GluR2 ligand-binding core dimer in complex with (S)-glutamate and the antagonist (S)-NS1209. *J. Mol. Biol. 357*, 1184−1201.

(26) Mayer, M. L., Ghosal, A., Duolman, N. P., and Jane, D. E. (2006) Crystal structures of the kainate receptor GluR5 ligand binding core dimer with novel GluR5-selective antagonists. *J. Neurosci. 26*, 2852−2861.

(27) Pøhlsgaard, J., Frydenvang, K., Madsen, U., and Kastrup, J. S. (2011) Lessons from more than 80 structures of the GluA2 ligand-binding domain in complex with agonists, antagonists and allosteric modulators. *Neuropharmacology 60*, 135−150.

(28) Assaf, Z., Larsen, A. P., Venskutonytė, R., Han, L., Abrahamsen, B., Nielsen, B., Gajhede, M., Kastrup, J. S., Jensen, A. A., Pickering, D. S., Frydenvang, K., Gefflaut, T., and Bunch, L. (2013) Chemoenzymatic Synthesis of New 2,4-*syn*-Functionalized (*S*)-Glutamate Analogues and Structure−Activity Relationship Studies at Ionotropic Glutamate Receptors and Excitatory Amino Acid Transporters. *J. Med. Chem. 56*, 1614−1628.

(29) Maclean, D. M., Wong, A. Y. C., Fay, A.-M., and Bowie, D. (2011) Cations but not anions regulate the responsiveness of kainate receptors. *J. Neurosci. 31*, 2136−2144.

(30) Naur, P., Vestergaard, B., Skov, L. K., Egebjerg, J., Gajhede, M., and Kastrup, J. S. (2005) Crystal structure of the kainate receptor GluR5 ligand-binding core in complex with (S)-glutamate. *FEBS Lett. 579*, 1154−1160.

(31) Kabsch, W. (2010) XDS. *Acta Crystallogr. D66*, 125−132.

(32) Evans, P. (2006) Scaling and assessment of data quality. *Acta Crystallogr. D62*, 72−82.

(33) Winn, M. D., Ballard, C. C., Cowtan, K. D., Dodson, E. J., Emsley, P., Evans, P. R., Keegan, R. M., Krissinel, E. B., Leslie, A. G. W., McCoy, A., McNicholas, S. J., Murshudov, G. N., Pannu, N. S., Potterton, E. A., Powell, H. R., Read, R. J., Vagin, A., and Wilson, K. S. (2011) Overview of the CCP4 suite and current developments. *Acta Crystallogr. D67*, 235−242.

(34) McCoy, A. J., Grosse-Kunstleve, R. W., Adams, P. D., Winn, M. D., Storoni, L. C., and Read, R. J. (2007) Phaser crystallographic software. *J. Appl. Crystallogr. 40*, 658−674.

(35) Emsley, P., Lohkamp, B., Scott, W. G., and Cowtan, K. (2010) Features and development of Coot. *Acta Crystallogr. D66*, 486−501.

(36) Moriarty, N. W., Grosse-Kunstleve, R. W., and Adams, P. D. (2009) electronic Ligand Builder and Optimization Workbench (eLBOW): A tool for ligand coordinate and restraint generation. *Acta Crystallogr. D65*, 1074−1080.

DOI: 10.1021/acschemneuro.5b00038
ACS Chem. Neurosci. XXXX, XXX, XXX−XXX

(37) Hayward, S., and Lee, R. A. (2002) Improvements in the analysis of domain motions in proteins from conformational change: DynDom version 1.50. *J. Mol. Graphics Modell. 21*, 181−183.
(38) Hayward, S., and Berendsen, H. J. (1998) Systematic analysis of domain motions in proteins from conformational change: New results on citrate synthase and T 4 lysozyme. *Proteins: Struct., Funct., Genet. 30*, 144−154.

DOI: 10.1021/acschemneuro.5b00038
ACS Chem. Neurosci. XXXX, XXX, XXX−XXX

APPENDIX C
$GABA_A$ Receptors

Foreword to Appendix C

Just as ionotropic glutamate receptors are important for mediating fast excitatory neurotransmission, $GABA_A$ receptors mediate inhibitory neurotransmission. The fine balance between excitatory and inhibitory neurotransmission is crucial for the proper function of neuronal circuits, and imbalances can lead to pathological states like epilepsy, as you will find in the first article in this Appendix (Lachance-Touchette et al., 2011). In this study, we characterized several mutant $GABA_A$ receptor subunits that were identified in patients with idiopathic generalized epilepsy (Lachance-Touchette et al., 2011). Interestingly, while some mutations in the $\alpha 1$ subunits altered the gating properties of the channels, a mutation in the $\gamma 2$ subunit did not appear to have any functional differences, suggesting that other factors, such as localization or auxiliary protein association, could be critical in this case (Lachance-Touchette et al., 2011). For this study, I performed the functional characterization of mutant $GABA_A$ subunits using recombinantly-expressed receptors and fast-application electrophysiology.

The following articles of this Appendix characterize the modulation of $GABA_A$ receptors by reactive oxygen species. In each of these articles, I performed recombinant electrophysiological experiments. In Accardi et al. (2014), I compared the decay kinetics of $\alpha 1$ and $\alpha 3$-containing $GABA_A$ receptors to help identify the mechanism underlying the change in EPSC kinetics caused by mitochondrial-derived reactive oxygen species. In Penna et al. (2014), I performed whole-cell experiments to assess the direct sensitivity of $GABA_A$ receptors to various concentrations of H_2O_2. These experiments were not included in the final version of the article, but were useful in the interpretation of a direct or indirect mechanism of receptor regulation. Finally, in Accardi et al. (2015), I assessed the

differential sensitivities of α1 and α6-containing $GABA_A$ receptors to furosemide, an antagonist that was used to identify the α6 subunits in cerebellar granule cells.

EJN fens European Journal of Neuroscience

European Journal of Neuroscience, Vol. 34, pp. 237–249, 2011 doi:10.1111/j.1460-9568.2011.07767.x

NEUROSYSTEMS

Novel α1 and γ2 $GABA_A$ receptor subunit mutations in families with idiopathic generalized epilepsy

Pamela Lachance-Touchette,[1,*] Patricia Brown,[2,3,*] Caroline Meloche,[1] Peter Kinirons,[1] Line Lapointe,[1] Hélène Lacasse,[1] Anne Lortie,[4] Lionel Carmant,[4] Fiona Bedford,[5] Derek Bowie[2] and Patrick Cossette[1]

[1]Centre for Excellence in Neuromics of University of Montreal (CENUM), CHUM Research Center, 1560 Sherbrooke est, Montreal, QC, Canada H2L 4M1

[2]Department of Pharmacology & Therapeutics, McGill University, Bellini Life Sciences Complex, Room 164, 3649 Sir William Osler Promenade, Montreal, QC, Canada H3G 0B1

[3]Integrated Program in Neuroscience, McGill University, Montreal, QC, Canada

[4]Centre Hospitalier Universitaire Sainte-Justine, Université de Montréal, Montreal, QC, Canada

[5]Department of Anatomy and Cell Biology, McGill University, Montreal, QC, Canada

Keywords: channelopathy, gating, genetics, seizure, synaptic inhibition

Abstract

Epilepsy is a heterogeneous neurological disease affecting approximately 50 million people worldwide. Genetic factors play an important role in both the onset and severity of the condition, with mutations in several ion-channel genes being implicated, including those encoding the $GABA_A$ receptor. Here, we evaluated the frequency of additional mutations in the $GABA_A$ receptor by direct sequencing of the complete open reading frame of the *GABRA1* and *GABRG2* genes from a cohort of French Canadian families with idiopathic generalized epilepsy (IGE). Using this approach, we have identified three novel mutations that were absent in over 400 control chromosomes. In *GABRA1*, two mutations were found, with the first being a 25-bp insertion that was associated with intron retention (i.e. K353delins18X) and the second corresponding to a single point mutation that replaced the aspartate 219 residue with an asparagine (i.e. D219N). Electrophysiological analysis revealed that K353delins18X and D219N altered $GABA_A$ receptor function by reducing the total surface expression of mature protein and/or by curtailing neurotransmitter effectiveness. Both defects would be expected to have a detrimental effect on inhibitory control of neuronal circuits. In contrast, the single point mutation identified in the *GABRG2* gene, namely P83S, was indistinguishable from the wildtype subunit in terms of surface expression and functionality. This finding was all the more intriguing as the mutation exhibited a high degree of penetrance in three generations of one French Canadian family. Further experimentation will be required to understand how this mutation contributes to the occurrence of IGE in these individuals.

Introduction

Epilepsy is one of the most common neurological conditions, with a prevalence of approximately 5–10 per 1000 in North America (Theodore *et al.*, 2006). For most patients (approximately 65%) with either generalized or partial epilepsies, the underlying cause is unknown and the condition is referred to as being 'idiopathic'. Overall, 30% of all individuals with epilepsy have idiopathic generalized epilepsy (IGE; McCorry *et al.*, 2006), a condition marked by generalized seizures and specific electroencephalographic abnormalities with no discernible defects in brain structure. In the past two decades, an increasing number of mutations in genes predisposing for various forms of IGE have been identified (Turnbull *et al.*, 2005; Macdonald *et al.*, 2010). Most of the mutations are found in genes encoding for voltage- or ligand-gated ion channels; they account for most familial forms of the disease (Scheffer & Berkovic, 2003; Hahn & Neubauer, 2009; Catterall *et al.*, 2010; Macdonald *et al.*, 2010; Zamponi *et al.*, 2010). This finding has led to the conclusion that IGE is primarily a 'channelopathy' (Kullmann & Waxman, 2010), although not all mutations encode for ion channels (e.g. Pal *et al.*, 2003).

γ-Amino-butyric acid $(GABA)_A$ receptors feature among several of the candidate ion channels thought to be involved in IGE (Galanopoulou, 2010; Kullmann & Waxman, 2010; Macdonald *et al.*, 2010). In keeping with this, signaling through $GABA_A$ receptors provides almost all inhibitory tone to the adult brain, balancing the tendency of excitatory neuronal circuits to induce convulsions (Ben Ari, 2006). To achieve this, $GABA_A$ receptors hyperpolarize neurons by fluxing chloride ions through a central anion-selective pore that is a pentamer assembled from 19 possible subunits, namely $\alpha1-\alpha6$, $\beta1-\beta3$, $\gamma1-\gamma3$,

Correspondence: Dr Derek Bowie and Dr Patrick Cossette, as above.
E-mails: derek.bowie@mcgill.ca and patrick.cossette@umontreal.ca

*Both authors contributed equally to this study.

Received 1 April 2011, revised 3 May 2011, accepted 16 May 2011

δ, ε, π, θ and $\rho 1 - \rho 3$ (Olsen & Sieghart, 2008). Subunit number and organization around this central pore is ordered (Chang *et al.*, 1996) with the most commonly expressed $GABA_A$ receptor thought to consist of two each of α and β and a γ_2 (Sarto-Jackson & Sieghart, 2008). To date, most $GABA_A$ receptor mutations associated with IGE have been found in the γ_2 (*GABRG2*) subunit (Baulac *et al.*, 2001; Wallace *et al.*, 2001; Harkin *et al.*, 2002; Kananura *et al.*, 2002; Audenaert *et al.*, 2006; Sun *et al.*, 2008; Shi *et al.*, 2010) though mutations in the α_1 (*GABRA1*; Cossette *et al.*, 2002; Maljevic *et al.*, 2006), δ (*GABRD*; Dibbens *et al.*, 2004) and β_3 (*GABRB3*; Lachance-Touchette *et al.*, 2010; Tanaka *et al.*, 2008) subunits have also been described.

Here, we identify three novel mutations from a population of French Canadians with IGE. Two mutations found in the *GABRA1* gene were associated with disrupted plasma membrane delivery of the fully assembled $GABA_A$ receptor as well as deficits in its signaling properties. In contrast, a single point mutation found in the *GABRG2* gene had little effect on surface membrane expression or the functional properties of the mature receptor, a property not yet described for any other IGE-related $GABA_A$ receptor mutants. Future experiments will be needed to ascertain whether this mutation disrupts a more nuanced aspect of $GABA_A$ receptor biology.

Materials and methods

Subjects and healthy-control samples

Ninety-five individuals with IGE were selected from the Quebec population of Canada. The methods used for the clinical characterization of this cohort have been described previously (Kinirons *et al.*, 2008). The phenotypes in these probands include 21 cases with juvenile myoclonic epilepsy, 12 with childhood absence epilepsy, eight with generalized epilepsy with febrile seizures plus and 54 with IGE not otherwise specified. This cohort includes 46 familial cases (17 families with two affected individuals, nine with three affected individuals and 20 with four or more affected individuals) and 49 singletons. A summary of clinical manifestations of affected individuals with mutations in *GABRA1* or *GABRG2* are provided in Supporting Information Table S1. All the individuals, including 190 healthy ethnically-matched controls, gave informed consent, after which patient information and blood samples were collected. DNA was extracted from peripheral blood through the use of standard protocols.

Screening for mutations and variation analysis

We detected a total of three novel variants in *GABRA1* and *GABRG2* genes by re-sequencing them in a cohort of 95 subjects (53 females and 42 males) with epilepsy (Table 1). The open reading frame of each gene codes for the $\alpha 1$ and $\gamma 2$ subunits of the $GABA_A$ receptor. The genomic organization of each gene was obtained from the UCSC Genome Browser (Hg18 build; http://genome.ucsc.edu/). All the coding regions of the genes were amplified by polymerase chain reaction (PCR, AppliedBiosystems9700; Applied Biosystems, Foster City, CA, USA). We designed primers from at least 50 bp of the exon–intron boundaries to examine the entire exonic sequences of the gene and splice sites. PCR primer pairs were designed using the software *Exon primer* from the UCSC Genome Browser. We used the sequence of reference NM_000806 and NM_000816 for the *GABRA1* and *GABRG2* genes respectively. The amplicons were analyzed on an ABI3730 automatic sequencer (Applied Biosystems) by using *Mutation Surveyor* software version 3.0 (SoftGenetics, State College, PA, USA). All mutations and variants were confirmed by

TABLE 1. Mutations identified in $GABA_A$ receptor genes

Gene	Nucleotide (genomic)	Nucleotide (mRNA)	Amino acid (protein)	Maf	Polyphen		SIFT		SNAP		Panther		Conservation (amino acid)
					PSIC score	Prediction	Score	Prediction	Score	Prediction	subP SEC	Pdeleterious	
GABRA1	g.chr5:161242237G>A	r.655G>A	p.D219N	0.01	0.787	Benign	0.33	Tolerated	89%	Neutral	−4.8313	0.86192	Highly conserved
GABRA1	g.chr5: 161256674_161256675ins25	r.1059_1060 ins1242	p.K353delins18X	0.01	N/A	N/A	N/A	N/A	N/A	N/A	N/A	N/A	N/A
GABRG2	g.chr5:161453551C>T	r.247C>T	p.P83S	0.01	1.982	Possibly damaging	0.00	Affects protein function	70%	Non-neutral	−5.5871	0.93003	Highly conserved

Maf, Minor allele frequency; PSIC, position-specific independent counts; subPSEC, substitution position-specific evolutionary conservation; Pdeleterious, probability of functional impairment.

resequencing. For the analyses of detected single-nucleotide polymorphisms (SNPs) in our cohort, we used the dbSNP Build 133 based on NCBI Human Genome (version 5.2) and The Human Gene Mutation Database at the Institute of Medical Genetics in Cardiff. The novel SNPs and known mutations were tested by sequencing the corresponding fragment in a control population of 190 individuals. These French Canadian controls underwent a systematic questionnaire in order to exclude symptoms compatible with seizures as well as any familial history of epilepsy. Transmission of any variant or mutation was tested in parents and relatives of the probands when available.

In silico predictions

The combination of four programs (*PolyPhen*, *SIFT*, *SNAP* and *PANTHER*) was used to predict the potential disruptiveness of an amino acid substitution on the structure and function of a human protein (Table 1). The genome information and homology searches were based on the UCSC Genome Browser database (NCBI36/hg18 assembly). Sequence cluster alignments were performed by using the Clustal W algorithm. All novel SNPs identified were also tested for their potential effects on splicing enhancer/inhibitor elements by using *ESEfinder* (Cartegni *et al.*, 2003) and *RESCUE-ESE* programs (data not shown; Fairbrother *et al.*, 2002).

Cloning and mutagenesis

For biochemical and functional analysis of each mutation we cloned human $\alpha1$, $\beta2$ and $\gamma2$ subunits of the $GABA_A$ receptor into the pcDNA3.1(-) vector (Invitrogen, Carlsbad, CA, USA). As a positive control, we also cloned the A322D mutant of *GABRA1* gene which has been described previously (Cossette *et al.*, 2002; Krampfl *et al.*, 2005). The QuickChange site directed mutagenesis kit (Stratagene, Agilent Technologies, Cedar Creek, TX, USA) was used to introduce D219N and P83S mutations in the *GABRA1* and *GABRG2* clones respectively, as described previously (Cossette *et al.*, 2002; Krampfl *et al.*, 2005). The sequence of the mutant *GABRA1* (K353delins18X) subunit was obtained by PCR from the cDNA of the patient A-III-I and subcloned into the vector containing the wildtype *GABRA1* to replace the 3′ part of the gene as described below. For the immunofluorescence experiments, a myc tag was inserted by PCR at the N-terminus between amino acids four and five of both the $\alpha1$ and the $\gamma2$ subunits. All constructs were sequenced to confirm the presence of the mutations and to exclude any other variants that may have been introduced during PCR amplification.

Reverse transcriptase PCR (RT-PCR)

To obtain the K353delins18X mutant, total cellular RNA from patient A-III-I was obtained from lymphoblastoid cell lines. RNA of the sample was reverse-transcribed to complementary DNA (cDNA) using the ThermoScript RT-PCR System kit (Invitrogen). PCR-amplification was performed on the cDNA using the Advantage kit (Applied Biosystems). The cDNA was amplified with *GABRA1*-specific primers flanking intron 11: *GABRA1*-5′ (exon 10): GAGCATCAGTGCCAGAAACTCCCTCCC, *GABRA1*-3′ (exon11): CGGGCTTGACCTCTTTAGGTTCTATGG and *GABRA1*-3′-UTR: CCCCCTCTTTTCTCTCTCATTCTGTCTCC. All primers were designed using NM_000806 as the reference sequence. PCR conditions were: 95 °C for 1 min, 40 cycles of 20 s at 95 °C, 30 s at 65 °C, 45 s at 98 °C, followed by 68 °C for 7 min. Reactions were cycled on an AppliedBiosystems9700 PCR instrument. The amplicons were analyzed on an ABI3730 automatic sequencer by using *Mutation Surveyor* software version 3.0.

Immunofluorescence

To assess the surface and cellular distribution of wildtype and mutant receptor subunits, myc-tagged wildtype and mutant $\alpha1$ subunits were co-transfected with wildtype $\beta2$ and $\gamma2$. Myc-tagged wildtype and mutant $\gamma2$ subunits were also co-transfected with wildtype $\alpha1$ and $\beta2$ in HEK 293 cells that had been plated on 22-mm glass coverslips coated with poly-L-lysine in DMEM containing 10% fetal bovine serum and incubated for 18 h. All transient transfections were performed at a ratio of 1 : 1 : 2 for $\alpha1$: $\beta2$: $\gamma2$ (2 : 2 : 4 μg per dish) using Lipofectamine 2000. For the endoplasmic reticulum (ER) colocalization experiments, a plasmid for the expression of the dsRed2-ER marker (Clontech, Mountain View, CA, USA) was co-transfected in a ratio of 1 : 1 : 2 : 1 for $\alpha1$: $\beta2$: $\gamma2$: dsRed2-ER respectively. After 24 h, cells were washed and fixed in 4% formaldehyde in PBS. Cells were washed and blocked once with PBS–glycine, 20 mM, and once with PBS containing 10% goat serum, 0.5% BSA and 0.1% Triton X-100 (10 min). Cells were then incubated with anti-myc-tag rabbit monoclonal antibody (1 : 200 dilution in blocker; cat, no. 2278; Cell Signaling, Millipore, Billerica, MA, USA) alone or with pan-Cadherin mouse monoclonal antibody for membrane co-localization (ab6528, 1 : 250 dilution, 1 h at room temperature; Abcam, Cambridge, MA, USA). This step was followed by three washes with blocking solution. Cells were then incubated for 1 h at room temperature with Alexa Fluor 488 rabbit IgG antibody (Molecular Probes, Invitrogen) and/or Alexa Fluor 568 mouse IgG antibody (Molecular Probes, Invitrogen) at a 1 : 400 dilution in blocking solution. Cells were washed three times with blocking solution and mounted onto glass slides. Fluorescently labelled cells were imaged using a confocal microscope (Leica TCS SP5).

Affinity purification of surface receptors

HEK 293 cells were plated in 10-cm dishes coated with poly-L-lysine in DMEM containing 10% fetal bovine serum and incubated for 18 h. Cells were transiently transfected with the cDNA encoding for wildtype or mutant $\alpha1$ and gamma2, together with the wildtype beta2 subunit using a ratio of 1 : 1 : 2 for $\alpha1$: $\beta2$: $\gamma2$ (12 : 12 : 24 μg). Twenty-four hours post-transfection, intact cells were washed twice with ice-cold PBS and incubated with the membrane-impermeable biotinylation reagent Sulfo-NHS SS-Biotin (0.5 mg/mL in PBS; Pierce, Rockford, IL, USA) for 30 min at 4 °C to label surface membrane proteins. To quench the reaction, cells were incubated with 10 mM glycine in ice-cold PBS twice for 5 min at 4 °C. Sulfhydryl groups were blocked by incubating the cells with 5 nM *N*-ethylmaleimide (NEM) in PBS for 15 min at room temperature. Cells were solubilized overnight at 4 °C in lysis buffer (Triton X-100, 1%; Tris–HCl, 50 mM; NaCl, 150 mM; and EDTA, 5 mM; pH 7.5) supplemented with protease inhibitors (Complete Mini; Roche, Mississauga, ON, Canada) and 5 mM NEM. Lysates were cleared by centrifugation (16 000 ***g***, 10 min at 4 °C). An aliquot of each lysate was saved. Biotinylated surface proteins were affinity-purified from the remaining cell lysates by incubating for 1 h at 4 °C with 100 μL of immobilized neutravidin-conjugated agarose bead slurry (Pierce). The samples were then subjected to centrifugation (16 000 ***g***, 10 min, at 4 °C), an aliquot of the supernatant was kept and the beads were washed six times with buffer (Triton X-100, 0.5%; Tris–HCl, 50 mM; NaCl, 150 mM; and EDTA, 5 mM; pH 7.5). Surface proteins were eluted from beads by incubating for 30 min at room temperature with 200 μL

of LSB/Urea buffer [2× Laemmli sample buffer (LSB) with 100 mM DTT and 6 M urea; pH 6.8]. Protein concentration of the lysates and the supernatants was determined using the Bradford method. Equal amounts of lysate and supertatant proteins were prepared by adding 2× LSB/urea buffer and loaded into an SDS-polyacrylamide gel (SDS-PAGE), as well as 30 μL of affinity-purified proteins.

Western blotting

Protein samples were run on 10% SDS-PAGE and transferred to PVDF membranes. Blots were incubated for 1 h at room temperature in blocking buffer containing 5% non-fat milk in TTBS (NaCl, 500 nM; Tris base, 20 mM; and Tween-20, 0.1%) followed by a 2-h incubation at room temperature with anti-α1 (1 : 2000; Chemicon MAB339; Chemicon, Millipore, Billerica, MA, USA) antibodies in blocking buffer. The blots were then washed (3 × 20 min) with TTBS and incubated for 1 h at room temperature in horseradish peroxidase-conjugated donkey anti-mouse IgG or horseradish peroxidase-conjugated donkey anti-rabbit IgG (Jackson Immuno Research, West Grove, PA, USA) at a 1 : 5000 dilution in blocking buffer. The blots were then washed (3 × 20 min in TTBS) and revealed by chemiluminescence with Western Lightning Plus-ECL (PerkinElmer, Waltham, MA, USA). GAPDH was used as a control to demonstrate that equal amounts of protein were loaded (mouse monoclonal anti-GAPDH; Chemicon MAB374, 1 : 2000 dilution). Similarly, pan-cadherin protein expression was used to normalize the loading of membrane proteins (mouse monoclonal pan-cadherin; Abcam ab6528, 1 : 5000 dilution).

Cell culture and transfection

Techniques used to culture and transfect mammalian cells have been described in detail elsewhere (Bowie, 2002). Briefly, tsA201 cells (provided by R. Horn, Jefferson Medical College, PA, USA) were maintained at a 70–80% confluency in minimal essential medium with Earle's salts, 2 mM glutamine and 10% fetal bovine serum supplemented with penicillin (100 units/mL) and streptomycin (100 μg/mL). After plating at low density (2×10^4 cells/mL) on 35-mm plastic dishes coated with poly-D-lysine, cells were transfected with the cDNAs encoding the human $GABA_A$ receptor subunits in a 1 : 1 : 2 ratio (α1 : β2 : γ2), using the calcium phosphate technique as previously described (Bowie, 2002). For analysis of the mutant subunits, the cDNAs encoding for the α1 (A322D), α1 (K353delins18X), α1 (D219N) and γ2 (P83S) replaced the corresponding wildtype subunits. The cDNA for enhanced green fluorescent protein was routinely co-transfected (0.1 μg per dish) to identify transfected cells.

Electrophysiological solutions and techniques

Experiments were performed 24–48 h after transfection. GABA (Sigma, Oakville, ON, Canada) was dissolved in external solution containing (in mM): NaCl, 150; HEPES, 5; $MgCl_2$, 2; and $CaCl_2$, 1; with 2% phenol red. Internal pipette solution contained (in mM): KCl, 150; EGTA, 5; $MgCl_2$, 1; and MgATP, 2. The pH and osmotic pressure of internal and external solutions were adjusted to 7.3–7.4 and 310 mOsm respectively. For Zn^{2+}-block experiments, $ZnCl_2$ (Sigma) was diluted to a 10-μM final concentration in control and agonist external recording solutions from 10-mM frozen stocks. Diazepam was diluted to a 1-μM final concentration in control and agonist external recording solutions from 1-mM frozen stocks. All recordings were performed with an Axopatch 200B amplifier (Molecular Devices, Inc., CA, USA) using thin-walled borosilicate glass pipettes (2–5 MΩ) coated with dental wax to reduce electrical noise. Control and agonist solutions were rapidly applied to outside-out patches excised from transfected tsA201 cells using a piezoelectric stack (Physik Instrumente, Germany). Solution exchange (10–90% rise-time, 150–250 μs) was routinely determined at the end of each experiment by measuring the liquid junction current (or exchange current) between the control and external solution containing an additional 10 mM NaCl. Current records were filtered at 5 kHz and digitized at 25 kHz, and series resistances (3–10 MΩ) compensated by 95%. All recordings were performed at a holding potential of −60 mV. Data acquisition was performed using pClamp9 software (Molecular Devices) and analysis and statistics were performed using Microsoft Excel (Microsoft Corporation, Redmond, WA, USA). All datasets reported in this study exhibited a normal distribution as determined by the Shapiro–Wilk normality test with *P*-values > 0.05. Figure illustrations were made using Origin 7.0 (OriginLab, Northampton, MA, USA). All experiments were carried out at room temperature (22–23 °C). For whole-cell recordings, control and agonist solutions were locally applied to the recorded cell.

Results

Identification of mutations in the GABRA1 and GABRG2 genes

We have identified three novel genetic mutations in the alpha1 (α1) and gamma2 (γ2) subunits of the $GABA_A$ receptor (Fig. 1). The amino acid numbering for these mutations refers to the immature protein including the signal peptide. Screening the *GABRA1* gene identified two variants, the first of which was an insertion of 25 nucleotides in the intron close to the splice acceptor site of exon 11 (Fig. 2A). The exact sequence of the insertion has been obtained by subcloning the PCR fragment of the mutated allele in a TOPO-cloning vector (Invitrogen). This 25-bp insertion in the genomic sequence of *GABRA1* (g.chr5:161256674_161256675ins25) changes the position of the putative branch site to a distance of 63 bp from exon 11. The maximal distance between the splice acceptor and the branch sites is usually between 20 and 50 bp (Keren *et al.*, 2010). We therefore hypothesized that this mutation prevents cleavage at the 3′ end of intron 10 (Fig. 2A). Consistent with this hypothesis, RT-PCR of the A-III-I individual has shown a 1242-bp insertion which corresponds to the retention of intron 10 (r.1059_1060ins1242). This splice mutation, which results in a complex rearrangement of the *GABRA1* transcript, predicts a deletion of the fourth transmembrane domain in the mature α_1 protein, as well as the insertion of 18 amino acids and a premature stop codon (p.K353delins18X; Fig. 2B). A total of three affected members from this family carry this K353delins18X mutation in *GABRA1*, as well as an obligated carrier (Fig. 1A). The second α1 variation was due to a missense mutation in the aspartate 219 residue to an asparagine (i.e. D219N) which was detected in four out of five affected individuals with either IGE or febrile seizures in pedigree B (Fig. 1B). Sequence analysis indicated that carriers are heterozygous with respect to a G>A substitution, which is predicted to change an aspartic acid to an asparagine at position 219 of the α1 $GABA_A$ receptor subunit. The K353delins18X and D219N mutations were not detected in 190 healthy controls (102 females and 88 males), nor were additional variations in *GABRA1* detected.

We also detected a missense mutation in the γ2 $GABA_A$ receptor subunit which changed the proline 83 residue of the immature protein to a serine (i.e. P83S; Fig. 1C), in a large family exhibiting febrile seizures and IGE over three generations. This P83S mutation was found in all affected individuals ($n = 9$) of this multiplex family (Fig. 1C). The heterozygous mutation Pro83Ser is found near a region which affects benzodiazepine binding on the extracellular ligand-

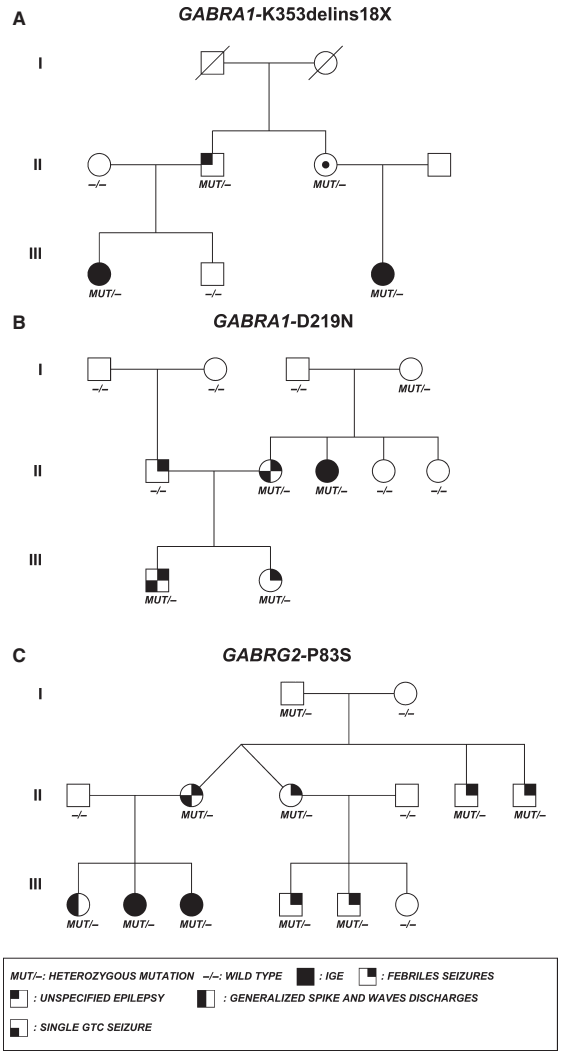

FIG. 1. Segregation profiles of the novel $GABA_A$ receptor mutants in French Canadian families affected with IGE and related phenotypes. (A and B) The (A) K353delins18X and (B) D219N mutations in *GABRA1* were found in four individuals of the same family over two generations. (C) The P83S mutation in *GABRG2* was found in nine individuals of the same family over two generations. Blackened symbols indicate affected individuals.

binding domain (Goldschen-Ohm *et al.*, 2010). Importantly, this mutation was not identified in the 190 French Canadian control subjects. In addition, no other additional mutations in *GABRG2* gene were detected in this cohort of IGE patients.

In silico analysis, using a combination of four different programs (*PolyPhen*, *SIFT*, *SNAP*, *PANTHER*), predicts that the P83S mutation should have a damaging effect on protein structure or function whereas the D219N in α1 is predicted to have a benign outcome (Table 1).

Subcellular distribution of mutant and wildtype $GABA_A$ receptors

Prior work has shown that other $GABA_A$ receptor mutations associated with IGE can affect the cellular distribution of the mature protein (Macdonald *et al.*, 2010). In many cases, the mutant receptor is held up in the ER and/or exhibits reduced surface expression (Macdonald *et al.*, 2010). To explore both of these issues, we examined the subcellular distribution of mutant α1 subunits that had been co-expressed with wildtype β2 and γ2 subunits (Figs 3 and 4). As controls, we compared the staining pattern of the wildtype α1 subunit which traffics normally and the α1 A322D mutant which accumulates in the ER and exhibits reduced plasma-membrane surface expression (Cossette *et al.*, 2002; Krampfl *et al.*, 2005; Maljevic *et al.*, 2006). As antibody recognition for the myc-tagged γ2 $GABA_A$ receptor subunit was variable, we focused only on examining its functional properties using electrophysiology (see below). Myc-tagged constructs of wildtype and mutant α1 subunits were expressed in HEK293 cells and visualized with a fluorescent-tagged myc antibody (Figs 3 and 4). ER localization was then estimated by overlaying the α1 subunit staining pattern with that of dsRed2-ER as a selective marker of this organelle (Fig. 3). Surface expression levels were determined in a similar manner using red-fluorescent pan-cadherin as a marker of the plasma membrane (Fig. 4).

As expected, there was little overlap in the staining pattern for the wildtype α1 subunit and that of the ER (Fig. 3, left column) whereas the distribution of the α1 A322D mutant co-localized almost exclusively with dsRed2-ER (Fig. 3, middle column) in agreement with prior work showing that this subunit is retained within the cell during protein synthesis and assembly. The staining pattern for the α1 K353delins18X also closely matched that of dsRed2-ER (Fig. 3, middle) whereas there was only partial, though substantial, overlap in the distribution of the α1 D219N mutant (Fig. 3, right column), indicating that some of this latter mutant protein may be trafficked to the surface of the plasma membrane. In support of this, the pattern of expression of both pan-cadherin and α1 D219N mutant were similar and comparable to the wildtype α1 subunit (Fig. 4A, left and right columns). In contrast, the staining pattern of pan-cadherin did not match that of α1 K353delins18X or α1 A322D subunits (Fig. 3, middle columns), further confirming that these mutations disrupt plasma membrane surface expression.

To examine more subtle defects in the targeting of the mutant subunits to the plasma membrane, we used cell surface biotinylation and Western blotting to quantify and compare surface expression of the mutants to wildtype subunits. To do this, HEK293 cells transfected with wildtype and mutant $GABA_A$ receptors were surface-biotinylated with the membrane-impermeable reagent Sulfo-NHS-SS-Biotin and biotinylated surface expressed proteins recovered from the soluble lysate fraction (i.e. L) by affinity purification (i.e. M; Fig. 4B). The unbound or nonbiotinylated fraction present in the supernatant (i.e. S) was also analysed as it represents the proportion of receptor subunits that are retained intracellularly. As expected of controls, the wildtype α1 subunit was found in both the membrane (M) and supernatant (S) fractions whereas the α1 A322D mutant was largely restricted to the supernatant (Fig. 4B, left and middle columns). Likewise, the K353delins18X mutant was also absent from the membrane fraction and, although it was detected in the supernatant, the band migrated at a lower molecular weight (Fig. 4B, middle column). This finding is consistent with the prediction that this mutation introduces a premature stop codon which truncates the fourth transmembrane domain of the mature α_1 protein. Although we were not able to detect the α1 A322D mutant and K353delins18X in the membrane fraction, it does not exclude the possibility that a small number of receptors were expressed at the plasma membrane. In contrast, the α1 D219N mutant was detected in both the membrane and supernatant fractions (Fig. 4B, right column), in agreement with the staining studies. Compared to the wildtype α1 subunit, there was a 50% decrease in the ratio of surface to total expression of the α1 D219N mutant ($P = 0.0013$, Student's *t*-test).

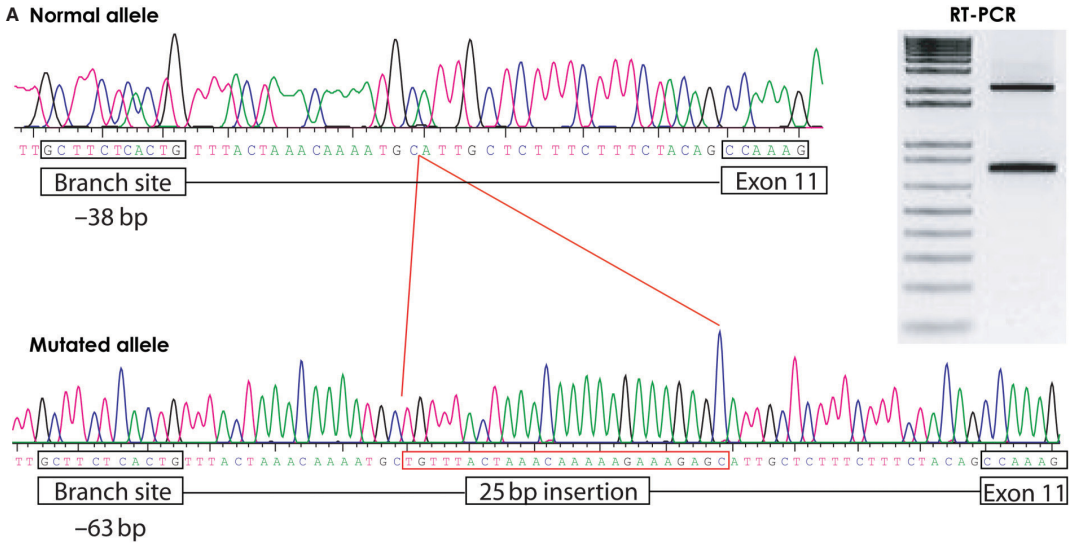

B WT α_1 subunit protein sequence length = 456

MRKSPGLSDCLWAWILLLSTLTGRSYGQPSLQDELKDNTTVFTRILDRLLDGYDNRLRPGLGERVTEVKTD
IFVTSFGPVSDHDMEYTIDVFFRQSWKDERLKFKGPMTVLRLNNLMASKIWTPDTFFHNGKKSVAHNMTMP
NKLLRITEDGTLLYTMRLTVRAECPMHLEDFPMDAHACPLKFGSYAYTRAEVVYEWTREPARSVVVAEDGS
RLNQYDLLGQTVDSGIVQSSTGEYVVMTTHFHLKRKIGYFVIQTYLPCIMTVILSQVSFWLNRESVPARTV
FGVTTVLTMTTLSISARNSLPKVAYATAMDWFIAVCYAFVFSALIEFATVNYFTKRGYAWDGKSVVPEKPK
KVKDPLIKKNNTYAPTATSYTPNLARGDPGLATIAKSATIEPKEVKPETKPPEPKKTFNSVSKIDRLSRIA
FPLLFGIFNLVYWATYLNREPQLKAPTPHQ

K353delins18X α_1 subunit protein sequence length = 371

MRKSPGLSDCLWAWILLLSTLTGRSYGQPSLQDELKDNTTVFTRILDRLLDGYDNRLRPGLGERVTEVKTD
IFVTSFGPVSDHDMEYTIDVFFRQSWKDERLKFKGPMTVLRLNNLMASKIWTPDTFFHNGKKSVAHNMTMP
NKLLRITEDGTLLYTMRLTVRAECPMHLEDFPMDAHACPLKFGSYAYTRAEVVYEWTREPARSVVVAEDGS
RLNQYDLLGQTVDSGIVQSSTGEYVVMTTHFHLKRKIGYFVIQTYLPCIMTVILSQVSFWLNRESVPARTV
FGVTTVLTMTTLSISARNSLPKVAYATAMDWFIAVCYAFVFSALIEFATVNYFTKRGYAWDGKSVVPEK**VN**
ALMVTVVHQYYVSLNLX

FIG. 2. Sequencing of the K353delins18X mutation in *GABRA1*. (A) The normal and mutant alleles were amplified by PCR, sub-cloned in a TOPO-cloning vector (Invitrogen) and sequenced separately. The mutation consists of a 25-bp insertion located between the splice acceptor and branching sites of exon 11 of the *GABRA1* gene. RT-PCR shows an abnormal lower band; sequencing of this band confirmed the retention of the intron leading to a premature stop codon. (B) The amino acid sequence of the wildtype (top) and mutant (bottom) $GABA_A$ receptor. The mutation results in the translation of 18 intronic amino acids and a premature stop codon (red) and the deletion of 103 amino acids.

Functional analysis of mutant α1 and γ2 $GABA_A$ receptor subunits

To measure the functionality of surface receptors, we performed electrophysiological recordings on outside-out patches excised from tsA201 cells transiently transfected with wildtype and mutant $GABA_A$ receptor subunits (Fig. 5). Following activation, $GABA_A$ receptors exhibit rapid desensitization kinetics with a time course of tens of milliseconds (Jones & Westbrook, 1996). Consequently, the advantage of performing experiments on excised membrane patches is that it permits rapid exchange of agonist solution (within 400–500 μs) prior to the onset of desensitization and therefore peak response amplitude and decay kinetics are determined with accuracy.

Typical membrane currents elicited by 10 mM GABA on wildtype or mutant $GABA_A$ receptors are shown in Fig. 5A. Note that peak responses of wildtype $\alpha_1\beta_2\gamma_2$ receptors were considerably larger than $\alpha_1\beta_2$ assemblies (Fig. 5A, upper row), an observation expected from earlier work highlighting the importance of subunit composition to agonist responsiveness (e.g. Verdoorn *et al.*, 1990; Boileau *et al.*, 2003). Likewise, patches containing α1(A322D)β2γ2 receptors elicited much weaker responses to GABA (Fig. 5A, middle row), which is consistent with their reduced surface expression (Fig. 4) and lower agonist sensitivity (Krampfl *et al.*, 2005). We failed to detect responses in any excised patches from cells transfected with the α1 K353delins18X subunit (Fig. 5A, middle row). The lack of responsiveness in excised patches is not due to detection failure as cells did not respond to GABA even in recordings performed in the whole-cell configuration (Fig. 6). Taken together with our staining and biochemical experiments, we conclude that the K353delins18X mutation completely eliminates surface expression of mature $GABA_A$ receptors, an observation supported by the fact that the α-subunit is required for the formation of functional receptors (Mizielinska *et al.*, 2006).

In contrast, we routinely recorded GABA-mediated responses from the cells expressing the α1 D219N and the γ2 P83S subunit mutations (Fig. 5A, lower row). The level of surface expression of α1 D219N-containing receptors, as estimated by peak response amplitude, was modest compared to wildtype $\alpha_1\beta_2\gamma_2$ receptors (Fig. 5B). Although reduced functionality may reflect changes in unitary conductance or

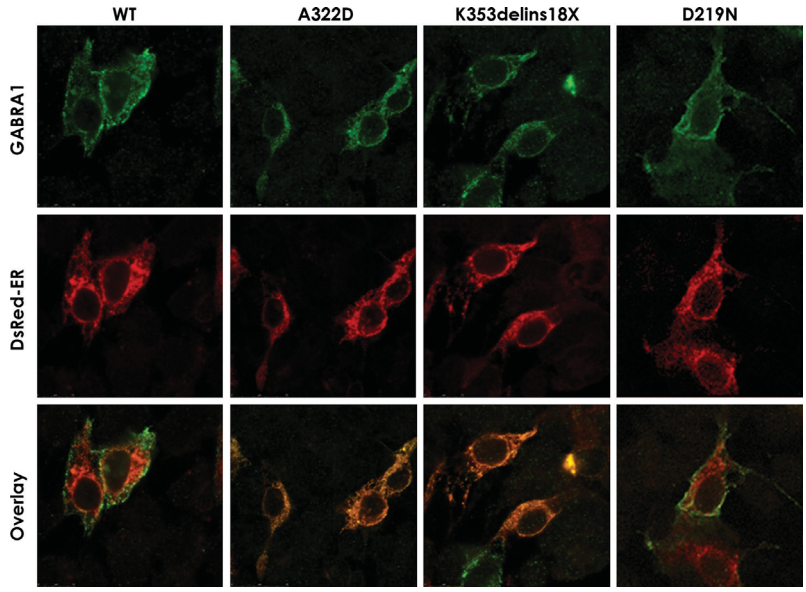

FIG. 3. Mutant α1 subunits co-localized with the ER. Immunostaining of the wildtype *GABRA1* subunit did not co-localize with the ER-marker DsRed-ER (left column). In contrast, the A322D and K353delins18X *GABRA1* mutants co-localized with the ER (middle columns), suggesting that the mutant subunits were retained in the ER and therefore did not reach the cell membrane. Staining for the D219N *GABRA1* mutant was partially co-localized with the ER.

agonist affinity/efficacy, much of it most probably reflects a genuine deficit in the delivery of mature $GABA_A$ receptors to the cell's surface, in agreement with immunohistochemical staining and Western blot analysis (Fig. 4A and B). Interestingly, peak membrane currents elicited by GABA at receptors containing the γ2 P83S subunit were indistinguishable from wildtype $\alpha_1\beta_2\gamma_2$ receptors (Fig. 5A and B). As peak responses of γ2 P83S-containing receptors were substantially larger than wildtype $\alpha_1\beta_2$ receptors (Fig. 5B), we tentatively concluded that this mutation does not affect the incorporation of γ2 subunits into mature $GABA_A$ receptors (see below). Finally, although the degree of equilibrium desensitization was similar for wildtype $\alpha_1\beta_2\gamma_2$ receptors compared to those containing the α1 D219N or γ2 P83S subunits (Fig. 5B, Table 2), we did observe a statistically significant difference between wildtype $\alpha_1\beta_2\gamma_2$ and $\alpha_1\beta_2$ receptors ($n = 22$ and 4 patches for $\alpha_1\beta_2\gamma_2$ and $\alpha_1\beta_2$ respectively, $P = 0.0013$, Student's *t*-test; Fig. 5B) which has been reported by others (Boileau *et al.*, 2003).

α1 D219N mutation altered $GABA_A$ receptor gating kinetics

Structural modeling of the pentameric $GABA_A$ receptor (Ernst *et al.*, 2005) places Asp219 at the interface of the α1 and β2 subunits (Fig. 7A) based on homology with the Torpedo nicotinic acetylcholine receptor (Unwin, 2005) (Fig. 7B). Given that this interface is important for agonist binding and gating (Olsen & Sieghart, 2009), we examined whether replacement of the positively-charged Asp residue with a neutral Asn affects re-equilibration rates following agonist application (i.e. macroscopic desensitization) or removal (i.e. off-kinetics; Fig. 7C and D). To do this, each experimental trace was fitted with two or three exponential components to estimate desensitization and off-kinetics (Fig. 7 and Table 2). For comparison, we also fitted agonist responses mediated by wildtype $\alpha_1\beta_2\gamma_2$ receptors and receptors containing the γ2 P83S subunit.

Typical responses to GABA (1–10 mM) in patches containing wildtype or mutant receptors are shown as overlays in Fig. 7C and D. In all cases, rates into desensitization were fit with either two or three time constants whereas most off-kinetic relaxations were well described by bi-exponential functions (Table 2). As fit values of the fastest ($\tau \sim 1.3$–2.8 ms) and slowest ($\tau \sim 93$–287 ms) desensitization time constants were almost identical in all recordings, the occurrence of an intermediate time constant ($\tau \sim 14$–21 ms) determined whether a third exponential component was included in the fit (Table 2). The biological basis of this intermediate component is not clear; however, prior work on native and recombinant $GABA_A$ receptors has noted variability in desensitization kinetics (e.g. Celentano & Wong, 1994). As we were able to exclude the possibility of variable proportions of $\alpha_1\beta_2$ and $\alpha_1\beta_2\gamma_2$ receptors in excised patches (see below), the distinct kinetic components of desensitization presumably correspond to an intrinsic property of the channel, perhaps modal gating (Lema & Auerbach, 2006).

Desensitization rates and off-kinetics of $GABA_A$ receptors containing the α1(D219N) subunit were appreciably faster than wildtype receptors and those containing the γ2 P83S subunit (Fig. 7C and D and Table 2). In contrast with the off-kinetics in wildtype patches, most of the off-kinetics for the α1 D219N-containing patches (7/9 patches) were fitted with three exponentials. Interestingly, the slowest component of desensitization had a larger contribution that in wildtype receptors (Table 2).

γ2 P83S mutation did not alter Zn^{2+} or benzodiazepine sensitivity

The expression levels (Fig. 5) and kinetic properties (Fig. 7) of $GABA_A$ receptors containing the γ2 P83S subunit were indistinguishable from wildtype $\alpha_1\beta_2\gamma_2$ receptors. To examine whether replacement of Pro83 with Ser affects the allosteric regulation of $GABA_A$

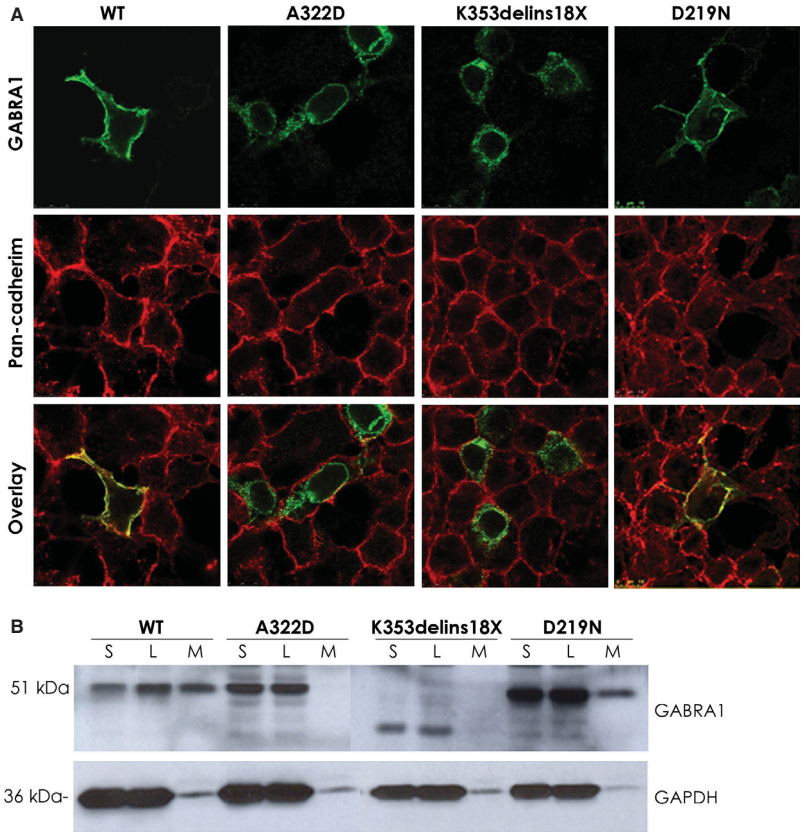

FIG. 4. Surface expression of the mutant α1 subunits. (A) In contrast to the wildtype α1 subunit (left column), immunostaining of A322D and K353delins18X *GABRA1* mutants did not co-localize with the marker for the cell membrane (pan-cadherin; red) when co-expressed with wildtype β2 and γ2 subunits. Staining for the D219N *GABRA1* mutant was also partially co-localized with pan-cadherin, suggesting that there is a reduction in surface expression of this subunit. (B) Western blot of total (L; lysate), biotinylated (M; membrane fraction) and non-biotinylated (S; supernatant) α1 proteins shows a reduction of approxiamtely 50% in the cell surface expression of the α1 D219N subunit. The absence of expression of the A322D and K353delins18X mutations at the cell surface is also shown. Consistent with the introduction of a premature stop codon, the K353delins18X subunit was detected at a lower molecular weight. GAPDH was used to normalize the supernatant and lysate proteins.

receptors, we examined their responsiveness to two known modulators, Zn^{2+} and the benzodiazepine diazepam, both of which are known to be dependent on the γ_2 subunit. For example, co-assembly with the γ2 subunit greatly diminishes sensitivity to Zn^{2+} block (Draguhn *et al.*, 1990) by disrupting some of its binding sites (Hosie *et al.*, 2003). Likewise, benzodiazepine potentiation of GABA-mediated responses is also γ2 subunit-dependent (Pritchett *et al.*, 1989) as it establishes a binding site at the interface with the α-subunit (Ernst *et al.*, 2005).

To examine Zn^{2+} sensitivity, block of 1 mM GABA-evoked responses by 10 μM $ZnCl_2$ was monitored in patches containing wildtype α1β2 or α1β2γ2 receptors which were compared with responses elicited by α1β2γ2(P83S) receptors (Fig. 8A). On average, Zn^{2+} reversibly antagonized α1β2 receptors by 86 ± 1% (n = 4 patches) whereas block of responses mediated by α1β2γ2 and α1β2γ2(P83S) receptors was much smaller (wildtype, 13 ± 4%, n = 6 patches; and P83S mutant, 13 ± 2%, n = 10 patches; $P < 0.0001$, one-tailed Student's t-test; Fig. 8B). Likewise, diazepam sensitivity was similar in α1β2γ2 and α1β2γ2(P83S) receptors (Fig. 9B and C). For example, although responses mediated by α1β2 receptors in 1 μM diazepam were unchanged (n = 3 patches), responses mediated by α1β2γ2 and α1β2γ2(P83S) receptors were potentiated by 20 ± 2 and 22 ± 2% respectively (n = 5 patches each, $P < 0.0001$, Student's paired t-test; Fig. 9B and C). The decrease in α1β2 receptors responses is most probably a consequence of time-dependent response rundown which probably leads to an underestimation of the potentiation of α1β2γ2 and α1β2γ2(P83S) receptors by diazepam. The summary plot in Fig. 9D reveals that there is a relationship between Zn^{2+} and diazepam sensitivity for the different $GABA_A$ receptors we have tested. α1β2 receptors were sensitive to Zn^{2+} block but insensitive to diazepam potentiation (blue squares). In contrast, wildtype α1β2γ2 receptors and those containing the mutant γ2 subunit (black circles and red triangles respectively) were resistant to block by Zn^{2+} but potentiated by diazepam. Taken together, these findings demonstrate that γ2 P83S mutation does not affect $GABA_A$ receptor sensitivity to Zn^{2+} or diazepam.

Discussion

Here we report the identification of three novel mutations in two $GABA_A$ receptor subunits found in patients with IGE and febrile seizures. The clinical manifestations observed in family C with the P83S mutation in *GABRG2* consist of a combination of febrile and absence seizures. This observation is consistent with the phenotype

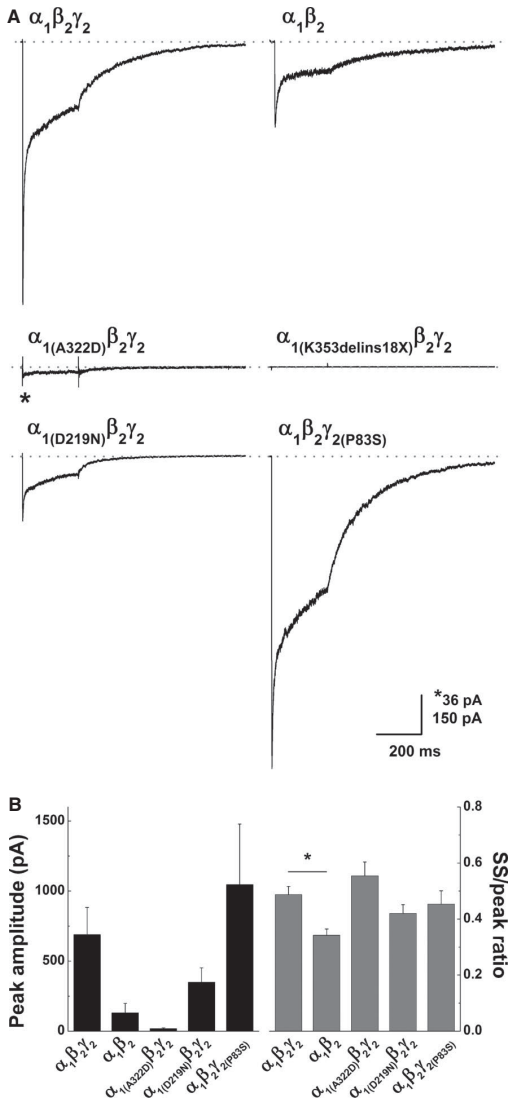

FIG. 5. Wildtype and mutant GABA-A receptors have different functional profiles. (A) Typical electrophysiological responses elicited by 1–10 mM GABA in the wildtype $\alpha1\beta2\gamma2$ (patch no. 081030p1) and $\alpha1\beta2$ (patch no. 090915p2), the α1 A322D (patch no. 081106p2), K353delins18X (patch no. 081219p3) and D219N (patch no. 090312p4) mutants, and in the γ2 P83S (patch no. 081219p1) mutant. (B) The left panel illustrates the mean peak current amplitudes obtained in patches containing each of the subunit combinations. Bars indicate means and error bars indicate SEM.

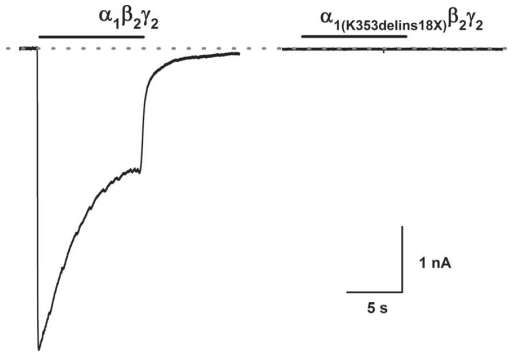

FIG. 6. α1 K353delins18X-containing $GABA_A$ receptors failed to express at the cell's surface. Typical whole-cell electrophysiological recordings of $GABA_A$ receptor responses elicited by 10-s GABA applications (100 μM) in tsA201 cells transfected with wildtype (patch no. 091001c5) or α1 K353delins18X-containing (patch no. 091001c9) receptors. All recordings in wildtype and mutant receptors were performed on the same day to control for transfection efficiency. Cells were voltage-clamped at −60 mV. Black bars indicate the duration of GABA application.

reported in other families with *GABRG2* mutations (Helbig *et al.*, 2008). So far, reports on mutations in *GABRA1* are limited to one family with juvenile myoclonic epilepsy (Cossette *et al.*, 2002) and a single individual with childhood absence epilepsy (Maljevic *et al.*, 2006). In contrast, family B with the D219N mutation in *GABRA1* exhibits mainly febrile seizures, with or without generalized tonic–clonic and absence seizures. Family A with the K353delins18X rather exhibits late-onset, afebrile, generalized tonic–clonic seizures as well as photosensitivity. Compared to *GABRG2*, febrile seizures thus seem to be less consistently associated with *GABRA1* mutations.

Mutations in the *GABRA1* gene, K353delins18X and D219N, segregate into two unrelated French Canadian families and were associated with disrupted plasma membrane delivery of mature protein as well as signaling deficits in the $GABA_A$ receptor. These mutations would be expected to reduce the strength of inhibitory transmission in neuronal circuits and, as a result, predispose the carrier to seizures; this line of reasoning is consistent with other studies purporting a prominent role of mutant $GABA_A$ receptors in IGE (Galanopoulou, 2010; Macdonald *et al.*, 2010). In contrast, we failed to identify any noticeable functional defect in the non-synonymous mutation P83S of the *GABRG2* gene. This observation is surprising as all other IGE-associated $GABA_A$ receptor mutants described to date exhibit defective behavior (Galanopoulou, 2010; Macdonald *et al.*, 2010). Considering its high degree of penetrance in three generations of a large extended French Canadian family and significant conservation across species (Supporting Information Fig. S1), as well as its absence in control chromosomes, all suggest that P83S is a real mutation and not a misclassified SNP. Whether this mutation disrupts a more nuanced aspect of $GABA_A$ receptor signalling such as may occur at the axon initial segment (Wimmer *et al.*, 2010), or it exhibits temperature sensitivity (Kang *et al.*, 2006), will require further experimentation.

Comparison with previous studies

Prior work has catalogued a total of 16 IGE-related variants in both translated and untranslated regions of $GABA_A$ receptor genes (Macdonald *et al.*, 2010). Although the specific molecular effects associated with each mutation can vary significantly from affecting mRNA transcript stability to disruption of channel gating (Macdonald *et al.*, 2010), their overall predicted effect at the level of the neuronal circuit is to undermine inhibition imposed by $GABA_A$ receptors. Consistent with this, electrophysiological experiments revealed that the kinetic properties of receptors assembled with the α1 D219N subunit are faster. Interestingly, the equivalent residue in the Torpedo nAChR is also negatively-charged, but in this case is a Glu which is thought to form an electrostatic interaction with the adjacent Arg (Unwin, 2005). If the α1 GABA receptor subunit adopts a similar structural arrangement, we would predict that this electrostatic

TABLE 2. Desensitization and off-kinetics of WT and mutant GABAA receptors

		Desensitization							Off-kinetics						
Comps	Receptor	τ fast	%	τ int.	%	τ slow	%	*n*	τ fast	%	τ int.	%	τ slow	%	*n*
2	α1β2γ2	2.8 ± 0.4	49	N/A		163 ± 39	51	13	27 ± 0	40	N/A		206 ± 26	60	21
	α1(D219N)β2γ2	2.2 ± 0.2	43	N/A		143 ± 52	57	4	6 ± 4	34	N/A		58 ± 6	66	2
	α1β2γ2(P83S)	2.3 ± 0.8	43	N/A		93 ± 36	57	5	34 ± 8	32	N/A		212 ± 38	69	7
3	α1β2γ2	2.4 ± 0.2	41	14 ± 2	22	279 ± 82	37	9	27 ± 0	17	70 ± 0	73	285 ± 0	10	1
	α1(D219N)β2γ2	1.3 ± 0.4	19	9 ± 4	35	121 ± 22	46	5	2.3 ± 0.4	21	26 ± 4	42	146 ± 18	37	7
	α1β2γ2(P83S)	2.4 ± 0.4	36	21 ± 5	31	287 ± 92	33	5	8 ± 2	4	66 ± 5	41	380 ± 102	55	3

Mean values for time constants (τ) are in ms and are ±SEM. Comps, number of exponential components; int, intermediate; %, percent contribution of component.

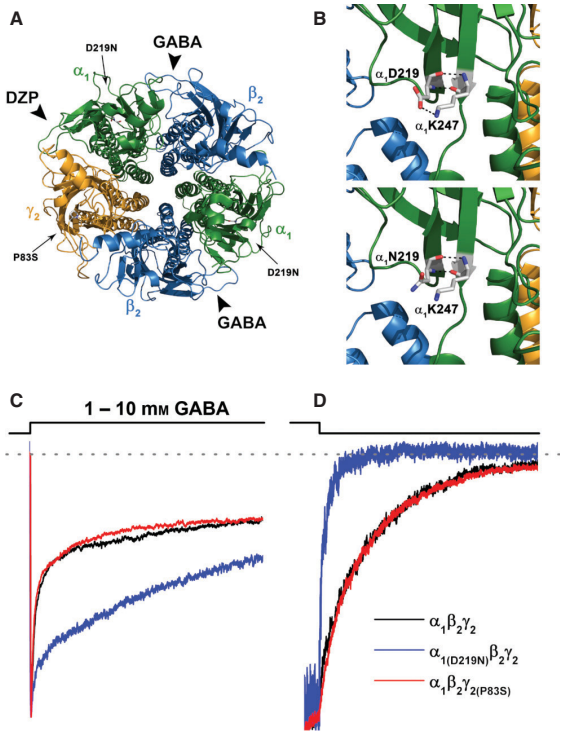

FIG. 7. The α1 D219N subunit disrupted receptor re-equilibration kinetics. (A) Structural model of the $GABA_A$ receptor (Ernst *et al.*, 2005) highlights the organization of the subunits within a pentameric complex as well as the proposed GABA and diazepam (DZP) binding sites. (B) Panels illustrate the possible location of the D219 and N219 residues at the interface between the putative transmembrane and extracellular domains using the *Torpedo marmorata* nAChR X-ray crystal structure [Protein Data Bank (PDB) accession number 2BG9]. (C) Typical electrophysiological responses elicited by 1–10 mM GABA in the wildtype α1β2γ2 (black, patch no. 081030p1), α1 D219N (blue, patch no. 081212p2) and γ2 P83S (red, patch no. 090914p2) mutants. The rates into desensitization for α1 D219N responses appear slower because of the increased contribution of the slow exponential component for this receptor. (D) Typical electrophysiological recordings showing the off-kinetics in the wildtype (patch no. 081030p1) and mutant (α1 D219N, patch no. 090312p2; γ2 P83S, patch no. 090803p1) receptors.

interaction is established between Asp219 and Lys247 (Fig. 7B). Replacement of Asp219 with an Asn would reduce the strength of this interaction and therefore may account for the accelerated $GABA_A$ receptor kinetics observed in our experiments.

The K353delins18X frameshift mutation alters the downstream amino acid sequence and results in the introduction of a premature translation–termination codon. This results in a truncation of the fourth transmembrane domain of the subunit and its retention in the ER (Figs 3 and 4). Other frameshift mutations in the coding sequence of *GABRA1* have been reported (975delC and S326fs328X; Kang *et al.*, 2009). Kang *et al.* suggest that premature translation can produce mRNA degradation through the activation of molecular pathways such as nonsense-mediated decay and reduced mutant α1 subunit mRNA. Because the α1 subunit is essential for the formation of functional $GABA_A$ receptors, a decrease in this subunit will also result in a decrease in surface $GABA_A$ receptors (Mizielinska *et al.*, 2006). In an intact neuronal system, the two novel *GABRA1* mutants, D219N and K353delins18X, could prove to be deleterious by causing an imbalance between excitation and inhibition. A decrease in function or expression could also lead to haploinsufficiency if the intact allele is not sufficient to produce the wildtype phenotype.

The paradox of the γ2 P83S subunit mutant

The $GABA_A$ receptor γ2 subunit fulfills a number of roles including the clustering of receptors and postsynaptic recruitment of the scaffolding protein gephyrin (Essrich *et al.*, 1998) as well as determining sensitivity to allosteric modulators such as Zn^{2+} and benzodiazepines (Olsen & Sieghart, 2009). The binding site for benzodiazepines occurs at the interface between α_1 and γ_2 (Sigel & Buhr, 1997; Boileau *et al.*, 1998) whereas the γ_2/β_2 subunit interface is the location of the γ_2 R82Q mutation that is implicated in childhood absence epilepsy and febrile seizures (Wallace *et al.*, 2001). As $GABA_A$ receptors containing the R82Q mutation exhibit altered kinetics and reduced benzodiazepine sensitivity (via a long-distance effect) as well as defective trafficking (Bowser *et al.*, 2002; Kang *et al.*, 2006; Goldschen-Ohm *et al.*, 2010), we anticipated a marked phenotype for the adjacent P83S mutant. Instead, we failed to observe any defective behaviour in terms of functional expression levels or sensitivity to benzodiazepines or Zn^{2+}. Given this, we conclude that Pro83 does not participate in the stability of the salt-bridge proposed to be a critical determinant of benzodiazepine efficacy (Goldschen-Ohm *et al.*, 2010). It would be interesting in future experiments to determine whether an appreciable phenotype can be assigned to the P83S mutant when $GABA_A$ receptors are assembled from β1 or β3 subunits rather than the β2 subunit used in the present study.

Working towards the molecular basis of IGE

Although the cause of the common IGE syndromes is unknown, there are increasing examples of familial cases that are genetic in origin

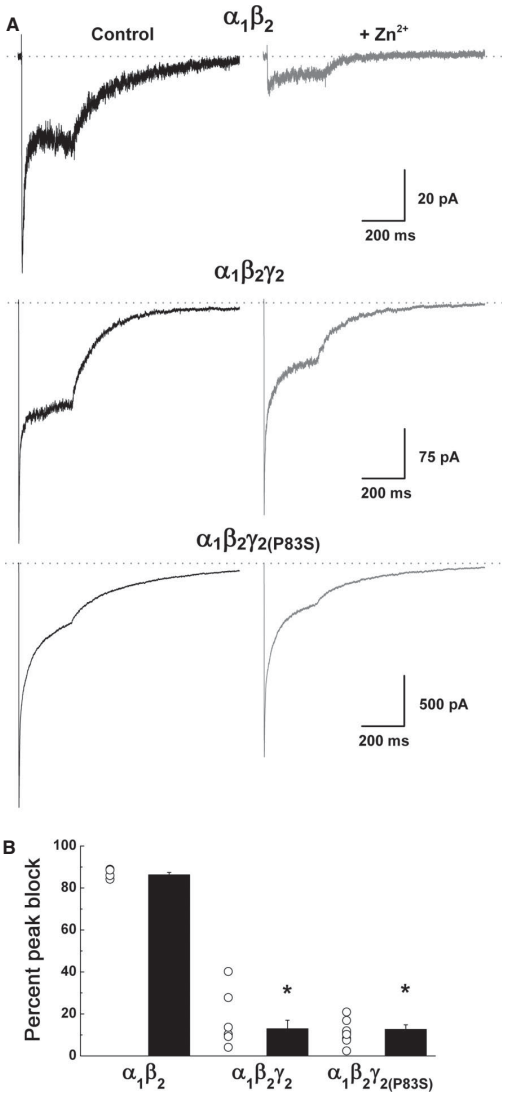

FIG. 8. The γ2 P83S mutation does not affect Zn^{2+} block of GABA-A receptors. (A) Typical electrophysiological responses elicited by 1 mM GABA in the absence (black) or presence (grey) of 10 μM Zn^{2+} for the wildtype $\alpha1\beta2$ (top row, patch no. 090914p1) and $\alpha1\beta2\gamma2$ (middle row, patch no. 090721p1) receptors, as well as the γ2 P83S-containing receptors (lower row, patch no. 090924p2). (B) This panel shows the mean percentage of peak current that was blocked by 10 μM Zn^{2+}. Bars indicate means and error bars indicate SEM. Circles are individual data.

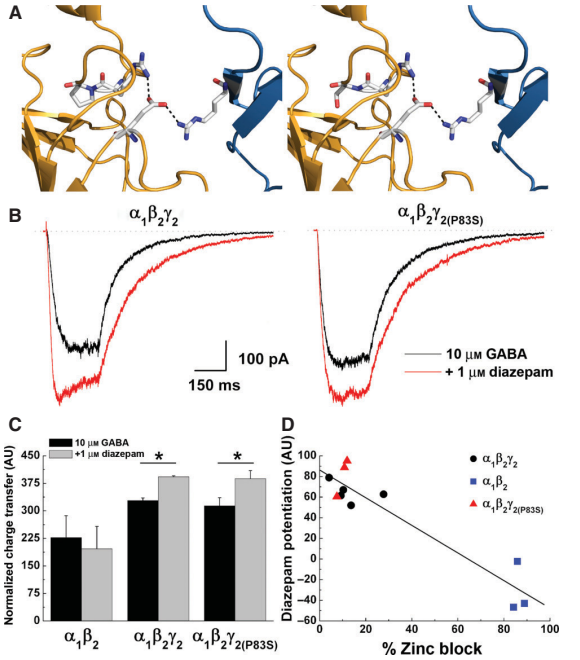

FIG. 9. The γ2 P83S mutation does not affect diazepam regulation of GABA-A receptors. (A) Homology model showing the possible conformation of the P83 and S83 residues at the interface between the γ2 and β2 subunits (PDB 2BG9). The three residues thought to allosterically modulate the benzodiazepine-binding site (γ2R82, γ2E178 and β2R117) are also shown, and do not appear to be disrupted by the P83S mutation. (B) Example electrophysiological traces in wildtype (patch no. 090713p4) and γ2 P83S-containing receptors (patch no. 090724p1) showing the response modulation by 1 μM diazepam. Mutant responses were indistinguishable from wildtype responses. (C) Diazepam potentiation was characterized by measuring the area under the curve for each response. This panel summarizes the mean charge transfer (in arbitrary units) for the $\alpha1\beta2$, $\alpha1\beta2\gamma2$ and $\alpha1\beta2\gamma2$(P83S) receptors. Bars indicate means and error bars indicate SEM. Responses from γ2-containing receptors were significantly potentiated by diazepam. (D) This graph demonstrates the relationship between Zn^{2+} block and diazepam potentiation for $\alpha1\beta2$, $\alpha1\beta2\gamma2$ and $\alpha1\beta2\gamma2$(P83S) receptors. Receptors containing a γ2 subunit (wildtype or mutant) exhibited substantial diazepam potentiation and little Zn^{2+} block, while receptors lacking a γ2 subunit showed the opposite relationship.

(Scheffer & Berkovic, 2003), most probably involving several interacting factors. It has also been proposed that it represents a 'channelopathy' given the preponderance of genetic defects found in ion channels expressed by individuals with familial IGE (Scheffer & Berkovic, 2003; Hahn & Neubauer, 2009; Catterall *et al.*, 2010; Macdonald *et al.*, 2010; Zamponi *et al.*, 2010). Understanding the molecular basis of IGE, as it relates to the $GABA_A$ receptor, also needs to take into account the effect of genetics on the susceptibility of individual neuronal cell types and their neuronal circuits as has emerged from studying $Na_V1.1$ channels in epilepsy (Catterall *et al.*, 2010). By comparing the phenotypic properties of homozygous null or heterozygous $Na_V1.1$ mice, several groups have noticed that lesions in the hippocampal circuit primarily affect the excitability of GABAergic interneurons, which control circuit inhibition, whilst having little or no effect on the firing properties of the excitatory pyramidal cells (Yu *et al.*, 2006; Ogiwara *et al.*, 2007). In other words, although all neuronal cell types either lack or have reduced $Na_V1.1$ signaling in either null or heterozygous mice respectively, the defect almost exclusively affects GABAergic interneurons, an observation that could not have been appreciated from genetic studies alone.

A similar strategy to examine the $GABA_A$ receptor γ2 subunit mutant R82Q, which is associated with familial childhood absence epilepsy, has also led to unexpected insights. Here, the onset of seizures in heterozygous mice occurs abruptly during development (around postnatal day 20) as occurs in the human condition (Tan *et al.*, 2007). In support of this, seizure susceptibility was significantly reduced when expression of the γ2 (R82Q) subunit was delayed until after development (Chiu *et al.*, 2008), confirming that the onset of symptoms is dependent on a critical period. Interestingly, more recent

work shows that, unlike its wildtype counterpart, the γ2 (R82Q) subunit is excluded from the axon initial segment (Wimmer *et al.*, 2010), the site of action potential initiation in neurons (Stuart *et al.*, 1997). Clearly, further insight into the three novel $GABA_A$ receptor mutants described in this study will require careful consideration of how they disrupt neuronal circuit behavior, from an appreciation of their developmental expression pattern to their distribution within distinct populations of neurons.

Supporting Information

Additional supporting information may be found in the online version of this article:

Fig. S1. Peptide sequence alignment of a portion of the GABRA1 and GABRG2 proteins from different species.

Table S1. Clinical manifestations of the 16 affected individuals carrying novel GABAA receptor mutations.

Please note: As a service to our authors and readers, this journal provides supporting information supplied by the authors. Such materials are peer-reviewed and may be re-organized for online delivery, but are not copy-edited or typeset by Wiley-Blackwell. Technical support issues arising from supporting information (other than missing files) should be addressed to the authors.

Acknowledgements

This work was supported by operating grants to D.B. and P.C. from the Canadian Institutes for Health Research as well as the Savoy Foundation. P.B. is supported by a Masters fellowship from the FRSQ and and P.L.-T. is supported by a doctoral fellowship from the Savoy Foundation. D.B. is the recipient of the Canada Research Chair award in Receptor Pharmacology. We would like to thank all the families and patients who participated in this study. We are grateful to Josée Poirier for performing DNA extraction and participating in the sequence and data analysis and Micheline Gravel for assisting in the collection of blood samples. We are grateful to members of the Bowie lab for providing a thoughtful critique of the manuscript and special thanks to Mark Aurousseau for discussions on the use of the homology models.

Abbreviations

ER, endoplasmic reticulum; GABA, γ-amino-butyric acid; IGE, idiopathic generalized epilepsy; PCR, polymerase chain reaction; RT-PCR, reverse transcriptase PCR; SNP, single-nucleotide polymorphism.

References

Audenaert, D., Schwartz, E., Claeys, K.G., Claes, L., Deprez, L., Suls, A., Van Dyck, T., Lagae, L., Van Broeckhoven, C., Macdonald, R.L. & De Jonghe, P. (2006) A novel GABRG2 mutation associated with febrile seizures. *Neurology*, **67**, 687–690.

Baulac, S., Huberfeld, G., Gourfinkel-An, I., Mitropoulou, G., Beranger, A., Prud'homme, J.F., Baulac, M., Brice, A., Bruzzone, R. & LeGuern, E. (2001) First genetic evidence of GABA(A) receptor dysfunction in epilepsy: a mutation in the gamma2-subunit gene. *Nat. Genet.*, **28**, 46–48.

Ben Ari, Y. (2006) Seizures beget seizures: the quest for GABA as a key player. *Crit. Rev. Neurobiol.*, **18**, 135–144.

Boileau, A.J., Kucken, A.M., Evers, A.R. & Czajkowski, C. (1998) Molecular dissection of benzodiazepine binding and allosteric coupling using chimeric gamma-aminobutyric acidA receptor subunits. *Mol. Pharmacol.*, **53**, 295–303.

Boileau, A.J., Li, T., Benkwitz, C., Czajkowski, C. & Pearce, R.A. (2003) Effects of gamma2S subunit incorporation on GABAA receptor macroscopic kinetics. *Neuropharmacology*, **44**, 1003–1012.

Bowie, D. (2002) External anions and cations distinguish between AMPA and kainate receptor gating mechanisms. *J. Physiol.*, **539**, 725–733.

Bowser, D.N., Wagner, D.A., Czajkowski, C., Cromer, B.A., Parker, M.W., Wallace, R.H., Harkin, L.A., Mulley, J.C., Marini, C., Berkovic, S.F., Williams, D.A., Jones, M.V. & Petrou, S. (2002) Altered kinetics and benzodiazepine sensitivity of a GABAA receptor subunit mutation [gamma 2(R43Q)] found in human epilepsy. *Proc. Natl Acad. Sci. USA*, **99**, 15170–15175.

Cartegni, L., Wang, J., Zhu, Z., Zhang, M.Q. & Krainer, A.R. (2003) ESEfinder: a web resource to identify exonic splicing enhancers. *Nucleic Acids Res.*, **31**, 3568–3571.

Catterall, W.A., Kalume, F. & Oakley, J.C. (2010) NaV1.1 channels and epilepsy. *J. Physiol.*, **588**, 1849–1859.

Celentano, J.J. & Wong, R.K. (1994) Multiphasic desensitization of the GABAA receptor in outside-out patches. *Biophys. J.*, **66**, 1039–1050.

Chang, Y., Wang, R., Barot, S. & Weiss, D.S. (1996) Stoichiometry of a recombinant GABAA receptor. *J. Neurosci.*, **16**, 5415–5424.

Chiu, C., Reid, C.A., Tan, H.O., Davies, P.J., Single, F.N., Koukoulas, I., Berkovic, S.F., Tan, S.S., Sprengel, R., Jones, M.V. & Petrou, S. (2008) Developmental impact of a familial GABAA receptor epilepsy mutation. *Ann. Neurol.*, **64**, 284–293.

Cossette, P., Liu, L., Brisebois, K., Dong, H., Lortie, A., Vanasse, M., Saint-Hilaire, J.M., Carmant, L., Verner, A., Lu, W.Y., Wang, Y.T. & Rouleau, G.A. (2002) Mutation of GABRA1 in an autosomal dominant form of juvenile myoclonic epilepsy. *Nat. Genet.*, **31**, 184–189.

Dibbens, L.M., Feng, H.J., Richards, M.C., Harkin, L.A., Hodgson, B.L., Scott, D., Jenkins, M., Petrou, S., Sutherland, G.R., Scheffer, I.E., Berkovic, S.F., Macdonald, R.L. & Mulley, J.C. (2004) GABRD encoding a protein for extra- or peri-synaptic GABAA receptors is a susceptibility locus for generalized epilepsies. *Hum. Mol. Genet.*, **13**, 1315–1319.

Draguhn, A., Verdorn, T.A., Ewert, M., Seeburg, P.H. & Sakmann, B. (1990) Functional and molecular distinction between recombinant rat GABAA receptor subtypes by Zn2+. *Neuron*, **5**, 781–788.

Ernst, M., Bruckner, S., Boresch, S. & Sieghart, W. (2005) Comparative models of GABAA receptor extracellular and transmembrane domains: important insights in pharmacology and function. *Mol. Pharmacol.*, **68**, 1291–1300.

Essrich, C., Lorez, M., Benson, J.A., Fritschy, J.M. & Luscher, B. (1998) Postsynaptic clustering of major GABAA receptor subtypes requires the gamma 2 subunit and gephyrin. *Nat. Neurosci.*, **1**, 563–571.

Fairbrother, W.G., Yeh, R.F., Sharp, P.A. & Burge, C.B. (2002) Predictive identification of exonic splicing enhancers in human genes. *Science*, **297**, 1007–1013.

Galanopoulou, A.S. (2010) Mutations affecting GABAergic signaling in seizures and epilepsy. *Pflugers Arch.*, **460**, 505–523.

Goldschen-Ohm, M.P., Wagner, D.A., Petrou, S. & Jones, M.V. (2010) An epilepsy-related region in the GABA(A) receptor mediates long-distance effects on GABA and benzodiazepine binding sites. *Mol. Pharmacol.*, **77**, 35–45.

Hahn, A. & Neubauer, B.A. (2009) Sodium and potassium channel dysfunctions in rare and common idiopathic epilepsy syndromes. *Brain Dev.*, **31**, 515–520.

Harkin, L.A., Bowser, D.N., Dibbens, L.M., Singh, R., Phillips, F., Wallace, R.H., Richards, M.C., Williams, D.A., Mulley, J.C., Berkovic, S.F., Scheffer, I.E. & Petrou, S. (2002) Truncation of the GABA(A)-receptor gamma2 subunit in a family with generalized epilepsy with febrile seizures plus. *Am. J. Hum. Genet.*, **70**, 530–536.

Helbig, I., Scheffer, I.E., Mulley, J.C. & Berkovic, S.F. (2008) Navigating the channels and beyond: unravelling the genetics of the epilepsies. *Lancet Neurol.*, **7**, 231–245.

Hosie, A.M., Dunne, E.L., Harvey, R.J. & Smart, T.G. (2003) Zinc-mediated inhibition of GABA(A) receptors: discrete binding sites underlie subtype specificity. *Nat. Neurosci.*, **6**, 362–369.

Jones, M.V. & Westbrook, G.L. (1996) The impact of receptor desensitization on fast synaptic transmission. *Trends Neurosci.*, **19**, 96–101.

Kananura, C., Haug, K., Sander, T., Runge, U., Gu, W., Hallmann, K., Rebstock, J., Heils, A. & Steinlein, O.K. (2002) A splice-site mutation in GABRG2 associated with childhood absence epilepsy and febrile convulsions. *Arch. Neurol.*, **59**, 1137–1141.

Kang, J.Q., Shen, W. & Macdonald, R.L. (2006) Why does fever trigger febrile seizures? GABAA receptor gamma2 subunit mutations associated with idiopathic generalized epilepsies have temperature-dependent trafficking deficiencies. *J. Neurosci.*, **26**, 2590–2597.

Kang, J.Q., Shen, W. & Macdonald, R.L. (2009) Two molecular pathways (NMD and ERAD) contribute to a genetic epilepsy associated with the GABA(A) receptor GABRA1 PTC mutation, 975delC, S326fs328X. *J. Neurosci.*, **29**, 2833–2844.

Keren, H., Lev-Maor, G. & Ast, G. (2010) Alternative splicing and evolution: diversification, exon definition and function. *Nat. Rev. Genet.*, **11**, 345–355.
Kinirons, P., Rabinowitz, D., Gravel, M., Long, J., Winawer, M., Senechal, G., Ottman, R. & Cossette, P. (2008) Phenotypic concordance in 70 families with IGE-implications for genetic studies of epilepsy. *Epilepsy Res.*, **82**, 21–28.
Krampfl, K., Maljevic, S., Cossette, P., Ziegler, E., Rouleau, G.A., Lerche, H. & Bufler, J. (2005) Molecular analysis of the A322D mutation in the GABA receptor alpha-subunit causing juvenile myoclonic epilepsy. *Eur. J. Neurosci.*, **22**, 10–20.
Kullmann, D.M. & Waxman, S.G. (2010) Neurological channelopathies: new insights into disease mechanisms and ion channel function. *J. Physiol.*, **588**, 1823–1827.
Lachance-Touchette, P., Martin, C., Poulin, C., Gravel, M., Carmant, L. & Cossette, P. (2010) Screening of GABRB3 in French-Canadian families with idiopathic generalized epilepsy. *Epilepsia*, **51**, 1894–1897.
Lema, G.M. & Auerbach, A. (2006) Modes and models of GABA(A) receptor gating. *J. Physiol.*, **572**, 183–200.
Macdonald, R.L., Kang, J.Q. & Gallagher, M.J. (2010) Mutations in GABAA receptor subunits associated with genetic epilepsies. *J. Physiol.*, **588**, 1861–1869.
Maljevic, S., Krampfl, K., Cobilanschi, J., Tilgen, N., Beyer, S., Weber, Y.G., Schlesinger, F., Ursu, D., Melzer, W., Cossette, P., Bufler, J., Lerche, H. & Heils, A. (2006) A mutation in the GABA(A) receptor alpha(1)-subunit is associated with absence epilepsy. *Ann. Neurol.*, **59**, 983–987.
McCorry, D., Nicolson, A., Smith, D., Marson, A., Feltbower, R.G. & Chadwick, D.W. (2006) An association between type 1 diabetes and idiopathic generalized epilepsy. *Ann. Neurol.*, **59**, 204–206.
Mizielinska, S., Greenwood, S. & Connolly, C.N. (2006) The role of GABAA receptor biogenesis, structure and function in epilepsy. *Biochem. Soc. Trans.*, **34**, 863–867.
Ogiwara, I., Miyamoto, H., Morita, N., Atapour, N., Mazaki, E., Inoue, I., Takeuchi, T., Itohara, S., Yanagawa, Y., Obata, K., Furuichi, T., Hensch, T.K. & Yamakawa, K. (2007) Na(v)1.1 localizes to axons of parvalbumin-positive inhibitory interneurons: a circuit basis for epileptic seizures in mice carrying an Scn1a gene mutation. *J. Neurosci.*, **27**, 5903–5914.
Olsen, R.W. & Sieghart, W. (2008) International Union of Pharmacology LXX. Subtypes of gamma-aminobutyric acid(A) receptors: classification on the basis of subunit composition, pharmacology, and function. Update. *Pharmacol. Rev.*, **60**, 243–260.
Olsen, R.W. & Sieghart, W. (2009) GABA A receptors: subtypes provide diversity of function and pharmacology. *Neuropharmacology*, **56**, 141–148.
Pal, D.K., Evgrafov, O.V., Tabares, P., Zhang, F., Durner, M. & Greenberg, D.A. (2003) BRD2 (RING3) is a probable major susceptibility gene for common juvenile myoclonic epilepsy. *Am. J. Hum. Genet.*, **73**, 261–270.
Pritchett, D.B., Sontheimer, H., Shivers, B.D., Ymer, S., Kettenmann, H., Schofield, P.R. & Seeburg, P.H. (1989) Importance of a novel GABAA receptor subunit for benzodiazepine pharmacology. *Nature*, **338**, 582–585.
Sarto-Jackson, I. & Sieghart, W. (2008) Assembly of GABA(A) receptors (Review). *Mol. Membr. Biol.*, **25**, 302–310.
Scheffer, I.E. & Berkovic, S.F. (2003) The genetics of human epilepsy. *Trends Pharmacol. Sci.*, **24**, 428–433.
Shi, X., Huang, M.C., Ishii, A., Yoshida, S., Okada, M., Morita, K., Nagafuji, H., Yasumoto, S., Kaneko, S., Kojima, T. & Hirose, S. (2010) Mutational analysis of GABRG2 in a Japanese cohort with childhood epilepsies. *J. Hum. Genet.*, **55**, 375–378.
Sigel, E. & Buhr, A. (1997) The benzodiazepine binding site of GABAA receptors. *Trends Pharmacol. Sci.*, **18**, 425–429.
Stuart, G., Spruston, N., Sakmann, B. & Hausser, M. (1997) Action potential initiation and backpropagation in neurons of the mammalian CNS. *Trends Neurosci.*, **20**, 125–131.
Sun, H., Zhang, Y., Liang, J., Liu, X., Ma, X., Wu, H., Xu, K., Qin, J., Qi, Y. & Wu, X. (2008) Gene symbol: GABRG2. Disease: generalized epilepsy with febrile seizures plus. *Hum. Genet.*, **124**, 298.
Tan, H.O., Reid, C.A., Single, F.N., Davies, P.J., Chiu, C., Murphy, S., Clarke, A.L., Dibbens, L., Krestel, H., Mulley, J.C., Jones, M.V., Seeburg, P.H., Sakmann, B., Berkovic, S.F., Sprengel, R. & Petrou, S. (2007) Reduced cortical inhibition in a mouse model of familial childhood absence epilepsy. *Proc. Natl Acad. Sci. USA*, **104**, 17536–17541.
Tanaka, M., Olsen, R.W., Medina, M.T., Schwartz, E., Alonso, M.E., Duron, R.M., Castro-Ortega, R., Martinez-Juarez, I.E., Pascual-Castroviejo, I., Machado-Salas, J., Silva, R., Bailey, J.N., Bai, D., Ochoa, A., Jara-Prado, A., Pineda, G., Macdonald, R.L. & Delgado-Escueta, A.V. (2008) Hyperglycosylation and reduced GABA currents of mutated GABRB3 polypeptide in remitting childhood absence epilepsy. *Am. J. Hum. Genet.*, **82**, 1249–1261.
Theodore, W.H., Spencer, S.S., Wiebe, S., Langfitt, J.T., Ali, A., Shafer, P.O., Berg, A.T. & Vickrey, B.G. (2006) Epilepsy in North America: a report prepared under the auspices of the global campaign against epilepsy, the International Bureau for Epilepsy, the International League Against Epilepsy, and the World Health Organization. *Epilepsia*, **47**, 1700–1722.
Turnbull, J., Lohi, H., Kearney, J.A., Rouleau, G.A., Delgado-Escueta, A.V., Meisler, M.H., Cossette, P. & Minassian, B.A. (2005) Sacred disease secrets revealed: the genetics of human epilepsy. *Hum. Mol. Genet.*, **14 Spec No. 2**, 2491–2500.
Unwin, N. (2005) Refined structure of the nicotinic acetylcholine receptor at 4A resolution. *J. Mol. Biol.*, **346**, 967–989.
Verdoorn, T.A., Draguhn, A., Ymer, S., Seeburg, P.H. & Sakmann, B. (1990) Functional properties of recombinant rat GABAA receptors depend upon subunit composition. *Neuron*, **4**, 919–928.
Wallace, R.H., Marini, C., Petrou, S., Harkin, L.A., Bowser, D.N., Panchal, R.G., Williams, D.A., Sutherland, G.R., Mulley, J.C., Scheffer, I.E. & Berkovic, S.F. (2001) Mutant GABA(A) receptor gamma2-subunit in childhood absence epilepsy and febrile seizures. *Nat. Genet.*, **28**, 49–52.
Wimmer, V.C., Reid, C.A., So, E.Y., Berkovic, S.F. & Petrou, S. (2010) Axon initial segment dysfunction in epilepsy. *J. Physiol.*, **588**, 1829–1840.
Yu, F.H., Mantegazza, M., Westenbroek, R.E., Robbins, C.A., Kalume, F., Burton, K.A., Spain, W.J., McKnight, G.S., Scheuer, T. & Catterall, W.A. (2006) Reduced sodium current in GABAergic interneurons in a mouse model of severe myoclonic epilepsy in infancy. *Nat. Neurosci.*, **9**, 1142–1149.
Zamponi, G.W., Lory, P. & Perez-Reyes, E. (2010) Role of voltage-gated calcium channels in epilepsy. *Pflugers Arch.*, **460**, 395–403.

nature COMMUNICATIONS

ARTICLE

Received 5 Nov 2013 | Accepted 20 Dec 2013 | Published 16 Jan 2014

DOI: 10.1038/ncomms4168

Mitochondrial reactive oxygen species regulate the strength of inhibitory GABA-mediated synaptic transmission

Michael V. Accardi[1], Bryan A. Daniels[1], Patricia M.G.E. Brown[1], Jean-Marc Fritschy[2], Shiva K. Tyagarajan[2] & Derek Bowie[1]

Neuronal communication imposes a heavy metabolic burden in maintaining ionic gradients essential for action potential firing and synaptic signalling. Although cellular metabolism is known to regulate excitatory neurotransmission, it is still unclear whether the brain's energy supply affects inhibitory signalling. Here we show that mitochondrial-derived reactive oxygen species (mROS) regulate the strength of postsynaptic $GABA_A$ receptors at inhibitory synapses of cerebellar stellate cells. Inhibition is strengthened through a mechanism that selectively recruits α3-containing $GABA_A$ receptors into synapses with no discernible effect on resident α1-containing receptors. Since mROS promotes the emergence of postsynaptic events with unique kinetic properties, we conclude that newly recruited α3-containing $GABA_A$ receptors are activated by neurotransmitter released onto discrete postsynaptic sites. Although traditionally associated with oxidative stress in neurodegenerative disease, our data identify mROS as a putative homeostatic signalling molecule coupling cellular metabolism to the strength of inhibitory transmission.

[1] Department of Pharmacology and Therapeutics, McGill University, Montréal, Québec, Canada H3B 0B1. [2] Institute of Pharmacology and Toxicology, University of Zurich, CH-8057, Zurich, Switzerland. Correspondence and requests for materials should be addressed to D.B. (email: derek.bowie@mcgill.ca).

Although the mammalian brain represents a small fraction of the total body mass, its energy requirements are substantial. Most neural energy is expended on sustaining excitatory signalling within the central nervous system[1] with action potential firing and glutamatergic transmission proposed to contribute as much as 80% of total expenditure[2]. Such high requirements, combined with limited energy reserves, place limits on the size of the evolving brain[3] obliging neuronal circuits to develop metabolically-efficient wiring[4] and signalling[5,6] strategies. How energy consumption is then distributed among different cell types is still unclear, although most work has focused on excitatory principal neurons and astrocytes[7–9]. While the bioenergetics of inhibitory GABAergic interneurons has received less attention[10], emerging data suggest a similar high demand on cellular metabolism. Inhibitory stellate and basket cells of the cerebellum, for example, are computed to use almost half their energy on postsynaptic receptor signalling[11] placing them on par with the energy demands of principal neurons such as Purkinje cells.

In keeping with this, GABAergic transmission at cerebellar stellate cells is particularly robust[12,13] implying that a significant proportion of energy is expended on reversing ion-gradients generated by synaptic activity. In fact, stellate cells are a particularly attractive model cell in which to study coupling of cellular metabolism with inhibitory transmission for two reasons. First, inhibitory transmission at stellate cells is relatively stable over time in terms of synaptic event amplitude and frequency making it ideal for quantitative analyses[13,14]. Second, prior work has established that stellate cell inhibitory synapses contain $GABA_A$ receptors of known composition which would be helpful in dissecting the molecular nature of any regulatory mechanism. Inhibitory stellate cell synapses of the young adult cerebellum contain $GABA_A$ receptors composed of α1, β2 and γ2 subunits[15,16]. α2- and/or α3-containing $GABA_A$ receptors may also play a minor role but their contribution is thought to diminish during development[17,18].

Here we have used the stellate cell inhibitory synapse to examine whether cellular metabolism regulates GABAergic signalling. Electrophysiological recordings demonstrate that GABAergic synapse strengthening occurs through a novel mechanism where mitochondrial-derived reactive oxygen species (mROS) recruit α3-containing $GABA_A$ receptors. Interestingly, mROS do not strengthen established synapses that contain α1-receptors. Taken together, our work highlights an unexpected role for mROS in signalling the metabolic state of the cell to the inhibitory synapse.

Results

Antimycin-A increases GABAergic synaptic event frequency. To determine whether inhibitory transmission is coupled to the metabolic state of the postsynaptic cell, we performed voltage-clamp recordings of miniature inhibitory postsynaptic currents (mIPSCs) that are mediated by $GABA_A$ receptors in cerebellar stellate cells. In agreement with other studies, our data revealed that event frequency and amplitude changed little during a typical 25–30 min recording (Fig. 1). For a more quantitative analysis, event frequency and amplitude were compared in each recording from synaptic events detected during the first (0–5) and last (20–25) 5 min (Fig. 1a) after seal breakthrough. Fits of the amplitude distributions from stellate cells ($n=6$) revealed that most tetrodotoxin (TTX)-insensitive GABAergic events were best fitted by 3 to 4 Gaussian components. For example, detected events from the first 5 min of the recordings gave peak values of −42 pA (13.7%), −75 pA (61.7%) and −139 pA (24.6%) (Fig. 1b, left). Similar fits were obtained with data obtained from the last 5 min of the recording after seal breakthrough (Fig. 1b, right), highlighting that inhibitory transmission is stable under these recording conditions.

To directly test the impact of cellular metabolism on inhibitory transmission, we performed identical experiments but included antimycin-A in the patch pipette solution to disrupt mitochondrial function. Prior biochemical studies have established the selective effect of antimycin-A on the mitochondria, where it concurrently blocks ATP production and generates the free radical superoxide[19]. This pharmacological effect is achieved by

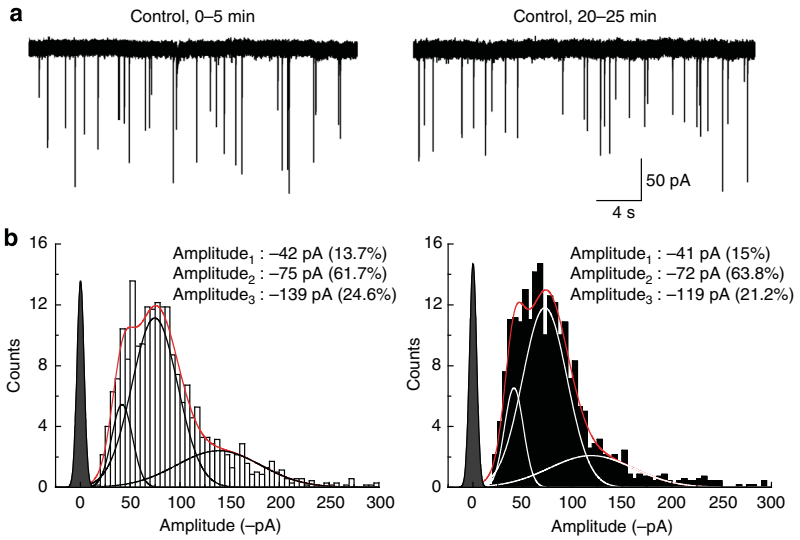

Figure 1 | Inhibitory transmission onto cerebellar stellate cells is stable. (**a**) mIPSCs recorded from the same stellate cell (cell no. 120202p2) at two time periods showing that event amplitude and frequency were similar throughout. (**b**) Amplitude distributions of inhibitory events from stellate cell recordings ($n=6$) comparing early (i.e., 0–5 min) and later (i.e., 20–25 min) events. Averaged data has been fit with the sum of three Gaussian functions (red line) with individual Gaussians shown in either black (left panel) or white (right panel). In this figure and other figures, closed point distribution (filled) has been scaled to the fitted peak of the lowest event amplitude and represents the average noise observed during the recordings.

inhibiting cytochrome c reductase, which disrupts the proton gradient needed by ATP synthase to make ATP[20]. Electrons made available by antimycin-A permit the formation of superoxide.

Inclusion of 2 μM antimycin-A in the patch pipette had an almost immediate effect on synaptic events mediated by $GABA_A$ receptors (Fig. 2). Unlike the control condition, the frequency of mIPSCs increased significantly over the duration of the recording (Fig. 2a). During the first 5 min, the total event frequency (mean ± s.e.m.) was 1.10 ± 0.07 Hz which increased to 1.78 ± 0.08 Hz after 20–25 min ($n = 5$; $P = 7.1 \times 10^{-9}$, paired, two-tailed Student's t-test). Gaussian fits of the amplitude distributions revealed that the increase in frequency was almost exclusively limited to synaptic events of smaller amplitudes (i.e., < − 100 pA). For example, fits of the control data estimate the contribution of the smallest events to be 13–15% (Fig. 1b, right) of all events that increases twofold after 20–25 min of antimycin-A treatment (Fig. 2b). Given this finding, we compared the frequency and amplitude of events smaller than − 100 pA in recordings where antimycin-A was absent or included in the patch pipette (Fig. 2c). In control conditions, both mIPSC amplitude and frequency were similar throughout the duration of the experiment (Fig. 2c, left). In contrast, however, small event frequency increased in a time-dependent manner in the presence of antimycin-A reaching a sustained maximum after 25 min (Fig. 2c, right).

Interestingly, we also observed what appeared to be a small time-dependent reduction in the averaged amplitude of small events in the presence of antimycin-A (Fig. 2c, right). For example, after 20–25 min, the event amplitude was − 54.6 ± 1.3 pA (mean ± s.e.m.) which declined to 93.9 ± 2.7% of the events observed at the start of the recording (i.e., − 57.7 ± 1.6 pA, $n = 5$). As discussed later, this trend towards a reduction in event amplitude is not due to a shift in the chloride equilibrium potential (Supplementary Fig. 1) but rather due to the recruitment of subunit-specific $GABA_A$ receptors.

An important concern was whether the effects described above for antimycin-A would impact inhibitory transmission in current-clamped stellate cells recorded in physiological levels of internal chloride. To examine this, we evoked inhibitory events on stellate cells by placing a stimulating electrode in the molecular layer of the cerebellum and then compared recordings in the presence and absence of antimycin-A (Fig. 3). Under these conditions, antimycin-A elicited a time-dependent increase in the extent to which inhibitory postsynaptic potentials hyperpolarized stellate cells (Fig. 3a,b). For example, in antimycin-A-treated cells, the peak hyperpolarization observed in the first 5 min increased to 132.5 ± 7.7% (mean ± s.e.m.; $n = 5$, $P = 0.035$, paired, two-tailed Student's t-test) which was not observed in control cells (e.g., 20–25 min: 93.7 ± 10.8% of control 0–5 min, $n = 3$, $P = 0.44$, paired, two-tailed Student's t-test; Fig. 3b). To account for the duration of the evoked event, we also measured the area under

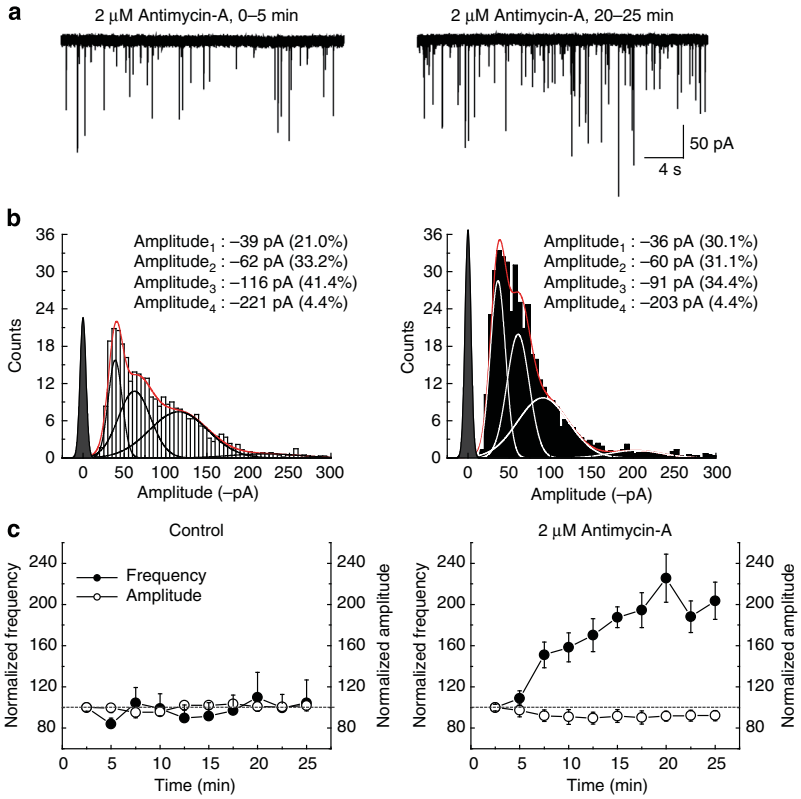

Figure 2 | Antimycin-A selectively enhances the occurrence of small amplitude inhibitory events. (**a**) mIPSCs from the same stellate cell (cell no. 111118p1) at two time periods in the presence of 2 μM antimycin-A. (**b**) Amplitude histograms comparing the data obtained at two time periods (0–5 min, left; 20–25 min, right) following the introduction of 2 μM antimycin-A ($n = 5$). Averaged data have been fit with the sum of four Gaussian functions (red line) with individual Gaussians shown in either black (left panel) or white (right panel). (**c**) Summary plot showing how normalized small event (i.e., < − 100 pA) amplitude (open circle) or frequency (filled circle) changed with time in the presence ($n = 5$) and absence ($n = 6$) of antimycin-A. Error bars, s.e.m. For clarity, the lower (frequency) and upper (amplitude) error bars were removed in the control panel (left).

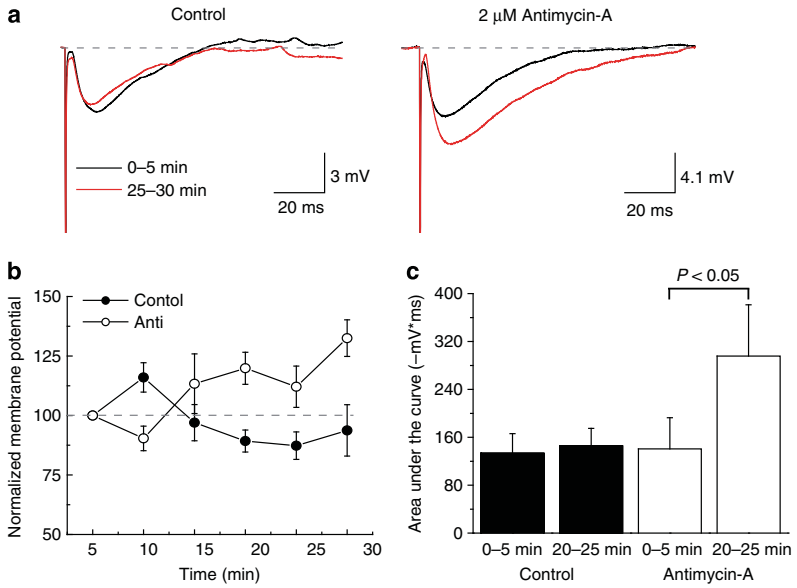

Figure 3 | Antimycin-A increases the amplitude of eIPSPs in the presence of physiological levels of chloride. (**a**) eIPSPs obtained in the presence (right) or absence (left) of 2 μM antimycin-A while cytosolic levels of chloride where maintained at physiological levels (i.e., $[Cl^-]_i = 4.1$ mM). The black traces represent the average response during the first 5 min (i.e., 0–5 min). The red traces represent the average response during the last 5 min (i.e., 25–30 min). (**b**) Summary plot showing the change of normalized membrane potentials of eIPSPs in the presence (white circle; $n = 5$) or absence (black circle; $n = 3$) of 2 μM antimycin-A (Anti). (**c**) Summary bar graph comparing the change in the area under the curve for the control and 2 μM antimycin-A condition at two time points. When compared with the first 5 min (0–5 min), antimycin-A elicits a significant increase ($P = 0.043$, paired two-tailed Student's *t*-test) in total area under the curve.

the curve for each hyperpolarization. In antimycin-A-treated cells, the time course of hyperpolarization (i.e., area under the curve) was -140.7 ± 51.9 mV*ms (mean ± s.e.m., $n = 5$) in the first 5 min which increased to -295.7 ± 85.7 mV*ms at the 20–25 min period ($P = 0.043$, paired, two-tailed Student's *t*-test; Fig. 3a,c). This change in the duration of hyperpolarization was absent in control cells (mean ± s.e.m., $n = 3$; 0–5 min: -133.5 ± 32.6 mV*ms; 20–25 min: -145.6 ± 29.3 mV*ms). Taken together, these data suggest that antimycin-A is able to affect stellate cell excitability by strengthening the degree of inhibitory tone.

Antimycin-A affects mIPSC frequency by generating mROS. Block of the electron transport chain impacts the cell in a number of ways; therefore, we performed several types of experiments to test whether the primary effect of antimycin-A was due to mROS. First, we imaged ROS levels by introducing the indicator dye, dichlorofluorescein (DCF) (see Methods), via the recording electrode while simultaneously measuring the frequency of mIPSCs in individual stellate cells (Fig. 4). Analysis of these data revealed that the increase in mIPSC frequency elicited by antimycin-A was concomitant with an elevation in intracellular ROS (Fig. 4b–d). Although the increase in intracellular ROS was robust, it is likely an underestimate of the actual signal due to the time delay required to fill the cell with fluorescent indicators (red circles, Fig. 4c). Second, the inclusion of the antioxidant, N-acetylcysteine (NAC; 1 mM), in the patch pipette attenuated the effect of antimycin-A on the frequency of small synaptic events (Fig. 5a–c). NAC contains a thiol group (Fig. 5a, red lettering) that acts as an electron donor thereby conferring anti-oxidant effects by reducing the superoxide generated by anti-mycin-A. NAC (1 mM) alone had little effect on GABAergic transmission (Fig. 5b). Third, other mitochondrial uncouplers, myxothiazol (Myxo; 5 μM, Fig. 5a,c) and rotenone (Rot; 2 μM, Fig. 5a,c), mimicked the effect of antimycin-A by increasing the frequency (Fig. 5c) with a modest reduction in the averaged amplitude (e.g., Myxo; 20–25 min: 96.5 ± 4.6% (mean ± s.e.m.) of control, $n = 5$) of small inhibitory synaptic events. Although myxothiazol is thought to bind to mitochondrial complex III, like antimycin-A[19], it has been proposed to generate ROS through an effect on complex I, much like rotenone[21], which may account for its apparently weaker effect on small event frequency (Fig. 5c). Finally, chemically derived ROS generated by the addition of the Fenton reaction (see Methods) in the patch pipette also elicited an increase in small GABAergic event frequency (Fig. 5c). Similar to antimycin-A, the Fenton reaction produced a steady increase in small event frequency over the first 15 min of the recordings but had a diminished effect over time (0.66 ± 0.12 Hz (mean ± s.e.m., $n = 5$) at 10–15 min period to 0.45 ± 0.07 Hz at 20–25 min, $P = 0.009$, paired, two-tailed Student's *t*-test). The return to basal levels of mIPSC frequency during prolonged exposure to the Fenton reaction was likely due to the time-dependent nature of the reaction. Furthermore, the modulating effects of Fenton-derived ROS may be impinged upon by the opposing effects of endogenous cytoplasmic antioxidants, such as glutathione, thus impeding ROS from reaching the synapse (i.e., the site of action). When taken together, these data suggest that mROS are responsible for the selective upregulation in frequency of small amplitude GABAergic synaptic events.

mROS promotes the occurrence of slow-decaying mIPSCs. A change in the frequency of synaptic activity, as observed with antimycin-A, is usually indicative of a presynaptic mechanism[22]. However, a comparison of event decay kinetics observed in the presence and absence of antimycin-A suggests that mROS may instead be primarily acting at a postsynaptic site. To perform the comparison, synaptic events were each fitted with a single exponential function and this value was plotted with respect to

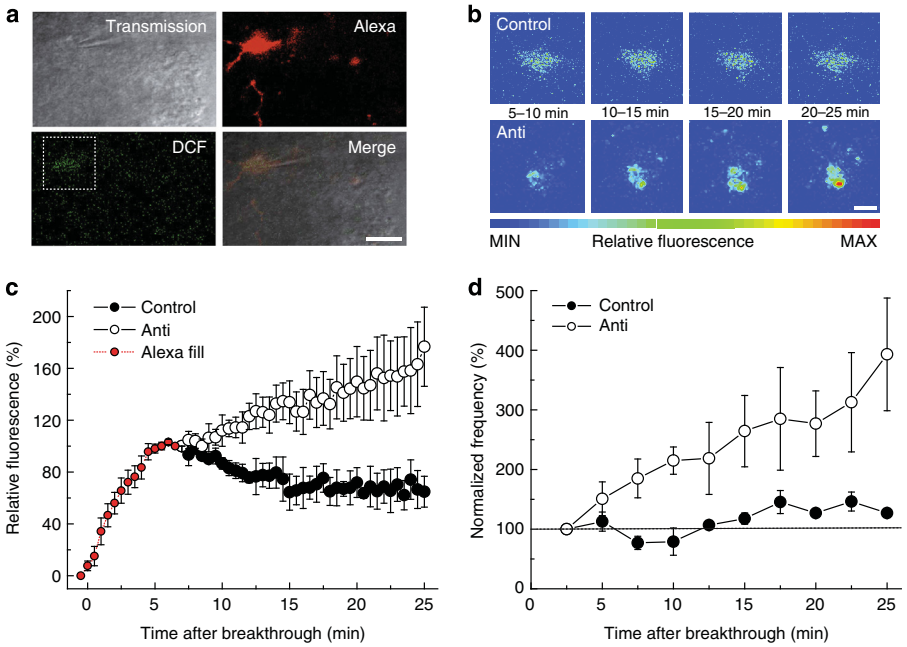

Figure 4 | Simultaneous fluorescence and electrophysiological measurements confirm that Antimycin-A increases intracellular ROS. (**a**) Representative scanning confocal images of a stellate cell loaded via the recording pipette with 100 μM Alexa 594 to assess the extent of cell filling and 100 μM H_2DCF-DA (DCF) to measure increases in intracellular ROS. The inset is the area depicted in panel **b** (Control) at 2 min after breakthrough. Scale bar, 10 μm. (**b**) Example DCF images from two separate experiments in the absence (Control, cell no. 131010p1) and presence of antimycin-A (Anti, cell no. 131010p4) in the recording pipette. The images are displayed using a range indicator from blue, pixels with no fluorescence, to red, the maximum signal for any pixel over the course of an individual experiment. Scale bar, 5 μm (**c**) The time course of mean intracellular DCF fluorescence in control ($n=3$) and antimycin-A ($n=4$) experiments. Fluorescence was normalized based on the time it took to acquire a stable Alexa signal (5–7 min, Alexa fill). Error bars, s.e.m. (**d**) Normalized mean frequency time course of small amplitude mIPSCs (<-100 pA) recorded concomitantly from the same cells in (**c**). Error bars, s.e.m.

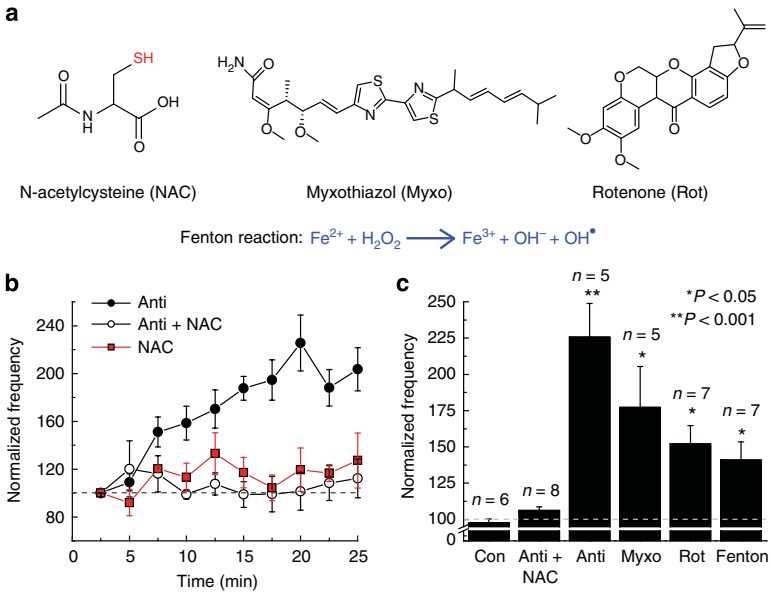

Figure 5 | Mitochondrial ROS increases the occurrence of small inhibitory events. (**a**) N-acetylcysteine (NAC), myxothiazol (Myxo), rotenone (Rot) structures as well as the Fenton reaction. The thiol group (highlighted in red) of NAC confers antioxidant properties. (**b**) Summary plot of antagonistic effect of NAC on the increase in small event frequency elicited by antimycin-A (2 μM Anti, $n=5$; 2 μM Anti + 1 mM NAC, $n=8$ and 1 mM NAC, $n=5$). Error bars, s.e.m. (**c**) Summary bar graph comparing the normalized small event frequency (i.e., <-100 pA) in different experimental conditions. When compared with control conditions (Con), the increase in event frequency observed with 2 μM antimycin-A ($n=5$, $P=0.0002$), 5 μM myxothiazol ($n=5$, $P=0.0123$), 2 μM rotenone ($n=7$, $P=0.0028$) and the Fenton reaction ($n=7$, $P=0.0072$) all reached statistical significance. All statistics were determined using an unpaired, two-tailed Student's *t*-test with the Bonferroni correction. Error bars, s.e.m.

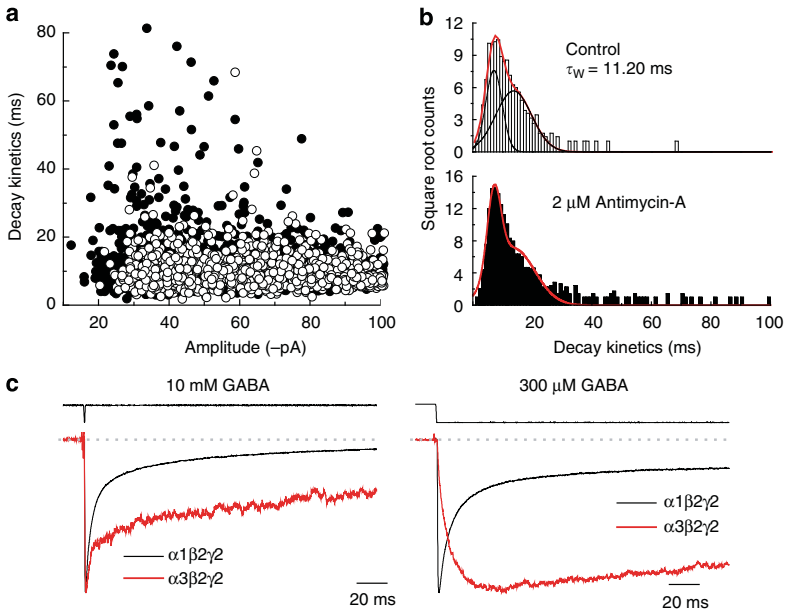

Figure 6 | Slow mIPSCs and recombinant α3-GABA$_A$ receptors have similar kinetics. (**a**) Plot of mIPSC amplitude and decay kinetics of small amplitude (i.e., < -100 pA) events observed in control (white circles, $n = 6$) or 2 μM antimycin-A (black circles, $n = 5$) conditions. (**b**, upper panel) Histograms showing the distribution of mIPSC decay kinetics fit with the sum of two Gaussian functions (red line). Individual Gaussians are shown in black. (**b**, lower panel) Similar plot of the distribution of decay kinetics observed in the presence of antimycin-A. The Gaussian fit (red line) from the upper panel has been scaled onto the data to identify the many more slow-decaying mIPSCs observed with antimycin-A exposure. (**c**) Overlay of typical membrane currents elicited by short 1 ms (left) or long 250 ms (right) applications of 10 mM or 300 μM GABA acting on recombinant α1β2γ2 (black line, patch no. 130322p7) or α3β2γ2 (red line, patch no. 130308p3) receptors. Response amplitudes have been normalized to allow a comparison of decay kinetics.

the peak response amplitude (Fig. 6a). In the absence of antimycin-A, most synaptic events (open circles) had a decay time constant of 10.16 ± 0.17 ms (mean ± s.e.m.; $n = 6$) irrespective of the peak amplitude (Fig. 6a). We did, however, observe a few events with slower decay kinetics, which were more readily identified in fits of the distribution in decay kinetics (Fig. 6b, upper panel). Of note, mIPSCs with slower decay kinetics were usually associated with smaller peak responses (Fig. 6a).

Antimycin-A affected synaptic activity in two ways. First, many more small amplitude events were observed with decay kinetics slower than 30 ms (Fig. 6a,b, lower panel). In the presence of antimycin-A, the number of events with slow decay kinetics increased about threefold, from ~0.7% (7/967 events) in control conditions to about 3% (51/1665 events). Second, antimycin-A substantially increased the number of events with amplitudes ≤ -30 pA (antimycin-A: 208 events or 12.5% of all small events; control: 34 events or 3.5% of all small events; Fig. 6a). This observation explains the modest reduction of the averaged response amplitude elicited by antimycin-A (Fig. 2c, right panel). It is unlikely that the occurrence of small amplitude, slow-decaying synaptic events was the result of poorly voltage-clamped synapses on distal dendritic branches, since their occurrence in ROS-generated solutions (i.e., antimycin-A, myxothiazol, rotenone and the Fenton reaction) was not associated with any change in the cells' biophysical properties. Consequently, we concluded that the appearance of small amplitude, slow-decaying mIPSCs has a biological origin and that mROS affect inhibitory transmission mainly through a postsynaptic mechanism.

Given the greater occurrence of small amplitude events with slow decay kinetics, we thus postulated that ROS may be strengthening inhibitory transmission by recruiting GABA$_A$ receptors possibly from extrasynaptic sites[23,24]. The slowing observed in decay kinetics would, in this case, correspond to recruited receptors responding to the neurotransmitter gradient emanating from inhibitory synapses. The subunit composition of extrasynaptic GABA$_A$ receptors expressed by stellate cells is not known, although it is most likely assembled from α1-(refs 15,16) and/or α3-containing receptors[17,18]. Therefore, we next determined whether the kinetic properties of recombinant α1- and/or α3-containing receptors matched that of the slow-decaying synaptic events observed during antimycin-A treatment.

To do this, we co-expressed α1- or α3 subunits with β2 and γ2 subunits in mammalian cells from which we excised outside-out patches (Fig. 6c, Supplementary Table 1). Brief (1 ms) applications of 10 mM γ-aminobutyric acid (GABA) to excised patches were used to mimic the response elicited by neurotransmitter released into the synaptic cleft, whereas long (250 ms) applications of 300 μM GABA were used to mimic the concentration profile of extrasynaptic GABA (see Barberis *et al.*[25] for details on the synaptic/extrasynaptic concentration profile of GABA). Using this approach, the decay kinetics of α1-containing GABA$_A$ receptors were dominated by a fast component of ~3 ms when activated by either 300 μM or 10 mM GABA (Fig. 6c, Supplementary Table 1), which does not match the slower kinetics of synaptic events observed in antimycin-A. In contrast, α3-containing receptors decayed at least an order of magnitude slower in response to both high and low GABA concentrations (Fig. 6c, Supplementary Table 1), which was more in line with the kinetic behaviour of synaptic events. In keeping with this, we concluded that the slowing of decay kinetics was not due to a direct pharmacological action on α3-containing GABA$_A$ receptors since application of antimycin-A to outside-out patches (external or cytoplasmic side of the membrane) did not affect their gating properties (Supplementary Fig. 2). Taken together, these data suggest that the increase in occurrence of slow-decaying events is consistent with the recruitment of

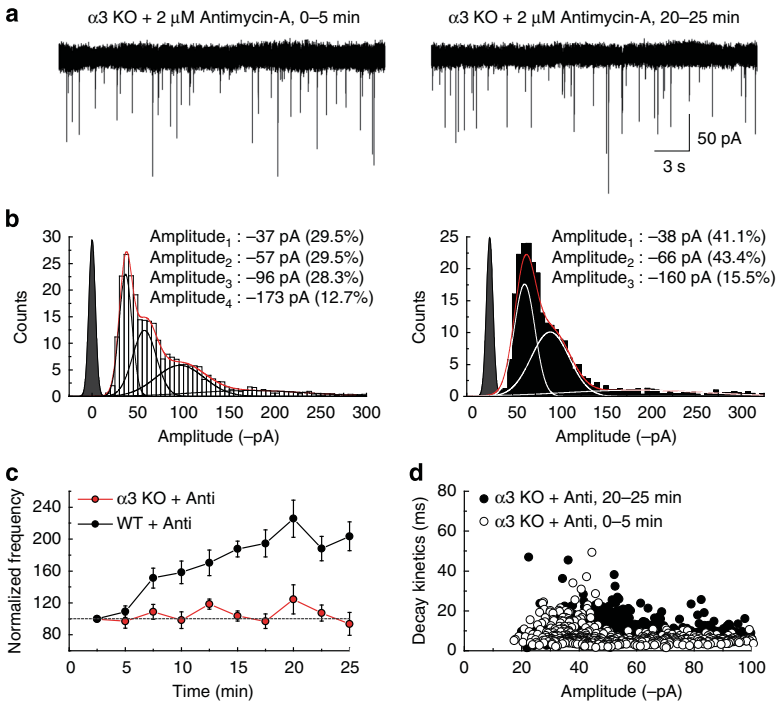

Figure 7 | Mitochondrial ROS do not strengthen inhibitory synapses lacking the α3 subunit. (**a**) mIPSCs recorded from the same stellate cell (cell no. 121130p1) in an α3-KO mouse during internal perfusion with 2 μM antimycin-A. (**b**) Amplitude histograms comparing data ($n=5$) obtained at two time periods (i.e., 0–5 min, left; 20–25 min, right). Pooled data has been fit with the sum of 3–4 Gaussian functions (red line) with individual Gaussians shown in either black (left panel) or white (right panel). (**c**) Summary plot comparing the effect of antimycin-A on small amplitude event frequency in wild-type ($n=6$) and α3-KO ($n=5$) mice. Error bars, s.e.m. (**d**) Scatter plot comparing decay kinetics and mIPSC amplitudes at two time points in stellate cells from α3-KO mice ($n=5$).

α3-containing $GABA_A$ receptors into inhibitory synapses. To test this hypothesis directly, we next examined the effect of antimycin-A on GABAergic currents recorded in mice lacking either α1 or α3 $GABA_A$ receptor subunits.

mROS have no effect on mIPSC frequency in α3-KO mice. We started with α3-knockout (KO) mice since the recombinant data suggested an important role for this subunit in mROS-mediated changes of GABAergic synapses. Similar to the wild-type mice, mIPSCs of stellate cells in α3-KO mice varied in amplitude between −20 pA and −300 pA, although a greater proportion of mIPSCs were of small amplitude (Fig. 7a,b). Unlike wild-type mice, however, the inclusion of antimycin-A in the patch electrode had no significant effect on small mIPSC frequency (Fig. 7c). For example, the frequency observed during the final 5 min was 0.85 ± 0.08 Hz (mean ± s.e.m.) which was similar to the frequency of 0.90 ± 0.1 Hz observed during the first 5 min ($n=5$, $P=0.35$, paired, two-tailed Student's t-test). Likewise, antimycin-A did not promote the occurrence of events with slow decay kinetics (Fig. 7d). The total number of events with decay kinetics >30 ms was 1.1% (5/466 events) for the first 5 min and 0.91% (5/549 events) in the last 5 min. The average decay time constant increased significantly in the last 5 min (10.03 ± 0.2 ms; mean ± s.e.m.) when compared with the first 5 min (7.23 ± 0.2 ms; $n=5$, $P<0.0001$, paired, two-tailed Student's t-test). It is not clear why there is a slowing in decay kinetics, although it is possible that antimycin-A may also act on α2-containing $GABA_A$ receptors, which have been reported to be expressed by stellate cells[17]. In terms of small event amplitudes, antimycin-A had no effect on their overall occurrence (i.e., < −30 pA; 0–5 min: 37/466 or 7.9%; 20–25 min: 46/549 or 8.4%). Taken together, these data suggest that the ROS-mediated increase in small amplitude, slow-decaying mIPSCs is absent in stellate cells lacking α3-containing $GABA_A$ receptors.

mROS increase mIPSC frequency in α1-KO mice. Inhibitory synapses of stellate cells in α1-KO mice differed from their wild-type counterpart in several important ways. First, all recorded mIPSCs in the α1-KO mice were much smaller in amplitude averaging about −30.6 ± 0.34 pA (mean ± s.e.m.; $n=5$) compared with −104.1 ± 0.73 pA of wild-type stellate cells (Fig. 8a). In fact, few synaptic responses ever surpassed −100 pA in amplitude consistent with a previous study[18]. Second, the decay kinetics of small mIPSCs in α1-KO mice were much slower (Fig. 8a) averaging about 20.2 ± 0.60 ms (mean ± s.e.m.; $n=5$) compared with 10.16 ± 0.17 ms (mean ± s.e.m.; $n=6$) in wild-type mice. A comparison of response amplitude versus decay kinetics of small mIPSCs observed in wild-type (open circles) and α1-lacking (black circles) mice revealed that the profile of inhibitory events in α1-KO mice were reminiscent of the small amplitude, slow-decaying responses observed in wild-type mice following antimycin-A treatment (Fig. 8b). Third and finally, mIPSC frequency in α1-lacking mice was lower at 0.52 ± 0.05 Hz (mean ± s.e.m.; $n=5$); an observation that might be expected given the preponderance of α1-containing $GABA_A$ receptors in stellate cells. Taken together, these observations suggest upregulation of the α3 subunit in the cerebellum of α1-KO mice, as suggested previously[26] and shown directly in Supplementary Fig. 3.

As predicted from the role of α3-containing $GABA_A$ receptors in wild-type mice, the frequency of mIPSCs in stellate cells of

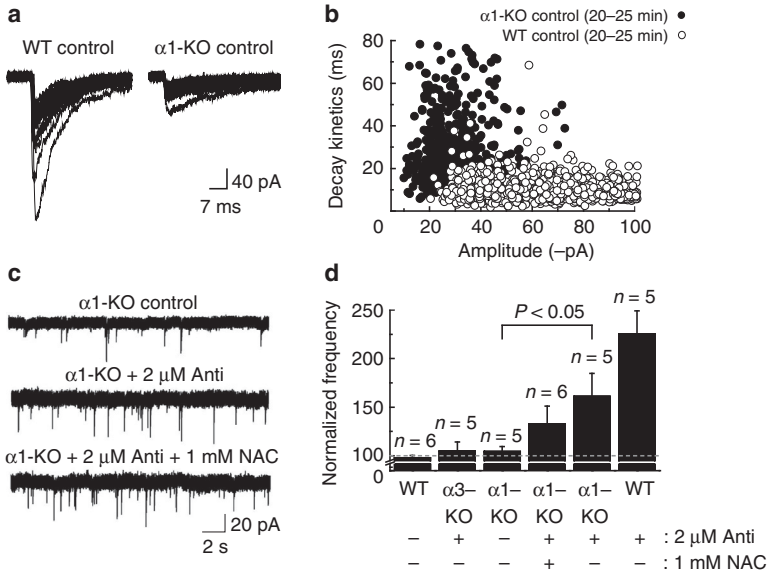

Figure 8 | Mitochondrial ROS increase mIPSC frequency in stellate cells lacking the α1-subunit. (**a**) Comparison of 15 randomly selected mIPSCs recorded in wild-type (left) and α1-KO (right) stellate cells. (**b**) Scatter plot comparing decay kinetics and amplitudes of mIPSCs from stellate cells in wild-type ($n=6$) and α1-KO mice ($n=5$). (**c**) Representative mIPSCs showing the effect of internal perfusion with 2 μM antimycin-A (top trace, cell no. 121025p2; middle trace, cell no. 121016p1 and bottom trace, cell no. 121206p1). (**d**) Bar graph summarizing the effect of antimycin-A on mIPSC frequency in wild-type and α1-KO cells. Statistics were determined using an unpaired, two-tailed Student's *t*-test; $P=0.0484$. Error bars, s.e.m.

α1-KO mice increased in a time-dependent manner when antimycin-A was included in the patch pipette (Fig. 8c,d). Antimycin-A increased event frequency from 0.63 ± 0.1 Hz (mean ± s.e.m.) within the first 5 min to 0.85 ± 0.1 Hz in the last 5 min ($n=5$, $P=3.24\times10^{-5}$, paired, two-tailed Student's *t*-test) of the recording corresponding to a normalized maximal peak increase of $68.6\pm28.7\%$ (Fig. 8c,d). We concluded that antimycin-A regulated mIPSC frequency by generating mROS since the effect of the mitochondrial uncoupler on event frequency (Fig. 8c,d) and amplitude (Supplementary Fig. 4) was attenuated by 1 mM NAC. Finally, in the last 5 min, antimycin-A increased the occurrence of slow-decaying mIPSCs with time constants greater than 30 ms (24%, 324 events). Thus, these data suggest that the ROS-mediated increase in small amplitude, slow-decaying mIPSCs occurs through the recruitment of α3-containing $GABA_A$ receptors.

It is interesting that antimycin-A increased event frequency in α1-lacking stellate cells less than in wild-type neurons (Fig. 8d). Since wild-type inhibitory synapses mainly possess α1-containing $GABA_A$ receptors[15,17], we reasoned that antimycin-A would be able to recruit more α3-containing $GABA_A$ receptors into these synapses. This explanation would explain the apparently weaker effect of mROS on α1-lacking stellate cells which, importantly, could be tested experimentally. Specifically, we hypothesized that mROS should increase not only the inhibitory event frequency in α1-lacking stellate cells but also their amplitude as more α3-containing $GABA_A$ receptors are recruited into the synapse.

mROS also increase mIPSC amplitude in α1-KO mice. As expected, neither the mIPSC frequency nor amplitude changed in control recordings of stellate cells lacking the α1-subunit (Fig. 9a, left panel). However, in antimycin-A-treated cells, the frequency of inhibitory events increased suggesting that the α1-subunit does not play a major role (Fig. 9a, right panel). The total event frequency during the first 5 min significantly increased after 20–25 min (Figs 8d, 9a, right). This increase was also observed by fitting the amplitude distributions (Fig. 9b). Interestingly, this analysis also uncovered an appreciable increase in the amplitude of mIPSCs (Fig. 9b, right panel). Fits of the amplitude distributions taken from the last 5 min of control α1-KO mice revealed that mIPSCs were best fit by the sum of two Gaussian components (-23 pA (43.1%) and -31 pA (56.9%)). However, after 20–25 min of antimycin treatment, data were best fit by four Gaussian components (-21 pA (41.5%), -32 pA (36.8%), -50 pA (15.0%) and -88 pA (6.7%)), where a sizeable proportion of all events (about 22%) exhibited amplitudes that were two- to threefold larger than any mIPSCs observed during the α1-KO-control condition. Taken together, these data demonstrate that antimycin-A increases both the frequency and amplitude of mIPSCs in stellate cells lacking the α1-subunit by recruiting α3-containing $GABA_A$ receptors to synaptic sites. Interestingly, when we repeated these experiments in younger wild-type mice (i.e., P10–12), where α3- and not α1-containing $GABA_A$ receptors dominate the synaptic response (see Vicini *et al.*[18]), antimycin-A increased event frequency, as expected, but did not increase mIPSC amplitude (Fig. 10) suggesting that the rules regulating synaptic strength are distinct in developing and mature stellate cells.

Discussion

The present study advances our understanding of inhibitory GABAergic synapses in two important ways. First, we show that cellular metabolism regulates the strength of inhibitory transmission by generating mROS. As discussed below, the traditional view that mROS are primarily involved in oxidative stress has broadened to encompass a more physiological role for these versatile signalling molecules[27]. Second, strengthening of stellate cell inhibitory synapses occurs through a mechanism that is selective for the recruitment of α3-containing $GABA_A$ receptors. Curiously, mROS have no apparent effect on α1-receptors which

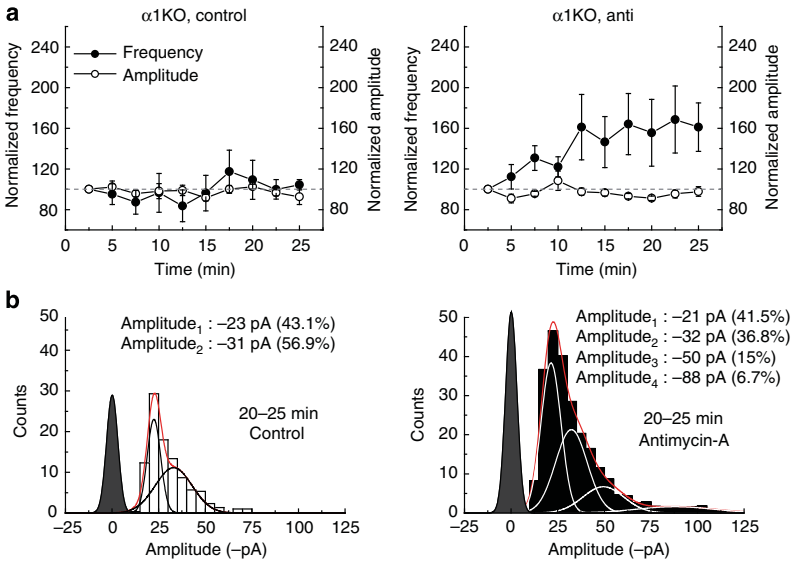

Figure 9 | ROS increase mIPSC frequency and amplitude in α1-KO mice. (**a**,**b**) Summary plots comparing mIPSC frequency and amplitude (i.e., < −100 pA) in α1-KO mice in the presence (right, $n = 5$) and absence (left, $n = 5$) of 2 μM antimycin-A. Error bars, s.e.m. (**b**) Amplitude distributions of mIPSCs observed during the last 5 min (i.e., 20–25 min) of stellate cell recordings from α1-KO mice both in the presence (right) and absence (left) of 2 μM antimycin-A. Averaged data have been fit with the sum of two or four Gaussian functions (red line) with individual Gaussians shown in either black (left panel) or white (right panel).

are the predominant $GABA_A$ receptor present at stellate cell inhibitory synapses. This apparent discrepancy can be explained if α3 receptors are recruited into synaptic sites that are distinct from α1 receptors. Given this, our data are consistent with the idea that α3-containing $GABA_A$ receptors occupy synaptic sites which are either entirely devoid of any $GABA_A$ receptor, reminiscent of silent glutamatergic[28] or GABAergic[29] synapses, and/or contain a small number of α3-containing receptors.

The generation of mROS has been traditionally linked to the cellular damage that accompanies chronic disease states such as diabetes[30], cancer[31] and neurodegenerative conditions such as Alzheimer's disease and Parkinsonism[32]. Given this, it might be concluded that our experiments using antimycin-A are more in line with these chronic disease states. However, recent work in the striatum suggests that the elevation in ROS elicited by mitochondrial uncouplers and physiological stimuli can be quite comparable[33]. Consequently, our findings may point to a more physiological role for mROS as already described for the innate immune response as well as the control of embryonic stem cell differentiation[27]. Exactly how mROS are elevated in inhibitory stellate cells awaits future study. However, given the emerging view that mROS lay at the heart of an important signalling hub[27], it is likely that numerous biochemical pathways converge on stellate cell synapses to elevate mROS.

We were initially surprised that mROS regulated α3-containing receptors with no apparent effect on α1-receptors. This observation can be explained in one of two ways. First, α1- and α3- containing $GABA_A$ receptors may be recruited to morphologically distinct stellate cell inhibitory synapses. In fact, subunit-specific synaptic segregation is not unusual for the cerebellum[34]. Granule cells, for example, form inhibitory synapses with Golgi cells which contain primarily α1β2/3γ2 (with some α6β2/3γ2 receptors), whereas mossy fibre to granule cell synapses contain only α6β2/3γ2 receptors[35]. In keeping with this, stellate cells are innervated by other cell types that include other stellate cells and basket cells of the molecular layer as well as Lugaro cells and globular cells, which are located beneath the Purkinje cell layer[34,36]. Consequently, it is possible that α1- and α3- containing $GABA_A$ receptors are targeted to synapses that are formed with different presynaptic partners. Second, α1- and α3- containing $GABA_A$ receptors may still share the same presynaptic terminal but are activated by neurotransmitter released from functionally-distinct active zones. In support of this, serial electron micrographs of inhibitory stellate cell synapses reveal their unusual architecture that places different active zones of the same presynaptic terminal in discrete locations[12]. This arrangement may allow α1- and α3- containing $GABA_A$ receptors to act in the distinct manner reported in our study. The physiological value of segregating $GABA_A$ receptors at stellate cell inhibitory synapses is not yet clear, although it is possible that the different kinetic properties of α1- and α3-receptors may allow neuronal excitability to be finely controlled.

In α1-lacking mice, the situation is similar but with the difference that α3-containing GABA receptors are now present to a greater extent at inhibitory synapses (see Fig. 8a and Supplementary Fig. 3). Given this, the relative increase in event frequency elicited by antimycin-A would be expected to be less, as we have observed, since many synapses already contain α3-receptors. Moreover, since the event amplitude increases in α1-lacking mice, this observation suggests that α3-containing GABA receptors are recruited to sites already containing α3-receptors.

In principle, a number of mechanisms may account for the increase in occurrence of α3-containing $GABA_A$ receptors with mROS which include lateral relocation of extrasynaptic receptors into inhibitory synapses[23,37], exocytotic insertion of synaptic $GABA_A$ receptors and/or mROS-directed increase in $GABA_A$ receptor open-channel probability. More work is required to delineate between these possibilities; however, our data are consistent with the recruitment of extrasynaptic α3-containing receptors. In agreement with this, lateral movement of extrasynaptic receptors has been proposed to be the dominating mechanism that strengthens GABAergic synapses[23,24,37]. Moreover, the time frame of lateral diffusion is also consistent

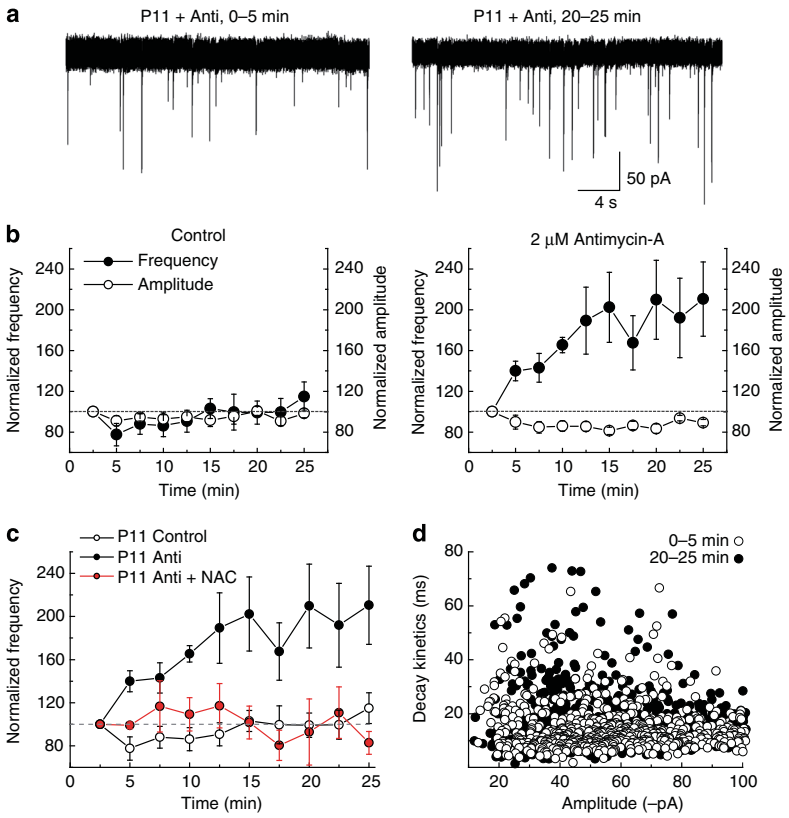

Figure 10 | Antimycin-A increases the occurrence of small inhibitory events during early stellate cell development. (**a**) mIPSCs from the same stellate cell (cell no. 138050p3) at two time periods in the presence of 2 μM antimycin-A (Anti). (**b**) Summary plot showing how normalized small event (i.e., < −100 pA) amplitude (open circle) or frequency (filled circle) changed with time in the presence ($n=7$) and absence ($n=8$) of antimycin-A. Error bars, s.e.m. (**c**) Summary plot showing the time course of the small mIPSC frequency increase elicited by 2 μM antimycin-A (Anti, black circle) and the antagonistic effect of NAC (red circle, $n=7$). The control condition (white circle) did not change over time. Error bars, s.e.m. (**d**) Plot of mIPSC amplitude and decay kinetics of small amplitude (i.e., < −100 pA) events observed in the first (i.e., 0–5 min, white circles) and last (i.e., 20–25 min, black circles) 5 min of young (P11) mice in the presence of 2 μM antimycin-A.

with the rates of mROS modulation described in the present study. Lateral relocation is dependent upon the diffusion rate of a receptor which interestingly, is higher for extrasynaptic $GABA_A$ receptors[23,37–39]. Finally, the occurrence of small amplitude, slow-decaying synaptic events elicited by mROS is also consistent with the lateral movement of α3-containing $GABA_A$ receptors, which would be expected to have these properties in response to low GABA concentrations. Clearly, more work is still required to understand how the generation of ROS in the mitochondria triggers the events that lead to the strengthening of inhibitory synapses of cerebellar stellate cells. Moreover, it would be important in future studies to examine if this effect of mROS is common to all inhibitory synapses.

Methods

Animals. Homozygous $GABA_A$ receptor α1-KO mice were generated on a mixed C57BL/6J-129Sv/SvJ background at the University of Pittsburgh (Pittsburgh, PA, USA)[18] and bred at the University of Zurich. Wild-type and α3-KO mice were maintained on a C57BL/6J background (B6.129 1-Gabra3tm2Uru/Uru)[40] and also bred at the University of Zurich. As the α3 subunit gene is located on the X chromosome, mutant mice were either hemizygote male or homozygote female obtained from heterozygous/hemizygous or α3-KO breeding pairs. Wild-type mice with a C57BL/6J background were obtained from Jackson Laboratories (Bar Harbor, ME, USA) and maintained as a breeding colony at McGill University. All animals were genotyped by PCR analysis of tail biopsies. Mutant mice were born at the expected Mendelian ratio and the mutant phenotypes were maintained across generations. Mice (WT and α1-KO: male and female, α3-KO: males only) used for the experiments ranged from 15 to 28 days old (P15–28; mean ± s.e.m. age: P22 ± 1, $n=46$) or 10–12 days old (P10–12; mean ± s.e.m. age: P11 ± 1, $n=7$; only for Fig. 10). All experiments have been approved by the local authorities and were performed in accordance with the guidelines of the Canadian Council on Animal Care and European Community Council Directive 86/609/EEC and were approved by the Animal Care Committee of McGill University (Protocol Number: 4564) or the Cantonal Veterinary Office of Zurich.

Cerebellum slice preparation. Mice were anaesthetized with isoflurane and immediately decapitated. The cerebellum was rapidly removed from the whole brain while submerged in oxygenated (95% O_2, 5% CO_2) ice-cold cutting solution. Cutting solution contained (in mM): 235 sucrose, 2.5 KCl, 1.25 NaH_2PO_4, 28 $NaHCO_3$, 0.5 $CaCl_2$, 7 $MgSO_4$ and 28 D-glucose (pH of 7.4; 305–315 mOsmol l^{-1}). The tissue was maintained in ice-cold solution while sagittal slices of cerebellum (250–300 μm) were cut using a vibrating tissue slicer (Leica VT100S, Leica Instruments, Nussloch, Germany). The slices were transferred to oxygenated, room temperature (20–23 °C) artificial cerebrospinal fluid (aCSF) for at least 1 h before recordings. aCSF contained (in mM): 125 NaCl, 2.5 KCl, 1.25 NaH_2PO_4, 26 $NaHCO_3$, 2 $CaCl_2$, 1 $MgSO_4$ and 25 D-glucose (pH of 7.4; 305–315 mOsmol l^{-1}).

Cell culture and transfection. Human embryonic kidney (HEK) 293T/17 cells (ATCC CRL-11268, Manassas, VA, USA) were maintained at 70–80% confluency in minimal essential medium with Earle's salts, 2 mM glutamine and 10% fetal bovine serum. After plating at low density (2×10^4 cells per ml) on 35 mm plastic dishes coated with poly-D-lysine, cells were transfected with the complementary DNAs (cDNAs) encoding the $GABA_A$ receptor subunits in a 1:1:2 ratio (α1:β2:γ2), using the calcium phosphate technique. All $GABA_A$ receptor subunits used were of human sequences, except the α3 subunit, which was of the rat sequence. The cDNA

for enhanced green fluorescent protein was routinely co-transfected (0.1 μg per dish) to identify transfected cells.

Electrophysiology. Slice experiments were performed on an Olympus BX51 upright microscope (Olympus, Southall, UK) equipped with differential interference contrast/infrared optics. Whole-cell patch-clamp recordings were made from stellate cells which were distinguished from misplaced or migrating granule, glial or basket cells by their small soma diameter (8–9 μm) and location in the outer two-thirds of the molecular layer. Patch pipettes were prepared from thick-walled borosilicate glass (GC150F-10, OD 1.5 mm, ID 0.86 mm; Harvard Apparatus Ltd, Kent, UK) and had open tip resistances of 3–8 MΩ when filled with an intracellular solution that contained (in mM): 140 CsCl, 4 NaCl, 0.5 $CaCl_2$, 10 HEPES, 5 EGTA, 2 Mg-ATP, 2 QX314 to block voltage-activated Na^+ channels and 0.5 mg ml^{-1} Lucifer Yellow as a *post hoc* dye indicator (pH 7.4 with CsOH, 300–310 mOsmol l^{-1}). Recordings were made with a Multiclamp 700A amplifier (Molecular Devices, Sunnyvale, CA, USA) at a holding potential of −60 mV. Series resistance and whole-cell capacitance were estimated by cancelling the fast current transients evoked at the onset and offset of brief (10–20 ms) 5 mV voltage-command steps. Series resistance during postsynaptic whole-cell recording (10–35 MΩ) was compensated between 40 and 65% and checked for stability throughout the experiments (>20% tolerance). The capacitance of the stellate cells was in the range of 6–11 pF. The bath was continuously perfused at room temperature (22–23 °C) with aCSF at a rate of 1–2 ml min^{-1}. mIPSCs were recorded in the presence of TTX (1 μM). Currents were filtered at 5 kHz with either a four-pole or eight-pole low-pass Bessel filter (Frequency Devices, Haverhill, MA, USA) and digitized at 25 kHz with a Digidata 1322A data acquisition board and Clampex9 (Molecular Devices) software.

For extracellular stimulation, thin-walled borosilicate glass electrodes (OD 1.65 mm, ID 1.15 mm; King Precision Glass Inc., Claremont, CA, USA) were used with a tip current of <3 MΩ when filled with aCSF. The intracellular solution used for evoked potentials contained (in mM): 126 K-Gluconate, 0.05 $CaCl_2$, 0.15 K_4BAPTA, 4 NaCl, 1 $MgSO_4$, 15 D-Glucose, 5 HEPES, 3 Mg-ATP, 0.1 NaGTP, 2 QX314 (pH 7.4 with KOH, 300–310 mOsmol l^{-1}). The ground electrode for the stimulation circuit was made with a platinum wire wrapped around the stimulation electrode. The stimulating electrode was positioned in the molecular layer at or just beneath the slice surface. Voltage pulses (1–25 V in amplitude, 200–400 ms in duration) were applied at low frequency stimulation (0.05–0.03 Hz) through the stimulating electrode. To minimize variability between responses, the stimulating electrode was positioned between 50 and 100 μm away from the cell of interest. The voltage that was used during each experiment was the lowest voltage intensity obtained that elicited the maximal eIPSPs response.

Experiments were also performed at room temperature on recombinant $GABA_A$ receptors 24–48 h after cDNA transfection. GABA (Sigma-Aldrich, St Louis, MO, USA) was dissolved in external solution containing (in mM): 150 NaCl, 5 HEPES, 2 $MgCl_2$ and 1 $CaCl_2$. Internal pipette solution contained (in mM): 150 KCl, 5 EGTA, 1 $MgCl_2$ and 2 Mg-ATP. The pH and osmotic pressure of internal and external solutions were adjusted to 7.3–7.4 and 300 mOsm l^{-1}, respectively. All recordings were performed with an Axopatch 200B amplifier (Molecular Devices) using thin-walled borosilicate glass pipettes (2–5 MΩ) coated with dental wax to reduce electrical noise. Control and agonist solutions were rapidly applied to outside-out patches excised from transfected HEK 239T/17 cells using a piezoelectric stack (Physik Instrumente, Karlsruhe/Palmbach, Germany). Solution exchange (10–90% rise-time = 150–250 μs) was determined by measuring the liquid junction current (or exchange current) between the control and external solution containing 10% additional NaCl. Current records were filtered at 5 kHz, digitized at 25 kHz and series resistances (3–10 MΩ) were compensated by 95%. All recordings were performed at a holding potential of −60 mV. Data acquisition were performed using pClamp10 software (Molecular Devices). Curve fitting and figure preparation of all electrophysiology data were performed with Origin 7.0 (OriginLab, Northampton, MA, USA), Microsoft Excel, Clampfit 10 (Molecular Devices) and the Strathclyde Electrophysiology WinWCP and WinEDR (John Dempster, Glasgow, UK) software.

Analysis of mIPSC events. mIPSCs were detected using WinEDR software with a detection threshold of four times the mean root square noise level. The accuracy of detection was visually confirmed for each recording. Only cells exhibiting mIPSC frequency of greater than 0.2 Hz were used for analysis. Amplitude distributions were fit with the sum of 2–4 Gaussian functions with the singular form of: $y = (Ai/wi*sqrt(\pi/2)))*exp(-2*((x-xci)/wi)2)$, where A is the area, xc is the centre of the peak and w is the error associated with the peak. The decay phase of mIPSCs was fit with a single exponential curve and both rise and decay phase were fitted between 10 and 90% of the peak amplitude. Data are expressed as mean ± s.e.m.; *P*-values represent the results of paired or unpaired, two-tailed Student's *t*-tests. A *P*-value of less than 0.05 was considered statistically significant. All data are from at least two different animals.

Intracellular ROS fluorescence. Scanning confocal images were collected on a Zeiss Axioexaminer microscope (Carl Zeiss Microscopy Jena GmbH, Jena, Germany) in the McGill University Life Sciences Complex Advanced BioImaging Facility. mIPSCs were simultaneously recorded on a HEKA EPC10 amplifier (HEKA Electronik Dr Schulze GmbH, Lambrecht/Pfalz, Germany) and visualized with HEKA Patchmaster software. Solutions for recording stellate cell mIPSCs were used as above except the internal solution included Alexa 594 (100 μM; Life Technologies Inc., Burlington, ON, Canada) to report the extent of indicator filling and CM-H_2DCF-DA (100 μM; Life Technologies Inc.) to report the relative increase in intracellular ROS[41]. Pairs of images were collected every 30 s, to reduce potential photo-oxidation of the ROS indicator, once a gigaohm seal was obtained until at least 25 min after membrane breakthrough for whole-cell recordings. Each image was 512 × 512 pixels with a 1 μs pixel dwell time. In some cases the Alexa laser was used to also capture a transmission image to indicate the electrode and cell position (Fig. 4a).

Pharmacological compounds. Glutamate antagonists, D-(-)-2-Amino-5-phosphonopentanoic acid (D-APV; 10 μM) and 6-Cyano-7-nitroquinoxaline-2,3-dione (CNQX; 5 μM), the glycine antagonist, strychnine (0.3 μM) and the $GABA_A$ receptor antagonist bicuculline (10 μM) were purchased from Tocris Bioscience (Ellisville, MO, USA). TTX (1 μM) was purchased from Alomone Labs (Jerusalem, Israel). Stock solutions of these antagonists were prepared in water and were stored at −20 °C and working solutions were diluted with aCSF shortly before application to the bath. The antioxidant, NAC (1 mM) (Sigma) was prepared as a stock solution in water and dissolved in patch electrode solution on the day of the experiment. Mitochondrial poisons (antimycin-A, myxothiazol and rotenone) were purchased from Sigma, dissolved in dimethyl sulfoxide (DMSO) and diluted in water to workable stock concentrations and stored at −20 °C. The final maximum DMSO concentration (0.1% v/v) had no effect on mIPSCs. Although we tested antimycin-A at a range of concentrations (0.5–10 μM), we used a final concentration of 2 μM since it had a relatively fast onset time and was not detrimental to the cell's health (based on the cell's appearance and biophysical properties (i.e., input resistance, holding current)). In support of this, a comparable concentration of antimycin-A (1 μM) has been used in a similar electrophysiological study of ROS effects on nAChRs[42]. Mg-ATP was included in our patch electrode solution to avoid compromising Na^+/K^+ ATPase function. For the Fenton reaction, H_2O_2 (10 mM) was added to a solution of ascorbate (44 mM) and $FeCl_3 \bullet 6H_2O$ (1 mM) at a 1:20 (v/v) dilution. This solution was added to the recording electrode solution at a 1:10 (v/v) dilution. The Fenton solution was prepared every 30 min from powdered ingredients at room temperature.

Immunohistochemistry. Three-week-old wild-type and α1-KO littermates were anesthetized with pentobarbital (50 mg kg^{-1}) and perfusion-fixed with 4% paraformaldehyde solution in 0.1 M sodium phosphate buffer, pH 7.4. The brain was postfixed for 6 h, cryoprotected in 30% sucrose in phosphate-buffered saline, and cut parasagittally with a freezing microtome. Sections were pretreated with pepsin (0.15 mg ml^{-1} in 0.2 M HCl) for 10 min at 37 °C[43] to unmask synaptic proteins and incubated overnight in a mixture of antibodies against the α1 subunit (rabbit; custom-made), α3 subunit (guinea pig; custom-made) and gephyrin (mouse; mAb7a, Synaptic Systems, Göttingen, Germany), followed by three washes and incubation in secondary antibodies coupled to Alexa488, Cy3 and Cy5 (Jackson Immunoresearch, West Grove, PA, USA). Images were acquired by confocal laser scanning microscopy (Zeiss LSM700, Carl Zeiss MicroImaging GmbH, Germany) using a ×40 objective (N.A. 1.4). Stacks of 3–10 confocal images spaced by 0.5 μm were projected for display.

References

1. Ames, III A. CNS energy metabolism as related to function. *Brain Res. Brain Res. Rev.* **34,** 42–68 (2000).
2. Attwell, D. & Laughlin, S. B. An energy budget for signaling in the grey matter of the brain. *J. Cereb. Blood Flow Metab.* **21,** 1133–1145 (2001).
3. Navarrete, A., van Schaik, C. P. & Isler, K. Energetics and the evolution of human brain size. *Nature* **480,** 91–93 (2011).
4. Mitchison, G. Axonal trees and cortical architecture. *Trends Neurosci.* **15,** 122–126 (1992).
5. Levy, W. B. & Baxter, R. A. Energy efficient neural codes. *Neural. Comput.* **8,** 531–543 (1996).
6. Balasubramanian, V., Kimber, D. & Berry, M. J. Metabolically efficient information processing. *Neural. Comput.* **13,** 799–815 (2001).
7. Attwell, D. & Gibb, A. Neuroenergetics and the kinetic design of excitatory synapses. *Nat. Rev. Neurosci.* **6,** 841–849 (2005).
8. Attwell, D. *et al.* Glial and neuronal control of brain blood flow. *Nature* **468,** 232–243 (2010).
9. Allaman, I., Belanger, M. & Magistretti, P. J. Astrocyte-neuron metabolic relationships: for better and for worse. *Trends Neurosci.* **34,** 76–87 (2011).
10. Buzsaki, G., Kaila, K. & Raichle, M. Inhibition and brain work. *Neuron* **56,** 771–783 (2007).
11. Howarth, C., Gleeson, P. & Attwell, D. Updated energy budgets for neural computation in the neocortex and cerebellum. *J. Cereb. Blood Flow Metab.* **32,** 1222–1232 (2012).
12. Nusser, Z., Cull-Candy, S. & Farrant, M. Differences in synaptic GABA(A) receptor number underlie variation in GABA mini amplitude. *Neuron* **19,** 697–709 (1997).

13. Nusser, Z., Naylor, D. & Mody, I. Synapse-specific contribution of the variation of transmitter concentration to the decay of inhibitory postsynaptic currents. *Biophys. J.* **80,** 1251–1261 (2001).
14. Auger, C., Kondo, S. & Marty, A. Multivesicular release at single functional synaptic sites in cerebellar stellate and basket cells. *J. Neurosci.* **18,** 4532–4547 (1998).
15. Persohn, E., Malherbe, P. & Richards, J. G. Comparative molecular neuroanatomy of cloned GABAA receptor subunits in the rat CNS. *J. Comp. Neurol.* **326,** 193–216 (1992).
16. Somogyi, P., Fritschy, J. M., Benke, D., Roberts, J. D. & Sieghart, W. The gamma 2 subunit of the GABAA receptor is concentrated in synaptic junctions containing the alpha 1 and beta 2/3 subunits in hippocampus, cerebellum and globus pallidus. *Neuropharmacology* **35,** 1425–1444 (1996).
17. Laurie, D. J., Seeburg, P. H. & Wisden, W. The distribution of 13 GABAA receptor subunit mRNAs in the rat brain. II. Olfactory bulb and cerebellum. *J. Neurosci.* **12,** 1063–1076 (1992).
18. Vicini, S. *et al.* GABA(A) receptor alpha1 subunit deletion prevents developmental changes of inhibitory synaptic currents in cerebellar neurons. *J. Neurosci.* **21,** 3009–3016 (2001).
19. Starkov, A. A. & Fiskum, G. Myxothiazol induces H(2)O(2) production from mitochondrial respiratory chain. *Biochem. Biophys. Res. Commun.* **281,** 645–650 (2001).
20. Smith, R. A., Hartley, R. C., Cocheme, H. M. & Murphy, M. P. Mitochondrial pharmacology. *Trends Pharmacol. Sci.* **33,** 341–352 (2012).
21. Adam-Vizi, V. Production of reactive oxygen species in brain mitochondria: contribution by electron transport chain and non-electron transport chain sources. *Antioxid. Redox Signal* **7,** 1140–1149 (2005).
22. Safiulina, V. F., Afzalov, R., Khiroug, L., Cherubini, E. & Giniatullin, R. Reactive oxygen species mediate the potentiating effects of ATP on GABAergic synaptic transmission in the immature hippocampus. *J. Biol. Chem.* **281,** 23464–23470 (2006).
23. Thomas, P., Mortensen, M., Hosie, A. M. & Smart, T. G. Dynamic mobility of functional GABAA receptors at inhibitory synapses. *Nat. Neurosci.* **8,** 889–897 (2005).
24. Luscher, B., Fuchs, T. & Kilpatrick, C. L. GABAA receptor trafficking-mediated plasticity of inhibitory synapses. *Neuron* **70,** 385–409 (2011).
25. Barberis, A., Petrini, E. M. & Mozrzymas, J. W. Impact of synaptic neurotransmitter concentration time course on the kinetics and pharmacological modulation of inhibitory synaptic currents. *Front Cell Neurosci.* **5,** 6 (2011).
26. Fritschy, J. M., Panzanelli, P., Kralic, J. E., Vogt, K. E. & Sassoe-Pognetto, M. Differential dependence of axo-dendritic and axo-somatic GABAergic synapses on GABAA receptors containing the alpha1 subunit in Purkinje cells. *J. Neurosci.* **26,** 3245–3255 (2006).
27. Sena, L. A. & Chandel, N. S. Physiological roles of mitochondrial reactive oxygen species. *Mol. Cell* **48,** 158–167 (2012).
28. Kerchner, G. A. & Nicoll, R. A. Silent synapses and the emergence of a postsynaptic mechanism for LTP. *Nat. Rev. Neurosci.* **9,** 813–825 (2008).
29. Inoue, W. *et al.* Noradrenaline is a stress-associated metaplastic signal at GABA synapses. *Nat. Neurosci.* **16,** 605–612 (2013).
30. Supale, S., Li, N., Brun, T. & Maechler, P. Mitochondrial dysfunction in pancreatic beta cells. *Trends Endocrinol. Metab.* **23,** 477–487 (2012).
31. Krysko, D. V. *et al.* Immunogenic cell death and DAMPs in cancer therapy. *Nat. Rev. Cancer* **12,** 860–875 (2012).
32. Jones, Q. R., Warford, J., Rupasinghe, H. P. & Robertson, G. S. Target-based selection of flavonoids for neurodegenerative disorders. *Trends Pharmacol. Sci.* **33,** 602–610 (2012).
33. Bao, L. *et al.* Mitochondria are the source of hydrogen peroxide for dynamic brain-cell signaling. *J. Neurosci* **29,** 9002–9010 (2009).
34. Fritschy, J. M. & Panzanelli, P. Molecular and synaptic organization of GABAA receptors in the cerebellum: Effects of targeted subunit gene deletions. *Cerebellum* **5,** 275–285 (2006).
35. Nusser, Z., Sieghart, W. & Somogyi, P. Segregation of different GABAA receptors to synaptic and extrasynaptic membranes of cerebellar granule cells. *J. Neurosci.* **18,** 1693–1703 (1998).
36. Simat, M., Parpan, F. & Fritschy, J. M. Heterogeneity of glycinergic and gabaergic interneurons in the granule cell layer of mouse cerebellum. *J. Comp Neurol.* **500,** 71–83 (2007).
37. Bogdanov, Y. *et al.* Synaptic GABAA receptors are directly recruited from their extrasynaptic counterparts. *EMBO J.* **25,** 4381–4389 (2006).
38. Peran, M., Hicks, B. W., Peterson, N. L., Hooper, H. & Salas, R. Lateral mobility and anchoring of recombinant GABAA receptors depend on subunit composition. *Cell Motil. Cytoskeleton* **50,** 89–100 (2001).
39. Jacob, T. C. *et al.* Gephyrin regulates the cell surface dynamics of synaptic GABAA receptors. *J. Neurosci.* **25,** 10469–10478 (2005).
40. Yee, B. K. *et al.* A schizophrenia-related sensorimotor deficit links alpha 3-containing GABAA receptors to a dopamine hyperfunction. *Proc. Natl Acad. Sci. USA* **102,** 17154–17159 (2005).
41. Avshalumov, M. V., Chen, B. T., Koos, T., Tepper, J. M. & Rice, M. E. Endogenous hydrogen peroxide regulates the excitability of midbrain dopamine neurons via ATP-sensitive potassium channels. *J. Neurosci.* **25,** 4222–4231 (2005).
42. Campanucci, V. A., Krishnaswamy, A. & Cooper, E. Mitochondrial reactive oxygen species inactivate neuronal nicotinic acetylcholine receptors and induce long-term depression of fast nicotinic synaptic transmission. *J. Neurosci.* **28,** 1733–1744 (2008).
43. Panzanelli, P. *et al.* Distinct mechanisms regulate GABAA receptor and gephyrin clustering at perisomatic and axo-axonic synapses on CA1 pyramidal cells. *J. Physiol.* **589,** 4959–4980 (2011).

Acknowledgements

This work was supported by operating grants from the Canadian Institutes of Health (CIHR) Research to D.B. and from the Swiss National Science Foundation to J.-M.F., as well as the Brain@McGill–Neuroscience Center Zurich partnership. M.V.A. was supported by the Van Gelder doctoral fellowship from the Savoy Foundation and the Brain@McGill, B.A.D. by a Fragile X Research Foundation of Canada/CIHR postdoctoral fellowship and PMGEB by a doctoral fellowship from the Fonds de la Recherche en Santé du Québec. D.B. is the recipient of a Canada Research Chair award. We wish to thank Dr Stefano Vicini for providing α3-subunit cDNA as well as members of the Bowie lab for discussions and comments on the manuscript.

Author contributions

M.V.A. performed the whole-cell electrophysiological recordings and analysis of the data; B.A.D. performed the whole-cell electrophysiological recordings in combination with imaging ROS and data analysis; P.M.G.E.B. performed all of the experiments on the recombinant $GABA_A$ receptors and analysis therein; S.K.T. provided additional electrophysiological slice data; J.-M.F. performed the immunohistochemistry; All authors contributed to the design of the experiments, interpretation of the results and the writing of the manuscript.

Additional information

Supplementary Information accompanies this paper at http://www.nature.com/naturecommunications

Competing financial interests: The authors declare no competing financial interests.

Reprints and permission information is available online at http://npg.nature.com/reprintsand permissions.

How to cite this article: Accardi, M. V. *et al.* Mitochondrial reactive oxygen species regulate the strength of inhibitory GABA-mediated synaptic transmission. *Nat. Commun.* 5:3168 doi: 10.1038/ncomms4168 (2014).

Cellular/Molecular

Hydrogen Peroxide Increases $GABA_A$ Receptor-Mediated Tonic Current in Hippocampal Neurons

Antonello Penna,[1]* Dian-Shi Wang,[1]* Jieying Yu,[1] Irene Lecker,[1] Patricia M.G.E. Brown,[4] Derek Bowie,[4] and Beverley A. Orser[1,2,3]

Departments of [1]Physiology and [2]Anesthesia, University of Toronto, Toronto, Ontario M5S 1A8, Canada, [3]Department of Anesthesia, Sunnybrook Health Sciences Centre, Toronto, Ontario M4N 3M5, Canada, and [4]Department of Pharmacology and Therapeutics, McGill University, Montréal, Québec H3G 1Y6, Canada

Hydrogen peroxide (H_2O_2), a key reactive oxygen species, is produced at low levels during normal cellular metabolism and at higher concentrations under pathological conditions such as ischemia-reperfusion injury. The mechanisms by which H_2O_2 contributes to physiological and pathological processes in the brain remain poorly understood. Inhibitory GABA type A ($GABA_A$) receptors critically regulate brain function by generating tonic and synaptic currents; however, it remains unknown whether H_2O_2 directly modulates $GABA_A$ receptor function. Here, we performed patch-clamp recordings, together with pharmacological and genetic approaches, to investigate the effects of H_2O_2 on $GABA_A$ receptor-mediated tonic and synaptic currents recorded in cultured mouse hippocampal neurons and CA1 pyramidal neurons in hippocampal slices. We found that H_2O_2 caused a dramatic increase in tonic current, whereas synaptic currents were unaffected. This increase in tonic current resulted from an extracellular oxidative reaction, which increased the potency of GABA, but only when $GABA_A$ receptors were activated by low concentrations of GABA. Oxygen-glucose deprivation, which produces high endogenous levels of H_2O_2, similarly increased the tonic current. These results suggest that $GABA_A$ receptor-mediated tonic current, which is potentiated by H_2O_2, might contribute to H_2O_2-induced brain dysfunction.

Key words: **$GABA_A$ receptor; hippocampus; hydrogen peroxide; ischemia-reperfusion; mouse; tonic current**

Introduction

Reactive oxygen species (ROS) are by-products generated during normal cellular oxidative metabolism in the brain and other organs (Giorgio et al., 2007; Rice, 2011). Excessive production of ROS occurs in a variety of neurological disorders including ischemic-reperfusion injury, stroke, and neurodegenerative disease (Andersen, 2004; Allen and Bayraktutan, 2009; Uttara et al., 2009). High levels of ROS can lead to oxidative stress, which in turn causes cellular dysfunction and neuronal death (Giorgio et al., 2007; Rice, 2011).

Received Jan. 24, 2014; revised June 26, 2014; accepted July 1, 2014.

Author contributions: A.P., D.-S.W., and B.A.O. designed research; A.P., D.-S.W., J.Y., I.L., and P.M.G.E.B. performed research; A.P., D.-S.W., J.Y., I.L., and P.M.G.E.B. analyzed data; A.P., D.-S.W., I.L., D.B., and B.A.O. wrote the paper.

This work was supported by Grants from the Canadian Institutes of Health Research (CIHR) to B.A.O. (MOP: 416838, 480143) and D.B. (FRN: 82804). A.P. was supported by a Fellowship Award from the Sleep and Biological Rhythms Toronto program and by a Postdoctoral Fellowship Award from Becas Chile. J.Y. was supported by a studentship from the Natural Sciences and Engineering Research Council of Canada. I.L. was supported by Savoy Foundation and CIHR studentships. P.M.G.E.B. was supported by a doctoral award from the Fonds des recherches en santé du Quebec. B.A.O. holds a Canada Research Chair. We thank Ella Czerwinska for her assistance with the cell cultures and Agnieszka A. Zurek, Sinziana Avramescu, Gang Lei, as well as all members of the B.A.O. laboratory for reading and critiquing the paper.

The authors declare no competing financial interests.

*A.P. and D.-S.W. contributed equally to this work.

Correspondence should be addressed to Dr Beverley A. Orser, Department of Physiology, University of Toronto, Room 3318 Medical Science Building, 1 King's College Circle, Toronto, Ontario M5S 1A8, Canada. E-mail: beverley.orser@utoronto.ca.

DOI:10.1523/JNEUROSCI.0335-14.2014

 0270-6474/14/3410624-11$15.00/0

One of the most important ROS is hydrogen peroxide (H_2O_2), a relatively stable molecule that diffuses through the cell membrane to interact with distant molecular targets (Giorgio et al., 2007; Rice, 2011). Low concentrations of H_2O_2 physiologically regulate synaptic plasticity (Kamsler and Segal, 2003; Rice, 2011), whereas higher concentrations are associated with neuronal dysfunction (Abramov et al., 2007; Giorgio et al., 2007). Concentrations of H_2O_2 as high as 200 μM occur during the early period of postischemic reperfusion (Hyslop et al., 1995). Despite being involved in a wide variety of physiological and pathological functions, the molecular substrates underlying H_2O_2 effects on neuronal function remain poorly understood.

GABA type A ($GABA_A$) receptors mediate the majority of inhibition in the brain and perturbations in GABAergic inhibition contribute to a variety of neurological disorders (Brickley and Mody, 2012). $GABA_A$ receptors generate two forms of inhibition: synaptic and tonic, which play distinct roles in regulating network synchrony and neuronal excitability (Farrant and Nusser, 2005; Brickley and Mody, 2012). Synaptic inhibition is generated by postsynaptic $GABA_A$ receptors that are activated by transient, near-saturating concentrations of GABA. In contrast, tonic inhibition is generated by extrasynaptic $GABA_A$ receptors that are activated by persistent, low ambient concentrations of GABA (Farrant and Nusser, 2005; Brickley and Mody, 2012).

H_2O_2 modulation of $GABA_A$ receptor function is of considerable interest as alterations in inhibitory neurotransmission dramatically change network activity (Farrant and Nusser, 2005;

Brickley and Mody, 2012). Previous studies that investigated the effects of H_2O_2 on GABAergic inhibition have produced conflicting results. Application of H_2O_2 (300 μM) to hippocampal slices increases the intracellular concentrations of chloride (Sah and Schwartz-Bloom, 1999). In contrast, very high concentrations of H_2O_2 (1.5–3.5 mM), reduce the amplitude of IPSPs recorded in the hippocampus, cerebral cortex, and thalamus (Pellmar, 1995; Frantseva et al., 1998). This reduction of IPSPs could result from a decrease in the release of GABA from presynaptic terminals or from direct inhibition of $GABA_A$ receptors. No previous studies have examined the direct effects of H_2O_2 on $GABA_A$ receptors that generate tonic and synaptic currents.

Here we show that H_2O_2 dramatically increases the amplitude of the tonic current in hippocampal neurons, whereas synaptic currents are unaffected. This increase in tonic current is due to an increase in potency of GABA, which results from an extracellular oxidative reaction. Oxygen-glucose deprivation, a pathological condition that generates high levels of endogenous H_2O_2 also increases the tonic current. Collectively, the results suggest that H_2O_2 could cause neuronal dysfunction, at least in part, by increasing $GABA_A$ receptor-mediated tonic current.

Materials and Methods

Experimental animals. All experimental procedures were approved by the Animal Care Committee of the University of Toronto (Toronto, ON, Canada). Three strains of mice of either sex were used to produce cultures of hippocampal neurons. Swiss White mice were obtained from Charles River Laboratories. $GABA_A$ receptor α5 subunit null-mutant (*Gabra5*$^{-/-}$) mice and wild-type (WT) mice (C57BL/6 × SvEv129) were obtained from Merck Sharp and Dohme Research Laboratories. $GABA_A$ receptor δ subunit null-mutant (*Gabrd*$^{-/-}$) mice and WT mice (C57BL/6 × SvJ129) were obtained from Dr Gregg E. Homanics at the University of Pittsburgh (Pittsburgh, PA). The generation, genotyping, and characterization of *Gabra5*$^{-/-}$ and *Gabrd*$^{-/-}$ mice were previously described (Mihalek et al., 1999; Collinson et al., 2002). Mice were housed in the animal care facility of the University of Toronto.

Cell culture. Cultures of embryonic hippocampal neurons were prepared as previously described (Wang et al., 2012). Briefly, fetal pups (embryonic day 18) were removed from mice killed by cervical dislocation. The hippocampi were dissected from each fetus and placed in an ice-cooled culture dish. Neurons were then dissociated by mechanical titration using two Pasteur pipettes (tip diameter, 150–200 μm) and plated on 35 mm culture dishes at a density of $\sim 1 \times 10^6$ cells/ml. The culture dishes were coated with collagen or poly-D-lysine (Sigma-Aldrich). For the first 5 d *in vitro*, cells were maintained in minimal essential media (MEM) supplemented with 10% fetal bovine serum and 10% horse serum (Life Technologies). The neurons were cultured at 37°C in a 5% CO_2-95% air environment. After the cells had grown to confluence, 0.1 ml of a mixture of 4 mg 5-fluorodeoxyuridine and 10 mg uridine in 20 ml MEM was added to the extracellular solution to reduce the number of dividing cells. Subsequently, the media was supplemented with 10% horse serum and changed every 3 or 4 d. Cells were maintained in culture for 14–20 d before use.

Whole-cell voltage-clamp recordings in cultured neurons. Before electrophysiological recordings, cultured neurons were rinsed with extracellular recording solution containing the following (in mM): 140 NaCl, 1.3 $CaCl_2$, 1 $MgCl_2$, 2 KCl, 25 *N*-2-hydroxy-ethylpiperazine-*N*′-2-ethanesulphonic acid (HEPES), 20 glucose, pH 7.4, 320–330 mOsm). 6-Cyano-7-nitroquinoxaline-2,3-dione (10 μM), and (2R)-amino-5-phosphonovaleric acid (20 μM) were added to the extracellular solution to block ionotropic glutamate receptors and tetrodotoxin (0.3 μM) was used to block voltage-dependent sodium channels. Patch pipettes (3–4 MΩ) were fabricated from borosilicate glass capillary tubing and filled with an intracellular solution containing the following (in mM): 140 CsCl, 10 HEPES, 11 EGTA, 4 MgATP, 2 $MgCl_2$, 1 $CaCl_2$, and 10 TEA (pH 7.3 with CsOH, 285–295 mOsm). All experiments were conducted at room temperature and whole-cell currents were recorded using the Axopatch 200B amplifier (Molecular Devices) controlled with pClamp 8.0 software via a Digidata 1322 interface (Molecular Devices). Membrane capacitance was measured using the membrane test protocol in pClamp 8.0. Currents were sampled at 10 kHz and filtered at 2 kHz by using an 8-pole low-pass Bessel filter. The extracellular solution was applied to neurons by a computer-controlled multibarreled perfusion system (SF-77B; Warner Instruments).

To measure the amplitude of the tonic current, the $GABA_A$ receptor competitive antagonist, bicuculline (100 μM), was applied as described previously (Caraiscos et al., 2004; Wang et al., 2012). All cells were recorded at a holding potential of −60 mV except for those used to study the current–voltage (*I–V*) relationship. *I–V* plots were constructed using a voltage step protocol, as previously described (Pavlov et al., 2009). Voltage steps of 20 mV were applied from −80 to +20 mV for 4 s, in the absence and presence of bicuculline (100 μM). The difference between current measured at the different membrane potentials, in the absence and presence of bicuculline, was used to generate the *I–V* plot. For each neuron, the voltage step protocol was repeated before and 5 min after the application of H_2O_2.

Whole-cell voltage-clamp recordings in hippocampal slices. Three-week old WT mice (C57BL/6 × SvEv129) of either sex were used for the recordings. After live decapitation, brains were removed and placed in ice-cold, oxygenated (95% O_2, 5% CO_2) artificial CSF (ACSF) that contained the following (in mM): 124 NaCl, 3 KCl, 1.3 $MgCl_2$, 2.6 $CaCl_2$, 1.25 NaH_2PO_4, 26 $NaHCO_3$, and 10 D-glucose with the solution osmolarity adjusted to 300–310 mOsm. Coronal brain slices (350 μm) were prepared with a VT1200S vibratome (Leica). The slices were allowed to recover for at least 1 h at room temperature (23–25°C) before being transferred to a submersion recording chamber where they were perfused with ACSF at 3–4 ml/min. All recordings were performed at room temperature using a MultiClamp 700B amplifier (Molecular Devices) that was controlled by pClamp 9.0 software via a Digidata 1322A interface (Molecular Devices). For whole-cell voltage-clamp recordings, the pipettes (2–3 MΩ) were filled with the same intracellular solution as described above for cell culture. Currents were sampled at 10 kHz. All cells were recorded at a holding potential of −60 mV. To measure the tonic current, the $GABA_A$ receptor competitive antagonist, bicuculline (20 μM) was applied. The tonic current was quantified by measuring the change in the holding current calculated from a Gaussian fitting of 30 s segments. Exogenous GABA (5 μM) was added to ACSF. The recorded neurons were perfused with ACSF containing H_2O_2 (1 mM) through a square-shaped barrel (ID 0.7 mm; Warner Instruments) whose tip was located in close proximity to the recorded neurons ($\approx$ 100 μM).

Oxygen-glucose deprivation. Ischemia-reperfusion injury was induced using the *in vitro* model of oxygen-glucose deprivation as previously described (Ohsawa et al., 2007). After establishing a stable baseline response, neurons were perfused for 10 min with a glucose- and O_2-deficient extracellular solution, in which the glucose was replaced with 2-deoxy-D-glucose (20 mM) and N_2 was continuously bubbled to remove O_2. The recorded neuron was then re-perfused with regular oxygenated extracellular solution for 5 min. The magnitude of the tonic current during the reperfusion period was compared with the baseline current. Only one neuron was used from each culture dish.

Statistical analyses. Data are represented as mean ± SEM. A Student's *t* test (paired or unpaired) was used to compare groups, where appropriate. For comparing three or more groups, one-way ANOVA followed by Newman–Keuls *post hoc* test was used. Two-way ANOVA (treatment × concentration) followed by Bonferroni *post hoc* test was also used, as indicated. Cumulative distributions of the amplitude and frequency of miniature IPSCs (mIPSCs) were compared using the Kolmogorov–Smirnov test. Statistical significance was set at $p < 0.05$.

Results

H_2O_2 markedly increases the tonic but not synaptic currents in hippocampal neurons

The tonic current was quantified by measuring the change in the holding current that occurred following an application of the competitive $GABA_A$ receptor antagonist bicuculline (BIC; 100

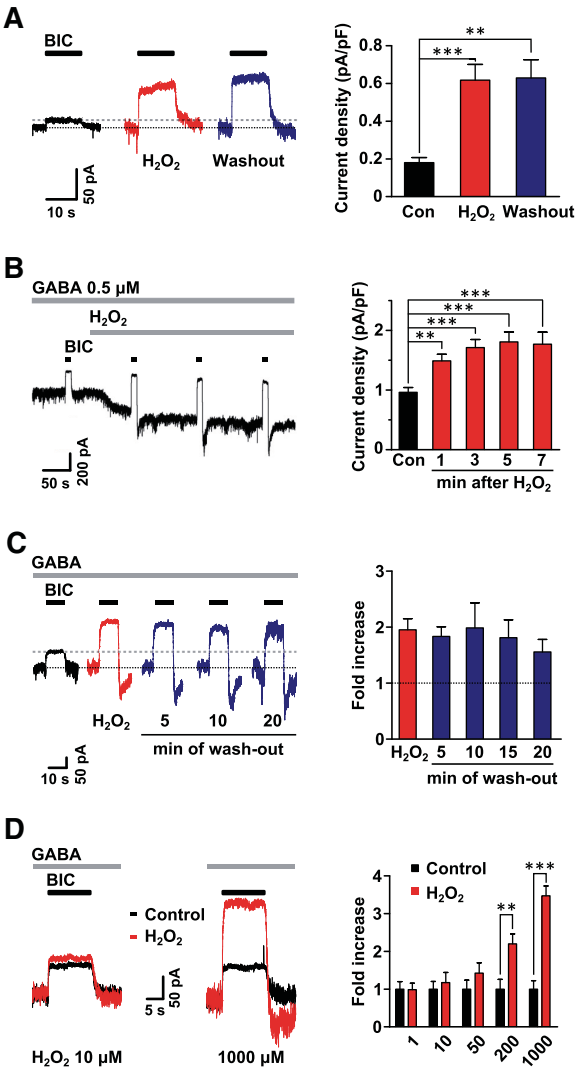

Figure 1. H_2O_2 increased tonic GABA currents in hippocampal neurons. ***A***, Representative traces and summarized data showing that the tonic current revealed by BIC (100 μM) was increased after 5 min of H_2O_2 (200 μM, $n = 21$) and this increase persisted for at least 5 min after washout ($n = 6$). ***B***, Representative trace and summarized data showing the time-dependent effects of H_2O_2 (200 μM) on tonic current in the presence of a low concentration of GABA (0.5 μM, $n = 17–23$). ***C***, Representative traces and summarized data demonstrate that tonic current was persistently increased even after 20 min of washout in the presence of GABA (0.5 μM, $n = 5–7$). One-way ANOVA: $F_{(2,47)} = 16.1$, for ***A***; $F_{(4,102)} = 6.7$ for ***B***, $F_{(4,24)} = 0.4$; and $p = 0.4$ for ***C***; Newman–Keuls *post hoc* test, $^{**}p < 0.01$ and $^{***}p < 0.001$. ***D***, Left, Representative traces showing the increase in tonic current induced by a low-concentration (10 μM) and a high-concentration (1000 μM) of H_2O_2 in the presence of GABA (0.5 μM). Right: Quantified data demonstrating the dose-dependent enhancing effects of H_2O_2 on tonic current ($n = 4$ for each concentration). Two-way ANOVA, effect of H_2O_2: $F_{(1,30)} = 32.0$, $p < 0.0001$; effect of concentration: $F_{(4,30)} = 9.2$, $p < 0.0001$; effect of interaction: $F_{(4,30)} = 9.2$, $p < 0.0001$; Bonferroni *post hoc* test, $^{**}p < 0.01$, $^{***}p < 0.001$. Con, Control (for here and in subsequent figures).

μM; Fig. 1*A*). For these initial experiments, no exogenous GABA was added to the extracellular solution. Pretreating the neurons with H_2O_2 (200 μM) for 5 min increased the amplitude of the tonic current 3.4 ± 0.5-fold (control: 0.18 ± 0.03 pA/pF; H_2O_2: 0.62 ± 0.08 pA/pF, $n = 21–23$, $p < 0.001$, one-way ANOVA followed by Newman–Keuls *post hoc* test; Fig. 1*A*). This increase persisted for at least 5 min after H_2O_2 was washed out.

The increase in tonic current by H_2O_2 could result from an increase in either the extracellular concentration of GABA or the $GABA_A$ receptor function. To exclude the possibility that changes in the extracellular concentration accounted for the increase, a low concentration of exogenous GABA (0.5 μM) was added to the extracellular perfusion solution. Under these conditions, neurons were "concentration clamped" at a stable, known concentration of agonist. GABA (0.5 μM) was selected as this concentration is similar to physiological levels of extracellular GABA that occur *in vivo* (Farrant and Nusser, 2005; Bright and Smart, 2013).

In the presence of exogenous GABA (0.5 μM), H_2O_2 (200 μM) gradually increased the holding current (control: −81.6 ± 8.7 pA; H_2O_2: −189.8 ± 21.8 pA, $n = 21–23$, $p < 0.001$, paired *t* test). Therefore, the amplitude of the tonic current revealed by BIC was enhanced in a time-dependent manner and peaked at 5–7 min (Fig. 1*B*). The enhancing effect of H_2O_2 was not reversible and was sustained for at least 20 min after washout (Fig. 1*C*). Notably, a transient, inward "rebound" current was observed after termination of the BIC application in H_2O_2-treated neurons. This rebound current has been attributed to BIC protecting $GABA_A$ receptors from entering an agonist-bound desensitized state (Bianchi and Macdonald, 2001; Chang et al., 2002). H_2O_2 dose-dependently increased the current with a threshold concentration of 10 μM and maximum effective concentration at 1 mM (3.5 ± 0.3-fold increase; Fig. 1*D*). Concentrations of H_2O_2 >1 mM were not studied because they caused instability of the recordings and cell death as reported previously (Schraufstatter et al., 1986; Kaneko et al., 2006).

To determine whether H_2O_2 similarly potentiated postsynaptic $GABA_A$ receptor currents, spontaneous mIPSCs were recorded from the cultured neurons. Surprisingly, pretreatment with H_2O_2 (200 μM) failed to change the amplitude or frequency of mIPSCs (Fig. 2; Table 1). The time course and charge transfer of the mIPSCs were also unaffected (Table 1).

We next investigated whether H_2O_2 also increased the tonic GABA current in CA1 pyramidal neurons of acutely isolated hippocampal slices. H_2O_2 (1 mM, 10 min) increased the amplitude of the tonic current recorded in the presence of 5 μM GABA (control: 0.05 ± 0.02 pA/pF; H_2O_2: 0.28 ± 0.08 pA/pF; $n = 6$ for each group, $p = 0.02$, unpaired *t* test; Fig. 3) but did not change the amplitude or time course of spontaneous synaptic GABA currents (Table 1). Collectively, these results show that H_2O_2 selectively increases the tonic but not synaptic currents in hippocampal neurons.

H_2O_2-induced increase in tonic current does not require α5$GABA_A$ receptors or δ$GABA_A$ receptors

Several factors could contribute to the differential sensitivity of tonic and synaptic currents to H_2O_2 including the subunit composition of the underlying $GABA_A$ receptors or the conditions under which the receptors are activated. To further investigate H_2O_2 enhancement of the tonic current, additional experiments were performed with cultured hippocampal neurons, as this preparation is a relatively high-throughput assay. In addition, cells can be effectively concentration-clamped and modulators can be applied and washed out rapidly.

A variety of $GABA_A$ receptor subtypes generate the tonic current although, most tonic current is generated by α5 subunit-containing $GABA_A$ (α5$GABA_A$) receptors and δ subunit-containing $GABA_A$ (δ$GABA_A$) receptors (Caraiscos et al., 2004; Farrant and Nusser, 2005; Mortensen and Smart, 2006; Brickley and Mody, 2012; Lee and Maguire, 2014). To study the subtypes

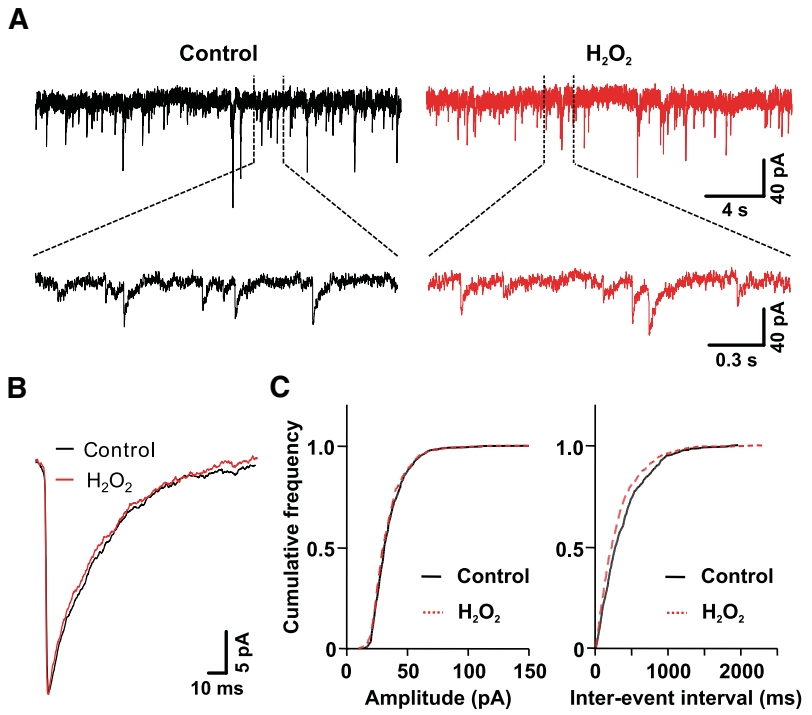

Figure 2. H_2O_2 had no effect on synaptic GABA currents. ***A***, Representative recordings of $GABA_A$ receptor-mediated mIPSCs recorded at −60 mV before (left) and after (right) 5 min of H_2O_2 (200 μM) treatment from the same neuron. ***B***, Traces were averaged from 475 (control) and 527 (H_2O_2) individual mIPSCs. ***C***, Cumulative amplitude (left) and frequency (right) distributions of mIPSCs showing that both the amplitude and the frequency were not affected by H_2O_2; $p = 0.24$ for the amplitude, $p = 0.06$ for the frequency, Kolmogorov–Smirnov test.

of $GABA_A$ receptors that mediate the H_2O_2 enhancement, a combination of pharmacological and genetic approaches was used. First, to investigate the role of α5$GABA_A$ receptors, the inhibitory effects of L-655,708 (L6, 20 nM), a selective inverse agonist for α5$GABA_A$ receptors (Quirk et al., 1996) were studied. The change in holding current produced by an application of L6 was measured before and after application of H_2O_2. BIC (100 μM) was applied after L6 to reveal the total tonic current generated by all subtypes of $GABA_A$ receptors. Despite the expected large increase in the BIC-sensitive current after H_2O_2, the amplitude of the L6-sensitive current was not significantly increased (control: 0.08 ± 0.02 pA/pF; H_2O_2: 0.10 ± 0.03 pA/pF; $n = 6$, $p = 0.36$, paired t test; Fig. 4*A*) and the ratio of the L6-sensitive to BIC-sensitive current was reduced from 47.1 ± 13.7% for control to 15.4 ± 3.9% for H_2O_2 ($n = 6$, $p = 0.03$, paired t test). These results show that α5$GABA_A$ receptors are not a major contributor to the H_2O_2-enhanced tonic current. To confirm that α5$GABA_A$ receptors are not necessary for the H_2O_2-sensitive current, hippocampal neurons were harvested from *Gabra5*$^{-/-}$ mice and WT mice (Fig. 4*B*). The relative magnitude of the tonic current recorded in these neurons was similarly increased by H_2O_2 between genotypes (*Gabra5*$^{-/-}$: 3.7 ± 0.7-fold increase, WT: 4.1 ± 0.6-fold increase; $n = 9$ and 10, respectively; $p = 0.70$, unpaired t test; Fig. 4*B*) confirming that α5$GABA_A$ receptors are not required for enhancement of tonic current. Note, the low amplitude tonic current observed in both genotypes under control conditions, may be attributed to a low ambient concentration of GABA (Caraiscos et al., 2004; Glykys and Mody, 2007; Wang et al., 2012).

To determine whether δ$GABA_A$ receptors generated the H_2O_2-enhanced tonic current, we applied the δ$GABA_A$ receptor-preferring agonist THIP (Brown et al., 2002). THIP-evoked inward current was measured before and after H_2O_2. The THIP (0.5 μM)-evoked current increased 3.3 ± 0.7-fold after H_2O_2 (control: 0.09 ± 0.04 pA/pF; H_2O_2: 0.30 ± 0.06 pA/pF; $n = 6$, $p = 0.007$, paired t test; Fig. 4*C*). The tonic current revealed by BIC was also greatly increased; but H_2O_2 did not change the THIP to BIC current ratio (Control: 59.6 ± 15.7%, H_2O_2: 34.6 ± 3.4%, $n = 5$; $p = 0.21$, paired t test). These results show that δ$GABA_A$ receptors contribute to, but do not exclusively generate the H_2O_2-enhanced tonic current. Next, to determine whether δ$GABA_A$ receptors were necessary for the H_2O_2 effects, the amplitude of the tonic current was measured in neurons harvested from *Gabrd*$^{-/-}$ and WT mice. H_2O_2 caused a similar increase in current in the two genotypes (WT: 9.6 ± 1.5-fold increase, *Gabrd*$^{-/-}$: 9.2 ± 1.4-fold increase; $n = 9$ for each genotype, $p = 0.85$, unpaired t test; Fig. 4*D*), indicating that δ$GABA_A$ receptors are not necessary for the H_2O_2 effects. Thus, the subtypes of $GABA_A$ receptors that typically generate the tonic current in hippocampal neurons are not required for H_2O_2 enhancement of the tonic current.

H_2O_2 increases the potency of GABA at the $GABA_A$ receptors

Given that the unique population of $GABA_A$ receptors that typically generates tonic current does not confer sensitivity to H_2O_2, we next studied whether the conditions of receptor activation contributed to the increase in tonic but not synaptic currents. The tonic current is generated by low concentrations of GABA whereas synaptic currents are activated by near-saturating concentrations of GABA (Farrant and Nusser, 2005; Brickley and Mody, 2012). Thus, we postulated that H_2O_2 increased the potency of GABA at the $GABA_A$ receptors and thereby enhanced the tonic current. If this was true, then the potentiating effects of H_2O_2 should increase with decreasing concentrations of GABA, and decrease with increasing GABA concentrations. Accordingly, we studied the effects of H_2O_2 on current evoked by a brief application of several concentrations of GABA. H_2O_2 (200 μM) increased the amplitude of GABA (0.5 μM)-evoked current 3.4 ± 0.5-fold (control: 1.6 ± 0.3 pA/pF; H_2O_2: 5.4 ± 0.7 pA/pF; $n = 13$ for each group, $p < 0.001$, one-way ANOVA followed by Newman–Keuls *post hoc* test). The increase in current developed slowly over 5 min and was irreversible (Fig. 5*A*). Decreasing GABA from 0.5 μM to 0.3 μM increased the potentiating effect of H_2O_2 (5.3 ± 1.1-fold increase; $n = 5$, $p < 0.001$, two-way ANOVA followed by Bonferroni *post hoc* test; Fig. 5*B*). Conversely, increasing GABA from 0.5 to 10 μM reduced the magnitude of the H_2O_2 effect (1.3 ± 0.2-fold increase; $n = 6$, $p > 0.05$, two-way ANOVA followed by Bonferroni *post hoc* test). Importantly, H_2O_2 caused no change in the current when a near-saturating concentration of GABA (100 μM) was applied. Thus,

Table 1. H_2O_2 did not modify mIPSCs recorded in cultured hippocampal neurons (200 μM, 5 min) or in CA1 pyramidal neurons from hippocampal slices (1 mM, 10 min)

	Treatment	Amplitude (pA)	Frequency (Hz)	Rise time (ms)	Decay time (ms)	Area (pA · ms)
Culture ($n = 9$)	Control	36.4 ± 1.5	2.3 ± 0.6	4.8 ± 0.2	12.4 ± 1.0	487.8 ± 48.5
	H_2O_2	36.1 ± 1.6	1.8 ± 0.4	4.9 ± 0.2	11.9 ± 0.8	454.5 ± 36.3
Slice ($n = 6$)	Control	34.5 ± 2.9	2.9 ± 0.4	3.1 ± 0.2	10.5 ± 0.7	360.5 ± 34.1
	H_2O_2	46.9 ± 4.8	2.8 ± 0.4	3.2 ± 0.2	10.9 ± 0.7	490.3 ± 52.8

Data are presented as mean ± SEM for all the parameters; $p > 0.05$, Student's paired t test.

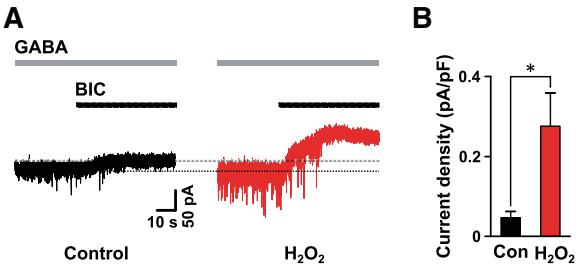

Figure 3. H_2O_2 increased tonic GABA currents in hippocampal slices. Representative traces (***A***) and summarized data (***B***) showing the increase in tonic current after 10 min of H_2O_2 (1 mM) treatment ($n = 6$); *$p = 0.02$, Student's unpaired t test.

H_2O_2 modifies the $GABA_A$ receptors at low but not high concentrations of GABA.

Next, GABA concentration-response plots were constructed for currents evoked by GABA (0.3–1000 μM) in the absence and presence of H_2O_2 (200 μM). H_2O_2 shifted the concentration-response plot to the left, but only for the lower components of the curve (Fig. 5*C*). The EC_{20} value was reduced from 5.5 ± 0.4 μM for control to 3.5 ± 0.4 μM for H_2O_2 ($n = 8$ and 11, respectively; $p = 0.003$, unpaired t test), whereas the EC_{50} values (control: 15.6 ± 1.3 μM; H_2O_2: 12.6 ± 1.1 μM; $n = 8$ and 11, respectively; $p = 0.11$, unpaired t test) and EC_{80} values (control: 44.5 ± 4.8 μM; H_2O_2: 47.3 ± 3.9 μM; $n = 8$ and 11, respectively; $p = 0.65$, unpaired t test) were unchanged. H_2O_2 also reduced the Hill coefficient (control: 1.35 ± 0.04; H_2O_2: 1.07 ± 0.05; $n = 8$ and 11, respectively; $p = 0.0005$, unpaired t test). Collectively, these results show that H_2O_2 increases the potency of GABA at the $GABA_A$ receptors, but only at low GABA concentrations.

H_2O_2 does not change the desensitization or voltage sensitivity of $GABA_A$ receptors

We next asked whether H_2O_2 modified the desensitization and voltage sensitivity of $GABA_A$ receptors, two factors that can modify the magnitude of tonic current (Chang et al., 2002; Pavlov et al., 2009). If H_2O_2 simply increased the potency of GABA without changing desensitization, then the extent of desensitization of the increased current should be similar to that observed with a higher concentration of GABA. Also, no change in current desensitization should be observed at a saturating concentration of GABA (Colquhoun, 1998; Chang et al., 2002). We quantified the extent of desensitization by recording whole-cell currents evoked by longer applications of GABA (20 s). The ratio of current at 20 s to peak current was measured before and after application of H_2O_2 (200 μM). In these experiments, H_2O_2 increased the extent of desensitization for current evoked by low concentrations of GABA (Fig. 5*D*), but did not influence desensitization of currents evoked by higher concentrations of GABA (e.g., 10 μM). We next plotted the relationship between the peak current and current at 20 s application of GABA (over a concentration range of 0.3–10 μM; Fig. 5*E*). A linear regression fit to data for the two conditions

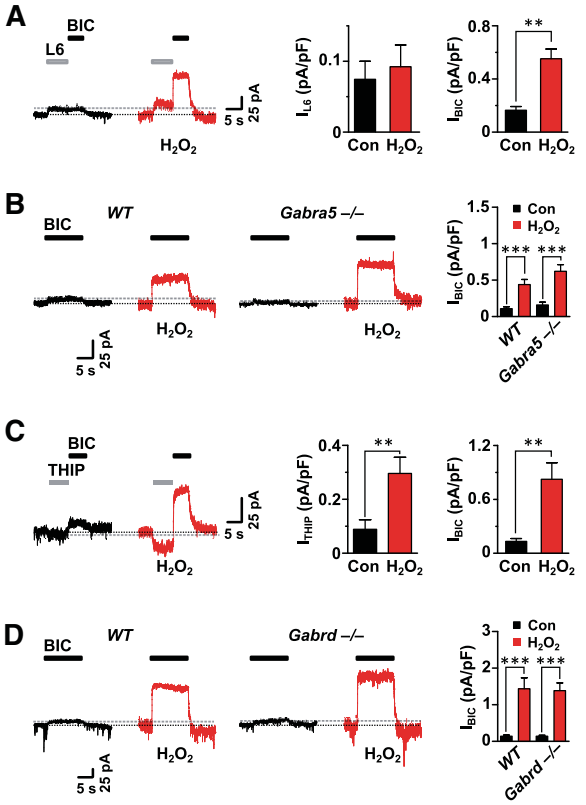

Figure 4. α5$GABA_A$ and $\delta GABA_A$ receptors were not required for the H_2O_2-dependent increase in current. ***A***, Left, Representative traces showing the tonic current revealed by a selective inverse agonist of α5$GABA_A$ receptors (L6, 20 nM) and BIC (100 μM). The L6-sensitive tonic current was unaffected, whereas BIC-sensitive current was greatly increased by H_2O_2. Right, Quantification of L6- and BIC-sensitive tonic current, before and after H_2O_2 ($n = 6$); **$p = 0.002$, Student's paired t test. ***B***, Left, Representative traces showing the tonic current revealed by BIC (100 μM) in neurons from WT and *Gabra5*$^{-/-}$ mice. Right, Quantification of the tonic current before and after H_2O_2 ($n = 10$ for WT, $n = 9$ for *Gabra5*$^{-/-}$). ***C***, Left, Representative traces showing the current activated by $\delta GABA_A$ receptor-preferring agonist THIP (0.5 μM) and the tonic current revealed by BIC (100 μM). Right, Quantification of THIP-activated inward current ($n = 6$) and the tonic current revealed by BIC ($n = 5$) before and after H_2O_2; **$p = 0.007$ for THIP, **$p = 0.008$ for BIC, Student's paired t test. ***D***, Left, Representative traces showing the tonic current revealed by BIC in neurons from WT and *Gabrd*$^{-/-}$ mice. Right, Quantification of the tonic current before and after H_2O_2 ($n = 9$ for each genotype).

showed that the slopes of the lines were similar (control: 1.2 ± 0.05; H_2O_2: 1.2 ± 0.06; $n = 23$ for each group, $p = 0.87$). Thus, H_2O_2 does not alter the intrinsic desensitization properties of $GABA_A$ receptors.

If H_2O_2 simply increases the potency of GABA, then no change in the voltage sensitivity of $GABA_A$ receptors should be observed (Colquhoun, 1998; Legendre et al., 2000; Pavlov et al., 2009). To test this prediction, *I–V* plots were constructed for

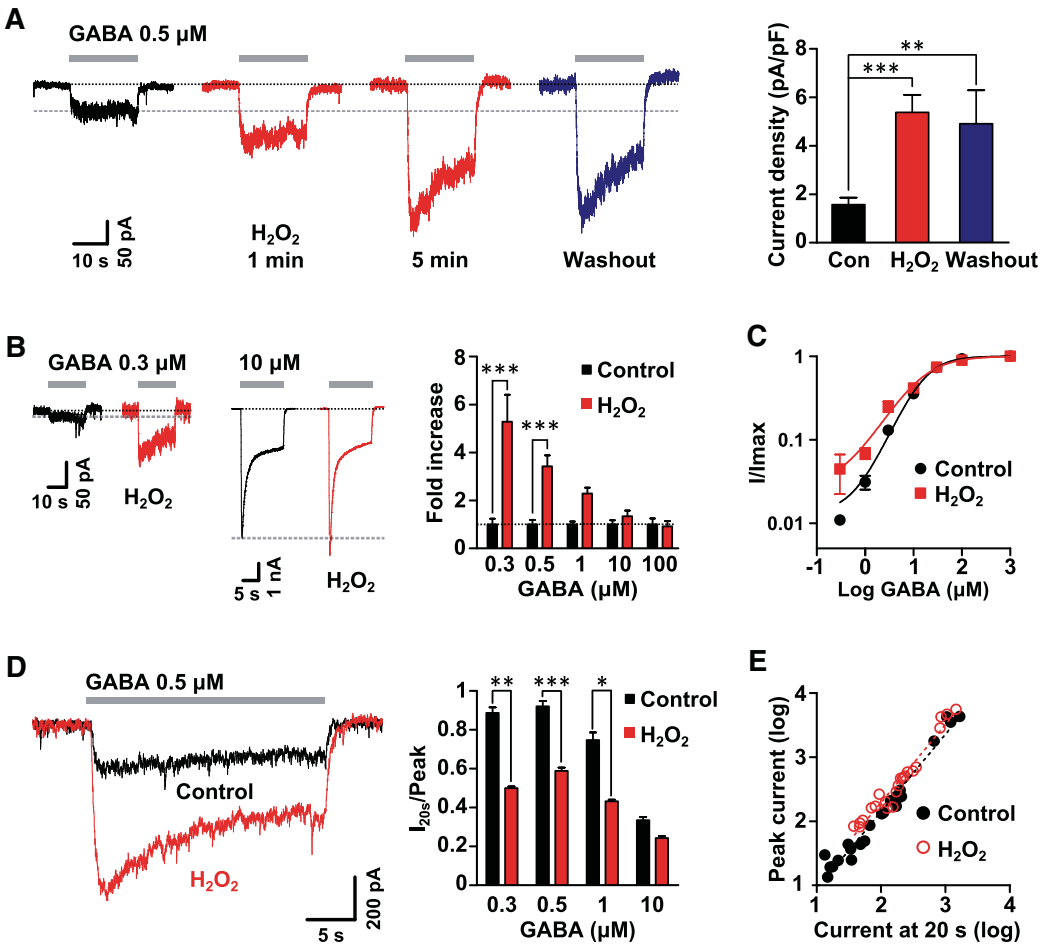

Figure 5. H_2O_2 increased the potency of low concentrations of GABA without modifying the desensitization properties. ***A***, Left, Representative traces showing the time-dependent effects of H_2O_2 (200 μM) on currents evoked by a low concentration of GABA (0.5 μM). Right, Summarized data ($n = 4–13$). One-way ANOVA: $F_{(2,27)} = 11.8$; Newman–Keuls *post hoc* test; $^{**}p < 0.01$, $^{***}p < 0.001$. ***B***, Left, Representative traces showing the effects of H_2O_2 (200 μM) on the currents evoked by 0.3 and 10 μM GABA. Right, Summarized data showing the fold increase in currents evoked by different concentrations of GABA by H_2O_2 (200 μM; $n = 5–13$). Two-way ANOVA, effect of H_2O_2: $F_{(1,58)} = 33.2$, $p < 0.0001$; effect of concentration: $F_{(4,58)} = 7.6$, $p < 0.0001$; effect of interaction: $F_{(4,58)} = 7.6$, $p < 0.0001$; Bonferroni *post hoc* test, $^{***}p < 0.001$. ***C***, Concentration-response plots in the absence and presence of H_2O_2 fitted with Hill equation ($n = 8–11$). ***D***, Left, Representative traces showing currents evoked by GABA (0.5 μM) before and after H_2O_2 (200 μM). Right, Summarized data showing the effects of H_2O_2 on desensitization of currents evoked by increasing concentrations of GABA. H_2O_2 decreased the ratio of current at 20 s to peak current only at low GABA concentrations but not at 10 μM ($n = 4–9$). Two-way ANOVA, effect of H_2O_2: $F_{(1,38)} = 33.5$, $p < 0.0001$; effect of concentration: $F_{(3,38)} = 18.0$, $p < 0.0001$; effect of interaction: $F_{(3,38)} = 1.8$, $p = 0.16$; Bonferroni *post hoc* test, $^{*}p < 0.05$, $^{**}p < 0.01$, $^{***}p < 0.001$. ***E***, Correlation between the current at 20 s and peak current, before and after H_2O_2 (200 μM). The linear regression fit generated similar slopes between control and H_2O_2 treatment ($n = 23$ for each condition).

tonic current recorded before and after application of H_2O_2 (200 μM). Specifically, GABA (0.5 μM) was added to the extracellular solution and currents were recorded using a voltage step protocol (−80 to +20 mV; Fig. 6*A*). BIC (100 μM) was then applied, and currents were recorded using the same voltage step protocol. The magnitude of the tonic current at the various potentials was calculated as the difference in current measured in the absence and presence of BIC. The control *I–V* plot exhibited a slight outward rectification (Fig. 6*A*), as previously described (Pavlov et al., 2009). H_2O_2 increased the slope of the *I–V* plot but did not change the outward rectifying properties or reversal potential (control: −1.9 ± 3.2 mV; H_2O_2: −6.3 ± 1.7 mV, $n = 6$, $p = 0.44$, paired *t* test) of the tonic current. The H_2O_2-induced increase in current was equivalent at all potentials between −80 mV and +20 mV (2.3 ± 0.1-fold; Fig. 6*B*), suggesting that H_2O_2 does not alter the voltage sensitivity of $GABA_A$ receptors.

H_2O_2 effects are independent of Zn^{2+}, Ca^{2+}, and $GABA_B$ receptors

The divalent cation Zn^{2+} inhibits subpopulations of high-affinity $GABA_A$ receptors that generate a tonic current in hippocampal neurons (Saxena and Macdonald, 1994; Mortensen and Smart, 2006), and trace levels of Zn^{2+} are present in the extracellular solution (Smart et al., 1994). Thus, it is plausible that H_2O_2 increased the current by relieving Zn^{2+}-induced inhibition of $GABA_A$ receptors. We tested this hypothesis in two ways. First, if Zn^{2+} inhibited the tonic current, then reducing the extracellular concentration of Zn^{2+} should mimic the effect of H_2O_2. The Zn^{2+} chelator TPEN (10 μM) was added to the extracellular solution to markedly reduce the concentration of Zn^{2+}. TPEN produced no change in the amplitude of the tonic current (control: 1.3 ± 0.3 pA/pF; TPEN: 1.3 ± 0.2 pA/pF; $n = 4$, $p = 0.55$, paired *t* test; Fig. 7*A*). Next, we studied whether increasing the extracel-

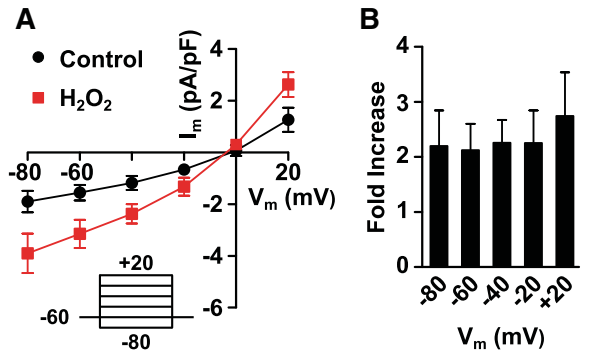

Figure 6. H_2O_2 did not modify the voltage sensitivity of the tonic GABA current. ***A***, The *I–V* relationship of tonic current before and after H_2O_2 treatment was studied using a voltage step protocol for holding potentials between −80 and +20 mV that had a duration of 4 s (n = 5–6). ***B***, Summarized data showing similar increase in tonic current by H_2O_2 at all membrane potentials (n = 5). One-way ANOVA: $F_{(4,20)} = 0.17$, $p = 0.95$.

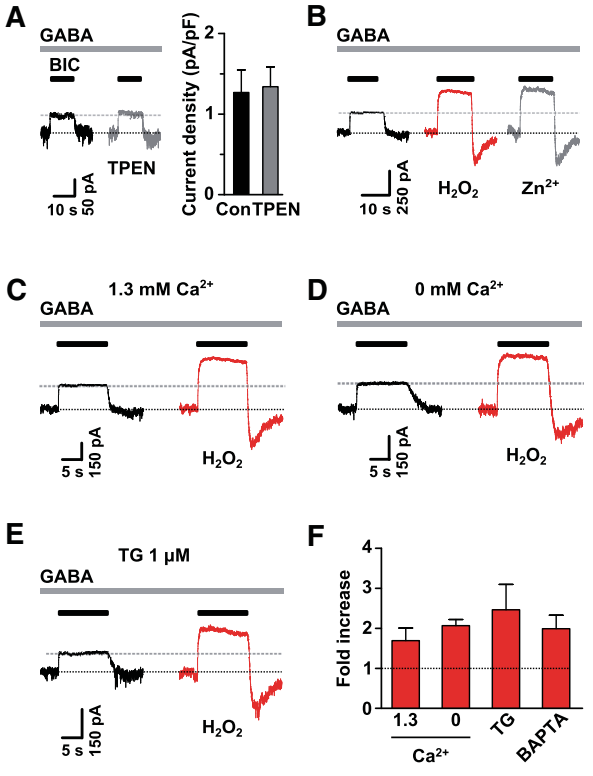

Figure 7. Changes in the concentration of Zn^{2+} and Ca^{2+} did not modify the effects of H_2O_2. ***A***, Left, Representative traces showing the effects of TPEN (10 μM) on the tonic current. Right, Quantification of the increase in tonic current before and after TPEN (n = 4). ***B***, Representative traces showing the effects of Zn^{2+} (10 μM) on tonic current after being potentiated by H_2O_2 (200 μM). Similar results were obtained from another three cells. ***C–E***, Representative traces showing the increase in tonic current by H_2O_2 (200 μM) in the presence of normal extracellular Ca^{2+} (***C***), in the absence of extracellular Ca^{2+} (***D***), or when intracellular Ca^{2+} was depleted with thapsigargin (TG, 1 μM; ***E***). ***F***, Summarized data for experiments in ***C–E*** (n = 5–9 for each condition). One-way ANOVA: $F_{(3,20)} = 0.7$, $p = 0.55$.

lular concentration of Zn^{2+} decreased the H_2O_2 effects on current. The addition of Zn^{2+} (10 μM) to the extracellular solution had no effect on H_2O_2 (200 μM) enhancement of the current (H_2O_2: 2.6 ± 0.5 pA/pF; Zn^{2+}: 2.4 ± 0.6 pA/pF; n = 4, p = 0.3, paired t test; Fig. 7*B*). Thus, H_2O_2 relief of Zn^{2+} blockade does not account for the increase in tonic current.

H_2O_2 is known to alter the intracellular concentration of Ca^{2+} (Smith et al., 2003) and the cytosolic concentration of Ca^{2+} alters the potency of GABA at $GABA_A$ receptors (Inoue et al., 1986; Martina et al., 1994). To determine whether H_2O_2-dependent changes in Ca^{2+} contributed to the increased current, extracellular and intracellular Ca^{2+} concentrations were modified. First, we reduced the extracellular concentration of Ca^{2+} and observed no change in the ability of H_2O_2 to increase the current (Fig. 7*C*,*D*,*F*). Depleting intracellular Ca^{2+} stores by treating the neurons with thapsigargin (TG; 1 μM; Fig. 7*E*,*F*) also had no effect. Similarly, chelating Ca^{2+} by perfusing the neurons with BAPTA-AM (100 μM; Fig. 7*F*) failed to change the H_2O_2-enhanced current. Thus, the H_2O_2 effects are independent of the extracellular and intracellular concentrations of Ca^{2+}.

It is plausible that the effects of H_2O_2 are secondary to its modulatory effects on other receptors or proteins. Upregulation of $GABA_B$ receptors increases tonic GABA current (Connelly et al., 2013; Tao et al., 2013) and H_2O_2 could increase the tonic current indirectly by increasing $GABA_B$ receptor function. However, when a $GABA_B$ receptor blocker CGP 55845 (1 μM) was added to the bath, H_2O_2 increased tonic GABA current 2.0 ± 0.2-fold (CGP: 1.2 ± 0.2 pA/pF; H_2O_2 and CPG: 2.4 ± 0.3 pA/pF; n = 5; p = 0.002, paired t test) suggesting that H_2O_2 does not act on $GABA_B$ receptors. Collectively, these results suggest that the increase in GABA potency by H_2O_2 does not result from relief of Zn^{2+}-induced inhibition and is independent of Ca^{2+} concentrations, as well as $GABA_B$ receptors.

H_2O_2 enhancement is mediated by an extracellular oxidative reaction

H_2O_2 regulates the function of several ion channels that span the cell membrane including TRPM4, TRPC6, and purinergic (P2X2 and P2X4) receptors via an oxidative reaction (Coddou et al., 2009; Graham et al., 2010; Simon et al., 2010). To determine whether H_2O_2 similarly regulated $GABA_A$ receptors via an oxidative reaction, the antioxidant glutathione (GSH, 1 mM) was added to the pipette solution and current was recorded before and after treatment with H_2O_2 (200 μM). Under these conditions, H_2O_2 increased the tonic current as reported above (control: 1.4 ± 0.2 pA/pF; H_2O_2: 3.6 ± 0.7 pA/pF; n = 6 for each group, p = 0.008, paired t test; Fig. 8*A*). In contrast, the effects of H_2O_2 were completely abolished when GSH was added to the extracellular solution (Fig. 8*B*). Similarly, when the antioxidant dithiothreitol (DTT, 1 mM) was added to the extracellular solution, H_2O_2 had no effect on the current (Fig. 8*C*). Collectively, the results show that the potentiating effects of H_2O_2 result from an extracellular oxidative reaction.

The oxidative reaction could be mediated either directly by H_2O_2 or indirectly through the production of hydroxyl radical ($\cdot$OH). H_2O_2 generates $\cdot$OH by interacting with ferrous irons (Fe^{2+}) via the Fenton reaction (Haber and Weiss, 1934). We tested whether inhibiting the Fenton reaction by adding the iron chelator deferoxamine (DFO; 100 μM) to the extracellular solution modified the effect of H_2O_2. DFO completely abolished the effect of H_2O_2 (Fig. 8*D*) confirming that the increase in current was dependent on the Fenton reaction.

Endogenous ROS increase tonic current

Finally, we investigated whether endogenous H_2O_2 increased the tonic current. Ischemia-reperfusion, which produces high levels of H_2O_2 and other ROS (Hyslop et al., 1995) can be mimicked *in*

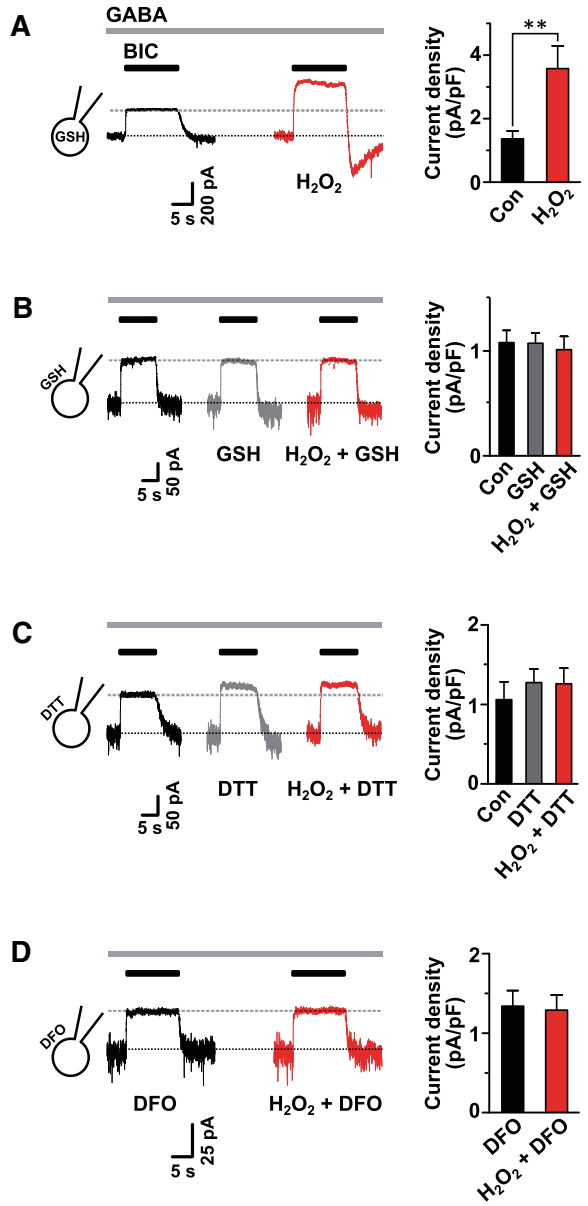

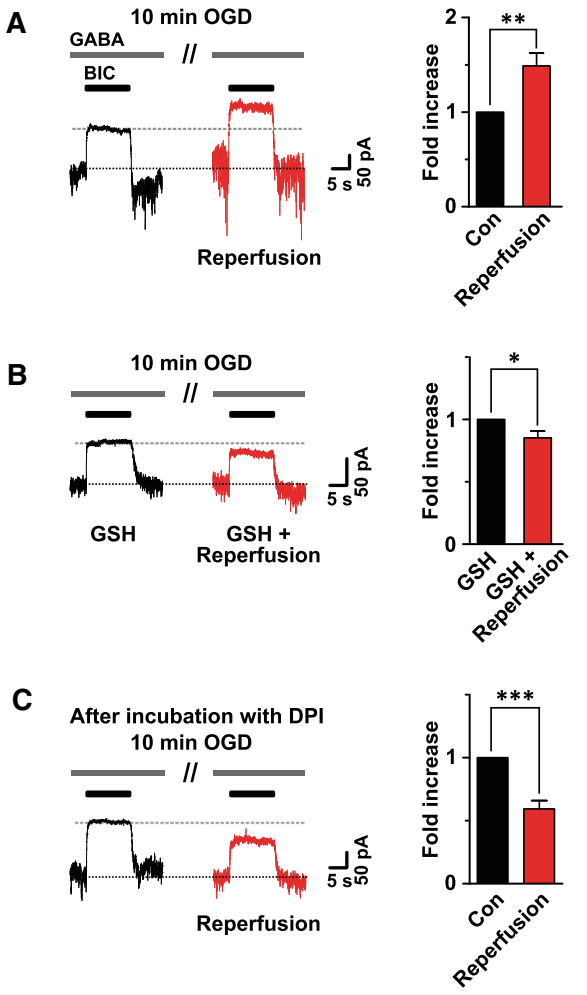

Figure 8. Extracellular oxidative reaction mediated the effects of H_2O_2. ***A***, Addition of the antioxidant GSH (1 mM) to the pipette solution did not modify the increase in tonic current by H_2O_2 (200 μM). $n = 6$ for each group, $^{**}p = 0.008$, Student's unpaired *t* test. ***B***, ***C***, Addition of the antioxidants GSH (1 mM) and DTT (1 mM) to the extracellular solution abolished the increase in tonic current by H_2O_2 (200 μM); $n = 4$. ***D***, DFO (100 μM) prevented the increase in tonic current by H_2O_2 (200 μM); $n = 6$.

Figure 9. OGD treatment increased tonic current through an oxidative reaction. ***A***, Reperfusion after OGD increased tonic current; $n = 9$, $^{**}p = 0.006$, Student's paired *t* test. ***B***, ***C***, The increase in tonic current by reperfusion was abolished and a decrease after reperfusion was observed for neurons treated with the antioxidant GSH (1 mM; ***B***) or pretreated for 30 min with NADPH oxidase inhibitor DPI (10 μM; ***C***). Student's paired *t* test; $n = 7$, $^{*}p = 0.03$ for ***B***; $n = 7$, $^{***}p < 0.001$ for ***C***.

vitro using an oxygen-glucose deprivation (OGD) protocol (Abramov et al., 2007). Following 10 min of OGD, cultures were re-perfused with the normal, oxygenated extracellular solution. OGD increased the amplitude of the current by 49 ± 13% ($n = 9$, $p = 0.006$, paired *t* test; Fig. 9*A*). Next, to confirm that this increase in current after OGD resulted from an oxidative reaction, the antioxidant GSH (1 mM) was added to the extracellular solution during period of ischemia. GSH completely abolished the increase in current following OGD (Fig. 9*B*). The current was also slightly reduced by GSH (15 ± 5%, $n = 7$, $p = 0.04$, paired *t* test).

We next sought to identify the source of the endogenous H_2O_2 produced during OGD and reperfusion. NADPH oxidase is the principal source of ROS during reperfusion and inhibition of this enzyme prevents the production of ROS in hippocampal neurons (Abramov et al., 2004; Riquelme et al., 2011). To examine whether NADPH oxidase generated H_2O_2, which increased the tonic current after OGD, cultured neurons were incubated with the NADPH oxidase inhibitor diphenyleneiodonium (DPI; 10 μM) for 30 min before being treated with OGD. DPI completely abolished the increase in tonic current after OGD and indeed, reduced tonic GABA current by 41 ± 1% ($n = 7$, $p < 0.0001$, paired *t* test; Fig. 9*C*). These results suggest that endogenous H_2O_2 produced by NADPH oxidase during ischemia-reperfusion might increase the tonic current via an oxidative reaction. The decrease in tonic current after GSH and DPI suggests that OGD may also have an inhibitory effect on tonic current that is masked by the potentiating effects of H_2O_2.

Discussion

The results show that H_2O_2 causes a robust increase in $GABA_A$ receptor-mediated tonic current whereas synaptic currents are unaffected. This selective increase in tonic current does not require the expression of typical extrasynaptic $GABA_A$ receptors and is due to an extracellular oxidative reaction that increases the potency of GABA. In addition, ischemia-reperfusion injury, which produces high endogenous levels of H_2O_2, similarly increases the tonic current.

H_2O_2 increases the potency of GABA, but only when $GABA_A$ receptors are activated by low concentrations of GABA. The GABA concentration-response plot is shifted to the left; however, only the EC_{20} value but not the EC_{50} or EC_{80} value is reduced. Several additional lines of evidence further support the conclusion that H_2O_2 increases the potency of GABA. First, a transient, inward "rebound" current is observed in H_2O_2-treated neurons (Fig. 1*B*). A similar rebound current can occur when currents are activated by high concentrations of GABA (Bianchi and Macdonald, 2001). Second, H_2O_2 did not modify the desensitization or voltage sensitivity, two intrinsic properties of the $GABA_A$ receptors that alter the current amplitude. Thirdly, the peak amplitude for current evoked by saturating concentration of GABA and mIPSCs was unaffected, which is consistent with the increased potency of GABA by H_2O_2 at only low concentrations of GABA. Two possible mechanisms might underlie the increased potency at low GABA concentrations. H_2O_2 can increase the open probability of $GABA_A$ receptors that reside in a monoliganded state, as occurs at low GABA concentrations (Petrini et al., 2011). H_2O_2 may stabilize such an open state and thereby increase the tonic current. Also, H_2O_2 may enhance the spontaneous opening probability of $GABA_A$ receptors that only activates the tonic current (McCartney et al., 2007; Wlodarczyk et al., 2013). Future studies, such as single channel recording, may provide insights into the underlying mechanisms responsible for the selective increase in potency of GABA at low concentrations.

The increase in GABA potency is attributed to an extracellular oxidative reaction as the addition of extracellular antioxidants (GSH and DTT) to the perfusion solution completely abolishes H_2O_2 effects, whereas intracellular application of GSH has no effect. Such oxidation by H_2O_2 may result from the production of $^{\cdot}OH$ by the Fenton reaction (Haber and Weiss, 1934) as inhibiting the Fenton reaction abolishes the effect. This result is consistent with previous reports that show H_2O_2, via the Fenton reaction, modulates the intracellular concentration of Cl^- (Sah and Schwartz-Bloom, 1999) and synaptic potentials (Pellmar, 1995) in hippocampal slices.

The onset of H_2O_2 enhancement of tonic current is slow and irreversible and occurs within the time frame of minutes. Most positive allosteric modulators of $GABA_A$ receptors, including benzodiazepines, barbiturates, and general anesthetics, increase current within the time frame of milliseconds to seconds and are fully reversible (Twyman et al., 1989; Orser et al., 1994; Walters et al., 2000). The slow time course of H_2O_2 increase in $GABA_A$ receptor activity is similar to H_2O_2 effects on P2X2 and TRPM4 channels, which results from oxidation of cysteine residues in the ion channels themselves (Coddou et al., 2009; Simon et al., 2010). For example, H_2O_2 oxidation of Cys^{430} in P2X2 channels increases receptor activity by increasing agonist potency (Coddou et al., 2009), whereas oxidation of Cys^{1093} in TRPM4 channels abolishes receptor desensitization (Simon et al., 2010).

It is plausible that the slow onset and irreversibility of H_2O_2 effects in our study are due to oxidation of cysteine residues of $GABA_A$ receptors. H_2O_2 predominantly oxidizes cysteine residues, but can also modify methionine, tyrosine, phenylalanine, histidine, and lysine residues (Chu et al., 2006; Calero and Calvo, 2008). H_2O_2 may oxidize amino acids that are located either in the binding pocket for GABA, or in a region close to the binding domain (Boileau et al., 1999). Alternatively, H_2O_2 may oxidize $GABA_A$ receptor-associated proteins, such as the transmembrane cell adhesion molecules dystroglycan (Pribiag et al., 2014) and neuroligin 2 (Hines et al., 2012), which regulate $GABA_A$ receptor function. It is of future interest to determine whether H_2O_2 via oxidation, acts directly on $GABA_A$ receptors or indirectly on receptor-associated proteins.

Extrasynaptic $\alpha5GABA_A$ receptors and $\delta GABA_A$ receptors are not necessary for the H_2O_2 effects. However, tonic current in neurons is not generated by a single population of $GABA_A$ receptors but rather by multiple subtypes including those containing $\alpha\beta$, $\alpha1\beta\delta$, $\alpha3\beta\gamma2$, $\alpha4\delta$, $\alpha6\delta$, and $\alpha\beta\varepsilon$ subunits (Mortensen and Smart, 2006; Lee and Maguire, 2014). These different receptor subtypes could contribute to the increased current produced by H_2O_2. Therefore, the major factor that confers sensitivity to H_2O_2 is unlikely the subunit composition of the receptor *per se*, but rather receptor occupancy by the agonist. When these multiple $GABA_A$ receptors are activated by low concentrations of GABA, oxidation by H_2O_2 increases the potency of GABA, which enhances the tonic current. H_2O_2 may also selectively potentiate yet-to-be-identified subpopulations of high affinity $GABA_A$ receptors. In support of this hypothesis, the increase in tonic current by H_2O_2 varied from 3.4-fold to 9.6-fold in cultured neurons from Swiss White mice and C57BL/6 × SvJ129 mice, respectively, studied in the absence of exogenous GABA (Figs. 1*B*, Fig. 4*D*). Different strains of mice may express different combinations of $GABA_A$ receptor subtypes (Caldji et al., 2004; Schlussman et al., 2013) that exhibit different sensitivities to H_2O_2. Future studies of combination of recombinant $GABA_A$ receptors might offer insights into possible mechanisms that account for the variable effects of H_2O_2.

Interestingly, several studies have suggested that H_2O_2 decreases $GABA_A$ receptor function. High concentrations of H_2O_2 (1.5–3.5 mM) reduce the amplitude of IPSPs in hippocampal, cerebral, cortical and thalamic neurons possibly due to a reduction in transmitter increase (Pellmar, 1995; Frantseva et al., 1998). In contrast, H_2O_2 (300 μM) induces an increase in intracellular Cl^- (Sah and Schwartz-Bloom, 1999), possibly by increasing the tonic current. We found that H_2O_2 has no effect on mIPSCs recorded in hippocampal neurons. This result is consistent with a study showing that H_2O_2 (100 μM) does not modify mIPSCs in spinal cord neurons, although, higher concentration of H_2O_2 (1 mM) increases both the amplitude and the frequency of mIPSCs possibly by increasing release of GABA (Takahashi et al., 2007).

H_2O_2 upregulation of tonic current may be particularly important under conditions where the concentration of H_2O_2 and other ROS increase dramatically (Andersen, 2004; Allen and Bayraktutan, 2009; Uttara et al., 2009). During ischemia-reperfusion injury, H_2O_2 levels in the brain can reach as high as 200 μM (Hyslop et al., 1995). OGD, which produces high endogenous levels of H_2O_2 as well as ROS, also increases the tonic current. Notably, the relative increase in current after OGD is similar to that produced by concentrations of H_2O_2 of 50–200 μM (Fig. 1*C*).

In summary, to the best of our knowledge, this study provides the first evidence that H_2O_2 dramatically increases the amplitude of tonic current generated by native $GABA_A$ receptors in neurons. This novel regulatory effect may have important clinical

implications, given that perturbations in tonic inhibition has been implicated in multiple neurological disorders and age-associated cognitive deficits (Brickley and Mody, 2012; Wang et al., 2012). Suppressing the H_2O_2-enhanced tonic GABA current might represent a novel strategy for preventing and/or treating such neurological disorders.

References

Abramov AY, Canevari L, Duchen MR (2004) β-Amyloid peptides induce mitochondrial dysfunction and oxidative stress in astrocytes and death of neurons through activation of NADPH oxidase. J Neurosci 24:565–575. CrossRef Medline

Abramov AY, Scorziello A, Duchen MR (2007) Three distinct mechanisms generate oxygen free radicals in neurons and contribute to cell death during anoxia and reoxygenation. J Neurosci 27:1129–1138. CrossRef Medline

Allen CL, Bayraktutan U (2009) Oxidative stress and its role in the pathogenesis of ischaemic stroke. Int J Stroke 4:461–470. CrossRef Medline

Andersen JK (2004) Oxidative stress in neurodegeneration: cause or consequence? Nat Med 10:S18–S25. CrossRef Medline

Bianchi MT, Macdonald RL (2001) Agonist trapping by $GABA_A$ receptor channels. J Neurosci 21:9083–9091. Medline

Boileau AJ, Evers AR, Davis AF, Czajkowski C (1999) Mapping the agonist binding site of the $GABA_A$ receptor: evidence for a β-strand. J Neurosci 19:4847–4854. Medline

Brickley SG, Mody I (2012) Extrasynaptic $GABA_A$ receptors: their function in the CNS and implications for disease. Neuron 73:23–34. CrossRef Medline

Bright DP, Smart TG (2013) Methods for recording and measuring tonic $GABA_A$ receptor-mediated inhibition. Front Neural Circuits 7:193. CrossRef Medline

Brown N, Kerby J, Bonnert TP, Whiting PJ, Wafford KA (2002) Pharmacological characterization of a novel cell line expressing human $\alpha4\beta3\delta$ $GABA_A$ receptors. Br J Pharmacol 136:965–974. CrossRef Medline

Caldji C, Diorio J, Anisman H, Meaney MJ (2004) Maternal behavior regulates benzodiazepine/$GABA_A$ receptor subunit expression in brain regions associated with fear in BALB/c and C57BL/6 mice. Neuropsychopharmacology 29:1344–1352. CrossRef Medline

Calero CI, Calvo DJ (2008) Redox modulation of homomeric ρ1 GABA receptors. J Neurochem 105:2367–2374. CrossRef Medline

Caraiscos VB, Elliott EM, You-Ten KE, Cheng VY, Belelli D, Newell JG, Jackson MF, Lambert JJ, Rosahl TW, Wafford KA, MacDonald JF, Orser BA (2004) Tonic inhibition in mouse hippocampal CA1 pyramidal neurons is mediated by α5 subunit-containing γ-aminobutyric acid type A receptors. Proc Natl Acad Sci U S A 101:3662–3667. CrossRef Medline

Chang Y, Ghansah E, Chen Y, Ye J, Weiss DS (2002) Desensitization mechanism of GABA receptors revealed by single oocyte binding and receptor function. J Neurosci 22:7982–7990. Medline

Chu XP, Close N, Saugstad JA, Xiong ZG (2006) ASIC1a-specific modulation of acid-sensing ion channels in mouse cortical neurons by redox reagents. J Neurosci 26:5329–5339. CrossRef Medline

Coddou C, Codocedo JF, Li S, Lillo JG, Acuña-Castillo C, Bull P, Stojilkovic SS, Huidobro-Toro JP (2009) Reactive oxygen species potentiate the P2X2 receptor activity through intracellular Cys^{430}. J Neurosci 29:12284–12291. CrossRef Medline

Collinson N, Kuenzi FM, Jarolimek W, Maubach KA, Cothliff R, Sur C, Smith A, Otu FM, Howell O, Atack JR, McKernan RM, Seabrook GR, Dawson GR, Whiting PJ, Rosahl TW (2002) Enhanced learning and memory and altered GABAergic synaptic transmission in mice lacking the α5 subunit of the $GABA_A$ receptor. J Neurosci 22:5572–5580. Medline

Colquhoun D (1998) Binding, gating, affinity and efficacy: the interpretation of structure-activity relationships for agonists and of the effects of mutating receptors. Br J Pharmacol 125:924–947. CrossRef Medline

Connelly WM, Fyson SJ, Errington AC, McCafferty CP, Cope DW, Di Giovanni G, Crunelli V (2013) $GABA_B$ receptors regulate extrasynaptic $GABA_A$ receptors. J Neurosci 33:3780–3785. CrossRef Medline

Farrant M, Nusser Z (2005) Variations on an inhibitory theme: phasic and tonic activation of $GABA_A$ receptors. Nat Rev Neurosci 6:215–229. CrossRef Medline

Frantseva MV, Perez Velazquez JL, Carlen PL (1998) Changes in membrane and synaptic properties of thalamocortical circuitry caused by hydrogen peroxide. J Neurophysiol 80:1317–1326. Medline

Giorgio M, Trinei M, Migliaccio E, Pelicci PG (2007) Hydrogen peroxide: a metabolic by-product or a common mediator of ageing signals? Nat Rev Mol Cell Biol 8:722–728. CrossRef Medline

Glykys J, Mody I (2007) Activation of $GABA_A$ receptors: views from outside the synaptic cleft. Neuron 56:763–770. CrossRef Medline

Graham S, Ding M, Ding Y, Sours-Brothers S, Luchowski R, Gryczynski Z, Yorio T, Ma H, Ma R (2010) Canonical transient receptor potential 6 (TRPC6), a redox-regulated cation channel. J Biol Chem 285:23466–23476. CrossRef Medline

Haber F, Weiss J (1934) The catalytic decomposition of hydrogen peroxide by iron salts. Proc R Soc Lond A 147:332–351. CrossRef

Hines RM, Davies PA, Moss SJ, Maguire J (2012) Functional regulation of $GABA_A$ receptors in nervous system pathologies. Curr Opin Neurobiol 22:552–558. CrossRef Medline

Hyslop PA, Zhang Z, Pearson DV, Phebus LA (1995) Measurement of striatal H_2O_2 by microdialysis following global forebrain ischemia and reperfusion in the rat: correlation with the cytotoxic potential of H_2O_2 *in vitro*. Brain Res 671:181–186. CrossRef Medline

Inoue M, Oomura Y, Yakushiji T, Akaike N (1986) Intracellular calcium ions decrease the affinity of the GABA receptor. Nature 324:156–158. CrossRef Medline

Kamsler A, Segal M (2003) Hydrogen peroxide modulation of synaptic plasticity. J Neurosci 23:269–276. Medline

Kaneko S, Kawakami S, Hara Y, Wakamori M, Itoh E, Minami T, Takada Y, Kume T, Katsuki H, Mori Y, Akaike A (2006) A critical role of TRPM2 in neuronal cell death by hydrogen peroxide. J Pharmacol Sci 101:66–76. CrossRef Medline

Lee V, Maguire J (2014) The impact of tonic $GABA_A$ receptor-mediated inhibition on neuronal excitability varies across brain region and cell type. Front Neural Circuits 8:3. CrossRef Medline

Legendre P, Ali DW, Drapeau P (2000) Recovery from open channel block by acetylcholine during neuromuscular transmission in zebrafish. J Neurosci 20:140–148. Medline

Martina M, Kilić G, Cherubini E (1994) The effect of intracellular Ca^{2+} on GABA-activated currents in cerebellar granule cells in culture. J Membr Biol 142:209–216. CrossRef Medline

McCartney MR, Deeb TZ, Henderson TN, Hales TG (2007) Tonically active $GABA_A$ receptors in hippocampal pyramidal neurons exhibit constitutive GABA-independent gating. Mol Pharmacol 71:539–548. CrossRef Medline

Mihalek RM, Banerjee PK, Korpi ER, Quinlan JJ, Firestone LL, Mi ZP, Lagenaur C, Tretter V, Sieghart W, Anagnostaras SG, Sage JR, Fanselow MS, Guidotti A, Spigelman I, Li Z, DeLorey TM, Olsen RW, Homanics GE (1999) Attenuated sensitivity to neuroactive steroids in γ-aminobutyrate type A receptor δ subunit knockout mice. Proc Natl Acad Sci U S A 96:12905–12910. CrossRef Medline

Mortensen M, Smart TG (2006) Extrasynaptic αβ subunit $GABA_A$ receptors on rat hippocampal pyramidal neurons. J Physiol 577:841–856. CrossRef Medline

Ohsawa I, Ishikawa M, Takahashi K, Watanabe M, Nishimaki K, Yamagata K, Katsura K, Katayama Y, Asoh S, Ohta S (2007) Hydrogen acts as a therapeutic antioxidant by selectively reducing cytotoxic oxygen radicals. Nat Med 13:688–694. CrossRef Medline

Orser BA, Wang LY, Pennefather PS, MacDonald JF (1994) Propofol modulates activation and desensitization of $GABA_A$ receptors in cultured murine hippocampal neurons. J Neurosci 14:7747–7760. Medline

Pavlov I, Savtchenko LP, Kullmann DM, Semyanov A, Walker MC (2009) Outwardly rectifying tonically active $GABA_A$ receptors in pyramidal cells modulate neuronal offset, not gain. J Neurosci 29:15341–15350. CrossRef Medline

Pellmar TC (1995) Use of brain slices in the study of free-radical actions. J Neurosci Methods 59:93–98. CrossRef Medline

Petrini EM, Nieus T, Ravasenga T, Succol F, Guazzi S, Benfenati F, Barberis A (2011) Influence of $GABA_AR$ monoliganded states on GABAergic responses. J Neurosci 31:1752–1761. CrossRef Medline

Pribiag H, Peng H, Shah WA, Stellwagen D, Carbonetto S (2014) Dystroglycan mediates homeostatic synaptic plasticity at GABAergic synapses. Proc Natl Acad Sci U S A 111:6810–6815. CrossRef Medline

Quirk K, Blurton P, Fletcher S, Leeson P, Tang F, Mellilo D, Ragan CI, McKernan RM (1996) [^{3}H]L-655,708, a novel ligand selective for the benzodiazepine site of $GABA_A$ receptors which contain the α5 subunit. Neuropharmacology 35:1331–1335. CrossRef Medline

Rice ME (2011) H_2O_2: a dynamic neuromodulator. Neuroscientist 17:389–406. CrossRef Medline

Riquelme D, Alvarez A, Leal N, Adasme T, Espinoza I, Valdés JA, Troncoso N, Hartel S, Hidalgo J, Hidalgo C, Carrasco MA (2011) High-frequency field stimulation of primary neurons enhances ryanodine receptor-mediated Ca^{2+} release and generates hydrogen peroxide, which jointly stimulate NF-κB activity. Antioxid Redox Signal 14:1245–1259. CrossRef Medline

Sah R, Schwartz-Bloom RD (1999) Optical imaging reveals elevated intracellular chloride in hippocampal pyramidal neurons after oxidative stress. J Neurosci 19:9209–9217. Medline

Saxena NC, Macdonald RL (1994) Assembly of $GABA_A$ receptor subunits: role of the δ subunit. J Neurosci 14:7077–7086. Medline

Schlussman SD, Buonora M, Brownstein AJ, Zhang Y, Ho A, Kreek MJ (2013) Regional mRNA expression of GABAergic receptor subunits in brains of C57BL/6J and 129P3/J mice: strain and heroin effects. Brain Res 1523:49–58. CrossRef Medline

Schraufstatter IU, Hyslop PA, Hinshaw DB, Spragg RG, Sklar LA, Cochrane CG (1986) Hydrogen peroxide-induced injury of cells and its prevention by inhibitors of poly(ADP-ribose) polymerase. Proc Natl Acad Sci U S A 83:4908–4912. CrossRef Medline

Simon F, Leiva-Salcedo E, Armisén R, Riveros A, Cerda O, Varela D, Eguiguren AL, Olivero P, Stutzin A (2010) Hydrogen peroxide removes TRPM4 current desensitization conferring increased vulnerability to necrotic cell death. J Biol Chem 285:37150–37158. CrossRef Medline

Smart TG, Xie X, Krishek BJ (1994) Modulation of inhibitory and excitatory amino acid receptor ion channels by zinc. Prog Neurobiol 42:393–441. CrossRef Medline

Smith MA, Herson PS, Lee K, Pinnock RD, Ashford ML (2003) Hydrogen-peroxide-induced toxicity of rat striatal neurones involves activation of a non-selective cation channel. J Physiol 547:417–425. CrossRef Medline

Takahashi A, Mikami M, Yang J (2007) Hydrogen peroxide increases GABAergic mIPSC through presynaptic release of calcium from IP3 receptor-sensitive stores in spinal cord substantia gelatinosa neurons. Eur J Neurosci 25:705–716. CrossRef Medline

Tao W, Higgs MH, Spain WJ, Ransom CB (2013) Postsynaptic $GABA_B$ receptors enhance extrasynaptic $GABA_A$ receptor function in dentate gyrus granule cells. J Neurosci 33:3738–3743. CrossRef Medline

Twyman RE, Rogers CJ, Macdonald RL (1989) Differential regulation of γ-aminobutyric acid receptor channels by diazepam and phenobarbital. Ann Neurol 25:213–220. CrossRef Medline

Uttara B, Singh AV, Zamboni P, Mahajan RT (2009) Oxidative stress and neurodegenerative diseases: a review of upstream and downstream antioxidant therapeutic options. Curr Neuropharmacol 7:65–74. CrossRef Medline

Walters RJ, Hadley SH, Morris KD, Amin J (2000) Benzodiazepines act on $GABA_A$ receptors via two distinct and separable mechanisms. Nat Neurosci 3:1274–1281. CrossRef Medline

Wang DS, Zurek AA, Lecker I, Yu J, Abramian AM, Avramescu S, Davies PA, Moss SJ, Lu WY, Orser BA (2012) Memory deficits induced by inflammation are regulated by α5-subunit-containing $GABA_A$ receptors. Cell Rep 2:488–496. CrossRef Medline

Wlodarczyk AI, Sylantyev S, Herd MB, Kersanté F, Lambert JJ, Rusakov DA, Linthorst AC, Semyanov A, Belelli D, Pavlov I, Walker MC (2013) GABA-independent $GABA_A$ receptor openings maintain tonic currents. J Neurosci 33:3905–3914. CrossRef Medline

Cellular/Molecular

α6-Containing GABA$_A$ Receptors Are the Principal Mediators of Inhibitory Synapse Strengthening by Insulin in Cerebellar Granule Cells

Michael V. Accardi,[1,2] Patricia M.G.E. Brown,[1,3] Loïs S. Miraucourt,[1] Beverley A. Orser,[4] and Derek Bowie[1]

[1]Department of Pharmacology and Therapeutics, [2]Graduate Program in Pharmacology, and [3]Integrated Program in Neuroscience, McGill University, Montréal, Québec H3A 2B4, Canada, and [4]Department of Physiology, University of Toronto, Toronto, Ontario M5S 1A8, Canada

Activity-dependent strengthening of central synapses is a key factor driving neuronal circuit behavior in the vertebrate CNS. At fast inhibitory synapses, strengthening is thought to occur by increasing the number of GABA$_A$ receptors (GABARs) of the same subunit composition to preexisting synapses. Here, we show that strengthening of mouse cerebellar granule cell GABAergic synapses occurs by a different mechanism. Specifically, we show that the neuropeptide hormone, insulin, strengthens inhibitory synapses by recruiting α6-containing GABARs rather than accumulating more α1-containing receptors that are resident to the synapse. Because α6-receptors are targeted to functionally distinct postsynaptic sites from α1-receptors, we conclude that only a subset of all inhibitory synapses are strengthened. Together with our recent findings on stellate cells, we propose a general mechanism by which mature inhibitory synapses are strengthened. In this scenario, α1-GABARs resident to inhibitory synapses form the hardwiring of neuronal circuits with receptors of a different composition fulfilling a fundamental, but unappreciated, role in synapse strengthening.

Key words: **inhibition; insulin; metabolism; mitochondria; plasticity mechanism; reactive oxygen species**

Introduction

Fast inhibitory transmission in the adult vertebrate CNS is primarily mediated by a family of ligand-gated ion-channels called GABA$_A$ receptors (GABARs) that stabilize the membrane potential by transporting chloride and bicarbonate ions (Belelli et al., 2009; Miller and Smart, 2010; Rudolph and Knoflach, 2011). GABARs assemble as a pentameric anion channel most commonly composed of 2 α (α1–6) and 2 β (β1–3) subunits with an additional subunit, typically a γ (γ1–3) subunit that may be replaced with a δ, ε, or θ subunit (Barnard et al., 1998; Moss and Smart, 2001; Rudolph et al., 2001). This richness in subunit diversity is a central factor in determining many aspects of GABAR signaling. For example, switches in subunit composition are commonly observed during neuronal development fulfilling roles in differentiation and maturation (Fritschy and Panzanelli, 2006). In cerebellar granule and stellate cells, there is a developmental change in the kinetics of synaptic events with slower rates ($\tau_{(fast)}$, 9–19 ms) observed in migrating P7-P11 neurons (Tia et al., 1996; Vicini et al., 2001) that express α1-α3 and α6 subunits (Laurie et al., 1992a, b), respectively. In adult P20-P35 neurons, however, synaptic events become faster ($\tau_{(fast)}$, 6–7 ms) (Tia et al., 1996; Vicini et al., 2001) due to the dominant expression of α1-containing GABARs (Somogyi et al., 1996; Vicini et al., 2001). Despite the prevalence of α1-receptors in adult synapses, stellate and granule neurons continue to express α2/3- and α6-containing receptors, respectively (Laurie et al., 1992a, b; Persohn et al., 1992; Tia et al., 1996; Vicini et al., 2001) whose role, if any, in signaling at the synapse is unclear.

Although numerous effector molecules strengthen inhibitory synapses, each is thought to change synaptic efficacy by increasing the number of GABARs per synapse (e.g., Otis et al., 1994; Nusser et al., 1997). It is generally assumed that inhibitory synapses are strengthened by the recruitment of GABARs of the same composition, more often than not, due to α1-containing receptors given their predominance in the adult CNS (Luscher et al., 2011; Rudolph and Knoflach, 2011). However, recent work from our laboratory has revealed that mitochondrial-derived reactive oxygen species (mROS) strengthen inhibitory synapses of cerebellar stellate cells by a mechanism distinct in two important ways. First, synapse strengthening is mediated by the recruitment of α3-containing receptors and not resident α1-receptors (Accardi et al., 2014). Second, α3-receptors are targeted to functionally separate postsynaptic sites from α1-receptors (Accardi et al., 2014), implying that not all synapses are strengthened by mROS. Whether this novel mechanism is unique to stellate cells or more

Received Feb. 5, 2015; revised May 4, 2015; accepted May 28, 2015.

Author contributions: M.V.A., P.M.G.E.B., L.S.M., B.A.O., and D.B. designed research; M.V.A., P.M.G.E.B., and L.S.M. performed research; M.V.A., P.M.G.E.B., L.S.M., and D.B. analyzed data; M.V.A., P.M.G.E.B., L.S.M., and D.B. wrote the paper.

This work was supported by Canadian Institutes of Health Research Operating Grants FRN:82804 to D.B. and MOP:416838 and MOP:480143 to B.A.O., M.V.A. was supported by a studentship from the Savoy Foundation. P.M.G.E.B. was supported by a doctoral fellowship from Fonds de la Recherche en Santé du Québec. D.B. and B.A.O. are the recipients of a Canada Research Chair award. We thank members of the D.B. laboratory, especially Dr. Bryan Daniels and Brent Dawe, for discussions and comments on the manuscript.

The authors declare no competing financial interests.

Correspondence should be addressed to Dr. Derek Bowie, Department of Pharmacology and Therapeutics, Bellini Building, Room 164, McGill University, 3649 Promenade Sir William Osler, Montreal, Quebec H3G 0B1, Canada. E-mail: derek.bowie@mcgill.ca.

DOI:10.1523/JNEUROSCI.0513-15.2015

 0270-6474/15/359676-13$15.00/0

commonly used throughout the CNS remains to be investigated. On that note, recruitment of α3-containing GABARs causes a slowing in decay kinetics of synaptic events (Accardi et al., 2014), an observation not observed in other studies (Otis et al., 1994; Luscher et al., 2011). This distinction raises the possibility that mROS have a unique effect on stellate cell inhibitory synapses that is not found elsewhere.

To address this issue directly, we have studied the mechanism by which ROS strengthen inhibitory synapses of cerebellar granule cells: the most abundant neuron in the vertebrate brain (Llinás, 1969). ROS was elevated by perfusing the mitochondrial uncoupler, antimycin-A, via the patch electrode or by bath application of the metabolic hormone, insulin. Like in stellate cells, ROS augment inhibitory synaptic transmission of granule cells by recruiting receptors of a different subunit composition, in this case, α6-containing GABARs, to postsynaptic sites that are distinct from resident α1-receptors. Unlike in stellate cells, however, synapse strengthening is not accompanied by a slowing of synaptic events. Together, we conclude that α1-containing GABARs form the hardwiring of inhibitory synapses of stellate and granule cells with α3- or α6-containing GABARs fulfilling a fundamental but unexpected role as the principal mediators of GABAergic synapse strengthening.

Materials and Methods

Animals. Breeder pairs for homozygous GABAR δ-knock-out (*Gabrd*$^{-/-}$; δ-KO) mice were generously provided by Dr. Gregg Homanics (University of Pittsburgh) and bred at the University of Toronto for experimentation. δ-KO mice were generated using a background of C57BL/6 × Sv129Ev mice as described previously (Mihalek et al., 1999). Wild-type mice were maintained on a C57BL/6J background (Charles River Laboratories) and maintained as a breeding colony at both McGill University (Montreal, Quebec, Canada) and University of Toronto (Toronto, Ontario, Canada). All KO animals were genotyped by PCR analysis of tail biopsies. Mice (Wild-type and δ-KO: male and female) used for the experiments ranged from postnatal day 15 to 28 (P15-P28; mean ± SEM age: P21 ± 1, $n = 51$). All experiments have been approved by the local authorities, were performed in accordance with the guidelines of the Canadian Council on Animal Care, and were approved by the Animal Care Committee of McGill University and University of Toronto.

Cerebellum slice preparation. Mice were anesthetized with isoflurane and immediately decapitated. The cerebellum was rapidly removed from the whole brain while submerged in oxygenated (95% O_2, 5% CO_2) ice-cold cutting solution, which contained (in mM) as follows: 235 sucrose, 2.5 KCl, 1.25 NaH_2PO_4, 28 $NaHCO_3$, 0.5 $CaCl_2$, 7 $MgSO_4$, 28 D-glucose (pH 7.4; 305–315 mOsmol/L). The tissue was maintained in ice-cold solution while sagittal slices of cerebellar vermis (300 μm) were cut using a vibrating tissue slicer (Leica VT100S, Leica Instruments). The slices were transferred to oxygenated aCSF and held at room temperature (20°C-23°C) for at least 1 h before recordings were performed. aCSF contained the following (in mM): 125 NaCl, 2.5 KCl, 1.25 NaH_2PO_4, 26 $NaHCO_3$, 2 $CaCl_2$, 1 $MgSO_4$, 25 D-glucose (pH of 7.4; 305–315 mOsmol/L).

Electrophysiology. Slice experiments were performed on an Olympus BX51 upright microscope (Olympus) equipped with differential interference contrast/infrared optics. Whole-cell patch-clamp recordings were performed on granule cells located in the granule cell layer, which were visually identified based on cell body size and were confirmed *post hoc* by imaging with Lucifer yellow. Patch pipettes were prepared from thick-walled borosilicate glass (GC150F-10, OD 1.5 mm, ID 0.86 mm; Harvard Apparatus) and had open tip resistances of 6–12 MΩ when filled with an intracellular solution that contained (in mM) as follows: 140 CsCl, 4 NaCl, 0.5 $CaCl_2$, 10 HEPES, 5 EGTA, 2 Mg-ATP, and 2 QX314 to block voltage-activated Na^+ channels with 0.5 mg/ml Lucifer yellow as a *post hoc* dye indicator (pH 7.4 with CsOH, 300–310 mOsmol/L). Recordings were made with a Multiclamp 700A amplifier (Molecular Devices) in voltage-clamp mode with a holding potential of −60 mV. Series resistance and whole-cell capacitance were estimated by cancelling the fast current transients evoked at the onset and offset of brief (10–20 ms) 5 mV voltage-command steps. Series resistance during whole-cell recording (10–35 MΩ) was compensated between 40% and 65% and checked for stability throughout the experiments (>20% tolerance). The capacitance of the granule cells was in the range of 1.5–4 pF. The bath was continuously perfused at room temperature (22°C–23°C) with aCSF at a rate of 1–2 ml/min. Miniature IPSCs (mIPSCs) were recorded in the presence of TTX (1 μM). Currents were filtered at 5 kHz with an eight-pole low-pass Bessel filter (Frequency Devices) and digitized at 25 kHz with a Digidata 1322A data acquisition board and Clampex9 (Molecular Devices) software. Data acquisition was performed using pClamp9 and pClamp10 software (Molecular Devices). Curve fitting and figure preparation of all electrophysiology data were performed with Origin 7.0 (OriginLab), Microsoft Excel, Clampfit 10 (Molecular Devices), and the Strathclyde Electrophysiology WinWCP and WinEDR (John Dempster) software.

mIPSCs from granule cells occur too infrequently to permit a proper characterization of their response characteristics in terms of event amplitude and decay times (Wall and Usowicz, 1997). In view of this, we performed all experiments in aCSF with elevated extracellular K^+ (18 mM), as described by others (Momiyama and Takahashi, 1994), which significantly increased baseline frequency approximately eightfold from 0.07 ± 0.01 Hz (aCSF, 2.5 mM KCl, $n = 5$) to 0.54 ± 0.01 Hz (aCSF, 18 mM KCl, $n = 5$; $p = 0.0001$, unpaired Student's t test). Other than the change in mIPSC frequency, all other characteristics (i.e., distribution of rise times, amplitudes, and decay kinetics) were indistinguishable between experiments in 2.5 and 18 mM K^+ aCSF solutions. This was also true with mice exposed to the internal perfusion of antimycin-A (aCSF, 2.5 mM KCl, $n = 6$: 0.13 ± 0.03 Hz; aCSF, 18 mM KCl, $n = 4$: 1.04 ± 0.25; $p = 0.002$, unpaired Student's t test) as well as δ-KO animals (aCSF, 2.5 mM KCl, $n = 6$: 0.13 ± 0.04 Hz; aCSF, 18 mM KCl, $n = 5$: 1.7 ± 0.2; $p = 0.0001$, unpaired Student's t test). Consequently, we concluded that the use of an elevated extracellular K^+ aCSF solution was a useful tool for increasing mIPSC frequency. aCSF (18 mM K^+) was only used as an external bathing solution during electrophysiological recordings and not during the recovery period before experimentation. To account for the increase in osmotic pressure with aCSF (18 mM K^+), sucrose was added to the internal pipette solution to achieve isomolarity (330 mOsmol/L).

Experiments were also performed at room temperature on recombinant GABARs 24–48 h after cDNA transfection. GABA (Sigma-Aldrich) was dissolved in external solution containing the following (in mM): 150 NaCl, 5 HEPES, 2 $MgCl_2$, and 1 $CaCl_2$. Internal pipette solution contained the following (in mM): 150 KCl, 5 EGTA, 1 $MgCl_2$, and 2 Mg-ATP. The pH and osmotic pressure of internal and external solutions were adjusted to 7.3–7.4 and 300 $mOsm1^{-1}$, respectively. Furosemide was dissolved as a 100 mM stock in DMSO, stored at −20°C, and diluted to a final concentration of 100 μM in external solutions. The control external solution also contained an equal amount of DMSO (0.1% v/v). Control and agonist solutions were rapidly applied to outside-out patches excised from transfected HEK 239T/17 cells using a piezoelectric stack (Physik Instrumente). Solution exchange (10%–90% rise-time = 150–250 μs) was determined in a separate experiment by measuring the liquid junction current (or exchange current) between the control and external solution containing 10% additional NaCl. All recordings were performed with an Axopatch 200B amplifier (Molecular Devices) using thin-walled borosilicate glass pipettes (2–5 MΩ) coated with dental wax to reduce electrical noise. Current records were filtered at 5 kHz, digitized at 25 kHz, and series resistances (3–10 MΩ) were compensated by 95%. All recordings were performed at a holding potential of −60 mV.

Analysis of mIPSC events. mIPSCs were detected using WinEDR software with a detection threshold of 4 × the mean square root of noise level. The accuracy of detection was visually confirmed for each event in each recording. Amplitude distributions were fit with the sum of 2–3 Gaussian functions with the singular form of the following: $y = (A1/(w1 * \mathrm{sqrt}(\pi/2))) * \exp(-2 * ((x - xc1)/w1)^2)$, where A is the area, xc is the center of the peak, and w is the error associated with the peak. The decay phase of mIPSCs was fit with a single exponential curve, and both rise and

decay phases were fitted between 10% and 90% of the peak amplitude. Data are expressed as mean ± SEM. p values represent the results obtained from either a paired or unpaired, two-tailed Student's t tests or a one-way ANOVA with Tukey's *post hoc* test. A p value of <0.05 was considered statistically significant. All data are from at least two different animals.

Intracellular ROS fluorescence. Slices for imaging experiments were incubated in oxygenated aCSF containing CM-H_2DCF-DA (5 μM DCF, Invitrogen) 45 min before imaging cytosolic ROS levels using a Zeiss Axioexaminer upright microscope (Carl Zeiss) equipped with a multiphoton chameleon (coherent) laser source set to excite at 780 nm (power = 0.3 W/cm^2). To visualize changes in DCF fluorescence intensity, XYZT series images of the cerebellar granule cell layer were acquired every 2 min using a 40× plan apochromatic objective (NA = 1.0). After baseline imaging (10 min), another 30 min of imaging followed, during which various drugs (insulin, 0.5 μM and/or genistein, 50 μM) were applied through the constant flow of oxygenated aCSF (1.5 ml/min). Slices during genistein treatment were incubated for ~45 min in aCSF + genistein (together with DCF) before the start of the 10 min baseline imaging. Images were acquired on an IBM-compatible computer using Zen software (Carl Zeiss) and subsequently analyzed using NIH Image/ImageJ.

Fluorescence image analysis. To analyze the change in fluorescence intensity, one or two focal planes of respective matching depth (z-axis) in every *XYZ* stacks were selected. Twenty ROIs were drawn per focal plane, to each surround individual granule cell soma (minimal *XY* drift was corrected using the ImageJ registration plugin). Raw measurements of all ROIs (mean pixel intensity) were used to perform Gaussian distributions of fluorescence intensity among the different groups ($n = 3$ slices for control; $n = 4$ slices for insulin; $n = 4$ slices for insulin + genistein). To compare the change of fluorescence intensity over time among groups, the Δfluorescence of each ROI ($\Delta F = F_t - F_0$, where F_0 is the mean ROI fluorescence during the first 10 min of the experiment) was determined. This analysis was restricted to granule cells (or ROIs) for which F_t did not vary >10% of F_0 during the first 10 min, to ensure a stable baseline before insulin application.

Pharmacological compounds. Ionotropic glutamate receptor antagonists, D-APV (for NMDARs; 10 μM) and CNQX (for non-NMDARs; 5 μM), the glycine receptor antagonist, strychnine (0.3 μM) and the GABAR antagonist bicuculline (10 μM) were purchased from Tocris Bioscience. TTX (1 μM) was purchased from Alomone Labs). Stock solutions of these antagonists were prepared in water and were stored at −20°C, and working solutions were diluted with aCSF shortly before application to the bath. The antioxidant, *N*-acetylcysteine (NAC, 1 mM) (Sigma) was prepared as a stock solution (100 mM) in water and dissolved in patch electrode solution on the day of the experiment. The mitochondrial uncoupler, antimycin-A (2 μM), was purchased from Sigma, dissolved in DMSO, and diluted in water to workable stock concentrations and stored at −20°C. The final maximum external DMSO concentration (0.1% v/v) had no effect on mIPSCs, consistent with other studies (Nakahiro et al., 1992). Mg-ATP (2 mM) was included in our patch electrode solution to maintain cytoplasmic ATP levels. Furosemide (100 μM; Tocris Bioscience) was dissolved in DMSO, stored at −20°C, and added directly into the aCSF on the day of the recordings. Although not significant ($p = 0.27$, paired Student's t test), furosemide application produced a small increase in mIPSC frequency of ~29% (22.5 min; see Fig. 4*D*, $n = 5$) immediately following the introduction of furosemide to the bath, an effect also observed by others (Mark Farrant, personal communication). Nevertheless, this change in mIPSC frequency was not sustained and returned to basal levels within 5–10 min. Insulin (0.5 μM, Sigma) was prepared from a 163 μM stock that required 0.1 M acetic acid to ensure complete dissolution. The concentration of insulin used is consistent with previous studies and also corresponds to circulating hormone levels (Wozniak et al., 1993; Wan et al., 1997). Genistein (50 μM; Tocris Bioscience), the protein tyrosine kinase and insulin receptor antagonist, was completely dissolved in DMSO and stored at −20°C at a final concentration of 50 mM. The phosphatidylinositol 3-kinase (PI3-kinase) inhibitor, wortmannin (1 μM; Tocris Bioscience), was dissolved in DMSO, diluted in water to a stock concentration of 500 μM, and stored at −20°C. The final maximum internal pipette DMSO concentration was <0.1% v/v.

Results

Mitochondrial ROS strengthens GABAergic synapses of cerebellar granule cells

To study the mechanism that strengthens GABAergic synapses, whole-cell recordings of mouse cerebellar granule cells were performed with an internal pipette solution containing the mitochondrial uncoupler, antimycin-A (2 μM, Fig. 1). Prior work from our laboratory on cerebellar stellate cells has established that antimycin-A and other uncouplers strengthen GABAergic transmission by elevating mROS (Accardi et al., 2014). We reasoned that they would have a similar effect on granule cells. In agreement with this, internal patch perfusion with antimycin-A elicited an increase in the frequency of inhibitory synaptic events by almost 1.5-fold during a typical 20–25 min recording (0–5 min, 0.74 ± 0.33 Hz; 20–25 min, 1.04 ± 0.25 Hz; $n = 4$, $p = 0.036$, paired two-tailed Student's t test; Fig. 1*A–C*), an observation absent from control recordings (Fig. 1*D*). Gaussian fits of the amplitude distributions revealed that antimycin-A selectively increased the occurrence of only mIPSCs of small amplitude with little effect on larger-amplitude events (Fig. 1*A*,*B*). For example, fits of the smallest events were 28% of all events within 0–5 min (Fig. 1*A*, bottom), which increased 1.5-fold, to 41%, after 20–25 min (Fig. 1*B*, bottom). As a consequence, we observed a small time-dependent reduction in the averaged amplitude of mIPSCs (e.g., 0–5 min, −38.3 ± 6.0 pA; 20–25 min, −31.2 ± 2.8 pA; 17% reduction; Fig. 1*C*,*D*), similar to our observations on stellate cells (Accardi et al., 2014). The increase in mIPSC frequency is due to an elevation in cytosolic mROS because the effect of antimycin-A was attenuated by inclusion of the antioxidant, NAC (1 mM, $n = 4$), in the patch electrode solution ($p < 0.01$, one-way ANOVA; Fig. 1*D*). Interestingly, we also observed an effect of antimycin-A on tonic GABA current baseline (25 min after seal breakthrough, Control, $n = 5$, 20.46 ± 4.7 pA; Antimycin-A, $n = 6$, 3.46 ± 0.93 pA; $p = 0.004$; unpaired Student's t test), suggesting that mROS also affect extrasynaptic receptors. These observations are similar to our earlier findings on cerebellar stellate cells suggesting that mROS are a common intermediary that couple cellular metabolism to the processes that strengthen GABAergic signaling.

mROS may strengthen GABAergic transmission by a presynaptic and/or postsynaptic mechanism. In stellate cells, the effect of mROS is abolished in mice lacking the α3 GABAR subunit (Accardi et al., 2014), which is primarily located in the perisynaptic and/or extrasynaptic space (Fritschy and Panzanelli, 2006). As a result, we concluded that mROS strengthen inhibitory transmission primarily by a postsynaptic mechanism via the recruitment of α3-containing GABARs into the synapse (Accardi et al., 2014). A similar mechanism may be at play in granule cells because mROS selectively augment the occurrence of inhibitory events of small amplitude (Fig. 1*A*,*B*) in a similar manner previously reported in stellate cells. Granule cells, however, do not express α3 subunits and thus may strengthen inhibitory transmission by recruiting any one of several GABARs. Adult granule cells express GABARs composed of α1/β2,3/γ2, α6/β2,3/γ2, and/or α1,6/β2,3/γ2 at their synapses, whereas α6/β2,3/γ2, α1,6/β2,3/γ2, and α6/β2,3/δ GABARs are found outside the synapse (Nusser et al., 1995, 1996, 1998a; Mapelli et al., 2014). Because only γ2-containing receptors are capable of entering synapses (Luscher et al., 2011), we concluded mROS do not mediate their effects by recruiting α6/β2,3/δ receptors. In agreement with this, bath application of Zn^{2+} (10 μM) elicited no noticeable reduc-

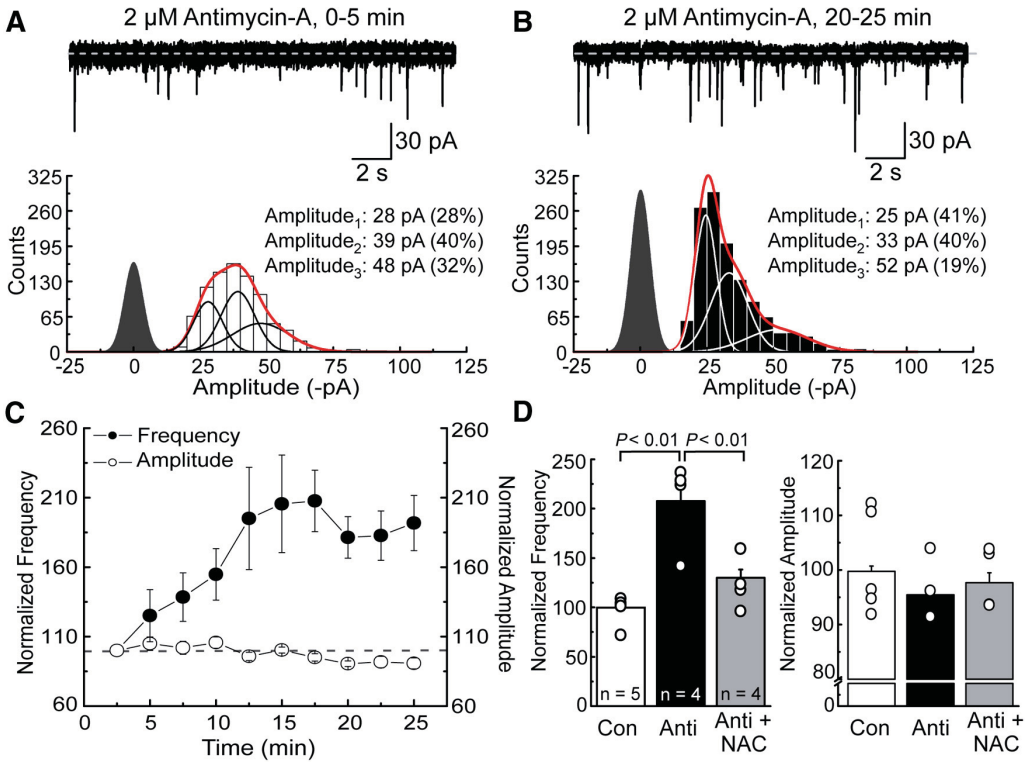

Figure 1. mROS selectively increase the occurrence of inhibitory events of small amplitude. ***A***, ***B***, Top, mIPSCs from the same granule cell (cell #140307000) at the beginning (0–5 min) and during (20–25 min) pipette perfusion with antimycin-A (2 μM). Bottom, Amplitude histograms comparing the data obtained at two time periods (i.e., 0–5 min, left; 20–25 min, right, $n = 4$). Each was fit with the sum of three Gaussian functions (red line), with individual functions shown in either black (left panel) or white (right panel). In this figure and elsewhere, the closed point distribution (filled; dark gray) was scaled to the fitted peak of the lowest event amplitude and represents the average baseline noise observed during the recordings. ***C***, Summary plot of the time course of mIPSC frequency (filled circle) and amplitude (open circle) during pipette perfusion with antimycin-A. Data are mean ± SEM. ***D***, Bar graphs of maximal normalized frequency (left) and amplitude (right) obtained in the different recording conditions. Anti, antimycin-A; NAC, *N*-acetylcysteine (1 mM). Statistical test was a one-way ANOVA with Tukey's *post hoc* test. The frequency comparison of "Control" versus "Anti + NAC" (***D***; left) was not significant and, for clarity, was not indicated in the figure. Amplitude comparisons were not significant ($p = 0.58$; one-way ANOVA).

tion on mIPSC amplitude (normalized: without Zn^{2+}, $n = 4$, 20–25 min: 90.7 ± 4.0%; with Zn^{2+}, $n = 5$, 20–25 min: 100.6 ± 6.4%; $p = 0.26$; unpaired Student's *t* test) or frequency (normalized: without Zn^{2+}, $n = 4$, 20–25 min: 207.65 ± 22.1%; with Zn^{2+}, $n = 5$, 20–25 min: 201.96 ± 15.7%; $p = 0.84$; unpaired Student's *t* test) induced by antimycin-A. Because Zn^{2+} blocks GABARs that do not contain the γ2 subunit (May and de Haën, 1979; Draguhn et al., 1990), we concluded that the effect of mROS on mIPSC frequency was not mediated through the recruitment of extrasynaptic δ-containing GABARs.

To explore the potential involvement of α1- and/or α6-containing GABARs, we looked for ways to discriminate between them at GABAergic synapses. Pharmacological studies on native and recombinant GABARs have reported that furosemide will selectively block α6-containing receptors (Korpi et al., 1995; Tia et al., 1996; Minier and Sigel, 2004). To confirm this, we first examined the degree of furosemide block on recombinant GABARs containing either α1 or α6 subunits where subunit composition would be known (Fig. 2; Table 1). Next, we determined the degree of furosemide block of native GABARs where the contribution of α6-containing GABARs is not known (Fig. 2*A*, right). Accordingly, we reasoned that a greater degree of block of mIPSCs would correspond to a greater presence of α6-containing receptors at GABAergic synapses.

As reported previously (Tia et al., 1996), 100 μM furosemide had almost no effect on the peak response amplitude or deactivation kinetics of α1-containing GABARs (Fig. 2*A*,*B*; Table 1). In contrast, however, furosemide reduced the peak response amplitude and affected deactivation kinetics of α6-containing GABARs (Fig. 2*A*; Table 1). Given these two effects, the charge transfer mediated by α6-containing GABARs was significantly reduced to 46 ± 9% ($n = 5$, $p = 0.009$, paired Student's *t* test) of the control in the presence of furosemide (100 μM; Fig. 2*B*; Table 1), demonstrating that furosemide is an ideal pharmacological agent to discriminate between the contribution of α1- or α6-containing GABARs. Interestingly, bath application of furosemide (100 μM) produced a modest effect on peak mIPSC amplitudes ($Peak_{before}$, − 43 ± 2.2 pA; $Peak_{after}$, − 34 ± 2.3 pA, $p = 0.03$, paired Student's *t* test) that was not statistically significant for charge transfer (Fig. 2*A*,*B*; $p = 0.10$, paired Student's *t* test), underscoring the minimal contribution of α6-containing GABARs under control conditions. Furthermore, a comparison of mIPSC decay kinetics revealed the time-dependent occurrence of some synaptic events with slower decay kinetics (i.e., ≥20 ms) during antimycin-A treatment (Fig. 2*C*, filled symbol). Although these slower events were too few in number to affect the overall decay kinetics of mIPSCs from granule cells (Fig. 2*A*, right), it is consistent with the possibility that mROS recruit α6-containing

GABARs, which have slower gating behavior (Fig. 2*A*, middle; Table 1).

In summary, these data highlight that α1- and α6-containing receptors can be distinguished by their sensitivity to block by furosemide. We therefore reasoned that, if mROS strengthen GABAergic synapses by the recruitment of α6-containing receptors, furosemide should block or attenuate the effect of antimycin-A on mIPSC frequency.

Pharmacological block of α6-containing GABARs abolishes synapse strengthening

To test this possibility, cerebellar slices were bathed in furosemide (100 μM) before and during whole-cell recordings from granule cells with internal perfusion of antimycin-A (Fig. 3). As expected, preincubation with furosemide had a modest effect on mIPSC baseline frequency and amplitude (Fig. 2*A*,*B*), consistent with our assertion that granule cell inhibitory synapses contain a small proportion of α6-containing GABARs. For example, baseline mIPSC frequency in slices before and after furosemide application were 0.96 ± 0.22 Hz and 0.87 ± 0.18 Hz (p = 0.46; paired Student's t test; n = 6), respectively. Interestingly, internal perfusion with antimycin-A had no detectable effect on mIPSC frequency (0–5 min, 1.08 ± 0.28 Hz; 20–25 min, 1.15 ± 0.088 Hz; p = 0.78; paired Student's t test, n = 6) (Fig. 3*A*–*D*) in marked contrast to its effects on naive slices (Fig. 1*C*,*D*). Moreover, fits of mIPSC amplitude distributions revealed that antimycin-A did not elicit a time-dependent increase in the occurrence of mIPSCs of events with small amplitude (Fig. 3*A*–*C*). Data obtained during the first 5 min of recording were best fit with the sum of 2 Gaussian functions with peak values of −29 ± 0.15 pA (81%) and −41 ± 1.3 pA (19%), which were indistinguishable from the peak values of −26 ± 0.15 pA (75%) and −38 ± 0.92 pA (25%) obtained in the last 5 min (i.e., 20–25 min) (Fig. 3*C*). These data are therefore consistent with the assertion that antimycin-A strengthens inhibitory synapses of granule cells by recruiting α6-containing GABARs.

Like all loop diuretics, furosemide acts on the anion/cation transporters, such as NKCC2 (Haas and Forbush, 1998) and KCC2 (Payne, 1997), but may have other pharmacological targets. Therefore, an immediate concern was that our observations may reflect furosemide's action on more than just α6-containing GABARs. We ruled out an effect on anion/cation transporters because transmembrane anion/cation gradients are constrained in the whole-cell recording configuration and because block usually occurs at concentrations greater than that used in the present study (Misgeld et al., 1986). To exclude the possibility of other targets, and provide additional evidence for the recruitment of α6-containing GABARs, we performed two separate experiments. First, we tested whether furosemide would exert a greater pharmacological block of mIPSCs after granule cells were treated with antimycin-A because mROS would be expected to recruit more α6-containing receptors into the synapse (Fig. 4). Second, we reasoned that furosemide would have a greater pharmacological block on mIPSCs of granule cells lacking the δ-subunit (Fig. 5) because mice lacking this subunit have been noted to have an upregulated expression of α6-containing GABARs (Tretter et al., 2001).

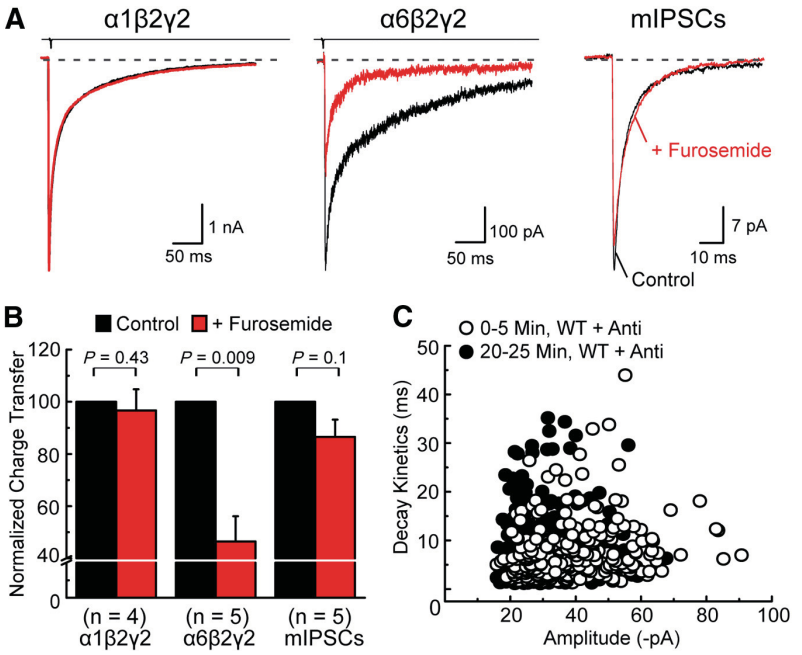

Figure 2. Furosemide block distinguishes between α1- and α6-containing $GABA_A$ receptors. ***A***, Overlay of typical membrane currents elicited by short 1 ms applications of 10 mM GABA on recombinant α1β2γ2 (left, patch #141219p8; n = 4) and α6β2γ2 (middle, patch #141219p3; n = 5) or averaged mIPSC from a granule cell (right, cell #140605000; n = 5) before (black line) and after (red line) bath application of 100 μM furosemide. ***B***, Bar graph comparing the degree of furosemide block on charge transfer between recombinant and native GABARs. Data are mean ± SEM, with paired Student's t tests and Bonferroni correction. ***C***, Plot comparing mIPSC amplitude versus decay kinetics observed in the first 5 min (0–5 min, open circles) and last 5 min (20–25 min, filled circles) of recording in antimycin-A (2 μM).

Furosemide block of α6-containing GABARs is more pronounced after antimycin-A treatment

Experiments comparing furosemide block of mIPSCs in control and antimycin-A-treated granule cells are summarized in Figure 4. In all cases, furosemide induced a significant reduction of the baseline membrane noise (compare Fig. 4*A*, top and bottom) consistent with antagonism of extrasynaptic α6- (and δ-) containing receptors. This effect represents a >50% reduction in baseline current for control (Pre-Furosemide, 14.36 ± 1.9 pA; Post-Furosemide, 6.93 ± 0.66 pA; p = 0.017; paired Student's t test; n = 5) and antimycin-A (53% reduction, Pre-Furosemide, 13.39 ± 0.94 pA; Post-Furosemide, 6.30 ± 0.54 pA; p = 0.0074; paired Student's t test; n = 5) conditions. In control granule cells, furosemide had a modest effect on mIPSC amplitude and almost no effect on mIPSC frequency (Fig. 4*A*,*B* left, *D*). In contrast, furosemide had a significant effect on mIPSC amplitude and frequency after antimycin-A treatment (Fig. 4*A*,*B* right, *C*,*D*). mIPSC amplitude was reduced by ~40% with 100 μM furosemide (p = 0.0007; paired Student's t test), representing an almost twofold greater block than control conditions (Fig. 4*B* right, *D*). Most strikingly, the increase in mIPSC frequency induced by antimycin-A was completely abolished following bath application of 100 μM furosemide (Fig. 4*C*,*D*). mIPSC frequency at 20–25 min was 1.43 ± 0.15 Hz compared with 0.87 ± 0.074 Hz at 40–45 min when block by furosemide had reached equilib-

Table 1. Kinetics of $\alpha1\beta2\gamma2$ and $\alpha6\beta2\gamma2$ $GABA_A$ receptors (1 ms pulse, 10 mM GABA)

	Components	t1 (mean ± SEM)	% A1	t2 (mean ± SEM)	% A2	t3 (mean ± SEM)	% A3	*n*
$\alpha1\beta2\gamma2$								
Control	3	2.7 ± 0.2	29	21.2 ± 2.4	39	130.1 ± 11.9	32	4
+100 μM furosemide	3	2.0 ± 0.2	31	19.8 ± 3.1	37	150.8 ± 19.5	32	4
$\alpha6\beta2\gamma2$								
Control	3	3.5 ± 0.4	16	23.1 ± 4.0	41	196.0 ± 5.1	43	5
+100 μM furosemide	3	6.4 ± 1.5	36	27.0 ± 3.7	48	337.9 ± 50.8	16	5

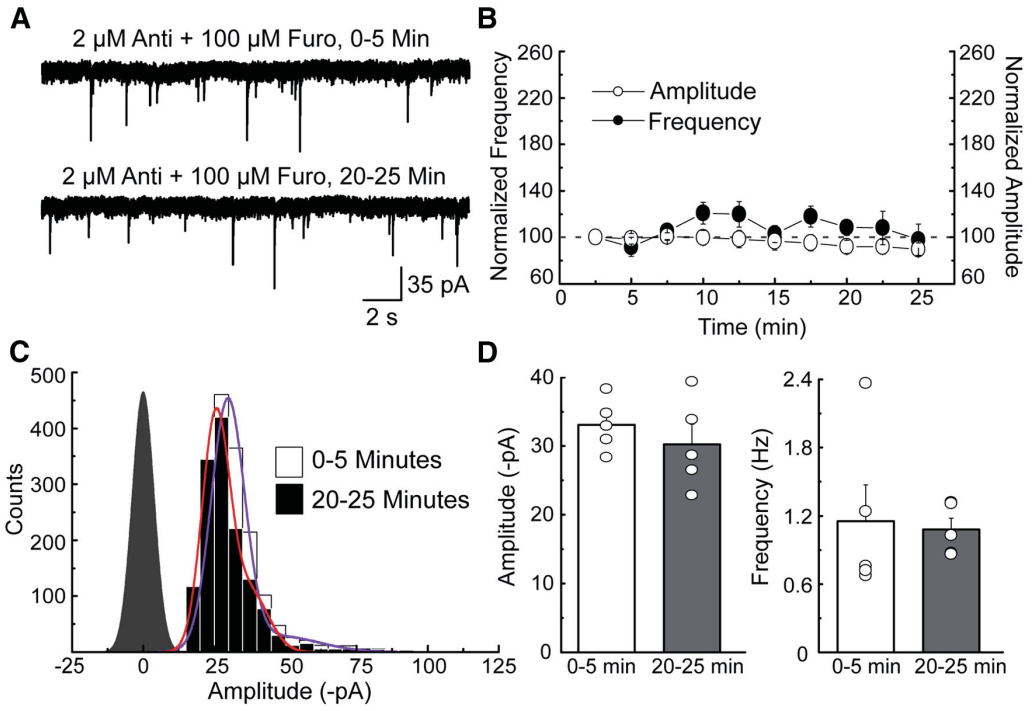

Figure 3. Pharmacological block of $\alpha6$-containing $GABA_A$ receptors prevents synaptic strengthening by mROS. ***A***, mIPSCs from two time points (cell #140329013) from the same cell during bath application of furosemide (100 μM) and internal perfusion with antimycin-A (2 μM). ***B***, Plot summarizing the effect of antimycin-A on event frequency (filled circle) and amplitude (open circle) ($n = 5$). ***C***, Amplitude histograms of data from the same cells at two time points fit with the sum of 2 Gaussian functions (purple represents 0–5 min; red represents 20–25 min). ***D***, Bar graphs comparing the effect of furosemide on mIPSC amplitude (left) and frequency (right) during internal patch perfusion with antimycin-A. In all cases, data are mean ± SEM.

rium (Fig. 4*C*,*D*). Indeed, mIPSC frequency was statistically indistinguishable ($p = 0.46$; paired Student's *t* test, $n = 6$) between measurements at the beginning (i.e., 0–5 min, 0.96 ± 0.091 Hz) and end (i.e., 40–45 min, 0.87 ± 0.074 Hz) of the experiment (Fig. 4*C*,*D*). These data support the assertion that strengthening of granule cell GABAergic synapses by mROS is due to the recruitment of $\alpha6$-containing GABARs. As discussed below, we further tested the involvement of $\alpha6$-containing GABARs by studying the effect of antimycin-A on granule cells that lack the δ-subunit.

Antimycin-A fails to strengthen GABAergic synapses of granule cells from δ-KO mice

Previous studies have shown that the overall surface expression of the $\alpha6$-subunit is unchanged in granule cells from δ-KO mice but that there is an increased surface expression of the $\gamma2$-subunit (Tretter et al., 2001), presumably because of a compensatory mechanism. Given this, we reasoned that granule cell inhibitory synapses would contain more $\alpha6/\gamma2$-containing GABARs, as proposed by others previously (Tretter et al., 2001). In keeping with this, we observed an increased basal frequency of mIPSCs by approximately twofold to threefold in δ-KO mice ($n = 5$) compared with wild-type (δ-KO: 1.69 ± 0.20 Hz; wild-type: 0.543 ± 0.087 Hz; $p = 0.0008$; unpaired Student's *t* test) consistent with an upregulation of inhibitory synaptic connections. More importantly, bath application of 100 μM furosemide elicited a much greater reduction in both mIPSC amplitude and frequency in granule cells from δ-KO than wild-type mice (Fig. 5). For instance, furosemide reduced mIPSC frequency in wild-type granule cells from 0.96 ± 0.22 Hz to 0.87 ± 0.18 Hz, which was much more modest than the effect in δ-KO mice where mIPSC frequency was reduced from 1.7 ± 0.2 Hz to 0.60 ± 0.19 Hz (Fig. 5*B*,*D*). Likewise, peak mIPSC amplitudes were reduced by ~20% in wild-type granule cells compared with a reduction of ~31% in granule cells lacking the δ-subunit (Fig. 5*B*–*D*). Together, these observations make two important conclusions regarding granule cells of δ-KO mice: (1) they exhibit a greater number of functional inhibitory synapses; and (2) inhibitory synapses contain a greater proportion of $\alpha6/\gamma2$-containing GABARs.

As a final test of the involvement of $\alpha6$-containing GABARs, we examined the effect of antimycin-A on granule cells of δ-KO mice (Fig. 5*E*). We reasoned that, because of the greater pro-

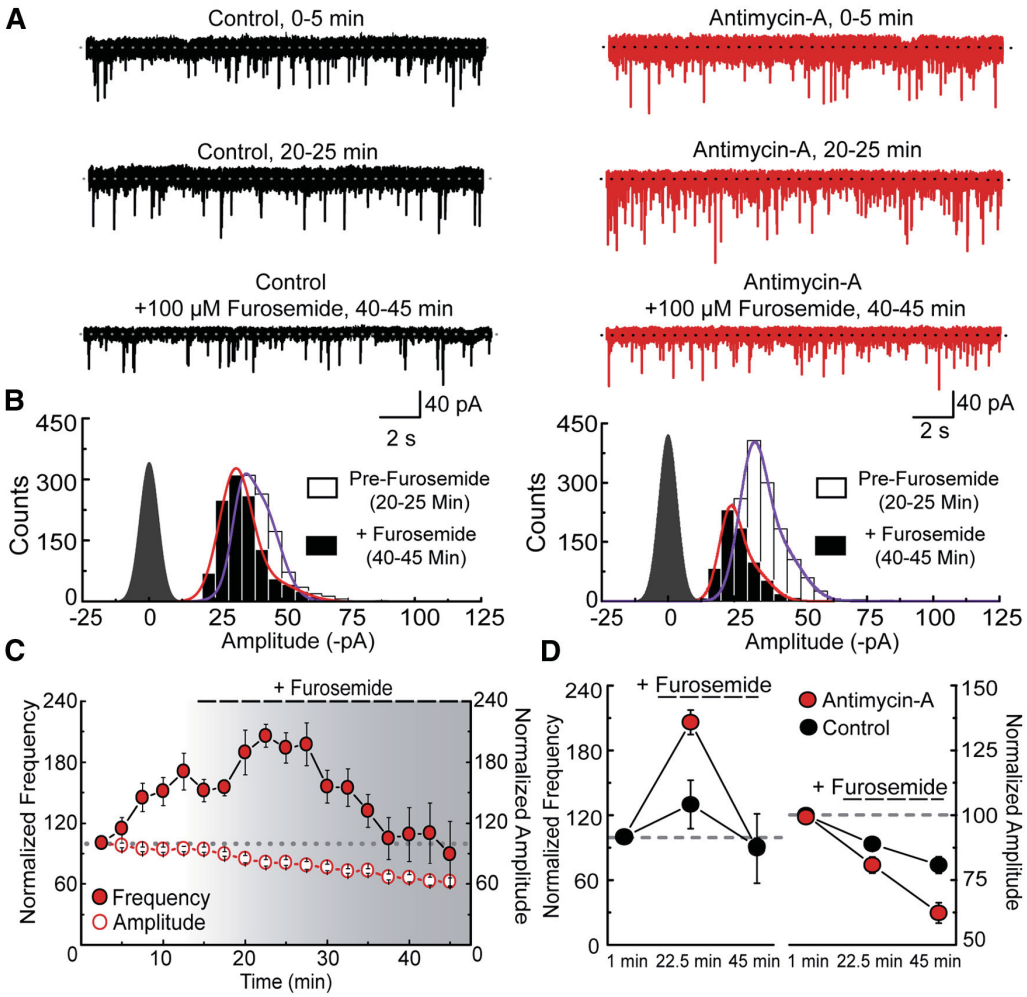

Figure 4. Synaptic strengthening induced by mROS is reversed by pharmacological block of α6-containing $GABA_A$ receptors. ***A***, Representative electrophysiological traces of a control (left, cell #140526000) and antimycin-A (2 μM, right, cell #140619000) treated granule cell at three separate time points. ***B***, Amplitude distributions of mIPSCs from two time points ($n = 5$ in each case). For clarity, only the summed Gaussian functions are shown (purple represents Pre-Furosemide; red represents + Furosemide). ***C***, Summary plot showing the time course of mIPSC frequency (red circle) and amplitude (open circle). Furosemide (100 μM) was added 15 min after the start of the experiment. Gray gradient represents the gradual equilibration of furosemide in the bath. ***D***, Summary plots of furosemide's effect on mIPSC frequency and amplitude. Data are mean ± SEM.

portion of α6/γ2-containing GABARs at these synapses, antimycin-A would have little or no effect on mIPSC frequency. That is, synapse strengthening by mROS via the recruitment of α6-containing GABARs would be limited because granule cell inhibitory synapses of δ-KO mice are already occupied by these receptors. In support of this, internal patch perfusion of antimycin-A exerted no effect on mIPSC frequency or peak amplitude (Fig. 5*E*). For example, mIPSC frequencies observed during the first (0–5 min) and last (20–25 min) 5 min were 1.1 ± 0.51 Hz and 1.32 ± 0.62 Hz, respectively ($p = 0.35$, paired Student's t test). Furthermore, the peaks of the fits of the antimycin-A treated δ-KO amplitude distribution (20–25 min: $Amplitude_1$, 37 pA; $Amplitude_2$, 48 pA) were very similar to that of the wild-type control (20–25 min: $Amplitude_1$: 39 pA; $Amplitude_2$: 55 pA). These data show that antimycin-A was ineffective in strengthening GABAergic synapses of δ-KO mice, in marked contrast to our observations on wild-type mice. We therefore conclude that strengthening of granule cell inhibitory synapses occurs by the recruitment of α6-containing GABARs.

Insulin elevates cytosolic ROS in granule cells of the mouse cerebellum

To determine whether a physiological signaling pathway strengthens GABAergic synapses in a similar manner, we examined the effect of the metabolic hormone, insulin. Prior work has established that insulin elevates cytosolic ROS (Mukherjee et al., 1978; May and de Haën, 1979; Zeng and Quon, 1996; Mahadev et al., 2001a, b; Goldstein et al., 2005) and, in separate experiments, insulin has been shown to strengthen GABAergic synapses (Wan et al., 1997; Vetiska et al., 2007). Given this, we reasoned that there may be a causal link between insulin's ability to elevate cytosolic ROS and its ability to strengthen inhibitory synapses.

To explore this, we first determined whether insulin can induce a change in the redox state of the cerebellum by loading granule cells with the fluorescent dye DCF and imaging for cytosolic ROS (Fig. 6; see Materials and Methods). Because DCF irreversibly reacts with cytosolic ROS, we anticipated that the fluorescent signal from individual cells would increase in a time-dependent manner, reflecting the constitutive turnover of their

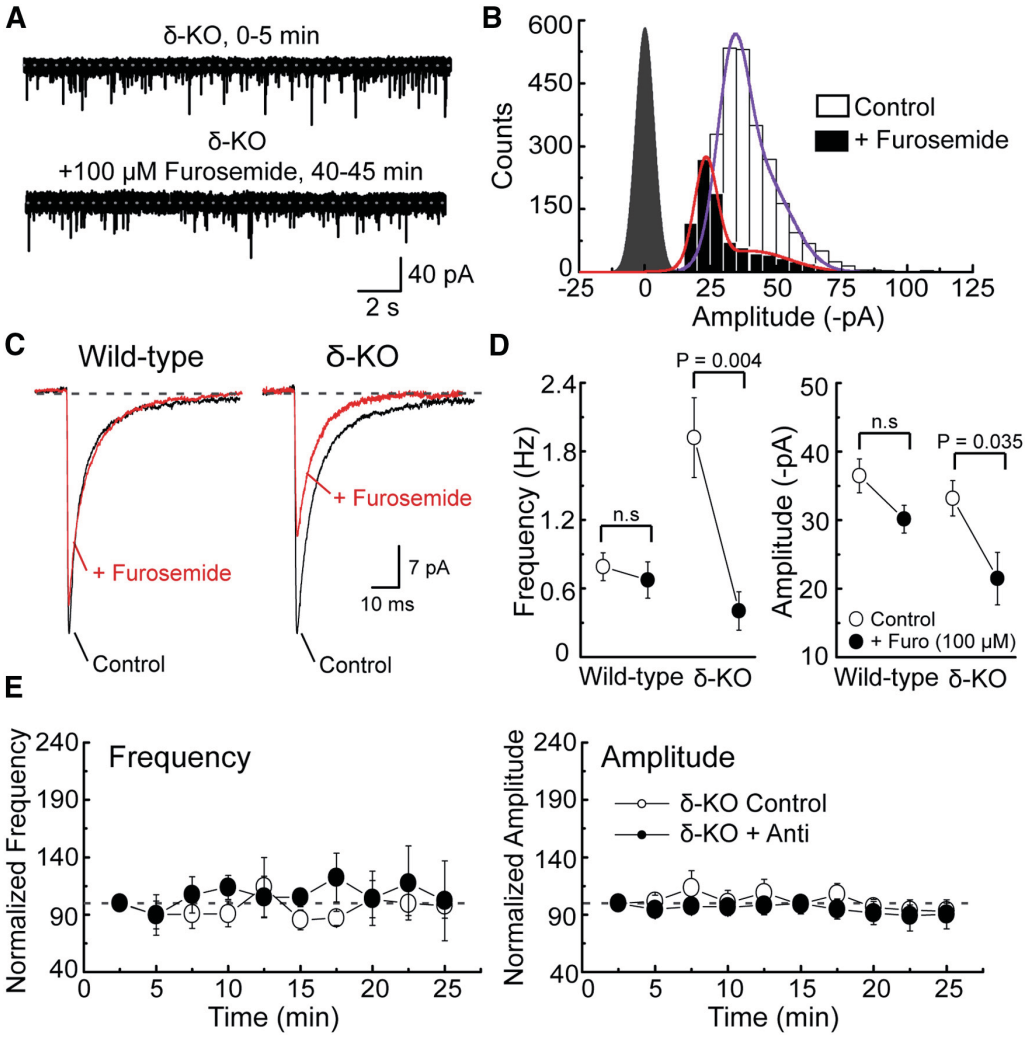

Figure 5. mROS fail to strengthen inhibitory synapses of δ-KO mice. ***A***, Representative recordings from a granule cell lacking the δ-subunit before (top) and after (bottom) applying furosemide (100 μM, cell #140621010) to the bath 15 min after the start of the experiment. ***B***, Amplitude distributions comparing mIPSCs at the two time points ($n = 5$). For clarity, summed Gaussian functions are shown (purple represents Control, 0–5 min; red represents + Furosemide, 40–45 min). ***C***, Averaged mIPSCs (from 15 random events) comparing the response profile of wild-type (cell #140605000) and δ-KO (cell #1406210010) cells before (black line) and after (red line) furosemide application. ***D***, Summary plot showing mIPSC frequency (left) and amplitude (right) before ("control," open circles, 0–5 min) and after ("+ furo," filled circle, 40–45 min) furosemide (100 μM) application. Statistical test is a paired Student's *t* test. n.s, Not significant. ***E***, Summary plots showing the time course of mIPSC frequency (left) and amplitude (right) of granule cells ($n = 5$) lacking the δ-subunit in the presence (filled circle) and absence (open circle) of antimycin-A (2 μM). Data are mean ± SEM.

metabolic and signaling state. In agreement with this, we observed a gradual increase in cytosolic ROS from cerebellar slices continuously perfused with aCSF over a 30–40 min time period (Fig. 6*B*). Interestingly, basal ROS levels were reduced significantly by pretreatment with the isoflavone, genistein (50 μM), which blocks a number of ubiquitous signaling pathways, including insulin's actions by inhibiting tyrosine kinase activity (Fig. 6*B*,*C*). At the start of the imaging experiments, the distribution of fluorescence intensity among granule cells bathed in aCSF was fit well with a single Gaussian function with a mean amplitude of 131 ± 2.7 a.u. (Fig. 6*C*, cyan bars), which was reduced significantly to 35 ± 3.5 a.u. by genistein (Fig. 6*C*, black bars; $p < 0.0001$, unpaired Student's *t* test). Despite this difference, the rate of change in fluorescence intensity was identical in both conditions over a typical 30–40 min imaging experiment (Fig. 6*B*) demonstrating that the constitutive production of cellular ROS was constant.

As expected, basal cytosolic ROS levels observed in granule cells before insulin application were comparable with measurements made in aCSF (Fig. 6*B*). Upon insulin (0.5 μM) application, however, we observed an almost immediate increase in cytosolic ROS generation (Fig. 6*A*,*B*) that reached statistical significance after 20 min ($p < 0.01$; two-way repeated-measures ANOVA with Holm-Sidak's multiple-comparison test). The distribution of DCF fluorescence intensity at the 24–30 min time point was fit well by the sum of two Gaussian functions with mean values of 191 ± 9.0 a.u. (55%) and 437 ± 202 a.u. (45%) (Fig. 6*D*). The emergence of a second peak, not observed in baseline recordings (Fig. 6*C*) or the control condition at 24–30 min (fit by a single Gaussian: 232 ± 5 a.u.), highlights the presence of

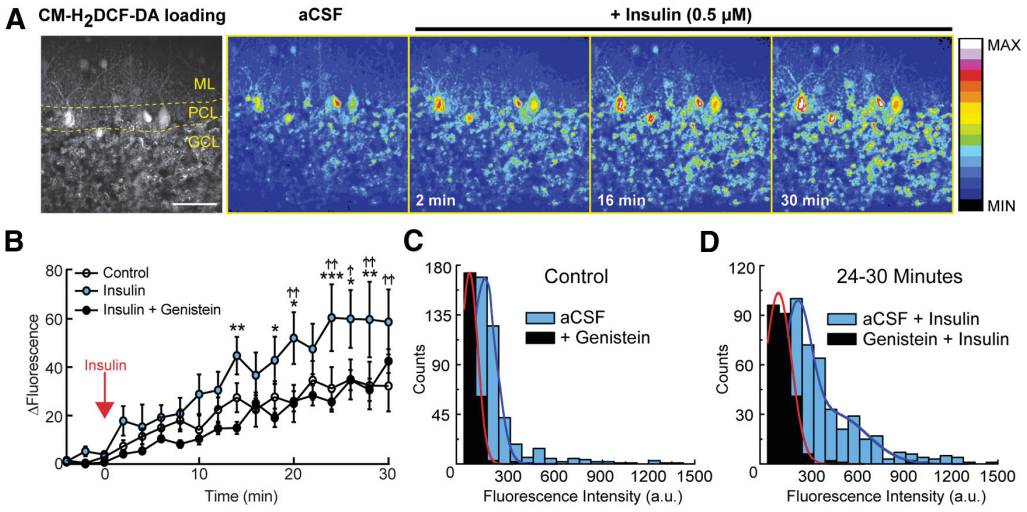

Figure 6. Insulin increases cytosolic ROS in cerebellar granule cells. ***A***, Example DCF images from a typical insulin-treated experiment showing elevations in cytosolic ROS. The images are displayed using a color-coded map of fluorescence intensity (16 colors) ranging from black (no fluorescence), to white (maximum signal for any pixel over the course of an individual experiment). A representative two-photon single focal plane image (far left) of a cerebellar parasagittal slice with the cellular layers denoted. Ml, Molecular layer; PCL, Purkinje cell layer; GCL, granule cell layer. Scale bar, 5 μm. Right, The 16 color version of this image. ***B***, Summary plot of the time course of fluorescence intensity changes in control (white circle), insulin (cyan circles), or insulin + genistein (black circles) treated conditions. Data are mean ± SEM. Two-way repeated-measures ANOVA with Holm-Sidak's multiple-comparison test: *Comparisons between "insulin" and "insulin + genistein." †Comparisons between "insulin" and "control." *$p < 0.05$. †$p < 0.05$. **$p < 0.01$. ††$p < 0.01$. ***$p < 0.001$. ***C***, Histograms comparing the level of fluorescence intensity obtained in the presence (black) or absence (cyan) of 50 μM genistein. Each histogram was fit with a single Gaussian function (red represents genistein; dark blue represents aCSF). ***D***, Histograms comparing the level of fluorescence intensity obtained after bath application of insulin (0.5 μM) in the presence (black) or absence (cyan) of 50 μM genistein at the end of a typical imaging recording. Each histogram was fit with either a single (red represents genistein + insulin) or the sum of two (dark blue represents aCSF + insulin), Gaussian functions.

a population of granule cells, which robustly respond to insulin. Importantly, genistein completely blocked the observed insulin-induced increase in cytosolic ROS generation (Fig. 6*B*,*D*), demonstrating that the action of insulin on cerebellar granule cells is due to an increase in tyrosine kinase activity. Together, these observations establish that cytosolic ROS levels in granule cells are regulated by the insulin receptor.

Elevating cytosolic ROS via the insulin receptor strengthens granule cell GABAergic synapses

To test for a causal relationship between ROS and strengthening of GABAergic synapses, we recorded mIPSCs from granule cells before and after bath application of insulin (0.5 μM; Fig. 7). Similar to antimycin-A (Fig. 1), insulin elicited a time-dependent increase in mIPSC frequency by almost twofold during a typical 20–25 min recording (Fig. 7*A–C*; $p = 0.0003$; paired two-tailed Student's *t* test, $n = 11$). Gaussian fits of the amplitude distributions before and after insulin treatment revealed that insulin primarily increased the occurrence of mIPSCs of small amplitude with little effect on larger events (Fig. 7*A*,*B*). Fits of the smallest events were 19% of all events within 0–5 min (Fig. 7*A*, bottom), which increased 2.2-fold, to 42%, after 20–25 min (Fig. 7*B*, bottom), resulting in the small, time-dependent reduction in the averaged mIPSC amplitude (e.g., 0–5 min: −47.9 ± 2.6 pA; 20–25 min: −42 ± 2.3 pA; 12% reduction; Fig. 7*C*,*D*). Furthermore, insulin's effect on mIPSCs was almost completely abolished by including the antioxidant, NAC (1 mM, $n = 4$), in the patch electrode solution ($p < 0.01$, one-way ANOVA; Fig. 7*D*) to diminish ROS levels. In view of this, our data establish a causal link between insulin's ability to elevate cytosolic ROS and strengthen GABAergic synapses of cerebellar granule cells.

Insulin recruits α6-containing receptors to GABAergic synapses via a wortmannin-sensitive pathway

To test whether insulin strengthens GABAergic synapses by recruiting α6-containing receptors, we examined the ability of furosemide to reduce inhibitory transmission during insulin treatment (Fig. 8). To do this, baseline mIPSC frequency was first augmented by bath application of insulin over the first 20–25 min of the recording (Fig. 8*A*,*B*). In control conditions, mIPSC frequency was 0.99 ± 0.3 Hz (0–5 min; Fig. 8*A*), increasing to 1.6 ± 0.4 Hz (20–25 min; Fig. 8*A*) following bath application of insulin (Fig. 8*A*,*B*; $p = 0.01$; paired Student's *t* test; $n = 6$). Having established an increase in mIPSC frequency with insulin, we tested for the recruitment of α6-containing GABARs by perfusion of the α6-GABAR antagonist, furosemide (Fig. 8*B*). As anticipated, bath application of 100 μM furosemide significantly reduced mIPSC frequency from 1.6 ± 0.4 Hz (20–25 min; Fig. 8*B*) in a time-dependent manner to levels observed at the beginning of the experiment (i.e., 0.73 ± 0.2 Hz, 40–45 min, $p = 0.03$; paired Student's *t* test; $n = 6$) (Fig. 8*B*). Indeed, mIPSC frequency was statistically indistinguishable ($p = 0.42$; paired Student's *t* test, $n = 6$) between measurements observed at the beginning (i.e., 0–5 min) and end (i.e., 40–45 min) of the experiment. As expected, furosemide also had a significant effect on mIPSC amplitudes (Fig. 8*B*,*C*), which were reduced by ~28% ($p = 0.02$; paired Student's *t* test), resulting in a leftward shift in the amplitude histogram. It is noteworthy to mention that furosemide reduced the baseline membrane noise (Fig. 8*A*) by ~40%, in a manner similar to that observed following antimycin-A treatment (Fig. 4), from 11.9 ± 0.7 pA (Pre-Furosemide) to 7.5 ± 0.3 pA (Post-Furosemide) ($p = 0.003$; paired Student's *t* test, $n = 6$) that was maintained throughout the recording (Fig. 8*A*, middle

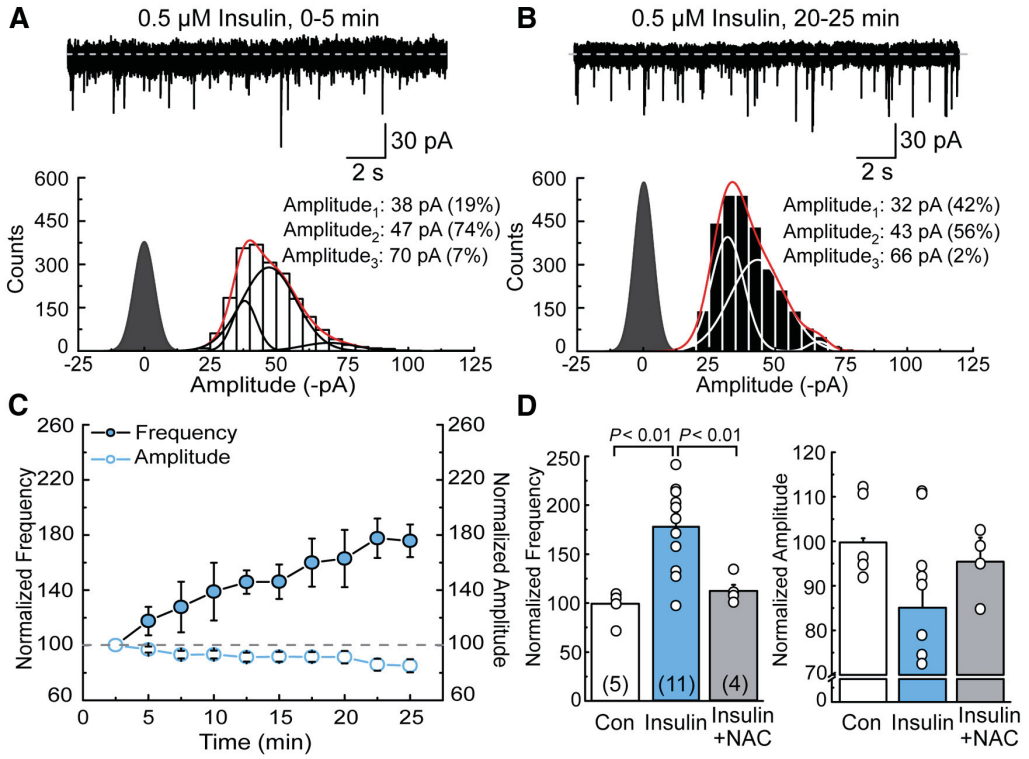

Figure 7. Insulin selectively increases the occurrence of inhibitory events of small amplitude. ***A***, ***B***, Top, mIPSCs from the same granule cell (cell #1503150007) at the beginning (0–5 min) and during (20–25 min) bath application with insulin (0.5 μM). Bottom, Amplitude histograms comparing the data obtained at two time periods (i.e., 0–5 min, left; 20–25 min, right; $n = 11$). Each was fit with the sum of three Gaussian functions (red line) with individual functions shown in either black (left) or white (right). ***C***, Summary plot of the time course of mIPSC frequency (filled circle) and amplitude (open circle) during constant bath application with insulin. Data are mean ± SEM. ***D***, Bar graphs of maximal normalized frequency (left) and amplitude (right) obtained in the different recording conditions. Control, Con ($n = 5$); *N*-acetylcysteine (1 mM), NAC ($n = 4$). Statistical test was a one-way ANOVA with Tukey's *post hoc* test. The frequency comparison of "Con" versus "Insulin + NAC" (***D***; left) was not significant and, for clarity, was not indicated in the figure. Amplitude comparisons were not significant ($p = 0.26$; one-way ANOVA).

and bottom). Together, these data establish that insulin strengthens GABAergic synapses by recruiting α6-containing receptors.

Insulin has been shown to strengthen GABAergic synapses via a PI3-kinase pathway (Vetiska et al., 2007). To establish whether a similar pathway accounts for our observations, we examined the effect of the PI3-kinase inhibitor, wortmannin, on the ability of insulin to strengthen GABAergic synapses (Fig. 8*D*). As anticipated, internal patch perfusion of 1 μM wortmannin completely blocked any change in mIPSC frequency and/or amplitude (Fig. 8*D*). mIPSC frequencies observed during the first (0–5 min) and last (20–25 min) 5 min were 0.58 ± 0.2 Hz and 0.60 ± 0.2 Hz, respectively ($p = 0.53$, paired Student's *t* test; $n = 6$). Additionally, the mIPSC amplitudes observed during the first (0–5 min) and last (20–25 min) 5 min were −46.6 ± 1.9 pA and −42.3 ± 2.1 pA, respectively ($p = 0.07$, paired Student's *t* test; $n = 6$). Together, these data show that wortmannin was effective in preventing the strengthening of GABAergic synapses by insulin. We therefore conclude that α6-selective strengthening of granule cell inhibitory synapses by insulin and ROS is mediated by activation of a wortmannin-sensitive, PI3-kinase pathway.

Discussion

We report three key findings that have important ramifications for our understanding of inhibitory synapse strengthening. First, ROS strengthen cerebellar granule cell GABAergic synapses by recruiting GABARs of a different composition, in this case, α6-containing GABARs, rather than accumulating more of the resident, α1-containing receptors. Second, α6-receptors are recruited to postsynaptic sites distinct from α1-receptors, implying that ROS strengthen only a subset of all possible inhibitory synapses. Third and finally, we reveal that insulin strengthens inhibitory GABAergic synapses of granule cells through this mechanism. Given the similarity to our recent findings on stellate cells, we propose that ROS uncover a novel mechanism by which inhibitory synapses are strengthened. In this case, GABARs that normally reside at inhibitory synapses, such as α1-receptors, form the hardwiring of neuronal circuits with receptors of a different subunit composition, α3-receptors in stellate cells or α6-receptors in granule cells, fulfilling a more prominent and unappreciated role in synapse strengthening. Because this mechanism is distinct from the predominant view of how inhibitory synapses are strengthened, our data suggest that more than one type of mechanism is responsible for strengthening inhibitory synapses in the adult CNS.

$GABA_A$ receptor synapses are strengthened by more than one mechanism

Numerous studies have described inhibitory synapse strengthening in different CNS regions underpinning its importance as a pervasive regulator of neuronal circuits (Kittler and Moss, 2003; Luscher et al., 2011). Strengthening is thought to occur by the lateral diffusion of extrasynaptic GABARs (Thomas et al., 2005; Bogdanov et al., 2006), although it may also occur by direct insertion of receptors (Luscher et al., 2011). It is generally thought

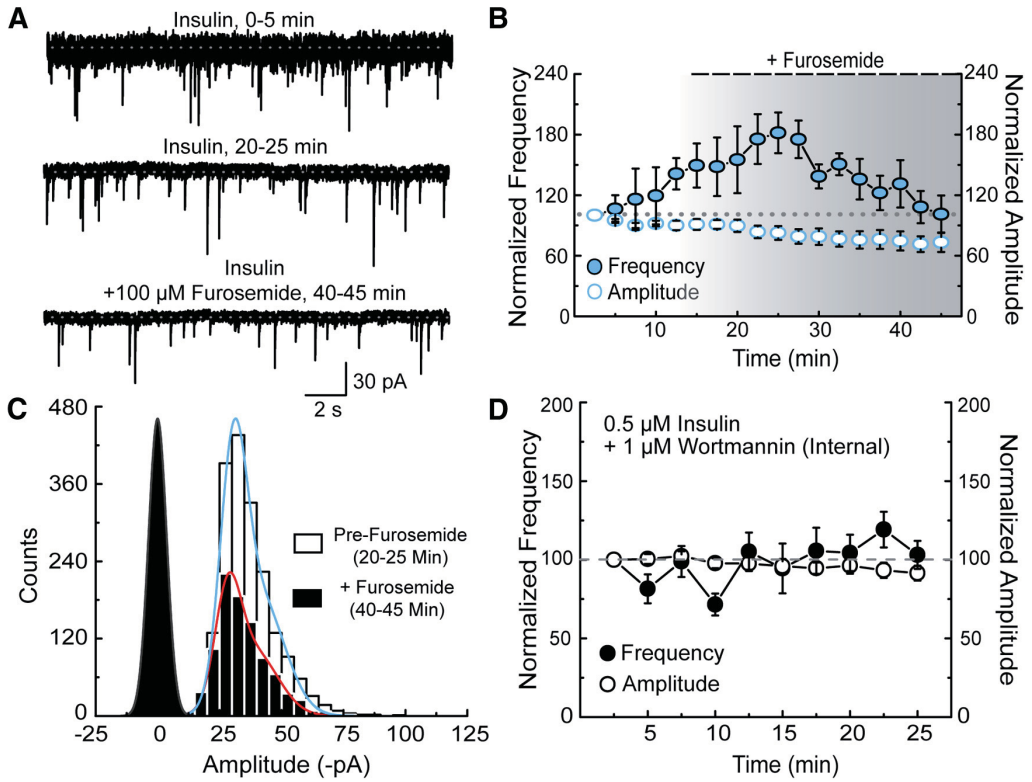

Figure 8. Synaptic strengthening induced by insulin is attenuated by pharmacological block of α6-containing $GABA_A$ receptors. ***A***, Representative electrophysiological traces of a cerebellar granule cell in the presence of insulin (0.5 μM, cell #150319000) at three separate time points. ***B***, Summary plot showing the time course of mIPSC frequency (filled cyan circle) and amplitude (open circle). Furosemide (100 μM) was added 15 min after the start of the experiment. Insulin was present within the bath throughout the duration of the experiment. Gray gradient represents the gradual equilibration of furosemide in the bath. ***C***, Amplitude distributions of mIPSCs from two time points ($n = 6$). For clarity, only the summed Gaussian functions are shown (cyan represents Pre-Furosemide: red represents + Furosemide). ***D***, Summary plot showing the time course of mIPSC frequency (filled circle) and amplitude (open circle) during internal perfusion of wortmannin (1 μM) during continuous bath application of insulin ($n = 6$). Data are mean ± SEM.

that inhibitory synapse strengthening is due to an effect on pre-existing synapses rather than the recruitment of receptors to a subset of postsynaptic sites, as described here for α6-receptors (see also Accardi et al., 2014), or even to silent synapses (Inoue et al., 2013). The most compelling evidence favoring the idea that synapse strengthening is due to an accumulation of more receptors per synapse comes from electrophysiological measurements of inhibitory synaptic events (e.g., Otis et al., 1994; Wan et al., 1997; Nusser et al., 1998b; Thomas et al., 2005; Houston et al., 2008; Rannals and Kapur, 2011). In these examples, spontaneous and/or mini-events increased in amplitude, in marked contrast to our observations. Whether synapse strengthening also involves more than one type of α-containing GABAR in these studies was not considered. Consequently, our observations described here on granule cells and elsewhere on stellate cells (Accardi et al., 2014) introduces an added complication for future studies to examine more closely. Whether α3- or α6-receptors of stellate or granule cells, respectively, are recruited into inhibitory synapses by lateral diffusion or by direct insertion also awaits future study. Together, however, the most parsimonious explanation of our data is that mROS uncover a novel mechanism by which inhibitory transmission can be strengthened. Moreover, given the emerging view that mROS lie at the center of many diverse biochemical pathways (Sena and Chandel, 2012), it is quite likely that strengthening of inhibitory synapses may be triggered by a myriad of signaling molecules that converge on this pathway.

Insulin strengthens inhibitory GABAergic synapses in a subunit-dependent manner

Our data identify an unexpected causal relationship between insulin signaling, cytosolic ROS, and the level of GABAergic inhibition. Most strikingly, insulin receptor activation promotes an increase in GABAergic transmission by selectively recruiting α6-containing GABARs and having little or no effect on resident α1-receptors. Exactly how insulin and ROS achieve this remains to be studied in greater detail. Prior work on nonexcitable tissue, however, has shown that activation of the insulin receptor elevates cytosolic ROS by coupling to the plasma membrane-bound NADPH oxidase system (Goldstein et al., 2005). These events then play a key role in modifying the activity of a plethora of thiol-dependent regulatory proteins (Papaconstantinou, 2009). Interestingly, the inhibitory synapse scaffolding protein, gephyrin, is modified by changes in the ROS signaling molecule, nitric oxide, causing the S-nitrosylation of gephyrin to regulate GABAR synapse clustering (Dejanovic and Schwarz, 2014). However, because post-translational modification of gephyrin reduces the size of putative inhibitory synapses, and presumably weakens synapse strength (Dejanovic and Schwarz, 2014), these findings seem inconsistent with our observations showing that ROS strengthen GABAergic synapses. Clearly, more work is required to elucidate the biochemical events linking elevations

in cytosolic ROS to changes in efficacy of inhibitory synapses of granule cells.

Our imaging data also reveal the constitutive presence of a basal cytosolic ROS background in naive slices due to appreciable constitutive, genistein-sensitive tyrosine kinase activity (Fig. 6). It is still not clear whether this observation is due to elevated levels of circulating insulin, which can be 10–100 times higher in the CNS compared with plasma levels (Havrankova et al., 1978), or the action of other tyrosine kinase receptors. Assuming insulin is implicated, it would suggest that its local production in acutely isolated cerebellar slices is substantial, similar to recent findings in the cerebral cortex where GABAergic neurogliaform cells have been shown to be a major source of insulin (Molnár et al., 2014). Our data also reveal that a substantial population of granule cells respond to insulin through either changes in ROS (Fig. 6) or the recruitment of α6-containing GABARs (Fig. 8). Exactly how insulin signaling impacts granule cells and the cerebellar circuit is still unclear, although it may act, as with cortical neurogliaform cells (Molnár et al., 2014), to locally regulate neurotransmission and firing rates in response to fluctuations in circulating glucose. Given that local blood flow and glucose levels are tightly regulated by neurons and glial cells in close proximity (Attwell et al., 2010), it is tempting to speculate that the release and action of insulin are part of an overall homeostatic mechanism that ensures the efficient coupling of cellular metabolism to neuronal signaling in the cerebellum.

$GABA_A$ receptor heterogeneity and its role in synapse strengthening

Since the cloning studies in the 1990s, it has been well established that different brain regions, and even individual neurons, can express multiple GABAR isoforms, raising the question of the significance of this receptor heterogeneity. In the context of the present study, the role of several granule cell GABAR subtypes has been identified and is linked to constraining granule cell excitability and output to other cerebellar regions. Inhibitory transmission onto granule cells occurs via two distinct mechanisms (i.e., phasic and tonic inhibition), which represents signaling by synaptic and extrasynaptic receptors, respectively (Semyanov et al., 2004). Phasic inhibition is largely mediated by α1-containing GABARs (Nusser et al., 1998a), whereas tonic inhibition occurs by activation of δ-containing GABARs (Nusser et al., 1996; Tia et al., 1996), which preferentially coassemble with α6-subunits (Nusser et al., 1996). Despite their presence at granule cell synapses (Nusser et al., 1996; Tia et al., 1996), the role fulfilled by α6/γ2 GABARs has been ill defined (Nusser et al., 1998a). Our study identifies an unexpected role for α6/γ2 GABARs that can enter inhibitory synapses under two conditions. First, in wild-type mice, elevations in ROS bring about a recruitment of α6/γ2 GABARs into postsynaptic sites. Second, in δ-KO mice, our data suggest that α6/γ2 GABARs overpopulate postsynaptic sites and thus compete with the functional role usually assigned to α1-receptors. Morphological evidence supporting this prominent role of α6/γ2 GABARs in wild-type mice is lacking (Nusser et al., 1996, 1998a), presumably because normal tissue fixations techniques do not initiate the events that would permit their recruitment. In keeping with this, there is a similar lack of morphological evidence supporting a prominent role of α3-containing GABARs at stellate cell inhibitory synapses (Nusser et al., 1997). However, functional data have shown that α3-containing GABARs become the dominant synaptic receptor in stellate cells of α1-KO mice (Vicini et al., 2001; Accardi et al., 2014) and are the primary mediator of strengthening of wild-type stellate cell synapses (Accardi et al., 2014), analogous to our observations on α6-receptors in granule cells. Whether our observations point to a more general role of other α-containing GABARs elsewhere in the CNS remains to be established. However, given the value of targeting GABARs to treat many types of CNS disorders (Rudolph and Knoflach, 2011; Rudolph and Möhler, 2014), the occurrence of receptor heterogeneity in individual neurons may be exploited to develop subunit-specific compounds that are clinically relevant.

References

Accardi MV, Daniels BA, Brown PM, Fritschy JM, Tyagarajan SK, Bowie D (2014) Mitochondrial reactive oxygen species regulate the strength of inhibitory GABA-mediated synaptic transmission. Nat Commun 5:3168. CrossRef Medline

Attwell D, Buchan AM, Charpak S, Lauritzen M, Macvicar BA, Newman EA (2010) Glial and neuronal control of brain blood flow. Nature 468:232–243. CrossRef Medline

Barnard EA, Skolnick P, Olsen RW, Möhler H, Sieghart W, Biggio G, Braestrup C, Bateson AN, Langer SZ (1998) International Union of Pharmacology: XV. Subtypes of gamma-aminobutyric acid A receptors: classification on the basis of subunit structure and receptor function. Pharmacol Rev 50:291–313. Medline

Belelli D, Harrison NL, Maguire J, Macdonald RL, Walker MC, Cope DW (2009) Extrasynaptic GABAA receptors: form, pharmacology, and function. J Neurosci 29:12757–12763. CrossRef Medline

Bogdanov Y, Michels G, Armstrong-Gold C, Haydon PG, Lindstrom J, Pangalos M, Moss SJ (2006) Synaptic GABAA receptors are directly recruited from their extrasynaptic counterparts. EMBO J 25:4381–4389. CrossRef Medline

Dejanovic B, Schwarz G (2014) Neuronal nitric oxide synthase-dependent S-nitrosylation of gephyrin regulates gephyrin clustering at GABAergic synapses. J Neurosci 34:7763–7768. CrossRef Medline

Draguhn A, Verdorn TA, Ewert M, Seeburg PH, Sakmann B (1990) Functional and molecular distinction between recombinant rat GABAA receptor subtypes by Zn^{2+}. Neuron 5:781–788. CrossRef Medline

Fritschy JM, Panzanelli P (2006) Molecular and synaptic organization of GABAA receptors in the cerebellum: effects of targeted subunit gene deletions. Cerebellum 5:275–285. CrossRef Medline

Goldstein BJ, Mahadev K, Wu X, Zhu L, Motoshima H (2005) Role of insulin-induced reactive oxygen species in the insulin signaling pathway. Antioxid Redox Signal 7:1021–1031. CrossRef Medline

Haas M, Forbush B 3rd (1998) The Na-K-Cl cotransporters. J Bioenerg Biomembr 30:161–172. CrossRef Medline

Havrankova J, Schmechel D, Roth J, Brownstein M (1978) Identification of insulin in rat brain. Proc Natl Acad Sci U S A 75:5737–5741. CrossRef Medline

Houston CM, Hosie AM, Smart TG (2008) Distinct regulation of beta2 and beta3 subunit-containing cerebellar synaptic GABAA receptors by calcium/calmodulin-dependent protein kinase II. J Neurosci 28:7574–7584. CrossRef Medline

Inoue W, Baimoukhametova DV, Füzesi T, Wamsteeker Cusulin JI, Koblinger K, Whelan PJ, Pittman QJ, Bains JS (2013) Noradrenaline is a stress-associated metaplastic signal at GABA synapses. Nat Neurosci 16:605–612. CrossRef Medline

Kittler JT, Moss SJ (2003) Modulation of GABAA receptor activity by phosphorylation and receptor trafficking: implications for the efficacy of synaptic inhibition. Curr Opin Neurobiol 13:341–347. CrossRef Medline

Korpi ER, Kuner T, Seeburg PH, Lüddens H (1995) Selective antagonist for the cerebellar granule cell-specific gamma-aminobutyric acid type A receptor. Mol Pharmacol 47:283–289. Medline

Laurie DJ, Seeburg PH, Wisden W (1992a) The distribution of 13 GABAA receptor subunit mRNAs in the rat brain: II. Olfactory bulb and cerebellum. J Neurosci 12:1063–1076. Medline

Laurie DJ, Wisden W, Seeburg PH (1992b) The distribution of thirteen GABAA receptor subunit mRNAs in the rat brain: III. Embryonic and postnatal development. J Neurosci 12:4151–4172. Medline

Llinás RH (1969) Physiological and morphological organization of the cerebellar circuits in various vertebrates. In: Neurobiology of cerebellar evolution and development (Llinás R, ed), pp 43–73. Chicago: American Medical Association.

Luscher B, Fuchs T, Kilpatrick CL (2011) GABAA receptor trafficking-mediated plasticity of inhibitory synapses. Neuron 70:385–409. CrossRef Medline

Mahadev K, Zilbering A, Zhu L, Goldstein BJ (2001a) Insulin-stimulated hydrogen peroxide reversibly inhibits protein-tyrosine phosphatase 1b in vivo and enhances the early insulin action cascade. J Biol Chem 276: 21938–21942. CrossRef Medline

Mahadev K, Wu X, Zilbering A, Zhu L, Lawrence JT, Goldstein BJ (2001b) Hydrogen peroxide generated during cellular insulin stimulation is integral to activation of the distal insulin signaling cascade in 3T3–L1 adipocytes. J Biol Chem 276:48662–48669. CrossRef Medline

Mapelli L, Solinas S, D'Angelo E (2014) Integration and regulation of glomerular inhibition in the cerebellar granular layer circuit. Front Cell Neurosci 8:55. CrossRef Medline

May JM, de Haën C (1979) Insulin-stimulated intracellular hydrogen peroxide production in rat epididymal fat cells. J Biol Chem 254:2214–2220. Medline

Mihalek RM, Banerjee PK, Korpi ER, Quinlan JJ, Firestone LL, Mi ZP, Lagenaur C, Tretter V, Sieghart W, Anagnostaras SG, Sage JR, Fanselow MS, Guidotti A, Spigelman I, Li Z, DeLorey TM, Olsen RW, Homanics GE (1999) Attenuated sensitivity to neuroactive steroids in gamma-aminobutyrate type A receptor δ subunit knockout mice. Proc Natl Acad Sci U S A 96:12905–12910. CrossRef Medline

Miller PS, Smart TG (2010) Binding, activation and modulation of Cys-loop receptors. Trends Pharmacol Sci 31:161–174. CrossRef Medline

Minier F, Sigel E (2004) Positioning of the alpha-subunit isoforms confers a functional signature to gamma-aminobutyric acid type A receptors. Proc Natl Acad Sci U S A 101:7769–7774. CrossRef Medline

Misgeld U, Deisz RA, Dodt HU, Lux HD (1986) The role of chloride transport in postsynaptic inhibition of hippocampal neurons. Science 232: 1413–1415. CrossRef Medline

Molnár G, Faragó N, Kocsis ÁK, Rózsa M, Lovas S, Boldog E, Báldi R, Csajbók É, Gardi J, Puskás LG, Tamás G (2014) GABAergic neurogliaform cells represent local sources of insulin in the cerebral cortex. J Neurosci 34: 1133–1137. CrossRef Medline

Momiyama A, Takahashi T (1994) Calcium channels responsible for potassium-induced transmitter release at rat cerebellar synapses. J Physiol 476:197–202. CrossRef Medline

Moss SJ, Smart TG (2001) Constructing inhibitory synapses. Nat Rev Neurosci 2:240–250. CrossRef Medline

Mukherjee SP, Lane RH, Lynn WS (1978) Endogenous hydrogen peroxide and peroxidative metabolism in adipocytes in response to insulin and sulfhydryl reagents. Biochem Pharmacol 27:2589–2594. CrossRef Medline

Nakahiro M, Arakawa O, Narahashi T, Ukai S, Kato Y, Nishinuma K, Nishimura T (1992) Dimethyl sulfoxide (DMSO) blocks GABA-induced current in rat dorsal root ganglion neurons. Neurosci Lett 138: 5–8. CrossRef Medline

Nusser Z, Roberts JD, Baude A, Richards JG, Somogyi P (1995) Relative densities of synaptic and extrasynaptic GABAA receptors on cerebellar granule cells as determined by a quantitative immunogold method. J Neurosci 15:2948–2960. Medline

Nusser Z, Sieghart W, Stephenson FA, Somogyi P (1996) The alpha 6 subunit of the GABAA receptor is concentrated in both inhibitory and excitatory synapses on cerebellar granule cells. J Neurosci 16:103–114. Medline

Nusser Z, Cull-Candy S, Farrant M (1997) Differences in synaptic GABA(A) receptor number underlie variation in GABA mini amplitude. Neuron 19:697–709. CrossRef Medline

Nusser Z, Sieghart W, Somogyi P (1998a) Segregation of different GABAA receptors to synaptic and extrasynaptic membranes of cerebellar granule cells. J Neurosci 18:1693–1703. Medline

Nusser Z, Hájos N, Somogyi P, Mody I (1998b) Increased number of synaptic GABA(A) receptors underlies potentiation at hippocampal inhibitory synapses. Nature 395:172–177. CrossRef Medline

Otis TS, De Koninck Y, Mody I (1994) Lasting potentiation of inhibition is associated with an increased number of gamma-aminobutyric acid type A receptors activated during miniature inhibitory postsynaptic currents. Proc Natl Acad Sci U S A 91:7698–7702. CrossRef Medline

Papaconstantinou J (2009) Insulin/IGF-1 and ROS signaling pathway cross-talk in aging and longevity determination. Mol Cell Endocrinol 299:89–100. CrossRef Medline

Payne JA (1997) Functional characterization of the neuronal-specific K-Cl cotransporter: implications for [K+]o regulation. J Physiol 273:C1516–C1525. Medline

Persohn E, Malherbe P, Richards JG (1992) Comparative molecular neuroanatomy of cloned GABAA receptor subunits in the rat CNS. J Comp Neurol 326:193–216. CrossRef Medline

Rannals MD, Kapur J (2011) Homeostatic strengthening of inhibitory synapses is mediated by the accumulation of GABA(A) receptors. J Neurosci 31:17701–17712. CrossRef Medline

Rudolph U, Knoflach F (2011) Beyond classical benzodiazepines: novel therapeutic potential of GABAA receptor subtypes. Nat Rev Drug Discov 10:685–697. CrossRef Medline

Rudolph U, Möhler H (2014) GABAA receptor subtypes: therapeutic potential in Down syndrome, affective disorders, schizophrenia, and autism. Annu Rev Pharmacol Toxicol 54:483–507. CrossRef Medline

Rudolph U, Crestani F, Möhler H (2001) GABA(A) receptor subtypes: dissecting their pharmacological functions. Trends Pharmacol Sci 22:188–194. CrossRef Medline

Semyanov A, Walker MC, Kullmann DM, Silver RA (2004) Tonically active GABA A receptors: modulating gain and maintaining the tone. Trends Neurosci 27:262–269. CrossRef Medline

Sena LA, Chandel NS (2012) Physiological roles of mitochondrial reactive oxygen species. Mol Cell 48:158–167. CrossRef Medline

Somogyi P, Fritschy JM, Benke D, Roberts JD, Sieghart W (1996) The gamma 2 subunit of the GABAA receptor is concentrated in synaptic junctions containing the alpha 1 and beta 2/3 subunits in hippocampus, cerebellum and globus pallidus. Neuropharmacology 35:1425–1444. CrossRef Medline

Thomas P, Mortensen M, Hosie AM, Smart TG (2005) Dynamic mobility of functional GABAA receptors at inhibitory synapses. Nat Neurosci 8:889–897. CrossRef Medline

Tia S, Wang JF, Kotchabhakdi N, Vicini S (1996) Developmental changes of inhibitory synaptic currents in cerebellar granule neurons: role of GABA(A) receptor alpha 6 subunit. J Neurosci 16:3630–3640. Medline

Tretter V, Hauer B, Nusser Z, Mihalek RM, Höger H, Homanics GE, Somogyi P, Sieghart W (2001) Targeted disruption of the GABA(A) receptor δsubunit gene leads to an up-regulation of gamma 2 subunit-containing receptors in cerebellar granule cells. J Biol Chem 276:10532–10538. CrossRef Medline

Vetiska SM, Ahmadian G, Ju W, Liu L, Wymann MP, Wang YT (2007) GABAA receptor-associated phosphoinositide 3-kinase is required for insulin-induced recruitment of postsynaptic GABAA receptors. Neuropharmacology 52:146–155. CrossRef Medline

Vicini S, Ferguson C, Prybylowski K, Kralic J, Morrow AL, Homanics GE (2001) GABA(A) receptor alpha1 subunit deletion prevents developmental changes of inhibitory synaptic currents in cerebellar neurons. J Neurosci 21:3009–3016. Medline

Wall MJ, Usowicz MM (1997) Development of action potential-dependent and independent spontaneous GABAA receptor-mediated currents in granule cells of postnatal rat cerebellum. Eur J Neurosci 9:533–548. CrossRef Medline

Wan Q, Xiong ZG, Man HY, Ackerley CA, Braunton J, Lu WY, Becker LE, MacDonald JF, Wang YT (1997) Recruitment of functional GABA(A) receptors to postsynaptic domains by insulin. Nature 388:686–690. CrossRef Medline

Wozniak M, Rydzewski B, Baker SP, Raizada MK (1993) The cellular and physiological actions of insulin in the central nervous system. Neurochem Int 22:1–10. CrossRef Medline

Zeng G, Quon MJ (1996) Insulin-stimulated production of nitric oxide is inhibited by wortmannin: direct measurement in vascular endothelial cells. J Clin Invest 98:894–898. CrossRef Medline